Cumhuriyet University

Cumhuriyet

Science

Journal

Cumhuriyet Science Journal (CSJ)

Derginin Eski Adı: Cumhuriyet Üniversitesi Fen-Edebiyat Fakültesi Fen Bilimleri Dergisi

Eski ISSN: 1300-1949

Baş Editör / Editor-in-Chief:

Prof. Dr. İdris ZORLUTUNA

Yazı İşleri Müdürü/ Managing Editor:

Assoc. Prof. Dr. Adil ELİK

Editörler / Editors:

Prof. Dr. Baki KESKİN

Assoc. Prof. Dr. Adil ELİK

Assoc. Prof. Dr. Nilüfer TOPSAKAL

Assoc. Prof. Dr. Serkan AKKOYUN

Assoc. Prof. Dr. Hülya KURŞUN

Assoc. Prof. Dr. Birnur AKKAYA

Assoc. Prof. Dr. Halil İbrahim ULUSOY

Akademik Dizin / Abstracted/Indexed in

Ulakbim TR-Dizin

Akademik Dizin

Arastirmax Bilimsel Yayın İndeksi

Bielefeld Academic Search Engine (BASE)

Directory of Open Access Journals (DOAJ)

Directory of Research Journal Indexing (DRJI)

Google Scholar

Index Copernicus

Research Gate

Thomson Reuters Zoological

WorldCat

CUMHURİYET SCIENCE JOURNAL

CONTENTS

A Simple and Cheap Ultrasound-Assisted Microextraction Procedure For Extraction of Tartrazine in Soft Drinks and Foodstuff

Nail ALTUNAY[1] (iD)

[1]Sivas Cumhuriyet University, Yıldızeli Vocational School, Medical Services and Techniques Department, Sivas, Turkey

Abstract. In this study, a simple and cheap ultrasound-assisted ionic liquid-based floating organic droplets microextraction (UA-IL-FODME) has been proposed for spectrophotometric determination of synthetic food dye (tartrazine) in soft drinks and food samples. 1-Octyl-3-methylimidazolium tetrafluoroborate [C8MIM][BF4] and 1-octanol were used as the extraction solvent and dispersant solvent, respectively. The method is based on extracting the tarrazine to the ionic phase with the help of ultrasonic effect at pH 5.5. Some experimental variables (pH, ionic liquid amount, type and volume of dispersive solvent, and ultrasonic conditions) were studied and optimized in detail. In optimum conditions, some analytical parameters of the method were as follows. Operating range, limit of detection, preconcentration factor, recovery % and RSD % values were 10-700 µg L-1, 3.2 µg L-1, 75, 94.7-104.7% and 2.7%, respectively. Following comprehensive validation studies, the recommended method was successfully applied to the extravasation and determination of tartrazine in soft drinks and foodstuff.

Keywords: Floating organic droplets, Ionic liquid, Ultrasound, Tartrazine, Soft drinks, Foodstuff.

Alkolsüz İçecekler ve Gıda Ürünlerinde Tartrazinin Özütlenmesi için Basit ve Ucuz Ultrason Destekli Mikroekstraksiyon Prosedürü

Özet. Bu çalışmada, basit ve ucuz ultrason destekli iyonik sıvı bazlı yüzer organik damlacıklar mikroekstraksiyonu (UA-IL-FODME), sentetik yiyecek boyalarının (tartrazin), alkolsüz içeceklerde ve gıda ürünlerinde spektrofotometrik olarak belirlenmesi için önerilmiştir.1-Oktil-3-metilimidazolyum tetrafloroborat [C8MIM] [BF4] ve 1-oktanol sırasıyla ekstraksiyon çözücü ve dağıtıcı çözücü olarak kullanılmıştır. Yöntem, pH 5.5'te tarrazin 'in iyonik faza ultrasonik etki yardımıyla özütlenmesine dayanır. Bazı deneysel değişkenler (pH, iyonik sıvı miktarı, dispersiv çözücü çeşidi ve hacmi ve ultrasonik koşullar) çalışıldı ve ayrıntılı olarak optimize edildi. Optimum koşullarda, yöntemin bazı analitik parametreleri aşağıda özetlenmiştir. Çalışma aralığı, seçme sınırı, ön konsantrasyon faktörü, geri kazanma yüzdesi ve %BBS değerleri sırasıyla 10-700 µg L-1, 3.2 µg L-1, 75, % 94.7-104.7 ve % 2.7 idi. Kapsamlı validasyon çalışmalarının ardından, önerilen yöntem, alkolsüz içecekler ve gıda maddelerinde tartrazininekstraksiyonu ve tayinine başarıyla uygulanmıştır.

Anahtar Kelimeler: Yüzen organik damlacıklar, İyonik sıvı, Ultrason, Tartrazin, Alkolsüz içecekler, Gıda ürünleri.

1. INTRODUCTION

In the world, food production and consumption are increasing due to population growth. Food additives should be used to prevent food spoilage during transportation and storage. [1]. Food dyes are defined by the International Food Codex Commission as additives to regulate the color of the dish. [2]. Nowadays, for technological reasons, it is suggested that foods should be colored [3]. Synthetic colorants are substances which can be produced by chemical synthesis. Synthetic colorants provide superiority in terms of color strengths, color ranges, stability, ease of use and price compatibility according to natural colorants. [4]. Tartrazine is water soluble synthetic food dye and its code is E102. Food additives are widely used for different purposes, including preservation, coloring and taste. However, some food additives are prohibited due to their toxicity [5]. Among the five azo dyes, Amaranth, Allura Red, New Coccine and Tartrazine (initially 10 ppm) lead to dose-related DNA fragmentation in the colon [6]. Tartrazine can cause allergic and asthma problems in delicate people. The analytical control of these compounds is important for the food industry due to their toxicity and carcinogenicity [7]. Therefore, simple, inexpensive and fast analytical methods are needed to determine synthetic dyes in food. Analytical methods for the analysis of synthetic colorants in food and beverages have been reported in literature. These methods are based on the basis of the thin layer chromatography (TLC) [8], high performance liquid chromatography (HPLC) with diode array detection (DAD) and ion-trap time-of-flight mass spectrometry (IT-TOF/MS) [9], spectrophotometry [10], electrochemical sensor [11], high performance liquid chromatography (HPLC)–diode array detector (DAD)–electrospray mass spectrometry (ESI-MS) [12]. It is also necessary to minimize possible matrix effects when analyzing at low levels. Therefore, different extraction methods such as solid phase extraction (SPE) [13], liquid–liquid extraction (LLE) [14], cloud point extraction (CPE) [15], molecularly imprinted solid-phase extraction (MISPE) [16], ultrasound-assisted extraction (UAE) [17-19] and ionic liquid based liquid phase microextraction (IL-

LPME) [20-22] were applied before determination step. In addition to these extraction methods, in the recent years, extraction methods using ionic liquid (IL) have become popular. Some of ILs properties are low toxicity, high vapor pressure, biodegradable and high hydrophobicity.

The purpose of this study is to develop a simple and cheap analytical method for the determination and extraction of tartrazine in soft drinks and foodstuff. In this context, the ultrasonic-assisted ionic liquid-based floating organic droplets microextraction procedure (UA-IL-FODME) was developed and UV-VIS spectrophotometry was used in the determination step. Factors affecting the extraction of tartrazine were investigated in detail. The proposed method can be applied for determination of tartrazine in soft drinks and foodstuff. After routine applications, the results shown that the proposed method is suitable for the extraction and determination of tartrazine in different food samples.

2. MATERIALS AND METHODS

2.1. Apparatus

In the study, tartrazine content in selected samples was determined at 425 nm using Shimadzu brand UV–VIS spectrophotometry (UV-1800 PC model, Kyoto, Japan). Ultrapure water with resistivity of 18.2 MΩ cm was obtained by a Milli-Q water purification system (Millipore Corp., USA). Extraction of tartrazine from sample solution was achieved by a universal hettich brand centrifuge (Hettich, London, England). The pH of samples solution was adjusted using a digital pH meter (Sartorius Docu-model, North America). An ultrasonic bath (UCS-10 model, Seoul, Korea) was used for both sample preparation and the formation of microsphere of ionic liquid.

2.2. Chemical and Reagents

The reagents used were of analytical purity, and were purchased from Sigma (St. Louis, MO. USA) and Merck (Darmstadt, Germany). The stock solutions of tartrazine (Sigma) was prepared in water. Working standards were prepared by dilution of the stock solution. 1-Octyl-3-

methylimidazolium tetrafluoroborate ([C8MIM][BF4]) (Sigma) was used as extraction solvent. Acetone (Merck), 1-heptanol (Merck), 1-octanol (Merck), ethanol (Sigma), 2-propanol (Sigma), and methanol (Merck) were tested as dispersive solvents. pH 5.5 of acetate buffer solution (0.1 M) was prepared by mixing an appropriate amount of sodium acetate and acetic acid in water. Before the experiment, all materials were washed in dilute nitric acid, followed by rinsing three times with distilled water, respectively.

2.3. Sample collection and preparation

Soft drinks and foodstuff were collected randomly from the local markets in Sivas, Turkey. Ultrasonic-assisted sample preparation step was carried out as follows: First, 50 mL centrifuge tubes were taken, and then 2 g of foodstuff and 3 mL of soft drinks were added to the tubes. Final volume of tubes was diluted to 50 mL, were placed in ultrasonic bath, and then sonicated for 15 min at 30 °C. The resulting mixture was filtered through the membrane filter after centrifugation at 4000 rpm for 5 min. The same experimental steps were performed to the blank sample. The proposed method was applied to 1.0 mL of the prepared samples.

2.4. UA-IL-FODME procedure

The UA-IL-FODME procedure was performed in 15-mL centrifuge tubes. First, an aliquot of 1.0 mL sample solution containing 25 µg L−1 of tartrazine was added to the tubes. Then the pH of the sample solution was adjusted to pH 5.5 with acetate buffer. To ensure the extraction of tartrazine from the sample solution, 400 µL of [C8MIM][BF4] (extraction solvent) and 300 µL of 1-octanol (dispersive solvent) were added rapidly with a micro syringe into the sample solution. The tubes were sonicated for 5 min at 45 oC in the ultrasonic bath to form the microspheres of the [C8MIM][BF4].The tubes were centrifuged at 4000 rpm for 2 min, and then were stored in an ice bath to facilitate phase separation. At this stage, the dispersive solvent (1-octanol) was solidified within 2 min. After decantation, the remaining phase was

completed to 500 µL using ethanol. Finally, the amount of tartrazine was determined at 425 nm by UV–Vis spectrophotometry. A blank solution was also carried out using the same experimental steps without tartrazine.

3. RESULTS AND DISCUSSION

3.1. Selection of working wavelength

The most important step of the experimental studies using UV–Vis spectrophotometry is the selection of the measurement wavelength. Because all the experimental measurements were performed at the selected wavelength. If the correct wavelength is not selected, all experimental results are affected. Therefore, the following experimental steps were taken to determine the appropriate wavelength. First, only the tartrazine in the aqueous solution was obtained at the spectrum. Second, the spectrum of tartrazine in the presence of other chemicals was taken. The results were given in Figure 1. As the results show, the tartrazine spectrum gave a weak spectrum at 435 nm, while in the presence of IL a sharp spectrum was obtained at 425 nm. In addition, the absorbance of the obtained spectrum shows a linear increase with the concentration of tartrazine. These reasons were chosen as the appropriate wavelength of 425 nm for optimization and analysis.
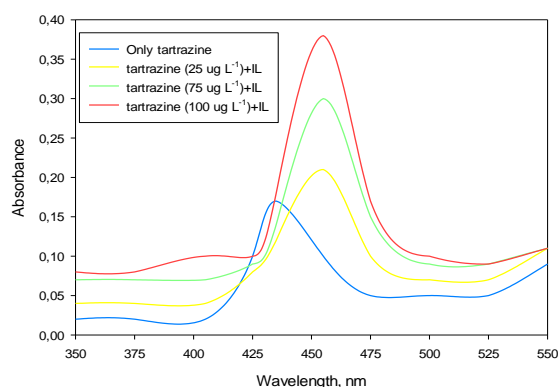
Figure 1. Absorbance spectra obtained in selected chemical conditions.

3.2. Effect of pH

Electrostatic interactions between chemical species vary depending on the pH of the aqueous solution. In the extraction experiments, the interaction between the analyte and the selected chemical

medium should be high. Depending on the interaction, the target analyte can be easily extracted from the aqueous solution. For a clearer view of this, the effect of the pH of the aqueous solution on the absorbance of tartrazine was investigated in the range of pH 3-9. As shown in Figure 2, the absorbance of tartrazine increased in the range of pH 3 to 5.5, and there was a decrease in absorbance at higher pH values. The reason for the decrease in absorbance at high pH is due to the loss of hydrogen from tartrazine. So, pH 5.5 of acetate buffer was selected as the optimum pH for higher absorbance and easy phase separation.
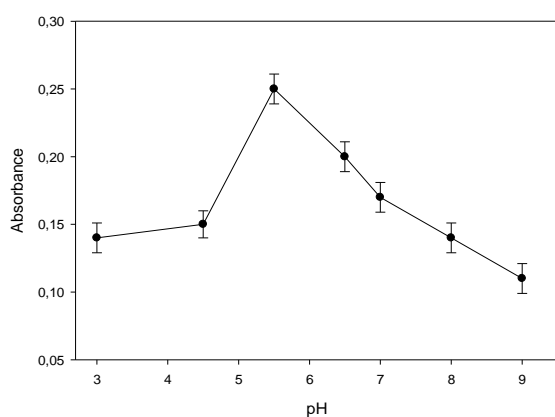
Figure 2. Effect of pH on absorbance of tartarazine

3.3. Effect of [C8MIM][BF4] amount

In these methods, the selection of the appropriate extraction solvent is necessary to good extraction. The following specifications should be taken into account when selecting the extraction solvent. (I) The selected solvent must be green. (II) A small amount of the extraction solvent should be sufficient for extraction. (III) the extraction solvent should be selective for the analyte. (IV) The extraction time should be short. Taking these properties into consideration, the ionic liquids (IL) such as [C8MIM][BF4] used in many fields were chosen as extraction solvents. The [C8MIM][BF4] must be in sufficient volume in the final volume in order to ensure the extraction. Therefore, the effect of the amount of [C8MIM][BF4] on the absorbance of the tartrazine was investigated in the range of 0-800 µL. As shown in Figure 3, the extraction depend on the amount of [C8MIM][BF4. Phase separation was not achieved in the absence of

[C8MIM][BF4], and maximum absorbance was obtained when the [C8MIM][BF4] amount was 400 µL. So, 400 µL of [C8MIM][BF4] was selected as the optimum value for higher absorbance and easy phase separation.
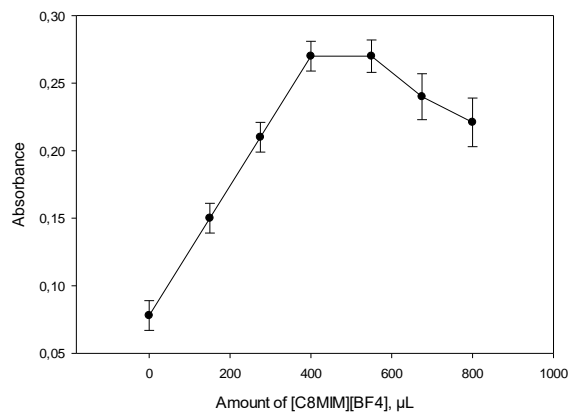
Figure 3. Effect of [C8MIM][BF4] amounton absorbance of tartarazine

3.4. The effect of the type and volume of dispersive solvent

The main purpose of the dispersive solvent is that the extraction solvent provides microsphere formation. The dispersive solvent should also be dispersible between the ionic liquid and the aqueous phase. For the selection of dispersive solvents, different solvents (acetone, 1-heptanol, 1-octanol, ethanol, 2-propanol, and methanol) preliminary tests were made, and the best signals and phase separation were obtained in the presence of 1-octanol. So, 1-octanol was chosen as the dispersive solvent. The effect of the amount of this dispersive solvent on the absorbance of tartrazine was investigated in the range of 0-600 µL. The results were given in Figure 4.
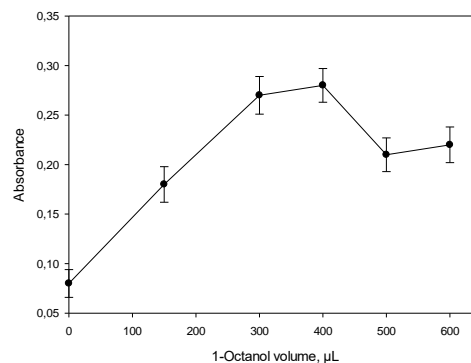
Figure 4. Effect of 1-octanolvolume on absorbance of tartarazine

Quantitative results could not be obtained when dispersive solvent volume was low. The reason for this is that there is not enough dispersive solvent in the medium to disperse the [C8MIM][BF4]. The highest absorbance values were obtained in the range of 300-400 µL of 1-octanol. At higher 1-octanol volumes, there was a partial reduction in absorbance. So, 300 µL of 1-octanol was selected as the optimum value for higher absorbance and easy phase separation.

3.5. Effect of ultrasonication time

Ultrasonication is an important variable that accelerates phase separation. The ultrasound-induced cavitation makes the ionic liquid molecules in the aqueous phase move faster. Selection of appropriate ultrasonic time is essential for extraction. The effect of ultrasonic time on the absorbance of the tartrazine was investigated in the range of 1-20 min. As shown in Figure 5, quantitative absorbances were obtained in a 5 min ultrasound. In addition, over 10 min of ultrasound absorbance decreased. In later studies, 5 min of ultrasonication time was selected as the optimum value for higher absorbance and easy phase separation.
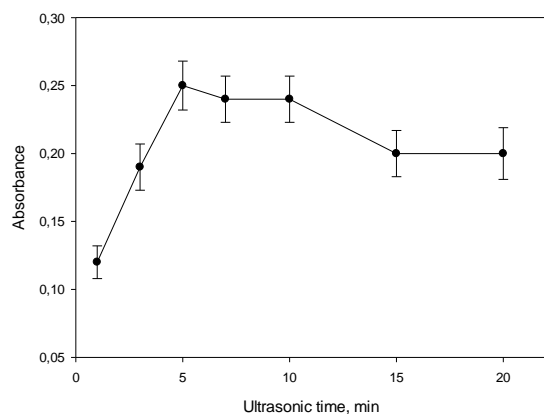
Figure 5. Effect of ultrasonic time on absorbance of tartarazine

3.6. Effect of temperature

Studies have been reported to provide phase separation at room temperature for ionic liquids. Additional experimental steps are implemented to increase the phase separation of ionic liquid. Some of them are vortexes, heating, and ultrasonic effect,

or a combination thereof. In this study, the heating effect is used to accelerate the phase separation of ionic fluid. And the effect of the working temperature on the absorbance of the tartrazine was investigated from room temperature to 60°C. The results were given in Figure 6. The highest absorbance was obtained at 45°C. The reason for the decrease in absorbance at high temperatures is the decrease in the effectiveness of the ionic liquid and dispersive solvent mixture. So, temperature (45°C) was selected as the optimum value for higher absorbance and easy phase separation.
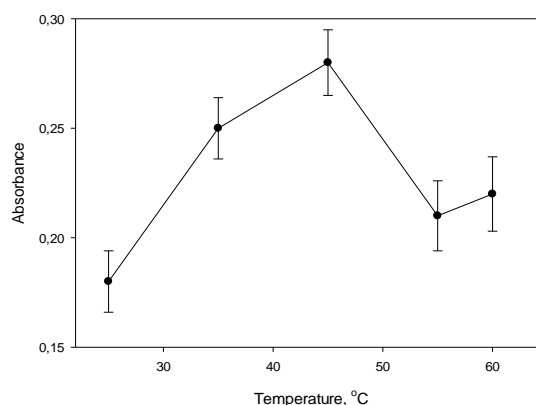
Figure 6. Effect of temperature on absorbance of tartarazine

3.7. Selectivity study

The selectivity of the analyte method is expressed as the interest of the selected chemical medium to the analyte in the sample medium. The higher the selectivity, the less analytical method has less interference. In general, experimental studies are performed with model solutions while developing a chemical method. The ability of the method developed when the real example is studied is not known. For this reason, it is necessary to carry out a selection study before the analysis of the real samples. These studies were carried out as follows. First, foreign ions at different proportions were added to the model solutions, and then the ability of the proposed method was tested in the presence of foreign ions by applying the proposed method. If an ion causes a ±5% change in the absorbance of the analyte, the ion is defined as an interference ion. In addition, the tolerance limits for the corresponding ion were determined by the ratio of the concentration caused by the interference to the

initial amonuts of tartrazine. The result of the study was given in Table 1. The results indicate no significant interference effect. Second, the analytical properties of the method were determined by studies on matrix matched solutions.

The impact of all possible initiatives was reflected in all analytical data. Studies have shown that the selected chemical medium was highly selective for the tartrazine.

Table 1. Selectivity of the method in the presence of potential interfering species and tolerance limits

Interfering species	Tolerance limits	Recovery (%)	RSD (%)
Sn^{2+}	1000	94.7	2.1
Cd^{2+}	1000	96.4	2.4
K^+	1000	98.1	2.2
Co^{2+}	1000	95.3	2.1
Mg^{2+}	1000	96.2	2.0
Ca^{2+}	750	96.8	2.8
Tartaric acid	750	97.5	2.5
Ponceau 4R	750	96.5	2.6
Fe^{3+}	750	98.2	1.8
SO_4^{2-}	500	94.4	2.7
Allura red AC	500	95.9	2.5
Ascorbic acid	500	97.1	2.6
Al^{3+}	500	96.3	2.9
Brilliant Blue	250	96.5	2.5
Sunset yellow	250	93.4	2.4
Erythrosine	250	93.1	2.1
Carmoisine	100	92.4	2.8
Amaranth	100	92.5	2.5

3.8. Analytical performance

After both chemical variables and experimental conditions were optimized, the analytical parameters of the method were determined in selected chemical conditions. The working matrix was performed on matched solutions. The experimental steps were as follows. Different amounts of tartarazine were added to the prepared samples, and then the recommended method was applied. Analytical properties such as the working linear range, regression equation, detection limit (LOD), quantification limit (LOQ), preconcentration factor, sensitivity improvement

factor (SIF) and recovery were calculated from the results. The linear working range of the method was calculated as 10-700 µg L^{-1}. The SIF was calculated from the slope ratio of the calibration graphs before and after the UA-IL-FODME procedure, and was found as 127. The LOD and LOQ were expressed as the ratio of three and ten times the standard deviation of the blank samples to the slope of the calibration graph. The LOD and LOQ values were 3.2 µg L^{-1} and 10 µg L^{-1}, respectively. Comprehensive analytical data was given in Table 2.

Table 2. Analytical parameters of the proposed method under optimum conditions

Parameters	For matrix-matched solutions
Regression equation	Abs.= $0.0018 \times$[Taratizine, µg L^{-1}] + 0.00024
Correlation coefficient, r^2	0.9935
Working linear range, µg L^{-1}	10-700
LOD, (µg L^{-1})	3.2
LOQ, (µg L^{-1})	10
Average RSD %	2.2
Average Recovery %	96.1
sensitivity improvement factor (SIF)	127
Pre-concentration factor (PF)	50

3.9. Validation study

The validation parameters (accuracy and precision) of the proposed method should be tested prior to the analysis of the real samples. Accuracy is expressed as the proximity of the experimental results to the actual accepting value. and the accuracy of the method was tested by recovery experiments. Precision refers to the proximity of the values found in an experiment. The precision of the method was assessed by the presence of relative standard deviation (RSDs%) value. The test of these parameters was evaluated with intra-day and inter-day studies. Both studies were tested for three different concentrations of tartarazine. Intra-day study, triplicate experimental study was carried out in one day for each concentration. In inter-day study, three repetitive studies were continued in three consecutive days. The RSD% values for intra-day and inter-day study ranged between 1.8-3.5% and 2.2-3.8%, respectively. In addition, quantitative recoveries (95.4-103.2% for intra-day 93.3-105.2% for inter-day) were obtained for both studies.

3.10.   Application

After all the analytical parameters of the method were tested, the applicability of the method was evaluated for the extraction and determination of taratizine from the soft drinks and foodstuff. Taking 1.0 mL of the prepared samples as described in Section 2.3, the recommended method was applied, and the amount of tartarazine in each sample was determined separately. Recovery experiments were also performed. Analytical results are given in Table 3.

Table 3. Analytical results of the proposed method

Sample	Tartarazine (µg L^{-1})		Recovery %	RSD %
	Added	Found		
Syrup-preserved fruit	-	75.4	-	1.4
	100	170.7	95.3	1.7
	200	269.0	96.8	1.8
Carbonated drink-green	-	117.5	-	2.1
	100	219.7	102.2	2.4
	200	320.9	101.7	2.5
Carbonated drink-orange	-	321.0	-	1.8
	100	417.4	96.4	1.7
	200	516.6	97.8	1.9
Chocolate candy-green	-	166.0	-	1.7
	100	259.8	93.8	1.8
	200	358.2	96.1	2.1
Chocolate candy-yellow	-	245.1	-	1.8
	100	340.8	95.7	2.0
	200	442.9	98.9	2.1
Lollipop	-	450.0	-	1.8
	100	511.4	101.4	2.1
	200	652.0	101.0	2.2
Icing sugar	-	314.7	-	2.3
	100	414.7	96.6	2.1
	200	510.3	97.8	2.0

The amount of tartrazine ranged from 75.4-321 µg L^{-1} for the soft drinks and ranged from 166 to 450 µg L^{-1} for foodstuff. Furthermore, the RSD% and recovery values for soft drinks and foodstuff samples were 1.4-2.5%, 95.3-102.2% and 1.7-2.3%, 93.8-101.4%, respectively. In order to understand the positive aspects of the proposed method in literature, the method used was compared analytically with the other methods reported. The analytical properties compared were the operating range, detection limit, preconcentration factor, RSD% and recovery. When the Table 4 was examined, it was understood that the proposed method has a wider working

range and a lower detection limit than other methods. According to other extraction methods, in this study, more environmentally friendly and cheap chemicals were used. In the determination step, the use of cheap and easy to use spectrophotometer that can be found in almost any laboratory is alternative to expensive and complex techniques such as HPLC.

Table 4. Comparison of analytical performance of the proposed method with other methods.

Extraction	Detection technique	Linearity ($\mu g\ L^{-1}$)	Detection limit ($\mu g\ L^{-1}$)	RSD (%)	References
IL-DPME	HPLC	0.5–2000	0.15	4.7	[23]
Without extraction	Electrochemical sensor	9–549	2.7	6.8	[24]
Without extraction	Spectrophotometry	0-10	-	4.2	[25]
IEME	HPLC	1.00–80	1.0	6.1	[26]
CPE	Spectrophotometry	0.05–5.00	37.19	3.2	[27]
UA-IL-FODME	Spectrophotometry	10-700	3.2	2.2	This study

Ionic liquid dispersive phase microextraction (IL-DPME),high-performance liquid chromatography (**HPLC**), in-tube electro-membrane extraction (IEME), ultrasound-assistedionicliquid-basedfloatingorganicdropletsmicroextraction (UA-IL-FODME)

4. CONCLUSION

In this study, a simple, innovative and inexpensive ultrasound-assisted ionic liquid-based floating organic droplets microextraction (UA-IL-FODME) method was proposed for the extravasation of synthetic food dye tartarazine in soft drinks and foodstuff. The amount of tartarazine was determined by spectrophotometer. The extraction of taratizine was provided in the mixture of ionic liquid ([C8MIM][BF4]) and dispersive solvent (1-octanol) at pH 5.5. The ultrasonic bath temperature during extraction was 45 °C. The most important advantages of the method were the use of chemicals in μL levels to ensure extraction. The use of environmentally friendly, inexpensive chemical and experimental material, rapid extraction, wide linear range, low detection limit are other outstanding advantages of the method. Detailed selectivity and validation studies were performed. The method was successfully applied to the extraction and determination of the tartarazine in selected samples. The results of recovery and RSD% were acceptable.

REFERENCES

[1] Amin K. A., Hameid H.A. and Elsttar A.A. Effect of food azo dyes tartrazine and carmoisine on biochemical parameters related to renal, hepatic function and oxidative stress biomarkers in young male rats. Food Chem. Toxicol., 48-10 (2010) 2994-2999.

[2] Ghoreishi S.M., Behpour M. and Golestaneh M. Simultaneous determination of sunset yellow and tartrazine in soft drinks using gold nanoparticles carbon paste electrode. Food chem., 132-1 (2012) 637-641.

[3] Kucharska M. and Grabka J. A review of chromatographic methods for determination of synthetic food dyes. Talanta, 80-3 (2010) 1045-1051.

[4] Soponar F., Moţ A.C. and Sârbu C. Quantitative determination of some food dyes using digital processing of images obtained by thin-layer chromatography. J. Chromatogr. A, 1188-2 (2008) 295-300.

[5] Hajimahmoodi M., Afsharimanesh M., Moghaddam G., Sadeghi N., Oveisi M.R., Jannat B. and Kanan H. Determination of eight synthetic dyes in foodstuffs by green liquid chromatography. Food Additives & Contaminants: Part A, 30-5 (2013) 780-785.

[6] El-Sheikh A.H. and Al-Degs Y.S. Spectrophotometric determination of food dyes in soft drinks by second order multivariate calibration of the absorbance spectra-pH data matrices. Dyes Pigm., 97-2 (2013) 330-339.

[7] Alves S.P., Brum D.M., Andrade E.C.B. and Netto A.D.P. Determination of synthetic dyes in selected foodstuffs by high performance liquid

chromatography with UV-DAD detection. Food Chem., 107-1 (2008) 489-496.

[8] Andrade F.I., Guedes M.I.F., Vieira Í.G.P., Mendes F.N.P., Rodrigues P.A.S., Maia C.S.C. and Matos L. Determination of synthetic food dyes in commercial soft drinks by TLC and ion-pair HPLC. Food Chem., 157 (2014) 193-198.

[9] Li X.Q., Zhang Q.H., Ma K., Li H.M. and Guo Z. Identification and determination of 34 water-soluble synthetic dyes in foodstuff by high performance liquid chromatography–diode array detection–ion trap time-of-flight tandem mass spectrometry. Food Chem., 182 (2015) 316-326.

[10] Asfaram A., Ghaedi M. and Goudarzi A. Optimization of ultrasound-assisted dispersive solid-phase microextraction based on nanoparticles followed by spectrophotometry for the simultaneous determination of dyes using experimental design. Ultrason. Sonochem., 32 (2016) 407-417.

[11] Song X., Shi Z., Tan X., Zhang S., Liu G. and Wu K. One-step solvent exfoliation of graphite to produce a highly-sensitive electrochemical sensor for tartrazine. Sens. Actuators, B., 197 (2014) 104-108.

[12] Ma M., Luo X., Chen B., Su S. and Yao S. Simultaneous determination of water-soluble and fat-soluble synthetic colorants in foodstuff by high-performance liquid chromatography–diode array detection–electrospray mass spectrometry. Journal of Chromatography A, 1103-1 (2006) 170-176.

[13] Qi P., Zeng T., Wen Z., Liang X. and Zhang X. Interference-free simultaneous determination of Sudan dyes in chili foods using solid phase extraction coupled with HPLC–DAD. Food Chem., 125-4 (2011) 1462-1467.

[14] Long C., Mai Z., Yang X., Zhu B., Xu X., Huang X. and Zou X. A new liquid–liquid extraction method for determination of 6 azo-dyes in chilli products by high-performance liquid chromatography. Food Chem., 126-3 (2011) 1324-1329.

[15] Altunay N., Elik A., Bulutlu C. and Gürkan R. Application of simple, fast and eco-friendly ultrasound-assisted-cloud point extraction for pre-concentration of zinc, nickel and cobalt from foods and vegetables prior to their flame atomic absorption spectrometric determinations. International journal of environmental analytical chemistry, 98-7 (2018) 655-675.

[16] Yan H., Qiao J., Pei Y., Long T., Ding W. and Xie, K. Molecularly imprinted solid-phase extraction coupled to liquid chromatography for determination of Sudan dyes in preserved beancurds. Food Chem., 132-1 (2012) 649-654.

[17] Chen D., Li X., Tao Y., Pan Y., Wu Q., Liu Z. and Yuan Z. Development of a liquid chromatography–tandem mass spectrometry with ultrasound-assisted extraction method for the simultaneous determination of sudan dyes and their metabolites in the edible tissues and eggs of food-producing animals. Journal of Chromatography B, 939 (2013) 45-50.

[18] Elik A. Ultrasonic-assisted leaching of trace metals from sediments as a function of pH. Talanta, 71-2 (2007) 790-794.

[19] Altunay N., Elik A. and Gürkan R. Extraction and reliable determination of acrylamide from thermally processed foods using ionic liquid-based ultrasound-assisted selective microextraction combined with spectrophotometry. Food Additives & Contaminants: Part A, 35-2 (2018) 222-232.

[20] Elik A., Altunay N. and Gürkan R. Microextraction and preconcentration of Mn and Cd from vegetables, grains and nuts prior to their determination by flame atomic absorption spectrometry using room temperature ionic liquid. J. Mol. Liq., 247 (2017) 262-268.

[21] Elik A., Altunay N. and Gürkan R. Ultrasound-Assisted Low-Density Solvent-Based Dispersive Liquid–Liquid Microextraction Coupled to Spectrophotometry for the Determination of Low Levels of Histamine in Fish and Meat Products. Food Anal. Methods., 12-2 (2019) 489-502.

[22] Altunay N., Elik A. and Gürkan R. Extraction and reliable determination of acrylamide from thermally processed foods using ionic liquid-based ultrasound-assisted selective microextraction combined with spectrophotometry. Food Additives & Contaminants: Part A, 35-2 (2018) 222-232.

[23] Wu H., Guo J.B., Du L.M., Tian H., Hao C.X., Wang Z.F. and Wang J.Y. A rapid shaking-based ionic liquid dispersive liquid phase microextraction for the simultaneous determination of six synthetic food colourants in soft drinks, sugar-and gelatin-based confectionery by high-performance liquid chromatography. Food Chem., 141-1 (2013) 182-186.

[24] Gan T., Sun J.Y., Meng W., Song L. and Zhang Y.X. Electrochemical sensor based on graphene and mesoporous TiO2 for the simultaneous determination of trace colourants in food. Food Chem., 141 (2013) 3731–3737.

[25] El-Sheikh A.H. and Al-Degs Y.S. Spectrophotometric determination of food dyes in soft drinks by second order multivariate calibration of the absorbance spectra-pH data matrices. Dyes Pigm., 97 (2013) 330–339.

[26] Bazregar M., Rajabi M., Yamini Y. and Asghari A. In-tube electro-membrane extraction with a sub-microliter organic solvent consumption as an efficient technique for synthetic food dyes determination in foodstuff samples. Journal of Chromatography A, 1410 (2015) 35-43.

[27] Nambiar A.P., Sanyal M. and Shrivastav P.S. Performance evaluation and thermodynamic studies for the simultaneous cloud point extraction of erythrosine and tartrazine using mixed micelles in food samples. Food Anal. Methods., 10 (2017) 3471-3480.

Analysis of a Random Zeeman Heartbeat Model with Differential Transformation Method

Pınar ORAL[1] iD *, Mehmet MERDAN[1]** iD *, Zafer BEKİRYAZICI[2]* iD

[1]Department of Mathematical Engineering, Gumushane University, Gumushane, TURKEY
[2]Department of Mathematics, Recep Tayyip Erdogan University, Rize, TURKEY

Abstract. In this paper, the differential transformation method is used to examine the random Zeeman Heartbeat Model. Some of the parameters and the initial conditions of the model are taken as random variables with Beta and Normal distributions, respectively. The approximate analytical solution of the random Zeeman Model is obtained and used to find the expectation and variance of the model components. The results from the random models including Beta and normal distributed random effects are compared and the approximate numerical characteristics are obtained for these cases. The approximate formulas are also modified by using Laplace-Padé Method to increase the convergence interval of the approximations.

Keywords: Zeeman Heartbeat Model, Random differential equation, Expected value, Variance, Padé approximation.

Diferansiyel Dönüşüm Yöntemi İle Rastgele Kalp Atış Modelinin Analizi

Özet. Bu çalışmada, rastgele Zeeman Kalpatış Modelinin incelenmesi için diferansiyel dönüşüm yöntemi kullanılmıştır. Modelin bazı parametreleri ve başlangıç koşulları sırasıyla Beta ve Normal dağılımlara sahip rastgele değişkenler olarak alınmıştır. Rastgele Zeeman Modelinin yaklaşık analitik çözümü elde edilmiş ve model bileşenlerinin beklenen değer ve varyansı elde edilmiştir. Beta ve normal olarak dağılmış rastgele etkiler altında, rastgele modellerin sonuçları karşılaştırılmış ve bu durumlar için elde edilen yaklaşık sayısal karakteristikler karşılaştırılmıştır. Elde edilen yaklaşık formüllere, yaklaşımların yakınsama aralığını artırmak için Laplace-Padé Metodu uygulanarak iyileştirilmiş çözümler bulunmuştur.

Anahtar Kelimeler: Zeeman Kalpatış Modeli, Rastgele diferansiyel denklem, Beklenen değer, Varyans, Padé yaklaşımı

1. INTRODUCTION

The majority of the investigations of mathematical models in various fields of science is performed by using deterministic components, ignoring the randomness of the natural course of events. This fact is a setback for an accurate description of the events through equation systems since there is always an unignorable amount of uncertainty in the natural realizations of all phenomena. The random effects approach of Merdan et al. aims to handle this issue swiftly by introducing random noise terms in the deterministic parameters of compartmental mathematical models [1,2]. Compartmental models are widely used in the modeling of infectious diseases and such a random modeling approach provides a straightforward modification of these models to effectively describe the random behavior of diseases.

The model used in this study has been introduced by E.C. Zeeman in 1972 [3-5]. It consists of differential equations that describe the heart activity under the control of electrical impulses produced by the body. The heart regulates the circulation of blood in the body through the contraction of heart muscles, an event which is triggered by an electrochemical activity. The equation systems of E.C. Zeeman represent the dynamics of the muscle fiber activity and stimulus which controls muscle fiber contraction over time. The parameters of the differential equation system will be added random effects with Gaussian (normal) and beta distribution to represent the natural fluctuations in the dynamics of heartbeat. Similar modeling studies have been made with random effects for bacterial resistance and biochemical reactions [2, 6] .

In this study, Differential Transformation Method (DTM) will be used to investigate the Zeeman's heartbeat models with random components. DTM [7,8] and similar methods related to DTM have been used for analyzing various mathematical models [17,18]. While DTM has many advantages for analyzing models such its adaptability for use in fractional, delay and partial differential equation systems, its power series form approximate-analytical solution which enables a detailed analysis of the problem of interest and its usability in many problems in applied mathematics. However, the series solution brings along a serious disadvantage as well, which arises when the problems are analyzed in wide time intervals, causing issues on the convergence of the approximate solution. One of the techniques for tackling this problem is the Laplace-Pade method, which proposes the use of a ratio two polynomial functions of orders p and q, where the orders are arbitrary positive integers. Applications have shown that every different selection of p, q results in a new approximate solution and generally the selection for $p = q$ provides the best convergence. Modifying the approximate analytical solution through Pade approximants provides a new approximate solution which is convergent to the exact solution on a wider time interval. Details of Laplace-Pade modification of DTM have been given in the literature [19-20].

Our study concentrates on the improvement of the approximate solutions of the Zeeman heartbeat model with random components obtained with DTM through Laplace-Pade method [18, 21]. The paper is organized as follows: Section 2 includes an analysis of the heartbeat model with two equations including an introduction of the Differential Transformation Method and the distributions used. Section 3 contains the analysis on the model with three equations. The last section contains the conclusions.

2. TWO DIMENSIONAL ZEEMAN MODEL

The Zeeman model is used for the modeling of heartbeat and the two dimensional version consists of the following differential equations, where x_1 represents the heart muscle fiber length and x_2 represents the stimulus:

$$\frac{dx_1}{dt} = -\frac{1}{\epsilon}(x_1^3 - Tx_1 + x_2),$$

$$\frac{dx_2}{dt} = x_1 - x_d. \tag{1}$$

The parameters of this system, ϵ, T, x_d are defined as follows: T represents the tension $(T > 0)$, ϵ is a constant that depends on the timescale and x_d is the typical relaxed fiber length. The deterministic values of the parameters have been given as $\epsilon = 0.2; T = 0.5$ and $x_d = 0$ or 0.41 whereas the initial values of (1) are given as $x_1(0) = 0.5$ and $x_2(0) = 0$ [3-5].

2.1. Differential Transformation Method

An outline of the Differential Transformation Method (DTM) can be given as follows. Let $x(t)$ be an analytical function in the domain D and $t = t_0$ be a point in D. The function $x(t)$ can be represented by using a t_0-centered power series. The k-th derivative of $x(t)$ is defined as:

$$X(k) = \frac{1}{k!}\left[\frac{d^k x(t)}{dt^k}\right]_{t=t_0}, \quad \forall t \in D. \tag{2}$$

In (2), $x(t)$ is the original function and $X(k)$ is the transformed function. The inverse differential transformation of $X(k)$ is given as [7,8]:

$$x(t) = \sum_{k=0}^{\infty} X(k)(t - t_0)^k, \quad \forall t \in D. \tag{3}$$

Using (2) and (3), we obtain

$$x(t) = \sum_{k=0}^{\infty} \frac{(t-t_0)^k}{k!}\left[\frac{d^k x(t)}{dt^k}\right]_{t=t_0}, \quad \forall t \in D. \tag{4}$$

The basic theorems for one-dimensional differential transformation are given as below.

Theorem 1. If $z(t) = x(t) \pm y(t)$, then $Z(k) = X(k) \pm Y(k)$.

Theorem 2. If $z(t) = cy(t)$, then $Z(k) = cY(k)$.

Theorem 3. If $z(t) = \frac{dy(t)}{dt}$, then $Z(k) = (k+1)Y(k+1)$.

Theorem 4. If $z(t) = \frac{d^n y(t)}{dt}$, then $Z(k) = \frac{(k+n)!}{k!}Y(k+n)$.

Theorem 5. If $z(t) = x(t)y(t)$, $Z(k) = \sum_{k_1=0}^{k} X(k_1)Y(k-k_1)$.

Theorem 6. If $z(t) = t^n$, then $Z(k) = \delta(k-n) = \begin{cases} 1 & k = n \\ 0 & k \neq n \end{cases}$.

In applications, the function $x(t)$ is represented by an infinite series and by using (4) we can write:

$$x(t) = \sum_{k=0}^{N} X(k)(t - t_0)^k, \quad \forall t \in D. \tag{5}$$

The equation (5) states that $\sum_{k=N+1}^{\infty} X(k)(t - t_0)^k$ has a negligibly small value.

Consider a system of ordinary differential equations

$$\frac{dx_1}{dt} + h_1(t, x_1, x_2, \dots, x_m) = g_1(t),$$

$$\frac{dx_2}{dt} + h_2(t, x_1, x_2, \dots, x_m) = g_2(t), \tag{6}$$

$$\frac{dx_m}{dt} + h_m(t, x_1, x_2, \dots, x_m) = g_m(t),$$

with the initial values

$$x_1(t_0) = d_1, \quad x_2(t_0) = d_2, \cdots, x_m(t_0) = d_m \tag{7}$$

Using DTM, the derivative of both sides in the equation system (6)-(7) is obtained as

$$(k + 1)X_1(k + 1) + H_1(k) = G_1(k),$$

$$(k + 1)X_2(k + 1) + H_2(k) = G_2(k),$$

$$\vdots$$

(8)

$$(k + 1)X_m(k + 1) + H_m(k) = G_m(k).$$

with

$$X_1(0) = d_1, \quad X_2(0) = d_2, \cdots, X_m(0) = d_m. \tag{9}$$

Similarly, the n-th term is obtained for (5) as

$$\varphi_{1,n}(t) = x_1(t) = \sum_{k=1}^{N} X_1(k)t^k,$$

$$\varphi_{2,n}(t) = x_2(t) = \sum_{k=1}^{N} X_2(k)t^k,$$

(10)

$$\vdots$$

$$\varphi_{m,n}(t) = x_m(t) = \sum_{k=1}^{N} X_m(k)t^k.$$

Using DTM for equation (1), we obtain:

$$(k + 1)X_1(k + 1) = -\frac{1}{\varepsilon}\left[\sum_{k_2=0}^{k}\sum_{k_1=0}^{k_2} X_1(k_1)X_1(k_2 - k_1)X_1(k - k_2) - TX_1(k) + X_2(k)\right],$$

(11)

$$(k + 1)X_2(k + 1) = X_1(k) - x_d\delta(k).$$

We will be choosing random parameters and initial values for the two dimensional Zeeman model to obtain a random model. In the next section, we introduce the beta and normal distributions which we will be using for these random components.

2.2. Beta Distribution

The Beta function $B(\alpha, \beta)$ for the parameters > 0, $\beta > 0$ is defined as

$$B(\alpha, \beta) = \int_0^1 x^{\alpha-1}(1 - x)^{\beta-1}dx. \tag{12}$$

Dividing both sides of (12) by $B(\alpha, \beta)$, we obtain

$$1 = \frac{1}{B(\alpha, \beta)}\int_0^1 x^{\alpha-1}(1 - x)^{\beta-1}dx. \tag{13}$$

Using the definition of a probability density function, we obtain [9]:

$$f(x) = \begin{cases} \dfrac{x^{\alpha-1}(1-x)^{\beta-1}}{B(\alpha,\beta)}, & 0 < x < 1 \\ 0, & elsewhere \end{cases}. \tag{14}$$

where

$$B(\alpha,\beta) = \frac{\Gamma(\alpha).\Gamma(\beta)}{\Gamma(\alpha+\beta)}. \tag{15}$$

If $X \sim B(\alpha,\beta)$ is a Beta distributed random variable then,

$$E[X] = \frac{\alpha}{\alpha+\beta}, \qquad Var[X] = \frac{\alpha\beta}{(\alpha+\beta)^2.(\alpha+\beta+1)},$$

$$E[X^2] = \frac{\alpha(\alpha+1)}{(\alpha+\beta+1)(\alpha+\beta)}, \qquad E[X^3] = \frac{\alpha(\alpha+1)(\alpha+2)}{(\alpha+\beta+2)(\alpha+\beta+1)(\alpha+\beta)}, \dots$$

$$E[X^N] = \frac{\alpha(\alpha+1)(\alpha+2)\dots(\alpha+(N-1))}{(\alpha+\beta+N-1)(\alpha+\beta+N-2)\dots(\alpha+\beta+1)(\alpha+\beta)}.$$

2.3. Expected Value of the Two Dimensional Zeeman Model

Using Differential Transformation Method [7,8] and its random counterpart [10-14], we can find the approximate solutions of a random process in the form of a power series by using the formula

$$x_N(t) = \sum_{k=0}^{N} X(k)t^k.$$

The variance and covariance for the approximate solution $x_N(t)$ are given as

$$E[x_N(t)] = \sum_{k=0}^{N} E[X(k)]t^k, \tag{16}$$

$$Var[x_N(t)] = \sum_{j=0}^{N}\sum_{i=0}^{N} cov(X(i),X(j))t^{i+j}, \tag{17}$$

where [11]

$$cov(X(i),X(j)) = E(X(i)X(j)) - E[X(i)]E[X(j)], \qquad \forall i,j = 0,1,\dots,N. \tag{18}$$

Let the parameter T in (1) be a Beta distributed random variable such that $T \sim Beta(\alpha = 2, \beta = 1)$. In addition, assume that the initial conditions are assumed to be random variables Y_0 and Y_1 where Y_0 and Y_1 are independent random variables with normal distribution, i.e. $Y_0, Y_1 \in N(\mu,\sigma^2)$. Let $\mu = 1, \sigma^2 = 1, \sigma = 1$. Then,

$$\begin{aligned}
&E[Y_0] = \mu = 1, E[Y_1] = \mu = 1, \\
&E[Y_0^2] = \mu^2 + \sigma^2 = 1 + 1 = 2, \\
&E[Y_1^2] = \mu^2 + \sigma^2 = 1 + 1 = 2, \\
&E[Y_0^3] = E[Y_1^3] = \mu^3 + 3\mu\sigma^2 = 1 + 3.1.1 = 4, \\
&E[Y_0^4] = E[Y_1^4] = \mu^3 + 6\mu^2\sigma^2 + 3\sigma^4 = 1 + 6.1.1 + 3.1 = 10, \\
&E[Y_0^5] = E[Y_1^5] = \mu^5 + 10\mu^3\sigma^2 + 15\mu\sigma^4 = 1 + 10.1.1 + 15.1 = 26, \\
&E[Y_0^6] = E[Y_1^6] = \mu^6 + 15\mu^4\sigma^2 + 45\mu^2\sigma^4 + 15\sigma^6 = 1 + 15.1. +45.1.1 + 15.1 = 76, \\
&E[Y_0^7] = E[Y_1^7] = \mu^7 + 21\mu^5\sigma^2 + 105\mu^3\sigma^4 + 105\mu^3\sigma^6 = 232.
\end{aligned} \tag{19}$$

Since $T > 0$ is Beta distributed such that $T \sim B(\alpha = 2, \beta = 1)$ [9],

$$
\begin{aligned}
E[T] &= \frac{\alpha}{\alpha + \beta} = \frac{2}{3}, \\
E[T^2] &= \frac{\alpha(\alpha + 1)}{(\alpha + \beta + 1)(\alpha + \beta)} = \frac{2.3}{3.4} = \frac{1}{2}, \\
E[T^3] &= \frac{\alpha(\alpha + 1)(\alpha + 2)}{(\alpha + \beta + 2)(\alpha + \beta + 1)(\alpha + \beta)} = \frac{2}{5}, \\
E[T^4] &= \frac{\alpha(\alpha + 1)(\alpha + 2)(\alpha + 3)}{(\alpha + \beta)(\alpha + \beta + 1)(\alpha + \beta + 2)(\alpha + \beta + 3)} = \frac{1}{3}.
\end{aligned}
\tag{20}
$$

Using (11), the approximate analytical solution of $x_1(t)$ in (1) using 4 terms is obtained as (denoted by X_1)

$$
\begin{aligned}
X1 = {}& Y_0 + (-5Y_1 + 5TY_0 - 5Y_0^3)t + \left(\frac{75}{2}Y_0^5 - 50Y_0^3 T + \frac{75}{2}Y_0^2 Y_1 + \frac{25}{2}Y_0 T^2 - \frac{25}{2}Y_1 T - \frac{5}{2}Y_0\right)t^2 \\
&+ \left(\frac{25}{6}Y_1 + \frac{50}{3}Y_0^3 - \frac{625}{2}Y_0^7 + \frac{125}{6}Y_0 T^3 - \frac{125}{6}Y_1 T^2 + \frac{1125}{2}Y_0^5 T - \frac{875}{2}Y_0^4 Y_1 \right. \\
&\left. - \frac{1625}{6}Y_0^3 T^2 - 125Y_0 Y_1^2 + 375Y_0^2 Y_1 T - \frac{25}{3}Y_0 T\right)t^3 + \cdots
\end{aligned}
$$

Hence, the approximate expected value of the random variable X_1 is obtained as

$$
\begin{aligned}
E[X1] = E\Big[{}& Y_0 + (-5Y_1 + 5TY_0 - 5Y_0^3)t \\
&+ \left(\frac{75}{2}Y_0^5 - 50Y_0^3 T + \frac{75}{2}Y_0^2 Y_1 + \frac{25}{2}Y_0 T^2 - \frac{25}{2}Y_1 T - \frac{5}{2}Y_0\right)t^2 \\
&+ \left(\frac{25}{6}Y_1 + \frac{50}{3}Y_0^3 - \frac{625}{2}Y_0^7 + \frac{125}{6}Y_0 T^3 - \frac{125}{6}Y_1 T^2 + \frac{1125}{2}Y_0^5 T - \frac{875}{2}Y_0^4 Y_1 \right. \\
&\left. - \frac{1625}{6}Y_0^3 T^2 - 125Y_0 Y_1^2 + 375Y_0^2 Y_1 T - \frac{25}{3}Y_0 T\right)t^3 \Big] + \cdots
\end{aligned}
$$

Using the independence of the random variables, we find

$$
E[X_1] = 1 - \frac{65}{3}t + \frac{10945}{12}t^2 - 67353.472t^3 + \cdots
\tag{21}
$$

The expected value of X_1 is shown in Figure 1.
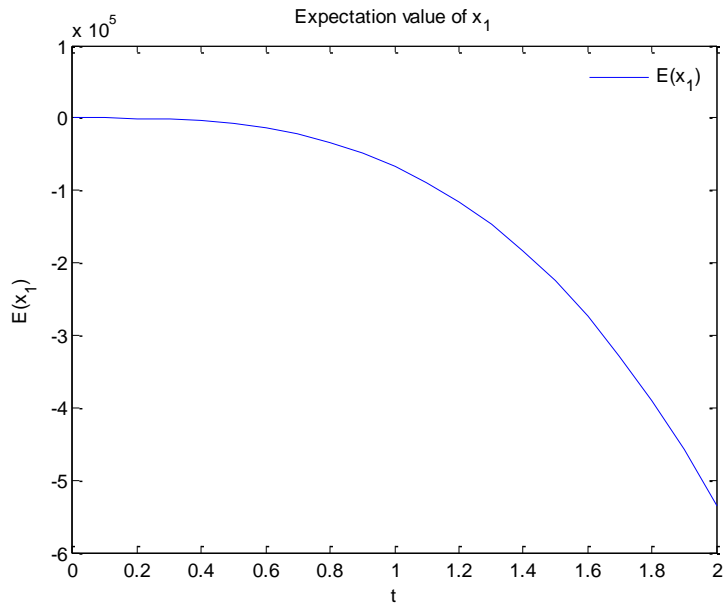
Figure 1. The expected value of X_1.

$$X_2 = Y_1 + Y_0 t + \left(-\frac{5}{2}Y_1 + \frac{5}{2}TY_0 - \frac{5}{2}Y_0^3\right)t^2$$
$$+ \left(\frac{25}{2}Y_0^5 - \frac{50}{3}Y_0^3 T + \frac{25}{2}Y_0^2 Y_1 + \frac{25}{6}Y_0 T^2 - \frac{25}{6}Y_1 T - \frac{5}{6}Y_0\right)t^3 + \cdots$$

Hence, its expectation becomes

$$E[X_2] = E\left[Y_1 + Y_0 t + \left(-\frac{5}{2}Y_1 + \frac{5}{2}TY_0 - \frac{5}{2}Y_0^3\right)t^2\right.$$
$$\left. + \left(\frac{25}{2}Y_0^5 - \frac{50}{3}Y_0^3 T + \frac{25}{2}Y_0^2 Y_1 + \frac{25}{6}Y_0 T^2 - \frac{25}{6}Y_1 T - \frac{5}{6}Y_0\right)t^3\right] + \cdots$$

$$E[X_2] = 1 + t - \frac{65}{6}t^2 + \frac{10945}{36}t^3 + \cdots \tag{22}$$

The approximate expected value of X_2 is shown in Figure 2. It should be noted that more terms are needed for accurate approximate expectations $E[X_1], E[X_2]$. The first three terms have been given to present the calculation method and to underline the improvements obtained by the modification.
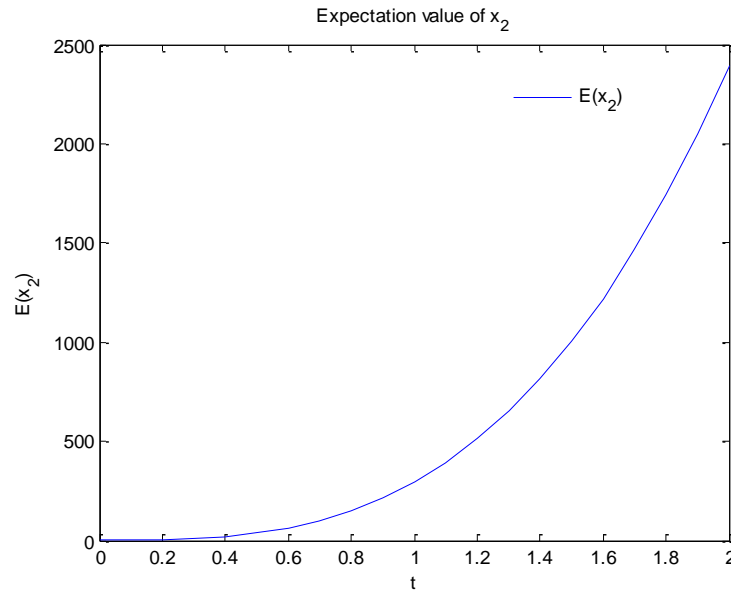
Figure 2. The expected value of X_2.

2.4. Laplace-Padé Method

If Laplace-Padé method [15,16] is used to improve the results, i.e. to obtain convergent results in a wider interval, the following result is obtained for (21):

$$
\begin{aligned}
M_1 &= \frac{1}{7424222958497731096191780362649627} e^{-\frac{56373593243647997}{418931110051840}t} \\
&\times \Bigg(7424222958497731096191780362649627 \\
&\times \cosh\left(\frac{1}{418931110051840} t\sqrt{247474098616591036539726012088 3209}\right) \\
&+ 141890257577574391\sqrt{247474098616591036539726012088 3209} \\
&\times \sinh\left(\frac{1}{418931110051840} t\sqrt{247474098616591036539726012088 3209}\right)\Bigg)
\end{aligned}
$$

This new expected value of X_1, denoted by $M1$, is shown in Figure 3.

Similarly, Laplace-Padé method for (22) gives:

$$
\begin{aligned}
M_2 &= \frac{1}{381232315} e^{-\frac{11075}{272}t} \Bigg(381232315\cosh\left(\frac{1}{816} t\sqrt{1143696945}\right) \\
&\qquad + 11347\sqrt{1143696945}\sinh\left(\frac{1}{816} t\sqrt{1143696945}\right)\Bigg)
\end{aligned}
$$

The modified expected value for X_2, denoted by M_2, is shown in Figure 4.
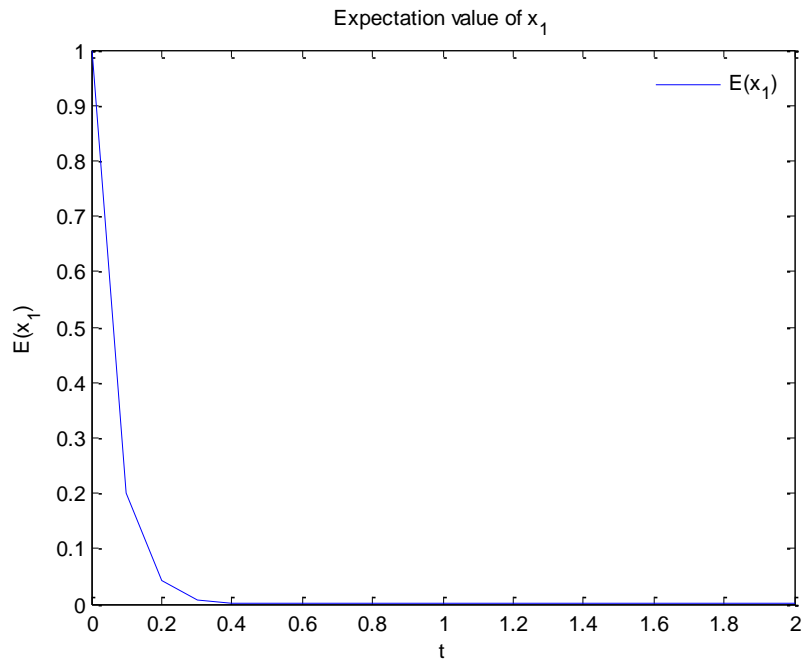
Figure 3. The expected value of X_1, obtained by modified DTM.
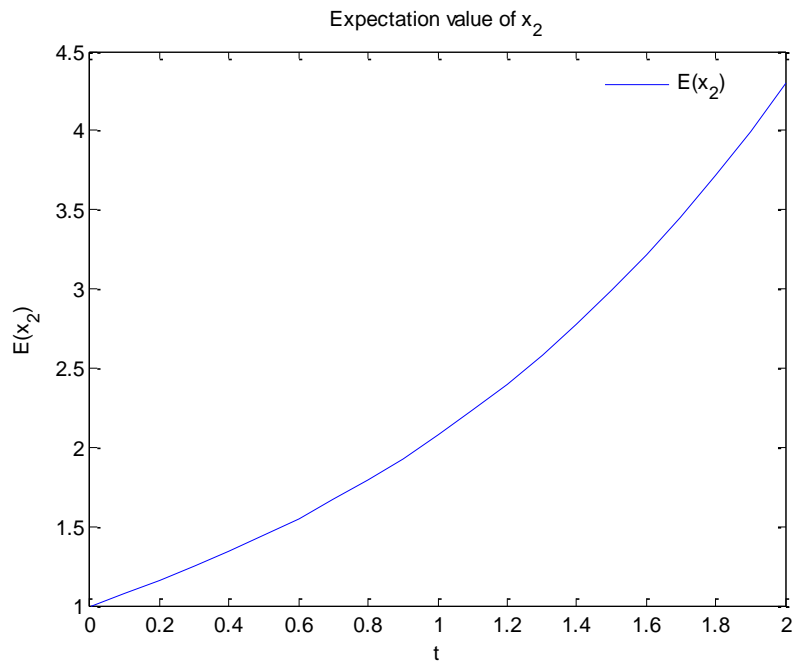
Figure 4. The expected value of X_2, obtained by modified DTM.

2.5. Variances for Two Dimensional Zeeman Model

Using the formulas (17) and (18), the variances for the two dimensional model is obtained as follows.

For the variance of x_1 (using a three term truncated approximation):

$$Var[X_1(t)] = \sum_{j=0}^{2}\sum_{i=0}^{2} cov(X_1(i), X_1(j))t^{i+j} = 1 - \frac{160}{3}t + \frac{87235}{18}t^2 + \cdots \tag{23}$$

Laplace-Padé method for (25) gives

$$M_3 = -\frac{1}{56738917631}e^{\left(\frac{1395760}{36981}t\right)}\left(-56738917631\cosh\left(\frac{73}{36981}t\sqrt{3886227235}\right)\right.$$
$$\left. + 673616\sqrt{3886227235}\sinh\left(\frac{73}{36981}t\sqrt{3886227235}\right)\right)$$

Similarly, the variance for X_2 is:

$$Var[X_2(t)] = \sum_{j=0}^{2}\sum_{i=0}^{2} cov(X_1(i), X_1(j))t^{i+j} = 1 - 4t^2 + \cdots \tag{24}$$

and the modified variance becomes

$$M_4 = cos(2\sqrt{2}t).$$

2.6. Expected Values for Initial Conditions with Normal Distribution

Assume that the initial conditions Y_0 and Y_1 of (1) are independent random variables with normal distribution. Using (19), the expected value of the (truncated) approximate solution X_1 becomes (note that unlike Section 2.3, the parameter T is not a random variable here):

$$E[X_1] = 1 - \frac{45}{2}t + \frac{7555}{8}t^2 - 69644.271t^3 + \cdots \tag{25}$$

If Laplace-Padé method is applied to (25), we obtain

$$M_5 = 0.1 \times 10^{-9}(9999999999\cosh(119.2044503t)$$
$$+ 9501091052\sinh(119.2044503t))e^{-135.7572336t}.$$

Similarly, the expected value of the approximate solution X_2 is

$$E[X_2] = 1 + t - \frac{45}{4}t^2 + \frac{7555}{24}t^3 + \cdots \tag{26}$$

Its modification is obtained as

$$M_6 = \frac{1}{60525305}e^{\left(-\frac{7645}{188}t\right)}\left(60525305\cosh\left(\frac{1}{188}t\sqrt{60525305}\right)\right.$$
$$\left. + 7833\sqrt{60525305}\sinh\left(\frac{1}{188}t\sqrt{60525305}\right)\right).$$

2.7.   Expected Values for Random *T* Parameter with Beta Distribution

If the parameter T in (1) is assumed to be Beta distributed, the approximate expected value of X_1 up to t^3 can be obtained by using (20) as follows (note that unlike Section 2.3, the initial values are not random variables here):

$$E[X_1] = \frac{1}{2} + \frac{25}{24}t - \frac{215}{192}t^2 - \frac{9625}{2304}t^3 + \cdots \tag{27}$$

Using Laplace-Padé on (27) gives

$$M_7 = -\frac{1}{1357422} e^{\left(\frac{1175}{508}t\right)} \left(-678711 cos\left(\frac{1}{508}\sqrt{2262370}t\right) \right.$$
$$\left. + 35\sqrt{2262370} sin\left(\frac{1}{508}\sqrt{2262370}t\right) \right).$$

Similarly, the expected value of the analytical solution X_2 becomes

$$E[X_2] = \frac{1}{2}t + \frac{25}{48}t^2 - \frac{215}{576}t^3 + \cdots$$

Its modification is obtained as

$$M_8 = \frac{4}{165}\sqrt{55}e^{\left(\frac{25t}{24}\right)} sin\left(\frac{3}{8}\sqrt{55}t\right).$$

3.   THREE DIMENSIONAL ZEEMAN MODEL

Let the initial conditions Y_1, Y_2, Y_3 be normal distributed and the model parameters ξ, μ, θ be (standard) Beta distributed random variables. Consider the three dimensional model (Zeeman, 1977)

$$\frac{dx_1}{dt} = -x_1^3 - x_2 x_1 - x_3$$

$$\frac{dx_2}{dt} = -\xi x_1 - \mu x_2 \tag{28}$$

$$\frac{dx_3}{dt} = -x_2 - \theta$$

$$x_1(0) = Y_1, x_2(0) = Y_2, x_3(0) = Y_3$$

Since the initial conditions are independent and identically distributed, $E[Y_1] = E[Y_2] = E[Y_3]$ as in (19) and (20). The deterministic values are given as $\xi = 2, \mu = 2, \theta = 1$ (Zeeman, 1977). We use $\xi, \mu, \theta \sim Beta(\alpha, \beta)$ where $\alpha = 1$ and $\beta = 1$. Using the properties of Beta distribution and (20), we get

$$E[\xi] = E[\mu] = E[\theta] = \frac{\alpha}{\alpha + \beta} = \frac{1}{2}$$

$$\tag{29}$$

$$E[\xi^2] = E[\mu^2] = E[\theta^2] = \frac{\alpha(\alpha + 1)}{(\alpha + \beta + 1)(\alpha + \beta)} = \frac{1}{3}$$

$$E[\xi^3] = E[\mu^3] = E[\theta^3] = \frac{\alpha(\alpha+1)(\alpha+2)}{(\alpha+\beta+2)(\alpha+\beta+1)(\alpha+\beta)} = \frac{1}{4}$$

$$E[\xi^4] = E[\mu^4] = E[\theta^4] = \frac{\alpha(\alpha+1)(\alpha+2)(\alpha+3)}{(\alpha+\beta)(\alpha+\beta+1)(\alpha+\beta+2)(\alpha+\beta+3)} = \frac{1}{5}.$$

Using this information, the expected values of X_1, X_2 and X_3 are obtained as below:

$$
\begin{aligned}
E[X_1] = E\Bigg[& Y_1 + (-Y_1 Y_2 - Y_1^3 - Y_3)t \\
& + \Big(\frac{1}{2}Y_1 Y_2 \mu + 2Y_1^3 Y_2 + \frac{3}{2}Y_1^2 Y_3 + \frac{1}{2}Y_1 Y_2^2 + \frac{1}{2}Y_2 Y_3 + \frac{1}{2}Y_1^2 \xi + \frac{3}{2}Y_1^5 + \frac{1}{2}Y_2 \\
& + \frac{1}{2}\theta \Big) t^2 \\
& + \Big(-3Y_1^2 Y_2 Y_3 - \frac{5}{6}Y_1^3 Y_2 \mu - \frac{2}{3}Y_1^2 Y_2 \xi - \frac{1}{2}Y_1 Y_2^2 \mu - \frac{1}{2}Y_1 Y_3 \xi - \frac{1}{6}Y_1^2 \mu \xi \\
& - \frac{1}{6}Y_1 Y_2 \mu^2 - \frac{1}{3}Y_2 Y_3 \mu - \frac{1}{6}Y_1 Y_2^3 - \frac{1}{6}Y_2^2 Y_3 - \frac{1}{6}Y_2 \theta - Y_1 Y_3^2 - \frac{9}{2}Y_1^5 Y_2 \\
& - \frac{7}{2}Y_1^4 Y_3 - \frac{13}{6}Y_1^3 Y_2^2 - Y_1^4 \xi - \frac{1}{2}Y_1^2 Y_2 - \frac{1}{2}Y_1^2 \theta - \frac{1}{6}Y_1 \xi - \frac{1}{6}Y_2 \mu - \frac{5}{7}Y_1^7 \\
& - \frac{1}{6}Y_2^2 \Big) t^3 \Bigg] + \cdots = 1 - 6t + 53t^2 - \frac{27677}{36}t^3 + \cdots
\end{aligned}
\tag{30}
$$

Using Laplace-Padé for the truncated approximation (30) gives

$$
\begin{aligned}
M_9 = \frac{1}{403622041} e^{\left(-\frac{23861}{840}t\right)} \Bigg(& 403622041 \cosh\left(\frac{1}{840}t\sqrt{403622041}\right) \\
& + 18821\sqrt{403622041}\sinh\left(\frac{1}{840}t\sqrt{403622041}\right) \Bigg).
\end{aligned}
$$

Similarly, the expected value of the approximate analytical solution X_2 is found as

$$
\begin{aligned}
E[X_2] = E\Bigg[& Y_2 + (-Y_1 \xi - Y_2 \mu)t + \Big(\frac{1}{2}Y_1^3 \xi + \frac{1}{2}Y_1 Y_2 \xi + \frac{1}{2}Y_3 \xi + \frac{1}{2}Y_1 \mu \xi + \frac{1}{2}Y_2 \mu^2 \Big)t^2 \\
& + \Big(-\frac{1}{2}Y_1^5 \xi - \frac{2}{3}Y_1^3 Y_2 \xi - \frac{1}{2}Y_1^2 Y_3 \xi - \frac{1}{6}Y_1 Y_2^2 \xi - \frac{1}{6}Y_2 Y_3 \xi - \frac{1}{6}Y_1^2 \xi^2 \\
& - \frac{1}{3}Y_1 Y_2 \mu \xi - \frac{1}{6}Y_2 \xi - \frac{1}{6}\xi\theta - \frac{1}{6}Y_1^3 \xi\mu - \frac{1}{6}Y_3 \xi\mu - \frac{1}{6}Y_1 \xi\mu^2 - \frac{1}{6}Y_2 \mu^3 \Big)t^3 \Bigg] \\
& + \cdots
\end{aligned}
\tag{31}
$$

$$\Rightarrow E[X_2] = 1 - t + \frac{43}{24}t^2 - \frac{661}{72}t^3 + \cdots$$

Using Laplace-Padé method, the modification is obtained as

$$
\begin{aligned}
M_{10} = \frac{1}{957199} e^{\left(-\frac{309}{31}t\right)} \Bigg(& 957199 \cosh\left(\frac{1}{186}t\sqrt{2871597}\right) \\
& + 556\sqrt{2871597}\sinh\left(\frac{1}{186}t\sqrt{2871597}\right) \Bigg).
\end{aligned}
$$

The expected value of X_3 is found as

$$E[X_3] = E\left[Y_3 + (-Y_2 - \theta)t + \left(\frac{1}{2}Y_1\xi + \frac{1}{2}Y_2\mu\right)t^2\right.$$
$$\left. + \left(-\frac{1}{6}Y_1^3\xi - \frac{1}{6}Y_1Y_2\xi - \frac{1}{6}Y_3\xi - \frac{1}{6}Y_1\mu\xi - \frac{1}{6}Y_2\mu^2\right)t^3\right] + \cdots \qquad (32)$$

$$\Rightarrow E[X_3] = 1 - \frac{3}{2}t + \frac{1}{2}t^2 - \frac{43}{72}t^3 + \cdots.$$

The Laplace-Padé modification of (32) becomes

$$M_{11} = -\frac{1}{151}e^{\left(\frac{5}{6}t\right)}\left(-151\cosh\left(\frac{1}{6}t\sqrt{151}\right) + 14\sqrt{151}\sinh\left(\frac{1}{6}t\sqrt{151}\right)\right).$$

4. CONCLUSION

In this study, we have used the random version of the Differential Transformation Method to investigate the approximate solutions of the two and three dimensional Zeeman models. The initial values Y_0, Y_1 and the parameter T were assumed to be normal and standard Beta distributed random variables, respectively. Using these random values, the expected values and variances were found for the two dimensional model. Similarly, the same approximate characteristics were investigated for the three dimensional model too. Finally, Laplace-Padé method was used to modify these approximations and obtain new functions for the approximate numerical characteristics. It is known from the literature that the modified approximations obtained by Laplace-Padé method are generally convergent to the exact solutions in a wider time interval. As the results show, it is seen that the modified approximate results are convergent to the exact solution, which are also consistent with the deterministic results in the literature. Results from Zeeman's studies [3-5] and other studies which do not contain random components show that the systems (1), (28) successfully model the contraction and relaxation of the heart muscles and the electrical signal transmission process. In this study, we have shown the use of random components in these models shows that similar results for the biological significance of the equation systems can be achieved with additional results for the variance and standard deviations of the results that imply deviations in the muscle and electrical signal transmission behavior. This study underlines the adaptability of DTM and Laplace-Pade methods to heartbeat models with random components and the applications can also be generalized to other mathematical models.

REFERENCES

[1] Merdan M. and Khaniyev T., On the Behavior of Solutions Under the Influence of Stochastic Effect of Avian-Human Influenza Epidemic Model, International Journal of Biotechnology and Biochemistry, 4-1 (2008) 75-100.

[2] Merdan M., Bekiryazici Z., Kesemen T. and Khaniyev T., Comparison of stochastic and random models for bacterial resistance. Advances in Difference Equations, 2017-1 (2017) 133.

[3] Zeeman E.C., Differential Equations for the Heartbeat and Nerve Impulse, Mathematics Institute, University of Warwick, Coventry, UK, 1972.

[4] Zeeman E.C., Catastrophe Theory, Selected Papers 1972–1977, Addison-Wesley, Reading, MA, 1977.

[5] Zeeman E.C., Differential equations for the heartbeat and nerve impulse, In: Waddington, C.H. (Ed.), Towards a Theoretical Biology 4: Essays, 8–67, Edinburgh University Press, 1972.

[6] Bekiryazici Z., Merdan M., Kesemen T. and Khaniyev T., Mathematical Modeling of Biochemical Reactions under Random Effects, Turkish Journal of Mathematics and Computer Science, 5 (2016) 8-18.

[7] Zhou J.K., Differential Transformation and its Applications for Electrical Circuits, Huarjung University Press, Wuuhahn, China, 1986.

[8] Ev Pukhov G.G., Differential Transforms and Circuit theory, Int. J. Circuit Theory Appl., 10-3 (1982) 265–276.

[9] Forbes C., Evans M., Hastings N. and Peacock B., Statistical Distributions, 4th Edition, John Wiley & Sons, New Jersey, 2011.

[10] Villafuerte L. and Chen-Charpentier B.M., A random differential transform method: Theory and applications, Applied Mathematics Letters, 25-10 (2012) 1490-1494.

[11] Khudair A.R., Haddad S.A.M. and Khalaf S.L., Mean square solutions of second-order random differential equations by using the differential transformation method, Open Journal of Applied Sciences, 6-4 (2016) 287-297.

[12] Villafuerte L. and Cortés J.-C., Solving Random Differential Equations by Means of Differential Transform Methods, Advances in Dynamical Systems and Applications, 8-2 (2013) 413-425.

[13] Calbo G., Cortés J.-C., Jódar L. and Villafuerte L., Solving the random Legendre differential equation: mean square power series solution and its statistical functions, Comput. Math. Appl., 61-9 (2011) 2782–2792.

[14] Villafuerte L., Braumann C.A., Cortés J.-C. and Jódar L., Random differential operational calculus: Theory and applications, Computers and Mathematics with Applications, 59-1 (2010) 115-125.

[15] Gökdoğan A., Merdan M. and Yildirim A., The Modified Algorithm for the Differential Transform Method to Solution of Genesio Systems, Communications in Nonlinear Science and Numerical Simulation, 17-1 (2012) 45-51.

[16] Benhammouda B. and Vazquez-Leal H., Analytical solutions for systems of partial differential–algebraic equations, SpringerPlus, 3-1 (2014) 137.

[17] Sungu, I.C. and Demir, H., A Computational Method for the Time-Fractional Navier-Stokes Equation, Cumhuriyet Science Journal, 39-4 (2018) 900-911.

[18] Merdan, M., Bekiryazici, Z., Kesemen, T. and Khaniyev, T., Analyzing the dynamics of Ebola transmission with random effects. Communications in Mathematical Biology and Neuroscience, 2018 (2018) Article-ID 22.

[19] Mehdi Rashidi, M. andErfani, E., The modified differential transform method for investigating nano boundary-layers over stretching surfaces. International Journal of Numerical Methods for Heat & Fluid Flow, 21-7 (2011) 864-883.

[20] Onwubuoya, C., Nwanze, D. E., Erejuwa, J. S. and Akinyemi, S. T., An Approximate Solution of a Computer Virus Model with Antivirus using Modifed Differential Transform Method, International Journal of Engineering Research & Technology, 7-4 (2018) 154-161.

[21] Bekiryazici, Z., Bazi Kompartmanli Modellerin Rastgele Ektiler Altinda Incelenmesi, PhD Thesis, Karadeniz Technical University, Trabzon, 2017.

Generalized Derivations of Hyperlattices

Seda OĞUZ ÜNAL[1] [iD] *, Hasret DURNA[2*]* [iD]

[1] *Cumhuriyet University, Education Faculty, Department of Science and Education, Sivas, Turkey*

[2] *Cumhuriyet University, Faculty of Science, Department of Mathematics, Sivas, Turkey*

Abstract. In this paper the notion of generalized derivation for a hyperlattice is introduced and some basic properties of them are derived.

2010 *Mathematics Subject Classification:* 06B35; 06B75.

*Keywords***:** Generalized derivations, Hyperlattice.

Hiperlatisler Üzerinde Genelleştirilmiş Türevler

Özet. Bu makalede hiperlatisler üzerinde genelleştirilmiş türev kavramı tanıtıldı ve bunların bazı temel özellikleri elde edildi.

*Anahtar Kelimeler***:** Genelleştirilmiş türevler, Hiperlatis.

1. INTRODUCTION AND PRELIMINARIES

Firstly, Marty introduced the notion of hyperstructure in [1] at 8th Congress of Scandinavian Mathematicians. Normally, the composition of two elements is an element in classical algebraic structures, but the composition of two elements is a set in algebraic hyperstructures. After this study, many authors studied this subject. The many concepts in pure and applied mathematics were applied to hyperstructures [2,3]. There come out many kinds of hyperalgebras such as hypergroups in [4, 5], hyperrings in [6,7] etc. In [8], Konstantinidou and Mittas introduced hyperlattices and in [9] superlattices in [9] (for more details see [10] and [11]). In particular some interesting results of the theory of hyperlattices studied by Rasouli and Davvaz in [12, 13].

Derivations in rings and near-rings have been studied by many mathematicians in several ways [14, 15]. Bresar [16] introduced the generalized derivation in rings and many mathematicians studied on this concept. N. O. Alshehri applied the notion of generalized derivation in ring theory to lattices [17]. Now, we define the notion of derivation on hyperlattice. In this paper we aim to generalize some results given in [17] and [18] to generalized derivations of hyperlattices. In this way, we define generalized derivation on hyperlattice and give an example.

In this section, we first recall some definitions and basic results (for more detailed information see [10,12,13]).

Definition 1.1 ([13]) *Let L be a nonempty set and $\vee\colon L \times L \to P^*(L)$ be a hyperoperation, where $P(L)$ is a power set of L and $P^*(L) = P(L) - \emptyset$ and $\wedge\colon L \times L \to L$ be an operation. Then $(L,\vee,\wedge)$ is a hyperlattice if*

    (1) for all $a \in L, a \in a \vee a, \ a \wedge a = a$;

    (2) for all $a, b \in L, a \vee b = b \vee a, \ a \wedge b = b \wedge a$;

    (3) for all $a, b, c \in L, (a \vee b) \vee c = a \vee (b \vee c); \ (a \wedge b) \wedge c = a \wedge (b \wedge c)$;

    (4) for all $a, b \in L, a \in [a \wedge (a \vee b)] \cap [a \vee (a \wedge b)]$;

    (5) if $a \in a \vee b$ for all $a, b \in L$, then $a \wedge b = b$.

Let A and B be nonempty subsets of L then, $A \wedge B = \{a \wedge b | a \in A, b \in B\}$, $A \vee B = \{a \vee b \mid a \in A, b \in B\}$.

Let L be a hyperlattice. For each $x, y \in L$, we define two relations on L as follows: $(x, y) \in \leq$ if and only if $x = x \wedge y$, $(x, y) \in \lessgtr$ if and only if $y \in x \vee y$. For all nonempty subsets A and B of L, we define $A \leq B$ if there exist $a \in A$ and $b \in B$ such that $a \leq b$.

A zero of a hyperlattice L is an element 0 with $0 \leq x$ for all $x \in L$. A unit 1, satisfies $x \leq 1$ for all $x \in L$, so it can be seen that there are at most one zero and at most one unit. A bounded hyperlattice is one that has both 0 and 1. In a bounded hyperlattice $L, \ y$ is a complement of x if $x \wedge y = 0$ and $1 \in x \vee y$. The set of complement elements of x is denoted by x^c. A complemented hyperlattice is a bounded hyperlattice in which every element has at least one complement.

Definition 1.2 ([3]) *An element $a \in L$ is called a scalar element if the set $a \vee x$ for all $x \in L$ has only one element.*

Proposition 1.3 ([13]) *Let $(L,\vee,\wedge)$ be a hyperlattice. Then the following hold:*

(1) $\leq = \lessgtr$ and $(L, \leq)$ is a poset. Also we can replace Definition 1.1 (4) by $x \in x \wedge (x \vee y)$ for all $x, y \in L$;

(2) $x \wedge y \leq x, \ y \leq x \vee y$ for all $x, y \in L$;

(3) $X \subseteq (X \vee X) \cap (X \wedge X)$ for a nonempty subset X of L;

(4) $X \vee (Y \vee Z) = (X \vee Y) \vee Z$ and $X \wedge (Y \wedge Z) = (X \wedge Y) \wedge Z$ for all nonempty subsets X, Y, Z of L;

(5) If $x \leq y$, then $x \wedge z \leq y \wedge z$ for all $x, y, z \in L$;

(6) If $x, y \in x \vee y$, then $x = y$, so $x \vee y = L$ implies that $x = y$ for all $x, y \in L$;

(7) If $x \vee y = \{0\}$, then $x = y = 0$ for all $x, y \in L$;

(8) If 0 is a scalar element of L, then $0 \vee 0 = 0, x \vee 0 = \{x\}$ for all $x \in L$.

Definition 1.4 ([13]) *A subhyperlattice of a hyperlattice L is a nonempty subset of L which is closed under the hyperoperation $\vee$ and operation $\wedge$ as defined in L.*

Definition 1.5 ([13]) *A hyperlattice $(L,\wedge,\vee, 0, 1)$ is said to be a distributive if for every $a, b, c \in L, a \wedge (b \vee c) = (a \wedge b) \vee (a \wedge c)$ is hold.*

Definition 1.6 ([13]) *Let* $(L, \wedge, \vee)$ *be a hyperlattice and* I *be a nonempty subset of* L. *Then* I *is called a hyperideal of* L *when:*

(i) I *is a subhyperlattice;*

(ii) $x \in I$ *and* $y \in L$ *imply* $x \wedge y \in I$.

Definition 1.7 *Let* L *be a hyperlattice. A mapping* $d: L \to L$ *such that, for all* $x, y \in L$, *we have*

(1) $d(x \vee y) \subseteq d(x) \vee d(y)$, (2) $d(x \wedge y) \in (d(x) \wedge y) \vee (x \wedge d(y))$

is said to be a derivation on L, and the pair (L, d) is said to be a differential hyperlattice, or more precisely, a hyperlattice with a derivation. If the map d such that $d(x \vee y) = d(x) \vee d(y)$ for all $x, y \in L$ and satisfies the condition (2), then d is called a strong derivation of L. In this case, the pair (L, d) is called a strongly differential hyperlattice

2. GENERALIZED DERIVATION OF HYPERLATTICES

In this section we define generalized derivation and strong generalized derivation of hyperlattice and give examples. Through this section L will denote a bounded hyperlattice and 0 be scalar element of L unless otherwise specified.

Definition 2.1 *A mapping* $D: L \to L$ *is called a generalized derivation on* L *if there exists a derivation* $d: L \to L$ *such that*

(1) $D(x \vee y) \subseteq D(x) \vee D(y)$

(2) $D(x \wedge y) \in (D(x) \wedge y) \vee (x \wedge d(y))$

for all $x, y \in L$. *The pair* (L, D) *is said to be a differential hyperlattice or is said to be hyperlattice with generalized derivation. The map* D *is called strong generalized derivation if* $D(x \vee y) = D(x) \vee D(y)$ *and satisfies the condition (2). Then the pair* (L, D) *is called a strongly differential hyperlattice.*

Example 2.2. *Let* $L = \{0, a, b, 1\}$ *and define* $\wedge$ *and* $\vee$ *by the following Cayley tables*

$\wedge$	0	a	b	1
0	0	0	0	0
a	0	a	0	a
b	0	0	b	b
1	0	a	b	1

$\vee$	0	a	b	1
0	$\{0\}$	$\{a\}$	$\{b\}$	$\{1\}$
a	$\{a\}$	$\{0, a\}$	$\{1\}$	$\{b, 1\}$
b	$\{b\}$	$\{1\}$	$\{0, b\}$	$\{a, 1\}$
1	$\{1\}$	$\{b, 1\}$	$\{a, 1\}$	L

Then $(L, \wedge, \vee)$ is a hyperlattice. Define the maps $d: L \to L$ by $dx = \begin{cases} 0, & x = 0, a \\ b, & x = b, 1 \end{cases}$ and $D: L \to L$ by $Dx = x$. Then we can see that D is a generalized derivation on L.

Definition 2.3 *Let* D *be a generalized derivation on* L. *If* $x \leq y$ *implies* $Dx \leq Dy$ *for all* $x, y \in L$, D *is called an isotone generalized derivation.*

Example 2.4 *Let L be a hyperlattice as in Example 2.2. It is easy to check that D is an isotone generalized derivation of L.*

Definition 2.5 *A generalized derivation D is said to be contractive if $Dx \leq x$ for all $x \in L$.*

Proposition 2.6 *Let D be a contractive generalized derivation and d be contractive derivation on L. Then the following hold for all $x, y \in L$*

a) If L is distributive hyperlattice then $dx \leq Dx$,

b) If I is a hyperideal of L then $DI \subseteq I$,

c) $D0 = 0$

d) $Dx \in Dx \vee (x \wedge d1)$

e) $D1 \in D1 \vee D1$

Proof. a) *For all $x \in L$, we have*

$$Dx \wedge dx = D(x \wedge x) \wedge dx \in \big((Dx \wedge x) \vee (x \wedge dx)\big) \wedge dx = (Dx \vee dx) \wedge dx.$$

Since L is distributive hyperlattice, we obtain

$Dx \wedge dx \in (Dx \wedge dx) \vee (dx \wedge dx)$. *By using Definition 1.1 (1) we have* $Dx \wedge dx \in (Dx \wedge dx) \vee dx$. *Also from Definition 1.1 (5) we get* $(Dx \wedge dx) \wedge dx = dx$. *Then it is a routine matter to show that* $Dx \wedge dx = dx$. *Consequently we have* $dx \leq Dx$.

b) Let $y \in DI$. Then there exist an $x \in I$ such that $y = Dx \leq x$. Since I is a hyperideal of L, we have $y \in I$.

c) It is a routine matter to show that $D0 = D(0 \wedge 0) \in (D0 \wedge 0) \vee (0 \wedge d0)$. By using [18] we have $D0 \in 0$. Hence the result.

d) $Dx = D(x \wedge 1) \in (Dx \wedge 1) \vee (x \wedge d1) = Dx \vee (x \wedge d1)$

e) It is clear from Definition 2.1.

Proposition 2.7 *Let D be a contractive generalized derivation, then we have*

a) If $d1 \leq x$, then $d1 \leq Dx$,

b) If $x \leq d1$, then $Dx = x$.

Proof. a) *Let $x \in L$ such that $d1 \leq x$, by using Proposition 2.6 d) we have $Dx \in Dx \vee (x \wedge d1)$ hence $Dx \in Dx \vee d1$. Therefore we obtain $d1 \leq Dx$.*

b) Let $x \in L$ such that $x \leq d1$, by using Proposition 2.6 d) we have $Dx \in Dx \vee (x \wedge d1) = Dx \vee x$, then $x \leq Dx$. On the other hand D is a contractive generalized derivation, therefore $Dx = x$.

Theorem 2.8 *Let D be a contractive generalized derivation on L. Then the following conditions are equivalent:*

1) $Dx = x$ for all $x \in L$,

2) $D(x \vee y) = (x \vee Dy) \wedge (Dx \vee y)$.

Proof. **(1)⇒(2)** *Since* $D(x \vee y) = x \vee y$ *and* $(x \vee Dy) \wedge (Dx \vee y) = x \vee y$, *we get* $D(x \vee y) = (x \vee Dy) \wedge (Dx \vee y)$.

(2)⇒(1) *By putting* $x = y$ *in (2) we have* $Dx = x$ *for all* $x \in L$ *since* D *is contractive generalized derivation.*

Theorem 2.9 *Let* D *be a generalized derivation on* L, *then the following conditions are hold.*

1) D *is an isotone generalized derivation.*

2) $Dx \vee Dy \leq D(x \vee y)$.

Proof. 1) *If* $x \leq y$, *then we get* $y \in x \vee y$. *Therefore* $Dy \in D(x \vee y)$. *By using Definition 2.1 we have* $Dy \in D(x \vee y) \subseteq Dx \vee Dy$. *Hence we conclude* $Dx \leq Dy$.

2) *Since* D *is isotone generalized derivation, we have* $Dx \leq D(x \vee y)$ *and* $Dy \leq D(x \vee y)$. *Hence we conclude* $Dx \vee Dy \leq D(x \vee y)$.

Acknowledgements

REFERENCES

[1] F. Marty, Sur une generalization de la notion de groupe, 8th Congress Math. Scandinaves, Stockholm (1934) 45–49.

[2] R. Ameri, M. Norouzi, New fundamental relation of hyperrings, European J. Combin. 34 (5) (2013) 884–891.

[3] P. Corsini, V. Leoreanu, Applications of Hyperstructure Theory, Kluwer Academic Publishers, Dordrecht (2003).

[4] J. Jantosciak, Transposition hypergroups: noncommutative join spaces. J. Algebra 187(1) (1997) 97–119.

[5] J. Zhan, B. Davvaz, P. K. Shun, Probability n-arybypergroups, Information Science 180 (2010) 1159–1166.

[6] R. Rosaria. Hyperaffine planes over hyperrings, Discrete Math. 155(1-3)(1996) 215–223.

[7] J. Zhan, C. Irina,Γ-hypermodules:isomorphism theorems and regularrelations, U.P.B. Sci Bull, Ser. A 73 (2011) 71–78.

[8] M. Konstantinidou, J. Mittas. An introduction to the theory of hyperlattices. Math. Balkanica,1977, 7: 187–193.

[9] Mittas, M. Konstantinidou, Sur unenouvellegeneration de la notion de treillis,Lessupertreilliset certaines de leursproprietiesgenerales,AnnSciUnivBlaise Pascal Ser Math, 25 (1989) 61–83.

[10] Xiaozhi Guo, Xiaolong Xin, Hyperlattices, Pure and Applied Mathematics (Xi'an) 20 (2004) 40–43.

[11] A. Rahnami-Barghi. The prime ideal theorem for distributive hyperlattices. Ital. J. Pure Appl. Math 10 (2001) 75–78.

[12] S. Rasouli, B. Davvaz, Construction and spectral topology on hyperlattices. Mediterr. J. Math.,7(2) (2010) 249–262.

[13] S. Rasouli, B. Davvaz, Lattices derived from hyperlattices, Commun. Algebra 38 (8) (2010) 2720–2737.

[14] H. E. Bell, G. Mason,Derivation in Near-Rings, North-Holland Math. Stud., North-Holland, Amsterdam 137 (1987).

[15] E. C. Posner, Derivations in prime rings, Proc. Amer. Math. Soc. 8(1957) 1093–1100.

[16] M. Bresar, On the distance of composition of the two derivations to the generalized derivations, Glasgow math. J., 33(1), (1991), 89-93.

[17] N. O. Alshehri, Generalized derivations of lattices, Int. J. Contemp. Math. Sciences, 5 (13) (2010) 629-640.

[18] J. Wang, Y. Jun, Xiaolong Xin, Y. Zou, On derivations of bounded hyperlattices, Journal of Mathematical Research and Applications 36(2) (2016) 151-161.

Interference-free determination of carmine in food samples using ultrasonic assisted cloud point extraction coupled with spectrophotometry

Adil ELİK[1] iD

[1]Cumhuriyet University, Faculty of Sciences, Department of Chemistry, TR-58140, Sivas, Turkey

Abstract. In this study, a simple, green and cost effective method of extraction and preconcentration of carmine used as a food additive in some food samples was developed using ultrasonic assisted cloud point extraction (UA-CPE) before spectrophotometric determination. Carmine was extracted from the aqueous solution using polyoxyethylenesorbitan monolaurate (Tween 20) as the extraction solvent in presence of Ni(II) at pH 6.5. Variables such as pH, amount of metal, temperature, ultrasonic effect, solvent type, type and concentration of nanionic surfactant have been optimized in detail. Under the optimum conditions, the analytical characteristics of the method are as follows; linear working range 1.5-350 μg L^{-1}; the detection limit, 0.4 μg L^{-1}; and preconcentration factor, 80. The relative standard deviation (RSD%) obtained for the 10 μg L^{-1} concentration (n: 5) of carmine was 3.7%. Recovery values for two different concentration levels were in the range of 94.8-104.7%. The accuracy and precision of the method were evaluated by intra- and inter-day studies. Finally, the method has been successfully applied to the determination of carmine in various foods.

Keywords: Carmine, food samples, ultrasound assisted extraction, green chemistry, spectrophotometry.

Spektrofotometri ile birleştirilmiş ultrasonik destekli bulutlanma noktası ekstraksiyonu kullanılarak gıda örneklerinde karminin girişimsiz tayini

Özet. Bu çalışmada, bazı gıda örneklerinde, carmine'nin spektrofotometrik tayin öncesi basit, yeşil ve düşük maliyetli özelliklere sahip ultrasonik yardımlı bulut noktası ekstraksiyonu (UA-CPE) geliştirilmiştir. Carmine, pH 6.5'de Ni (II) varlığında ekstraksiyon çözücüsü olarak polioksietilensorbitan monolaurat (Tween 20) kullanılarak sulu çözeltiden özütlenmiştir. pH, metal miktarı, sıcaklık, ultrasonik etki, solvent tipi, nanyonik yüzey aktif madde türü ve konsantrasyonu gibi değişkenler en uygun şekilde optimize edilmiştir. Optimum koşullar altında, yöntemin analitik özellikleri aşağıdaki gibidir; doğrusal çalışma aralığı 1.5-350 μg L^{-1}; tespit limiti, 0,4 μg L^{-1}; ve ön konsantrasyon faktörü, 80. Karminin 10 μg L^{-1} konsantrasyonu (n: 5) için elde edilen bağıl standart sapma (% BSS) % 3.7 idi. İki farklı konsantrasyon seviyesi için geri kazanım değerleri % 94.8-104.7 arasındaydı. Yöntemin doğruluğu ve kesinliği, gün içi ve günler arası çalışmalarla değerlendirildi. Son olarak, yöntem çeşitli gıdalarda karmin tayini için başarıyla uygulanmıştır.

Anahtar Kelimeler: Carmine, gıda örnekleri, ultrason destekli ekstraksiyon, yeşil kimya, spektrofotometri.

1. INTRODUCTION

Synthetic food dyes are used in different industries such as paper, textile, ink, plastics, cosmetics, pharmaceuticals, beverages and food. Food dyes are widely used to make food more attractive and appetizing. Generally, food dyes have complex aromatic structures and are stable. Therefore, they

are biodegradable. Carmine (E120), used as a food colouring, is a bright red pigment derived from the aluminium salt of carminic acid [1]. It is used as colouring pigments in cosmetic products such as pharmaceutical formulations, eye fir and lipstick as well as many different products such as carmine, fruit juices, ice cream, yogurt and sugar. Carmine, one of the synthetic food colors, is approved for use in the USA, Canada, Korea and the European Union [2]. Acceptable daily of carmine intake (ADI) is average 5 mg based on body weight [3]. Although the amounts of carmine added to foods and drinks are strictly controlled, their use may exceed the tolerable limit. Therefore, it is very important to observe the carmine dye levels in high-consumption food products.

In recent years, the number of studies on this subject has witnessed the importance of this problem. For the analysis of food dyes fast, accurate and emphasizes the need to develop selective techniques. Until now, various methods like differential pulse polarography (DPP) [4], stripping voltammetry (SV) [5], high performance liquid chromatography (HPLC) [6], and spectrophotometry [7] have been proposed for the determination of carmine in food samples. Chromatography and polarography methods are not considered as green analytical methods due to the use of hazardous organic solvents in the chromatography and the reduction of mercury in the polarography [8]. On the other hand, HPLC and capillary electrophoresis (CE) methods are interpreted as more effective alternative methods. However, these methods are expensive, time consuming, and generates waste containing a high proportion of organic solvent [9]. Despite the high sensitivity of electroanalytical methods, its selectivity is low. Disadvantages of the stripping voltammetry (SV) include longer analysis times compared to spectroscopic methods, as well as interference that can lead to limitations [10]. UV-visible spectrometry is an important tool in this area, with a low weight and low cost. In addition, it is often used in many areas such as chemistry, food, and environment. There are two main limitations to the spectrometric determinations of food dyes. The first is the lower analytical quantity than the

quantitative limits of the UV-visible spectrometry, and the other is the possible interference effect of other chemical species present in the samples. Preconcentration-separation methods such as solid phase extraction (SPE) [11,12], cloud point extraction (CPE) [13-16], solvent extraction (SE) [17], and ion exchange (IE) [18,19] were widely used to solve these problems. The current trend in analytical chemistry, especially for quality control applications, is the development of methods that include environmentally friendly less reactive consumption. For this reason, the cloud point extraction (CPE) method, which uses surfactants for the separation and preconcentration of carmine, was used in the study. The basis of the CPE method depends on the non-ionic surfactant in the aqueous solutions becoming cloudy (forming miscellaneous) when heated to a temperature known as cloud point temperature [20]. The micelle solution, which is above the cloud point temperature, forms two separate phases as the small volume surfactant rich phase and the diluted aqueous phase [21]. By centrifugation, the surfactant-rich phase tube is collected at the bottom and the aqueous phase is separated by decantation. The surfactant phase which is then dissolved in a suitable solvent can be analyzed by a suitable technique. In addition, this method is an alternative to conventional liquid liquid extraction (LLE) due to its high enrichment factor, less desirable sample size, lower toxic reagent use, elimination of large amounts of organic solvents, use of non-toxic surfactants, safer, simpler and more economical [22].

Sonication is a powerful aid in accelerating the various steps of the analytical process especially extraction and sample preparation steps [24]. Ultrasonic energy is released at the end through a cavitation process, which involves evacuation of the formation and breakdown of microbubbles to high temperatures [24]. This energy is of great help in the pre-treatment of solid and liquid samples as it facilitates and accelerates operations such as the extraction of different chemical species (organic, biological, and inorganic compounds) from different samples such as biologicals, environmental and foods [25-28].

The purpose of this study, for the determination of carmine dye used in food samples, was to develop an analytical method that is selective, sensitive, consuming less reagents, and environmentally friendly. To achieve this goal, a combination of ultrasound-assisted cloud point extraction and spectrophotometry was used to provide environmental and low-reagent consumption. The factors affecting the efficiency of extraction were examined systematically. The proposed method was compared with some methods in the literature in terms of analytical properties. After validation of the method, the method was successfully applied to the determination of carmine in various food samples with satisfactory results.

2. MATERIALS AND METHODS

2.1. Instrumentations

Spectrophotometric analysis was performed on a double-beamed Shimadzu UV-1800 PC spectrophotometry (Kyoto, Japan) equipped with 1.0 cm quartz cells. The injection volume and detection wavelength were 500 μL and 510 nm, respectively. Ultrasonic bath (UCP-10 model, Seoul, Korea) was used for extraction of carmine and sample preparation. A Universal Hettich model centrifuge (London, UK) was used to separate the extract from the aqueous phase. All pH measurements were performed using a Selecta 2001 Sartorius model (North America) pH meter combined with a glass calomel electrode. A Labconco ultrapure water system (Kansas City, USA) was used to obtain ultra-pure water used in the experiments and 18.2 MΩ cm^{-1} resistant water was obtained.

2.2. Reagents

All working reagents were purchased from Sigma (St. Louis, Mo., USA). Standard work solutions were prepared by gradual dilution of stock solutions. The stock carmin solution was prepared in ethanol-water (50:50, v/v) at a concentration of 0.1 mol L^{-1} and stored at 4 ° C in a refrigerator. The standard Ni (II) solution (1000 mg L^{-1}) was prepared by dissolving the nitrate salt in water. 5.0% (w/v) polyoxyethylene-isobutyl monolaurate (Tween 20) was prepared by dissolving 5.0 g of Tween 20 in methanol using an ultrasonic bath and diluting to 100 mL with water. The phosphate-

citrate buffer solution was prepared by mixing 35.2 mL of 0.2 mol L^{-1} Na$_2$HPO$_4$ and 14.8 mL of 0.1 mol L^{-1} citrate solutions for pH 6.5. Prior to the experiments, all vessels (glassware, low density and high density polyethylene bottles) were kept in 10% (v / v) HNO$_3$ for at least one day and then washed five times with ultrapure water.

2.3. Sample preparation

In order to investigate the feasibility of the developed method, some food samples (strawberries, rice, sour cherry, syrup, powdered drinks, biscuits and jellybeans) were randomly selected from the markets in Sivas/Turkey. Ultrasonically assisted extraction (UAE) method was used to prepare the selected samples for analysis. Sample preparation steps were performed as follows.

First, a mixer was used to homogenize 5.0 grams of food samples. These milled samples were then transferred to a 100 mL beaker and final volume was adjusted to 50 mL with pure water by adding 0.05 mol L^{-1} NaOH solution. The extraction was performed by applying ultrasonic energy (300 W at 40 kHz ultrasound frequency) at room temperature in an ultrasonic bath until a clear solution was obtained [29]. The extract was then centrifuged at 4000 rpm for 5 minutes, and the pore size was adjusted to 0.45 mm by filtration through a membrane filter.

2.4. Ultrasonic assisted cloud point extraction

The recommended procedure was resumed as follows. First, a 3 mL aqueous sample solution containing 50 μg L^{-1} carmine was added to a 50 mL centrifuge tube, and then 1.25 mL of phosphate-citrate buffer solution was added to adjust the pH of the sample solution to 6.5. After adjusting the pH, 2.5 mL of 10 mg L^{-1} Ni (II) solution was added to form a hydrophobic complex with carmine, and the solutions were diluted to about 45 mL with distilled water. After waiting 2 minutes to form the appropriate complex (Carmine-Ni), 1.0 mL of 5.0% (w / v) Tween 20 was added to the solution

and the final volume was 50 mL. The mixture was then sonicated in an ultrasonic bath for 10 minutes at 55 °C to provide cloudiness of the surfactant. The surfactant phase was separated from the aqueous phase by centrifugation at 4000 rpm for 5 minutes. The upper aqueous phase was then withdrawn with a syringe. To reduce the viscosity of the surfactant rich phase, the remaining phase was added to 500 μL of methanol and transferred to a quartz cell. Finally, the absorbance reactivated versus schooled at 510 nm.

3.   RESULTS AND DISCUSSION
3.1. Optimization of UV detection wavelength

To determine the wavelength of the complex, the absorption spectrum as a function of reactive vacancy and the carmine concentration was investigated in the wavelength range of 350-650 nm. The studies were conducted under optimum conditions for three different concentrations of carmine.
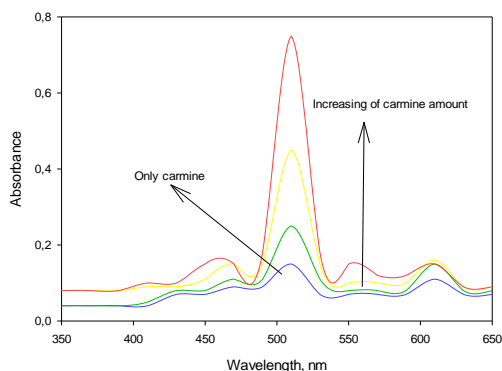
Figure 1. Spectra obtained depending on concentration of carmine (10, 50, 100 μg L^{-1}) under optimal conditions

As can be seen in Figure 1, it is understood that in the presence of Ni (II) there is a large absorption peak at about 510 nm with a significant sensitivity difference and a linear relationship with the carmine concentration. Therefore, the absorbance measurements were continued at 510 nm to increase the detection sensitivity. This shows luminescence with a red shift of 65 nm with fluorescence-specific carminic acid (λex: 493 nm, λem: 593 nm) with Al (III) (λex: 517 nm, λem: 582 nm) in contrast to the luminescence of carmine, which forms stable complexes with Ni (II) ions but does not cause any wavelength shift due to the effect of low energetic ligand [30]. In the aqueous mica medium, the absorption wavelength of the NiL_2^{2-} or H_2Ni_2 complex in the presence of Tween 20 shifted to 13 nm due to H-bonding, π-π staking and hydrophobic interactions.

3.2. Optimization of extraction conditions

In this study, the optimization of the variables that could affect the extraction efficiency was carried out by monitoring the recovery. Recovery for each variable was calculated according to the following formula.

$$\text{Recovery, } \%R = \frac{C_{int}.V_{int} - C_{final}.V_{final}}{C_{int}.V_{int}} \, 100$$

The meanings of the indices in the form are as follows. C_{int}: initial concentration, V_{int}: initial volume, C_{final} post-concentration, V_{final} final volume. For each optimal point worked, % R is calculated according to the formula above. The amount at which the highest %R ratio is obtained is chosen as the most appropriate value for that variable. The operating range and optimum value of each parameter are given in Table 1.

Table 1. Optimization of analytical variables affecting the complex formation and extraction efficiency of carmine

Parameters	Working Range	Optimum Value
pH	2.5-10.5	6.5
Ni(II) volume (10 μg L^{-1}), mL	0.0-3.0	2.5
Tween 20 volume (%5.0, a/h), mL	0.0-3.0	1.0
Sample volume, mL	5-150	40
Equilibrium Temperature, °C	25–70	55
Ultrasonic time, dk	1-30	10
Centrifugal rate, rpm	1000–4000	4000
Centrifugal time, min	1–10	2

The first parameter to be optimized in the extraction procedure is the pH of the solution. Because the pH of the solution directly affects the chemical form of the reagents. The optimum pH value should be selected to form the complex containing analyte. For these reasons, the effect of pH on the recovery of Carmine was studied in the presence of Ni (II) in the range of 2.5-10.5. The results obtained are given in Figure 2 (a). From pH 2.5 to 6.5, % R rapidly increased, but there was no significant change from pH 6.5 to 8.5. There was a significant decrease in %R at higher pH values. This decrease in extraction yield comes from the hydrolysis of Ni (II) ions. In further studies, the pH for the extraction of carmine was chosen as the optimal value of 6.5 and the pH adjustment was carried out with 0.1 mol L^{-1} phosphate-citrate buffer solution.
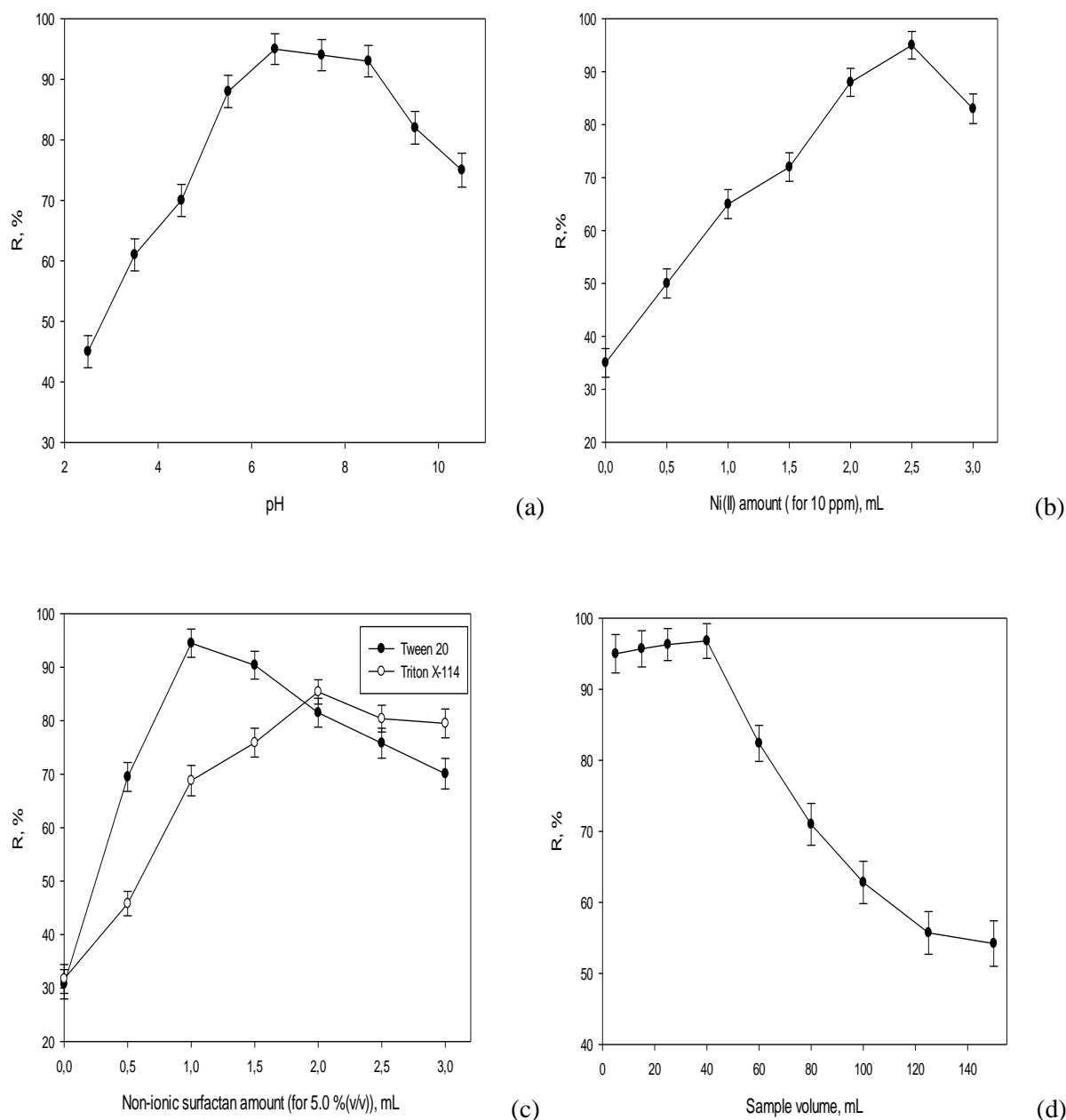
Figure 2 (a-d). Optimization study of some parameters affecting the extraction method

Preliminary experiments were carried out at pH 6.5 with some transition metal ions such as Cu (II), Fe (III) and Ni (II) in equal molar concentrations to form a chelate complex at the appropriate and sufficient consistency with the carmine in the phosphate-citrate buffer. It has been found that the best chelate complex formation and phase separation are obtained in a manner that gives maximum sensitivity when Ni(II) is used. This is due to the coordination of the positive charge of the Ni(II) ion with the phenol and keto groups of the ligand as a result of the concentration-dependent displacement-based complex formation with the $Al(OH)L_2^{2-}$ (Which can give ionic and stable metal complexes with pKa values of 2.81, 5.43 and 8.10) can be explained by the formation of chelates as a result of the decrease of the polarity of the Ni (II) ion [31].

$$Ni^{2+} + HCitrate^{3-} \rightarrow NiHCitrate^{-}, \text{ a stability constant of about } 5.11 \qquad (1)$$

$$Al(OH)L_2^{2-} + NiHCitrate^{-} \rightarrow NiL_2^{2-} + Al(Citrate)^{-} + H_2O \qquad (2)$$

$$NiL_2^{2-} + 2H_2O \rightarrow H_2NiL_2 + 2OH^{-} \qquad (3)$$
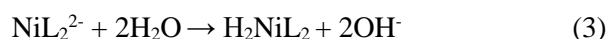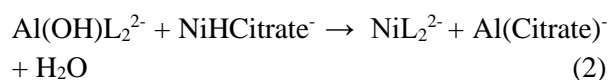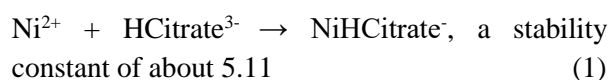
As a consequence of the increased acidity of the complex over the critical micelle concentration (CMC), the H_2NiL_2 chelate complex will readily pass through the surfactant-rich surfactant complex in a hydrophobic interaction with the hydroxyl and polar ethoxy groups of Tween 20. Then, the effect of the amount of Ni (II) in the constant concentration (10 mg L^{-1}) of carmine in% GC was investigated between 0.0-3.0 mL, keeping other parameters constant. As can be seen from Figure 2 (b), the % R is about 35% in the absence of Ni (II), but increases rapidly with increasing Ni (II) content. When 2.5 mL of the Ni (II) solution was used, the % R value was not quantitatively (~ 95%). On the other hand, in the presence of higher Ni (II), a decrease in % R was observed because the excess of Ni (II) ions pass into the surfactant phase. For these reasons, 2.5 mL Ni (II) solution was used for carmine extraction in subsequent studies.

Surfactant concentration and species are critical factors to shift to the surfactant phase of the resulting Carmine-Ni complex and should be sufficient for the quantitative extraction of the analyte. In addition, as the non-ionic surfactant volume increases, a more efficient mass transfer from the sample solution to the surfactant-rich phase can be expected. Therefore, in order to obtain the highest possible recovery value, the extraction procedure should be carefully investigated to identify the minimum required surfactant volume. For this purpose, the effect of Tween 20 and Triton X-114 non-ionic surfactants on carmine recovery was investigated at a constant concentration (5%, w/v) in the range of 0.0-3.0 mL. As can be seen in Figure 2 (c), the best recovery was obtained when 1.0 mL of Tween 20 was used. As the volume of the surfactant-rich phase obtained after centrifugation is increased, the dilution agent in the higher volumes is used. Therefore, the final volume has increased. Hence, in subsequent experiments 1.0 mL of 5.0% (w / v) Tween 20 was used to achieve good phase separation and high recovery.

Optimization of sample volume is important for both the sensitivity and the enrichment factor because carmine is found in trace quantities in food samples. The effect of sample volume on the recovery of carmine was investigated under optimum conditions from 5 mL to 150 mL and the obtained data is given in Figure 2 (d). The results of the study show that extraction after 40 mL of sample volume is reduced. For this reason, the enrichment factor was calculated as 80 with the highest sample volume (40 mL) to final volume (500 μL).

Ultrasonic time is an important parameter to accelerate the surfactant mass transfer. The time required for the two phases (aqueous phase and surfactant phase) to reach equilibrium is called the extraction time. The effect of ultrasonic time on the % GK was investigated for 1 to 30 minutes by applying ultrasonic power to the same specimens (300 W, 40 kHz). From studies, mass transfer is not

quantitatively complete, so it can be said that the% R was very low when the duration of sonication was below 5 minutes. The best recovery was achieved within 10 minutes and no significant change in recovery was observed for longer periods. In subsequent studies, 10 min was selected as the ultrasound duration for carmine extraction.

The temperature may facilitate clouding by affecting the water solubility of the extracting non-ionic surfactant (Tween 20). Furthermore, in extractions experiments, the temperature of the experimental environment must be above its clouding temperature in order for the surface-active material used to obtain a cloudy appearance, or clouding does not occur. For this reason, the effect of equilibrium temperature on recovery is investigated under optimum conditions from room temperature to 70°C. At temperatures lower than 55°C, the phase separation is very low as cloud formation is not complete. At higher temperatures, there was no phase separation due to possible degradation of the complex inverse. For this reason, the optimum equilibrium temperature for extraction of carmine was 55°C in subsequent studies.

After subjecting the test tubes to centrifugation at 4000 rpm for 5 minutes, the resulting surfactant rich phase was highly viscous and low in volume. For this reason, the final volume of the phase prior to spectrophotometric determination was set to 500 μL with methanol.

3.3. Selectivity study

After optimizing the variables that could affect the extraction, the selectivity of the selected chemical medium was tested. Method selectivity is very important for carmine extraction. As the method is developed using model solutions, potential chemical species in food samples can reduce recovery by affecting carmine's complex formation. For this reason, a wide range of intervention studies have been conducted and tolerance limits and recovery values have been determined for each species. The tolerance limit is defined as the ratio of the concentration to the concentration of carmine in the entrepreneurial

analytical signal that causes a failure of less than ± 5%. It is clear that there is no significant interference effect as shown in Table 2. In short, the proposed method has a high tolerance limit for foreign ions and can be reliably applied to the identification and extraction of carmine in food samples.

Table 2. Effect of possible interfering species on the extraction efficiency of carmine

Foreign Ions	Tolerance Limit	Recovery, %
Cd^{2+}	1000	102.1
Mg^{2+}	1000	97.7
Al^{3+}	1000	98.5
Br^-	750	101.4
SO_4^{2-}	750	96.9
Ag^+	750	96.7
Co^{2+}	750	96.8
Pb^{2+}	500	102.5
Tartrazine	500	97.7
Amaranth	500	95.3
Sudan (I-III)	500	96.4
Cr^{3+}	250	103.9
Brilliant Blue	250	95.4
Ponceau 4RC	200	95.1
Cu^{2+}	100	95.0
Mn^{2+}	50	94.4
Zn^{2+}	50	93.7

3.4. Analytical features of proposed method

The analytical properties of the method were tested in two different ways, after optimizing the variables that might affect the extraction process. First, a calibration equation using the model solution under optimum conditions, linear working range, limit of detection (LOD) and the limit of quantification (LOQ), the enrichment factor (EF), the relative standard deviation (% RSD) and some analytical including recovery% parameters were determined. In the second study, the same analytical properties were found by matrix matching by adding carmine to sample solutions at different concentrations. Both studies were repeated five times.

Calculation graphs were generated for both model solutions and matched solutions and the slopes were compared with the Student t-test. For possible matrix effect, the matrix is 95% with the

slopes of the matching standard curve, there is no significant difference between the model standard curve for confidence level and four degrees of freedom. The calculated t-factor (1.73) was below the critical Student's t (2.78), so that calibration equation obtained using model solutions in the analysis of food products could be used reliably. The detail result was shown in Table 3.

Table 3. Analytical characteristics of the method for model solutions and matrices-matched solutions

Analytical Features	For model solutions	For matrix-match solutions
Calibration equation	$A=8.25\times10^{-3}[carmine]+3.21\times10^{-4}$	$A=7.85\times10^{-3}[carmine]+4.38\times10^{-4}$
Linear range, $\mu g\ L^{-1}$	1.5–350	2-300
Limit of detection (LOD, n:12, $3\sigma_b/m$), $\mu g\ L^{-1}$	0.4	1.1
Limit of quantification (LOQ, n:12, $10\sigma_b/m$), $\mu g\ L^{-1}$	1.5	3.6
Relative standard deviation (%RSD)	3.7	3.9
Recovery, %	94.8-104.7	92.4-102.7
Preconcentration factor (PF)	80	80

Table 4. Results for the determination of carmine in food samples by the proposed method

Food Samples	Added ($\mu g\ L^{-1}$ or $\mu g\ kg^{-1}$)	Found ($\mu g\ L^{-1}$ or $\mu g\ kg^{-1}$)	Recovery (%)	RSD (%)
Candy	-	120.7	-	2.6
	20	136.2	96.8	2.8
	50	167.3	98.0	3.2
Apricot jam	-	116.7	-	2.9
	20	140.1	103.1	3.1
	50	170.7	102.4	3.3
Cherry jam	-	95.4	-	2.9
	20	110.2	95.5	3.1
	50	140.7	96.8	3.3
Strawberry jam	-	183.1	-	3.0
	20	198.8	97.5	3.2
	50	229.8	98.6	3.4
Powder beverage (sour cherry)	-	195.8	-	3.1
	20	204.6	94.8	3.3
	50	235.9	96.7	3.4
Powder beverage (peach)	-	145.6	-	2.8
	20	158.3	95.9	2.9
	50	189.9	97.1	3.2
Strawberry biscuit	-	55.7	-	2.7
	20	77.7	102.6	28
	50	108.3	101.2	3.1
Banana biscuit	-	30.8	-	2.4
	20	52.7	104.7	2.5
	50	82.8	102.5	2.7
Jelibon	-	125.5	-	2.8
	20	142.2	97.7	2.9
	50	173.0	98.6	3.1

3.5. Precision, accuracy and applications

Since we do not have a certified reference material containing carmine, two different studies have been conducted to test the correctness and accuracy of the proposed method. The accuracy of the proposed procedure was evaluated by intra-day (x) and inter-day (y) reproducibility studies. This process was performed as follows. For each study, three different carmine concentrations were added to the food samples and the results of three replicate analyses on three different days were calculated from the coefficient of variation (CV) $\% = 2^{(1-0.5 \log C)}$ from the Horwitz equation.[32] Where C is concentration with $\mu g\ L^{-1}$ units. CV_x and CV_y were calculated as described in the ISO 5725-2 guidelines [32] and ranged between 1.8-3.4% and 2.1-3.5% respectively. All CVs, intra-day (7.2%) and inter-day (11.3%), It was below the maximum values allowed by the Horwitz equation. The proposed procedure has examined the correctness of the recovery process. This process was performed as follows. Two different carmine concentrations were added to each food sample, and then the general extraction procedure was applied to these samples for the carmine assay. Quantitative recovery values were obtained during the studies. This suggests that the correctness of the proposed method has been tested safely. Detailed results are given in Table 4.

As is known, carmine is used as food dye. For this reason, food samples that are important for human health and that are consumed more are selected to test the analytical feasibility and reliability of the proposed method. Food samples were prepared for analysis as described in Section 2.3. 3.0 mL of the prepared samples were subjected to the recommended extraction procedure. The standard addition method was used to test for correctness during the analysis.

3.6. Comparison with the other methods

The contribution of the proposed method to the literature has been shown more clearly compared to other methods. The results are detailed in Table 5. As can be seen, it has been observed that the analytical properties obtained using this method are better or comparable to those of other methods. The present method has certain advantages such as low toxicity, simplicity and low cost compared to expensive, time consuming, complex but precise techniques which require a specialist user in his field such as HPLC-PDA, SWV and DPP.

Table 5. Comparison of analytical parameters of the proposed method with some of the methods reported in literature

Samples	Method	LOD	liner range	RSD, %	Recovery, %	Reference
Foods	SE/HPLC	$0.4\ mg\ L^{-1}$	$1.0\text{–}100.0\ mg\ L^{-1}$	6.8	94.1	[33]
Ice cream and soft drinks	SV	$0.002\ mg\ L^{-1}$	$0.05\text{–}0.14\ mg\ L^{-1}$	2.2	97.2	[34]
Confectionery and milk	DPP	$0.18\ mg\ L^{-1}$	$1.1\text{–}100.5\ mg\ L^{-1}$	7.8	95.0	[35]
Foods	Spectrophotometry	$0.012\ mg\ L^{-1}$	$0.04\text{–}5.0\ mg\ L^{-1}$	4.0	100.0	[36]
Foods	Spectrophotometry	$0.4\ \mu g\ L^{-1}$	$1.5\text{–}350\ \mu g\ L^{-1}$	3.7	94.8-104.7	The current method

4. CONCLUSION

In this study, a simple, easy to use, low cost and environmentally friendly method for the carmine determination of food samples was developed using ultrasonically assisted extraction before spectrophotometric detection. The effects of the main parameters such as solution pH, surfactant and metal concentration, ultrasonic time and temperature have been researched and optimized. After optimization of the experimental conditions, satisfactory results were obtained for the accuracy and precision of the method. According to our

literature review, this study is one of a limited number of studies done spectrophotometric for ultrasound-assisted extraction of carmine for trace levels in food samples. The method is simple, sensitive, selective and environmentally friendly to determine carmine in food samples and also does not require complex techniques such as high performance liquid chromatography or stripping voltammetry. Therefore, this method can be safely applied to effectively monitor carmine in terms of food safety in food products.

ACKNOWLEDGMENTS

REFERENCES

[1] Hsiu-Mei C., Ting-Chien C., San-De P., Chiang, H. L., Adsorption characteristics of Orange II and Chrysophenine on sludge adsorbent and activated carbon fibers, Journal of Hazardous Materials, 161-2,3 (2009) 1384-1390.

[2] Dinç E, Baydan E., Kanbur M., Onur, F., Spectrophotometric multicomponent determination of sunset yellow, tartrazine and allura red in soft drink powder by double divisor-ratio spectra derivative, inverse least-squares and principal component regression methods, Talanta, 58-3 (2002) 579-594.

[3] Watson D.H., Food chemical safety, volume 2: additives, Woodhead Publishing Limited, Abington Hall, Abington, Cambridge CB1 6AH, UK, (2002).

[4] Yilmaz U. T., Ergun F., Yilmaz H., Determination of the food dye carmine in milk and candy products by differential pulse polarography, Journal of Food and Drug Analysis, 22-3 (2014) 329-335.

[5] Alghamdi A.H., Alshammery H.M., Abdalla M.A., Alghamdi A.F., Determination of carmine food dye (E120) in foodstuffs by stripping voltammetry, Journal of AOAC

International, 92-5 (2009) 1454-1459.

[6] Silva T.A., Pereira G.F., Fatibello-Filho O., Eguiluz K.I.B., Salazar-Banda G.R., Electroanalytical sensing of indigo carmine dye in water samples using a cathodically pretreated boron-doped diamond electrode, Journal of Electroanalytical Chemistry, 769 (2016) 28-34.

[7] Heydari R., Hosseini M., Zarabi S., A simple method for determination of carmine in food samples based on cloud point extraction and spectrophotometric detection, Spectrochimica Acta Part A: Molecular and Biomolecular Spectroscopy, 150 (2015) 786-791.

[8] González M., Méndez J., Carnero A., Lobo M.G., Afonso, A., Optimizing conditions for the extraction of pigments in cochineals (Dactylopius coccus Costa) using response surface methodology, Journal of Agricultural and Food Chemistry, 50-24 (2002) 6968-6974.

[9] Yilmaz U.T., Ergun F., Yilmaz, H., Determination of the food dye carmine in milk and candy products by differential pulse polarography, Journal of Food and Drug Analysis, 22-3 (2014) 329-335.

[10] Zhang L., Wang H., Cao, J., Determination of carmine, allura red and erythrosine in meat product by high performance liquid chromatography, Journal of Food Safety and Quality, 7-3 (2016) 1006-1010.

[11] Qi P., Zeng T., Wen Z., Liang X., Zhang X., Interference-free simultaneous determination of Sudan dyes in chili foods using solid phase extraction coupled with HPLC–DAD, Food Chemistry, 125-4 (2011) 1462-1467.

[12] Soylak M., Unsal Y. E., Yilmaz E., Tuzen, M., Determination of rhodamine B in soft drink, waste water and lipstick samples after solid phase extraction, Food and Chemical Toxicology, 49-8 (2011) 1796-1799.

[13] Altunay N., Gürkan, R., A new cloud point extraction procedure for determination of inorganic antimony species in beverages and biological samples by flame atomic absorption spectrometry, Food Chemistry, 175 (2015) 507-515.

[14] Gürkan R., Korkmaz S., Altunay N., Preconcentration and determination of vanadium and molybdenum in milk, vegetables

and foodstuffs by ultrasonic-thermostatic-assisted cloud point extraction coupled to flame atomic absorption spectrometry, Talanta, 155 (2016) 38-46.

[15] Altunay N., Gürkan R., Orhan U., A new ultrasonic-assisted cloud-point-extraction procedure for pre-concentration and determination of ultra-trace levels of copper in selected beverages and foods by flame atomic absorption spectrometry, Food Additives & Contaminants: Part A, 32-9 (2015) 1475-1487.

[16] Elik A., Altunay N., Gürkan R., Determination of trace levels of nitrite in beverages samples through micellar improved catalytic kinetic spectrophotometry, Cumhuriyet Sci. J., 38-3 (2017) 400-411.

[17] Zaghdoudi K., Pontvianne S., Framboisier X., Achard M., Kudaibergenova R., Ayadi-Trabelsi M., Guiavarc Y., Accelerated solvent extraction of carotenoids from: Tunisian Kaki (Diospyros kaki L.), peach (Prunus persica L.) and apricot (Prunus armeniaca L.), Food Chemistry, 184 (2015) 131-139.

[18] Xia X., Zhu C., Luo J., Zeng Z., Guan C., Ng C. F., Fan H. J., Synthesis of Free-Standing Metal Sulfide Nanoarrays via Anion Exchange Reaction and Their Electrochemical Energy Storage Application. Small, 10-4 (2014) 766-773.

[19] Hong J. G., Zhang B., Glabman S., Uzal N., Dou X., Zhang H., Chen Y., Potential ion exchange membranes and system performance in reverse electrodialysis for power generation: a review, Journal of Membrane Science, 486 (2015) 71-88.

[20] Gürkan R., Altunay N., Quantification of 5-hydroxymethylfurfural in honey samples and acidic beverages using spectrophotometry coupled with ultrasonic-assisted cloud point extraction, Journal of Food Composition and Analysis, 42 (2015) 141-151.

[21] Altunay N., Gürkan R., Sertakan K., Indirect determination of free, total, and reversibly bound sulfite in selected beverages by spectrophotometry using ultrasonic-assisted cloud point extraction as a preconcentration step, Food Analytical Methods, 8-8 (2015) 2094-2106.

[22] Pourreza N., Sharifi H., Golmohammadi H., Curcumin nanoparticles combined with cloud point extraction for citrate determination in food and drug samples, Microchemical Journal, 129 (2016) 213-218.

[23] Oh J. Y., Choi S. D., Kwon H. O., Lee S. E., Leaching of polycyclic aromatic hydrocarbons (PAHs) from industrial wastewater sludge by ultrasonic treatment, Ultrasonics Sonochemistry, 33 (2016) 61-66.

[24] Lin S., Zhou X., Ge L., Ng S. H., Zhou X., Chang, V.W.C., Development of an accelerated leaching method for incineration bottom ash correlated to toxicity characteristic leaching protocol, Electrophoresis, 37-19 (2016) 2458-2461.

[25] Doche M.L., Mandroyan A., Mourad-Mahmoud M., Moutarlier V., Hihn J.Y., An ultrasonic-assisted process for copper recovery in a des solvent: Leaching and re-deposition, Chemical Engineering and Processing: Process Intensification, 121 (2017) 90-96.

[26] Güney M., Elik A. Comparison of probe with bath ultrasonic leaching procedures for preparation to heavy metal analysis of bio-collectors prior to atomic absorption spectrometry, Communications in Soil Science and Plant Analysis, 48-15 (2017) 1741-1752.

[27] Kakavandi M.G., Behbahani M., Omidi F., and Hesam G., Application of ultrasonic assisted-dispersive solid phase extraction based on ion-imprinted polymer nanoparticles for preconcentration and trace determination of lead ions in food and water samples, Food Analytical Methods, 10-7 (2017) 2454-2466.

[28] Dağdeviren S., Altunay N., Sayman,Y., Gürkan R., A new method of UA_CPE coupled with spectrophotometry for the faster and cost-effective detection of proline in fruit juice, honey, and wine, Food Chemistry, 255 (2018) 31-40.

[29] Lim H. S., Choi J. C., Song S. B., Kim M., Quantitative determination of carmine in foods by high-performance liquid chromatography, Food Chemistry, 158 (2014) 521-526.

[30] Kunkely H., Vogler A., Absorption and luminescence spectra of cochineal, Inorganic Chemistry Communications, 14-7 (2014) 1153-

1155.

[31] Wyrzykowski D., Chmurzyński L., Thermodynamics of citrate complexation with Mn^{2+}, Co^{2+}, Ni^{2+} and Zn^{2+} ions, Journal of Thermal Analysis and Calorimetry, 102-1 (2009) 61-64.

[32] Goscinny S., Hanot V., Halbardier J.F., Michelet J. Y., Van Loco J., Rapid analysis of melamine residue in milk, milk products, bakery goods and flour by ultra-performance liquid chromatography/tandem mass spectrometry: From food crisis to accreditation, Food Control, 22-2 (2011) 226-230.

[33] Lim H. S., Choi J. C., Song S. B., Kim M., Quantitative determination of carmine in foods by high-performance liquid chromatography, Food Chemistry, 158 (2014) 521-526.

[34] Alghamdi A.H., Alshammery H.M., Abdalla M.A., Alghamdi A.F., Determination of carmine food dye (E120) in foodstuffs by stripping voltammetry, Journal of AOAC International, 92-5 (2009) 1454-1459.

[35] Yilmaz U.T., Ergun F., Yilmaz H., Determination of the food dye carmine in milk and candy products by differential pulse polarography, Journal of Food and Drug Analysis, 22-3 (2014) 329-335.

[36] Heydari R., Hosseini M., Zarabi, S.A., simple method for determination of carmine in food samples based on cloud point extraction and spectrophotometric detection, Spectrochimica Acta Part A: Molecular and Biomolecular Spectroscopy, 150 (2015) 786-791.

Interval-Valued Fuzzy Parameterized Intuitionistic Fuzzy Soft Sets and Their Applications

Hüseyin KAMACI [1]

[1] *Yozgat Bozok University, Faculty of Science and Arts, Department of Mathematics, Yozgat, TURKEY*

Abstract. In recent years, the fuzzy sets, interval-valued fuzzy sets, intuitionistic fuzzy sets and soft sets, which offer different perspectives for the structures containing the uncertainties, have attracted the interest of many researchers. Also, the intuitionistic fuzzy soft sets produced by combining the intuitionistic fuzzy sets with the soft sets have been widely studied. In this work, the concept of interval-valued fuzzy parameterized intuitionistic fuzzy soft set (IVFPIFS set) is introduced. This set is the generalization of soft sets, fuzzy soft sets, fuzzy parameterized (fuzzy) soft sets, interval-valued fuzzy parameterized (fuzzy) soft sets, intuitionistic fuzzy soft sets and fuzzy parameterized intuitionistic fuzzy soft sets. For the IVFPIFS sets, basic operations such as complement, union and intersection are defined. Also, the properties of these operations are investigated in detail. Lastly, an algorithm by using the aggregation operators based on the IVFPIFS sets is constructed. The examples are given to verify the feasibility and validity of the proposed algorithm.

Keywords: Fuzzy set, Interval-valued fuzzy set, Intuitionistic fuzzy set, Intuitionistic fuzzy soft set, IVFPIFS set [2000] 03E72, 03B52,94D05.

Aralık Değerli Bulanık Parametreli Sezgisel Bulanık Esnek Kümeler ve Uygulamaları

Özet. Son yıllarda, belirsizlik içeren yapılar için farklı perspektifler sunan bulanık kümeler, aralık değerli bulanık kümeler, sezgisel bulanık kümeler ve esnek kümeler birçok araştırmacının ilgisini çekmiştir. Ayrıca, sezgisel bulanık kümeleri esnek kümelerle birleştirerek oluşturulan sezgisel bulanık esnek kümeler de geniş ölçüde çalışılmıştır. Bu çalışmada, aralık değerli bulanık parametreli sezgisel bulanık esnek küme (ADBPSBE küme) kavramı tanıtılmıştır. Bu küme, esnek kümelerin, bulanık esnek kümelerin, bulanık parametreli (bulanık) esnek kümelerin, aralık değerli bulanık parametreli (bulanık) esnek kümelerin, sezgisel bulanık esnek kümelerin ve bulanık parametreli sezgisel bulanık esnek kümelerin genelleştirilmesidir. ADBPSBE kümeler için tümleyen, birleşim ve kesişim gibi temel işlemler tanımlanmıştır. Ayrıca, bu işlemlerin özellikleri detaylı olarak araştırılmıştır. Son olarak, ADBPSBE kümeler üzerine temellenmiş birleştirme operatörlerini kullanarak bir algoritma oluşturulmuştur. Önerilen algoritmanın uygulanabilirliğini ve geçerliliğini test etmek için örnekler verilmiştir.

Anahtar Kelimeler: Bulanık küme, Aralık değerli bulanık küme, Sezgisel bulanık küme, Sezgisel bulanık esnek küme, ADBPSBE küme [2000] 03E72, 03B52,94D05.

1. INTRODUCTION

It is natural to deal with uncertainties and imprecise data in various areas such as economics, environmental science, social science, medical science and engineering. This situation is part of the complexity of the real world. Some kinds of uncertainties are major problems which cannot be dealt with by classical methods. Therefore, the researchers need new mathematical tools to overcome these difficulties. Fuzzy set theory, offered by Zadeh [1], was developed as an important mathematical tool to resolve the uncertainty and ambiguity issues. Sambuc [2] proposed a new approach using Int([0,1]) consisting of all closed subintervals of the interval [0,1] instead of the interval [0,1] in the membership function of the fuzzy set. Moreover, Atanassov [3] defined an intuitionistic fuzzy set which is an extension of the concept of a fuzzy set. Afterwards, Atanassov and Gargov [4] presented the concept of interval-valued intuitionistic fuzzy set developed by taking the interval-valued fuzzy values instead of fuzzy values of membership and non-membership in the intuitionistic fuzzy soft set.

In 1999, Molodtsov [5] introduced the soft set theory which is a general mathematical tool for dealing with uncertain data. In [6-8], the researchers contributed to the operations of soft sets. Furthermore, Aktaş and Çağman [9] focused on the notion of soft group, thus they pioneered the idea of algebraic structures on the soft sets. Immediately after, the algebraic structures such as the soft semiring, soft ring, soft module and soft near-ring were discussed [10-13]. In [14,15], the authors addressed the fuzzification of the parameters of the soft sets. Moreover, the products [16], means [17] and relations [18] of fuzzy parameterized soft sets were derived. Deli and Çağman [19] discussed the soft set, whose parameters have intuitionistic fuzzy weights. Also, Deli and Karataş [20] introduced interval valued intuitionistic fuzzy parameterized soft sets and their some operations. While the operational and structural improvements in the soft sets continued, Çağman et al. [21] initiated a new theory called the fuzzy soft set. Later, they created a selection algorithm using the fs-aggregation operator based on the fuzzy soft set. Many researchers aimed to improve and further extend these theories by using the matrix representations of the soft sets and fuzzy soft sets [22-27]. Maji et al. [28] introduced an intuitionistic fuzzy soft set by embedding the idea of the intuitionistic fuzzy set into the soft set. Xu et al. [29] further researched on the intuitionistic fuzzy soft sets. Çağman and Karataş [30] redefined intuitionistic fuzzy soft set by utilizing the concept of fuzzy soft set defined in [21]. Also, they derived new operations for intuitionistic fuzzy soft sets and obtained several propositions and conclusions. In [31], the authors focused on the similarity measure between two intuitionistic fuzzy soft sets. In addition to these developments in the soft set theory, many studies were published about new findings and results on the different types of soft sets such as interval-valued fuzzy soft sets, intuitionistic fuzzy sets and neutrosophic soft sets [32-39].

In this paper, we define IVFPIFS sets and their operations. Also, we give various propositions which are related to the relations and operations on the IVFPIFS sets. Additionally, we present two IVFPIFS-aggregation operators and accordingly the aggregate interval-valued intuitionistic fuzzy sets produced by employing these operators. By using new notions, we give an algorithm with illustrative examples.

2. PRELIMINARIES

In this section, the concepts of fuzzy set, interval-valued fuzzy set, intuitionistic fuzzy set, interval-valued intuitionistic fuzzy set, soft set and intuitionistic fuzzy soft set are given.

Definition 2.1. ([1]) Let A be a collection of objects (points) denoted by a_i. Then, a fuzzy set W in A is defined as

$$W = \{\alpha_W(a_i)/a_i : a_i \in A\}$$

where $\alpha_W: A \longrightarrow [0,1]$ is called the membership function of W. The value $\alpha_W(a_i)$ denotes the degree of membership of the element $a_i \in A$ into the set W.

Definition 2.2. ([2]) Let A be a collection of objects (points) denoted by a_i. Also, let $Int([0,1])$ be the set of all closed subintervals of the interval $[0,1]$. Then, an interval-valued fuzzy set X in A is defined as

$$X = \{\beta_X(a_i)/a_i: \ a_i \in A\}$$

where $\beta_X: A \longrightarrow Int([0,1])$ is called the membership function of X such that $\beta_X(a_i) = [\underline{\beta_X}(a_i), \overline{\beta_X}(a_i)]$ and $0 \leq \underline{\beta_X}(a_i) \leq \overline{\beta_X}(a_i) \leq 1$. The values $\underline{\beta_X}(a_i)$ and $\overline{\beta_X}(a_i)$ denote the lower and upper degrees of membership of the element $a_i \in A$ into the set X, respectively.

State that the set of all interval-valued fuzzy sets on the set A is denoted by $IVFS(A)$.

Definition 2.3. ([3]) Let A be a collection of objects (points) denoted by a_i. Then, an intuitionistic fuzzy set Y in A is defined as

$$Y = \{< \gamma_Y^+(a_i), \gamma_Y^-(a_i) >/a_i: \ a_i \in A\}$$

where $\gamma_Y^+, \gamma_Y^-: A \longrightarrow [0,1]$ are respectively called the membership function and the non-membership function of Y with property $0 \leq \gamma_Y^+(a_i) + \gamma_Y^-(a_i) \leq 1$. The values $\gamma_Y^+(a_i)$ and $\gamma_Y^-(a_i)$ denote the degrees of membership and non-membership of the element $a_i \in A$ into the set Y, respectively.

The remaining part $\gamma_Y^*(a_i) = 1 - \gamma_Y^+(a_i) - \gamma_Y^-(a_i)$ is called the indeterministic part of $a_i \in A$.

State that the set of all intuitionistic fuzzy sets on the set A is denoted by $IFS(A)$.

Remark: If $\gamma_Y^+(a_i) + \gamma_Y^-(a_i) = 1$ for all a_i then intuitionistic fuzzy set Y degenerates into a fuzzy set.

Proposition 2.4. ([3]) Let Y_1 and Y_2 be two intuitionistic fuzzy sets on A. Then,

i) $Y_1 \subseteq Y_2 \iff \gamma_{Y_1}^+(a_i) \leq \gamma_{Y_2}^+(a_i)$ and $\gamma_{Y_1}^-(a_i) \geq \gamma_{Y_2}^-(a_i)$ for all $a_i \in A$.

ii) $Y_1 \cap Y_2 = \{< inf\{\gamma_{Y_1}^+(a_i), \gamma_{Y_2}^+(a_i)\}, sup\{\gamma_{Y_1}^-(a_i), \gamma_{Y_2}^-(a_i)\} >/a_i: \ a_i \in A\}$.

iii) $Y_1 \cup Y_2 = \{< sup\{\gamma_{Y_1}^+(a_i), \gamma_{Y_2}^+(a_i)\}, inf\{\gamma_{Y_1}^-(a_i), \gamma_{Y_2}^-(a_i)\} >/a_i: \ a_i \in A\}$.

iv) $Y_1^c = \{< \gamma_{Y_1}^-(a_i), \gamma_{Y_1}^+(a_i) >/a_i: \ a_i \in A\}$.

Definition 2.5. ([4]) Let A be a collection of objects (points) denoted by a_i. Also, let $Int([0,1])$ be the set of all closed subintervals of the interval $[0,1]$. Then, an interval-valued intuitionistic fuzzy set Z in A is defined as

$$Z = \{< \gamma_Z^+, \gamma_Z^- >/a_i: a_i \in A\}$$

where $\gamma_Z^+ = [\underline{\gamma_Z^+}(a_i), \overline{\gamma_Z^+}(a_i)], \gamma_Z^- = [\underline{\gamma_Z^-}(a_i), \overline{\gamma_Z^-}(a_i)]: A \longrightarrow Int([0,1])$ are respectively called the membership function and the non-membership function of Z with property $0 \leq \overline{\gamma_Z^+}(a_i) + \overline{\gamma_Z^-}(a_i) \leq 1$ and $0 \leq \underline{\gamma_Z^+}(a_i) + \underline{\gamma_Z^-}(a_i) \leq 1$. Here, the values $\underline{\gamma_Z^+}(a_i)$ and $\overline{\gamma_Z^+}(a_i)$ denote the lower and upper degrees of membership of the element $a_i \in A$, and also the values $\underline{\gamma_Z^-}(a_i)$ and $\overline{\gamma_Z^-}(a_i)$ denote the lower and upper degrees of non-membership of the element $a_i \in A$, respectively.

State that the set of all interval-valued intuitionistic fuzzy sets on the set A is denoted by $IVIFS(A)$.

Note: If we use notations γ_i^+ and γ_i^- instead of $\gamma_Z^+(a_i)$ and $\gamma_Z^-(a_i)$ for $a_i \in A$, then $\gamma_i = <\gamma_i^+, \gamma_i^- > = <[\underline{\gamma_i^+}, \overline{\gamma_i^+}], [\underline{\gamma_i^-}, \overline{\gamma_i^-}] >$ denotes interval-valued intuitionistic fuzzy value (shortly, IVIF value) of $a_i \in A$.

Definition 2.6. ([40,41]) Let $\gamma_i = <\gamma_i^+, \gamma_i^- > = <[\underline{\gamma_i^+}, \overline{\gamma_i^+}], [\underline{\gamma_i^-}, \overline{\gamma_i^-}] >$ be the IVIF value of $a_i \in A$. Then, the score function and accuracy function of γ_i are respectively defined as follows:

$$Scr(\gamma_i) = \frac{1}{2}(\underline{\gamma_i^+} - \underline{\gamma_i^-} + \overline{\gamma_i^+} - \overline{\gamma_i^-}),$$

$$Acr(\gamma_i) = \frac{1}{2}(\underline{\gamma_i^+} + \underline{\gamma_i^-} + \overline{\gamma_i^+} + \overline{\gamma_i^-}).$$

To compare two IVIF values γ_1 and γ_2, Tan [40] and Xu [41] introduced a simple method as follows:

(1) If $Scr(\gamma_1) < Scr(\gamma_2)$ then $\gamma_1 < \gamma_2$

(2) If $Scr(\gamma_1) = Scr(\gamma_2)$ then

    (i) if $Acr(\gamma_1) < Acr(\gamma_2)$ then $\gamma_1 < \gamma_2$

    (ii) if $Acr(\gamma_1) = Acr(\gamma_2)$ then $\gamma_1 = \gamma_2$.

Definition 2.7. ([41]) Let $\gamma_1 = <[\underline{\gamma_1^+}, \overline{\gamma_1^+}], [\underline{\gamma_1^-}, \overline{\gamma_1^-}] >$ and $\gamma_2 = <[\underline{\gamma_2^+}, \overline{\gamma_2^+}], [\underline{\gamma_2^-}, \overline{\gamma_2^-}] >$ be two IVIF values. Then, the operations $\oplus$ and $\otimes$ for γ_1 and γ_2 are respectively defined as follows:

a) $\gamma_1 \oplus \gamma_2 = <[\underline{\gamma_1^+} + \underline{\gamma_2^+} - \underline{\gamma_1^+}\cdot\underline{\gamma_2^+}, \overline{\gamma_1^+} + \overline{\gamma_2^+} - \overline{\gamma_1^+}\cdot\overline{\gamma_2^+}], [\underline{\gamma_1^-}\cdot\underline{\gamma_2^-}, \overline{\gamma_1^-}\cdot\overline{\gamma_2^-}] >.$

b) $\gamma_1 \otimes \gamma_2 = <[\underline{\gamma_1^+}\cdot\underline{\gamma_2^+}, \overline{\gamma_1^+}\cdot\overline{\gamma_2^+}], [\underline{\gamma_1^-} + \underline{\gamma_2^-} - \underline{\gamma_1^-}\cdot\underline{\gamma_2^-}, \overline{\gamma_1^-} + \overline{\gamma_2^-} - \overline{\gamma_1^-}\cdot\overline{\gamma_2^-}] >.$

Definition 2.8. ([5,42]) Let U be a universal set and $P(U)$ be the power set of U. Also, let $\mathcal{E}$ be the set of parameters and $\mathcal{A} \subseteq \mathcal{E}$. Then, a soft set $\mathcal{F}_{\mathcal{A}}$ on U is a set of ordered pairs

$$\mathcal{F}_{\mathcal{A}} = \{(\varepsilon_j, f_{\mathcal{A}}(\varepsilon_j)) : \varepsilon_j \in \mathcal{E}, f_{\mathcal{A}}(\varepsilon_j) \in P(U)\}$$

where the function $f_{\mathcal{A}} : \mathcal{E} \longrightarrow P(U)$ such that $f_{\mathcal{A}}(\varepsilon_j) = \emptyset$ if $\varepsilon_j \notin \mathcal{A}$. Also, $f_{\mathcal{A}}$ is called an approximate function of the soft set $\mathcal{F}_{\mathcal{A}}$.

Definition 2.9. ([30]) Let U be a universal set. Also, let $\mathcal{E}$ be the set of parameters and $\mathcal{A} \subseteq \mathcal{E}$. Then, an intuitionistic fuzzy soft set (shortly, IFS set) $\Psi_{\mathcal{A}}$ on U is a set of ordered pairs

$$\Psi_{\mathcal{A}} = \{(\varepsilon_j, \psi_{\mathcal{A}}(\varepsilon_j)) : \varepsilon_j \in \mathcal{E}, \psi_{\mathcal{A}}(\varepsilon_j) \in IFS(U)\}$$

where the function $\psi_{\mathcal{A}} : \mathcal{E} \longrightarrow IFS(U)$ such that $\psi_{\mathcal{A}}(\varepsilon_j) = \emptyset$ if $\varepsilon_j \notin \mathcal{A}$. Also, $\psi_{\mathcal{A}}$ is called an approximate function of the intuitionistic fuzzy soft set $\Psi_{\mathcal{A}}$.

State that the set of all intuitionistic fuzzy soft sets on the set U is denoted by $IFSS(U)$.

3. INTERVAL-VALUED FUZZY PARAMETERIZED INTUITIONISTIC FUZZY SOFT SET

In this section, the interval-valued fuzzy parameterized intuitionistic fuzzy soft set (shortly, IVFPIFS set) is defined. Also, it is given some specific findings and results for the IVFPIFS sets.

Definition 3.1. Let U be a universal set and $\mathcal{E}$ be the set of parameters. Also, let X be a interval-valued fuzzy set over $\mathcal{E}$ with the membership function $\beta_X: \mathcal{E} \longrightarrow Int([0,1])$. Then, an interval-valued fuzzy parameterized intuitionistic fuzzy soft set (IVFPIFS set) Ψ_X on U is a set of ordered pairs

$$\Psi_X = \{(\beta_X(\varepsilon_j)/\varepsilon_j, \psi_X(\varepsilon_j)): \varepsilon_j \in \mathcal{E}, \psi_X(\varepsilon_j) \in IFS(U)\}$$

where the function $\psi_X: \mathcal{E} \longrightarrow IFS(U)$ such that $\psi_X(\varepsilon_j) = \emptyset$ if $\beta_X(\varepsilon_j) = [\underline{\beta_X}(\varepsilon_j), \overline{\beta_X}(\varepsilon_j)] = [0,0]$.

State that the set of all interval-valued fuzzy parameterized intuitionistic fuzzy soft sets on U is denoted by $IVFPIFSS(U)$.

Example 3.2. Let us assume that $U = \{u_1, u_2, u_3, u_4\}$ is the set of cars which can be purchased in a car showroom. To evaluate these cars, there may be five parameters $\mathcal{E} = \{\varepsilon_1, \varepsilon_2, \varepsilon_3, \varepsilon_4, \varepsilon_5\}$, where ε_j, $j = 1,2,3,4,5$ stand for "equipped", "speedy", "sport", "cheap" and "modern", resp. If it is taken $X_1 = \{[0.2,0.6]/\varepsilon_1, [0.55,0.75]/\varepsilon_2, [0.1,0.85]/\varepsilon_3, [0,1]/\varepsilon_4, [0.2,0.25]/\varepsilon_5\}$ and $\psi_{X_1}(\varepsilon_1) = \{< 0.4,0.3 > /u_1, < 0.7,0.2 > /u_3, < 0.11,0.7 > /u_4\}$, $\psi_{X_1}(\varepsilon_2) = \{< 0.6,0.1 > /u_2\}$, $\psi_{X_1}(\varepsilon_3) = < 0.5,0.25 > /U$, $\psi_{X_1}(\varepsilon_4) = \{< 0.6,0.35 > /u_1, < 0.4,0 > /u_2, < 0.4,0.47 > /u_4\}$, $\psi_{X_1}(\varepsilon_5) = \{< 0.5,0.4 > /u_3\}$, then the IVFPIFS set is written as

$$\Psi_{X_1} = \{([0.2,0.6]/\varepsilon_1, \{< 0.4,0.3 > /u_1, < 0.7,0.2 > /u_3, < 0.11,0.7 > /u_4\}),$$
$$([0.55,0.75]/\varepsilon_2, \{< 0.6,0.1 > /u_2\}), ([0.1,0.85]/\varepsilon_3, < 0.5,0.25 > /U),$$
$$([0,1]/\varepsilon_4, \{< 0.6,0.35 > /u_1, < 0.4,0 > /u_2, < 0.4,0.47 > /u_4\}),$$
$$([0.2,0.25]/\varepsilon_5, \{< 0.5,0.4 > /u_3\})\}.$$

Definition 3.3. Let $\Psi_X \in IVFPIFSS(U)$. Then, Ψ_X is called

a) an empty IVFPIFS set if it is denoted and defined as

$$\Psi_{\overline{\emptyset}} = \{([0,0]/\varepsilon_j, \{< 0,1 > /u_i: u_i \in U\}): \varepsilon_j \in \mathcal{E} \}.$$

b) a universal IVFPIFS set if it is denoted and defined as

$$\Psi_{\overline{\mathcal{E}}} = \{([1,1]/\varepsilon_j, \{< 1,0 > /u_i: u_i \in U\}): \varepsilon_j \in \mathcal{E} \}$$

Definition 3.4. Let Ψ_{X_1}, $\Psi_{X_2} \in IVFPIFSS(U)$. Then,

a) Ψ_{X_1} is an interval-valued fuzzy parameterized intuitionistic fuzzy soft subset of Ψ_{X_2} if and only if $\underline{\beta_{X_1}}(\varepsilon_j) \leq \underline{\beta_{X_2}}(\varepsilon_j)$, $\overline{\beta_{X_1}}(\varepsilon_j) \leq \overline{\beta_{X_2}}(\varepsilon_j)$ and $\psi_{X_1}(\varepsilon_j) \subseteq \psi_{X_2}(\varepsilon_j)$ for all $\varepsilon_j \in \mathcal{E}$. This is denoted by $\Psi_{X_1} \widetilde{\subseteq} \Psi_{X_2}$.

b) Ψ_{X_1} and Ψ_{X_2} are interval-valued fuzzy parameterized intuitionistic fuzzy soft equal if and only if $\underline{\beta_{X_1}}(\varepsilon_j) = \underline{\beta_{X_2}}(\varepsilon_j)$, $\overline{\beta_{X_1}}(\varepsilon_j) = \overline{\beta_{X_2}}(\varepsilon_j)$ and $\psi_{X_1}(\varepsilon_j) \subseteq \psi_{X_2}(\varepsilon_j)$, $\psi_{X_1}(\varepsilon_j) \supseteq \psi_{X_2}(\varepsilon_j)$ for all $\varepsilon_j \in \mathcal{E}$. This is denoted by $\Psi_{X_1} = \Psi_{X_2}$.

Example 3.5. We consider the IVFPIFS set Ψ_{X_1} in Example 3.2. Also, we take the following IVFPIFS set, for $X_2 = \{[0,0.2]/\varepsilon_1, [0.3,0.5]/\varepsilon_2, [0.1,0.85]/\varepsilon_3, [0,0.7]/\varepsilon_4, [0.1,0.2]/\varepsilon_5\}$,

$$\Psi_{X_2} = \{([0,0.2]/\varepsilon_1, \{< 0.2,05 >/u_1, < 0.11,0.8 >/u_4\}), ([0.3,0.5]/\varepsilon_2, \{< 0.3,0.65 >/u_2\}),$$
$$([0.1,0.85]/\varepsilon_3, \{< 0.22,0.51 >/u_2, < 0.37,0.25 >/u_3\}, < 0.45,0.65 >/u_4\}),$$
$$([0,0.7]/\varepsilon_4, \{< 0.3,0.5 >/u_1, < 0.3,0 >/u_2\}), ([0.1,0.2]/\varepsilon_5, \{< 0.1,0.8 >/u_3\})\}.$$

Then, we can say that $\Psi_{X_2} \tilde{\subseteq} \Psi_{X_1}$.

Proposition 3.6. Let $\Psi_{X_1}, \Psi_{X_2}, \Psi_{X_3} \in IVFPIFSS(U)$. Then,

i) $\Psi_{X_1} \tilde{\subseteq} \Psi_{\bar{\mathcal{E}}}$.

ii) $\Psi_{\bar{\emptyset}} \tilde{\subseteq} \Psi_{\bar{\mathcal{E}}}$.

iii) $\Psi_{X_1} \tilde{\subseteq} \Psi_{X_1}$.

iv) $\Psi_{X_1} \tilde{\subseteq} \Psi_{X_2}$ and $\Psi_{X_2} \tilde{\subseteq} \Psi_{X_1} \Leftrightarrow \Psi_{X_1} = \Psi_{X_2}$.

v) $\Psi_{X_1} \tilde{\subseteq} \Psi_{X_2}$ and $\Psi_{X_2} \tilde{\subseteq} \Psi_{X_3} \Rightarrow \Psi_{X_1} \tilde{\subseteq} \Psi_{X_3}$.

vi) $\Psi_{X_1} = \Psi_{X_2}$ and $\Psi_{X_2} = \Psi_{X_3} \Rightarrow \Psi_{X_1} = \Psi_{X_3}$.

Proof. The proofs are straightforward, hence omitted.

Definition 3.7. Let $\Psi_X \in IVFPIFSS(U)$. Then, the complement of Ψ_X, symbolized by Ψ_X^c, is defined by

$$\Psi_X^c = \{(\beta_{X^{\tilde{c}}}(\varepsilon_j)/\varepsilon_j, \psi_{X^{\tilde{c}}}(\varepsilon_j)): \varepsilon_j \in \mathcal{E}, \psi_{X^{\tilde{c}}}(\varepsilon_j) \in IFS(U)\}$$

where $\beta_{X^{\tilde{c}}}(\varepsilon_j) = 1 - \beta_X(\varepsilon_j) = [1 - \overline{\beta_X}(\varepsilon_j), 1 - \underline{\beta_X}(\varepsilon_j)]$ and $\psi_{X^{\tilde{c}}}(\varepsilon_j)$ is the complement of intuitionistic fuzzy set $\psi_X(\varepsilon_j)$.

Example 3.8. We consider the IVFPIFS set Ψ_{X_1} given in Example 3.2. The complement of the IVFPIFS set Ψ_{X_1} is

$$\Psi_{X_1}^c = \{([0.4,0.8]/\varepsilon_1, \{< 0.3,0.4 >/u_1, < 1,0 >/u_2, < 0.2,0.7 >/u_3, < 0.7,0.11 >/u_4\}),$$
$$([0.25,0.45]/\varepsilon_2, \{< 1,0 >/u_1, < 0.1,0.6 >/u_2, < 1,0 >/u_3, < 1,0 >/u_4\},$$
$$([0.15,0.9]/\varepsilon_3, < 0.25,0.5 >/U),$$
$$([0,1]/\varepsilon_4, \{< 0.35,0.6 >/u_1, < 0,0.4 >/u_2, < 1,0 >/u_3, < 0.47,0.4 >/u_4\}),$$
$$([0.75,0.8]/\varepsilon_5, \{< 1,0 >/u_1, < 1,0 >/u_2, < 0.4,0.5 >/u_3\}), < 1,0 >/u_4\}.$$

Proposition 3.9. Let $\Psi_X \in IVFPIFSS(U)$.

i) $\Psi_{\bar{\mathcal{E}}}^c = \Psi_{\bar{\emptyset}}$.

ii) $\Psi_{\bar{\emptyset}}^c = \Psi_{\bar{\mathcal{E}}}$.

iii) $(\Psi_X^c)^c = \Psi_X$.

Proof. The proofs are trivial.

Definition 3.10. Let $\Psi_{X_1}, \Psi_{X_2} \in IVFPIFSS(U)$. Then, the union of Ψ_{X_1} and Ψ_{X_2}, symbolized by $\Psi_{X_1} \tilde{\sqcup} \Psi_{X_2}$, is defined by

$$\Psi_{X_1} \tilde{\sqcup} \Psi_{X_2} = \{(\beta_{X_1 \tilde{\sqcup} X_2}(\varepsilon_j)/\varepsilon_j, \psi_{X_1 \tilde{\sqcup} X_2}(\varepsilon_j)): \varepsilon_j \in \mathcal{E}, \psi_{X_1 \tilde{\sqcup} X_2}(\varepsilon_j) \in IFS(U)\}$$

where $\beta_{X_1 \tilde{\sqcup} X_2}(\varepsilon_j) = sup[\beta_{X_1}(\varepsilon_j), \beta_{X_2}(\varepsilon_j)] = [sup\{\underline{\beta_{X_1}}(\varepsilon_j), \underline{\beta_{X_2}}(\varepsilon_j)\}, sup\{\overline{\beta_{X_1}}(\varepsilon_j), \overline{\beta_{X_2}}(\varepsilon_j)\}]$ and
$\psi_{X_1 \tilde{\sqcup} X_2}(\varepsilon_j) = \psi_{X_1}(\varepsilon_j) \cup \psi_{X_2}(\varepsilon_j)$.

Example 3.11. Let's consider the IVFPIFS set Ψ_{X_1} in Example 3.2. Also, we take the IVFPIFS set

$\Psi_{X_2} = \{([0.3,0.7]/\varepsilon_1, \{< 0.5,0.4 >/u_1, < 0.1,0.7 >/u_4\}),$
$([0.55,0.8]/\varepsilon_2, \{< 0.2,0.75 >/u_1, < 0.35,0.35 >/u_3\}),$
$([0.3,0.9]/\varepsilon_3, \{< 0.6,0.3 >/u_1, < 0.6,0.2 >/u_2\}),$
$([0.1,0.5]/\varepsilon_4, \{< 0.5,0.35 >/u_1, < 0.2,0.4 >/u_2, < 0.5,0.47 >/u_4\}),$
$([0.2,0.25]/\varepsilon_5, \{< 0.1,0.5 >/u_3\})\}.$

Then, the union of the IVFPIFS sets Ψ_{X_1} and Ψ_{X_2} is

$\Psi_{X_1} \tilde{\sqcup} \Psi_{X_2} = \{([0.3,0.7]/\varepsilon_1, \{< 0.5,0.3 >/u_1, < 0.7,0.2 >/u_3, < 0.11,0.7 >/u_4\}),$
$([0.55,0.8]/\varepsilon_2, \{< 0.2,0.75 >/u_1, < 0.6,0.1 >/u_2, < 0.35,0.35 >/u_3\}),$
$([0.3,0.9]/\varepsilon_3, \{< 0.6,0.25 >/u_1, < 0.6,0.2 >/u_2, < 0.5,0.25 >/u_3, < 0.5,0.25 >/u_4\}),$
$([0.1,1]/\varepsilon_4, \{< 0.6,0.35 >/u_1, < 0.4,0 >/u_2, < 0.5,0.47 >/u_4\}),$
$([0.2,0.25]/\varepsilon_5, \{< 0.5,0.4 >/u_3\})\}.$

Proposition 3.12. Let $\Psi_{X_1}, \Psi_{X_2}, \Psi_{X_3} \in IVFPIFSS(U)$. Then,

i) $\Psi_{X_1} \tilde{\sqcup} \Psi_{X_1} = \Psi_{X_1}$.

ii) $\Psi_{X_1} \tilde{\sqcup} \Psi_{\overline{\emptyset}} = \Psi_{X_1}$.

iii) $\Psi_{X_1} \tilde{\sqcup} \Psi_{\bar{\mathcal{E}}} = \Psi_{\bar{\mathcal{E}}}$.

iv) $\Psi_{X_1} \tilde{\sqcup} \Psi_{X_2} = \Psi_{X_2} \tilde{\sqcup} \Psi_{X_1}$.

v) $\Psi_{X_1} \tilde{\sqcup} (\Psi_{X_2} \tilde{\sqcup} \Psi_{X_3}) = (\Psi_{X_1} \tilde{\sqcup} \Psi_{X_2}) \tilde{\sqcup} \Psi_{X_3}$.

Proof. The proofs of (i)-(iv) are trivial, therefore omitted.

v) For all $\varepsilon_j \in \mathcal{E}$,
$\beta_{X_1 \tilde{\sqcup}(X_2 \tilde{\sqcup} X_3)}(\varepsilon_j) = sup[\beta_{X_1}(\varepsilon_j), \beta_{X_2 \tilde{\sqcup} X_3}(\varepsilon_j)]$

$= sup[\beta_{X_1}(\varepsilon_j), sup[\beta_{X_2}(\varepsilon_j), \beta_{X_3}(\varepsilon_j)]]$

$= sup[\beta_{X_1}(\varepsilon_j), [sup\{\underline{\beta_{X_2}}(\varepsilon_j), \underline{\beta_{X_3}}(\varepsilon_j)\}, sup\{\overline{\beta_{X_2}}(\varepsilon_j), \overline{\beta_{X_3}}(\varepsilon_j)\}]]$

$= [sup\{\underline{\beta_{X_1}}(\varepsilon_j), sup\{\underline{\beta_{X_2}}(\varepsilon_j), \underline{\beta_{X_3}}(\varepsilon_j)\}\}, sup\{\overline{\beta_{X_1}}(\varepsilon_j), sup\{\overline{\beta_{X_2}}(\varepsilon_j), \overline{\beta_{X_3}}(\varepsilon_j)\}\}]$

$= [sup\{sup\{\underline{\beta_{X_1}}(\varepsilon_j), \underline{\beta_{X_2}}(\varepsilon_j)\}, \underline{\beta_{X_3}}(\varepsilon_j)\}, sup\{sup\{\overline{\beta_{X_1}}(\varepsilon_j), \overline{\beta_{X_2}}(\varepsilon_j)\}, \overline{\beta_{X_3}}(\varepsilon_j)\}]$

$= sup[sup\{\underline{\beta_{X_1}}(\varepsilon_j), \underline{\beta_{X_2}}(\varepsilon_j)\}, sup\{\overline{\beta_{X_1}}(\varepsilon_j), \overline{\beta_{X_2}}(\varepsilon_j)\}], \beta_{X_3}(\varepsilon_j)]$

$= sup[sup[\beta_{X_1}(\varepsilon_j), \beta_{X_2}(\varepsilon_j)], \beta_{X_3}(\varepsilon_j)]$

$= sup[\beta_{X_1 \tilde{\sqcup} X_2}(\varepsilon_j), \beta_{X_3}(\varepsilon_j)]$

$= \beta_{(X_1 \tilde{\sqcup} X_2) \tilde{\sqcup} X_3}(\varepsilon_j),$

$\psi_{X_1 \tilde{\sqcup}(X_2 \tilde{\sqcup} X_3)}(\varepsilon_j) = \psi_{X_1}(\varepsilon_j) \cup \psi_{X_2 \tilde{\sqcup} X_3}(\varepsilon_j)$

$= \psi_{X_1}(\varepsilon_j) \cup (\psi_{X_2}(\varepsilon_j) \cup \psi_{X_3}(\varepsilon_j))$

$$= (\psi_{X_1}(\varepsilon_j) \cup \psi_{X_2}(\varepsilon_j)) \cup \psi_{X_3}(\varepsilon_j)$$

$$= \psi_{X_1 \tilde{\sqcup} X_2}(\varepsilon_j) \cup \psi_{X_3}(\varepsilon_j)$$

$$= \psi_{(X_1 \tilde{\sqcup} X_2) \tilde{\sqcup} X_3}(\varepsilon_j).$$

Hence, we obtain that $\Psi_{X_1} \tilde{\sqcup} (\Psi_{X_2} \tilde{\sqcup} \Psi_{X_3}) = (\Psi_{X_1} \tilde{\sqcup} \Psi_{X_2}) \tilde{\sqcup} \Psi_{X_3}$.

Definition 3.13. Let $\Psi_{X_1}, \Psi_{X_2} \in IVFPIFSS(U)$. Then, the intersection of Ψ_{X_1} and Ψ_{X_2}, symbolized by $\Psi_{X_1} \tilde{\sqcap} \Psi_{X_2}$, is defined by

$$\Psi_{X_1} \tilde{\sqcap} \Psi_{X_2} = \{(\beta_{X_1 \tilde{\sqcap} X_2}(\varepsilon_j)/\varepsilon_j, \psi_{X_1 \tilde{\sqcap} X_2}(\varepsilon_j)): \varepsilon_j \in \mathcal{E}, \psi_{X_1 \tilde{\sqcap} X_2}(\varepsilon_j) \in IFS(U)\}$$

where $\beta_{X_1 \tilde{\sqcap} X_2}(\varepsilon_j) = inf[\beta_{X_1}(\varepsilon_j), \beta_{X_2}(\varepsilon_j)] = [inf\{\underline{\beta_{X_1}}(\varepsilon_j), \underline{\beta_{X_2}}(\varepsilon_j)\}, inf\{\overline{\beta_{X_1}}(\varepsilon_j), \overline{\beta_{X_2}}(\varepsilon_j)\}]$ and $\psi_{X_1 \tilde{\sqcap} X_2}(\varepsilon_j) = \psi_{X_1}(\varepsilon_j) \cap \psi_{X_2}(\varepsilon_j)$.

Example 3.14. We take the IVFPIFS set Ψ_{X_1} in Example 3.2 and the IVFPIFS set Ψ_{X_2} in Example 3.11. Then, the intersection of the IVFPIFS sets Ψ_{X_1} and Ψ_{X_2} is

$$\Psi_{X_1} \tilde{\sqcap} \Psi_{X_2} = \{([0.2,0.6]/\varepsilon_1, \{< 0.4,0.4 >/u_1, < 0.1,0.7 >/u_4\}), ([0.55,0.75]/\varepsilon_2, \emptyset),$$
$$([0.1,0.85]/\varepsilon_3, \{< 0.5,0.3 >/u_1, < 0.5,0.25 >/u_2\}),$$
$$([0,0.5]/\varepsilon_4, \{< 0.5,0.35 >/u_1, < 0.2,0.4 >/u_2, < 0.4,0.47 >/u_4\}),$$
$$([0.2,0.25]/\varepsilon_5, \{< 0.1,0.5 >/u_3\})\}.$$

Proposition 3.15. Let $\Psi_{X_1}, \Psi_{X_2}, \Psi_{X_3} \in IVFPIFSS(U)$. Then,

i) $\Psi_{X_1} \tilde{\sqcap} \Psi_{X_1} = \Psi_{X_1}$.

ii) $\Psi_{X_1} \tilde{\sqcap} \Psi_{\overline{\emptyset}} = \Psi_{\overline{\emptyset}}$.

iii) $\Psi_{X_1} \tilde{\sqcap} \Psi_{\overline{\mathcal{E}}} = \Psi_{X_1}$.

iv) $\Psi_{X_1} \tilde{\sqcap} \Psi_{X_2} = \Psi_{X_2} \overline{\sqcap} \Psi_{X_1}$.

v) $(\Psi_{X_1} \tilde{\sqcap} \Psi_{X_2}) \tilde{\sqcap} \Psi_{X_3} = \Psi_{X_1} \tilde{\sqcap} (\Psi_{X_2} \tilde{\sqcap} \Psi_{X_3})$.

Proof. The proofs of (i)-(iv) are trivial, therefore omitted.

v) For all $\varepsilon_j \in \mathcal{E}$,

$$\beta_{X_1 \tilde{\sqcap} (X_2 \tilde{\sqcap} X_3)}(\varepsilon_j) = inf[\beta_{X_1}(\varepsilon_j), \beta_{X_2 \tilde{\sqcap} X_3}(\varepsilon_j)]$$

$$= inf[\beta_{X_1}(\varepsilon_j), inf[\beta_{X_2}(\varepsilon_j), \beta_{X_3}(\varepsilon_j)]]$$

$$= inf[\beta_{X_1}(\varepsilon_j), [inf\{\underline{\beta_{X_2}}(\varepsilon_j), \underline{\beta_{X_3}}(\varepsilon_j)\}, inf\{\overline{\beta_{X_2}}(\varepsilon_j), \overline{\beta_{X_3}}(\varepsilon_j)\}]]$$

$$= [inf\{\underline{\beta_{X_1}}(\varepsilon_j), inf\{\underline{\beta_{X_2}}(\varepsilon_j), \underline{\beta_{X_3}}(\varepsilon_j)\}\}, inf\{\overline{\beta_{X_1}}(\varepsilon_j), inf\{\overline{\beta_{X_2}}(\varepsilon_j), \overline{\beta_{X_3}}(\varepsilon_j)\}\}]$$

$$= [inf\{inf\{\underline{\beta_{X_1}}(\varepsilon_j), \underline{\beta_{X_2}}(\varepsilon_j)\}, \underline{\beta_{X_3}}(\varepsilon_j)\}, inf\{inf\{\overline{\beta_{X_1}}(\varepsilon_j), \overline{\beta_{X_2}}(\varepsilon_j)\}, \overline{\beta_{X_3}}(\varepsilon_j)\}]$$

$$= inf[inf\{\underline{\beta_{X_1}}(\varepsilon_j), \underline{\beta_{X_2}}(\varepsilon_j)\}, inf\{\overline{\beta_{X_1}}(\varepsilon_j), \overline{\beta_{X_2}}(\varepsilon_j)\}], \beta_{X_3}(\varepsilon_j)]$$

$$= inf[inf[\beta_{X_1}(\varepsilon_j), \beta_{X_2}(\varepsilon_j)], \beta_{X_3}(\varepsilon_j)]$$

$$= inf[\beta_{X_1 \tilde{\sqcap} X_2}(\varepsilon_j), \beta_{X_3}(\varepsilon_j)]$$

$$= \beta_{(X_1 \tilde{\cap} X_2) \tilde{\cap} X_3}(\varepsilon_j),$$

$$\psi_{X_1 \tilde{\cap} (X_2 \tilde{\cap} X_3)}(\varepsilon_j) = \psi_{X_1}(\varepsilon_j) \cap \psi_{X_2 \tilde{\cap} X_3}(\varepsilon_j)$$

$$= \psi_{X_1}(\varepsilon_j) \cap (\psi_{X_2}(\varepsilon_j) \cap \psi_{X_3}(\varepsilon_j))$$

$$= (\psi_{X_1}(\varepsilon_j) \cap \psi_{X_2}(\varepsilon_j)) \cap \psi_{X_3}(\varepsilon_j)$$

$$= \psi_{X_1 \tilde{\cap} X_2}(\varepsilon_j) \cap \psi_{X_3}(\varepsilon_j)$$

$$= \psi_{(X_1 \tilde{\cap} X_2) \tilde{\cap} X_3}(\varepsilon_j).$$

Thus, we have $\Psi_{X_1} \tilde{\cap} (\Psi_{X_2} \tilde{\cap} \Psi_{X_3}) = (\Psi_{X_1} \tilde{\cap} \Psi_{X_2}) \tilde{\cap} \Psi_{X_3}$.

Proposition 3.16. Let $\Psi_{X_1}, \Psi_{X_2}, \Psi_{X_3} \in IVFPIFSS(U)$. Then,

i) $\Psi_{X_1} \tilde{\sqcup} (\Psi_{X_2} \tilde{\cap} \Psi_{X_3}) = (\Psi_{X_1} \tilde{\sqcup} \Psi_{X_2}) \tilde{\cap} (\Psi_{X_1} \tilde{\sqcup} \Psi_{X_3})$.

ii) $\Psi_{X_1} \tilde{\cap} (\Psi_{X_2} \tilde{\sqcup} \Psi_{X_3}) = (\Psi_{X_1} \tilde{\cap} \Psi_{X_2}) \tilde{\sqcup} (\Psi_{X_1} \tilde{\cap} \Psi_{X_3})$.

Proof. The proofs can be proved in a similar manner to the proofs of Propositions 3.12 and 3.15.

Proposition 3.17. Let $\Psi_{X_1}, \Psi_{X_2} \in IVFPIFSS(U)$. Then, the following De-Morgan laws are valid.

i) $(\Psi_{X_1} \tilde{\sqcup} \Psi_{X_2})^c = \Psi_{X_1}{}^c \tilde{\cap} \Psi_{X_2}{}^c$.

ii) $(\Psi_{X_1} \tilde{\cap} \Psi_{X_2})^c = \Psi_{X_1}{}^c \tilde{\sqcup} \Psi_{X_2}{}^c$.

Proof. i) For all $\varepsilon_j \in \mathcal{E}$,

$$\beta_{(X_1 \tilde{\sqcup} X_2)^{\tilde{c}}}(\varepsilon_j) = 1 - \beta_{X_1 \tilde{\sqcup} X_2}(\varepsilon_j)$$

$$= 1 - [sup(\underline{\beta_{X_1}}(\varepsilon_j), \underline{\beta_{X_2}}(\varepsilon_j)), sup(\overline{\beta_{X_1}}(\varepsilon_j), \overline{\beta_{X_2}}(\varepsilon_j))]$$

$$= [1 - sup(\overline{\beta_{X_1}}(\varepsilon_j), \overline{\beta_{X_2}}(\varepsilon_j)), 1 - sup(\underline{\beta_{X_1}}(\varepsilon_j), \underline{\beta_{X_2}}(\varepsilon_j))]$$

$$= [inf(1 - \overline{\beta_{X_1}}(\varepsilon_j), 1 - \overline{\beta_{X_2}}(\varepsilon_j)), inf(1 - \underline{\beta_{X_1}}(\varepsilon_j), 1 - \underline{\beta_{X_2}}(\varepsilon_j))]$$

$$= inf[\beta_{X_1 \tilde{c}}(\varepsilon_j), \beta_{X_2 \tilde{c}}(\varepsilon_j)]$$

$$= \beta_{X_1{}^{\tilde{c}} \tilde{\cap} X_2{}^{\tilde{c}}}(\varepsilon_j),$$

$$\psi_{(X_1 \tilde{\sqcup} X_2)^{\tilde{c}}}(\varepsilon_j) = (\psi_{X_1 \tilde{\sqcup} X_2}(\varepsilon_j))^c$$

$$= (\psi_{X_1}(\varepsilon_j) \cup \psi_{X_2}(\varepsilon_j))^c$$

$$= (\psi_{X_1}(\varepsilon_j))^c \cap (\psi_{X_2}(\varepsilon_j))^c$$

$$= \psi_{X_1 \tilde{c}}(\varepsilon_j) \cap \psi_{X_2 \tilde{c}}(\varepsilon_j)$$

$$= \psi_{X_1 \tilde{c} \tilde{\cap} X_2 \tilde{c}}(\varepsilon_j).$$

Hence, we obtain that $(\Psi_{X_1} \tilde{\sqcup} \Psi_{X_2})^c = \Psi_{X_1}{}^c \tilde{\cap} \Psi_{X_2}{}^c$.

The proof of (ii) can be proved similarly.

4.IVFPIFS-AGGREGATION OPERATORS

In this section, the IVFPIFS-aggregation operators which create the aggregate interval-valued intuitionistic fuzzy sets from an IVFPIFS set and its interval-valued fuzzy parameter set are introduced. By using these operators, an algorithm for selection is proposed.

Definition 4.1. Let $\Psi_X = \{(\beta_j/\varepsilon_j, \{< \gamma_{ij}^+, \gamma_{ij}^- >/u_i: u_i \in U\}): \varepsilon_j \in \mathcal{E}\}$ be an IVFPIFS set, where $\gamma_{ij} =< \gamma_{ij}^+, \gamma_{ij}^- > \ i = 1,2,\dots,n$ indicates an intuitionistic fuzzy value when the alternative u_i is assessed with respect to the parameter ε_j and $\beta_j = [\underline{\beta_j}, \overline{\beta_j}]$ indicates an interval-valued fuzzy value of the parameter ε_j. Then, the first IVFPIFS-aggregation operator, denoted by $IVFPIFS_{agg}^1$, is defined by

$$IVFPIFS_{agg}^1 : IVFS(\mathcal{E}) \times IVFPIFSS(U) \longrightarrow IVIFS(U), \ IVFPIFS_{agg}^1(X, \Psi_X) = \dot{\Psi}_X \quad (4.1)$$

where $\dot{\Psi}_X = \{< [\underline{\dot{\gamma}_i^+}, \overline{\dot{\gamma}_i^+}], [\underline{\dot{\gamma}_i^-}, \overline{\dot{\gamma}_i^-}] >/u_i: u_i \in U\}$ which is an interval-valued intuitionistic fuzzy set on U.

Here, the membership degree $\dot{\gamma}_i^+ = [\underline{\dot{\gamma}_i^+}, \overline{\dot{\gamma}_i^+}]$ and the non-membership degree $\dot{\gamma}_i^- = [\underline{\dot{\gamma}_i^-}, \overline{\dot{\gamma}_i^-}]$ of $u_i \in U$ is defined as follows:

$$\dot{\gamma}_i^+ = [1 - \prod_{j=1}^m (1 - \underline{\beta_j}\gamma_{ij}^+), 1 - \prod_{j=1}^m (1 - \overline{\beta_j}\gamma_{ij}^+)] \text{ and } \dot{\gamma}_i^- = [\prod_{j=1}^m \underline{\beta_j}\gamma_{ij}^-, \prod_{j=1}^m \overline{\beta_j}\gamma_{ij}^-]$$

where m denotes the number of parameters in $\mathcal{E}$.

Definition 4.2. Let $\Psi_X = \{(\beta_j/\varepsilon_j, \{< \gamma_{ij}^+, \gamma_{ij}^- >/u_i: u_i \in U\}): \varepsilon_j \in \mathcal{E}\}$ be an IVFPIFS set, where $\gamma_{ij} =< \gamma_{ij}^+, \gamma_{ij}^- > \ i = 1,2,\dots,n$ indicates an intuitionistic fuzzy value when the alternative u_i is assessed with respect to the parameter ε_j and $\beta_j = [\underline{\beta_j}, \overline{\beta_j}]$ indicates an interval-valued fuzzy value of the parameter ε_j. Then, the second IVFPIFS-aggregation operator, denoted by $IVFPIFS_{agg}^2$, is defined by

$$IVFPIFS_{agg}^2 : IVFS(\mathcal{E}) \times IVFPIFSS(U) \longrightarrow IVIFS(U), \ IVFPIFS_{agg}^2(X, \Psi_X) = \ddot{\Psi}_X \quad (4.2)$$

where $\ddot{\Psi}_X = \{< [\underline{\ddot{\gamma}_i^+}, \overline{\ddot{\gamma}_i^+}], [\underline{\ddot{\gamma}_i^-}, \overline{\ddot{\gamma}_i^-}] >/u_i: u_i \in U\}$ which is an interval-valued intuitionistic fuzzy set on U.

Here, the membership degree $\ddot{\gamma}_i^+ = [\underline{\ddot{\gamma}_i^+}, \overline{\ddot{\gamma}_i^+}]$ and the non-membership degree $\ddot{\gamma}_i^- = [\underline{\ddot{\gamma}_i^-}, \overline{\ddot{\gamma}_i^-}]$ of $u_i \in U$ is defined as follows:

$$\ddot{\gamma}_i^+ = [\prod_{j=1}^m \underline{\beta_j}\gamma_{ij}^+, \prod_{j=1}^m \overline{\beta_j}\gamma_{ij}^+] \text{ and } \ddot{\gamma}_i^- = [1 - \prod_{j=1}^m (1 - \underline{\beta_j}\gamma_{ij}^-), \prod_{j=1}^m (1 - \overline{\beta_j}\gamma_{ij}^-)]$$

where m denotes the number of parameters in $\mathcal{E}$.

Now, we construct an algorithm using the interval-valued intuitionistic fuzzy sets which are found by utilizing $IVFPIFS_{agg}^1$ and $IVFPIFS_{agg}^2$.

Algorithm

Step 1. Construct an IVFPIFS set Ψ_X on U.

Step 2. By using the first IVFPIFS-aggregation operator given in Eq. (4.1), obtain the first aggregate interval-valued intuitionistic fuzzy set $\dot{\Psi}_X = \{< [\underline{\dot{\gamma}_i^+}, \overline{\dot{\gamma}_i^+}], [\underline{\dot{\gamma}_i^-}, \overline{\dot{\gamma}_i^-}] >/u_i: u_i \in U\}$ of the IVFPIFS set Ψ_X on U.

Step 3. By using the second IVFPIFS-aggregation operator given in Eq. (4.2), obtain the second aggregate interval-valued intuitionistic fuzzy set $\ddot{\Psi}_X = \{< [\underline{\ddot{\gamma}_i^+}, \overline{\ddot{\gamma}_i^+}], [\underline{\ddot{\gamma}_i^-}, \overline{\ddot{\gamma}_i^-}] >/u_i : u_i \in U\}$ of the IVFPIFS set Ψ_X on U.

Step 4. Find the IVIF values $< \ddot{\gamma}_i^+, \ddot{\gamma}_i^- >=< \dot{\gamma}_i^+, \dot{\gamma}_i^- > \oplus < \ddot{\gamma}_i^+, \ddot{\gamma}_i^- >$ for $i = 1,2,\ldots,n$ (or $< \ddot{\gamma}_i^+, \ddot{\gamma}_i^- >=< \dot{\gamma}_i^+, \dot{\gamma}_i^- > \otimes < \ddot{\gamma}_i^+, \ddot{\gamma}_i^- >$) by employing any of the operations $\oplus$ and $\otimes$ given in Definition 2.7.

Step 5. Compare the IVIF values by using the score function and accuracy function of $\ddot{\gamma}_i =< \ddot{\gamma}_i^+, \ddot{\gamma}_i^- >$ for $i = 1,2,\ldots,n$.

Step 6. As a result of these comparisons, obtain opportune element of U which is denoted and defined by

$$U_{opp} = \{u_i : u_i \in U \text{ and } \ddot{\gamma}_i > \ddot{\gamma}_{i'} \text{ for all } i' \neq i\}.$$

Let us give two illustrative examples to better understand the steps of this algorithm.

Example 4.3. Let's consider a retailer planning to open a new store in the city. There are five streets to be selected, i.e. $U = \{u_1, u_2, u_3, u_4, u_5\}$. Three parameters are considered: ε_1=traffic, ε_2=rent price, ε_3= crowdedness and ε_4=competition. We aim to determine opportune street, where the retailer can open a new store. For this purpose, we apply the above algorithm as follows:

Step 1. After evaluating the streets under the specified parameters, the IVFPIFS set is generated as below:

$\Psi_X = \{([0.4, 0.7]/\varepsilon_1\{< 0.6, 0.3 >/u_1, < 0.5, 0.3 >/u_2, < 0.4, 0.6 >/u_3, < 0.4, 0.3 >/u_4,$
$< 0.7, 0.1 >/u_5\}), ([0.6, 0.9]/\varepsilon_2, \{< 0.4, 0.5 >/u_1, < 0.7, 0.1 >/u_2, < 0.2, 0.7 >/u_3,$
$< 0.35, 0.35 >/u_4, < 0.5, 0.3 >/u_5\}), ([0.5, 0.8]/\varepsilon_3\{< 0.7, 0.2 >/u_1, < 0.85, 0.1 >/u_2$
$< 0.1, 0.7 >/u_3, < 0.4, 0.6 >/u_4, < 0.6, 0.4 >/u_5\}), ([0.3, 0.6]/\varepsilon_4, \{< 0.5, 0.5 >/u_1,$
$< 0.6, 0.4 >/u_2, < 0.25, 0.7 >/u_3, < 0.2, 0.4 >/u_4, < 0.85, 0.1 >/u_5\})\}.$

In order to follow the steps of the algorithm more easily, let's present this IVFPIFS set Ψ_X with the table as follows.

Table 1: The tabular form of IVFPIFS set Ψ_X.

Ψ_X	$[0.4, 0.7]/\varepsilon_1$	$[0.6, 0.9]/\varepsilon_2$	$[0.5, 0.8]/\varepsilon_3$	$[0.3, 0.6]/\varepsilon_4$
u_1	$< 0.6, 0.3 >$	$< 0.4, 0.5 >$	$< 0.7, 0.2 >$	$< 0.5, 0.5 >$
u_2	$< 0.5, 0.3 >$	$< 0.7, 0.1 >$	$< 0.85, 0.1 >$	$< 0.6, 0.4 >$
u_3	$< 0.4, 0.6 >$	$< 0.2, 0.7 >$	$< 0.1, 0.7 >$	$< 0.25, 0.7 >$
u_4	$< 0.4, 0.3 >$	$< 0.35, 0.35 >$	$< 0.4, 0.6 >$	$< 0.2, 0.4 >$
u_5	$< 0.7, 0.1 >$	$< 0.5, 0.3 >$	$< 0.6, 0.4 >$	$< 0.85, 0.1 >$

The value in the ith row and jth column of this table denotes the intuitionistic fuzzy value of the alternative u_i evaluated according to the parameter ε_j.

Step 2. The first aggregate interval-valued intuitionistic fuzzy set $\dot{\Psi}_X$ of the IVFPIFS set Ψ_X is obtained as in Table 2.

Table 2: The tabular form of $\dot{\Psi}_X$.

$\dot{\gamma}_i/u_i$	$\dot{\gamma}_i =< \dot{\gamma}_i^+, \dot{\gamma}_i^- >=< [\underline{\dot{\gamma}_i^+}, \overline{\dot{\gamma}_i^+}], [\underline{\dot{\gamma}_i^-}, \overline{\dot{\gamma}_i^-}] >$
u_1	$< [0.680876, 0.8856704], [0.00054, 0.004536] >$
u_2	$< [0.781224, 0.9507456], [0.0000432, 0.00036288] >$
u_3	$< [0.350428, 0.5383072], [0.0074088, 0.06223392] >$
u_4	$< [0.5009728, 0.70486912], [0.0009072, 0.00762048] >$
u_5	$< [0.737164, 0.9285286], [0.0000432, 0.00036288] >$

Step 3. The second aggregate interval-valued intuitionistic fuzzy set $\ddot{\Psi}_X$ of the IVFPIFS set Ψ_X is obtained as in Table 3.

Table 3: The tabular form of $\ddot{\Psi}_X$.

$\ddot{\gamma}_i/u_i$	$\ddot{\gamma}_i =< \ddot{\gamma}_i^+, \ddot{\gamma}_i^- >=< [\underline{\ddot{\gamma}_i^+}, \overline{\ddot{\gamma}_i^+}], [\underline{\ddot{\gamma}_i^-}, \overline{\ddot{\gamma}_i^-}] >$
u_1	$< [0.003024, 0.0254016], [0.52876, 0.744514] >$
u_2	$< [0.006426, 0.0539784], [0.3084608, 0.49734512] >$
u_3	$< [0.000072, 0.0006048], [0.7736492, 0.94523408] >$
u_4	$< [0.0004032, 0.00338688], [0.5717568, 0.78613752] >$
u_5	$< [0.006426, 0.0539784], [0.3891328, 0.56604712] >$

Step 4. By using the operation $\oplus$ in Definition 2.7, we have Table 4.

Table 4: The tabular form of $\dddot{\gamma}_i$ obtained by using $\oplus$.

$\dddot{\gamma}_i/u_i$	$\dddot{\gamma}_i =< \dddot{\gamma}_i^+, \dddot{\gamma}_i^- >=< \dot{\gamma}_i^+, \dot{\gamma}_i^- > \oplus < \ddot{\gamma}_i^+, \ddot{\gamma}_i^- >$
u_1	$< [0.68184103, 0.8887455], [0.0002855304, 0.003377116] >$
u_2	$< [0.78262985, 0.95340427], [0.0000133255, 0.0001804766] >$
u_3	$< [0.35047475, 0.53858643], [0.005731812, 0.05882562] >$
u_4	$< [0.50114701, 0.70586912], [0.0005186978, 0.005990745] >$
u_5	$< [0.73885298, 0.93251502], [0.00001681053, 0.0002054072] >$

Step 5. We give the results of score function of $\dddot{\gamma}_i =< \dddot{\gamma}_i^+, \dddot{\gamma}_i^- >$ for $i = 1,2,3,4,5$ as in Table 5.

Table 5: The tabular form of the results of score function for $\oplus$.

$i/Scr(\dddot{\gamma}_i)$	1	2	3	4	5
$Scr(\dddot{\gamma}_i)$	0.78346194	0.86792016	0.41225188	0.60025334	0.83557289

By Definition 2.6, we have $\dddot{\gamma}_2 > \dddot{\gamma}_5 > \dddot{\gamma}_1 > \dddot{\gamma}_4 > \dddot{\gamma}_3$ since $Scr(\dddot{\gamma}_2) > Scr(\dddot{\gamma}_5) > Scr(\dddot{\gamma}_1) > Scr(\dddot{\gamma}_4) > Scr(\dddot{\gamma}_3)$.

Here, if the results obtained by using the score function for some IVIF values are the same, then new comparison results will be obtained by using the accuracy function for these IVIF values.

Step 6. As a result of these comparisons, we obtain the opportune element of U is $U_{opp} = \{u_2\}$. Thus, we can say that the most appropriate street in the city for a new store is u_2.

Example 4.4. Let us consider Example 4.3. If the operation $\otimes$ is taken instead of the operation $\oplus$ in Step 4, then the following table is obtained.

Table 6: The tabular form of $\ddot{\gamma}_i$ obtained by using $\otimes$.

$\ddot{\gamma}_i/u_i$	$\ddot{\gamma}_i = < \ddot{\gamma}_i^+, \ddot{\gamma}_i^- > = < \dot{\gamma}_i^+, \dot{\gamma}_i^- > \otimes < \ddot{\gamma}_i^+, \ddot{\gamma}_i^- >$
u_1	$< [0.002058969, 0.02249745], [0.52901447, 0.74567288] >$
u_2	$< [0.005020145, 0.05131973], [0.30849067, 0.49752752] >$
u_3	$< [0.0000252308, 0.0003255682], [0.77532619, 0.94864238] >$
u_4	$< [0.0002019922, 0.002387307], [0.5721453, 0.78776725] >$
u_5	$< [0.004737016, 0.05012049], [0.38915919, 0.56947051] >$

Thus, we have the results of score function of $\ddot{\gamma}_i = < \ddot{\gamma}_i^+, \ddot{\gamma}_i^- >$ for $i = 1,2,3,4,5$ as in Table 7.

Table 7: The tabular form of the results of score function for $\otimes$.

i/$Scr(\ddot{\gamma}_i)$	1	2	3	4	5
$Scr(\ddot{\gamma}_i)$	-0.6250654	-0.3748392	-0.8618089	-0.6786616	-0.4518861

Then, we obtain $\ddot{\gamma}_2 > \ddot{\gamma}_5 > \ddot{\gamma}_1 > \ddot{\gamma}_4 > \ddot{\gamma}_3$ since $Scr(\ddot{\gamma}_2) > Scr(\ddot{\gamma}_5) > Scr(\ddot{\gamma}_1) > Scr(\ddot{\gamma}_4) > Scr(\ddot{\gamma}_3)$. Hence, according to these comparisons, we say that the opportune element of U is $U_{opp} = \{u_2\}$.

By Tables 6 and 7, it is easily seen that the values $\ddot{\gamma}_i$ and $Scr(\ddot{\gamma}_i)$ for each u_i $(i = 1,2,3,4,5)$ have changed. However, the comparison results and also the opportune element are the same.

5. CONCLUSION

In this paper, we defined the interval-valued fuzzy parameterized intuitionistic fuzzy soft sets by combining the interval-valued fuzzy sets and the intuitionistic fuzzy soft sets from parameterization point of view. Their basic operations and some interesting results were introduced. Also, we proposed a decision making model based on the IVFPIFS-aggregation operators, which is described in this study.

We think that the IVFPIFS sets can be applied not only to decision making problems but also problems of many fields containing uncertainty. Moreover, we hope that the findings in this work will help researchers promote and enhance the further study on intuitionistic fuzzy soft sets.

REFERENCES

[1] Zadeh, L.A., Fuzzy sets, Inform. Control, 8 (1965) 338-353.
[2] Sambuc, R., Fonctions Φ-floues. Application a l'aide au diagnostic en pathologie thyroidienne. Ph. D. Thesis, Univ. Marseille, France, 1975.
[3] Atanassov, K.T., Intuitionistic fuzzy sets, Fuzzy Set. Syst., 20 (1986) 87-96.
[4] Atanassov, K. and Gargov, G., Interval-valued intuitionistic fuzzy sets, Fuzzy Set. Syst., 31 (1989) 343-349.
[5] Molodtsov, D., Soft set theory-first results, Comput. Math. Appl., 37 (1999) 19-31.

[6] Ali, M.I., Feng, F., Liu, X., Min, W.K. and Shabir, M., On some new operations in soft set theory, Comput. Math. Appl., 57 (2009) 1547-1553.

[7] Maji, P.K., Biswas, R. and Roy, A.R., Soft set theory, Comput. Math. Appl., 45 (2003) 555-562.

[8] Sezgin, A. and Atagün, A.O., On operations of soft sets, Comput. Math. Appl., 61 (2011) 1457-1467.

[9] Aktaş, H. and Çağman, N., Soft sets and soft groups, Inform. Sci., 177 (2007) 2726-2735.

[10] Feng, F., Jun, Y.B. and Zhao, X., Soft semirings, Comput. Math. Appl., 56 (2008) 2621-2628.

[11] Acar, U., Koyuncu, F. and Tanay, B., Soft sets and soft rings, Comput. Math. Appl., 59 (2010) 3458-3463.

[12] Atagün, A.O. and Sezgin, A., Soft substructures of rings, fields and modules, Comput. Math. Appl., 61 (2011) 592-601.

[13] Sezgin, A., Atagün, A.O. and Aygün, E., A note on soft near-rings and idealistic soft near-rings, Filomat, 25 (2011) 53-68.

[14] Çağman, N., Çıtak, F. and Enginoğlu, S., FP-soft set theory and its applications, Ann. Fuzzy Math. Inform., 2 (2011) 219-226.

[15] Zorlutuna, I. and Atmaca, S., Notes on fuzzy parametrized soft sets, Cumhuriyet Science Journal, 39 (2018) 818-827.

[16] Çağman, N. and Deli, I., Products of FP-soft sets and their applications, Hacet. J. Math. Stat., 41 (2012) 365-374.

[17] Çağman, N. and Deli, I., Means of FP-soft sets and their applications, Hacet. J. Math. Stat., 41 (2012) 615-625.

[18] Deli, I. and Çağman, N., Relations on FP-soft sets applied to decision making problems, Journal of New Theory, 3 (2015) 98-107.

[19] Deli, I. and Çağman, N., Intuitionistic fuzzy parameterized soft set theory and its decision making, Appl. Soft Comput., 28 (2015) 109-113.

[20] Deli, I. and Karataş, S., Interval valued intuitionistic fuzzy parameterized soft set theory and its decision making, J. Intell. Fuzzy Syst., 30 (2016) 2073-2082.

[21] Çağman, N., Enginoğlu, S. and Çıtak, F., Fuzzy soft set theory and its applications, Iran. J. Fuzzy Syst., 8 (2011) 137-147.

[22] Atagün, A.O., Kamacı, H. and Oktay, O., Reduced soft matrices and generalized products with applications in decision making, Neural Comput. Applic., 29 (2018) 445-456.

[23] Çağman, N. and Enginoğlu, S., Soft matrix theory and its decision making, Comput. Math. Appl., 59 (2010) 3308-3314.

[24] Çağman, N. and Enginoğlu, S., Fuzzy soft matrix theory and its application in decision making, Iran. J. Fuzzy Syst., 9 (2012) 109-119.

[25] Kamacı, H., Atagün, A.O. and Sönmezoğlu, A., Row-products of soft matrices with applications in multiple-disjoint decision making, Appl. Soft Comput., 62 (2018) 892-914.

[26] Kamacı, H., Atagün, A.O. and Aygün, E., Difference operations of soft matrices with applications in decision making, Punjab Univ. J. Math., 51 (2019) 1-21.

[27] Petroudi, S.H.J., Nabati, Z. and Yaghobi, A., Some new results on fuzzy soft matrices, Turkish Journal of Fuzzy Systems, 8 (2017) 52-62.

[28] Maji, P.K., Biswas, R. and Roy, A.R., Intuitionistic fuzzy soft sets, The Journal of Fuzzy Mathematics, 9 (2001) 677-692.

[29] Xu, Y.-J., Sun, Y.-K. and Li, D.-F., Intuitionistic fuzzy soft set, 2nd International Workshop on Intelligent Systems and Applications IEEE, Wuhan, China, 2010.

[30] Çağman, N. and Karataş, S., Intuitionistic fuzzy soft set theory and its decision making, J. Intell. Fuzzy Syst., 24 (2013) 829-836.

[31] Deli, I. and Çağman, N., Similarity measure of IFS-sets and its application in medical diagnosis, Ann. Fuzzy Math. Inform., 11 (2016) 841-854.

[32] Broumi, S., Majumdar, P. and Smarandache, F., New operations on intuitionistic fuzzy soft sets based on first Zadeh's logical operator*s*, Journal of New Results in Science, 4 (2014) 71-81.

[33] Chetia, B., Das, P.K., Some results of intuitionistic fuzzy soft sets and its application in decision making, Appl. Math. Sci., 7 (2013) 4693-4712.

[34] Deli, I., *npn*-soft sets theory and applications, Ann. Fuzzy Math. Inform., 10 (2015) 847-862.

[35] Deli, I., Interval-valued neutrosophic soft sets and its decision making, Int. J. Mach. Learn. Cyber., 8 (2017) 665-676.

[36] Deli, I., Eraslan, S. and Çağman, N., ivnpiv-neutrosophic soft sets and their decision making based on similarity measure, Neural Comput. Applic., 29 (2018) 187-203.

[37] Dinda, B. and Samanta, T.K., Relations on intuitionistic fuzzy soft sets, General Mathematics Notes., 1 (2010) 74-83.

[38] Karaaslan, F., Intuitionistic fuzzy parameterized intuitionistic fuzzy soft sets with applications in decision making, Ann. Fuzzy Math. Inform., 11 (2016) 607-619.

[39] Yin, Y., Li, H. and Jun, Y.B., On algebraic structure of intuitionistic fuzzy soft sets, Comput. Math. Appl., 64 (2012) 2896-2911.

[40] Tan, C., A multi-criteria interval-valued intuitionistic fuzzy group decision making with Choquet integral-based TOPSIS, Expert Syst. Appl., 38 (2011) 3023-3033.

[41] Xu, Z., Choquet integrals of weighted intuitionistic fuzzy information, Inf. Sci., 180 (2010) 726-736.

[42] Çağman, N. and Enginoğlu, S., Soft set theory and uni-int decision making, Eur. J. Oper. Res., 207 (2010) 615-625.

Investigation of the effect of Aflatoxin B1 and Aflatoxin G1 on DNA Hybridization by Using Electrochemical DNA Biosensor

Gültekin GÖKÇE[1]* iD , Songül GÖKÇE[2] iD , Şenay ÇETİNUS[2] iD

[1] Cumhuriyet University, Education Faculty, Department of Mathematics and Science Education, Sivas, Turkey
[2] Cumhuriyet University, Science Faculty, Department of Biochemistry, 58140 Sivas, Turkey

Abstract. Biomolecular detection has become a current issue together with the increase in electrochemical sensor studies. The effect of Aflatoxin B1 and Aflatoxin G1 on DNA hybridization was analyzed with electrochemically by using pencil graphite electrode. For this purposes; the changes in guanine currents were monitored before and after hybridization occurred between DNA complementary base sequences using differential pulse voltammetry (DPV). In the first step of this work the capture probe was immobilized by wet adsorption onto the surface of PGE optimizing concentration and immobilization time and then hybridization event was performed between capture and its target probe. In the second step the hybridization experiments were repeated using inosine modified capture probe instead of capture probe which used in the first step. As differently from the first step the inosine modified probe was interacted with 2 µg/mL and 4 µg/mL of AFB1 for 10 min before allowing hybridization and the same protocol was repeated for AFG1. The decrease in guanine current after hybridization was the reference for the genotoxic effects of aflatoxins. The decrease in guanine oxidations in the cases of 2 µg/mL and 4 µg/mL AFG1 and 2 µg/mL and 4 µg/mL AFB1 concentrations were found to be 18% and 26 % for AFG1; and 50% and 61% for AFB1, respectively. AFB1 showed the maximum genotoxic effect to DNA hybridization.

*Keywords***:** Aflatoxin B1, Aflatoxin G1, Pencil Graphite Electrode, Hybridization, Differential Pulse Voltammetry

Aflatoksin B1 ve Aflatoksin G1'in DNA Hibridizasyonuna Etkisinin Elektrokimyasal DNA Biyosensörü ile İncelenmesi

Özet. Biyomoleküler analizlerde yeni teknolojilerin gelişmesi, elektrokimyasal sensör alanındaki çalışmaların da katılmasıyla güncel bir konu olmuştur. Bu çalışmada Aflatoksin B1'in (AFB1) ve Aflatoksin G1'in (AFG1) DNA hibridizasyonu üzerindeki etkisi, kalem grafit elektrot (PGE) kullanılarak elektrokimyasal yöntemlerle analiz edildi. Bu amaçla; guanin oksidasyon akımlarındaki değişiklikler, diferansiyel puls voltametrisi (DPV) ile birbirlerini eşleniği olan DNA baz sekansları arasında hibridizasyon oluşmadan önce ve sonra izlendi. Çalışmanın ilk aşamasında, yakalama probu ıslak adsorpsiyonla PGE yüzeyine immobilize edilirken prob derişimi ve adsorpsiyon süresi optimize edildi ve sonra, hedef prop ile hibritleşmeye tabi tutulurken hedef proba ait konsantrasyon ve hibridizasyon süresi optimize edildi. İkinci aşamada, hibridizasyon deneyleri, birinci aşamada kullanılan yakalama probu yerine inosin modifiye edilmiş yakalama probu kullanılarak tekrarlandı. Ancak, ilk aşamadan farklı bir şekilde inosin modifiye edilmiş prob, hibridizasyona tabi tutulmadan önce 10 dakika süre ile 2 µg / mL ve 4 µg / mL AFB1 ile etkileştirildi ve aynı protokol, aynı koşullarda AFG1 için de tekrarlandı. Hibridizasyondan sonra guanin oksidasyon akımındaki azalma, aflatoksinlerin DNA sekanslarının hibridizasyonuna etkisinin bir sonucu olup, AFB1 ve AFGl'in DNA üzerine genotoksik etkisinin bir göstergesidir. Guanin oksidasyon sinyalindeki azalmalar 2 µg/mL ve 4 µg/mL AFG1 için % 18 ve % 26; 2

* Corresponding author. *Email address:*   *ggokce2000@gmail.com*

μg/mL ve 4 μg/mL AFB1 için % 50 ve % 61 olarak bulundu. Sonuç olarak AFB1'in DNA üzerindeki genotoksik etkisi AFG1'e göre çok daha fazla olarak tespit edildi.

***Anahtar Kelimeler*:** Aflatoksin B1, Aflatoksin G1, Kalem Grafit Elektrot, Hibridizasyon, Diferansiyel Puls Voltametrisi

1. INTRODUCTION

The biosensors in which DNA molecule is used for recognition surface is defined as DNA biosensors or genosensors [1]. DNA biosensors have been frequently used for diagnosis of hereditary and infectious diseases [2, 3], for detection of the microorganisms which trigger food [4] and environment [5] and biological weapons [6]. Particularly DNA biosensors which are used in health field are interesting. Efforts for detection of certain diseases from biological materials like blood, serum, tissue, cell etc. have gained importance in recent years and these studies have begun to be used for detection of bacterial, viral, parasitic and fungal diseases and the mutations [2, 3] which lead to many hereditary diseases.

Hybridization-based DNA biosensors work through binding of the probe which has a short base sequence (20-40 bases) that corresponds to the target sequence to the electrode surface [7, 8]. Hybrid is formed by applying the sensor to the analyte solution which contains the target sequence. This formation converts to an observable signal through the converting system which is found in electrochemical or optic systems.

Hybridization detection of the genes with certain sequences has been performed based on the changes in the oxidation signal (non-indicator method) or the changes in reduction or oxidation signal of a hybridization indicator which interacts with at least one of these bases or an inter-catalyzer hybridization indicator (indicator method) [9, 10]. In recent years, hybridization detection has been carried out by using oxidation signals of DNA bases, guanine and adenine, without using an indicator in electrochemical DNA biosensors and progressed rapidly. Studies are carried out for diagnosis of some infectious and hereditary diseases with non-indicator DNA hybridization method [11, 12]. Nucleic acid recognition-based electrochemical DNA biosensors is a more rapid, inexpensive and easy method than the routine analysis methods in diagnosis of hereditary and infectious diseases [13].

The toxic substances which are synthesized from the secondary metabolisms of molds are defined as "mycotoxin". Mycotoxins are the substances which have various chemical and biological activities on the contrary to the bacterial toxins which are mainly in protein structure and which have antigenic properties. Mycotoxins are accepted as very important natural toxins due to being available and producing toxins by being formed in many food and feedstuff. Aflatoxins which are the most studied mycotoxins were discovered in 1960 and understood to have "hepatotoxic" and "hepatocarcinogen" effects [14]. Aflatoxins are the substances which have the greatest potential to cause hepatocellular cancer and evaluated in the context of Group I carcinogens by The International Agency for Research on Cancer (IARC) [15-17]. Aflatoxins have many significant toxic effects like immune-supression, protein metabolism impairment besides leading to hepatocellular cancer [18]. Aflatoxins are produced by some strains of Aspergillus flavus and by almost all strains of Aspergillus parasiticus [19, 20].

In the present study, the effect of interaction between DNA and aflatoxin (B1 and G1) on the hybridization was investigated by using differential pulse voltammetry (DPV). An inosine modified probe (inosine was used instead of guanine in the sequence of main probe) was immobilized onto the surface of PGE by using wet adsorption (probe concentration and immobilization time were optimized) and hybridization with target probe was performed under optimum conditions. AFB1 and AFG1 were interacted with main probe before hybridization and the changes in guanine oxidation

current signals were monitored before and after hybridization by using differential pulse voltammetry (DPV) technique. To the best of our knowledge, this is the first report on that the effect of interaction between DNA and aflatoxin on the hybridization of DNA.

2. MATERIAL AND METHOD

2.1. Devices

The guanine oxidation peak current was monitored by using DPV technic with an potentiostat/galvanostat analysis system (AUTOLAB PGSTAT 302 N) and GPES 4.8 software. A 7 mL voltammetric cell was used to electrochemical determinations carried out under ambient conditions (23 ± 2 °C). The triple electrode system composed of disposable PGE (as working electrode), platinum wire (as counter electrode) and silver/silver chloride (as reference electrode) was used to perform electrochemical measurements. A Rotring T 0,5 pencil model was the holder of graphite bars. A thin metallic wire was used to provided electrical contact between conductive parts of the pencil.

2.2. Chemical Substances

The oligonucleotides (probes and its complementary) were supplied from IONTEK (İstanbul, Turkey). Concentrated (1000 µg/mL) stock solutions of the lyophilize nucleotide were prepared in Tris-EDTA buffer containing of 10 mM Tris–HCl and 1 mM EDTA (pH: 8.0) and stored as frozen. The experiment solutions were prepared by diluting the concentrated stock solution with 0.5 M acetate buffer (contained 20 mM NaCl; pH 4.8).

0.05 M PBS (phosphate buffer solution which contains 20 mM NaCl; pH 7.4) was used to prepare diluted target solution. All the other chemical reagents used in experiments were in analytical purity grade and supplied from Sigma-Aldrich (Germany). In every case deionized water was used to prepare all solutions.

The sequences of the oligonucleotides (probes and its complementary) were as below:

5'   –   NH2-(CH2)6-GCTCCCCTACTGCTGGCGAAAAG-3': Capture probe

5′-NH2(CH2)6-ICTCCCCTACTICTIICIAAAAI-3′:Probe substituted with inosine

5′-CTTTTCGCCAGCAGTAGGGGAGC-3′:Target probe

AFB1 and AFG1 stock solution were prepared so as to contain 1000 µg/ml in 99.8% methanol (MeOH) solution.

2.3. Guideline for AFB1 and AFG1
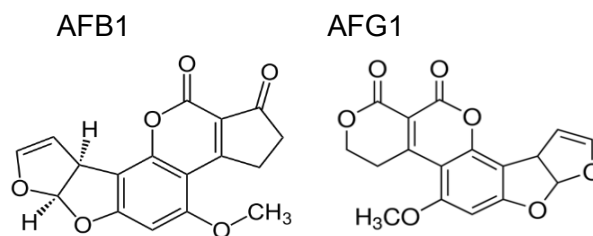
Figure 1. Structural formula of AFB1 ($C_{17}H_{12}O_6$) and AFG1 ($C_{17}H_{12}O_7$).

2.4. Method

AUTOLAB PGSTAT 302 N (Eco Chemie, Netherland) was used as potentiostat device and GPES was used as software program in the present study which was conducted by using differential pulse voltammetry. As triple electrode system, pencil graphite electrode (PGE) was used as working electrode, Ag/AgCl as reference electrode and platin wire was used as counter electrode. All electrodes were bond to the system with metallic connector and measurement solution was adjusted in 7 mL volume.

Activation of PGE:

All in voltammetric measurements the renewable PGE was used to electrochemical determination of DNA hybridization. Graphite ends of the PGE (Rotring T 0,5 pencil, Tombo HB model and 0.5 mm graphite bar) which was 6 cm was cut as 3 cm [21, 22]. 1,5 cm of this 3 cm was marked and

inserted to the voltammetric cell so as the part of 1 cm to be dipped into the solution.

The working electrodes were pretreated in ABS by applying a potential of +1.4 V for 0,5 min. The oxidation peak currents of guanine were monitored with DPV after baseline fitting.

Immobilization of the capture probe and inosine modified probe:

The pencil bars activated by electrochemically were dipped into the vials containing 120 μL capture probe solution at different concentrations ranged between 8- 48 μg/mL in ABS for 30 min. Thus the single stranded capture probe was attached to PGE's surface by adsorption. In order to remove unbounded probe parts the electrodes were immersed in ABS for 3 s. After optimization of probe concentration as 24 μg/mL, optimum adsorption time also optimized as 40 min. In the second step inosine modified probe sequence was immobilized on to surface of PGE at the same conditions.

Hybridization and Aflatoxin interaction:

The hyridization experiments between inosine modified probe and its target were carried out following of inosine modified probe immobilized wit wet adsorption. For this purposes the PGE's which probe modified on their surface were immersed into the vials containing 120 μL target probe solution at different concentrations ranged between 10 - 60 μg/mL in PBS for 30 min. In order to remove unbounded probe parts the electrodes were immersed in PBS for 3 s. After optimization of hybridized target probe concentration as 40 μg/mL, optimum hybridization time also optimized as 50 min. In another step, inosine probe modified PGE were immersed in 2 μg/mL AFB1 and 4 μg/mL AFB1 solutions for 10 min in order to analyze interaction effect on hybridization. This step was repeated for AFG1.

Voltammetric measurement:

The guanine oxidation peak current was determined by using DPV in the potential range of

+ 0.8 V - + 1.4 V in 0.5 M ABS (pulse amplitude and scan rate were 50 mV and 50 mV/s respectively). All experiments were repeated for at least 5 times.

3. RESULTS AND DISCUSSION

In this work, the DNA biosensor (without labeling) based on DPV measurement of the hybridization occured between capture probes (one is interacted with aflatoxins another one is without interacted) and target. This study was aimed to develop a label-free DNA biosensor to analyze the effect on hybridization of interaction between aflatoxins and DNA by using disposable sensor (PGE). The detection of hybridization was monitored according to guanine oxidation peak current occurred at + 1.0 V. The critical event that the probe modified inosine didn't give any oxidation signal before hybridization.

When the capture probe was immobilized by wet adsorption, its concentration (Fig. 2) and the immobilization time (Fig. 3) were optimized according to the guanine oxidation current. According to the optimization experiments, capture probe concentration was found as 24 μg/mL and the immobilization time as 40 min.
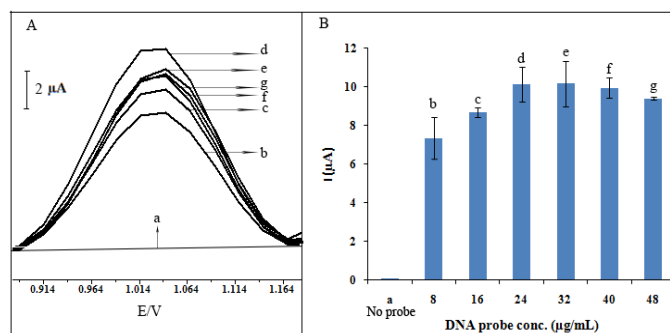
Fig. 2. (A) Voltamograms and (B) Histograms related to guanine oxidation currents according to different capture probe concentrations (immobilization time was constant as 30 min).
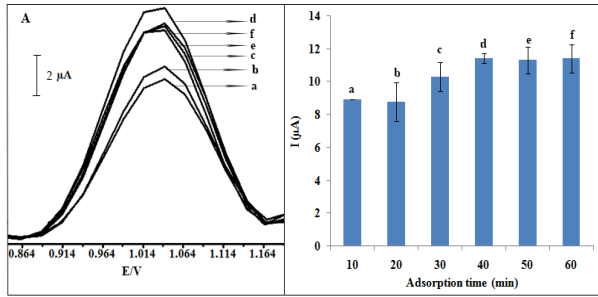
Fig. 3.(A) Voltammograms and (B) Histograms related to guanine oxidation currents according to different capture probe immobilization time (for constant concentration of 24 µg/mL)

The following experiments were related to optimizing the hybridization between capture probe and its complementary target in different hybridization times range of 15 and 60 min (Fig. 4) and the value of the optimum hybridization time was found as 50 min and in different target concentration range of 15 and 60 µg/mL (Fig. 5) and the value of the optimum target concentration was found as 40 µg/mL.
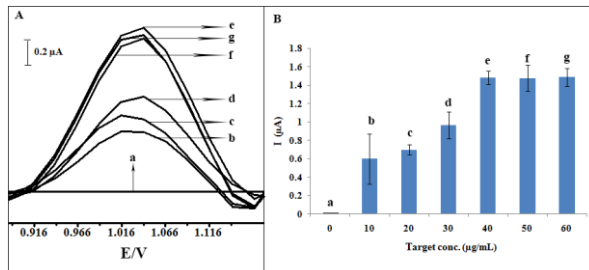
Fig. 4.(A) Voltammograms and (B) Histograms related to guanine oxidation currents according to different concentrations of the target at constant hybridization time of 30 min.
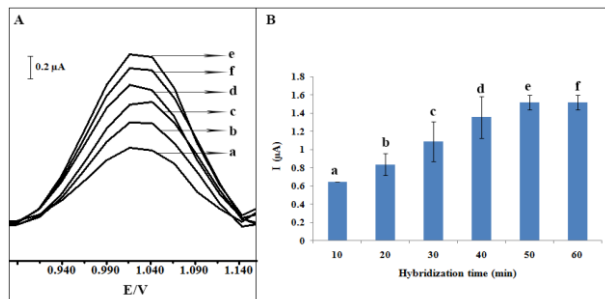
Fig. 5 (A) Voltammograms and (B) Histograms related to guanine oxidation currents according to different hybridization times at constant target concentrations (40 µg/mL).

In the optimization experiments, 50 min hybridization time and 40 ppm complementary target concentration were chosen according to the guanine oxidation signal with a better reproducibility and these values were used for further hybridization studies.

The effects of 2 µg/mL and 4 µg/mL AFB1 and AFG1 (at the same concentrations) on DNA hybridization were analyzed through the changes in oxidation signals of guanine. The obtained voltammograms and histograms were given in Fig. 6 and Fig. 7, respectively.
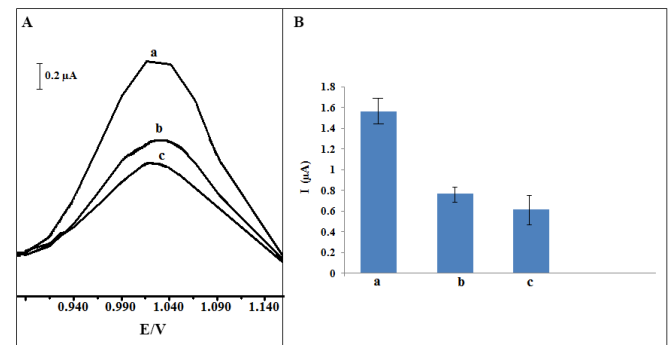
Figure 6 (A) Voltammograms and (B) Histograms related to guanine oxidation currents according to hybridization [without AFB1 interaction (a), interaction with 2 µg/mL AFB1 (b), interaction with 4 µg/mL AFB1 (c)] with target probe.

Figure 7 (A) Voltammograms and (B) Histograms related to guanine oxidation currents according to hybridization [without AFB1 interaction (a), interaction with 2 µg/mL AFB1 (b), interaction with 4 µg/mL AFB1 (c)] with target probe.

Figure 6 shows that the effect of interaction between AFB1 and DNA on hybridization of inosine modified probe with its target according to oxidation signal obtained before interaction with AFB1 (a) and after interaction with 2 µg/mL (b) and 4 µg/mL (c) AFB1. When increased of AFB1 concentration to 4 µg/mL the guanine oxidation current decreased more. So AFB1 was concluded to prevent DNA hybridization with proportion to the concentration of AFB1. The guanine oxidation current was found to decrease 50 % after interaction with AFB1 and this reduction was found to be about 60% when the amount of AFB1 was increased to 4 µg/mL.

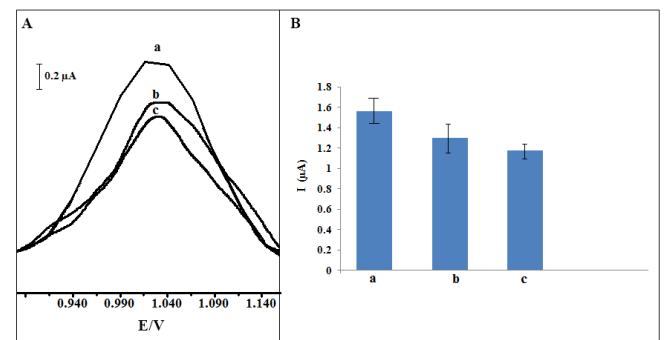The effect of interaction between AFG1 and DNA on hybridization of inosine modified probe with its target according to oxidation signal obtained before interaction with AFG1 (a) and after interaction with 2 µg/mL (b) and 4 µg/mL (c) AFG1 (Figure 7). When increased of AFG1 concentration to 4 µg/mL the guanine oxidation current decreased more. It was concluded that AFG1 also prevented DNA hybridization with proportion to its concentration. The guanine oxidation current was found to decrease 18 % after interaction with AFG1 and this reduction was found to be about 26 % when the amount of AFG1 was increased to 4 µg/mL.

4.   CONSCLUSION

In our study conducted for assessment of sensor technologies-based DNA analyses, activation of pencil graphite electrodes (PGE) and the effect of AFB1 and AFG1 on DNA hybridization on electrode surface were analyzed with electrochemical method. The effect of AFB1 and AFG1 on DNA hybridization was analyzed through the changes in guanine oxidation signal by using DPV with hybridization method using PGE as a working electrode without any labeling. The biosensor consisting of the immobilization of probe which doesn't contain guanine (modified with inosine) onto the surface of PGE was utilized successfully to evaluate of interactions between DNA and Aflatoxins. The duplex formed between inosine modified probe and its target was detected in connection with DPV by measuring the guanine oxidation peak current. In the first step, capture probe modified with inosine was immobilized by wet adsorption onto the pretreated PGE surface.

The hybridization occurred between the modified probe and its target on the PGE's surface was then determined according to the guanine oxidation current [23, 24]. Before hybridization experiments, the inosine modified probe was interacted with AFB1 and AFG1 at the same concentrations and the same time. It was seen that the aflatoxins had genotoxic effect on the hybridization of DNA. It's well known that the aflatoxins have very much genotoxic properties among the mycotoxins and also known that these carcinogenic toxins damage DNA [25]. The aflatoxins contained furan ring when covalently binds to DNA form an epoxide. Studies related to in vitro reaction of synthetic AFB1 –8,9-epoxide with DNA showed that the adduct formation proceed by a pre-covalent intercalation complex between double-stranded DNA and AFB1–exo-8,9-epoxide isomer [26]. Our results in this study also showed that the genotoxic effect could be easily understood and compared each other by utilized hybridization event and AFB1has much more genotoxic effect than AFG1.

ACKNOWLEDGMENTS

REFERENCES

[1]   Kerman, K., Meric, B., Ozkan, D., Kara., P., Erdem, A. and Ozsoz, M., Electrochemical DNA biosensor for the determination of Benzo[a]pyrene–DNA adducts, Analytica Chimica Acta, 450 (2001) 45-52.

[2]   Ozsoz M., Erdem A., Kerman K., Ozkan D., Tugrul B., Topcuoglu N., Ekren H. and Taylan M., Electrochemical genosensor based on colloidal gold nanoparticles for the detection of factor V Leiden mutation using disposable pencil graphite electrodes, Anal Chem., 75 (2003) 2181-2187.

[3]   Palecek E., Fojta, M., Tomschik M., and Wang J., Electrochemical biosensors for DNA damage, Biosensors and Bioelectronics, 13 (1998) 621-628.

[4] Del Giallo M.L., Ariksoysal D.O., Marrazza G., Mascini M. and Ozsoz M., Disposable Electrochemical Enzyme-Amplified Genosensor for Salmonella Bacteria Detection, Analytical Letters, 38 (2005) 2509–2523.

[5] Lin Y., Lu F. and Wang J., Disposable Carbon Nanotube Modified Screen-Printed Biosensor for Amperometric Detection of Organophosphorus Pesticides and Nerve Agents, Electroanalysis, 16-1,2 (2004) 145-149.

[6] Sing Virendra V., Recent Advances in Electrochemical Sensors for Detecting Weapons of Mass Destruction. A Review, Electroanalysis, 28-5 (2016) 920-935.

[7] Chen, J. H., Zhang, J., Huang, L. Y., Lin, X. H. and Chen, G. N., Hybridization biosensor using 2-nitroacridone as electrochemical indicator for detection of short DNA species of Chronic Myelogenous Leukemia, Biosensors & Bioelectronics, 24 (2008) 349-355.

[8] Marrazza, G., Chianella, I. and Mascini, M., Disposable DNA electrochemical sensor for hybridization detection, Biosensors & Bioelectronics, 14 (1999) 43-51.

[9] Brabec V. and Koudelka J., Oxidation of DNA at carbon electrodes the effect of the quality of the DNA sample, J. Electroanal. Chem., 116 (1980) 793-799.

[10] Erdem A, Meriç B., Kerman K., Dalbastı T. and Özsöz M., Detection of interaction between metal complex indicator and DNA by using electrochemical biosensor, Electroanal., 11 (1999) 1372-1377.

[11] Jelen, F., Erdem A. and Palecek, E., Cyclic voltammetry of echinomycin and its interaction with double-stranded and single-stranded DNA adsorbed at the electrode, Bioelectrochemistry,55 (2002) 165-173.

[12] Özkan D., Karadeniz H., Erdem A., Mascini M. and Özsöz M., Electrochemical genosensor for Mitomycin C- DNA interaction based on guanine signal, J. Pharmaceutical and Biomedical Analysis, 35 (2004) 905-912.

[13] Wang A.H.J., Interactions between anti tumor drugs and DNA, Nucleic Acids and Molecular Biology, 1 (1987) 52-58.

[14] Pohland, A.E., Mycotoxins in review, Food Additives Contaminants, 10, (1993) 17-28.

[15] Gündüz, S Kimyacılar için istatistik, Gazi Kitabevi, Ankara (1998) 89.

[16] Hazır, Z. and Çoksöyler, N., Farklı bölgelerde ve farklı yöntemlerle elde edilen kırmızı biberlerde aflatoksin düzeyleri, Gıda Mühendisliği Kongre ve Sergisi (1998) 479-483.

[17] Trucksess, M.W. and Scott, P.M., Mycotoxins in botanicals and dried fruits: a review. Food Additives and Contaminants. 25 (2008) 181–192.

[18] Williams, J.H., Phillips, T.D., Jolly, P.E., Stiles, J.K., Jolly, C.M., Aggerwal, D. Human aflatoxicosis in developing countries: a review of toxicology, exposure, potential health consequences, and interventions, The American Journal Clinical Nutrition. 80 (2004) 1106-1122.

[19] Fernández-Cruz, M.L., Mansilla, M.L. and Tadeo, J.L., Mycotoxins in fruits and their processed products: Analysis, occurrence and health implications, Journal of Advanced Research, 1 (2010) 113–122.

[20] Zinedine, A., González-Osnaya, L., Soriano, J.M., Moltó, J.C., Idrissi and L., Mañes, J. Presence of aflatoxin M1 in pasteurized milk from Morocco. International journal of food microbiology, 114 (2007) 25–29.

[21] Wang, J., Kawde, A. N. , Erdem A. and Salazar, M., Magnetic bead-based label-free electrochemical detection of DNA hybridization, Analyst, 126 (2001) 2020-2025.

[22] Kuralay, F., Erdem, A., Abacı, S. Ozyoruk, H. and Yıldız, A., Poly (vinylferrocenium) coated disposable pencil graphite electrode for DNA hybridization, Electrochem. Commun., 11-6 (2009) 1242-1246.

[23] Smrdel K.S., Seret M., Duh D., Knap N. and Avsic-Zupanc T., Anaplasma phagocytophilum in ticks in Slovenia, Parasitesand Vectors, 3 (2010) 210-215.

[24] Wang J., Cai X., Rivas G. and Shiraishi H., Stripping potentiometric transduction of DNA hybridization processes, Anal. Chim. Act., 326 (1996) 141-145.

[25] Wang, J.S. and Groopman, J.D., DNA damage by mycotoxins, Mutation Research, 424 (1999) 167–181.

On The Synchronization of Van Der Pol-Duffing Oscillator

Selahattin Kındıkoğlu[1]* , *Rıfat Yazıcı[2]*

[1]*Department of Physics, Karadeniz Technical University, Trabzon, TURKEY*
2*Department of Computer Engineering, Istanbul Commerce University, Istanbul,, TURKEY*

Abstract. The most well known property of chaotic systems is their sensitivity to initial conditions. In this work the criterion presented in literature for synchronizing two chaotic systems is applied to a system consisting of two Van der Pol-Duffing oscillators. First, the route to chaos is investigated for the Duffing oscillator. Furthermore, the Lyapunov function approach is used to design a high dimensional chaotic system. Then certain subsystems of a nonlinear chaotic system are synchronized by linking them with a common signal. Synchronization has been observed when there exists an asymptotic stability and an appropriate Lyapunov function, also by computing all the Lyapunov exponents and Kolmogorov entropy.

Keywords: Chaotic systems, Lyapunov exponent, Kolmogorov entropy.

Van Der Pol-Duffing Osilatöründe Senkronizasyon

Özet. Kaotik sistemlerin bilinen en önemli özelliği başlangıç koşullarına duyarlılıktır. Bu çalışmada, literatürde sunulmuş iki kaotik sistemin senkronizasyon kriteri, iki Van Der Pol-Duffing osilatörüne uygulandı. İlk olarak Duffing osilatörü için kaos yolu araştırıldı. Sonra Lyapunov fonksiyon yaklaşımı yüksek boyutlu kaotik bir sistemin oluşturulmasında kullanıldı. Daha sonra doğrusal olmayan bir kaotik sistemin belirli alt sistemleri ortak bir sinyal ile bağlanarak senkronize edildi. Senkronizasyon, uygun Lyapunov fonksiyonu ve asimptotik kararlığının varlığı ile gözlendi.

1. INTRODUCTION

Two identical autonomous chaotic systems started at virtually identical initial conditions would be observed to quickly diverge from one another [1]. That is, their trajectories become uncorrelated, even if each maps out the same attractor in phase space. It is thus impossible to build up two identical, chaotic, synchronized and separated systems. Pecora and Carroll showed that two chaotic systems can be synchronized by dividing each of them into two subsystems, namely, a drive subsystem and a response subsystem and by keeping the variable values of the drive subsystems the same [2]. When the Lyapunov exponents are all negative for the response subsystem, synchronization is achieved [12].

A possible application of synchronization of chaotic signal is to implement a secure communication system. Since chaotic signals are usually broadband, noise like, and difficult to predict, they can be used for masking information bearing waveforms. A chaotic masking signal is added at the transmitter to a message, and at the receiver the masking is reproduced and removed from the received signal [3]. Also, the Van der Pol-Duffing oscillator can be used as model in

---

* Corresponding author. *Email address:*   *kindik@ktu.edu.tr*

physics, engineering electronics, biology, neurology and many other disciplines [13].

Pecora and Carroll have extended the synchronization of chaotic circuits to periodically forced circuits [4]. When one of the subsystem is periodically forced, all the Lyapunov exponents for the subsystem are not negative, the periodical forcing introduces a zero exponent. To make the zero Lyapunov exponent in the response system negative, they use a phase correction circuit to match the phase in a response circuit to the phase in a drive circuit. They also show that the chaotic behavior is a good candidate to keep period-multiplied systems in phase (synchronized) [5]. There is a need for this when many devices are coupled into arrays to increase the sensitivity or power output beyond what one device would provide.

A method of controlling nonlinear and chaotic systems which can synchronize the phase space trajectory to a desired unstable orbit is discussed in [6]. This method utilizes the principles of adaptive control and time dependent changes in the system parameters. The system parameter values are changed according to the deviations of the system variables from desired orbit and the deviations of the controlled parameters from their values for the desired orbit.

A method of transmitting signals in a secure way through chaos synchronization in a physical model has been discussed in [7]. A criterion for synchronization of chaos based on the asymptotic stability has been created and the model developed has been proved to be useful in analog signal transmission.

2. THEORETICAL FRAMEWORK

2.1. Asymptotic Stability

Asymptotic stability commonly appears in linear damped forced systems. When the transient part of the system response is completed and only the forced part remains, the system response no longer depends on the initial conditions, namely, it has converged to stable point or a desired orbit. This state of forgetting the initial conditions, steady state response in forced systems, is known as asymptotic stability.

There is a very close relationship between synchronization and asymptotic stability. The term synchronization denotes an eventual coincidence of two different systems starting with different initial conditions. Asymtotic, however, indicates a case where both systems converge, after sufficient time, to the same eventual state without respect to the initial conditions.

Since chaotic systems very much remember the initial conditions, asymptotic stability for the total chaotic system would be almost impossible. But, it is reasonable that a subsystem of a total chaotic system can exhibit a characteristic of asymptotic stability. Such a system can be considered to be constructed from two parts, namely, master and slave. Now this master-slave system can operate synchronously.

An outline of the Differential Transformation Method (DTM) can be given as follows. Let $x(t)$ be an analytical function in the domain D and $t = t_0$ be a point in D. The function $x(t)$ can be represented by using a t_0-centered power series. The k-th derivative of $x(t)$ is defined as:

2.2. Synchronization of Systems

The phenomena of synchronization is that the slave system knows which state (attractor) to go to when driven (stimulated) by a parameter signal. A dynamical system may be described by the following ordinary differential equation

$$\dot{x} = f(x, \alpha). \tag{1}$$

Where x and f are n-dimensional vectors of the form $x = (x_1, \dots, x_n)$ and $f(x, \alpha) = \{f_1(x, \alpha), \dots, f_n(x, \alpha)\}$ respectively where α is a set of parameters such that the system lies in the chaotic regime. The desired orbit may be chaotic or periodic. The system is then divided into two subsystem a drive subsystem $x_d = (x_1, \dots, x_m)$ and a response subsystem $x_r = (x_{m+1}, \dots, x_n)$ such that $x = (x_d, x_r)$.

A master system $u = (u_d, u_r)$ may be governed by

$$u_d \cdot = f_d(u_d, u_r, \alpha), \qquad (2)$$

$$\dot{u}_r = f_r(u_d, u_r, \alpha). \qquad (3)$$

Furthermore, let the slave system $u' = (u'_d, u'_r)$ be governed by

$$\dot{u'_d} = f_d(u'_d, u'_r, \alpha'), \qquad (4)$$

$$\dot{u'_r} = f_r(u'_d, u'_r, \alpha') \qquad (5)$$

If the derive subsystem of the master is allowed to drive that of the slave (see Fig. 1), then

$$u'_d = u_d \qquad (6)$$

In order to lock the given system onto a given unstable orbit, start the evolution of the system with an initial condition $u'_o = (u'_{do}, u'_{ro})$ which slightly deviates from the desired orbit such that $u'_d = u_d$ but $u'_r = u_r + \delta u_r$. The drive variable u'_d now evolves according to Eq. (2) and the response variable u'_r evolves according to the following equation.

$$\dot{u'_r} = f_r(u_d, u'_r, \alpha') \qquad (7)$$
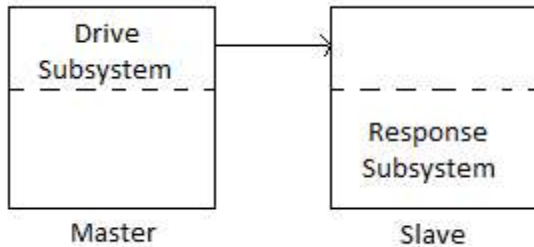
Figure 1. Block diagram of a master-slave system.

Thus the drive variables of the slave are continuously set to those of the desired orbit while the response variables are allowed to evolve freely. The total system will settle down onto the desired orbit, when the drive variables are such that the Lyapunov exponents of the response system are all negative. In this case the difference $u'_r - u_r = \Delta u_r$ goes to zero as $t \to \infty$.

2.3. A Model System-Duffing Oscillator

The Duffing oscillator with a double-well potential can be described by a nonlinear Langevin equation of the form

$$m\ddot{x} + \gamma\dot{x} + \frac{d\phi}{dx} = f(t), \qquad (8)$$

where γ is the damping constant, φ is a double-well potential, and f is a random force or white noise [8,9].

The physical realization of the Duffing oscillator circuit is shown in Fig. 2. The circuit element denoted by N represents a nonlinear negative resistor and can be constructed by using a set of diodes and an operational amplifier. The unfolding parameter is represented by the parameter γ which is controlled by the offset votage of the amplifier. Such a nonlinear element can be described as

$$I_N(V) = \gamma + aV + bV^3, \qquad (9)$$

where $a < 0$ and b$>$ 0. The circuit equations are easily obtained by Kirchoff's laws to the various branches of the circuit as follows

$$\dot{x} = -m(x^3 - \alpha x + \mu - y), \qquad (10a)$$

$$\dot{y} = x - y - z, \qquad (10b)$$

$$\dot{z} = \beta y, \qquad (10c)$$

where differentiation is with respect to time. Here x, y and z correspond to the rescaled form of the voltage across capacitor C_1, the voltage across capacitor C_2, and the current through L, respectively. The rescaled circuit parameters m, α, β, and μ are given as

$$m = \frac{C_2}{C_1}, \qquad \alpha = -(1+\alpha r), \qquad \beta = \frac{C_2 r^2}{L},$$

$$\mu = (br^3)^{1/2}V \qquad (11)$$
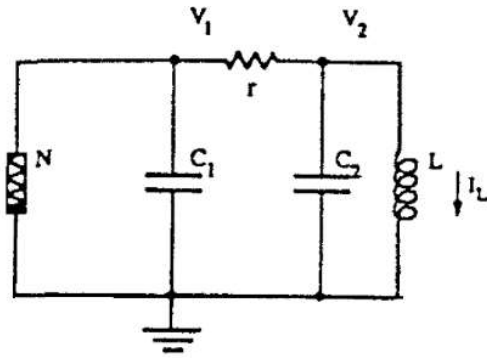
Figure 2. Equivalent circuit of the Duffing oscillator.

Here μ unfolds the double well, if μ = 0 then the wells have equal probability and the system becomes

$$\dot{x} = -m(x^3 - \alpha x - y), \qquad (12a)$$

$$\dot{y} = x - y - z, \qquad (12b)$$

$$\dot{z} = \beta y. \qquad (12c)$$

There are several types of synchronization. One of them holds for systems which are not chaotic, but follow periodic limit cycles. Here a chaotic synchronization approach is introduced together with the necessary and sufficient condition for synchronization of linear or nonlinear systems. This approach exploits an appropriate Lyapunov function to globally establish the asymptotic stability of subsystem. The Lyapunov function can be further used to create a high–dimensional chaotic system, with a nonlinear subsystem. Here we obtained Lyapunov exponents ($\lambda_1 = 2.13$, $\lambda_2 = 0.44$, $\lambda_3 = 0.00$, $\lambda_4 = 0.00$, $\lambda_5 = -75.52$). Also we obtained Kolmogorov entropy and Lyapunov dimension (h_K=2.48 and D_L = 4.04) [13].

For a slave system governed by the subsystem (12a), the following set of equations can be written

$$\dot{x}' = x, \qquad (13a)$$

$$\dot{y}' = x - y' - z', \qquad (13b)$$

$$\dot{z}' = \beta y'. \qquad (13c)$$

Considering the differences between the unprimed and primed quantities and starring them,

$$\dot{y}^* = -y^* - z^*, \qquad (14a)$$

$$\dot{z}^* = \beta y. \qquad (14b)$$

If the Lyapunov function is chosen as in [7], i.e., as

$$E = \frac{1}{2}[(\beta y^* + z^*)^2 + \beta y^{*2} + (1+\beta)z^{*2}], \quad (15)$$

then

$$\dot{E} = -\beta(y^{*2} + z^{*2}) \leq 0. \qquad (16)$$

The equality sign applies only at the origin, therefore the subsystem [(12b) and (12c)] is globally asymptotically stable. Thus the master and slave systems eventually synchronize.

3. CALCULATIONS

The choice of system form should be based on the fact that master and slave systems would be synchronous. Thus a 5-dimensional Duffing system (17a-e) which is derived from the system (12a-c) has been taken.

$$\dot{x}_1 = -mx_1^3 + \alpha m x_1 + m x_2 + x_5, \qquad (17a)$$

$$\dot{x}_2 = x_1 - x_2 - x_3, \qquad (17b)$$

$$\dot{x}_3 = \beta x_2, \qquad (17c)$$

$$\dot{x}_4 = -x_4^3 + x_5 \qquad (17d)$$

$$\dot{x}_5 = -x_1 - x_4 - x_5, \qquad (17e)$$

where $x_i = x_i$(t), i=1,2,3,4,5. The slave has an identical set of equations with the master expect the signal x_3 which is common. Notice that the subsystems are nonlinear, although this is not always necessary. For dissipative system it must be ensured that the divergence of the system is negative. This condition is readily satisfied by the system (17a-e). If all the Lyapunov exponents for the slave system are less than zero, then after initial transients decay, x_1', x_2', x_4', and x_5' will be equal to x_1', x_2', x_4', and, x_5'; that is, the subsystems synchronize. Thus, the first step is to calculate the rest points of the system (17), and the corresponding Jacobian eigenvalues. The Jacobian matrix can be formed as

$-3\mathrm{m}x_1^2 + \alpha\mathrm{m}$	m	0	0	1
1	−1	−1	0	0
0	β	0	0	0
0	0	0	$-3x_4^2$	1
−1	0	0	−1	−1

where x_1, x_2, x_3, x_4, x_5 denote the rest points. When m = 100, α = .35 and β = 300, the system has been found chaotic because it has at least one positive Lyapunov exponent. At the same time, this situation has been observed from the phase portrait of the dynamical variables x_1 and x_2. For m = 100, α =0.11 and β = 300, the solution of the system is found to be periodic, Fig.3b. For the system (17) the rest points and the corresponding Jacobian eigenvalues are shown in Table 1.

Table 1. Rest points and Jacobian eigenvalues of Eq. (17).

Rest Points					Jacobian Eigenvalues		
x_1	x_2	x_3	x_4	x_5			
0.00	0.00	0.00	0.00	0.00	37.1376	$-1.5828 \pm 16.7355i$	$-48.60 \pm 0.8743i$
0.59	0.00	0.59	0.479	0.11	-70.7669	$-0.8524 \pm 0.9868i$	$0.1757 \pm 17.154i$
−0.59	0.00	−0.59	0.479	0.11	-70.7669	$-0.8524 \pm 0.9868i$	$0.1757 \pm 17.154i$

The slave system driven by x_3 is given as

$$\dot{x}_1' = -mx_1'^3 + \alpha m x_1' + m x_2' + x_5', \qquad (18a)$$

$$\dot{x}_2' = x_1' - x_2' - x_3, \qquad (18b)$$

$$\dot{x}_4' = -x_4'^3 + x_5', \qquad (18c)$$

$$\dot{x}_5' = -x_1' - x_4' - x_5'. \qquad (18d)$$

Because Eqs.(17a-e) and (18a-d) establish a unique dynamical system it is possible to observe chaos in the slave system even though all the Lyapunov exponents are negative. If the differences between the corresponding dynamic variables of the master and slave are established and starred, then

$$\dot{x}_1^* = m(\alpha - k_1)x_1^* + m x_2^* + x_5^*, \qquad (19a)$$

$$\dot{x}_2^* = x_1^* - x_2^*, \qquad (19b)$$

$$\dot{x}_4^* = -k_2 x_4^* + x_5^*, \qquad (19c)$$

$$\dot{x}_5^* = -x_1^* - x_4^* - x_5^*. \qquad (19d)$$

where $k_1 = (x_1^2 + x_1 x_1' + x_1'^2) \geq 0$ and $k_2 = (x_4^2 + x_4 x_4' + x_4'^2) \geq 0$.

Consider the Lyapunov function given by

$$E = \frac{1}{2} (x_1^{*2} + x_2^{*2} + x_4^{*2} + x_5^{*2}). \qquad (20)$$

The derivative of Eq. (20) with respect to time is given by

$$\dot{E} = (m(\alpha - k_1) x_1^{*2} + 101 x_1^* x_2^*$$

$$- x_2^{*2} - k_2 x_4^{*2} - x_5^{*2}). \qquad (21)$$

It is clear that $\dot{E} \leq 0$ if x_1^* and x_2^* are of opposite sign and $\alpha \leq k_1$ and the equality sign holds only at the origin ($x_1^* = x_2^* = x_4^* = x_5^* = 0$). Therefore the slave system is glabally asymptotically stable [10, 11, a]. The master (Eqs. (17a-e)) and slave (Eqs.(18a-d)) systems will eventually synchronize as shown in Fig. (3a-d). Furthermore, Lyapunov exponents of the slave are also not positive ($\lambda_1 = -1.05$, $\lambda_2 = -504.6$, $\lambda_3 = -2.39$, $\lambda_4 = 0.00$).
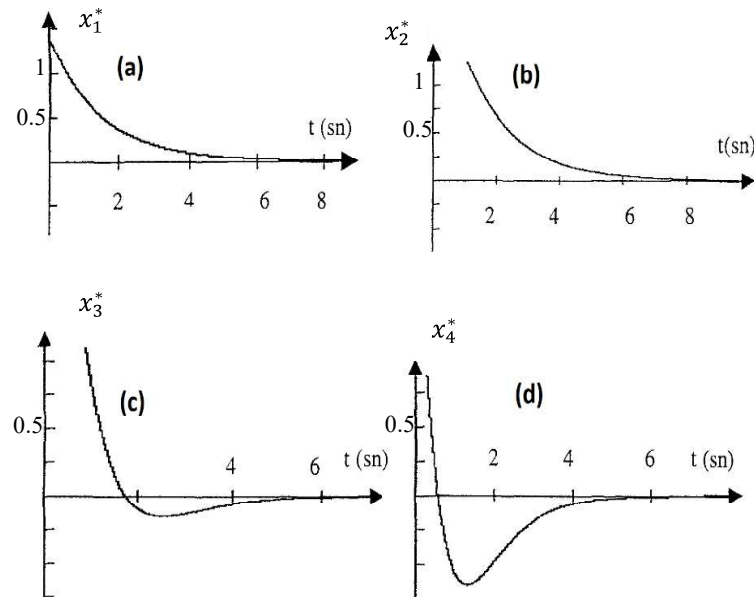
Figure 3(a-d). Synchronization of the dynamics variables of the master and slave systems for β=300 when t→ ∞.

4. CONCLUSION

In this work a criterion for synchronization of chaos, based on the asymptotic stability has been investigated for the Duffing oscillator. This criterion holds for only if the appropriate Lyapunov function is available. This criterion makes it possible to create a high dimensional chaotic system with a nonlinear subsystem. Such a chaotic system has exhibited synchronization in the case of both periodic limits cycles and chaos, Fig. 3a-b. The ability to be able to design a synchronous system consisting of nonlinear and especially chaotic systems has created new opportunities for modelling complex systems and applications of chaos to communications.

REFERENCES

[1] R. He, P. G. Vaidya , Analysis and Synthesisof synchronous Periodic and Chaotic Systems, Physical Review A, 46 (1992) 7387-7392.

[2] L. M. Pecora , T. L. Carroll, Synchronization in Chaotic Systems, Physical Review Letters, 64 (1990) 821-824.

[3] K. M. Cuomo, A.W. Oppenheim, S. H. Strogatz, Synchronization of Lorenz-Based Chaotic Circuits with Applications to communication, IEEE Trans. On Circuit and Systems-II, 40 (1993) 626-633.

[4] T. L. Carroll, L. M. Pecora, Synchronizing Nonautonomous Chaotic Circuits, IEEE Trans.

[5] On Circuits and Systems-II, 40 (1993) 646-650.

[6] T. L. Carroll, L. M. Pecora, Using Chaos to keep Period-Multiplied Systems in Phase, Physical Review E, 48 (1993) 2426-2436.

[7] J. K. John, R. E. Amritkar, Synchronization of Unstable Orbits Using Adaptive Control,physical Review E, 49 (1994) 4843-4847.

[8] K. Murali, M. Lakshmanan, Transmission of Signals by Synchronization in a Chaotic Van der Pol-Duffing Oscillator, Physical Review E, 48 (1993) R1624-R1626.

[9] G. P. King, S. T. Gaito, Bistable Chaos I Unfolding the Cusp, Physical Review A, 46 (1992) 3092- 3099.

[10] V. English, W. Lauterborn, Regular Window Sructure of a Double-Well Duffing Oscillator, Physical Review A, 44 (1991) 916-924.

[11] Shinners, S. M., Modern Control System Theory and Desing, John Wiley and Sons, Inc., 1992.

[12] Hilborn, R. C., Chaos and Nonlinear Dynamics, An Introduction for Scientists and

Engineers, New York, Oxford , Oxford University Press, 1994.

[13] U. E. Vincent, B. R. Nana Nbendjo, A. A. Ajayi, A. N. Njah, P. V. E. McClintock, Hyperchaos and bifurcations in a driven Van der Pol-Duffing Oscillator circuit, Int. J. Dynam. Control (2015) 3:363-370.

[14] S. Kındıkoğlu, R. Yazıcı, A. I. Kopya, hyperchaos in Van der Pol-Duffing Oscillaor, 19.04. 2000, Turkish Pyhsical Society.

Dose Calculations of SPECT Simulations on Dynamical Targets with GATE / GEANT4

Sinan KUDAY [1] iD

[1] *Istanbul Aydın University, Application and Research Center For Advanced Studies, 34295, Istanbul, TURKEY*

Abstract. Simulations of SPECT studies have been taken attention with the fact that more accurate results can be constructed in medical imaging with developing computing techniques. As a result, one can visualize new ideas or improvements with the help of medical simulations before applying on real incidents for clinical purposes acquiring high level of statistics without harming live tissues. In this study, we focused on the capability of GATE (a simulation toolkit for PET & SPECT) that is developed under GEANT4 simulation framework and applications on the effects such as activity degradations, displacements and overlapping of the tissues. Energy histograms and dose calculations are obtained by using built-in tissues and analyzing virtual data using ROOT analysis software. Results show the magnitudes of effects that may have a significant disturbance on SPECT images and their dependence on spesific parameters.

*Keywords***:** SPECT, CT, Geant4, GATE, ROOT, Simulation.

GATE / GEANT4 ile Dinamik Kaynaklar üzerinde SPECT Benzetimlerinin Doz Hesaplamaları

Özet. SPECT çalışmalarının simülasyonları, gelişen bilgisayar teknikleriyle birlikte tıbbi görüntülemede daha doğru sonuçların elde edilebileceği gerçeğine dikkat çekmektedir. Sonuç olarak, canlı dokulara zarar vermeden yüksek düzeyde istatistik elde etmek için gerçek olaylara uygulanmadan önce tıbbi simülasyonların yardımıyla yeni fikirler veya iyileştirmeler görselleştirilebilir. Bu çalışmada, GEANT4 simülasyonları çerçevesinde geliştirilmiş GATE (a simulation toolkit for PET & SPECT) yazılımının yetenekleri ile aktivite azalmaları, yer değiştirmeler ve dokuların üst üste gelmeleri gibi etkilerin uygulamaları üzerine yoğunlaştık. Enerji histogramları ve doz hesaplamaları, öntanımlı dokular kullanılarak ve ROOT analiz yazılımı kullanılarak sanal verilerin analiz edilmesiyle elde edildi. Sonuçlar, SPECT görüntülerde ve bunların spesifik parametrelere bağımlılıklarında önemli bir bozulmaya neden olabilecek etkilerin büyüklüğünü göstermektedir.

*Anahtar Kelimeler***:** SPECT, CT, Geant4, GATE, ROOT, Benzetim.

1.   INTRODUCTION

Single photon emission computed tomography (SPECT), as one of the most effective techniques in nuclear imaging for functional visualization of human or animal bodies [1], is based on the detection and reconstruction of gamma photons that decayed by the radiotracers introduced into the body before the process. A SPECT system contains gamma cameras that is fixed on the gantry and rotates around the target (body) that is of interest recording the two-dimensional projection of a three-dimensional activity distribution of radiotracers [2]. Afterwards, a serial algorithms are executed to reconstruct the three

dimensional real-like images from acquired two-dimensional images by the SPECT system. As a medical imaging technique, SPECT, can be considered together with a CT system that forms the hybrid usage of both technologies named as SPECT / CT. Considering their scan geometries, 5 generations of CT systems may be classified for multi purposes by the time they are firstly introduced in 1960s [3, 4]. Fifth generation CT systems are convenient to make detections with cylindrical scanners and prepare source as a cone beam from higher energy X-ray sources. On the other hand, third and fourth generation CT systems use fan beam scanners with multiple array of detectors in different geometries. Recent hybrid systems are quite succesfull processing and superposing both SPECT and CT images allowing to detect targeted lesions [5, 6]. Because of their fast scanning features, it is not surprising to see handheld SPECT devices used in combination with a thoracoscopic gamma detector that are already introduced to mark smal sized nodules during surgical excision [7].

In the fundamental principles of SPECT data acquisitions, it needs to be reconstructed 3D/4D models from 2D spectrums of target using a Fourier transform. This process actually corresponds a modelling simulation taking into account the attenuation effects and the measurement errors [8]. Thus one can understand the simulation need in a hybrid procedure as SPECT / CT imaging in two ways: i. modelling from CT image reconstructions, ii. modelling from irradiation of radiotracers injected in the target. Note that since both of the simulation types help oncologists providing different certainities and sensitivities, a hybrid imaging procedure overlaps two models together to obtain a better conclusion: CT reconstruction algorithms are based on grey scale measurements from X-ray frequencies and SPECT algorithms use track distributions of lesions from radiated gamma measurements. Thus one can understand the aim of a SPECT simulation as creating a realistic model to trace development of diseases [9]. In order to complete this task, not only visually but also numericaly realistic model needs to be simulated to obtain quantitative changes in dose volumes and

irradiation distributions. In addition to the above mentioned, for educational purposes, simulations of medical techniques seem to be the most accurate and harmless solution.

In this work, we have used a setup based on the SPECT benchmark of GATE v8.1 (a simulation toolkit for PET & SPECT) running under the GEANT4 framework that is developed as a detector simulation for general purposes at CERN [10]. Thus, one can consider GATE package as a medical physics oriented tool that consists of several applications in imaging, radiotherapy, realistic phantom categories as well as internal dosimetry for preclinical applications. It is worthwhile to mention that GATE is more comphrensive and precise than some of its successors that is also developed uder Geant4 framework [11] while we are noting that all of these softwares are still under development.

For years, CERN as a major experimental laboratory based on the nuclear researhes, also issued studies that has brought high technology and insights in to medical researches. Not only producing isotopes that are needed ingredients of radiopharmaceuticals in ISOLDE collaboration but also supporting new design ideas of medical accellerators on cancer treatments in university/institute collaborations [12]. Especially after the major upgrade of Geant4 in 2015 releasing the version 10.0, medical simulations based on Geant4 frameworks began to be considered as the detailed detector simulations that have the highest resolution in imaging and complex geometries in setup.

The outline of our paper has been prepared as; the definitions of main simulation setup and geometries in section II, considered dynamical cases in data acquisition in section III, analysis and dose calculations in section IV and presenting the results with a brief interpretation in section V.

2.　GATE/GEANT4 SIMULATIONS

2.1. GATE/GEANT4 Simulation Setup

At the first stage of this study, we have followed the procedure preparing a macro to create a SPECT

geometry as mentioned in GATE user manual [13]. In Fig.1, a simple box geometry that has the dimensions of 7x21x30 cm is shielded with lead and repeated 4 times to obtain SPECT heads. (Note that some of the SPECT systems already have 3 heads.) SPECT head system is made of three levels: base (white), collimator (red) and crystal (yellow). Base geometry of SPECT heads are placed in a ring orbit with 0.15 deg/s fixed velocity. A collimator geometry with lead shielding is created in 3x19x28 cm (3 cm thickness) dimensions and hexagone paralell holes are placed around Y-Z axis. For the last level, a NaI crystal volume has been created as the main read-out of the system in 1 cm thickness and placed after collimator layer. A back compartment in 2.5 cm thickness made of glass is placed as the last layer. For the middle stage; a table surface made of glass, cylindrical phantom and cylindrical source geometries are created with 20 cm height and 15 cm radius. Translations and materials for these geometries are chosen from different tissues during the data taking to simulate dynamic effects that will be mentioned in the next sections. For simulated activity, a source confinement is defined in the phantom and a gamma source set at 140 KeV energy with 15 KBq activity by default.
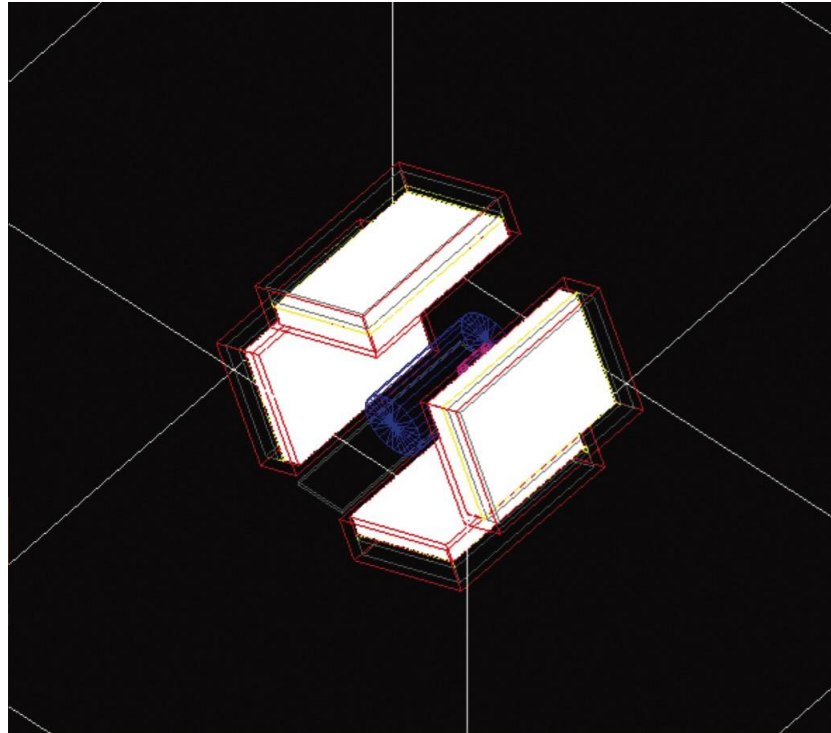
Figure 1: Virtualization of SPECT scene with the placements of base, four NaI cameras, collimators and cylindrical phantom on the table surface.

2.2. Simulation Specifications

Dominant physics processes are included as standard model e- interactions, rayleigh & compton scattering, photoelectric effect, electron ionisation and bremsstrahlung. The simulated data acquired by 5 second intervals from 4 different angles along a circular orbit. Compton events occurring in the phantom, collimator, back compartment, shielding and table are recorded. However, defining a dose actor into propoer regions of the simulation setup can record direct dose values obtained from the source. In order to observe detector outputs from SPECT device, one should modelize data digitization process in a simulation. An output is obtained more realisticly after applying blurring process that will gain resolution and distribution. Gaussian energy blur is applied to the events detected in the crystal, using an energy resolution of 10% at 140 keV. The limited spatial resolution

of the photomultipliers and associated electronic is modelled using a Gaussian blur with a standard deviation of 2 mm. Thus, one can calculate FWHM of a pulse if it is assumed to has a Gaussian distribution as E × R where E is the peak energy and R is the resolution. Default random number generator is used and seeded differently for each run.

Dose calculations are calculated from the acquired gammas from the located source in the center of the cylindrical phantom. A dose actor element is created attaching to the SPECT head volumes and the root analysis outputs are obtained at the end of each run. As running a previously coded a root macro over outputs, DVH (Dose Volume Histograms) are calculated and plotted as described in section IV. Profile histograms in Fig.2 shows the outputs for the world volume with default activity values in X-Y, X-Z and Y-Z point of views respectively.
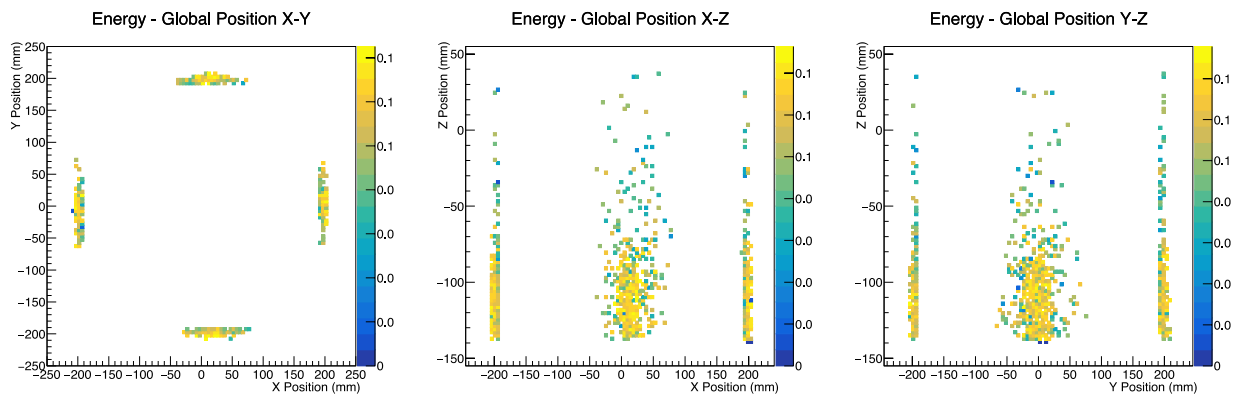
Figure 2: Global distributions based on the world volume for X-Y, X-Z and Y-Z surfaces respectively.

3.   SIMULATED DATA PRODUCTION

In this work, we considered several dynamical cases for target, namely a cylindirical phantom, that may cause possible failures in SPECT imaging as follows:

1. Activity Degradations: Intravenously or intracavitary injected radiopharmaceutical include high-affinity molecules as carriers to tumor cells. Thus, radiopharmaceutical has two important components: Chemical compound and radionuclide. One of the most common problems in radiopharmaceutical productions is impurity of substances due to the fact that it is not possible to treat molecules one by one in atomic level. Such impurities can not be observed directly but may block bonding of radionuclide molecules to targeted tissues. If this is the case, one can expect activity degradations during medical imaging processes such as SPECT.   We simulated activity degradations by reducing gamma activity in data taking from SPECT-head starting from 40000 Bq with 5000 Bq intervals. Total activities are

acquired similar to Fig. 2 but with less entries after each reduction. We give statistical analysis and related DVHs from our calculation in the next section.

2. Volume Displacements: We refer here natural displacements and movements during radiological imaging such as breathing, heart beating or reflex-induced motions of patient that have the small amplitudes. In order to simulate the motions, one can categorize them according their coordinates and directions: translational and rotational motions. SPECT devices usually apply built-in correction algorithms for correcting rotational movements but not for translational movements. The main reason for that translational movements may be unrepeated movements to predict before the action comparing with the rotational movements. It is possible to create such an algorithm defining a fourier transform from a given reference frame to acquired image. Hence that calculating the transform phase and peak will yield the idea of how much correction is needed in the frame or confidence level. In this work to simulate volume

displacements, we set translations for the phantom with 0.5, 1, 1.5 and 2 cm respectively. Profile histograms for the source has reflected the direct image of a squeezing phantom as in Fig.3 for 20 seconds time intervals. For this dynamical case, each run has been merged to form one single continuous run.
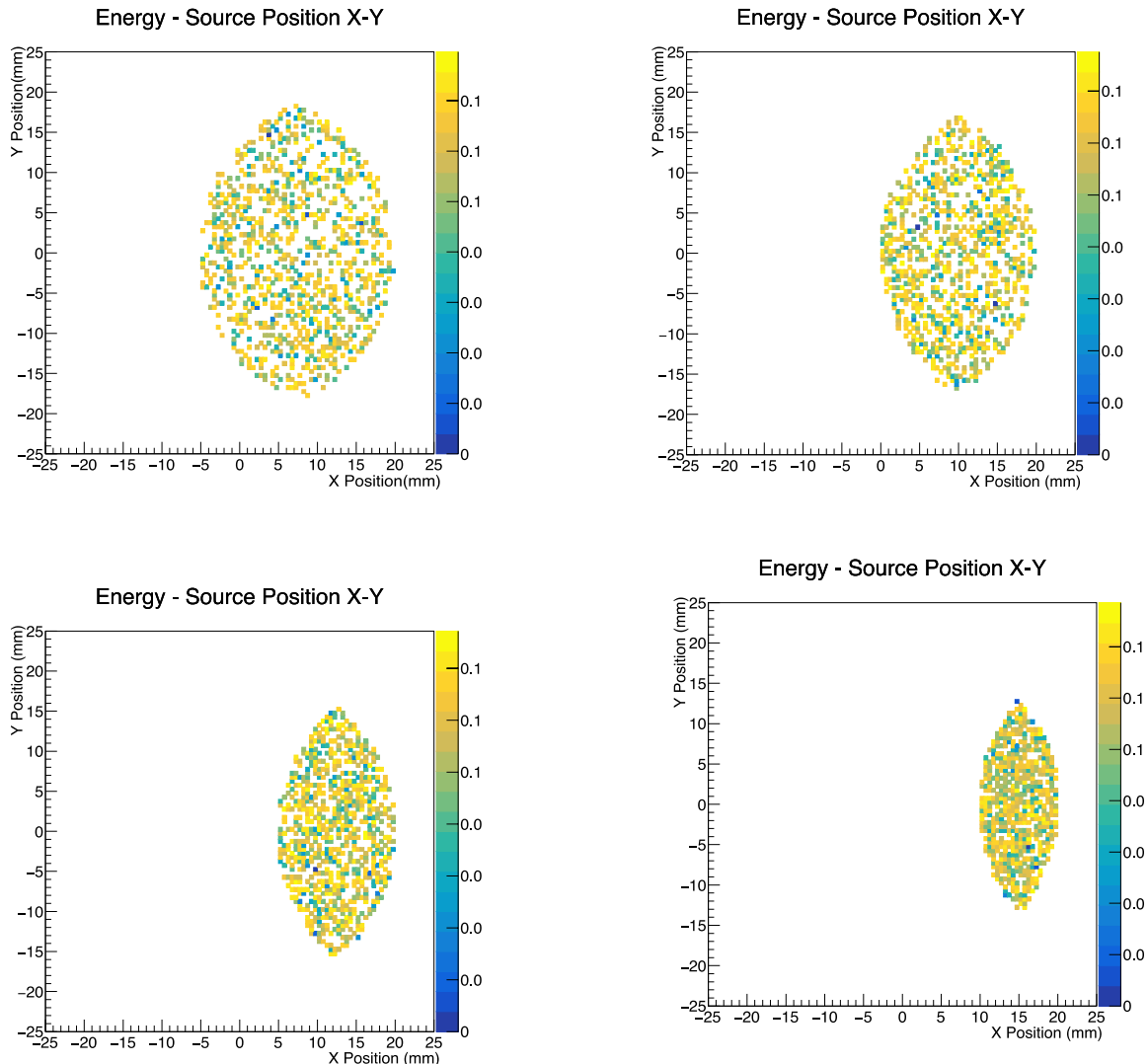
Figure 3: As an example to respirational motion, source profile histograms of small displacements with 0.5, 1, 1.5 and 2 cm respectively on the X-Y surface.

3. Tissue / Material Overlapping: A common and inevitable problem in nuclear imaging can be considered as tissue overlapping that refers to intervening of untargeted organs during diagnosis or treatment. Succesively, that problem increases the attenuation probability since the untargeted organs have potential to absorb doses. SPECT / CT system, that applies attenuation correction algorithms removing soft tissue artifacts from medical images, allows a better accuracy. However it is an important knowledge that how much energy will be absorbed by those tissues and in what significances. We have defined several tissues and materials as below (where d is the density and NoA is number of atoms) and placed around the gamma source and calculated the absorbed dose distributions as in the next section. A statistical analysis of the data yields the significances if those distribution differences are at the important levels. Differences from vacuum and 100% overlapping cases are considered where the source completely covered by the material.

Air: d=1.29 mg/cm^3; State = gas; Elements (Fraction) : Nitrogen (0.755268); Oxygen (0.231781); Argon (0.012827); Carbon (0.000124).

Blood: d=1.06 g/cm^3; State = liquid; Elements (Fraction) = Hydrogen (0.102); Carbon (0.11); Nitrogen (0.033); Oxygen (0.745); Sodium (0.001); Phosphor (0.001); Sulfur (0.002); Chlorine (0.003); Potassium (0.002); Iron (0.001).

Body: d=1.00 g/cm^3; State = solid; Elements (Fraction) = Hydrogen (0.112); Oxygen (0.888).

Plastic: d=1.18 g/cm^3; State=solid; Elements (NoA) = Carbon (5); Hydrogen (8); Oxygen (2).

Water: d=1.00 g/cm^3; State=liquid ;Elements (NoA) = Hydrogen (2) ; Oxygen(1).
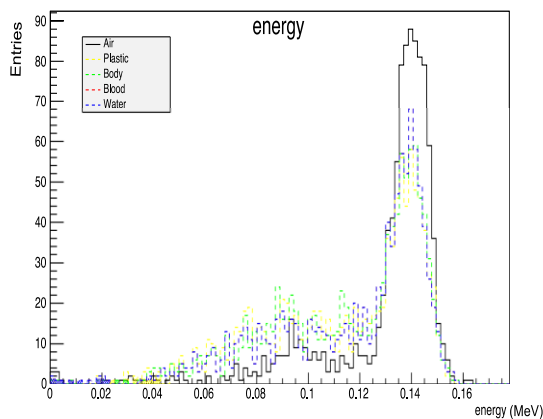
Figure 4: Energy histogram based on the different materials show the overlapping effect on tissues in arbitrary units.

4. ANALYSIS OF ENERGY & DOSE CALCULATIONS

After data is obtained in root file format, a simple macro script is created to calculate absorbed dose percentages in a given volume *V* as $d(D_0 - D) / dV$ where D_0 is the dose of the source and D is the measured dose by the SPECT system. Target volume has been differantiated in a loop and dose values against each volume calculated as in Fig.5, Fig.6, Fig.7. Apparent dose differences are observed except for similarly defined materials such as blood and water in Fig.7. Thus, instead of using built-in materials, one should define

materials with more details to conclude dose separations in such plots. However, in order to realize if those values are at important levels, one can implement a χ^2 test of indepence as statistical analysis separetely constructing null and alternative hypothesis. One can call null hypothesis as "A single image case (Activity Degradations / Volume Displacements / Tissue Overlapping) has no effect on dose measurements" and its opposite as the alternative hypothesis. Therefore, we calculated the χ^2 values as follows where *O* is the observed values, *E* is the expected values and i is the number index for the measurement;

$$\chi^2 = \sum_i (O_i - E_i) / E_i \qquad (1)$$

Here we call expected value as 40000 Bq for activity degredations, 0 cm for volume displacements and vacuum environment for tissue overlappings. In Table 1, χ^2 values are revealed for each case to decide accepting the null hypothesis or not. Basicly, a standart χ^2 table should be used for relevant significance levels.
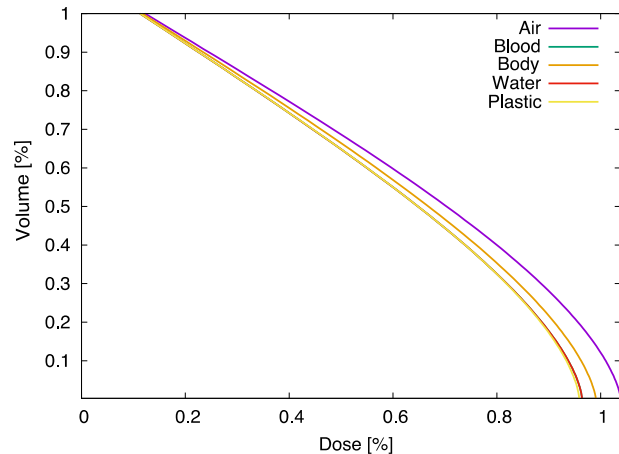
Figure 5: DVHs for tissue / material overlapping around the 40000 Bq gamma source.

Table 1. Calculated χ² values of doses for the considered imaging cases

Activity Degradations	15000 Bq	20000 Bq	25000 Bq	30000 Bq	35000 Bq
	1.48	1.023	0.77	0.3	0.073
Volume Displacements	0.5 cm	1 cm	1.5 cm	2 cm	2.5 cm
	0.0034	0.008	0.014	0.048	0.07
Tissue / Material Overlapping	Blood	Body	Plastic	Water	Air
	0.087	0.036	0.092	0.087	~ 0

5. CONCLUSION

In this letter, we have qualitatively investigated that if one can observe significant disturbances in imaging via the SPECT simulations of GATE / Geant4. Note that for $\alpha = 0.9$, volume displacements with more than 2.5 cm, activity degradations with more than 15000 Bq and tissue / material overlappings with heavier than 1.25 g/m³ density will significantly effect on dose measurements. Thus, one should have to apply additional correction methods if any of the SPECT runs have suffered from above mentioned issues. According to recent medical publications, those result show that the SPECT calibration of GATE is quite accurate meeting the realistic expectations.

REFERENCES

[1] Buck K. A., Nekolla S., Ziegler S., Beer A., Krause A. J., Herrmann K., Scheidhauer K., Wester H., Rummeny E. J., Schwaiger M., Drzezga A., SPECT/CT , J. Nucl. Med., 49-8 (2008) 1305-1319.

[2] Bybel B., Brunken R. C., DiFilippo F. P., Neumann D. R., Wu G., Cerqueira M. D., SPECT/CT Imaging: Clinical Utility of an Emerging Technology, Radiographics, 28-4 (2008) 1097-1113.

[3] Madsen, M.T., Recent advances in SPECT imaging., J Nucl. Med., 48-4 (2007) 661–673.

[4] Groch, M.W., Erwin, W. D., SPECT in the year 2000: Basic Principles, J. Nucl. Med. Technol., 28-4 (2000) 233-244.

[5] Habib, Z., Hasegawa, B., Determination of the Attenuation Map in Emission Tomography, J. Nucl. Med., 44-2 (2003) 291-315.

[6] Khalil M. M., Tremoleda J. L., Tamer B. Bayomy, and W. Gsell, Molecular SPECT Imaging: An Overview, International Journal of Molecular Imaging, 796025 (2011) 1-15

[7] Müller J., Putora P. M., Schneider T., Zeisel C., Brutsche M., Baty F., Markus A., Kick J., Handheld single photon emission computed tomography (handheld SPECT) navigated video-assisted thoracoscopic surgery of computer tomography-guided radioactively marked pulmonary lesions, Interactive CardioVascular and Thoracic Surgery, 23-3 (2016) 345–350.

[8] Patton, J.A., Turkington T.G., SPECT/CT physical principles and attenuation correction., J. Nucl Med Technol., 36-1 (2008) 1-10.

[9] Keenan, M. A., Stabin M. G., Segars W. P., Fernald M. J., RADAR Realistic Animal Model Series for Dose Assessment, J. Nucl. Med., 51-3 (2010) 471-6.

[10] Jan, S., *et. al.,* GATE - Geant4 Application for Tomographic Emission: a simulation toolkit for PET and SPECT, Phys Med Biol. , 49-19 (2004) 4543–4561.

[11] Arce P., Mendes P. R., Lagares J. I., GAMOS: a GEANT4-based Easy and Flexible Framework for Nuclear Geant4 Simulations, IEEE Proc. Nuc. Sci. Symp. Conf. Rec., 1 (2008) 3162 - 3168.

[12] CERN-MEDICIS Collaboration, CERN-MEDICIS (Medical Isotopes Collected from ISOLDE): A New Facility, Appl. Sci., 4-2 (2014) 265-281.

[13] http://www.opengatecollaboration.org/sites/default/files/GATE-UsersGuideV8.0.pdf

On Solvability of An Inverse Boundary Value Problem For The Elliptic Equation Of Second Order With Periodic And Integral Condition

Amirov R. Kh.[1]* iD *, Mehraliyev Y.T.[2]* iD *, Heydarzade N.A[2]* iD

[1]Sivas Cumhuriyet University, Faculty of Science, Department of Mathematics Sivas , TURKEY,

[2]Baku Statet University, Faculty of Mathematics, Baku, AZERBAYCAN

Abstract. An inverse boundary value problem for a second-order elliptic equation with periodic and integral condition is investigated. The definition of a classical solution of the problem is introduced. The goal of this paper is to determine the unknown coefficient and to solve the problem of interest. The problem is considered in a rectangular domain. To investigate the solvability of the inverse problem, we perform a conversion from the original problem to some auxiliary inverse problem with trivial boundary conditions. By the contraction mapping principle we prove the existence and uniqueness of solutions of the auxiliary problem. Then we make a conversion to the stated problem again and, as a result, we obtain the solvability of the inverse problem.

*Keywords***:** *Inverse boundary value problem, Elliptic equation, Fourier method, Classical solution.*

İkinci Mertebeden Periyodik ve İntegral Koşullu Eliptik Denklemler İçin Ters Sınır-Değer Problemlerin Çözümü

Özet. Sunulan çalışmada dikdörtgensel bölgede periyodik ve integral tipli koşullarla verilen ikinci mertebeden eliptik tip diferansiyel denklemler için bazı ters problemlerin çözümü ele alınmıştır. Matematiksel fiziğin denklemleri için ters problemler olarak verilen denklemlerin çözümü ile ilgili bilinen ek bilgiler yardımıyla onun katsayıların veya sağ taraftaki fonksiyonların, veya katsayıların ve sağ taraftaki bilinmeyen fonksiyonların birlikte belirlenmesi problemleri düşünülmektedir. Ters problemler bilimin birçok dallarında ortaya çıkmakta olup, özellikle fiziksel ve kimyasal süreçlerin takibi sırasında bazı büyüklüklerin belirlenmesinde önem taşımaktadır. Genelde fiziksel ve kimyasal süreçler diferansiyel denklemlerle ifade edildiğinden ve bu diferansiyel denklemlerin katsayıları da süreçleri ifade eden fiziksel ve kimyasal büyüklüklere bağlı olduğundan, süreçlerin akışının belirlenmesi için bu süreci ifade eden diferansiyel denklemin katsayılarının belirlenmesi önemlidir. Dolayısıyla, ters problemlerin konumu ve çözümü bilimsel açıdan çok önem taşımaktadır.

*Anahtar Kelimeler***:** Ters sınır-değer problemleri,Elliptik denklem, Fourier yöntemi, Klasik çözüm

1. INTRODUCTION

In this paper, we discuss solutions of some inverse problems for second order elliptic differential equations under the periodic and integral type conditions in the rectangular area. By using well known additional information for the solution of inverse problems in mathematical physics equations, we think

---

about the problem to determine their coefficients or right-hand side functions, or state coefficients and right-hand side unknown functions together. Inverse problems have wide-ranging applications in science, in particular, they are very important to determine some scalar quantities during the follow-up physical and chemical processes. In general, physical and chemical processes are expressed by differential equations and their coefficients depend on physical and chemical scalar quantities on which express their process, for these reasons, it is very important to determine these coefficients of differential equations to identify the flow of the process. Hence the position of inverse problem and their solutions are essential in science.

Among them we should mention the papers of A.N. Tikhonov [1], M.M. Lavrentyev [2, 3], V.K. Ivanov [4] and their followers. For a comprehensive overview, the reader should see the monograph by A.M. Denisov [5].

In this paper, we prove existence and uniqueness of the solution for the inverse boundary value problem for the elliptic equation of second order with periodic and integral type conditions.

2. Problem statement and its reduction to an equivalent problem

Consider the equation

$$u_{tt}(x,t) + u_{xx}(x,t) = a(t)u(x,t) + b(t)g(x,t) + f(x,t) \tag{1}$$

in the interior the domain $D_T = \{(x,t) : 0 \le x \le 1, 0 \le t \le T\}$ with the boundary conditions:

$$u(x,0) - \delta u_t(x,0) = \varphi(x), \ u_t(x,T) = \psi(x) + \int_0^T p(t)u(x,t)dt \ (0 \le x \le 1), \tag{2}$$

periodic boundary condition

$$u(0,t) = u(1,t) \quad (0 \le t \le T), \tag{3}$$

nonlocal integral condition

$$\int_0^1 u(x,t)dx = 0 \quad (0 \le t \le T) \tag{4}$$

and the additional conditions

$$u(x_i,t) = h_i(t) \quad (i = 1,2; x_1 \neq x_2; 0 \le t \le T), \tag{5}$$

where $\delta, x_i \in (0,1)$ $(i = 1,2)$-are fixed numbers, $f(x,t), g(x,t), \varphi(x), \psi(x), p(t), h(t)$ -are given functions, $u(x,t)$, $a(t)$ and $b(t)$ - are the unknown functions.

Definition . The triplet $\{u(x,t), a(t), b(t)\}$ is said to be a classical solution of problem (1)–(5), if the functions $u(x,t)$, $a(t)$ and $b(t)$ satisfy the following conditions:

1) The function $u(x,t)$ and its derivatives $u_t(x,t), u_{tt}(x,t)$, $u_x(x,t)$, $u_{xx}(x,t)$ are continuous in the domain D_T;

2) the functions $a(t)$ and $b(t)$ are continuous on the interval $[0,T]$;

3) equation (1) and conditions (2)–(5) are satisfied in the classical (usual) sense.

In order to investigate problem (1) - (5), we first consider the following auxiliary problem: it is required to define a triplet $\{u(x,t),a(t),b(t)\}$ of functions $u(x,t) \in C^2(D_T), a(t) \in C[0,T]$ and $b(t) \in C[0,T]$, from relations (1) - (3),

$$u_x(0t) = u_x(1,t) \quad (0 \le t \le T), \tag{6}$$

$$h_i''(t) + u_{xx}(x_i,t) = a(t)h_i(t) + b(t)g(x_i,t) + f(x_i,t) \quad (i = 1,2; \ 0 \le t \le T). \tag{7}$$

Analogously [6], the following lemma was proved.

Lemma1. Suppose that $\varphi(x), \psi(x) \in C[0,1]$, $p(t) \in C[0,T]$, $h_i(t) \in C^2[0,T](i = 1,2)$,

$$h(t) \equiv h_1(t)g(x_2,t) - h_2(t)g(x_1,t) \ne 0 \ (0 \le t \le T), \ f(x,t) \in C(D_T), \ \int_0^1 f(x,t)dx = 0 \ (0 \le t \le T)$$

, $g(x,t) \in C(D_T)$, $\int_0^1 g(x,t)dx = 0 \ (0 \le t \le T)$ and the compatibility conditions

$$\int_0^1 \varphi(x)dx = 0, \ \int_0^1 \psi(x)dx = 0, \tag{8}$$

$$\varphi(x_i) = h_i(0) - \delta h_i'(0), \ \psi(x_i) = h_i'(T) - \int_0^T p(t)h_i(t)dt \ (i = 1,2). \tag{9}$$

hold. Then the following assertions are valid:

• each classical solution $\{u(x,t),a(t),b(t)\}$ of problem (1)-(5) is a solution of problem (1)-(3), (6), (7);

• each solution $\{u(x,t),a(t),b(t)\}$ of problem (1)-(3), (6), (7), satisfying the condition

$$T\Big((2T + \delta)\|a(t)\|_{C[0,T]} + (T + \delta)\|p(t)\|_{C[0,T]}\Big) < 1, \tag{10}$$

is a classical solution of problem (1)-(5).

3. Existence and uniqueness of the classical solution to the inverse boundary value problem

It is known [7] that the system

$$1, \cos\lambda_1 x, \sin\lambda_1 x, ..., \cos\lambda_k x, \sin\lambda_k x, ... \tag{11}$$

is a basis in $L_2(0,1)$, where $\lambda_k = 2k\pi$ $(k = 1,.2,..)$.

Since the system (11) form a basis in $L_2(0,1)$, we shall seek the first component $u(x,t)$ of classical solution $\{u(x,t), a(t), b(t)\}$ of the problem (1)-(3), (6),(7) in the form

$$u(x,t) = \sum_{k=0}^{\infty} u_{1k}(t)\cos\lambda_k x + \sum_{k=1}^{\infty} u_{2k}(t)\sin\lambda_k x \quad (\lambda_k = 2\pi k), \tag{12}$$

where

$$u_{10}(t) = \int_0^1 u(x,t)dx \ ,$$

$$u_{1k}(t) = 2\int_0^1 u(x,t)\cos\lambda_k x dx \quad (k = 1,2,...),$$

$$u_{2k}(t) = 2\int_0^1 u(x,t)\sin\lambda_k x dx \quad (k = 1,2,...).$$

Then applying the formal scheme of the Fourier method, for determining of unknown coefficients $u_{1k}(t)$ $(k = 0,1,...)$ and $u_{2k}(t)$ $(k = 1,2,...)$ of function $u(x,t)$ from (1) and (2) we have

$$u_{10}''(t) = F_{10}(t;u,a,b) \quad (0 \leq t \leq T), \tag{13}$$

$$u_{ik}''(t) - \lambda_k^2 u_{ik}(t) = F_{ik}(t;u,a,b) \quad (0 \leq t \leq T; \ i = 1,2; \ k = 1,2,...), \tag{14}$$

$$u_{10}(0) - \delta u_{10}'(0) = \varphi_{10}, \ u_{10}'(T) = \psi_{10} + \int_0^T p(t)u_{10}(t)dt \ , \tag{15}$$

$$u_{ik}(0) - \delta u_{ik}'(0) = \varphi_{ik}, \ u_{ik}'(T) = \psi_{ik} + \int_0^T p(t)u_{ik}(t)dt \ (i = 1,2; \ k = 1,2,...), \tag{16}$$

where

$$F_{1k}(t;u,a,b) = a(t)u_{1k}(t) + b(t)g_{1k}(t) + f_{1k}(t) \quad (k = 0,1,...) \ ,$$

$$g_{10}(t) = \int_0^1 g(x,t)dx, \quad f_{10}(t) = \int_0^1 f(x,t)dx, \quad \varphi_{10} = \int_0^1 \varphi(x)dx, \quad \psi_{10} = \int_0^1 \psi(x)dx,$$

$$g_{1k}(t) = 2\int_0^1 g(x,t)\cos\lambda_k x\,dx \ \ (k=1,2,...), \quad f_{1k}(t) = 2\int_0^1 f(x,t)\cos\lambda_k x\,dx \ \ (k=1,2,...),$$

$$\varphi_{1k} = 2\int_0^1 \varphi(x)\cos\lambda_k x\,dx, \quad \psi_{1k} = 2\int_0^1 \psi(x)\cos\lambda_k x\,dx \quad (k=1,2,...),$$

$$F_{2k}(t;u,a,b) = a(t)u_{2k}(t) + b(t)g_{2k}(t) + f_{2k}(t),$$

$$g_{2k}(t) = 2\int_0^1 g(x,t)\sin\lambda_k x\,dx \ \ (k=1,2,...), \quad f_{2k}(t) = 2\int_0^1 f(x,t)\sin\lambda_k x\,dx \ \ (k=1,2,...) ,$$

$$\varphi_{2k} = 2\int_0^1 \varphi(x)\sin\lambda_k x\,dx \quad , \quad \psi_{2k} = 2\int_0^1 \psi(x)\sin\lambda_k x\,dx \quad (k=1,2,...).$$

Solving the problem (13)–(16), we find

$$u_{10}(t) = \varphi_{10} + \left(\psi_{10} + \int_0^T p(\tau)u_{10}(\tau)dt\right)t + \int_0^T G_0(t,\tau)F_{10}(\tau;u,a,b)d\tau \ , \tag{17}$$

$$u_{ik}(t) = \frac{ch(\lambda_k(T-t))}{ch(\lambda_k T) + \lambda_k\delta\,sh(\lambda_k T)}\varphi_{ik} + \frac{sh(\lambda_k t) + \lambda_k\delta\,ch(\lambda_k t)}{\lambda_k\big(ch(\lambda_k T) + \lambda_k\delta\,sh(\lambda_k T)\big)}\left(\psi_{ik} + \int_0^T p(\tau)u_{ik}(\tau)dt\right) +$$

$$+ \int_0^T G_k(t,\tau)F_{ik}(\tau;u,a,b)d\tau \quad (i=1,2; \ k=1,2,...), \tag{18}$$

where

$$G_0(t,\tau) = \begin{cases} -t-\delta, \ t\in[0,\tau] \\ -\tau-\delta, \ t\in[\tau,T], \end{cases}$$

$$G_k(t,\tau) = \begin{cases} \dfrac{ch(\lambda_k(T-\tau))}{\lambda_k\big(ch(\lambda_k T) + \lambda_k\delta\,sh(\lambda_k T)\big)}[\lambda_k\delta\,ch(\lambda_k t) + sh(\lambda_k t)], \ t\in[0,\tau], \\[4mm] \dfrac{ch(\lambda_k(T-t))}{\lambda_k\big(ch(\lambda_k T) + \lambda_k\delta\,sh(\lambda_k T)\big)}[\lambda_k\delta\,ch(\lambda_k\tau) + sh(\lambda_k\tau)], \quad t\in[\tau,T]. \end{cases}$$

After substituting the expressions $u_{1k}(t) \ (k=0,1,...)$ and $u_{2k}(t) \ (k=1,2,...)$ into (12), for the component $u(x,t)$ of the solution $\{u(x,t),a(t),b(t)\}$ to the problem (1)–(3), (6), (7) we get

$$u(x,t) = \varphi_{10} + \left(\psi_{10} + \int_0^T p(\tau)u_{10}(\tau)dt\right)t + \int_0^T G_0(t,\tau)F_{10}(\tau;u,a,b)d\tau +$$

$$+ \sum_{k=1}^{\infty}\left\{\frac{ch(\lambda_k(T-t))}{ch(\lambda_k T) + \lambda_k\delta\, sh(\lambda_k T)}\varphi_{1k} + \frac{sh(\lambda_k t) + \lambda_k\delta\, ch(\lambda_k t)}{\lambda_k\big(ch(\lambda_k T) + \lambda_k\delta\, sh(\lambda_k T)\big)}\left(\psi_{1k} + \int_0^T p(\tau)u_{1k}(\tau)dt\right) + \right.$$

$$\left. + \int_0^T G_k(t,\tau)F_{1k}(\tau;u,a,b)d\tau\right\}\cos\lambda_k x +$$

$$+ \sum_{k=1}^{\infty}\left\{\frac{ch(\lambda_k(T-t))}{ch(\lambda_k T) + \lambda_k\delta\, sh(\lambda_k T)}\varphi_{2k} + \frac{sh(\lambda_k t) + \lambda_k\delta\, ch(\lambda_k t)}{\lambda_k\big(ch(\lambda_k T) + \lambda_k\delta\, sh(\lambda_k T)\big)}\left(\psi_{2k} + \int_0^T p(\tau)u_{2k}(\tau)dt\right) + \right.$$

$$\left. + \int_0^T G_k(t,\tau)F_{2k}(\tau;u,a,b)d\tau\right\}\sin\lambda_k x. \tag{19}$$

Now, using (7) and (12) we have

$$a(t) = \big[h(t)\big]^{-1}\Big\{g(x_2,t)\big(h_1''(t) - f(x_1,t)\big) - g(x_1,t)\big(h_2''(t) - f(x_2,t)\big) -$$

$$- \sum_{k=1}^{\infty}\lambda_k^2 u_{1k}(t)(g(x_2,t)\cos\lambda_k x_1 - g(x_1,t)\cos\lambda_k x_2) -$$

$$- \sum_{k=1}^{\infty}\lambda_k^2 u_{2k}(t)(g(x_2,t)\sin\lambda_k x_1 - g(x_1,t)\sin\lambda_k x_2)\Big\}, \tag{20}$$

$$b(t) = \big[h(t)\big]^{-1}\Big\{h_1(t)\big(h_2''(t) - f(x_2,t)\big) - h_2(t)\big(h_1''(t) - f(x_1,t)\big) -$$

$$- \sum_{k=1}^{\infty}\lambda_k^2 u_{1k}(t)(h_1(t)\cos\lambda_k x_2 - h_2(t)\cos\lambda_k x_1) -$$

$$- \sum_{k=1}^{\infty}\lambda_k^2 u_{2k}(t)(h_1(t)\sin\lambda_k x_2 - h_2(t)\sin\lambda_k x_1)\Big\}. \tag{21}$$

We substitute expression (18) into (20), (21) and have

$$a(t) = \big[h(t)\big]^{-1}\Big\{g(x_2,t)\big(h_1''(t) - f(x_1,t)\big) - g(x_1,t)\big(h_2''(t) - f(x_2,t)\big) -$$

$$- \sum_{k=1}^{\infty}\lambda_k^2\left[\frac{ch(\lambda_k(T-t))}{ch(\lambda_k T) + \lambda_k\delta\, sh(\lambda_k T)}\varphi_{1k} + \frac{sh(\lambda_k t) + \lambda_k\delta\, ch(\lambda_k t)}{\lambda_k\big(ch(\lambda_k T) + \lambda_k\delta\, sh(\lambda_k T)\big)}\left(\psi_{1k} + \int_0^T p(\tau)u_{1k}(\tau)dt\right) - \right.$$

$$+ \int_0^T G_k(t,\tau) F_{1k}(\tau; u, a, b) d\tau \Bigg] (g(x_2, t) \cos \lambda_k x_1 - g(x_1, t) \cos \lambda_k x_2) -$$

$$- \sum_{k=1}^{\infty} \lambda_k^2 \Bigg[\frac{ch(\lambda_k(T-t))}{ch(\lambda_k T) + \lambda_k \delta \, sh(\lambda_k T)} \varphi_{2k} + \frac{sh(\lambda_k t) + \lambda_k \delta \, ch(\lambda_k t)}{\lambda_k \big(ch(\lambda_k T) + \lambda_k \delta \, sh(\lambda_k T)\big)} \Bigg(\psi_{2k} + \int_0^T p(\tau) u_{2k}(\tau) dt \Bigg) -$$

$$+ \int_0^T G_k(t,\tau) F_{2k}(\tau; u, a, b) d\tau \Bigg] (g(x_2, t) \sin \lambda_k x_1 - g(x_1, t) \sin \lambda_k x_2) \Bigg\}, \qquad (22)$$

$$b(t) = \big[h(t)\big]^{-1} \Big\{ h_1(t) \big(h_2''(t) - f(x_2, t)\big) - h_2(t) \big(h_1''(t) - f(x_1, t)\big) -$$

$$- \sum_{k=1}^{\infty} \lambda_k^2 \Bigg[\frac{ch(\lambda_k(T-t))}{ch(\lambda_k T) + \lambda_k \delta \, sh(\lambda_k T)} \varphi_{1k} + \frac{sh(\lambda_k t) + \lambda_k \delta \, ch(\lambda_k t)}{\lambda_k \big(ch(\lambda_k T) + \lambda_k \delta \, sh(\lambda_k T)\big)} \Bigg(\psi_{1k} + \int_0^T p(\tau) u_{1k}(\tau) dt \Bigg) -$$

$$+ \int_0^T G_k(t,\tau) F_{1k}(\tau; u, a, b) d\tau \Bigg] (h_1(t) \cos \lambda_k x_2 - h_2(t) \cos \lambda_k x_1) -$$

$$- \sum_{k=1}^{\infty} \lambda_k^2 \Bigg[\frac{ch(\lambda_k(T-t))}{ch(\lambda_k T) + \lambda_k \delta \, sh(\lambda_k T)} \varphi_{2k} + \frac{sh(\lambda_k t) + \lambda_k \delta \, ch(\lambda_k t)}{\lambda_k \big(ch(\lambda_k T) + \lambda_k \delta \, sh(\lambda_k T)\big)} \Bigg(\psi_{2k} + \int_0^T p(\tau) u_{2k}(\tau) dt \Bigg) -$$

$$+ \int_0^T G_k(t,\tau) F_{2k}(\tau; u, a, b) d\tau \Bigg] (h_1(t) \sin \lambda_k x_2 - h_2(t) \sin \lambda_k x_1) \Bigg\}, \qquad (23)$$

Thus, the problem (1)–(3), (6), (7) is reduced to solving the system (19), (22), (23) with respect to the unknown functions $u(x,t)$, $a(t)$ and $b(t)$.

Using the definition of the solution of the problem (1)-(3), (6),(7), we prove the following lemma.

Lemma 2. *If* $\{u(x,t), a(t), b(t)\}$ *is any solution to the problem (1)–(3), (6), (7), then the functions*

$$u_{10}(t) = \int_0^1 u(x,t) dx \ ,$$

$$u_{1k}(t) = 2 \int_0^1 u(x,t) \cos \lambda_k x \, dx \quad (k = 1, 2, \ldots),$$

$$u_{2k}(t) = 2\int_0^1 u(x,t)\sin\lambda_k x\, dx \quad (k = 1,2,...)$$

satisfy the system (17), (18) in $[0,T]$.

Remark. *It follows from lemma 2 that to prove the uniqueness of the solution to the problem (1)–(3), (6), (7), it suffices to prove the uniqueness of the solution to the system (19), (22), (23)*

. In order to investigate the problem $(1) - (3)$, (6), (7), consider the following spaces

Denote by $B_{2,T}^3$ [6] the set of all functions $u(x,t)$ of the form

$$u(x,t) = \sum_{k=0}^{\infty} u_{1k}(t)\cos\lambda_k x + \sum_{k=1}^{\infty} u_{2k}(t)\sin\lambda_k x \quad (\lambda = 2k\pi),$$

defined on D_T such that the functions $u_{1k}(t)$ $(k = 0,1,2,...)$, $u_{2k}(t)$ $(k = 1,2,...)$ are continuous on $[0,T]$ and

$$\left\| u_{10}(t) \right\|_{C[0,T]} + \left(\sum_{k=1}^{\infty} \left(\lambda_k^3 \left\| u_{1k}(t) \right\|_{C[0,T]} \right)^2 \right)^{\frac{1}{2}} + \left(\sum_{k=1}^{\infty} \left(\lambda_k^3 \left\| u_{2k}(t) \right\|_{C[0,T]} \right)^2 \right)^{\frac{1}{2}} < +\infty.$$

The norm on this set is given by

$$\left\| u(x,t) \right\|_{B_{2,T}^3} = \left\| u_{10}(t) \right\|_{C[0,T]} + \left(\sum_{k=1}^{\infty} \left(\lambda_k^3 \left\| u_{1k}(t) \right\|_{C[0,T]} \right)^2 \right)^{\frac{1}{2}} + \left(\sum_{k=1}^{\infty} \left(\lambda_k^3 \left\| u_{2k}(t) \right\|_{C[0,T]} \right)^2 \right)^{\frac{1}{2}}.$$

Denote by E_T^3 the space $B_{2,T}^3 \times C[0,T]]$ of the vector-functions $z(x,t) = \{u(x,t),a(t),b(t)\}$ with the norm

$$\left\| z(x,t) \right\|_{B_{2,T}^3} = \left\| u(x,t) \right\|_{B_{2,T}^3} + \left\| a(t) \right\|_{C[0,T]} + \left\| b(t) \right\|_{C[0,T]}.$$

It is known that $B_{2,T}^3$ and E_T^3 are Banach spaces.

Now, in the space E_T^3 consider the operator

$$\Phi(u,a,b) = \{\Phi_1(u,a,b), \Phi_2(u,a,b), \Phi_3(u,a,b)\},$$

where

$$\Phi_1(u,a,b) = \tilde{u}(x,t) \equiv \sum_{k=0}^{\infty} \tilde{u}_{1k}(t)\cos\lambda_k x + \sum_{k=1}^{\infty} \tilde{u}_{2k}(t)\sin\lambda_k x, \; \Phi_2(u,a,b) = \tilde{a}(t), \; \Phi_3(u,a,b) = \tilde{b}(t), \text{a}$$

$\tilde{u}_{10}(t)$, $\tilde{u}_{ik}(t)$ $(i = 1,2; k = 0,1,2,...)$, $\tilde{a}(t)$ and $\tilde{b}(t)$ equal to the right hand sides of (17), (18), (22)

and (23), respectively.

It is easy to see that

$$\frac{ch(\lambda_k(T-t))}{ch(\lambda_k T)+\lambda_k \delta\, sh(\lambda_k T)}<1 \quad (0\le t\le T), \quad \frac{sh(\lambda_k t)+\lambda_k \delta\, ch(\lambda_k t)}{\lambda_k\big(ch(\lambda_k T)+\lambda_k \delta\, sh(\lambda_k T)\big)}<1+\delta \quad (0\le t\le T),$$

$$\frac{ch(\lambda_k(T-\tau))}{\lambda_k\big(ch(\lambda_k T)+\lambda_k \delta\, sh(\lambda_k T)\big)}[\lambda_k \delta\, ch(\lambda_k t)+sh(\lambda_k t)]<(1+\delta) \quad (0\le t\le \tau\le T),$$

$$\frac{ch(\lambda_k(T-t))}{\lambda_k\big(ch(\lambda_k T)+\lambda_k \delta\, sh(\lambda_k T)\big)}[\lambda_k \delta\, ch(\lambda_k \tau)+sh(\lambda_k \tau)]<(1+\delta) \quad (0\le \tau\le t\le T) \ .$$

Taking into account these relations, with the help of simple transformations we find:

$$\|\tilde{u}_{10}(t)\|_{C[0,T]}\le |\varphi_{10}|+T\Big(|\psi_{10}|+T\|p(t)\|_{C[0,T]}\|u_{10}(t)\|_{C[0,T]}\Big)+\Bigg[\sqrt{T}\Big(\int_0^T |f_{10}(\tau)|^2 d\tau\Big)^{\frac{1}{2}}+$$

$$+T\|a(t)\|_{C[0,T]}\|u_{10}(t)\|_{C[0,T]}+\sqrt{T}\Big(\int_0^T |g_{10}(\tau)|^2 d\tau\Big)^{\frac{1}{2}}\|b(t)\|_{C[0,T]}\Bigg](T+\delta), \tag{24}$$

$$\Big(\sum_{k=1}^{\infty}(\lambda_k^3\|\tilde{u}_{ik}(t)\|_{C[0,T]})^2\Big)^{\frac{1}{2}}\le \sqrt{6}\Big(\sum_{k=1}^{\infty}(\lambda_k^3|\varphi_{ik}|)^2\Big)^{\frac{1}{2}}+$$

$$+\sqrt{6}(1+\delta)\Bigg[\Big(\sum_{k=1}^{\infty}(\lambda_k^3|\psi_{ik}|)^2\Big)^{\frac{1}{2}}+T\|p(t)\|_{C[0,T]}\Big(\sum_{k=1}^{\infty}(\lambda_k^3\|u_{ik}(t)\|_{C[0,T]})^2\Big)^{\frac{1}{2}}\Bigg]+$$

$$+\sqrt{6}(1+\delta)\Bigg[\sqrt{T}\Big(\int_0^T\sum_{k=1}^{\infty}(\lambda_k^3|f_{ik}(\tau)|)^2\Big)^{\frac{1}{2}}+T\|a(t)\|_{C[0,T]}\Big(\sum_{k=1}^{\infty}(\lambda_k^3\|u_{ik}(t)\|_{C[0,T]})^2\Big)^{\frac{1}{2}}+$$

$$+\sqrt{T}\Big(\int_0^T\sum_{k=1}^{\infty}(\lambda_k^3|g_{ik}(\tau)|)^2\Big)^{\frac{1}{2}}\|b(t)\|_{C[0,T]}\Bigg], \tag{25}$$

$$\|\tilde{a}(t)\|_{C[0,T]}\le \big\|[h(t)]^{-1}\big\|_{C[0,T]}\Big\{\big\|g(x_1,t)\big(h_1''(t)-f(x_1,t)\big)-g(x_1,t)\big(h_2''(t)-f(x_2,t)\big)\big\|_{C[0,T]}+$$

$$
+ \left(\sum_{k=1}^{\infty} \lambda_k^{-2} \right)^{\frac{1}{2}} \Big\| |g(x_1,t)| + |g(x_2,t)| \Big\|_{C[0,T]} \left[\sum_{i=1}^{2} \left(\sum_{k=1}^{\infty} (\lambda_k^3 |\varphi_{ik}|)^2 \right)^{\frac{1}{2}} + (1+\delta) \left[\sum_{i=1}^{2} \left(\sum_{k=1}^{\infty} (\lambda_k^3 |\psi_{ik}|)^2 \right)^{\frac{1}{2}} + \right. \right.
$$

$$
\left. + T \|p(t)\|_{C[0,T]} \sum_{i=1}^{2} \left(\sum_{k=1}^{\infty} (\lambda_k^3 \|u_{ik}(t)\|_{C[0,T]})^2 \right)^{\frac{1}{2}} \right] + (1+\delta) \left[\sqrt{T} \sum_{i=1}^{2} \left(\int_0^T \sum_{k=1}^{\infty} (\lambda_k^3 |f_{ik}(\tau)|)^2 \, d\tau \right)^{\frac{1}{2}} + \right.
$$

$$
\left. \left. + T \|a(t)\|_{C[0,T]} \sum_{i=1}^{2} \left(\sum_{k=1}^{\infty} (\lambda_k^3 \|u_{ik}(t)\|_{C[0,T]})^2 \right)^{\frac{1}{2}} + \sqrt{T} \sum_{i=1}^{2} \left(\int_0^T \sum_{k=1}^{\infty} (\lambda_k^3 |g_{ik}(\tau)|)^2 \, d\tau \right)^{\frac{1}{2}} \|b(t)\|_{C[0,T]} \right] \right] \right\},
$$

(26)

$$
\left\| \tilde{b}(t) \right\|_{C[0,T]} \leq \left\| [h(t)]^{-1} \right\|_{C[0,T]} \left\{ \Big\| h_1(t) \big(h_2''(t) - f(x_2,t) \big) - h_2(t) \big(h_1''(t) - f(x_1,t) \big) \Big\|_{C[0,T]} + \right.
$$

$$
+ \left(\sum_{k=1}^{\infty} \lambda_k^{-2} \right)^{\frac{1}{2}} \Big\| |h_1(t)| + |h_2(t)| \Big\|_{C[0,T]} \left[\sum_{i=1}^{2} \left(\sum_{k=1}^{\infty} (\lambda_k^3 |\varphi_{ik}|)^2 \right)^{\frac{1}{2}} + (1+\delta) \left[\sum_{i=1}^{2} \left(\sum_{k=1}^{\infty} (\lambda_k^3 |\psi_{ik}|)^2 \right)^{\frac{1}{2}} + \right. \right.
$$

$$
\left. + T \|p(t)\|_{C[0,T]} \sum_{i=1}^{2} \left(\sum_{k=1}^{\infty} (\lambda_k^3 \|u_{ik}(t)\|_{C[0,T]})^2 \right)^{\frac{1}{2}} \right] + (1+\delta) \left[\sqrt{T} \sum_{i=1}^{2} \left(\int_0^T \sum_{k=1}^{\infty} (\lambda_k^3 |f_{ik}(\tau)|)^2 \, d\tau \right)^{\frac{1}{2}} + \right.
$$

$$
\left. \left. + T \|a(t)\|_{C[0,T]} \sum_{i=1}^{2} \left(\sum_{k=1}^{\infty} (\lambda_k^3 \|u_{ik}(t)\|_{C[0,T]})^2 \right)^{\frac{1}{2}} + \sqrt{T} \sum_{i=1}^{2} \left(\int_0^T \sum_{k=1}^{\infty} (\lambda_k^3 |g_{ik}(\tau)|)^2 \, d\tau \right)^{\frac{1}{2}} \|b(t)\|_{C[0,T]} \right] \right] \right\}.
$$

(27)

Suppose that the data of the problem (1)–(3), (6), (7) satisfy the following condition

Q_1. $\varphi(x) \in C^2[0,1], \varphi'''(x) \in L_2(0,1), \varphi(0) = \varphi(1), \varphi'(0) = \varphi'(1), \varphi''(0) = \varphi''(1)$.

Q_2. $\psi(x) \in C^2[0,1], \psi'''(x) \in L_2(0,1), \psi(0) = \psi(1), \psi'(0) = \psi'(1), \psi''(0) = \psi''(1)$.

Q_3. $f(x,t), f_x(x,t), f_{xx}(x,t) \in C(D_T), f_{xxx}(x,t) \in L_2(D_T),$

$f(0,t) = f(1,t), f_x(0,t) = f_x(1,t), f_{xx}(0,t) = f_{xx}(1,t) \ (0 \leq t \leq T)$.

Q_4. $g(x,t), g_x(x,t), g_{xx}(x,t) \in C(D_T), g_{xxx}(x,t) \in L_2(D_T),$

$$g(0,t) = g(1,t), g_x(0,t) = g_x(1,t), g_{xx}(0,t) = g_{xx}(1,t) \ (0 \le t \le T) \ .$$

Q_5 . $\delta \ge 0, p(t) \in C[0,T], h(t) \in C^2[0,T], h(t) \ne 0 \ (0 \le t \le T).$

Then, from (25)–(27), we get

$$\left\|\widetilde{u}(x,t)\right\|_{B_{2,T}^3} \le A_1(T) + B_1(T)\left\|a(t)\right\|_{C[0,T]}\left\|u(x,t)\right\|_{B_{2,T}^3} + C_1(T)\left\|u(x,t)\right\|_{B_{2,T}^3} + D_1(T)\left\|b(t)\right\|_{C[0,T]},$$

$$(28)$$

$$\left\|\widetilde{a}(t)\right\|_{C[0,T]} \le A_2(T) + B_2(T)\left\|a(t)\right\|_{C[0,T]}\left\|u(x,t)\right\|_{B_{2,T}^3} + C_2(T)\left\|u(x,t)\right\|_{B_{2,T}^3} + D_2(T)\left\|b(t)\right\|_{C[0,T]},$$

$$(29)$$

$$\left\|\widetilde{b}(t)\right\|_{C[0,T]} \le A_3(T) + B_3(T)\left\|a(t)\right\|_{C[0,T]}\left\|u(x,t)\right\|_{B_{2,T}^3} + C_3(T)\left\|u(x,t)\right\|_{B_{2,T}^3} + D_3(T)\left\|b(t)\right\|_{C[0,T]}, \qquad (30)$$

where

$$A_1(T) = \left\|\varphi(x)\right\|_{L_2(0,1)} + T\left\|\psi(x)\right\|_{L_2(0,1)} + (T+\delta)\sqrt{T}\left\|f(x,t)\right\|_{L_2(D_T)} +$$

$$+ \sqrt{6}\left\|\varphi'''(x)\right\|_{L_2(0,1)} + \sqrt{6}(1+\delta)\left\|\psi'''(x)\right\|_{L_2(0,1)} + (1+\delta)\sqrt{6T}\left\|f_{xxx}(x,t)\right\|_{L_2(D_T)},$$

$$B_1(T) = T(T+\delta) + \sqrt{6}(1+\delta)T \ ,$$

$$C_1(T) = T\left\|p(t)\right\|_{C[0,T]}(T + \sqrt{6}(1+\delta)) \ ,$$

$$D_1(T) = (T+\delta)\sqrt{T}\left\|g(x,t)\right\|_{L_2(D_T)} + (1+\delta)\sqrt{6T}\left\|g_{xxx}(x,t)\right\|_{L_2(D_T)} \ ,$$

$$A_2(T) = \left\|[h(t)]^{-1}\right\|_{C[0,T]}\left\{\left\|g(x_1,t)\left(h_1''(t) - f(x_1,t)\right) - g(x_1,t)\left(h_2''(t) - f(x_2,t)\right)\right\|_{C[0,T]} +$$

$$+ \left(\sum_{k=1}^{\infty} \lambda_k^{-2}\right)^{\frac{1}{2}}\left\||g(x_1,t)| + |g(x_2,t)|\right\|_{C[0,T]}\left(2\left\|\varphi'''(x)\right\|_{L_2(0,1)} + 2(1+\delta)\left\|\psi'''(x)\right\|_{L_2(0,1)} +\right.$$

$$\left.+ 2(1+\delta)\sqrt{T}\left\|f_{xxx}(x,t)\right\|_{L_2(D_T)}\right)\right\},$$

$$B_2(T) = \left\|[h(t)]^{-1}\right\|_{C[0,T]}\left(\sum_{k=1}^{\infty} \lambda_k^{-2}\right)^{\frac{1}{2}}\left\||g(x_1,t)| + |g(x_2,t)|\right\|_{C[0,T]}(1+\delta)T \ ,$$

$$C_2(T) = \left\| [h(t)]^{-1} \right\|_{C[0,T]} \left(\sum_{k=1}^{\infty} \lambda_k^{-2} \right)^{\frac{1}{2}} \left\| |g(x_1,t)| + |g(x_2,t)| \right\|_{C[0,T]} (1+\delta) \|p(t)\|_{C[0,T]} T,$$

$$D_2(T) = 2\left\| [h(t)]^{-1} \right\|_{C[0,T]} \left(\sum_{k=1}^{\infty} \lambda_k^{-2} \right)^{\frac{1}{2}} \left\| |g(x_1,t)| + |g(x_2,t)| \right\|_{C[0,T]} (1+\delta)\sqrt{T} \|g_{xxx}(x,t)\|_{L_2(D_T)},$$

$$A_3(T) = \left\| [h(t)]^{-1} \right\|_{C[0,T]} \left\{ \left\| h_1(t)\left(h_2''(t) - f(x_2,t)\right) - h_2(t)\left(h_1''(t) - f(x_1,t)\right) \right\|_{C[0,T]} + \right.$$

$$+ \left(\sum_{k=1}^{\infty} \lambda_k^{-2} \right)^{\frac{1}{2}} \left\| |h_1(t)| + |h_2(t)| \right\|_{C[0,T]} \left(2\|\varphi'''(x)\|_{L_2(0,1)} + 2(1+\delta)\|\psi'''(x)\|_{L_2(0,1)} + \right.$$

$$\left. \left. + 2(1+\delta)\sqrt{T} \|f_{xxx}(x,t)\|_{L_2(D_T)} \right) \right\},$$

$$B_2(T) = \left\| [h(t)]^{-1} \right\|_{C[0,T]} \left(\sum_{k=1}^{\infty} \lambda_k^{-2} \right)^{\frac{1}{2}} \left\| |h_1(t)| + |h_2(t)| \right\|_{C[0,T]} (1+\delta)T,$$

$$C_2(T) = \left\| [h(t)]^{-1} \right\|_{C[0,T]} \left(\sum_{k=1}^{\infty} \lambda_k^{-2} \right)^{\frac{1}{2}} \left\| |h_1(t)| + |h_2(t)| \right\|_{C[0,T]} (1+\delta)\|p(t)\|_{C[0,T]} T,$$

$$D_2(T) = 2\left\| [h(t)]^{-1} \right\|_{C[0,T]} \left(\sum_{k=1}^{\infty} \lambda_k^{-2} \right)^{\frac{1}{2}} \left\| |g(x_1,t)| + |g(x_2,t)| \right\|_{C[0,T]} (1+\delta)\sqrt{T} \|g_{xxx}(x,t)\|_{L_2(D_T)},$$

It follows from the inequalities (28)-(30) that.

$$\left\| \tilde{u}(x,t) \right\|_{B_{2,T}^3} + \left\| \tilde{a}(t) \right\|_{C[0,T]} + \left\| \tilde{b}(t) \right\|_{C[0,T]} \leq$$

$$\leq A(T) + B(T)\|a(t)\|_{C[0,T]} \|u(x,t)\|_{B_{2,T}^3} + C(T)\|u(x,t)\|_{B_{2,T}^3} + D(T)\|b(t)\|_{C[0,T]}, \tag{31}$$

where

$$A(T) = A_1(T) + A_2(T) + A_3(T), \quad B(T) = B_1(T) + B_2(T) + B_3(T),$$

$$C(T) = C_1(T) + C_2(T) + C_3(T), \quad D(T) = D_1(T) + D_2(T) + D_3(T).$$

So, we can prove the following theorem:

Theorem 1. *Let conditions Q_1 - Q_5 be satisfied, and*

$$(B(T)(A(T) + 2) + C(T) + D(T))(A(T) + 2) < 1 . \qquad (32)$$

Then   problem   (1)-(3),   (6),   (7)   has   a   unique   solution   in   the   sphere $K = K_R(\|z\|_{E_T^3} \leq R = A(T) + 2)$ *of the space* E_T^3.

Proof. In the space E_T^3 consider the equation

$$z = \Phi z , \qquad (33)$$

where $z = \{u, a, b\}$,, the components $\Phi_i(u, a, b)$ $(i = 1,2,3)$ of the operator $\Phi(u, a, b)$ are determined by the right hand sides of equations (19), (22) and (23). Consider the operator $\Phi(u, a, b)$ in the sphere $K = K_R$ from E_T^3. Similar to (31), we get that for any $z_1, z_2, z_3 \in K_R$ the following estimations are valid:

$$\|\Phi z\|_{E_T^3} \leq A(T) + B(T)\|a(t)\|_{C[0,T]}\|u(x,t)\|_{B_{2,T}^3} + C(T)\|u(x,t)\|_{B_{2,T}^3} + D(T)\|b(t)\|_{C[0,T]} \leq$$

$$\leq A(T) + B(T)(A(T) + 2)^2 + C(T)(A(T) + 2) + D(T)(A(T) + 2) , \qquad (34)$$

$$\|\Phi z_1 - \Phi z_2\|_{E_T^3} \leq B(T)R(\|a_1(t) - a_2(t)\|_{C[0,T]} + \|u_1(x,t) - u_2(x,t)\|_{B_{2,T}^3}) +$$

$$+ C(T)\|u_1(x,t) - u_2(x,t)\|_{B_{2,T}^3} + D(T)\|b_1(t) - b_2(t)\|_{C[0,T]} , \qquad (35)$$

Then, it follows from (32 together with the estimates (34) and (35) that the operator Φ acts in the ball $K = K_R$ and is contractive. Therefore, in the ball $K = K_R$ the operator Φ has a unique

fixed point $\{z\} = \{u, a, b\}$, that is a unique solution to the equation (33), i.e. a unique solution to the system (19),(22), (23).

The function $u(x,t)$, as an element of the space $B_{2,T}^3$, is continuous and has continuous derivatives $u_x(x,t), u_{xx}(x,t)$ in D_T .

Now, from (13) and (14) we get

$$\|u_{10}''(t)\|_{C[0,T]} \leq \|a(t)\|_{C[0,T]}\|u_{10}(t)\|_{C[0,T]} + \|b(t)\|_{C[0,T]}\left\|\|g(x,t)\|_{C[0,T]}\right\|_{L_2(0,1)} + \left\|\|f(x,t)\|_{C[0,T]}\right\|_{L_2(0,1)},$$

$$\left(\sum_{k=1}^{\infty}(\lambda_{ik}\|u_{ik}(t)\|_{C[0,T]})^2\right)^{\frac{1}{2}} \leq \sqrt{2}\left(\sum_{k=1}^{\infty}(\lambda_k^3\|u_{ik}(t)\|_{C[0,T]})^2\right)^{\frac{1}{2}} +$$

$$+ \sqrt{2}\left\|\|a(t)u_x(x,t) + b(t)g_x(x,t) + f_x(x,t)\|_{C[0,T]}\right\|_{L_2(0,1)}.$$

Hence it follows that $u_{tt}(x,t)$ is continuous in D_T . It is easy to verify that equation (1) and conditions (2), (3) ,(6) and (7) are satisfied in the ordinary sense.

Consequently, $\{u(x,t), a(t), b(t)\}$ is a solution of problem (1)–(3), (6), (.7), and by Lemma 2 it is unique in the bal $K = K_R$ .The theorem is proved..

By Lemma 1 the unique solvability of the initial problem (1)–(5) follows from the theorem.

Theorem 2. Let all the conditions of Theorem 1 be fulfilled and

$$\int_0^1 f(x,t)dx = 0, \int_0^1 g(x,t)dx = 0 \ (0 \le t \le T),$$

$$\int_0^1 \varphi(x)dx = 0, \ \int_0^1 \psi(x)dx = 0,$$

$$\varphi(x_i) = h_i(0) - \delta h_i'(0), \ \psi(x_i) = h_i'(T) - \int_0^T p(t)h_i(t)dt \ (i = 1,2),$$

$$T\big((2T + \delta)(A(T) + 2) + (T + \delta)\|p(t)\|_{C[0,T]}\big) < 1.$$

Then the problem (1)–(5) has a unique classical solution in the ball $K = K_R \big(\|z\|_{E_T^3} \le A(T) + 2\big)$ of the space E_T^3 .

REFERENCES

[1] Tikhonov A.N., On stability of inverse problems, Dokl. AN SSSR, 39-5 (1943) 195–198 (in Russian).

[2] Lavrent'ev M.M., On an inverse problem for a wave equation, Dokl. AN SSSR, 157-3 (1964) 520–521 (in Russian).

[3] Lavrent'ev M.M., Romanov V.G., Shishatsky S.T. Ill-posed problems of mathematical physics and analysis, M., Nauka, 1980 (in Russian).

[4] Ivanov V.K., Vasin V.V., Tanana V.P., Theory of linear ill-posed problems and its applications, M., Nauka, 1978 (in Russian).

[5] Denisov A.M., Introduction to theory of inverse problems, M., MGU, 1994 (in Russian).

[6] Mehraliyev Ya.T., On solvability of an inverse boundary value problem for a second order elliptic equation, Vest. Tverskogo Gos. Univ., Ser. Prikladnaya Matematika, 23 (2011) 25–38 (in Russian).

[7] Budak B.M., Samarskii A.A.,.Tikhonov A.N, A Collection of Problems in Mathematical Physics, M. Nauka, 1972 (in Russian).

On The Inverse Sum In Degree Index and Co Index

Gülistan KAYA GÖK

¹ Hakkari University, Department of Mathematics Education, Hakkari, TURKEY

Abstract. The inverse sum in degree index of G is specified the degrees d_i and d_j. Some bounds are found for inverse sum in degree index in this study. Also, some definitions and relations are obtained in terms of degrees.

Keywords: İnverse sum in degree index, co index.

Derece Endeksinde ve Ko Endeksinde Ters Toplam

Özet. G' nin derece endeksinde ters toplam d_i ve d_j dereceleri ile belirtilir. Bu çalışmada, derece endeksinde toplam için bazı sınırlar bulunur. Ayrıca, dereceler açısından bazı tanımlar ve bağıntılar elde edilir.

Anahtar Kelimeler: Derece endeksinde ters toplam, Eş endeks.

1. INTRODUCTION

Let G be a simple, connected graph on the vertex set V(G) and the edge set E(G). For $v_i \in V(G)$, the degree of vertex v_i denoted by d_i, the maximum degree is denoted by Δ and the minimum degree is denoted by δ.

The inverse sum in degree matrix $[ISI](G)$ of graphs is defined as

$$[ISI]_{ij} = \begin{cases} \dfrac{d_i + d_j}{d_i d_j} & if\ i\ adjacent\ to\ j \\ 0 & otherwise. \end{cases}$$

The eigenvalues of $[ISI](G)$ are denoted by δ^+. New bounds for these eigenvalues are reported in terms of the degrees.

The Inverse Sum In Degree Index (ISI) index of G is defined as

$$\sum_{v_i v_j \in E(G)} \frac{d_i + d_j}{d_i d_j}.$$

(See [2] for details.)

In this study, different bounds are set using the Estrada index and Zagreb index for ISI index.

The Estrada index of graph G is explained as

$$EE(G) = \sum_{i=1}^{n} e^{\lambda_i}$$

where λ is the eigenvalue of adjacency matrix of G. ([1], [10])

The Zagreb co index of G is described in [5], [7] as

$$\overline{Z_1}(G) = \sum_{v_i v_j \notin E(G),}(d_G(i) + d_G(j)),$$

$$\overline{Z_2}(G) = \sum_{v_i v_j \notin E(G),}(d_G(i)d_G(j)).$$

The Harmonic index of G is specified in [8] as

$$H(G) = \sum_{v_i v_j \in E(G)} \frac{2}{d_i + d_j}.$$

Considering these topological indices, Estrada inverse sum in degree index and inverse sum in degree co index are defined. Indeed, some inequalities are obtained concerned with these indices.

(See [6] for more details deal with this topic.)

2. PRELIMINARIES

In this section, some lemmas and theorems that are needed in main results will be given.

Lemma 2.1. [9]

Let $M = (m_{ij})$ be an $n x n$ irreducible nonnegative matrix and $\lambda_1(M)$ be the greatest eigenvalue with $R_i(M) = \sum_{j=1}^{m} m_{ij}$. Then,

$$(min R_i(M): 1 \leq i \leq n) \leq \lambda_1(M) \leq (max R_i(M): 1 \leq i \leq n)$$

Lemma 2.2. [4]

If G is a simple connected graph and $\lambda_1(G)$ is the spectral radius , then

$$\lambda_1(G) \leq max\left(\sqrt{m_i m_j}: 1 \leq i, j \leq n, v_i, v_j \in E\right)$$

Theorem 2.1. [3]

If $a_i, b_i \in R^+, 1 \leq i \leq n$, then

$$\sum_{i=1}^{n} a_i{}^2 \sum_{i=1}^{n} b_i{}^2 - \left(\sum_{i=1}^{n} a_i b_i\right)^2 \leq \frac{n^2}{4} (M_1 M_2 - m_1 m_2)^2$$

where $M_1 = \max_{1 \leq i \leq n} a_i, M_2 = \max_{1 \leq i \leq n} b_i, m_1 = \min_{1 \leq i \leq n} a_i, m_2 = \min_{1 \leq i \leq n} b_i.$

Theorem 2.2. [5]

Let G be a graph with n vertices and m edges. Then,

$$Z_1(\bar{G}) = Z_1(G) + n(n-1)^2 - 4m(n-1)$$

$$\overline{Z_1}(G) = 2m(n-1) - Z_1(G) = \overline{Z_1}(\bar{G}).$$

Lemma 2.3. [7]

If G is a regular graph, then

$$Z_1(G) \geq \frac{4m^2}{n},$$

$$Z_2(G) \geq \frac{4m^3}{n^2},$$

$$\overline{Z_1}(G) \leq \frac{-4m^2}{n} + 2m(n-1),$$

$$\overline{Z_2}(G) \leq 2m^2 \left(1 - \frac{2m}{n^2} - \frac{1}{n}\right).$$

3. MAIN RESULTS

3.1. Inverse Sum In Degree Index and Estrada Inverse Sum In Degree Index

Firstly, a relation is given for the largest eigenvalue of *ISI* matrix including degrees in this subsection. After, an inequality is obtained for *ISI* index using this relation. In addition, Estrada inverse sum in degree index is defined and some relations are found in terms of degrees and vertices.

Theorem 3.1.1. Let G be graph on n vertices and m edges. Then,

$$ISI(G) \geq \sqrt{\left(Z_2(G) H(G)\right)^2 - \frac{n^2}{4}\left(\frac{\Delta^3 - \delta^3}{2\Delta\delta}\right)}.$$

Proof. Let choose $a_k = d_i d_j$, $b_k = \frac{1}{d_i + d_j}$, $M_1 = \Delta^2$, $m_1 = \delta^2$, $M_2 = \frac{1}{2\delta}$, $m_2 = \frac{1}{2\Delta}$.

By Theorem 2.1, it is seen that

$$\sum_{v_i v_j \in E(G)} (d_i d_j)^2 \sum_{v_i v_j \in E(G)} \left(\frac{1}{d_i + d_j}\right)^2 - \left(\sum_{v_i v_j \in E(G)} \frac{d_i d_j}{d_i + d_j}\right)^2 \le \frac{n^2}{4}\left(\frac{\Delta^2}{2\delta} - \frac{\delta^2}{2\Delta}\right).$$

If necessary organizing is applied, this inequality is obtained as follows:

$$\left(\sum_{v_i v_j \in E(G)} (d_i d_j)\right)^2 \left(\sum_{v_i v_j \in E(G)} \left(\frac{1}{d_i + d_j}\right)\right)^2 - \frac{n^2}{4}\left(\frac{\Delta^2}{2\delta} - \frac{\delta^2}{2\Delta}\right)$$

$$\le \left(\sum_{v_i v_j \in E(G)} \frac{d_i d_j}{d_i + d_j}\right)^2.$$

Putting the definitions in the above inequality, it gets

$$\left(Z_2(G)\right)^2 \left(H(G)\right)^2 - \frac{n^2}{4}\left(\frac{\Delta^3 - \delta^3}{2\Delta\delta}\right) \le (ISI\ (G))^2.$$

Hence,

$$ISI(G) \ge \sqrt{\left(Z_2(G)\ H(G)\right)^2 - \frac{n^2}{4}\left(\frac{\Delta^3 - \delta^3}{2\Delta\delta}\right)}.$$

Lemma 3.1.1. For a simple connected graph of $ISI\ (G)$,

$$\gamma_1^+ \le \frac{\Delta}{n^{1/n}\sqrt{(d_i^n + \Delta)(d_j^n + \Delta)}}$$

where Δ is the maximum degree of G.

Proof. Let $D(G)^{-1} ISI(G) D(G) = Q(G)$ and $X = (x_1,\ x_2, \ldots, x_n)^T$ be an eigen vector of $Q(G)$ corresponding to an eigen value γ^+. Also, $x_i = 1$ and $0 < x_k \le 1$ for every k. Let $x_j = max_k(x_k: v_i v_k \in E,\ i\ is\ adjacent\ to\ k)$. It is known that $(Q(G))X = \gamma_1^+(G)X$. If $i\_$th equation from above equation is taken, then $\gamma_1^+(G)x_i = \sum_k \left(\frac{d_i d_k}{d_i + d_k}\right) x_k = \left(d_i \sum_k \frac{d_k}{d_i + d_k}\right) x_k$. By the Aritmetic-Geometric mean inequality, it gives

$$\frac{\sum_k \frac{d_k}{d_i+d_k}}{n} \geq \left(\frac{\prod_{k=1}^n \frac{d_k}{d_i+d_k}}{n}\right)^{1/n} \geq \frac{\left(\frac{\prod_{k=1}^n d_k}{\prod_{k=1}^n (d_i+d_k)}\right)^{1/n}}{n^{1/n}}$$

$$\geq \frac{\frac{(\Delta^n)^{1/n}}{(d_i^n+\prod_{k=1}^n d_k)^{1/n}}}{n^{1/n}} \geq \frac{\Delta}{n^{1/n}\left(d_i^n + (\Delta^n)^{1/n}\right)}.$$

Using the Lemma 2.1,

$$\gamma_1^+(G) \leq \frac{d_i\Delta}{n^{1/n}\left(d_i^n + \Delta\right)}$$

The j_th equation of same equation has

$$\gamma_1^+(G) \leq \frac{d_j\Delta}{n^{1/n}\left(d_j^n + \Delta\right)}$$

From Lemma 2.2, it is expressed that

$$\gamma_1^+(G) \leq \sqrt{\left(\frac{d_i\Delta}{n^{1/n}\left(d_i^n + \Delta\right)}\right)\left(\frac{d_j\Delta}{n^{1/n}\left(d_j^n + \Delta\right)}\right)}.$$

Hence,

$$\gamma_1^+ \leq \frac{\Delta}{n^{1/n}\sqrt{\left(d_i^n + \Delta\right)\left(d_j^n + \Delta\right)}}.$$

Since, $\Delta = d_1 \geq d_2 \geq, \dots, \geq d_n = \delta$, it is clear that

$$\gamma_1^+ \leq \frac{\Delta}{n^{1/n}\sqrt{\left(\Delta^n + \Delta\right)\left(\delta^n + \Delta\right)}}.$$

Definition 3.1.1. Let G be a graph and $\gamma_1^+ \geq \gamma_2^+ \geq \cdots \geq \gamma_n^+$ be eigenvalues of inverse sum in degree matrix of G. Estrada inverse sum in degree index is defined as

$$E_{\iota s\iota} = \sum_{j=1}^n e^{\gamma_j^+}.$$

Theorem 3.1.2. Let G be a graph with n vertices and $E_{\iota s\iota}$ be an Estrada inverse sum in deg index. Then,

$$E_{\iota s\iota} \geq e^K + \frac{(n-1)}{e^{1/n-1}}$$

where $K = \frac{\Delta}{n^{1/n}\sqrt{(\Delta^n+\Delta)(\delta^n+\Delta)}}$.

Proof. $E_{ısı} = \sum_{j=1}^{n} e^{\gamma_j^+} \geq e^{\gamma_1^+} + (n-1)\left(\prod_{j=2}^{n} e^{\gamma_j^+}\right)^{1/n-1}$ using the Aritmetic-Geometric mean inequality. Since, $\sum_{i=1}^{n} e^{\gamma_j^+} = 0$ then $E_{ısı} \geq e^{\gamma_j^+} + \frac{(n-1)}{e^{1/n-1}}$. It is known that $\gamma_j^+ \leq K$. Hence,

$$E_{ısı} \geq e^K + \frac{(n-1)}{e^{1/n-1}}.$$

Theorem 3.1.3. Let G be a graph with n vertices and $E_{ısı}$ be an Estrada inverse sum in deg. index. Then,

$$E_{ısı} \leq \sqrt{-Kn\sum_{k\geq0}^{\infty}\frac{2^k}{k!}}.$$

Proof. It is easy to see that $\frac{1}{n}\sum_{j=1}^{n}\left(e^{\gamma_j^+}\right)^2 \geq \left(\frac{1}{n}\sum_{j=1}^{n}e^{\gamma_j^+}\right)^2$. On the other hand, $\frac{1}{n}\sum_{j=1}^{n}e^{2\gamma_j^+} \geq \frac{1}{n^2}E_{ısı}^2$. Hence,

$$n.\sum_{k\geq0}^{\infty}\frac{1}{k!}\sum_{j=1}^{n}\left(2\gamma_j^+\right)^k \geq E_{ısı}^2$$

and thus,

$$E_{ısı}^2 \leq n.\sum_{k\geq0}^{\infty}\frac{2^k}{k!}\sum_{j=1}^{n}\left(\gamma_j^+\right)^k.$$

Knowing that $\gamma_1^+ \geq \cdots \geq \gamma_n^+$ and $\gamma_1^+ \leq K$, it is obtained that

$$E_{ısı}^2 \leq n.\sum_{k\geq0}^{\infty}\frac{2^k}{k!}.n.K^k.$$

It is clear that the equality holds

$$E_{ısı} \leq \sqrt{n^2.\sum_{k\geq0}^{\infty}\frac{(2K)^k}{k!}}.$$

Theorem 3.1.4. Let G be a graph with n vertices and $E_{ısı}$ be an Estrada inverse sum in degree index. Then,

$$E_{ısı} \leq \sqrt{e^{2K} - 2e^K} + e^K.$$

Proof. $\left(E_{ısı} - e^{\gamma_1^+}\right)^2 = \left(\sum_{j=1}^n e^{\gamma_j^+}\right)^2 - 2\left(\sum_{j=1}^n e^{\gamma_j^+} e^{\gamma_1^+}\right) + e^{2\gamma_1^+}$

$$\leq \left(\sum_{j=1}^n e^{\gamma_j^+}\right)^2 - 2ne^{\gamma_1^+}\left(\prod_{j=1}^n e^{\gamma_j^+}\right)^{1/n} + e^{2\gamma_1^+}.$$

Since $\left(\sum_{j=1}^n e^{\gamma_j^+}\right)^2 = \left(\sum_{k\geq 0}^{\infty} \frac{1}{k!}\sum_{j=1}^n (\gamma_j^+)^k\right)^2 \leq \left(\sum_{k\geq 0}^{\infty} \frac{1}{k!}\left(\sum_{j=1}^n \gamma_j^+\right)^k\right)^2$ and $\sum_{j=1}^n \gamma_j^+ = 0$, then

$$\left(E_{ısı} - e^{\gamma_1^+}\right)^2 \leq -2ne^{\gamma_1^+} + e^{2\gamma_1^+} = e^{\gamma_1^+}\left[e^{\gamma_1^+} - 2n\right].$$

The inequality states that

$$E_{ısı} \leq \sqrt{e^{\gamma_1^+}\left(e^{\gamma_1^+} - 2n\right)} + e^{\gamma_1^+}.$$

In the sequel, Theorem 3.1.2 says that

$$E_{ısı} \leq \sqrt{e^K(e^K - 2n)} + e^K.$$

3.2 Inverse Sum In Degree Co Index

In this subsection, *ISI* co index is described and different bounds are yielded concerned with Zagreb co indices, the vertices and the edges.

Definition 3.2.1.

Let *G* be a simple, connected graph. *ISI* co index is defined as follows:

$$ISI(\bar{G}) = \sum_{v_i v_j \notin E(G)} \frac{d_G(i)d_G(j)}{d_G(i) + d_G(j)}.$$

Theorem 3.2.1. Let $ISI(\bar{G})$ be the complement of inverse sum in degree index. If G is regular then,

$$ISI(\bar{G}) \leq \frac{(n-1)^2\left[\binom{n}{2} - m\right] - (n-1).\left(-\frac{4m^2}{n} + 2m(n-1)\right) + \left(2m^2\left(1 - \frac{2m}{n^2} - \frac{1}{n}\right)\right)}{2.(n-1).\left[\binom{n}{2} - m\right] + \frac{4m^2}{n} - \left(2m(n-1)\right)}.$$

Proof. By the definition of $ISI(\bar{G})$; $ISI(\bar{G}) = \sum_{v_i v_j \in E(\bar{G})} \frac{d_{\bar{G}}(i)d_{\bar{G}}(j)}{d_{\bar{G}}(i) + d_{\bar{G}}(j)}$. Since $d_{\bar{G}}(i) = (n - 1 - d_i)$ and $d_{\bar{G}}(j) = (n - 1 - d_j)$, then

$$ISI\,(\bar{G}) = \sum_{v_i v_j \in E(\bar{G})} \frac{(n-1-d_i).(n-1-d_j)}{(n-1-d_i)+(n-1-d_j)}$$

$$= \sum_{v_i v_j \in E(\bar{G})} \frac{(n-1)^2 - (n-1)(d_i+d_j) + d_i d_j}{2(n-1) - (d_i+d_j)}$$

$$\leq \frac{\sum_{v_i v_j \in E(\bar{G})}(n-1)^2 - (n-1)(d_i+d_j) + d_i d_j}{\sum_{v_i v_j \in E(\bar{G})} 2(n-1) - (d_i+d_j)}$$

$$ISI\,(\bar{G}) \leq \frac{(n-1)^2 \sum_{v_i v_j \in E(\bar{G})} 1 - (n-1) \sum_{v_i v_j \in E(\bar{G})}(d_i+d_j) + \sum_{v_i v_j \in E(\bar{G})} d_i d_j}{2.(n-1).\left[\binom{n}{2}-m\right] - \sum_{v_i v_j \in E(\bar{G})}(d_i+d_j)}.$$

Because, G has $\binom{n}{2}-m$ edges. By Theorem 2.2, it is stated that

$$ISI\,(\bar{G}) \leq \frac{(n-1)^2\left[\binom{n}{2}-m\right] - (n-1)Z_1\,(\bar{G}) + Z_2\,(\bar{G})}{2.(n-1).\left[\binom{n}{2}-m\right] - Z_1\,(\bar{G})}$$

Since $Z_1\,(\bar{G}) = \overline{Z_1}\,(G)$, then

$$ISI\,(\bar{G}) \leq \frac{(n-1)^2\left[\binom{n}{2}-m\right] - (n-1).\overline{Z_1}\,(G) + \overline{Z_2}\,(G)}{2.(n-1).\left[\binom{n}{2}-m\right] - \overline{Z_1}\,(G)}.$$

Using the Lemma 2.3, it is concluded that

$$ISI\,(\bar{G}) \leq \frac{(n-1)^2\left[\binom{n}{2}-m\right] - (n-1).\left(-\frac{4m^2}{n} + 2m(n-1)\right) + \left(2m^2\left(1-\frac{2m}{n^2}-\frac{1}{n}\right)\right)}{2.(n-1).\left[\binom{n}{2}-m\right] + \frac{4m^2}{n} - (2m(n-1))}.$$

Corollary 3.2.1. Let $ISI(\bar{G})$ be the complement of inverse sum in degree index. If G is regular then,

$$\overline{ISI}\,(\bar{G}) \leq \frac{(n-1)m - (n-1).\left(-\frac{4m^2}{n} + 2m(n-1)\right) + \left(2m^2\left(1-\frac{2m}{n^2}-\frac{1}{n}\right)\right)}{2.(n-1)m + \frac{4m^2}{n} - (2m(n-1))}$$

Proof. Applying similar steps to the Theorem 3.2.1, it is obtained that

$$\overline{ISI}\,(\bar{G}) = \sum_{v_i v_j \notin E(\bar{G})} \frac{d_{\bar{G}}(i).d_{\bar{G}}(j)}{d_{\bar{G}}(i)+d_{\bar{G}}(j)}$$

$$= \sum_{v_i v_j \in E(G)} \frac{(n-1)^2 - (n-1)(d_i+d_j) + d_i d_j}{2(n-1) - (d_i+d_j)}$$

$$\leq \frac{(n-1)^2 m - (n-1).\overline{Z_1}(G) + \overline{Z_2}(G)}{2.(n-1)m - \overline{Z_1}(G)}.$$

By Lemma 2.3, it is resulted that

$$\overline{ISI}(\bar{G}) \leq \frac{(n-1)^2 m - (n-1).\left(-\frac{4m^2}{n} + 2m(n-1)\right) + \left(2m^2\left(1 - \frac{2m}{n^2} - \frac{1}{n}\right)\right)}{2.(n-1)m + \frac{4m^2}{n} - \left(2m(n-1)\right)}$$

4. CONCLUSION

In this study, the inverse sum in degree index is expanded, the Estrada inverse sum in degree index is defined and some bounds are found deal with these indices. In the sequel, inverse sum in degree co index is described and some inequalities are obtained in terms of the edges and vertices.

5. ACKNOWLEDGEMENT

6. REFERENCES

[1] Estrada E., Characterization of 3D molecular structure, Chem. Phys. Lett., 319 (2000) 713-718.

[2] Sedlar J., Stevanović D. and Vasilyev A., On the inverse sum in degree index, Discrete Applications Mathematics, 184 (2015) 202-212.

[3] Kaya Gök G., Some bounds on the distance-sum-connectivity matrix, Journal of Inequalities and Applications, (2018) 171.

[4] Das K. C. and Kumar P., Some new bounds on the spectral radius of graphs, Discrete Mathematics, 281 (2004) 149-161.

[5] Gutman I., Furtula B., Vukićević Z.V. and Popivoda G., On Zagreb Indices and Co indices, MATCH Commun. Math. Comput. Chem., 74 (2015) 5-16.

[6] Sorgun S. and Büyükköse Ş., The new upper bounds on the spectral radius of weighted graphs, Applied Mathematics and Computation, 218 (2012) 5231-5238.

[7] Hossein-Zadeh S., Hamzeh A. and Ashrafi A. R., Extremal Properties of Zagreb Co indices and Degree Distance of Graphs, Miskolc Mathematical Notes, 11-2 (2010) 129-137.

[8] Fajtlowicz S., On conjectures on Graffiti-II, Congr. Number, 60 (1987) 187-197.

[9] Horn R.A. and Johnson C.R., Matrix Analysis: Cambridge University Press, New York, 1985.

[10] Du Z. and Zhongzhu L., On the Estrada and Laplacian Estrada indices of graphs, Linear Algebra and its Applications, 435 (2011) 2065-2076.

APT-Pareto Distribution and its Properties

İsmail Kınacı[1] (iD)**, Coşkun Kuş[2]** (iD)**, Kadir Karakaya[2*]** (iD)**, Yunus Akdoğan[2]** (iD)

[1]Department of Actuarial Sciences, Selçuk University, 42250, Konya, TURKEY

[2]Department of Statistics, Selçuk University, 42250, Konya, TURKEY

Abstract. Recently, the APT-family has been introduced as a new family of distributions. A special case of this family with exponential distribution is examined in details. In this paper, Pareto is considered as a baseline distribution in APT-family. Several properties of the APT-Pareto distribution such as the moments, hazard rate and survival functions are derived. The maximum likelihood and least square methods are discussed. Simulation study is also performed to get the bias and mean square errors of estimates. A numerical example is given to illustrate the capability of APT-Pareto distribution for modelling real data.

*Keywords***:** Distribution family, Estimation, Pareto distribution, Simulation.

APT-Pareto Dağılımı ve Özellikleri

Özet. Son zamanlarda, APT-dağılım ailesi adında yeni bir dağılım ailesi tanıtılmıştır. Bu dağılım ailesi için üstel dağılım durumunu detaylı bir şekilde ele alınmıştır. Bu makalede, APT-dağılım ailesinde Pareto dağılımı çalışılmıştır. APT-Pareto dağılımına ilişkin momentler, hazard fonksiyonu, yaşam fonksiyonu gibi özellikleri elde edilmiştir. En çok olabilirlik ve en küçük kareler yöntemleri tartışılmıştır. Tahmin edicilerin yan ve hata kareler ortalamalarını elde edebilmek için simülasyon çalışması yapılmıştır. APT-Pareto dağılımının modellemedeki kullanılabilirliğini göstermek amacıyla gerçek bir veri uygulaması yapılmıştır.

Anahtar Kelimeler: Dağılımlar ailesi, Tahmin, Pareto dağılımı, Simülasyon

1. INTRODUCTION

Distribution theory is one of the most important areas of statistics. In the last two decades, there are too many statistical distributions are introduced by including an extra parameter to an existing family of distribution functions. Azzalini [1] introduced the skew normal distribution by adding an extra parameter λ to the normal distribution. Let Z be the skew-normal random variable, then the density function of Z is of

$$\phi(z;\lambda) = 2\phi(z)\Phi(\lambda z),\ z \in \mathbb{R},$$

where ϕ and Φ are the standard normal density and distribution function, respectively. It is clear that the skew-normal distribution is reduced standard normal distribution for $\lambda = 0$.

Mudholkar and Srivastava [2] proposed a method to include an extra parameter to a two-parameter Weibull distribution. If a random variable Z has distribution function $F(z)$, then $(F(z))^\theta$ $(\theta > 0)$ is also distribution function and it is called exponentiated family, where $F(z)$, is baseline distribution. Mudholkar and Srivastava [2] considered $F(z) = (1 - \exp(-z/\sigma)^\alpha)$ as a baseline distribution and they get the distribution with cdf

$$F(z) = \left(1 - \exp(-z/\sigma)^\alpha\right)^\theta$$

and called it as exponentiated-Weibull family, where θ is an extra parameter. Some exponentiated distributions have been introduced by several authors, see for example Gupta et al. [3], Gupta and Kundu [4] and etc.

Marshall and Olkin [5] proposed another method to introduce an additional parameter to any distribution function as follows. Let Z is a random variable with cdf F and density f, then

$$g(z) = \frac{\alpha f(z)}{\{1 - (1 - \alpha)(1 - F(z))\}^2}$$

is also pdf of a random variable, where α is an extra parameter. Marshall and Olkin [5] cosidered exponential and Weibull distribution for baseline distribution $f(z)$.

Eugene et al. [6] proposed the beta generated method which is defined as follows: Let Z is a random variable with cdf F, then

$$G(z) = \frac{\Gamma(\alpha + \beta)}{\Gamma(\alpha)\Gamma(\beta)} \int\limits_0^{F(z)} t^{\alpha - 1}(1 - t)^{\beta - 1}\, dt,$$

is a distribution function as well, where $(\alpha, \beta) \in \mathbb{R}_+^2$ is an extra parameter vector.

Alzaatreh et al. [7] introduced a new method for generating families of continuous distributions called T-X family using same idea of Eugene et al. [6]

Mahdavi and Kundu [8] introduced an extra parameter to a family of distributions functions to bring more flexibility to the given family. This new method is called α-power transformation (APT) method. The proposed APT method is very easy to use, hence it can be used extensively for the data modelling purposes. The pdf and cdf of APT-family are given, respectively, by

$$f_{APT}(x) = \begin{cases} \frac{\log(\alpha)}{\alpha - 1} f(x)\alpha^{F(x)} I_A(x) & , \quad \alpha \neq 1 \\ f(x) & , \quad \alpha = 1 \end{cases} \tag{1}$$

and

$$F_{APT}(x) = \begin{cases} \frac{\alpha^{F(x)} - 1}{\alpha - 1} I_A(x) & , \quad \alpha \neq 1 \\ F(x) & , \quad \alpha = 1, \end{cases} \tag{2}$$

where $\alpha > 0$ is an extra parameter and $I_A(x)$ is indicator function on set A which is domain of baseline distribution. Mahdavi and Kundu [8] applied the α-power transformation to exponential

distribution.

An extra parameter supplies more flexibility to a class of distribution functions and it can be very useful for the data analysis. It should be point out that the adding extra parameter caused the estimation problem, but it can be solved by numerical methods. R and Matlab have several numerical algorithms for this job.

In this paper, α-power transformation is applied to Pareto distribution. In Section 2, moments, hazard rate and survival functions are given. The maximum likelihood and least square methods are discussed in Section 3. In Section 4, a simulation study is also performed to observe the performance of the estimates. A numerical example with the real data is given to illustrate the flexibility of APT-Pareto distribution for modelling real data in Section 5.

2. α -POWER PARETO DISTRIBUTION

In this paper, Pareto distribution is considered. The pdf and cdf of the Pareto distribution are given, respectively, by

$$f_p(x) = \beta x^{-\beta-1} I(1, \infty) \tag{3}$$

and

$$F_p(x) = 1 - x^{-\beta} I(1, \infty) \tag{4}$$

where $\beta > 0$ is a shape parameter and $I_A(.)$ is indicator function.

Using Eqs. (3)-(4) in Eqs. (1)-(2), the pdf and cdf of APT-Pareto distribution are defined by

$$f_{APTP}(x) = \begin{cases} \frac{\log(\alpha)}{\alpha-1} \beta x^{-\beta-1} \alpha^{1-x^{-\beta}} I_{(1,\infty)}(x) & , \quad \alpha \neq 1, \\[2em] \beta x^{-\beta-1} & , \quad \alpha = 1 \end{cases} \tag{5}$$

and

$$F_{APTP}(x) = \begin{cases} \frac{\alpha^{\left(1-x^{-\beta}\right)}-1}{\alpha-1} I_{(1,\infty)}(x) & , \quad \alpha \neq 1 \\[2em] \left(1-x^{-\beta}\right) & , \quad \alpha = 1, \end{cases} \tag{6}$$

respectively. The random variable X is said to have a two-parameter APT-Pareto distribution and it is denoted by $APTP(\alpha, \beta)$.

Fig. 1 presents the plots pdf of $APTP(\alpha, \beta)$ for some choices of α and β.
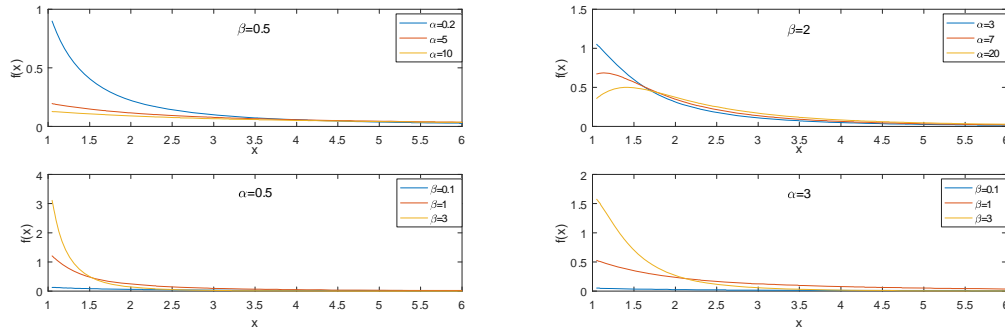
Figure 1. Pdf of APTP distribution for some choices of α and β

In the rest of paper, the case $\alpha \neq 1$ is only considered. The survival function and the hazard rate function for *APTP* distribution are given in the following forms

$$S_{APTP}(x) = \frac{\alpha - \alpha^{\left(1 - x^{-\beta}\right)}}{\alpha - 1}$$

and

$$h_{APTP}(x) = \frac{\log(\alpha)\beta x^{-\beta-1}\alpha^{1-x^{-\beta}}}{\alpha - \alpha^{\left(1 - x^{-\beta}\right)}},$$

respectively. Fig. 2 presents the plots the hazard rate function of $APTP(\alpha,\beta)$ for some choices of α and β.
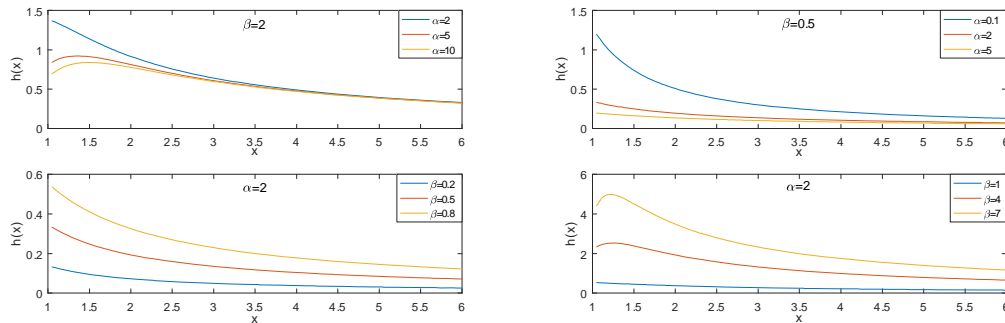
Figure 2. Hazard rate function of APTP distribution for some choices of α and β

The r th moment of *APTP* distribution is obtained by

$$E(X^r) = \int_1^\infty x^r \frac{\log(\alpha)}{\alpha - 1}\beta x^{-\beta-1}\alpha^{1-x^{-\beta}}\,dx$$

$$= \frac{\log(\alpha)}{1-\alpha}\alpha\beta\sum_{i=0}^\infty (-1)^i \frac{\log(\alpha)^i}{i!}\left(\frac{1}{r-\beta(i+1)}\right).$$

$$= \frac{\log(\alpha)^{\left(\frac{r-2\beta}{2\beta}\right)}\beta\sqrt{a}\left((r-2\beta)^2\, WhittakerM\left(\frac{-r+2\beta}{2\beta},\frac{-r+3\beta}{2\beta},\log(\alpha)\right)\right)}{(r-2\beta)(r-3\beta)(\alpha-1)(\beta-r)}$$

$$- \frac{\log(\alpha)^{\left(\frac{1-2\beta}{2\beta}\right)}\beta\sqrt{a}\left(\beta WhittakerM\left(\frac{-r}{2\beta},\frac{-r+3\beta}{2\beta},\log(\alpha)\right)(r-\log(\alpha)\beta-2\beta)\right)}{(r-2\beta)(r-3\beta)(\alpha-1)(\beta-r)},$$

where the WhittakerM(a, b, c) is a Whittaker function and it can be easily calculated by Maple or Matlab. It should be noted that r th moments works for only $\beta > \frac{3}{2} r$. This restriction has been observed in simulation study. It is not proved here.

Moment generating function of *APTP* distribution is given by

$$M_X(t) = \int_1^\infty \exp(tx) \frac{\log(\alpha)}{\alpha - 1} \beta x^{-\beta - 1} \alpha^{1 - x^{-\beta}} dx$$

$$= \frac{\log(\alpha)\beta\alpha}{\alpha - 1} \sum_{i=0}^\infty \frac{(-t)^{\beta(i+1)} (-\log(\alpha))^i \, \Gamma(-\beta(i+1), -t)}{i!}$$

where $\Gamma(a, b)$ is the incomplete gamma function.

3. ESTIMATION

3.1. Maximum-Likelihood Method

Let $X_1, X_2, \ldots, X_n$ be a random sample from $APTP(\alpha, \beta)$, then log-likelihood function is given by

$$\ell(\alpha, \beta) = n \log\left(\frac{\log(\alpha)}{\alpha - 1} \right) + n \log(\beta) - (\beta + 1) \sum_{i=1}^n \log(x_i) + \left(n - \sum_{i=1}^n x_i^\beta \right) \log(\alpha).$$

The likelihood equations are found to be

$$\frac{\partial \ell(\alpha, \beta)}{\partial \alpha} = n \left(\frac{\alpha - 1}{\log(\alpha)} \right) \left(\frac{1}{\alpha(\alpha - 1)} - \frac{\log(\alpha)}{(\alpha - 1)^2} \right) + \frac{n - \sum_{i=1}^n x_i^\beta}{\alpha} = 0,$$

$$\frac{\partial \ell(\alpha, \beta)}{\partial \beta} = \frac{n}{\beta} - \sum_{i=1}^n \log(x_i) - \log(\alpha) \sum_{i=1}^n x_i^\beta \log(x_i) = 0.$$

Maximum likelihood estimates (MLE) of α and β are obtained by solving likelihood equations. The likelihood equations cannot be solved explicitly. Likelihood function can be maximized by numerical method. **fminsearch** MATLAB command can be used for this job. **fminsearch** uses the simplex search method of Lagarias et al. [9].

3.2. Least-squares Method

Let $x_{(1)} < x_{(2)} < \cdots < x_{(n)}$ denote the ordered observations from $APTP(\alpha, \beta)$ distribution. Using the distribution function given in Eq. (6), we can write

$$F\left(x_{(i)}\right) = \frac{\alpha^{\left(1 - x_{(i)}^{-\beta}\right)} - 1}{\alpha - 1}, \qquad i = 1, 2, \ldots, n \tag{7}$$

Empirical distribution function, denoted by F^* can be used to estimate $F\left(x_{(i)}\right)$ in (7). Substituting the empirical distribution function in Eq. (7), we have the following model:

$$F^*\left(x_{(i)}\right) = \frac{\alpha^{\left(1-x_{(i)}^{-\beta}\right)} - 1}{\alpha - 1} + \varepsilon_i, \qquad i = 1, 2, \ldots, n,$$

where ε_i is the error term for i th observation. Now, the least squares estimators ($\tilde{\alpha}, \tilde{\beta}$) of parameters can be obtained by minimizing the following equation with respect to α and β :

$$L(\alpha, \beta) = \sum_{i=1}^{n} \varepsilon_i^2 = \sum_{i=1}^{n}\left(F^*\left(x_{(i)}\right) - \frac{\alpha^{\left(1-x_{(i)}^{-\beta}\right)} - 1}{\alpha - 1}\right)^2, \qquad i = 1, 2, \ldots, n.$$

Least-squares estimates (LSE) of α and β can be obtained by numerical methods. **fminsearch** MATLAB command can be used for this job.

4. SIMULATION STUDY

In this section, a simulation study is conducted to compare the ability of estimation procedures discussed in the previous section. In the simulation, $X_1, X_2, \ldots, X_n$ from the *APTP* distribution are generated and then computed the MLEs and LSEs of α and β with 10000 repetitions. We then compared the performance of these estimates in terms of their biases and mean square errors (MSE). We reported the biases and MSEs of these estimates in Tables 1-2, for different values of n and (α, β) .

From Tables 1-2, it is observed that both estimates are biased but asymptotically unbiased. Also, as the sample size n increases, the bias and MSEs of the estimators decreases as expected.

Table 1: Bias of MLEs and LSEs for some parameter values of α and β

α	β	n	$\hat{\alpha}$	$\hat{\beta}$	$\tilde{\alpha}$	$\tilde{\beta}$
2	2	50	1.3612	0.0939	1.5310	0.1023
		100	0.5514	0.0420	0.5679	0.0413
		200	0.2525	0.0196	0.2718	0.0226
		300	0.1734	0.0146	0.1764	0.0151
		400	0.1341	0.0120	0.1395	0.0137
		500	0.1031	0.0094	0.1053	0.0102
3	1	50	2.1219	0.0398	2.4204	0.0439
		100	0.8103	0.0178	0.8230	0.0196
		200	0.3690	0.0085	0.3904	0.0107
		300	0.2532	0.0063	0.2573	0.0071
		400	0.1809	0.0044	0.1837	0.0050
		500	0.1532	0.0043	0.1553	0.0051
0.5	0.8	50	0.4662	0.0908	0.6711	0.1070
		100	0.1950	0.0402	0.2800	0.0435
		200	0.0912	0.0173	0.1241	0.0131
		300	0.0620	0.0109	0.0849	0.0073
		400	0.0477	0.0088	0.0648	0.0059
		500	0.0392	0.0071	0.0506	0.0039

Table 2: MSEs of MLEs and LSEs for some parameter values of α and β

α	β	n	$\hat{\alpha}$	$\hat{\beta}$	$\tilde{\alpha}$	$\tilde{\beta}$
2	2	50	21.6056	0.2314	29.8067	0.3724
		100	3.4502	0.1083	4.4688	0.1694
		200	1.1274	0.0540	1.5549	0.0812
		300	0.6866	0.0365	0.9176	0.0556
		400	0.4863	0.0269	0.6272	0.0398
		500	0.3657	0.0213	0.4724	0.0318
3	1	50	46.9261	0.0463	165.8959	0.0686
		100	7.6548	0.0221	9.6245	0.0322
		200	2.4231	0.0109	3.2240	0.0154
		300	1.4694	0.0074	1.8830	0.0106
		400	1.0050	0.0055	1.2791	0.0076
		500	0.7841	0.0043	0.9722	0.0061
0.5	0.8	50	1.9843	0.0835	4.0642	0.1515
		100	0.4171	0.0446	0.7355	0.0797
		200	0.1338	0.0224	0.2367	0.0439
		300	0.0818	0.0152	0.1480	0.0312
		400	0.0564	0.0114	0.1050	0.0243
		500	0.0430	0.0088	0.0788	0.0190

5.   REAL DATA ANALYSIS

In this section, we illustrate the ability of the *APTP* distribution. We fit this distribution to two real data sets and compare the results with the distributions in the literature. In order to compare the models, we used following three criterions: Akaike Information Criterion(AIC), Bayesian Information Criterion (BIC) and log-likelihood (ℓ) values, where the lower values of AIC, BIC and the upper value of ℓ values for models indicate that these models could be chosen as the best model to fit the data sets.

First real data: First real data set is given in Feigl and Zelen [10] for the patients who died of acute myelogenous leukemia. Feigl and Zelen [10] represent observed survival times (weeks) for AG negative. The data set is: 56, 65, 17, 17, 16, 22, 3, 4, 2, 3, 8, 4, 3, 30, 4, 43. APTP, Weibull, Alpha-Power Exponential(Mahdavi and Kundu [8]), Exponentiated Exponential (Gupta and Kundu, [3]), Beta Generalized-Exponential (BGE) (Barreto-Souza et al. [11]), Beta-Exponential (BE) (Nadarajah and Kotz [12]), Beta-Pareto (BP)(Akinsete et al. [13]), Generalized Exponential (GE)(Gupta and Kundu [14]), Exponential Poisson (EP) (Kus [15]), Beta Generalized Half-Normal (BGHN) (Pescim et al. [16]), Generalized Half-Normal (GHN)(Cooray and Ananda [17]) and Gamma-Uniform (GU) (Torabi

and Montazeri [18]) distributions are fitted to data. Table 3 shows that the APTP distribution gives a better fit than the other models for all criteria except GU distribution.

Table 3. Results of AIC, BIC and log-likelihood for APTP and other distributions for the data set

Model	ML Estimates of Parameters	AIC	BIC	ℓ
APTP	$\hat{\alpha} = 485.771, \hat{\beta} = 1.034$	127.3	128.9	-61.6
Pareto	$\hat{\alpha} = 0.431$	135.2	135.9	-66.6
BGHN	$\hat{a} = 0.09, \hat{b} = 0.40, \hat{\alpha} = 5.99, \quad \hat{\theta} = 132.49$	131.9	134.9	-61.9
GHN	$\hat{\alpha} = 0.76, \hat{\theta} = 73.62$	130.2	131.8	-63.1
GE	$\hat{\alpha} = 0.757, \hat{\theta} = 0.013$	129.5	131	-62.7
EP	$\hat{\alpha} = 0.01, \hat{\theta} = 0.016$	129.1	130.6	-62.5
BP	$\hat{a} = 20.35, \hat{b} = 32.71, \hat{\alpha} = 0.01, \hat{\theta} = 0.06$	129.7	132.8	-62.8
Weibull	$\hat{\alpha} = 0.948, \hat{\beta} = 0.055$	129.4	130.9	-62.6
EE	$\hat{\alpha} = 0.968, \hat{\theta} = 0.053$	129.5	131.0	-62.7
APE	$\hat{\alpha} = 0.364, \hat{\beta} = 0.042$	129.1	130.6	-62.5
BGE	$\hat{a} = 37.95, \hat{b} = 3.33, \hat{\alpha} = 0.013, \hat{\theta} = 0.04$	132.9	135.9	-62.4
BE	$\hat{b} = 2.998, \hat{\alpha} = 0.96, \hat{\theta} = 0.017$	131.5	133.8	-62.7
GU	$\hat{a} = 1.99, \hat{b} = 165.39, \hat{\alpha} = 0.46, \hat{\theta} = 0.30$	123	126.1	-57.5
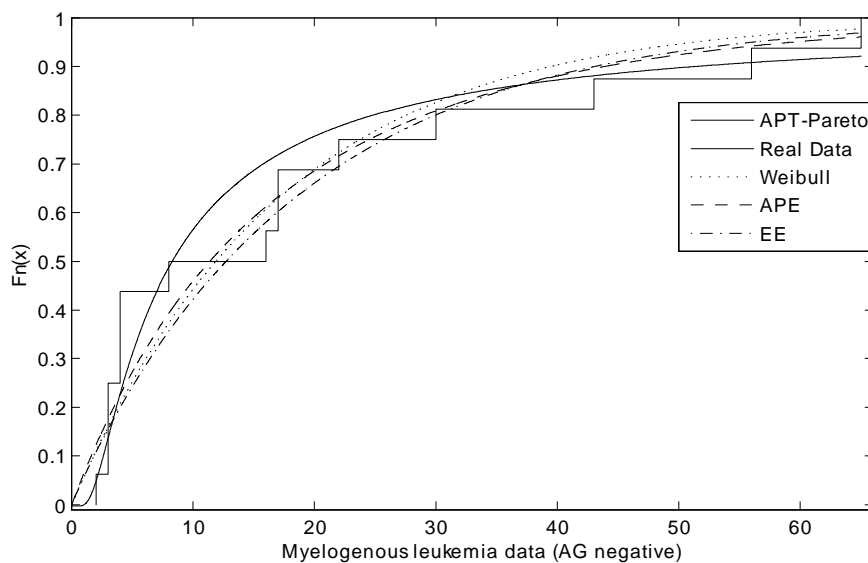
Figure 3. Empirical and some fitted distribution functions based on myelogenous leukemia data

Second real data set: The real dataset is taken from Nassar and Nada [19], which gives the relief times of 32 patients receiving an analgesic. The data are: 5.9, 20.4, 14.9, 16.2, 17.2, 7.8, 6.1, 9.2, 10.2, 9.6, 13.3, 8.5, 21.6, 18.5, 5.1,6.7, 17, 8.6, 9.7, 39.2, 35.7, 15.7, 9.7, 10, 4.1, 36, 8.5, 8, 9.2, 26.2, 21.9,16.7, 21.3, 35.4, 14.3, 8.5, 10.6, 19.1, 20.5, 7.1, 7.7, 18.1, 16.5, 11.9, 7, 8.6,12.5, 10.3, 11.2, 6.1, 8.4, 11, 11.6, 11.9, 5.2, 6.8, 8.9, 7.1, 10.8. APTP, Burr XII distribution by Burr[20], Kumaraswamy Rayleigh (Kum-R) by Rashwan [21], Beta Bur XII (Beta-BXII) by Paranaíba et al.[22], Weibull Lomax (W-L) by Tahir et al. [23]. Odd log-logistcWeibull (OLL-W) by Cruz et al. [24], and Exponentiated Generated Weibull (EG-W) by Cordeiro et al. [25] distributions are fitted to data. From Table 4, it is clear that the APTP distribution provides the overall best fit and therefore could be chosen as the most adequate model among the fitted models to second data.

Table 4. Results of AIC and log-likelihood for APTP and other distributions for the data set.

Model	ML Estimates of Parameters	AIC	BIC	ℓ
APTP	$\hat{\alpha} = 485.77, \hat{\beta} = 1.03$	221.9	228.8	109.2
Pareto	$\hat{\alpha} = 0.39$	285.9	287.4	142.0
Burr XII	$\hat{\lambda} = 0.07, \hat{\theta} = 5.61$	518.5	521.3	257.2
Kum-R	$\hat{\alpha} = 1.49, \hat{\theta} = 73.62, \hat{\lambda} = 4.70, \hat{\beta} = 0.19$	400.9	401.8	196.5
Beta-Burr XII	$\hat{\alpha} = 37.30, \hat{\theta} = 1.09, \hat{\lambda} = 0.89, \hat{\beta} = 3.84$	385.9	386.8	188.9
W-L	$\hat{\alpha} = 3.94, \hat{\beta} = 3.26, \hat{\lambda} = 2.61, \hat{\theta} = 0.26$	396.6	397.5	194.3
OLL-W	$\hat{\alpha} = 28.15, \hat{\lambda} = 0.08, \hat{\theta} = 793.68$	387.5	389.4	190.8
EG-W	$\hat{\alpha} = 0.19, \hat{\beta} = 11.15, \hat{\lambda} = 0.77, \hat{\theta} = 0.38$	387.5	388.3	189.7
TLG-Burr XII	$\hat{\alpha} = 6.29, \hat{\beta} = 7.32, \hat{\lambda} = 0.68, \hat{\theta} = 1.81$	385.5	386.4	188.8
APE	$\hat{\alpha} = 328.19, \hat{\beta} = 1.64$	223.5	226.4	109.7
Weibull	$\hat{\beta} = 1.76, \hat{\lambda} = 0.06$	225.5	228.4	110.8
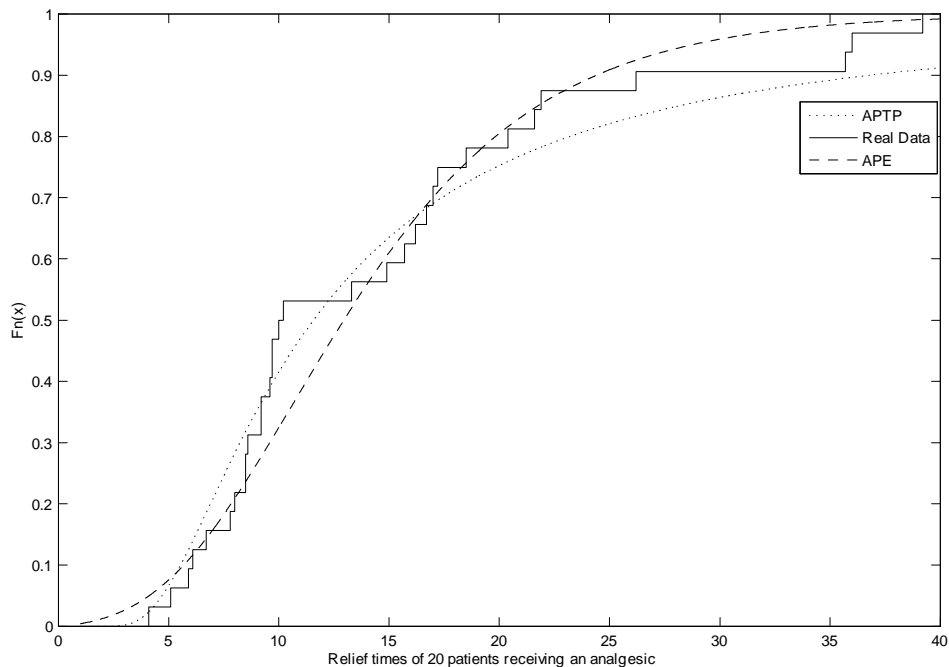
Figure 4. Empirical and some fitted distribution functions based on relief times data

6. CONCLUSION

In this study, APT family is considered with baseline Pareto distribution. ML and LS estimation are discussed for the parameters. An application of the *APTP* distribution to a real data set is given to demonstrate that this distribution can be used quite effectively to provide better fit than other available models.

REFERENCES

[1] Azzalini A., A class of distributions which includes the normal ones, Scandinavian journal of statistics, 24 (1985), 171-178.

[2] Mudholkar G.S. and Srivastava D.K., Exponentiated weibull family for analyzing bathtub failure-rate data, IEEE Transactions on Reliability, 42-2 (1993), 299-302.

[3] Gupta R.C., Gupta P.L. and Gupta R.D., Modeling failure time data by lehman alternatives, Communications in Statistics-Theory and Methods, 27-4 (1998), 887-904.

[4] Gupta R.D. and Kundu D., Exponentiated exponential family: an alternative to gamma and Weibull distributions, Biometrical Journal: Journal of Mathematical Methods in Biosciences, 43-1 (2001), 117-130.

[5] Marshall A.W. and Olkin I., A new method for adding a parameter to a family of distributions with application to the exponential and weibull families, Biometrika, 84-3 (1997), 641-652.

[6] Eugene N., Lee C. and Famoye F., Beta-normal distribution and its applications, Communications in Statistics-Theory and Methods, 31-4 (2002), 497-512.

[7] Alzaatreh A., Lee C. and Famoye F., A new method for generating families of continuous distributions, Metron, 71-1 (2013), 63-79.

[8] Mahdavi A. and Kundu D., A new method for generating distributions with an application to exponential distribution, Communications in Statistics - Theory and Methods, 46-13 (2017), 6543-6557.

[9] Lagarias J.C., Reeds J.A., Wright M.H. and Wright P.E., Convergence Properties of the Nelder-Mead Simplex Method in Low Dimensions, SIAM Journal of Optimization, 9-1 (1998), 112-147.

[10] Feigl P. and Zelen M., Estimation of Exponential Survival Probabilities with Concomitant Information, Biometrics, 21-4 (1964), 826-838.

[11] Barreto-Souza W., Santos A.H.S. and Cordeiro G.M., The Beta generalized exponential distribution, Statist. Comput. Simul., 80 (2010), 159-172.

[12] Nadarajah S. and Kotz S., The Beta exponential distribution, Reliability Engrg. System Safety, 91 (2006), 689-697.

[13] Akinsete A., Famoye F. and Lee C. The Beta-Pareto distribution, Statistics, 42-6(2008), 547-563.

[14] Gupta R.D. and Kundu D., Generalized exponential distributions, Australian and New Zealand Journal of Statistics, 41-2 (1999), 173-188.

[15] Kus C, A new lifetime distribution, Comput. Statist. Data Anal., 51(2007), 4497-4509.

[16] Pescim R.R., Dem´etrio C.G.B., Cordeiro G.M., Ortega E.M.M. and Urbano M.R., The Beta generalized half-Normal distribution, Comput. Statist. Data Anal., 54 (2009), 945-957.

[17] Cooray K. and Ananda M.M.A., A generalization of the half-normal distribution wit applications to lifetime data, Comm. Statist. Theory Methods, 37 (2008), 1323-1337.

[18] Torabi H. and Montazeri N.H., The Gamma-Uniform distribution ans its applications, Kybernetika, 48-1 (2012), 16-30.

[19] Nassar M.M. abd Nada N.K., The beta generalized Pareto distribution, Journal of Statistics: Advances in Theory and Applications, 6 (2011), 1-17.

[20] Burr, I.W., Cumulative frequency functions, Annals of Mathematical Statistics, 13(1942), 215-232.

[21] Rashwan N.I., A note on Kumaraswamy exponentiated Rayleigh distributioni, Journal of Statistical Theory and Applications, 5 (2016), 286-295.

[22] Paranaíba P.F., Ortega E. M., Cordeiro G. M. and Pescim R.R., The beta Burr XII distribution with application to lifetime data, Computational Statistics and Data Analysis, 55-2 (2011), 1118-1136.

[23] Tahir, M.H., Cordeiro G. M., Mansoor M. and Zubair M., The Weibull-Lomax distribution: properties and applications, Hacettepe Journal of Mathematics and Statistics, 44-2 (2015), 461-480.

[24] Cruz J.N.D., Ortega E.M. and Cordeiro G.M., The log-odd log-logistic Weibull regression model: modelling, estimation, influence diagnostics and residual analysis, Journal of Statistical Computation and Simulation, 86-8 (2016), 1516-1538.

[25] Cordeiro G.M., Gomes A.E., da-Silva C.Q. and Ortega E.M., The beta exponentiated Weibull distribution, Journal of Statistical Computation and Simulation, 83-1 (2013), 114-138.

Analyzing of Production Conditions of ⁸⁹Zr in the Particle Accelerator

Buğra Gökhun Bulduk[1]* iD *, Perihan Ünak[1]* iD *, Ayfer Yurt Kılçar[1]* iD *, Özge Kozguş Güldü[1]* iD *, Volkan Tekin[1]* iD

[1] Ege University, Institute of Nuclear Sciences, Department of Nuclear Applications, 35100 Bornova-İZMİR / TURKEY

Abstract. Nowadays 89Zr is outstanding PET radionuclide with its physical half-life (t1/2 ~ 78 hours), useful decay specifications and so that it is suitable for antibody-based immuno-PET. Relatively oscillated positrons' low decay energies supply to take high-resolution. 89Zr-labeled radiopharmaceuticals, especially as 89Zr-labeled antibodies applications are getting increase day by day.

In this study, calculations about production of 89Zr were done and used (p,n) reaction of 89Y target system. For this Q-value, Threshold Energy, Minimum Coulomb Barrier Energy of the reaction were calculated then the cross-sections of this reaction were found using Empire3.2/MALTA code. After determining the irradiation calculations, the bombardment performed. The irradiation was performed in Ankara Sarayköy Nuclear Research and Training Center, proton accelerator. The cyclotron is IBA type Cyclone-30. Then separation part was done with Dowex resine system. After separation 89Zr from the irradiated target system, radioactive 89Zr was obtained purely..

Keywords: 89Zr, 89Y, Cyclone-30, Empire3.2/MALTA, Radionuclide, Dowex, PET Radionuclides

89Zr'un Proton Hızlandırıcıda Üretim Koşullarının İncelenmesi

Özet. ⁸⁹Zr, uygun bozunum özellikleri, fiziksel yarı ömrü (t1/2 ~ 78 saat) nedeniyle artan ilgi görmüştür ve bu nedenle de antikor temelli immüno-PET için uygun görülmektedir. Relatif olarak salınan pozitronların düşük bozunum enerjisi yüksek çözünürlüklü görüntü alınmasını sağlar. ⁸⁹Zr-işaretli radyofarmasötiklerinin insanda kullanımı özellikle ⁸⁹Zr işaretli antikorlar olarak immuno-PET de kullanımı günden güne artmaktadır.

Bu çalışmada, ⁸⁹Zr üretimi ile ilgili hesaplamalar yapılmış ve ⁸⁹Y hedef sisteminin kullanıldığı (p, n) reaksiyonu kullanılmıştır. Bunun için reaksiyon sonucu Bağ Enerjisi, Eşik Enerjisi, Minimum Coulomb Bariyeri Enerjisi hesaplanmış, daha sonra bu reaksiyonun tesir kesitleri Empire3.2/MALTA kodu kullanılarak bulunmuştur. Işınlama hesaplamaları belirlendikten sonra proton bombardımanı yapılmıştır. Bu ışınlama Ankara Sarayköy Nükleer Araştırma ve Eğitim Merkezi'ndeki proton hızlandırıcısında gerçekleştirilmiştir. Kullanılan siklotron IBA tipi Siklon-30'dur. Daha sonra ayırma kısmı Dowex reçine sistemi ile yapılmıştır. Işınlanmış ⁸⁹Zr, hedef sistemden ayrıldıktan sonra, radyoaktif ⁸⁹Zr saf olarak elde edilmiştir.

Anahtar Kelimeler: ⁸⁹Zr, ⁸⁹Y, Siklon-30, Empire3.2/MALTA, Radyonüklid, Dowex, PET Radyonüklidleri

1. INTRODUCTION

Positron Emission Tomography (PET) uses short-lived organic β⁺-emitters however, in the case of the slow metabolic processes, longer-lived β⁺-emitters are needed. ^{89}Zr is an important positron releasing radionuclide with its half-life of 78.41

hours and approximately 23% low positron energy emission. Besides its chemistry is useful labeling of antibodies (mAbs) for PET imaging in radio-immunotherapy and personal medicine. In nuclear medicine, usage of ^{89}Zr as a PET radionuclide increased recently [1, 2, 3, 4, 6, 16, 18, 21]. ^{89}Zr decays to ^{89m}Y with 22.7% of positron emission (β⁺ decay) and 77.3% of electron capture (EC). Because of EC, about 15-keV low energy X-ray irradiation is also seen. Moreover, there is 909-keV energy gamma radiation with this decay. 511 keV energy annihilation photons are far away from noise relatively and this situation causes to increase the quality of image. In addition ^{89}Zr with 902 keV positron energy and 78.41 hours half-life is more ideal PET radionuclide than ^{18}F with 110 minute half-life for production and transportation to the hospital [12, 21].

^{89}Zr can produce in medical cyclotrons with proton or deuteron irradiation with ^{89}Y(p,n)^{89}Zr or ^{89}Y(d,2n)^{89}Zr reaction [13, 23]. ^{89}Zr is a specific radionuclide, which can be used in immuno-PET applications with monoclonal antibodies (mAbs) in-vivo monitoring and quantifications [2, 12], and with the half-life of 78.41 hours is an ideal time to connect the antibodies to the target tissue [20, 23, 24].

When the comparison of gamma scintillation or Single-Photon Emission Computed Tomography (SPECT), PET is higher attenuation correction, resolution and sensitivity [10, 17, 20, 21, 22]. According to that, ^{89}Zr-labeled antibodies used in tumor detection at preclinic and clinic, successively [7, 8, 9]. On the other hand ^{89}Zr-labeled antibodies with cancer detection and research, there is also a potential for usage in autoimmune diseases [5, 15]. There are also more studies about labeled of white-blood cells, cytokines and labeling of these cells are also important [11, 14, 19].

2. MATERIALS and METHODS

2.1. Calculation of Q-value, Threshold Energy and Minimum Coulomb Barrier Energy of ^{89}Y(p,n)^{89}Zr Reaction

$$Q = [m_P + m_T - (m_X + m_R)]c^2 \text{ MeV}$$

- m_P is projectile mass in MeV/c^2,

- m_T is target mass in MeV/c^2,

- m_X is emitted particle mass in MeV/c^2,

- m_R is residual nucleus mass in MeV/c^2,

- c is the speed of the light.

After calculating the Q-value, the Threshold Energy (E_{Th}) is,

$$E_{Th} = -Q \frac{m_P + m_T}{m_T} \text{ MeV}$$

Threshold energy for the reaction, which occurs at this energy level, is significant. The other necessary term is Minimum Coulomb Barrier Energy ($E_{cb_{\min}}$) so,

$$E_{cb_{\min}} = 1.109(A_P + A_T) \frac{Z_P Z_T}{A_T(A_P^{1/3} + A_T^{1/3})} \text{ MeV}$$

- A_P is atomic number of projectile,

- A_T is atomic number of target,

- Z_p is mass number of projectile,

- Z_T is mass number of target.
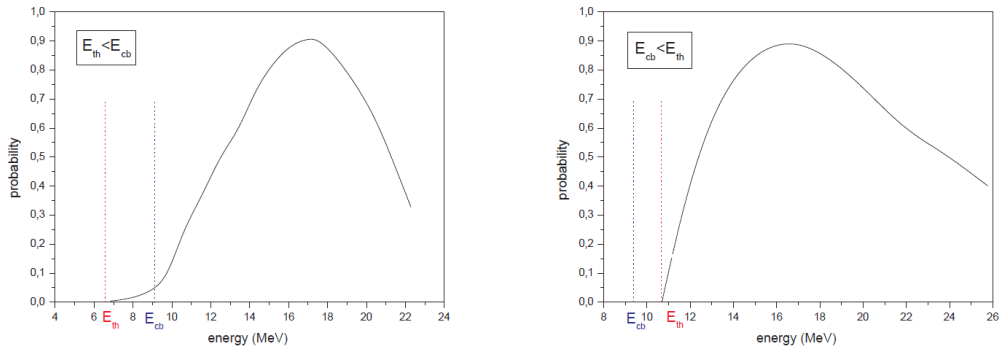
Figure 1. Comparison of Threshold Energy and Minimum Coulomb Barrier Energy

- σ is the reaction cross-section, or probability of interaction, expressed in cm² and is a function of energy,

2.2. Nuclear Cross-section and Irradiation Yield

The general formula of the nuclear cross-section is,

$$\sigma_R = \pi r_0^2 (A_p^{1/3} + A_T^{1/3})^2$$

where r_0 is radius of nucleus and about 1.6 fm and the unit of this total cross-section is barn (10^{-24} cm²). In this project, all the cross-sections of the reactions will be calculated by Empire3.2/MALTA code.

The rate of production is given by the simplest equation,

$$R = n_T I \sigma$$

Nonetheless, the cross-section is not always constant and function of energy so that the more exact expression is,

$$R = n_T I \int_{E_s}^{E_0} \frac{\sigma(E)}{dE/dx} dE$$

- R is the number of nuclei formed per second,

- n_T is the target thickness in nuclei/cm²,

- I is the incident particle flux per second and is related to the beam current,

- E is the energy of the incident particles,

- x is the distance travelled by the particle and

- $\int_{E_s}^{E_0}$ is the integral from the initial energy to the

final energy of the incident particle along its path.

$$n_T = \frac{\rho x}{A_T} N_A$$

is the equation of target thickness also and,

- A_T is the atomic weight of the target material in grams,

- ρ is the density in g/cm3,

- N_A is Avogadro's number and

- x is the distance the particle travels through the material in cm.

Then the overall rate of production is,

$$-\frac{dn}{dt} = n_T I \int_{E_s}^{E_0} \frac{\sigma(E)}{dE/dx} dE - \lambda N$$

- λ is the decay constant and is equal to ln $2/t_{1/2}$ ($t_{1/2}$ is half-life),

- t is the irradiation time in seconds and

- N is the number of produced nuclei in the target.

For all, the yield of the nuclear reaction is,

$$Y_{EOB} = \frac{N_A I}{A_T}(1 - e^{-\lambda t}) \int_{E_s}^{E_0} \frac{\sigma(E)}{S_T(E)} dE$$

- $S_T(E)$ *is the stopping power, dE/dx actually.*

2.3. Energy Loss after bombardment, Stopping Power and Range of Ions in Matter

For Bethe and Bloch (Bethe et al., 1932), stopping power with the simplest form is,

$$S = \frac{4\pi e^4 Z_1^2 Z_2}{mv^2}[\ln(\frac{2mv^2}{I}) + \ln(\frac{1}{1-\beta^2}) - \beta^2 - \frac{C}{Z_2}]$$

MeV/cm

- m is the mass of electron,

- Z_1 and Z_2 are the atomic numbers of the particle and target,

- e is the electron charge,

- v is the velocity of the particle,

- I is the ionization (excitation) potential,

- β is v/c and v is the speed of particle in cm/s and

- C/Z_2 is the shell correction.

2.4. SRIM (Stopping Powers and Ranges in All Elements, 2013)

SRIM is the program, which can calculate and simulate the energies of the charged or uncharged particles in the system. These particles can be electrons, protons, neutrons, helium, deuterium or tritium. According to SRIM2013, it gives the range of the projectile into the target depends on stopping power.

2.5. Reaction Q-values and Threshold Energies for ^{89}Y+^{1}H

According to Table 1, the reaction Q-value is about 3.6 MeV and so the reactions occur after this energy level. Also from the equations (1) and (2), the results are about -4 MeV and 4.1 MeV. Then the Coulomb Barrier energy (3) for this reaction is 8 MeV. Since Threshold Energy is smaller than Minimum Coulomb Barrier Energy, the reaction initiates at the Threshold Energy level.

Table 1. Q-values and Threshold Energies for different reactions of ^{89}Y+p until 15 MeV

Reaction Products	Q-value (keV)	Threshold Energy (keV)
^{90}Zr+γ	8353.380	0.0
^{86}Sr+α	1678.100	0.0
^{89}Y+p	0.0	0.0
^{89}Zr+n	-3615.110	3656.070
^{82}Kr+2α	-4679.690	4732.720
^{88}Sr+2p	-7076.770	7156.970
^{85}Rb+p+α	-7966.740	8057.020
^{88}Y+d	-9257.150	9362.060
^{85}Sr+n+α	-9813.140	9924.350
^{87}Sr+^{3}He	-10471.360	10590.030
^{78}Se+3α	-10669.020	10789.930
^{88}Y+n+p	-11481.720	11611.840
^{87}Y+t	-12351.640	12491.610
^{88}Zr+2n	-12934.490	13081.070
^{81}Br+p+2α	-14583.330	14748.600
^{84}Kr+2p+α	-14983.700	15153.500

2.6. Cross-sections for the Reaction of ^{89}Y+^{1}H

According to Empire3.2, the cross-sections of some reactions of ^{89}Y+p are below;

Table 2. Cross-sections of the different reactions after the proton bombardment to the target of ^{89}Y (*=the main reaction)

Energy (MeV)	(p,γ) reaction cross-section (mb)	(p,n) reaction cross-section (mb)*	(p,2n) reaction cross-section (mb)	(p,d) reaction cross-section (mb)	(p,2p) reaction cross-section (mb)	(p,α) reaction cross-section (mb)
10	0.22577	654.357	0	0	0	0.48568
11	0.18951	681.768	0	5.1E-08	5.8E-06	0.85182
12	0.19406	709.748	0	5.2E-05	0.00156	1.78121
13	0.17922	684.621	0	0.00182	0.03143	3.83865
14	0.17308	682.809	30.3097	0.17112	0.23038	8.97375
15	0.16944	619.156	106.859	4.38041	1.07919	17.9847

From Table 2, the probable radiochemical purities will be ^{90}Zr, ^{89}Zr, ^{88}Zr, ^{88}Y, ^{88}Sr and ^{86}Sr using Table 1. The reactions' cross-sections except the main reaction (p,n), is too small to produce another impurity so they are negligible.
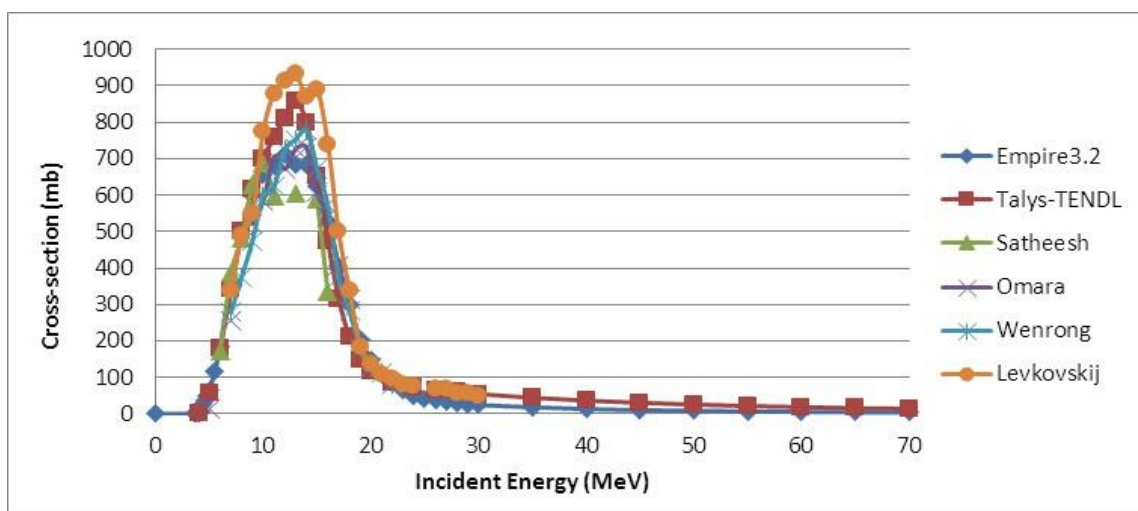
Figure 2. Comparison of the Empire3.2, Talys-TENDL2014 and EXFOR cross-section data for the reaction of ^{89}Y(p,n)^{89}Zr

When incident energy is increased, different reactions occur directly so minimum energy is always preferable. Furthermore 12 MeV energy range is optimum and other probable reactions are (p,γ), (p,d), (p,2p) and (p,α) but if it is compared, these reactions cross-sections are extremely small from the main reaction. From these results, other isotopes can occur actually like ^{90}Zr, ^{88}Y, ^{88}Sr and ^{86}Sr as seen in Table 1 then ^{90}Zr and ^{86}Sr cannot produce because of the threshold energy of the main reaction.

2.7. Stopping Power of the Target System

From SRIM(2013), the target thickness is the most important parameter and for 12 MeV proton energy, energy loss against thickness result is in Figure 3.
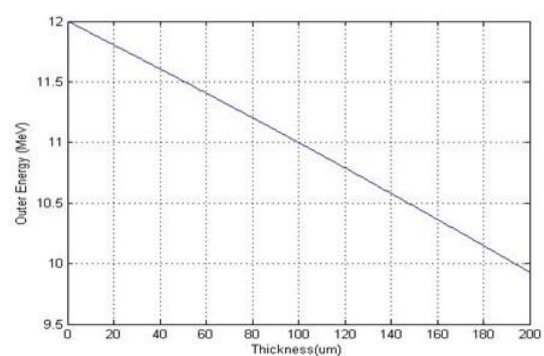
Figure 3. Energy loss with 12 MeV proton beam after target of ^{89}Y using MATLAB code

2.8. Rate of Production

The calculations about the bombardment was performed with MATLAB using IAEA data for irradiation. According to Figure 4 to produce ^{89}Zr from ^{89}Y with proton bombardment under 12 MeV in Cyclone-30 cyclotron.
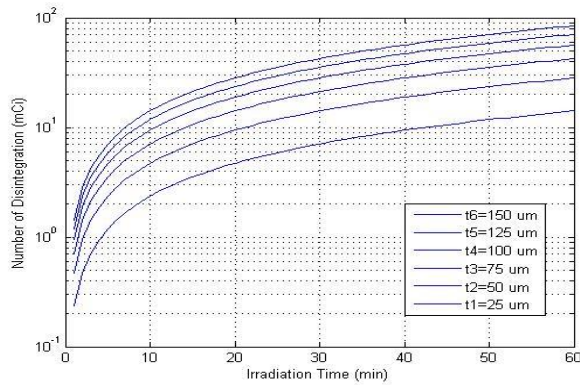
Figure 4. Activity for the irradiation of target ^{89}Y with proton beam for 1 hour.

2.9. Preparation of Dowex Resine

First, the activation of the resine was obtained. For this 10% NaCl solution and 0.2% NaOH was heated at 80 C° for 2 hours. Then Dowex (1x8) was passed through the mixture with 0.5% HCl solution. Before the elution, the column was conditioned with 12 M HCl. In the first step, the target will be washed with 12 M HCl and will be passed through the resine. It is expected that ^{89}Zr will stay in the resine in this way then after washing the resine with 2 M HCl, ^{89}Zr will also come from there.

3. RESULTS AND DISCUSSION

From all the calculations, it is decided that irradiation parameters were like below;

Table 3. Irradiation Parameters

Target Material	Yttrium metal foil (99.99% pure)
Irradiation Time	30 minutes
Irradiation flux	20 µA (1.25x10^{14} proton/cm^2)
Proton beam angle	6°
Thickness of the target	150 µm

Proton beam energy	15 MeV
Expected activity	10 mCi
Cooling time	1 day

After bombardment, ORTEC LaBr3 scintillation detector performed the counting method. In the first spectroscopy (Figure 5), it is seen that there are 3 main peaks which are annihilation photon (511 keV), ^{89}Zr gamma peak (909 keV) and ^{65}Zn gamma peak (1116 keV) because of copper target plate. Then the impurity was removed using Dowex resine, there are only 2 peaks can be seen in Figure 6.
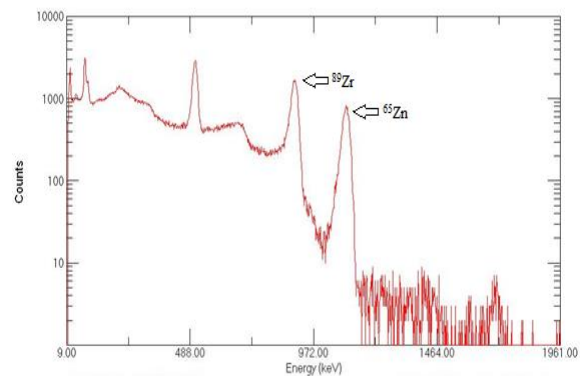
Figure 5. The first gamma spectroscopy of the target after irradiation
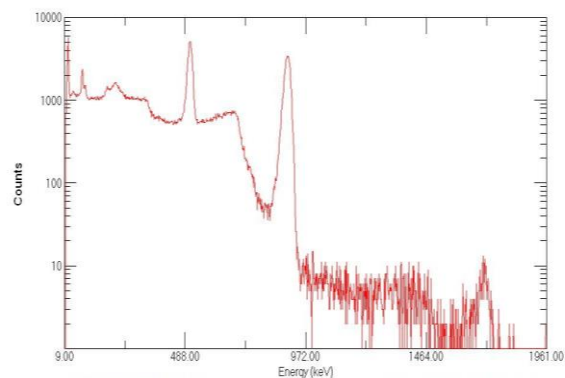
Figure 6. The gamma spectroscopy of target after washing with resine

Totally 3.5 mCi of activity was observed in the dose calibrator after the irradiation. According to the spectrum obtained after the initial washing of the copper target system with 12M HCl, the ^{65}Zn impurity was removed from the system and the amount of residual activity decreased to 2.5 mCi.

This is calculated to be around 7 mCi of ^{89}Zr immediately after irradiation. According to the calculations made, a radiation efficiency of 70% was achieved. It is believed that the cause of the error is caused by the heat spread of the yttrium foil. As a result, ^{89}Zr was obtained in pure form.

4. CONCLUSION

Using new metallic PET radionuclides like 89Zr is increasing all over the world. With a single photon energy and half-life, it is useful and more efficient than other PET radionuclides. To product this radionuclide, there is a nuclear reaction named (p,n) and the target for this reaction is 89Y. IBA Cyclone-30 proton accelerator, which has a 30-MeV maximum energy of protons, is very common in the world and the irradiation was performed in this cyclotron.

To sum up, it is matched that the theoretical data and experimental outputs. It was calculated that after irradiation, it was waited about 10 mCi activity from the target but only 7 mCi total activity was obtained because of the damaged target due to high temperature. Last of all, the irradiation was successfully completed taking radioactive 89Zr without any radiochemical impurity.

5. ACKNOWLEDGMENTS

REFERENCES

[1]　Adonai N., Nguyen K.N., Walsh J., Iyer M., Toyokuni T., Phelps M.E., McCarthy T., McCarthy D.W. and Gambhir S.S., Ex-vivo Cell Labeling with ^{64}Cu-pyruvaldehyde-bis(N4-methylthiosemicarbazone) for Imaging Cell Trafficking in Mice with Positron Emission Tomography, Proc. Natl. Acad. Sci. U.S.A., 99-5 (2002) 3030-3035.

[2]　Aerts H.J.W.L., Dubois L., Perk L., Vermaelen P., van Dongen G.A.M.S., Wouters B.G. and Lambin P., Disparity Between in-vivo EGFR Expression and ^{89}Zr Labeled Cetuximab Uptake Assessed with PET, J. Nucl. Med., 50 (2009), 123–131.

[3]　Alfuraih A., Alzimami K., Ma A.K. and Alghamdi A, Optimization of ^{89}Zr Production Using Monte Carlo Simulations, J. Radioanal. Nucl. Chem., 296 (2013), 1025–1029.

[4]　Avila-Rodriguez M.A., Selwyn R.G., Converse A.K. and Nickles R.J., ^{86}Y and ^{89}Zr as PET Imaging Surrogates for ^{90}Y: A Comparative Study, Proceedings of Ninth Mexican Symposium on Medical Physics, (2006) 45–47.

[5]　Becker W., Emmrich F., Horneff G., Burmester G., Seiler F., Schwarz A., Kalden J. and Wolf F., Imaging Rheumatoid Arthritis Specifically with Technetium-99m CD4-specific (T-helper lymphocytes) Antibodies, Eur. J. Nucl. Med., 17 (1990), 156159.

[6]　Borjesson P.K.E., Jauw Y.W.S., de Bree R., Roos J.C., Castelijns J., Leemans C.R., van Dongen G.AM.S. and Boellaard R., Radiation Dosimetry of ^{89}Zr-Labeled Chimeric Monoclonal Antibody U36 as Used for Immuno-PET in Head and Neck Cancer Patients, J. Nucl. Med., 50-11 (2009), 1828–1836.

[7]　Borjesson P.K.E., Jauw Y.W.S., Boellaard R., de Bree R., Comans E.F.I., Roos J.C., Castelijns J.A., Vosjan M.J., Kummer J.A., Leemans C.R., Lammertma A.A. and van Dongen G.A., Performance of Immuno-Positron Emission Tomography with Zirconium-89-Labeled Chimeric Monoclonal Antibody U36 in the Detection of Lymph Node Metastases in Head and Neck Cancer Patients, Clinical Cancer Research, 12 (2006), 2133-2140.

[8] Dijkers E.C., Oude Munnink T.H., Kosterink J.G., Brouwers A.H., Jager P.L., de Jong J.R., van Dongen G.A., Schröder C.P., Lub-de Hooge M.N. and de Vries E.G., Biodistribution of ^{89}Zr-Trastuzumab and PET Imaging of HER2-Positive Lesions in Patients with Metastatic Breast Cancer, Clin. Pharmacol. Ther., 87 (2010), 586–592.

[9] Dijkers E.C.F., Kosterink J.G.W., Rademaker A.P., Perk L.R., van Dongen G.A.M.S., Bart J., de Jong J.R., de Vries E.G.E. and Lub-de Hooge M.N., Development and Characterization of Clinical-Grade ^{89}Zr-Trastuzumab for HER2/neu ImmunoPET Imaging, J. Nucl. Med., 50 (2009), 974–981.

[10] Disselhorst J.A., Brom M., Laverman P., Slump C.H., Boerman O.C., Oyen W.J.G., Gotthardt M. and Visser E.P., Image-Quality Assessment for Several Positron Emitters Using the NEMA NU 4-2008 Standards in the Siemens Inveon Small Animal PET Scanner, J. Nucl. Med., 51 (2010), 610617.

[11] Firestein G.S., Evolving Concepts of Rheumatoid Arthritis, Nature 423 (2003) 356 361.

[12] Holland J.P., Sheh Y. and Lewis J.S., Standardized Methods for the Production of High Specific-Activity Zirconium-89, Nucl. Med. Biol., 36 (2009) 729–739.

[13] IAEA, IAEA-TRS-468: Cyclotron Produced Radionuclides: Physical Characteristics and Production Methods, (2009), Vienna.

[14] Lampropoulou V., Calderon-Gomez E., Roch T., Neves P., Shen P., Stervbo U., Boudinot P., Anderton S.M. and Fillatreau S., Suppressive Functions of Activated B Cells in Autoimmune Diseases Reveal the Dual Roles of Toll-like Receptors in Immunity, Immunol. Rev., 233 (2010), 146161.

[15] Malviya G., Vries E.F.J.D., Dierckx R.A. and Signore, A., Radiopharmaceuticals for Imaging Chronic Lymphocytic Inflammation. Braz. Arch. Biol. Technol., 50 (2007), 1–13.

[16] Meijs W.E., Haisma H.J., Klok R.P., van Gog F.B., Kievit E., Pinedo H.M. and Herscheid J.D., Zirconium-Labeled Monoclonal Antibodies and Their Distribution in Tumor-Bearing Nude Mice, J. Nucl. Med., 38 (1997), 112–118.

[17] Nayak T.K. and Brechbiel M.W., Radioimmunoimaging with Longer-Lived Positron-Emitting Radionuclides: Potentials and Challenges, Bioconjugate Chem., 20 (2009), 825–841.

[18] Perk L.R., Visser O.J., van Walsum M.S., Vosjan M.J.W.D., Visser G.W.M., Zijlstra J.M., Huijgens P.C. and van Dongen G.A.M.S., Preparation and Evaluation of (89)Zr-Zevalin for Monitoring of (90)Y-Zevalin Biodistribution with Positron Emission Tomography, Eur. J. Nucl. Med. Mol. Imaging, 33 (2006), 1337–1345.

[19] Toh M.L. and Miossec, P., The Role of T Cells in Rheumatoid Arthritis: New Subsets and New Targets, Curr. Opin. Rheumatol., 19 (2007), 284288.

[20] Van Dongen G.A.M.S., Visser G.W.M., Hooge M.N.L., De Vries E.G. and Perk L., Immuno-PET: a Navigator in Monoclonal Antibody Development and Applications, The Oncologist, 12 (2007), 1379–1389.

[21] Verel I., Visser G.W.M., Boellaard R., van Walsum M.S., Snow G.B. and van Dongen G.A.M.S., ^{89}Zr Immuno-PET: Comprehensive Procedures for the Production of ^{89}Zr-Labeled Monoclonal Antibodies, J. Nucl. Med., 44 (2003), 1271–1281.

[22] Verel I., Visser G.W.M. and van Dongen G.A.M.S., The Promise of Immuno-PET in Radioimmunotherapy, J. Nucl. Med., 46 (2005), 164s–171s.

[23] Walther M., Gebhardt P., Grosse-Gehling P., Wurbach L., Irmler I., Preusche S., Khalid M., Opfermann T., Kamradt T., Steinbach J. and Saluz H.P., Implementation of ^{89}Zr Production and In-vivo Imaging of B-cells in Mice with ^{89}Zr-Labeled Anti-B-Cell Antibodies by Small Animal PET/CT, Applied Radiation and Isotopes, 69 (2011), 852–857.

[24] Wu A.M., Antibodies and Antimatter: the Resurgence of Immuno-PET, J. Nucl. Med., 50-1 (2009) 2-5.

Investigation of Benzimidazole Derivates as Corrosion Inhibitor by DFT

*Burak TÜZÜN[1],** iD

[1] *Science Faculty, Department of Chemistry, Cumhuriyet University, Sivas 58140, Turkey*

Abstract. Benzimidazole derivates are investigated the activity of corrosion inhibitor molecules.In quantum chemical calculation, different parameters such as E_{HOMO}, E_{LUMO}, ΔE (HOMO-LUMO energy gap), electronegativity, chemical hardness, global softness, nucleophilicity are calculated by Gaussian 09 software. Studied molecules were performed using the Hartree-Fock (HF) and Becke, 3-parameter, Lee-Yang-Parr (B3LYP) method with sdd, cep-4g, 3-21G, 6-31G, 6-31++G, lanl2dz basis set in gas and aqueous phase. We can see the corrosion inhibitor ranking as: 4NPBI > 4APBI > 2NPBI > 2APBI > 4BPBI > 4MPBI > 4CPBI > PBI in B3lyp method with sdd and lanl2dz.

Keywords: Benzimidazole, DFT, corrosion, activity.

DFT ile benzimidazol türevlerinin korozyon inhibitörü olarak incelenmesi

Özet. Benzimidazol türevleri, korozyon önleyici moleküllerin aktivitesini araştırıldı. Kuantum kimyasal hesaplamasında, E_{HOMO}, E_{LUMO}, ΔE (HOMO-LUMO enerji aralığı), elektronegatiflik, kimyasal sertlik, global yumuşaklık, nükleofilik gibi farklı parametreler gaussian 09 yazılımı ile hesaplandı. Çalışılan moleküller, Hartree-Fock (HF) ve Becke, 3-parametre Lee-Yang-Parr (B3LYP) yöntemi kullanılarak sdd, cep-4g, 3-21G, 6-31G, 6-31 ++ G, lanl2dz temel sette gaz ve sulu fazda hesaplamaları yapıldı. Korozyon inhibitörü sıralamasını aşağıdaki gibi görebiliriz: 4NPBI> 4APBI> 2NPBI> 2APBI> 4BPBI> 4MPBI> 4CPBI> PBI, b3lyp metodunda lanl2dz ve sdd settinde.

Anahtar Kelimeler: Benzimidazol, DFT, korozyon, aktivite.

1. INTRODUCTION

Metal corrosion is a very important problem in various industrial processes which is widely used water, alcohol and acid. The acid solutions used cause too much corrosion in the metal that is an iron, copper, aluminum. Corrosion inhibitors that are containing nitrogen, oxygen, Sulphur and aromatic ring, are used to prevent corrosion caused by acid solutions.

As it is well known that experimental studies have been used to understand the corrosion inhibition mechanism of molecules and to explain corrosion inhibition efficiencies. Quantum chemical calculations provide preliminary information on the activities of molecules. In quantum chemical calculations, parameters related to the activity of molecules are calculated using density functional theory (DFT) that are calculated HOMO (highest occupied molecular orbital), LUMO (lowest unoccupied molecular orbital), electrophilicity, electronegativity, chemical potential, chemical hardness and nucleophilicity.

In this study, we can be seen that activity of studied molecules whose names are 2-(4-nitrophenyl) benzimidazole (4NPBI), 2-(4-aminophenyl) benzimidazole (4APBI), 2-(2-nitrophenyl) benzimidazole (2NPBI), 2-(2-aminophenyl) benzimidazole (2APBI), 2-phenyl benzimidazole (PBI), 2-(4-chlorophenyl) benzimidazole (4CPBI), 2-(4-metilphenyl) benzimidazole (4MPBI), 2-(4-bromophenyl) benzimidazole (4BPBI) in Figure 1 [1].

2. COMPUTATIONAL DETAILS

DFT calculation is the most popular method for the activity of molecules.In this study, we prepared the input files of the molecules studied by gaussian view 5.08 programs [2]. Calculations of studied molecules were performed with Gaussian IA32W-G09RevA.02 and Gaussian AS64L-G09RevD.01 programs [3-4]. Studied molecules were performed using the Hartree-Fock (HF)[5] and Becke, 3-parameter, Lee-Yang-Parr (B3LYP) [6-8] method with sdd, cep-4g, 3-21G, 6-31G, 6-31++G, lanl2dz basis set in gas and an aqueous phase. HOMO and LUMO are given information about activity of molecules.Chemical reactivity parameter of molecules isgiven to found a good corrosion inhibitor such as E_{HOMO}, E_{LUMO}, ΔE (HOMO-LUMO energy gap), electronegativity (χ), chemical potential (μ), chemical hardness (η), electrophilicity (ω), nucleophilicity (ε), global softness (σ) and proton affinity (PA) [9-18].

$$\mu = -\chi = \left(\frac{\partial E}{\partial N} \right)_{\upsilon(r)} \tag{1}$$

$$\eta = \frac{1}{2} \left(\frac{\partial^2 E}{\partial N^2} \right)_{\upsilon(r)} = \frac{1}{2} \left(\frac{\partial \mu}{\partial N} \right) \tag{2}$$

Ionization energy (I) and electron affinity (A) [19] of studied molecules are calculated with HOMO and LUMO energy that are interested Electronegativity, global softness and chemical hardness obtaining the following equations.

$$\chi = -\mu = \left(\frac{I+A}{2} \right) \tag{3}$$

$$\eta = \frac{I-A}{2} \tag{4}$$

As it is well known that global softness is defined as the inverse of the chemical hardness [20].

$$\sigma = 1/\eta \tag{5}$$

$$\chi = -\mu = \left(\frac{-E_{HOMO} - E_{LUMO}}{2} \right) \tag{6}$$

$$\eta = \left(\frac{E_{LUMO} - E_{HOMO}}{2} \right) \tag{7}$$

The global electrophilicity index (ω) that is investigated by Parr et al., is the inverse of nucleophilicity and are given inequality (8). Electrophilicity and nucleophilicity are used for the prediction organic and inorganic reaction mechanisms. Nucleophilicity (ε) is defined as the inverse of the electrophilicity in equations (9).

$$\omega = \mu^2 / 2\eta = \chi^2 / 2\eta \tag{8}$$

$$\varepsilon = 1/\omega \tag{9}$$

3. RESULTS AND DISCUSSION

The corrosion inhibitor reactivity of benzimidazole derivatives is studied by quantum chemical calculation. The chemical reactivity of studied molecules that is obtained by the Gaussian software program, it is shown that a good inhibitor against different metal atoms. The studied of molecules are obtained the results are given in below.

The studied molecules are investigated quantum chemical parameter such as E_{HOMO}, E_{LUMO}, ΔE (HOMO-LUMO energy gap), electronegativity, chemical potential, chemical hardness, electrophilicity, nucleophilicity, global softness and proton affinity. These parameters are very important parameters which are compared the reactivity of studied molecules.

As it is well known that the properties of chemical reactivity of studied molecules were compared by molecular orbitals of an inhibitor molecule that have got two molecular orbitalswhose the name is

Highest Occupied Molecular Orbital (HOMO) and Lowest Unoccupied Molecular Orbital (LUMO).

The energy level of HOMO has defined the electron donating ability of studied molecules. The molecule has got the high values of energy of HOMO that is showingthe tendency to donate electrons of the molecule to appropriate that the acceptor molecules have low energy and empty molecular orbital [9-18]. From the light of the result given in the information, the energy level of LUMO of molecules is indicated electron accepting abilities of studied molecules. When the energy value of LUMO of inhibitor molecule is lower, this molecule has more electron accepting ability in lower energy of molecular orbitals. The calculated of HOMO and LUMO energy value is given in Table 1, 2, 3 and 4.
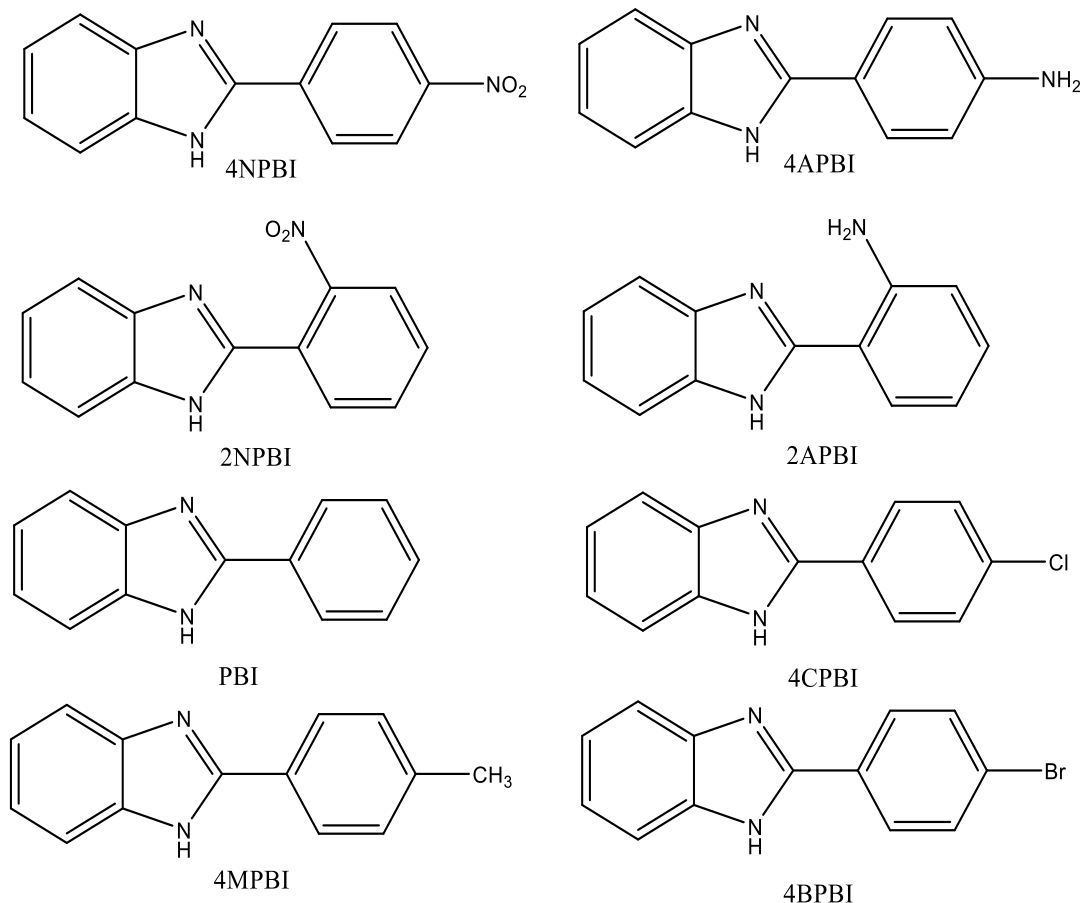
Figure 1. The structure and schematic representation of molecules of benzimidazole derivatives

In figure 2, structure of HOMO, LUMO and ESP studied molecules are given about some information of this molecule. In figure of HOMO of molecule, we look where highest occupied molecular orbital is. In this picture, HOMO orbitals appear to cover the entire molecule. In figure of LUMO of molecule, we look where lowest unoccupied molecular orbital is. In this picture, LUMO orbitals appear to cover the entire molecule. Last picture is ESP that is Molecular electrostatic potential (ESP) figure that given information about distribution of electrons in molecular. In this picture, the different value of the electrostatic potential represented by different colors [14]. This potential increases in the order red > orange > yellow > green > blue. The highest potential is on oxygen atoms.

The energy gap value (ΔE) in chemical reactivity of inhibitor molecule is a very important parameter in corrosion. As it is well known that inhibitor molecule has a small energy gap value, this molecule is a good corrosion inhibitor. Since the energy gap value of inhibitor molecule is indicated

that the binding ability of inhibitor molecules on metal surfaces [21]. On the basis of the calculated the energy gap value given in Table 1, 2, 3 and 4, the corrosion inhibition activity of benzimidazole derivatives molecules can be written as:4NPBI > 4APBI > 2NPBI > 2APBI > 4BPBI > 4MPBI > 4CPBI > PBI in B3lyp method with sdd and lanl2dz.

Figure 2. Structures of HOMO, LUMO and ESPs of benzimidazole derivatives

Table 1. The calculated quantum chemical parameters with B3LYP method in gas phase (eV)

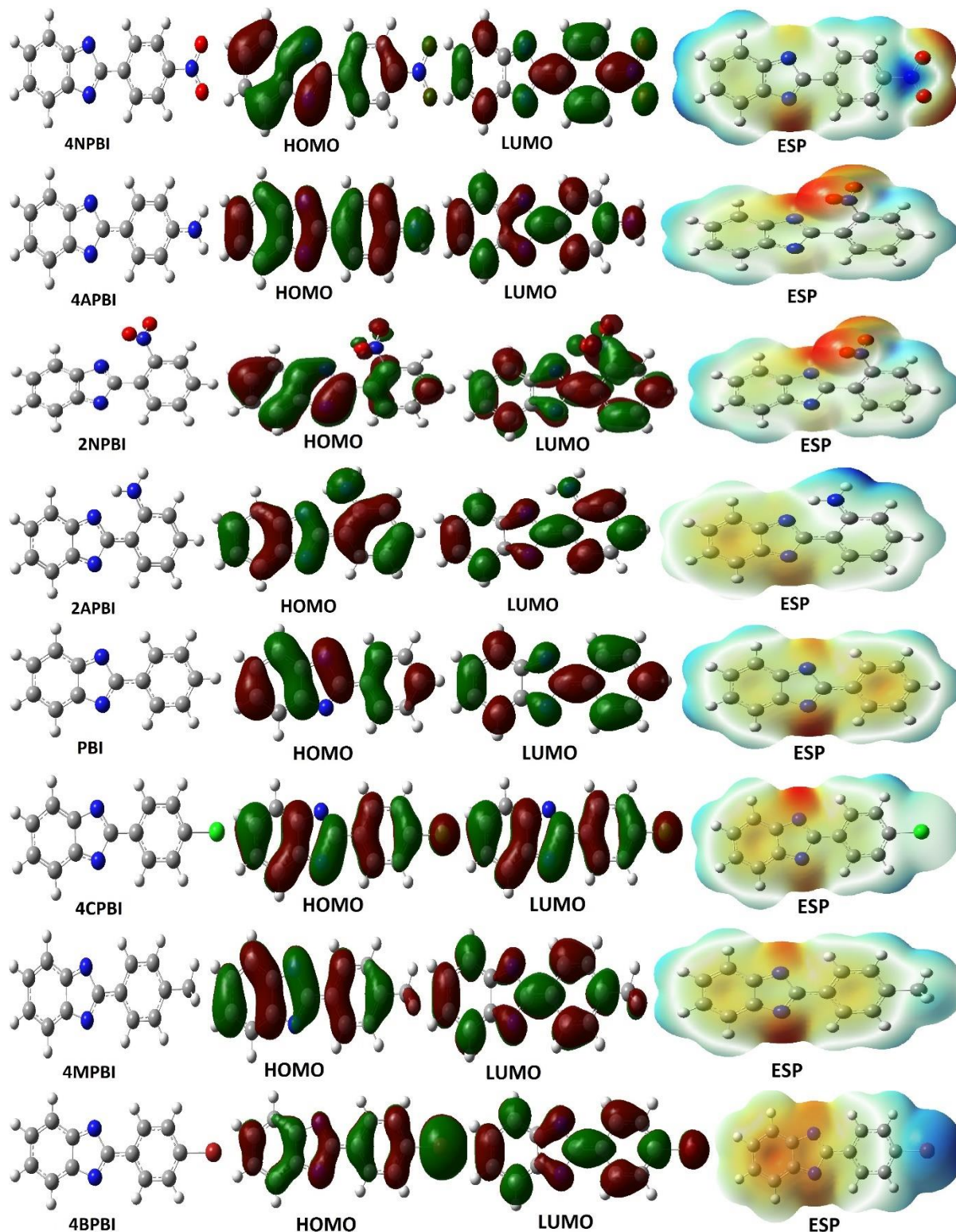|	E_{HOMO}	E_{LUMO}	I	A	ΔE	η	σ	χ	Pİ	ω	ε	dipol	Energy
B3LYP/SDD													
4NPBI	-6,903	-3,324	6,903	3,324	3,579	1,790	0,559	5,113	-5,113	7,305	0,137	8,811	-22163,416
4APBI	-5,376	-1,259	5,376	1,259	4,117	2,059	0,486	3,317	-3,317	2,673	0,374	5,861	-18105,389
2NPBI	-6,701	-2,566	6,701	2,566	4,136	2,068	0,484	4,633	-4,633	5,191	0,193	4,634	-22162,904
2APBI	-5,618	-1,471	5,618	1,471	4,147	2,073	0,482	3,544	-3,544	3,030	0,330	2,949	-18105,611
PBI	-6,193	-1,703	6,193	1,703	4,490	2,245	0,445	3,948	-3,948	3,471	0,288	0,998	-16599,339
4CPBI	-6,345	-1,920	6,345	1,920	4,425	2,213	0,452	4,132	-4,132	3,858	0,259	3,522	-29105,350
4MPBI	-6,009	-1,597	6,009	1,597	4,413	2,206	0,453	3,803	-3,803	3,277	0,305	0,391	-17668,447
4BPBI	-6,337	-1,939	6,337	1,939	4,398	2,199	0,455	4,138	-4,138	3,893	0,257	3,421	-16947,196
B3LYP/Cep-4g													
4NPBI	-8,192	-4,904	8,192	4,904	3,288	1,644	0,608	6,548	-6,548	13,041	0,077	8,251	-3762,591
4APBI	-6,682	-3,025	6,682	3,025	3,657	1,829	0,547	4,853	-4,853	6,440	0,155	3,823	-2932,975
2NPBI	-8,018	-4,466	8,018	4,466	3,552	1,776	0,563	6,242	-6,242	10,968	0,091	4,138	-3762,160
2APBI	-6,936	-3,193	6,936	3,193	3,743	1,872	0,534	5,065	-5,065	6,852	0,146	2,577	-2933,299
PBI	-7,652	-3,443	7,652	3,443	4,209	2,105	0,475	5,547	-5,547	7,310	0,137	1,906	-2649,286
4CPBI	-7,793	-3,739	7,793	3,739	4,054	2,027	0,493	5,766	-5,766	8,201	0,122	4,731	-3038,153
4MPBI	-7,498	-3,327	7,498	3,327	4,171	2,085	0,480	5,413	-5,413	7,024	0,142	0,913	-2833,735
4BPBI	-7,507	-3,506	7,507	3,506	4,001	2,000	0,500	5,507	-5,507	7,579	0,132	2,813	-2997,697
B3LYP/3-21g													
4NPBI	-6,653	-2,814	6,653	2,814	3,839	1,920	0,521	4,733	-4,733	5,836	0,171	7,293	-22043,816
4APBI	-5,108	-0,876	5,108	0,876	4,231	2,116	0,473	2,992	-2,992	2,116	0,473	6,020	-18008,316
2NPBI	-6,514	-2,448	6,514	2,448	4,067	2,033	0,492	4,481	-4,481	4,938	0,203	4,463	-22043,329
2APBI	-5,362	-1,146	5,362	1,146	4,216	2,108	0,474	3,254	-3,254	2,511	0,398	3,212	-18008,695
PBI	-6,055	-1,394	6,055	1,394	4,660	2,330	0,429	3,724	-3,724	2,977	0,336	1,122	-16510,517
4CPBI	-6,256	-1,660	6,256	1,660	4,595	2,298	0,435	3,958	-3,958	3,409	0,293	3,943	-28957,276
4MPBI	-5,886	-1,311	5,886	1,311	4,575	2,288	0,437	3,598	-3,598	2,830	0,353	0,200	-17573,972
4BPBI	-6,092	-1,568	6,092	1,568	4,524	2,262	0,442	3,830	-3,830	3,242	0,308	2,607	-86205,409
B3LYP/6-31g													
4NPBI	-6,699	-3,019	6,699	3,019	3,681	1,840	0,543	4,859	-4,859	6,414	0,156	8,360	-22160,493
4APBI	-5,171	-0,971	5,171	0,971	4,200	2,100	0,476	3,071	-3,071	2,246	0,445	5,850	-18103,585
2NPBI	-6,499	-2,190	6,499	2,190	4,309	2,154	0,464	4,345	-4,345	4,381	0,228	4,369	-22159,960
2APBI	-5,420	-1,196	5,420	1,196	4,224	2,112	0,474	3,308	-3,308	2,591	0,386	2,862	-18103,805
PBI	-6,008	-1,428	6,008	1,428	4,580	2,290	0,437	3,718	-3,718	3,018	0,331	0,968	-16597,877
4CPBI	-6,200	-1,682	6,200	1,682	4,519	2,259	0,443	3,941	-3,941	3,437	0,291	3,765	-29103,991
4MPBI	-5,838	-1,343	5,838	1,343	4,495	2,247	0,445	3,590	-3,590	2,868	0,349	0,307	-17666,882
4BPBI	-6,124	-1,644	6,124	1,644	4,479	2,240	0,446	3,884	-3,884	3,368	0,297	3,096	-86558,506
B3LYP/6-31++g													
4NPBI	-6,977	-3,443	6,977	3,443	3,534	1,767	0,566	5,210	-5,210	7,679	0,130	8,847	-22161,453
4APBI	-5,483	-1,352	5,483	1,352	4,130	2,065	0,484	3,417	-3,417	2,827	0,354	5,786	-18104,341
2NPBI	-6,769	-2,745	6,769	2,745	4,025	2,012	0,497	4,757	-4,757	5,623	0,178	4,581	-22160,962
2APBI	-5,716	-1,536	5,716	1,536	4,180	2,090	0,478	3,626	-3,626	3,145	0,318	2,846	-18104,506
PBI	-6,277	-1,757	6,277	1,757	4,520	2,260	0,442	4,017	-4,017	3,571	0,280	0,942	-16598,523
4CPBI	-6,440	-1,981	6,440	1,981	4,460	2,230	0,448	4,211	-4,211	3,975	0,252	3,607	-29104,649
4MPBI	-6,095	-1,664	6,095	1,664	4,431	2,216	0,451	3,879	-3,879	3,396	0,294	0,456	-17667,551
4BPBI	-6,385	-1,962	6,385	1,962	4,423	2,212	0,452	4,174	-4,174	3,939	0,254	3,097	-86559,996
B3LYP/Lanl2dz													
4NPBI	-6,908	-3,330	6,908	3,330	3,578	1,789	0,559	5,119	-5,119	7,323	0,137	8,827	-22163,371
4APBI	-5,379	-1,261	5,379	1,261	4,117	2,059	0,486	3,320	-3,320	2,677	0,374	5,862	-18105,360
2NPBI	-6,706	-2,574	6,706	2,574	4,131	2,066	0,484	4,640	-4,640	5,212	0,192	4,640	-22162,858
2APBI	-5,620	-1,473	5,620	1,473	4,147	2,074	0,482	3,547	-3,547	3,033	0,330	2,955	-18105,584
PBI	-6,196	-1,705	6,196	1,705	4,491	2,246	0,445	3,950	-3,950	3,475	0,288	1,003	-16599,313
4CPBI	-6,362	-1,931	6,362	1,931	4,430	2,215	0,451	4,147	-4,147	3,881	0,258	3,656	-16989,793
4MPBI	-6,013	-1,598	6,013	1,598	4,414	2,207	0,453	3,806	-3,806	3,281	0,305	0,387	-17668,421
4BPBI	-6,311	-1,920	6,311	1,920	4,391	2,195	0,455	4,116	-4,116	3,858	0,259	3,211	-16941,355

Table 2. The calculated quantum chemical parameters with B3LYP method in aqueous phase (eV)

	E$_{HOMO}$	E$_{LUMO}$	I	A	ΔE	η	σ	χ	Pİ	ω	ε	dipol	Energy
B3LYP/SDD													
4NPBI	-6,795	-3,598	6,795	3,598	3,197	1,599	0,626	5,196	-5,196	8,446	0,118	11,794	-22163,836
4APBI	-5,643	-1,564	5,643	1,564	4,079	2,040	0,490	3,604	-3,604	3,184	0,314	11,666	-18105,943
2NPBI	-6,733	-3,252	6,733	3,252	3,481	1,740	0,575	4,992	-4,992	7,161	0,140	5,936	-22163,388
2APBI	-5,853	-1,665	5,853	1,665	4,188	2,094	0,478	3,759	-3,759	3,375	0,296	6,213	-18105,980
PBI	-6,402	-1,910	6,402	1,910	4,492	2,246	0,445	4,156	-4,156	3,845	0,260	1,504	-16599,635
4CPBI	-6,467	-2,028	6,467	2,028	4,439	2,220	0,451	4,248	-4,248	4,065	0,246	4,841	-29105,633
4MPBI	-6,235	-1,846	6,235	1,846	4,390	2,195	0,456	4,041	-4,041	3,719	0,269	0,928	-17668,758
4BPBI	-6,457	-2,046	6,457	2,046	4,411	2,205	0,453	4,252	-4,252	4,098	0,244	4,653	-16947,477
B3LYP/Cep-4g													
4NPBI	-8,178	-5,203	8,178	5,203	2,976	1,488	0,672	6,690	-6,690	15,043	0,066	10,258	-3763,007
4APBI	-7,004	-3,391	7,004	3,391	3,613	1,807	0,554	5,197	-5,197	7,476	0,134	7,187	-2933,601
2NPBI	-8,168	-5,044	8,168	5,044	3,124	1,562	0,640	6,606	-6,606	13,968	0,072	5,275	-3762,659
2APBI	-7,426	-3,335	7,426	3,335	4,091	2,045	0,489	5,381	-5,381	7,077	0,141	6,980	-2934,065
PBI	-7,914	-3,733	7,914	3,733	4,182	2,091	0,478	5,824	-5,824	8,111	0,123	2,767	-2649,691
4CPBI	-7,968	-3,940	7,968	3,940	4,027	2,014	0,497	5,954	-5,954	8,802	0,114	6,076	-3038,525
4MPBI	-7,811	-3,658	7,811	3,658	4,153	2,077	0,482	5,735	-5,735	7,918	0,126	1,585	-2834,169
4BPBI	-7,701	-3,739	7,701	3,739	3,962	1,981	0,505	5,720	-5,720	8,259	0,121	3,496	-2998,069
B3LYP/3-21g													
4NPBI	-6,621	-3,036	6,621	3,036	3,585	1,793	0,558	4,829	-4,829	6,503	0,154	9,425	-22044,112
4APBI	-5,384	-1,216	5,384	1,216	4,168	2,084	0,480	3,300	-3,300	2,612	0,383	11,861	-18008,855
2NPBI	-6,593	-2,818	6,593	2,818	3,775	1,887	0,530	4,706	-4,706	5,866	0,170	5,702	-22043,682
2APBI	-5,620	-1,355	5,620	1,355	4,265	2,133	0,469	3,487	-3,487	2,851	0,351	6,313	-18009,045
PBI	-6,281	-1,619	6,281	1,619	4,662	2,331	0,429	3,950	-3,950	3,346	0,299	1,734	-16510,766
4CPBI	-6,391	-1,785	6,391	1,785	4,606	2,303	0,434	4,088	-4,088	3,628	0,276	5,402	-28957,519
4MPBI	-6,133	-1,565	6,133	1,565	4,567	2,284	0,438	3,849	-3,849	3,244	0,308	0,297	-17574,226
4BPBI	-6,261	-1,731	6,261	1,731	4,530	2,265	0,442	3,996	-3,996	3,526	0,284	3,579	-86205,643
B3LYP/6-31g													
4NPBI	-6,601	-3,273	6,601	3,273	3,328	1,664	0,601	4,937	-4,937	7,324	0,137	11,136	-22160,860
4APBI	-5,421	-1,262	5,421	1,262	4,158	2,079	0,481	3,341	-3,341	2,685	0,372	11,164	-18104,077
2NPBI	-6,534	-2,835	6,534	2,835	3,699	1,849	0,541	4,684	-4,684	5,932	0,169	5,584	-22160,389
2APBI	-5,639	-1,381	5,639	1,381	4,258	2,129	0,470	3,510	-3,510	2,893	0,346	5,802	-18104,128
PBI	-6,202	-1,622	6,202	1,622	4,581	2,290	0,437	3,912	-3,912	3,341	0,299	1,437	-16598,127
4CPBI	-6,305	-1,773	6,305	1,773	4,532	2,266	0,441	4,039	-4,039	3,600	0,278	5,210	-29104,238
4MPBI	-6,046	-1,571	6,046	1,571	4,475	2,237	0,447	3,809	-3,809	3,242	0,308	0,679	-17667,162
4BPBI	-6,246	-1,755	6,246	1,755	4,491	2,246	0,445	4,000	-4,000	3,563	0,281	4,269	-86558,747
B3LYP/6-31++g													
4NPBI	-6,842	-3,731	6,842	3,731	3,111	1,556	0,643	5,286	-5,286	8,982	0,111	12,184	-22161,881
4APBI	-5,706	-1,608	5,706	1,608	4,098	2,049	0,488	3,657	-3,657	3,263	0,306	11,631	-18104,879
2NPBI	-6,834	-3,491	6,834	3,491	3,343	1,671	0,598	5,162	-5,162	7,972	0,125	6,520	-22161,520
2APBI	-5,908	-1,691	5,908	1,691	4,217	2,109	0,474	3,799	-3,799	3,423	0,292	6,113	-18104,858
PBI	-6,446	-1,927	6,446	1,927	4,519	2,259	0,443	4,186	-4,186	3,878	0,258	1,385	-16598,804
4CPBI	-6,522	-2,049	6,522	2,049	4,473	2,236	0,447	4,286	-4,286	4,106	0,244	5,005	-29104,924
4MPBI	-6,278	-1,877	6,278	1,877	4,401	2,200	0,454	4,078	-4,078	3,778	0,265	1,185	-17667,850
4BPBI	-6,477	-2,044	6,477	2,044	4,433	2,217	0,451	4,260	-4,260	4,094	0,244	4,225	-86560,265
B3LYP/Lanl2dz													
4NPBI	-6,801	-3,606	6,801	3,606	3,195	1,598	0,626	5,203	-5,203	8,473	0,118	11,813	-22163,791
4APBI	-5,648	-1,568	5,648	1,568	4,080	2,040	0,490	3,608	-3,608	3,191	0,313	11,672	-18105,916
2NPBI	-6,738	-3,263	6,738	3,263	3,475	1,738	0,575	5,000	-5,000	7,194	0,139	5,944	-22163,343
2APBI	-5,858	-1,668	5,858	1,668	4,189	2,095	0,477	3,763	-3,763	3,380	0,296	6,222	-18105,954
PBI	-6,408	-1,913	6,408	1,913	4,495	2,247	0,445	4,161	-4,161	3,851	0,260	1,520	-16599,610
4CPBI	-6,482	-2,037	6,482	2,037	4,444	2,222	0,450	4,259	-4,259	4,082	0,245	5,016	-16990,077
4MPBI	-6,240	-1,849	6,240	1,849	4,391	2,195	0,455	4,045	-4,045	3,726	0,268	0,921	-17668,733
4BPBI	-6,442	-2,039	6,442	2,039	4,403	2,202	0,454	4,241	-4,241	4,084	0,245	4,386	-16941,636

Table 3. The calculated quantum chemical parameters with HF method in gas phase (eV)

	E$_{HOMO}$	E$_{LUMO}$	I	A	ΔE	η	σ	χ	Pİ	ω	ε	dipol	Energy
HF/SDD													
4NPBI	-9,731	1,063	9,731	-1,063	10,793	5,397	0,185	4,334	-4,334	1,740	0,575	8,069	-22027,634
4APBI	-7,518	2,499	7,518	-2,499	10,017	5,009	0,200	2,509	-2,509	0,629	1,591	1,251	-17988,851
2NPBI	-9,606	0,988	9,606	-0,988	10,593	5,297	0,189	4,309	-4,309	1,753	0,570	5,060	-22026,633
2APBI	-7,286	2,280	7,286	-2,280	9,566	4,783	0,209	2,503	-2,503	0,655	1,527	5,928	-17987,967
PBI	-8,307	2,265	8,307	-2,265	10,572	5,286	0,189	3,021	-3,021	0,863	1,158	1,206	-16492,155
4CPBI	-9,140	0,209	9,140	-0,209	9,349	4,675	0,214	4,466	-4,466	2,133	0,469	4,423	-28979,512
4MPBI	-8,148	2,403	8,148	-2,403	10,552	5,276	0,190	2,872	-2,872	0,782	1,279	0,584	-17553,403
4BPBI	-9,059	2,072	9,059	-2,072	11,131	5,565	0,180	3,494	-3,494	1,097	0,912	4,188	-16834,371
HF/Cep-4g													
4NPBI	-11,048	-0,994	11,048	0,994	10,054	5,027	0,199	6,021	-6,021	3,606	0,277	7,817	-3662,891
4APBI	-8,991	1,491	8,991	-1,491	10,481	5,241	0,191	3,750	-3,750	1,342	0,745	0,917	-2849,671
2NPBI	-11,022	0,115	11,022	-0,115	11,136	5,568	0,180	5,453	-5,453	2,670	0,374	4,664	-3662,380
2APBI	-8,604	1,346	8,604	-1,346	9,951	4,975	0,201	3,629	-3,629	1,323	0,756	2,482	-2849,719
PBI	-10,075	1,128	10,075	-1,128	11,203	5,601	0,179	4,473	-4,473	1,786	0,560	1,478	-2573,138
4CPBI	-10,547	0,580	10,547	-0,580	11,127	5,564	0,180	4,984	-4,984	2,232	0,448	4,665	-2955,887
4MPBI	-9,973	1,282	9,973	-1,282	11,256	5,628	0,178	4,345	-4,345	1,678	0,596	0,721	-2751,804
4BPBI	-10,274	2,506	10,274	-2,506	12,780	6,390	0,156	3,884	-3,884	1,180	0,847	3,356	-2916,891
HF/3-21g													
4NPBI	-9,509	1,425	9,509	-1,425	10,934	5,467	0,183	4,042	-4,042	1,494	0,669	7,167	-21909,792
4APBI	-7,264	2,858	7,264	-2,858	10,122	5,061	0,198	2,203	-2,203	0,479	2,086	0,472	-17893,170
2NPBI	-9,416	1,386	9,416	-1,386	10,802	5,401	0,185	4,015	-4,015	1,492	0,670	4,741	-21908,839
2APBI	-7,310	2,611	7,310	-2,611	9,921	4,960	0,202	2,349	-2,349	0,556	1,798	1,916	-17893,832
PBI	-8,354	2,571	8,354	-2,571	10,925	5,462	0,183	2,892	-2,892	0,765	1,307	1,096	-16404,596
4CPBI	-8,659	2,177	8,659	-2,177	10,836	5,418	0,185	3,241	-3,241	0,969	1,032	4,153	-28832,859
4MPBI	-8,181	2,665	8,181	-2,665	10,845	5,423	0,184	2,758	-2,758	0,701	1,426	0,553	-17460,279
4BPBI	-8,490	2,259	8,490	-2,259	10,749	5,375	0,186	3,115	-3,115	0,903	1,108	3,201	-86052,485
HF/6-31g													
4NPBI	-9,507	1,349	9,507	-1,349	10,856	5,428	0,184	4,079	-4,079	1,533	0,652	7,884	-22024,747
4APBI	-7,504	3,068	7,504	-3,068	10,572	5,286	0,189	2,218	-2,218	0,465	2,150	1,393	-17987,154
2NPBI	-8,786	1,942	8,786	-1,942	10,727	5,364	0,186	3,422	-3,422	1,092	0,916	4,966	-22023,629
2APBI	-7,769	2,864	7,769	-2,864	10,633	5,316	0,188	2,453	-2,453	0,566	1,768	1,602	-17987,206
PBI	-8,150	2,601	8,150	-2,601	10,751	5,375	0,186	2,775	-2,775	0,716	1,396	1,157	-16490,647
4CPBI	-8,422	2,264	8,422	-2,264	10,686	5,343	0,187	3,079	-3,079	0,887	1,127	4,171	-28977,756
4MPBI	-7,993	2,697	7,993	-2,697	10,690	5,345	0,187	2,648	-2,648	0,656	1,524	0,608	-17551,797
4BPBI	-8,350	2,280	8,350	-2,280	10,630	5,315	0,188	3,035	-3,035	0,867	1,154	3,734	-86402,492
HF/6-31++g													
4NPBI	-9,086	0,216	9,086	-0,216	9,302	4,651	0,215	4,435	-4,435	2,114	0,473	8,026	-22024,899
4APBI	-7,524	1,058	7,524	-1,058	8,582	4,291	0,233	3,233	-3,233	1,218	0,821	0,384	-17988,099
2NPBI	-9,541	0,832	9,541	-0,832	10,373	5,186	0,193	4,355	-4,355	1,828	0,547	5,083	-22024,461
2APBI	-7,948	1,053	7,948	-1,053	9,001	4,501	0,222	3,447	-3,447	1,320	0,757	1,618	-17987,709
PBI	-8,323	1,056	8,323	-1,056	9,379	4,689	0,213	3,633	-3,633	1,408	0,710	1,159	-16491,100
4CPBI	-8,557	0,974	8,557	-0,974	9,531	4,766	0,210	3,792	-3,792	1,508	0,663	4,066	-28978,198
4MPBI	-8,155	1,084	8,155	-1,084	9,239	4,619	0,216	3,535	-3,535	1,353	0,739	0,536	-17552,232
4BPBI	-8,506	0,982	8,506	-0,982	9,489	4,744	0,211	3,762	-3,762	1,492	0,670	3,766	-86403,766
HF/Lanl2dz													
4NPBI	-9,686	0,357	9,686	-0,357	10,044	5,022	0,199	4,664	-4,664	2,166	0,462	8,602	-22027,001
4APBI	-7,512	2,501	7,512	-2,501	10,013	5,006	0,200	2,506	-2,506	0,627	1,595	1,248	-17988,792
2NPBI	-9,598	0,989	9,598	-0,989	10,587	5,293	0,189	4,305	-4,305	1,750	0,571	5,061	-22026,572
2APBI	-7,922	2,486	7,922	-2,486	10,407	5,204	0,192	2,718	-2,718	0,710	1,409	1,681	-17988,964
PBI	-8,306	2,262	8,306	-2,262	10,568	5,284	0,189	3,022	-3,022	0,864	1,157	1,210	-16492,099
4CPBI	-9,153	2,081	9,153	-2,081	11,233	5,617	0,178	3,536	-3,536	1,113	0,898	4,567	-16877,010
4MPBI	-8,143	2,404	8,143	-2,404	10,546	5,273	0,190	2,869	-2,869	0,781	1,281	0,587	-17553,340
4BPBI	-9,042	2,096	9,042	-2,096	11,138	5,569	0,180	3,473	-3,473	1,083	0,924	4,187	-16828,705

Table 4. The calculated quantum chemical parameters with HF method in aqueous phase (eV)

	E_{HOMO}	E_{LUMO}	I	A	ΔE	η	σ	χ	Pİ	ω	ε	dipol	Energy
HF/SDD													
4NPBI	-9,572	0,857	9,572	-0,857	10,428	5,214	0,192	4,358	-4,358	1,821	0,549	9,390	-22028,075
4APBI	-8,474	2,114	8,474	-2,114	10,587	5,294	0,189	3,180	-3,180	0,955	1,047	2,646	-17989,032
2NPBI	-9,607	0,626	9,607	-0,626	10,233	5,116	0,195	4,490	-4,490	1,970	0,508	6,386	-22027,146
2APBI	-8,186	2,262	8,186	-2,262	10,447	5,224	0,191	2,962	-2,962	0,840	1,191	2,161	-17989,338
PBI	-8,525	2,050	8,525	-2,050	10,576	5,288	0,189	3,237	-3,237	0,991	1,009	1,492	-16492,429
4CPBI	-8,633	1,922	8,633	-1,922	10,555	5,277	0,189	3,355	-3,355	1,067	0,937	4,965	-28979,199
4MPBI	-8,392	2,167	8,392	-2,167	10,559	5,279	0,189	3,112	-3,112	0,917	1,090	0,749	-17553,678
4BPBI	-8,596	1,864	8,596	-1,864	10,460	5,230	0,191	3,366	-3,366	1,083	0,923	4,650	-16834,047
HF/Cep-4g													
4NPBI	-11,038	-1,211	11,038	1,211	9,827	4,913	0,204	6,125	-6,125	3,817	0,262	8,804	-3663,269
4APBI	-8,517	1,842	8,517	-1,842	10,359	5,179	0,193	3,337	-3,337	1,075	0,930	19,751	-2847,722
2NPBI	-11,159	-0,967	11,159	0,967	10,192	5,096	0,196	6,063	-6,063	3,607	0,277	5,968	-3662,986
2APBI	-9,023	0,973	9,023	-0,973	9,996	4,998	0,200	4,025	-4,025	1,621	0,617	2,910	-2850,076
PBI	-10,381	0,826	10,381	-0,826	11,207	5,604	0,178	4,777	-4,777	2,036	0,491	1,638	-2573,449
4CPBI	-10,770	0,403	10,770	-0,403	11,173	5,587	0,179	5,184	-5,184	2,405	0,416	5,309	-2956,186
4MPBI	-10,326	0,937	10,326	-0,937	11,262	5,631	0,178	4,695	-4,695	1,957	0,511	0,767	-2752,114
4BPBI	-10,176	0,713	10,176	-0,713	10,888	5,444	0,184	4,732	-4,732	2,056	0,486	3,325	-2915,754
HF/3-21g													
4NPBI	-9,143	0,508	9,143	-0,508	9,651	4,826	0,207	4,318	-4,318	1,931	0,518	8,571	-21909,680
4APBI	-7,485	2,568	7,485	-2,568	10,053	5,027	0,199	2,458	-2,458	0,601	1,663	1,165	-17894,129
2NPBI	-9,442	1,506	9,442	-1,506	10,948	5,474	0,183	3,968	-3,968	1,438	0,695	5,566	-21909,660
2APBI	-8,609	3,072	8,609	-3,072	11,681	5,841	0,171	2,769	-2,769	0,656	1,524	3,304	-17893,970
PBI	-8,607	2,313	8,607	-2,313	10,920	5,460	0,183	3,147	-3,147	0,907	1,102	1,341	-16404,854
4CPBI	-8,796	2,030	8,796	-2,030	10,826	5,413	0,185	3,383	-3,383	1,057	0,946	5,007	-28833,117
4MPBI	-9,120	3,045	9,120	-3,045	12,165	6,082	0,164	3,037	-3,037	0,758	1,319	1,831	-17460,878
4BPBI	-8,664	2,083	8,664	-2,083	10,747	5,373	0,186	3,291	-3,291	1,008	0,992	3,817	-86052,729
HF/6-31g													
4NPBI	-8,831	0,336	8,831	-0,336	9,167	4,584	0,218	4,247	-4,247	1,968	0,508	9,396	-22024,616
4APBI	-7,350	2,192	7,350	-2,192	9,541	4,771	0,210	2,579	-2,579	0,697	1,435	13,029	-17986,720
2NPBI	-8,817	1,732	8,817	-1,732	10,549	5,274	0,190	3,542	-3,542	1,189	0,841	6,228	-22024,133
2APBI	-8,042	2,633	8,042	-2,633	10,675	5,337	0,187	2,704	-2,704	0,685	1,460	2,063	-17987,498
PBI	-8,373	2,377	8,373	-2,377	10,750	5,375	0,186	2,998	-2,998	0,836	1,196	1,445	-16490,898
4CPBI	-8,522	2,162	8,522	-2,162	10,684	5,342	0,187	3,180	-3,180	0,947	1,056	5,078	-28978,014
4MPBI	-8,241	2,455	8,241	-2,455	10,696	5,348	0,187	2,893	-2,893	0,782	1,278	0,783	-17552,044
4BPBI	-8,469	2,164	8,469	-2,164	10,633	5,316	0,188	3,152	-3,152	0,935	1,070	4,524	-86402,741
HF/6-31++g													
4NPBI	-8,942	-0,031	8,942	0,031	8,911	4,456	0,224	4,486	-4,486	2,259	0,443	9,556	-22025,334
4APBI	-7,956	1,127	7,956	-1,127	9,083	4,541	0,220	3,414	-3,414	1,283	0,779	1,791	-17988,068
2NPBI	-8,769	1,250	8,769	-1,250	10,018	5,009	0,200	3,760	-3,760	1,411	0,709	0,050	-5258,296
2APBI	-8,199	1,136	8,199	-1,136	9,335	4,667	0,214	3,532	-3,532	1,336	0,748	2,086	-17988,013
PBI	-8,522	1,118	8,522	-1,118	9,640	4,820	0,207	3,702	-3,702	1,422	0,703	1,465	-16491,364
4CPBI	-8,639	1,136	8,639	-1,136	9,775	4,888	0,205	3,751	-3,751	1,440	0,695	4,977	-28978,465
4MPBI	-8,384	1,137	8,384	-1,137	9,521	4,760	0,210	3,623	-3,623	1,379	0,725	0,731	-17552,497
4BPBI	-6,477	-2,044	6,477	2,044	4,433	2,217	0,451	4,260	-4,260	4,094	0,244	4,225	-86560,265
HF/Lanl2dz													
4NPBI	-9,464	0,170	9,464	-0,170	9,633	4,817	0,208	4,647	-4,647	2,242	0,446	10,080	-22027,451
4APBI	-7,719	2,243	7,719	-2,243	9,962	4,981	0,201	2,738	-2,738	0,753	1,329	0,565	-17989,775
2NPBI	-9,598	0,627	9,598	-0,627	10,225	5,112	0,196	4,486	-4,486	1,968	0,508	6,389	-22027,085
2APBI	-7,820	1,992	7,820	-1,992	9,812	4,906	0,204	2,914	-2,914	0,865	1,156	5,161	-17988,423
PBI	-8,518	2,053	8,518	-2,053	10,571	5,285	0,189	3,232	-3,232	0,988	1,012	1,495	-16492,373
4CPBI	-8,636	1,915	8,636	-1,915	10,551	5,276	0,190	3,360	-3,360	1,070	0,934	5,144	-16876,701
4MPBI	-8,384	2,170	8,384	-2,170	10,554	5,277	0,190	3,107	-3,107	0,915	1,093	0,752	-17553,614
4BPBI	-8,585	1,891	8,585	-1,891	10,475	5,238	0,191	3,347	-3,347	1,069	0,935	4,679	-16828,383

Chemical hardness [20,22-24] is the resistance to electron cloud polarization or deformation of chemical species.Chemical hardness is a very important parameter that is investigating a reactivity of molecules in both experimental and theoretical chemistry.Global softness, ΔE, and chemical hardness are related to each other.In the light of information of Koopman's theory [23], both chemical hardness value and global softness value are taken place HOMO and LUMO energy value. If the hard molecules have high HOMO-LUMO energy gap, this molecule is not a good corrosion inhibitor. This molecule can't very easy give electron of HOMO to metal. From the light of

the result given in table 1, 2, 3, and 4, we can see the corrosion inhibitor ranking of chemical hardness value as: 4NPBI > 4APBI > 2NPBI > 2APBI > 4BPBI > 4MPBI > 4CPBI > PBI in B3lyp method with sdd and lanl2dz.

The electronegativity value of molecules is a parameter that helps to compare the reactivity of molecules. Value of this parameter is given to predict the electron transfer between the metal and inhibitor. The molecule that has high electronegativity value, this molecule is hardly given the valances electron. Because these electrons are attracted more than other molecules by the nucleus. According to Sanderson's electronegativity equalization [24-25], we are work out the value of electrons transferred from corrosion inhibitor molecule by the following equation:

$$\Delta N_{max} = \frac{\chi_M - \chi_{inh}}{2(\eta_M + \eta_{inh})}$$

(10)

where χ_M and χ_{inh} are electronegativity of metal and inhibitor molecule, respectively. η_M and η_{inh} are chemical hardness of inhibitor molecule and metal, respectively.

In all parameter, we can write that 4NPBI is the best corrosion inhibitor more than another molecule. The activities of these molecules may be calculated using different programs [26-27].Moreover, a similar ranking was given in the experimental study managed by Dutta and his co-worker [1].

4. CONCLUSION

Benzimidazole derivatives were performed at Hartree-Fock and b3lyp with different basis set to investigate the corrosion inhibition activity.The result of quantum chemical parameters was shown that the corrosion inhibition efficiency ranking of these molecules can be givenas: 4NPBI > 4APBI > 2NPBI > 2APBI > 4BPBI > 4MPBI > 4CPBI > PBI in B3lyp method with sdd and lanl2dz.From the light of the result given in table 1, 2, 3, and 4, these molecules are very important towards rational design new benzimidazole derivate as corrosion inhibitor.

REFERENCES

[1] Dutta, A., Saha, S. K., Adhikari, U., Banerjee, P., & Sukul, D.,Effect of substitution on corrosion inhibition properties of 2-(substituted phenyl) benzimidazole derivatives on mild steel in 1 M HCl solution: a combined experimental and theoretical approach. Corrosion Science, 123 (2017) 256-266.

[2] Dennington R.D., Keith T.A., Millam J.M., GaussView 5.0, 2009. Wallingford CT.

[3] Frisch M.J., Trucks G.W., Schlegel H.B., Scuseria G.E., Robb M.A., Cheseman J.R., Scalmani G., Barone V., Mennucci B., Petersson G.A., Nakatsuji H., Caricato H., Li X., Hratchian H.P., Izmaylov A.F., Bloino J., Zheng G., Sonnerberg J.L., Hada M., Ehara M., Toyota K., Fukuda R., Hasegawa J., Ishida M., Nakajima T., Honda Y., Kitao O., Nakai H., Vreven T., Montgomery J.A., Peralta J.E., Ogliaro F., Bearpark M., Heyd J.J., Brothers E., Kudin K.N., Staroverov V.N., Kobayashi R., Normand J., Raghavachari K., Rendell A., Burant J.C., Iyengar S.S., Tomasi J., Cossi M., Nega R., Millam J.M., Klene M., Knox J.E., Cross J.B., Bakken V., Adamo C., Jaramillo J., Gomperts R., Stratmann R.E., Yazyev O., Austin A.J., Cammi R., Pomelli C., Ochterski J.W., Martin R.L., Morokuma K., Zakrzewski V.G., Voth G.A., Salvador P., Dannenberg J.J., Daprich S., Daniels A.D., Farkas A., Foreaman J.B., Ortiz JV, Cioslowski J, Fox DJ. Gaussian 09, Revision D.01, Gaussian, Inc., WallingfordCT, 2009.

[4] Frisch M.J., Trucks G.W., Schlegel H.B., Scuseria G.E., Robb M.A., Cheseman J.R., Scalmani G., Barone V., Mennucci B., Petersson G.A., Nakatsuji H., Caricato H., Li X., Hratchian H.P., Izmaylov A.F., Bloino J., Zheng G., Sonnerberg J.L., Hada M., Ehara M., Toyota K., Fukuda R., Hasegawa J., Ishida M., Nakajima T., Honda Y., Kitao O., Nakai H., Vreven T., Montgomery J.A., Peralta J.E., Ogliaro F., Bearpark M., Heyd J.J., Brothers E., Kudin K.N., Staroverov V.N., Kobayashi R., Normand J., Raghavachari K., Rendell A., Burant J.C., Iyengar S.S., Tomasi J., Cossi M., Nega R., Millam J.M., Klene M., Knox J.E., Cross J.B., Bakken V., Adamo C., Jaramillo J., Gomperts R., Stratmann R.E., Yazyev O., Austin A.J., Cammi R., Pomelli C., Ochterski J.W., Martin R.L., Morokuma K., Zakrzewski V.G., Voth G.A., Salvador P., Dannenberg J.J., Daprich S., Daniels A.D., Farkas A., Foreaman J.B., Ortiz JV, Cioslowski J, Fox DJ., Gaussian

09, Revision A.02, Gaussian, Inc., Wallingford CT, 2009.

[5] Becke A.D., A new mixing of Hatree-Fock and local density-functional theories, J.Chem. Phys., 98 (1993) 1372-1377.

[6] WibergK.B.. Basis set effects on calculated geometries: 6-311++G** vs. aug-cc-pVDZ. J. Comput. Chem., 25 (2004) 1342–1346.

[7] Beck A.D., Density-functional thermochemistry III. the role of exact, Exchange The Journal of Chemical Physics 98 (1993) 5648-5652.

[8] Lee C., Yang W., Parr R.G., Development of the Colle-Savletti correlation-energy formula into a functional of the electron density, Physical Review, 37 (1988) 785-789.

[9] Kaya S., Banerjee P., Saha S. K., Tüzün B., Kaya C., Theoretical evaluation of some benzotriazole and phospono derivatives as aluminum corrosion inhibitors: DFT and molecular dynamics simulation approaches, RSC Advances, 6 (2016) 74550-74559.

[10] Kaya S., Tüzün B., Kaya C., Obot I.B., Determination of corrosion inhibition effects of amino acids: Quantum chemical and molecular dynamic simulation study, Journal of the Taiwan Institute of Chemical Engineers, 58 (2016) 528-553.

[11] Kaya S., Kaya C., Guo L., Kandemirli F., Tüzün B., Uğurlu İ., Madkour L.H., Saraçoğlu M., Quantum chemical and molecular dynamics simulation studies on inhibition performances of some thiazole and thiadiazole derivatives against corrosion of iron. Journal of Molecular Liquids, 219 (2016) 497-504.

[12] Tüzün B., Selectivity of Salicylaldoxime and its Derivatives, Journal of New Results in Science, 3-5 (2014) 67-85.

[13] E. Kose, A. Atac, F. Bardak, the structural and spectroscopic investigation of 2-chloro-3-methylquinoline by DFT method and UV–Vis, NMR and vibrational spectral techniques combined with molecular docking analysis. Journal of Molecular Structure, 1163 (2018) 147-160.

[14] Z. Zhang, W. Li, W. Zhang, X. Huang, L. Ruan, L. Wu, Experimental, quantum chemical calculations and molecular dynamics (MD) simulation studies of methionine and valine as corrosion inhibitors on carbon steel in phase change materials (PCMs) solution. Journal of Molecular Liquids, 272 (2018) 528-538.

[15] R. Nabah, F. Benhiba, Y. Ramli, M. Ouakki, M. Cherkaoui, H. Oudda, A. Zarrouk, Corrosion Inhibition Study of 5, 5-diphenylimidazolidine-2, 4-dione for Mild Steel Corrosion in 1 M HCl Solution: Experimental, Theoretical Computational and Monte Carlo Simulations Studies. Analytical & Bioanalytical Electrochemistry, 10-10 (2018) 1375-1398.

[16] M. Alam, D.U. Lee, Synthesis, spectroscopic and computational studies of 2-(thiophen-2-yl)-2, 3-dihydro-1H-perimidine: An enzymes inhibition study. Computational Biology and Chemistry, 64 (2016) 185-201.

[17] Madkour L.H., Elshamy I.H. Experimental and computational studies on the inhibition performances of benzimidazole and its derivatives for the corrosion of copper in nitric acid. Int. J. Ind. Chem., 7 (2016) 195–221.

[18] Pearson RG. Chemical hardness: applications from molecules to solids. Germany: Wiley-VCH: Weinheim; 1997.

[19] Obot I.B., Obi-Egbedi N.O., Eselo A.O., Anticorrosion potential of 2-mesityl-1H-imidazol[4,5-][1,10]-phenanthroline on mild steel in sulfuric acid solution; experimental and theoretical study, Ind. Eng. Chem. Res., 50 (2011) 2098-2110.

[20] Makov G., Chemical hardness in density functional theoryJ. Phys. Chem., 99 (1995) 9337-9339

[21] Pearson R.G., Hard and soft acids and bases, J. Am. Chem. Soc., 85 (1963) 3533-3539

[22] Pearson R.G., Hard and soft acids and bases, HSAB, part 1: Fundamental principles, J. Chem. Educ., 45 (1968) 581-587.

[23] Koopmans T., Ordering of wave functions and eigen-energies to the individual electrons of an atom, Physica, 1 (1993) 104-113.

[24] Sanderson R.T., Chemical bond and bond energy, Academic Press, New York 1976.

[25] Sanderson R.T., Electronegativities in inorganic chemistry, J. Chem. Educ., 31 (1954) 2-7.

[26] Özalp A.; Yavuz S. Ç.; Sabancı N.; Çopur F.; Kökbudak Z.; Sarıpınar E. 4D-QSAR investigation and pharmacophore identification of pyrrolo[2,1-c][1,4] benzodiazepines using electron conformational-genetic algorithm method. SAR and QSAR in Environmental Research, 27-4 (2016) 317-342.

[27] Tüzün B., Yavuz S. Ç., Sarıpınar E., 4D-QSAR analysis and pharmacophore modeling: propoxy methylphenyl oxasiazole derivatives by electron conformatitional-genetic algorithm method, Journal of Physical and Theoretical Chemistry of Islamic Azad University of Iran, 14-2 (2018) 149-164.

Humic Acid/Quercetin Coated Magnetic Fe₃O₄ Nanoparticles For Adsorptive Removal of Cu²⁺ and Ni²⁺

Fatoş Ayça ÖZDEMİR OLGUN[1,*] , *Birsen DEMİRATA ÖZTÜRK*[1]

¹ *Istanbul Technical University, Department of Chemistry, Istanbul TURKEY*

Abstract. Removal of metals and heavy metals from industrial wastewaters is a serious concern for water systems. In this study, environmentally friendly natural polymer coated, cost-effective, easy to operate HA/QR magnetic nanoparticles were suggested to overcome this problem, for the first time in literature. Fe₃O₄ magnetic nanoparticles were synthesized with co-precipitation technique and a core-shell structure was obtained with humic acid sodium salt (HA) solution. At the second step of the procedure, synthesized magnetic nanoparticles were coated with quercetin solution. Scanning electron microscopy (SEM), X-Ray diffraction (XRD) and particle size analyses were performed to enlighten and characterize the structure. The newly synthesized nanoparticles were used for the batch-wise adsorption of copper and nickel metals, successfully. Maximum adsorption capacities were calculated as 14.61 mg/g for copper and 28.30 mg/g using 0.03 g adsorbents, at pH=7. Adsorption isotherms were evaluated and it was concluded that adsorption equilibrium fitted to both Langmuir and Freundlich isotherm models, better correlated with Langmuir isotherm model.

Keywords: Humic acid, Fe₃O₄ magnetic nanoparticles, metal removal, adsorption isotherm.

Hümik Asit/Kuversetin Kaplı Fe₃O₄ Manyetik Nanoparçacıklar ile Cu²⁺ ve Ni²⁺ Metallerinin Adsorpsiyon Yöntemiyle Giderimi

Özet. Endüstriyel atıksulardan metal ya da ağır metal giderilmesi su sistemleri için ciddi sorunlar oluşturabilmektedir. Bu çalışmada, bu sorunları tamamen gidermek ya da en aza indirmek için bir çözüm yolu önerildi. Çalışma kapsamında, literatürde ilk kez, doğal polimer olan hümik asit sodyum tuzu ile kaplı olduğu için çevre dostu olan, ekonomik ve manyetik özelliğinden dolayı kullanım kolaylığı sağlayan HA/QR manyetik nanoparçacıklar sentezlendi. Sentez prosedürünün birinci adımında birlikte çöktürme tekniğiyle Fe₃O₄ manyetik nanoparçacıklar sentezlendi ve çekirdek-kabuk (core-shell) modeline uygun olarak hümik asit çözeltisi ile muamele edilerek kaplandı. İkinci adımda ise, sentezlenen partiküller kuersetin çözeltisi ile kaplandı. Oluşan nano yapının aydınlatılması için SEM (Taramalı Elektron Mikroskopisi), X ışını kırınımı (XRD) ve parçacık boyut analizi teknikleri kullanıldı. Yeni sentezlenen parçacıklar Cu²⁺ ve Ni²⁺ metallerinin giderimi için adsorban olarak başarıyla kullanıldı. pH=7 değerinde 0.03 g adsorban kullanılarak hesaplanan adsorpsiyon kapasiteleri Cu²⁺ için 14.61 mg/g; Ni²⁺ için 28.30 mg/g olarak hesaplandı. Adsorpsiyon izotermleri değerlendirildiğinde, elde edilen adsorpsiyon izoterm eğrisinin hem Langmuir hem Freundlich modeline uyum sağladığı gözlemlendi.

Anahtar Kelimeler: Hümik asit, Fe3O4 manyetik nanoparçacıklar, metal giderimi, adsorpsiyon izotermi.

1. INTRODUCTION

As industry develops, waste products become a concerning issue. Heavy metals found in discharged sewage show toxic impacts with their resistance against biodegradation and ability of accumulation. Livers, nervous system, female and male reproductive system, connective tissues such as hair, skin and nails are the first places affected by metal accumulation [1]. Heavy metals such as nickel and copper are used in many production plants and often met in their aqueous effluents [2]. The ability of metal ions to accumulate in plant, fish and mammals tissues poses a serious threat to human health through bioaccumulation in the food chain [3,4]. Several methods for heavy metal removal are found in literature such as; ultrafiltration, ion exchange chromatography, precipitation [5-7], reverse osmosis [8], nanofiltration [9]. Among these methods, adsorption process is commonly used with its flexible operation and high-quality effluent production [10]. In recent years, advances in nanoscale sciences, offer more effective adsorbents with many specific physiochemical properties. Nanosized ferric oxides are preferable for adsorption process with their low-cost, eco-friendly and easy-to-operate magnetic properties [11]. Moreover surface modified Fe_3O_4 nanoparticles are more efficient as their surface functionality improved. Humic acid, which is the end product of microbiological decomposition of plants and animals, is a good candidate for a surface coating material to provide a long-time stability. Quercetin, a naturally derived polyhydroxy (3, 3', 4', 5,7-OH) compound that can form complexes with metal cations, also prevents oxidation and growth of bacteria in water.

In this study Fe_3O_4 magnetic nanoparticles were synthesized and coated with humic acid sodium salt and quercetin, respectively. HA/QR magnetic nanoparticles were installed in copper and nickel adsorption process in batch-wise. Essential adsorption parameters as pH, adsorbent dose and incubation time [12] were investigated for the optimization. Adsorption equilibrium data were studied for a better understanding of adsorption process.

2. MATERIALS AND METHOD

All the reagents used in the experiments were of analytical grade. Iron (III) chloride hexahydrate (98%, Merck), ammonium iron (II) sulfate hexahydrate, humic acid sodium salt (Sigma Aldrich), quercetin (Sigma Aldrich), hydrochloric acid (Merck), ammonia solution (25%, Merck), NaOH (Merck), standard solutions of Cu^{2+} and Ni^{2+} for atomic absorption spectrometry were used during experiments. Ultrapure water was used when required, at each step of procedure.

Gec Avery analytical balance was used to weigh the chemicals at solid phase. Magnetic stirrer (VWR) and ultrasonic bath (Bandelin Sonorex) were used at solution preparation step. MSE Mistral 2000 centrifuge was used at synthesis of nanoparticles. The batch adsorption experiments were performed with the aid of shaker (Edmund Bühler 7400 Tubingen). For pH measurements Knick pH-meter was used. JOEL JSM-7600F Scanning Electron Microscope and FEI Quanta 250 FEG was used for the SEM analysis. Ultrapure water used during all experiments were obtained by Millipore Direct Q-UV 3. Varian 280-FS atomic absorption spectrometer was used for the determination of metals. Air/ acetylene gas mixture was used for atomization step. Hollow cathode lamps peculiar to each metal were installed during analyses. The absorbance measurements were performed at 324.8nm for Cu and 232.0 nm for Ni^{2+}.

2.1. Preparation of Solutions

1000 mgL^{-1} humic acid sodium salt solution was prepared by dissolving 0.25 g humic acid sodium salt in 0.25 L ultrapure water. 1×10^{-2} M quercetin solution in ethyl alcohol medium and 1% (w/v) SDS solution were prepared to use at nanoparticle synthesis step. Standard solutions of Cu^{2+} and Ni^{2+} were prepared by dilution of 1000 mgL^{-1} stock solutions to be in the required concentration level.

2.2. Synthesis of Nanoparticles

15.25 g $FeCl_3.6H_2O$ and 10.50 g $NH_4FeSO_4.6H_2O$ were weighed and mixed and dissolved in 250.0 mL of ultrapure water. 5.0 mL of 25% ammonia

solution was added to 50.0 mL portion of the mixture mentioned above. After the addition 25% ammonia solution, precipitation occurred. In order to modify and improve the surface properties of nanoparticles, 25.0 mL of humic acid sodium salt solution and 25.0 mL 1×10^{-2} M quercetin solutions were added, respectively. The synthesis procedure occurred at 90 ^{0}C for 1h. After humic acid quercetin magnetic nanoparticles were obtained, the particles were washed twice with ultrapure water to remove the excess impurities. Finally, synthesized nanoparticles were filtered and allowed to dry at 50^0C for 12 h in drying oven. Dried particles were pestled in mortar to powder form.

2.3. Characterization of Synthesized Nano particles

As the HA/QR magnetic nanoparticles were synthesized for the first time in the literature, the structure should be understood. For this reason, SEM, XRD and particle size analyses were performed.

Qualitative analyses of synthesized nanoparticles were performed by X-ray diffractometer. The analyte was stabilized between the positions of 0^0C-90^0C 2θ angles. By using the software of the instrument the collected data was transferred to graphic art for a better understanding.

Particle sizes of nanoparticles were measured by size analyzer. Synthesized nanoparticles were added to the reservoir of the instrument after ultrapure water. At pre-analysis step the particles were exposed to ultrasonic waves for 5 minutes allowing the particles dispersed in water. The results were achieved by taking the refractive index values of water and analyte into consideration. The reservoir was discharged and washed regularly after each measurement.

2.4. Adsorption Studies

Batch adsorption method was used to investigate the adsorption characteristics of the synthesized HA/QR magnetic nanoparticles. Batch-wise experiments were performed in glass flasks with a reaction volume of 50.0 mL at room temperature (25.0±0.1 ^{0}C). Metal solutions with desired concentration values were shaken with

synthesized QR/HA magnetic nanoparticles. The particles were easily collected from the slurry with a regular magnet, leaving a clear effluent behind. Prior to the adsorption isotherm studies, adsorption parameters such as; pH, contact time and amount of adsorbent were optimized. For pH optimization, 2 mgL^{-1} Cu^{2+} and 3 mgL^{-1} Ni^{2+} solutions were prepared by adequate dilutions of their stock solutions. The pH values of the prepared solutions were adjusted with 0.1 M NaOH and 0.1 M HCl solutions. 0.01g of HA/QR magnetic nanoparticles were let to contact with freshly prepared solutions at varying pH values for 10 min at 400 rpm. The effect of contact time was investigated by allowing to contact 0.1 g of HA/QR magnetic nanoparticles with 2 mgL^{-1} Cu^{2+} and 3 mgL^{-1} Ni^{2+} solutions at pH=7, for increasing periods of time. Finally, the amount of HA/QR magnetic nanoparticles to be used in adsorption experiments were optimized at pH=7, using 2 mgL^{-1} Cu^{2+} and 3 mgL^{-1} Ni^{2+} solutions. After these optimizations, the adjusted adsorption parameters were employed in subsequent experiments.

The concentration of the residual metal in solution was determined by fast-sequential flame atomic absorption spectrometer. Solutions not to contain metal were used as blank. The difference between the initial and final concentration values was calculated in order to obtain adsorbed metal concentration and adsorbent capacity.

3. RESULTS AND DISCUSSIONS
3.1. Characterization of HA/QR magnetic nanoparticles

The scanning electron microscopy (SEM) images of the synthesized nanoparticles was displayed in Figure 1. Lighter and brighter shades of the image belong to the coated nanoparticles. The particles exhibit a uniform size of approximately 40 nm.
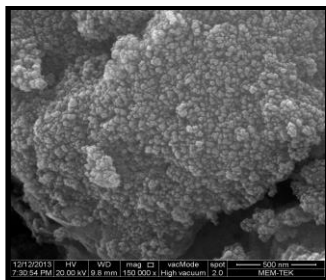
Figure 1. SEM micrograph of HA/QR magnetic nanoparticles.

The crystal structures of the samples were analyzed using X-ray diffraction method. The samples were analyzed between 0^0C- 90^0C at diffraction angle of 2θ. In Figure 2, the first image belongs to the core-shell magnetic nanoparticle before coating and the second image belongs to the magnetite coated with QR and HA solutions. As we compare the scan images, it can be concluded that five peaks existing in both of the images are the characteristics of the magnetic nanoparticle. The sharpest peak of number 2 only existing in the first scan image is thought to be as a result of coating procedure.
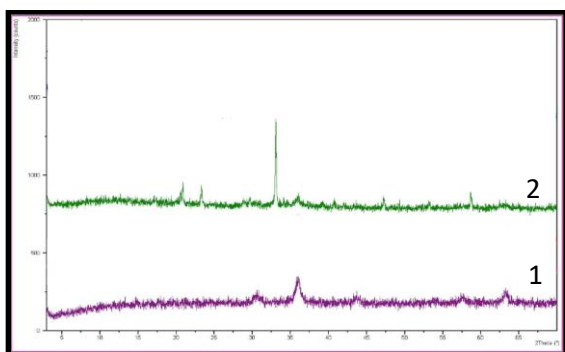
Figure 2. XRD patterns of 1)Magnetic nanoparticle 2) HA/QR coated magnetic nanoparticle.
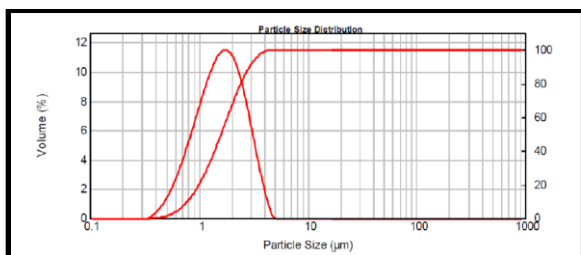
Figure 3. Particle size distribution of HA/QR magnetic nanoparticles measured by particle size analyzer.

Particle size analyzer was used to measure the particle size distribution and surface area of the synthesized HA/QR magnetic nanoparticles. Figure 3 shows the distribution of the synthesized nanoparticles after ultrasonicated in water for complete dispersion.

Using Figure 3, the average particle diameter was measured at 1.59 μm with a surface area of 4.42 m^2/g. The values measured by particle size analyzer are higher than those measured by SEM, as the attractive forces between dry particles are so great. This can be explained by the dispersion of HA/QR magnetic nanoparticles in water and subsequent sonication. Besides, the average particle diameter and surface area of uncoated magnetic nanoparticles were also measured. As the results were compared, the average particle diameter decreased after coating (17.53 μm for uncoated; 1.59 μm for HA/QR coated) when the surface area increased (0.97 m^2/g for uncoated; 4.42 μm for coated).

3.2. Adsorption of Cu^{2+} and Ni^{2+} with HA/QR Magnetic Nanoparticles

3.2.1. Optimization of Adsorption Parameters

In order to explain the adsorption characteristics of the synthesized nanoparticles, some basic parameters such as pH, contact time should be examined. One parameter at a time procedure was employed during optimization experiments.

For the optimization of pH value, 2 mgL^{-1} Cu^{2+} and 3 mgL^{-1} Ni^{2+} solutions were prepared. 0.01g of synthesized nanoparticles were shaken with freshly prepared solutions at varying pH values for 10 min at 400rpm. Removal percentages were calculated using the equation given below.

$$\%\text{Removal}= [(c_i-c_f)/ c_i] \times 100 \qquad (1)$$
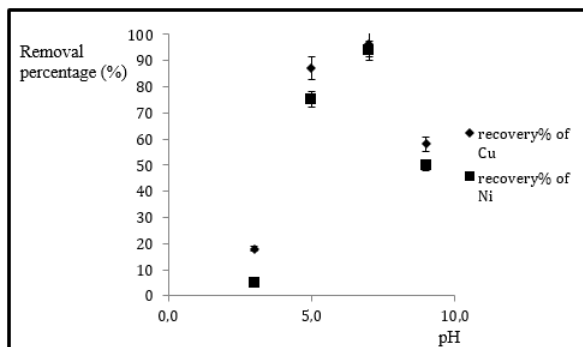
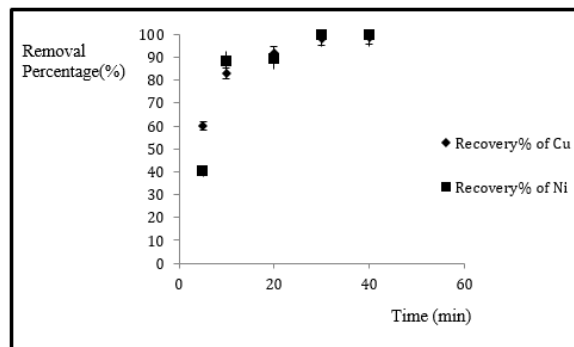**Figure 4.** Effect of pH on Cu^{2+} and Ni^{2+} adsorption by HA/QR magnetic nanoparticles.

As it is seen from the graph above, maximum removal percentage of both metal is at pH=7. The most effective amount of adsorbent to be used in further adsorption experiments must be decided. For this purpose, 0.01g ; 0.02g, 0.03g and 0.04g of adsorbent were weighed. 2 $mgL^{-1}Cu^{2+}$ and 4 $mgL^{-1}Ni^{2+}$ solutions were prepared by accurate dilution of stock solutions. The particles were allowed to contact with the metal solutions for 10 min with a rotation rate of 400 rpm. in batch system. It is obviously seen from Figure 5 that, the maximum metal removal was obtained with 0.03 mg of nanoparticle. Afterward, the more particles used in batch system do not make a remarkable change in removal percentage.
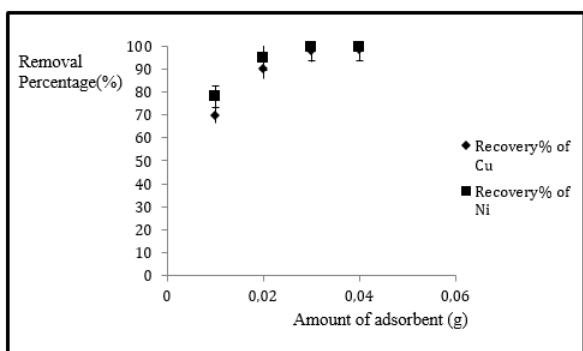
Figure 5. Effect of amount of HA/QR magnetite on Cu^{2+} and Ni^{2+} adsorption by HA/QR magnetite nanoparticles.

Using the adsorption parameters optimized in previous experiments (0.03 g of magnetite; pH=7), removal percentages of metals were calculated at increasing periods of time. For 30 min of contact time, it was observed that removal

percentage reaches its maximum (99.5% for Ni; 98.0% for Cu^{2+}) and stays stable as time passes.

Figure 6. Effect of batch-wise contact time on Cu^{2+} and Ni^{2+} adsorption by HA/QR magnetite nanoparticle adsorption.

3.2.2. Adsorption Isotherms

Adsorption equilibrium must be well investigated and analyzed in order to have an opinion about the design of adsorption process. In this study Langmuir and Freundlich isotherm models were used to define the adsorption of metal ions by synthesized magnetite nanoparticles. For a more realistic approach to adsorption phenomena as a function of concentration, the concentration range was selected in geometric order (between 0.01-0.08 mgL^{-1}). Langmuir isotherm that represents the simplest theoretical model for monolayer adsorption is in the following form;

$$1/q_e = 1/Q_{max} + 1/ Q_{max} K_L \quad (2)$$

where;

$$q_e = [(c_i-c_f)/V] /m \quad (3)$$

In the equation given above; Q_{max} (Maximum adsorption capacity of the adsorbent) and K_L (Equilibrium constant represented in Gibbs free energy change of adsorption) represent the Langmuir adsorption parameters. The concentration terms c_i and c_f represent the initial and equilibrium concentrations of metals in solution, V represents the volume of solution and m stands for the amount of magnetite used during batch experiments.
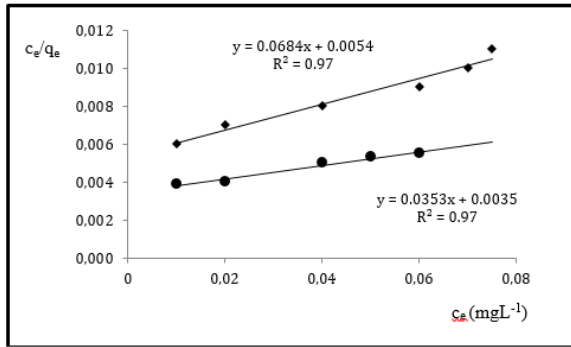
Figure 7. Linearized Langmuir isotherm graphs of Cu^{2+} and Ni^{2+} adsorption by HA/QR magnetite nanoparticles.
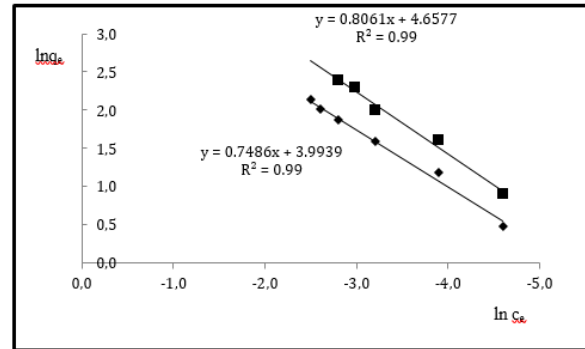
The Freundlich isotherm equation is as follows;

$$q_e = K_f \times C_e^{1/n} \quad (4)$$

may be linearized with a similar algorithm;

$$\ln q_e = K_f + 1/n \; C_e \quad (5)$$

Freundlich equation represents a line with a slope of $1/n$ and an intercept of K_f corresponding to the adsorption capacity and intensity, respectively[13].

Figure 8. Linearized Freundlich isotherm graphs of Cu^{2+} and Ni^{2+} adsorption by HA/QR magnetic nanoparticles.

Freundlich equilibrium constants were determined from the graph drawn $\ln q_e$ versus $\ln c_e$. In linearized Freundlich equation, n indicates the degree of nonlinearity[14]. When n is smaller than 1, adsorption process is assumed to be chemical phenomena; n value between 1 and 10 (which was calculated as 1.33 for Cu^{2+} and 1.24 for Ni^{2+}) adsorption is physical and good when considered [14-16].

Taking the advantage of the linearized isotherms shown in Figure 7 and Figure 8, Langmuir and Freundlich isotherm equations for batch adsorption of Cu^{2+} and Ni^{2+} metals were obtained and summarized in Table 1.

Table 1. Parameters of Linearized Langmuir and Freundlich Isotherm.

Metal Adsorbed	Parameters obtained by Langmuir Isotherm				Parameters obtained by Freundlich Isotherm			
	Langmuir Isotherm Equation	Slope $^{-1}$ of Linearized Langmuir Isotherm	K_L	R^2	Freundlich Isotherm Equation	Slope $^{-1}$ of Linearized Freundlich Isotherm	K_f	R^2
Cu^{2+}	$Q_e = \frac{6.84 \times 10^{-2}}{(1+ 0.079)\,c_e}$	$Q_{max}=14.61$ mg/g adsorbent	12.67 L/mg	0.97	$Q_e = 3.99 c_e^{0.75}$	n= 1.33 mg/g adsorbent	3.99 L/mg	0.99
Ni^{2+}	$Q_e = \frac{3.53 \times 10^{-2}}{(1+ 10.09)\,c_e}$	$Q_{max}=28.30$ mg/g adsorbent	10.08 L/mg	0.97	$Q_e = 4.65 c_e^{0.81}$	n=1.24 mg/g adsorbent	4.66 L/mg	0.98

When Table 1 is inspected carefully, one can see that the adsorption models of Cu^{2+} and Ni^{2+} metals by HA/QR magnetic nanoparticles are well fitted to both isotherm models (when the regression coefficients were taken into consideration). However, the overall data are slightly better fitted to Langmuir isotherm for both metals.

4. CONCLUSION

In this study, HA/QR magnetite nanoparticles were synthesized for the adsorption of metals from aqueous systems, as the first time in literature. Fe_3O_4 magnetic nanoparticles are rather preferred for their easy to operate properties at batch-wise adsorption process. The particles were

coated with humic acid, for longtime usage. Considering economical issues in large-scaled installation of newly synthesized nano-composite materials, long-term usage is another issue to be evaluated. In previous studies found in literature, the nanoparticles were coated with many different polymers to be more stable[17-18]. However, humic acid, which is a natural, biodegradable and environmentally friendly polymer was installed for the first time within this assay. At the second step of coating, quercetin was chosen as the hydroxyls on the molecule may enhance the adsorption capability of HA/magnetite nanoparticles. And more than it was presumed, the particle size analyses showed an obvious decrease from 17.53 μm to 1.59 μm at diameters. The synthesized particles were measured to have a diameter of 40 nm. and used in adsorption experiments. Batch-wise adsorption process was easily operated with HA/QR magnetite nanoparticles taking the advantage of their magnetic behaviors. The adsorption isotherm of Cu^{2+} and Ni^{2+} -as model metals- fitted both to Langmuir and Freundlich isotherm models. The optimal removal of metals occurred contacting metal solutions with only 0.03 g adsorbent at pH=7, for 30 min. There are many studies found in literature introducing new composite materials for the adsorption of metals [19- 21] This study shows superiority to others, obtaining high removal percentages (99.5% for Ni; 98.0% for Cu^{2+}) at neutral pH values by installing a biodegradable and eco-friendly material as adsorbent.

ACKNOWLEDGMENTS

REFERENCES

[1] Ashish B., Naeti K., Himanshu K., Copper toxicity: A comprehensive study, Res. J. Recent Sci., 2 (2013) 58-67.

[2] Azouaou N., Sadaoi Z., Mokaddem H., Removal of cadmium from aqueous solution by adsorption on vegetable wastes, O. J. App., 24 (2008) 4638-4643.

[3] Liu D., Li Z., Zhu Y., Kumar R., Recycled chitosan nanofibril as an effective Cu(II), Pb(II), and Cd(II) ionic chelating agent: adsorption and desorption performance, Carbohydr. Polym., 111 (2014) 469-476.

[4] Liphadzi M. S., Kirkham M. B., Preperation of magnetic carboxy methyl chitosan nanoparticles for adsorption of heavy metal ions, S. Afr. J. Bot., 72 (2006) 391-397.

[5] Chang Y. C., Chen D. H., Preparation and adsorption properties of monodisperse chitosan-bound Fe_3O_4 magnetic nanoparticles for removal of Cu(II) ions, J. Colloid Interface Sci., 283 (2005) 446- 451.

[6] Savage N., Diallo M. S., Nanomaterials and water purification: opportunities and challenges, J. Nanopart. Res., 7 (2005) 331-342.

[7] Erdem E., Karapınar N., Donat R., The removal of heavy metal cations by natural zeolites, J. Colloid Interface Sci., 284 (2004) 309-314.

[8] Shatialam A. M., Al-Harthy A., Al-Zawhry A., Feed water pretreatment in RO systems in middleeast, Desalination, 150 (2002) 235-245.

[9] Murthy Z. V. P., Chaudhai L. B., Seperation of binary heavy metals from aqueous solutions by nanofiltration and characterization of the membrane using Spiegler-Kedem model, Chem. Eng. J., 150 (2008) 181-187.

[10] Fenglian F., Wang Q., Removal of heavy metal ions from wastewaters, a review, J. Environ. Manage., 92 (2011) 407-418.

[11] Yean S., Cong L., Yavuz J. T., Yu M., Effect of material particle size on adsorption and desorption of arsenite and arsenate, J. Mater. Res. Technol., 20 (2005) 3255-3264.

[12] Shen Y. F., Tang J., Me Z. N., Wang Y. D., Ren Y., Zou L., Preperation and application of Fe_3O_4 nanoparticles for wastewater purification, Sep. Purif. Technol., 68 (2009) 312-319.

[13] Ozdemir F. A., Demirata B., Apak R., Adsorptive removal of methylene blue from simulated dyeing wastewater with melamine-formaldehyde-urea resin, J. Appl. Polym. Sci.,

112 (2009) 3442-3448.

[14] Ajenifuja E., Ajao J. A. , Ajayi E. O. B., Adsorption isotherm studies of Cu (II) and Co (II) in high concentration Aaqueous solutions on photocatalytically modified diatomaceous ceramic adsorbents, Appl. Water Sci., 7 (2017) 3793-3801.

[15] McKay G., Otterburn M. S., Sweenay A. G., The removal of color from effluent using various adsorbents, Water Res., 14 (1980) 15-20.

[16] Ozer A., Pirincci H. B., The adsorption of Cd(II) ions on sulphuric acid-treated wheat Bran, J. Hazard. Mater., 137 (2006) 849-855.

[17] Du S., Lou Y., Zou F., Li X., Li D., Polydopamine-coated Fe_3O_4 nanoparticles as synergistic redox mediators for catalytic reduction of azo dyes, Nano, (2017)12-21.

[18] Wan Q., Huang Q., Liu M., Xu D., Huang H., Zhang Z., Wei Y., Aggregation-induced emission active luminescent polymeric nanoparticles: Non-covalent fabrication methodologies and biomedical applications, Applied Materials Today, 9 (2017) 145-160.

[19] Ghaemi N., A new approach to copper ion removal from water by polymeric nanocomposite membrane embedded with γ-alumina nanoparticles, Appl. Surf. Sci., 364 (2016) 221-228.

[20] Fouldagar M., Behestiti M., Salozyan H., Single and binary adsortpon of nickel and copper from aqueous solution by γ-alumina nanoparticle equilibrium and kinetic modelling, J. Mol. Liq., 211 (2015) 1060-1073.

[21] Thanh D. N., Novak P., Vejpravova J., Vu H. N., Lederer J., Munshi T., Removal of copper and nickel from water using nanocomposite of magnetic hydroxyapatite nanorods, J. Magn. Magn. Mater., 456 (2018) 451-460.

Hydrogen generation by *Rhodobacter sphaeroides* O.U.001 using pretreated waste barley

Gökhan KARS[1]* , Ayça EMSEN[2]

[1]*Necmettin Erbakan University, Faculty of Science, Molecular Biology and Genetics Department, Konya, TURKEY*

[2]*Selçuk University, Faculty of Medicine, Department of Pediatric Immunology, Konya, TURKEY*

Abstract. In the present study, valorization of waste barley by producing hydrogen (H_2) and 5-aminolevulinic acid (5-ALA) using *Rhodobacter sphaeroides* O.U.001 was aimed. Firstly, 3 % (w/v) waste barley hydrolysate was prepared by treating 3 g of powdered waste barley with H_2SO_4 in a total volume of 100 mL mixture and then autoclaving this mixture at 121 ºC for 30 min. Upon generation of fermentable simple sugars by pretreatment and analytical examination of the hydrolysate in terms of ammonium content, element composition and light transmittance, various types of growth media containing various concentrations of sugar (5 - 6 - 7 - 8 g/L) were prepared. The cells were cultivated in these media under photo-heterotrophic conditions which favor H_2 and 5-ALA generations. pH changes, growth, H_2 production and 5-ALA generation were monitored in the media. The results showed that all the media prepared from 3 % (w/v) waste barley hydrolysate sustained the cell growth appreciably. The highest OD value (OD_{660}: 1.71) was attained when using 8 g/L sugar. Furthermore, biological H_2 evolution was seen in each bioreactor. In particular, the highest hydrogen accumulation (0.29 L H_2/L) was achieved in 6 g/L sugar-containing medium. However, 5-ALA was not detected in any of the media. To conclude, considerable cell growth and biological hydrogen production was achieved using 3 % (w/v) waste barley hydrolysate under the conditions tested but there was no detectable 5-ALA generation.

*Keywords***:** Biological hydrogen, 5-aminolevulinic acid, *Rhodobacter sphaeroides,* waste barley.

Ön işlemden geçirilmiş atık arpa kullanarak *Rhodobacter sphaeroides* O.U.001 ile hidrojen üretimi

Özet. Bu çalışmada, *Rhodobacter sphaeroides* O.U.001 kullanılarak hidrojen (H_2) ve 5-aminolevulinik asitin (5-ALA) üretilmesi ile atık arpa'nın değerlendirilmesi hedeflendi. Öncelikle, 3 g toz halindeki atık arpa H_2SO_4 ile karıştırılarak 100 mL toplam hacimde karışım elde edildi ve sonrasında bu karışım 121 °C' de 30 dakika boyunca otoklavlanarak % 3'lük (a/h) atık arpa hidrolizatı hazırlandı. Fermente edilebilir basit şekerlerin önişlem ile ortaya çıkarılması ve hidrolizatın amonyum muhtevası, element bileşimi ve ışık geçirgenliği bakımından analitik olarak incelenmesinin ardından, farklı şeker konsantrasyonlarına sahip çeşitli büyüme ortamları (5 - 6 - 7 - 8 g/L) hazırlandı. Hücreler bu ortamlarda H_2 ve 5-ALA yapımlarını destekleyen foto-heterotrofik koşullar altında çoğaltıldı. Ortamlardaki pH değişimleri, büyüme, hidrojen üretimi ve 5-ALA üretimi izlendi. Sonuçlar, % 3'lük (a/h) atık arpa hidrolizatından hazırlanan tüm ortamların hücre büyümesini önemli ölçüde desteklediğini gösterdi. En yüksek OD değeri (OD_{660}: 1.71) 8 g/L şeker kullanılarak elde edildi. Ayrıca, her bir biyoreaktörde biyolojik H_2 üretimi gözlemlendi. Özellikle, en yüksek hidrojen birikimi

(0.29 L H$_2$/L), 6 g/L şeker içeren ortamda elde edildi. Ancak, hiçbir ortamda 5-ALA tespit edilmedi. Sonuç olarak, test edilen koşullar altında % 3'lük (a/h) atık arpa hidrolizatı kullanılarak önemli miktarda hücre büyümesi ve biyolojik hidrojen üretimi sağlandı, ancak saptanabilir miktarda 5-ALA üretimi yoktu.

***Anahtar Kelimeler*:** Biyolojik hidrojen, 5-aminolevulinik asit, *Rhodobacter sphaeroides,* atık arpa.

1. INTRODUCTION

Currently, there is increasing energy demand in the world and it is primarily supplied from the fossil-based fuels. However, it is generally recognized that the use of fossil-based fuels has negative impacts on environment. Sulfur oxides (SO$_x$), carbon monoxide (CO), nitrogen oxides (NO$_x$), and carbon dioxide (CO$_2$) are the main pollutant gasses emitted as a consequence of the use of fossil-based fuels [1, 2]. For instance, while CO$_x$ emissions cause greenhouse effect, SO$_x$ and NO$_x$ emissions lead to acid rains. Moreover, these emissions might also cause serious health problems. Therefore, alternative and clean energy sources need to be developed to alleviate these environmental and health problems.

There are several alternative renewable and sustainable sources like geothermal energy, hydropower, solar energy, wind energy and biomass energy. Hydrogen can be considered as an energy carrier since there is no hydrogen source in nature but rather it is produced through biological and non-biological means [3, 4]. If hydrogen could be produced in a renewable and sustainable way, it can partially meet the world's energy demand. In our country, there are also sustainable and renewable sources for the generation of hydrogen and considerable amount of electricity could potentially be generated from the hydrogen produced [5]. Moreover, when used as a fuel, it does not produce any toxic chemicals. Biological hydrogen production occurs mainly by dark fermentation and photo-biological processes. In some processes, a combination of two was realized and called as two-stage hydrogen production method [6]. In biological hydrogen processes, the microorganisms take role and the responsible enzymes are hydrogenases and nitrogenases [7]. There are various types of these enzymes in microorganism [7, 8]. Photo fermentative hydrogen production is mainly performed by purple non-sulfur (PNS) bacteria. The representatives of them could be listed as *Rhodopseudomonas palustris* (*Rps. palustris*), *Rhodospirullum rubrum* (*Rsp. rubrum*), *Rhodobacter capsulatus* (*R. capsulatus*) and *Rhodobacter sphaeroides* (*R. sphaeroides*). The responsible enzyme in PNS bacteria is nitrogenase and hydrogen production is an inherent character of the enzyme [7]. Under anoxic conditions and nitrogen limitations, the hydrogen is evolved at the expense of ATP using light energy [7, 8]. PNS bacteria are versatile in that they can grow under different physiological conditions and they can produce various valuable chemicals like 5-aminolevulinic acid (5-ALA), poly-hydroxy butyrate (PHB) and vitamin B$_{12}$ [9-13]. In a recently developed concept called biorefinery, more than one product (more than one fuel or fuel and value-added chemicals) is produced in the same bioprocess [12-16]. The logic behind this approach is to maximize the benefit from the biomass. In this way, cost-efficient bioprocesses will be developed. Kars et al. [12] reported the production of 5-ALA (23 mM) and hydrogen (1.01 L H$_2$/L) in the same bioprocess from sugar beet molasses.

In biological hydrogen production processes, different types of carbon sources could be used [17]. Industrial waste streams, agricultural and forestry lignocellulosic materials could effectively be used as substrate in the biological hydrogen production processes [12, 13, 17]. The selected carbon source should be cheap, found in large amount, easily fermentable by microbe and non-toxic to the cells. The case of using lignocellulosic biomass, the pretreatment of biomass is of great importance to produce useable simple sugars and organic acid. The basic pretreatment methods may be listed as mechanical, biological, chemical and physical techniques [18]. The motivation behind

this study is to find cheap and accessible feedstock for biological hydrogen and 5-ALA productions. For this purpose, waste barley was chosen, pretreated and used as carbon source. In the present study, 3 % (w/v) waste barley hydrolysate was obtained. The growth media containing various quantities of sugar (5, 6, 7 and 8 g/L) were prepared using this hydrolysate. And, the formation of hydrogen and 5-ALA by *R. sphaeroides* O.U.001 in the bioreactors was monitored.

2. MATERIAL AND METHOD

2.1. The microbial strain and its cultivation conditions

In this study, *R. sphaeroides* O.U. 001 whose DSM number is 5864 was chosen for both photo-biological hydrogen and 5-aminolevulinic acid productions. The medium used for the general maintenance of this bacterium was Biebl and Pfennig minimal medium [19]. One liter of minimal medium includes K_2HPO_4 (0.5 g), $MgSO_4 \cdot 7H_2O$ (0.2 g), DL-Malic acid (2 g), Na·Glutamate·H_2O (0.37 g), NaCl (0.4 g), $CaCl_2 \cdot 2H_2O$ (0.05 g), trace element solution (0.05 mL from 20X stock solution), $FeSO_4$ (1 mL from 2X stock solution) and vitamin solution (0.05 mL from 20X stock solution). One liter of 20X concentrated stock trace element solution includes $Na_2MoO_4 \cdot 2H_2O$ (40 mg), $NiCl_2 \cdot 6H_2O$ (20 mg), $CuCl_2 \cdot 2H_2O$ (20 mg), $CoCl_2 \cdot 6H_2O$ (200 mg), H_3BO_3 (60 mg), $MnCl_2 \cdot 4H_2O$ (100 mg), $ZnCl_2$ (70 mg) and HCl (0.675 mL from % 37). 2X concentrated $FeSO_4$ solution was prepared by adding 0.02 g of $FeSO_4$ into 10 mL of dH_2O. One liter of 20X concentrated vitamin stock solution contains Thiamin (500 mg), Nicotinic acid or Niacin (500 mg) and Biotin (15 mg). The trace elements solution and $FeSO_4$ solution were sterilized by autoclave while vitamin element solution was sterilized through micro filtration since vitamins were heat-labile. The trace elements solution and $FeSO_4$ solution were separately autoclaved and added to the basal media to prevent possible precipitations such as calcium phosphate precipitate. When solid media were needed, 1.5 % agar was used in minimal media. 55 ml glass bottles were used as bioreactors. The incubation temperature for the cultures was 29 ºC and the light energy was provided by incandescent lamps (100 W). The intensity of the light bioreactor surface was circa 775 ± 25 lux. For general purposes, either aerobic or anaerobic condition was used.

2.2. Pretreatment of waste barley

R. sphaeroides is a versatile bacterium since it has the capability to utilize a wide variety of substrate as a source carbon [12, 20, 21]. However, the waste materials and lignocellulosic biomass should be pretreated to decompose the complex biomaterials into its monomers so that it could be utilized by the PNS bacteria. In the present study, waste barley was utilized as carbon source so that a cost-efficient hydrogen production process could be achieved. Firstly, 3 g of powdered waste barley was dissolved in certain amount of dH_2O after which the pH of the concoction was set to 3 by adding H_2SO_4 before completion of the final volume to 100 mL. The acid hydrolysis of waste barley (3 % w/v) was performed by autoclaving this mixture at 121 ºC for 30 min. To remove the insoluble components, the suspension was spun at high speed (9418 x g) for about 10 min and then the liquid part above the pellet was filtered (Whatman Grade No: 41) to eliminate remaining insoluble particles. After completion of pretreatment process, the neutralization of the hydrolysate to pH: 7 was done by NaOH addition. Upon neutralization, color of the hydrolysate became darker and some precipitates were formed. These were removed by re-centrifugation of the hydrolysate at 9418 x g for 10 min and then the amounts of total sugar, organic acids, total phenol and ammonium were analyzed.

2.3. Analytical methods

Many factors like a type of carbon source [20], presence of ammonia [22] and existence of necessary elements such as molybdenum and iron [23] influence biological hydrogen production. These factors exert their effect either directly on the nitrogenase enzyme or on the selected PNS bacterium. For this reason, waste barley

hydrolysate was analyzed in terms of these aspects in order to prepare a suitable medium for biological hydrogen production. Acid-phenol spectrophotometric method applied for the determination of total simple sugar concentration of the waste barley hydrolysate [24]. First of all, a series of samples with pre-determined sugar concentrations were prepared and then their spectrophotometric measurements were done. After the graph was drawn, the unknown sample concentration was calculated by interpolation. After knowing the sugar content of the hydrolysate, 4 different culture media were prepared so as to contain 5, 6, 7 and 8 g/L sugar concentration from % 3 waste barley hydrolysate. The total ammonium ion content of the hydrolysate was found out with the use of an ammonium test kit (Norateks, Turkey). For this, 1 mL of barley hydrolysate was put into a glass tube and mixed with 4 mL of dH_2O. Then, 2 drops from the NH_4-1 solution and 4 drops from the NH_4-2 solution were put onto the diluted hydrolysate in order. The suspension was held at room temperature (RT) for 5 min. for the formation of color. Finally, the color of the suspension was matched with the identical reference color on the manual to find out the ammonium concentration. The elements found in the 3 % barley hydrolysate were identified by inductively coupled plasma mass spectrometry (ICP-MS, Perkin Elmer elanDRC-e, USA).

The produced hydrogen was collected in graduated glass tubes by water displacement method and purity of collected gas was measured by gas chromatography (GC, Agilent, 6890N). Supelco carboxen 1010 column and thermal conductivity detector were used in GC. The argon gas was utilized as carrier gas and the flow rate was set to 22.3 mL/min. The temperature of detector, injector and oven was adjusted to 170 ºC, 160 ºC and 140 ºC, respectively. The amount of 5-ALA in media was quantified by a spectrophotometric technique [25] and explained in detail in [26]. Similar to other methods mentioned above, 8 samples having pre-determined amounts of 5-ALA were first made and then their spectrophotometric measurements

were performed. Afterward, the quantities of 5-ALA in the studied samples were calculated from the graph.

2.4. Media preparation and culture conditions

For the hydrogen and 5-ALA productions, four kinds of medium with various sugar concentrations (5, 6, 7 and 8 g/L) were made from % 3 barley hydrolysate. The contents of the 5-ALA and hydrogen production media were same as the contents of the Biebl and Pfennig minimal medium except that glutamate, malate and NaCl were not added since barley hydrolysate contains sufficient amount of carbon, nitrogen and NaCl sources. After putting all the ingredients of the medium into the bioreactors (55 mL glass bottles), the pH of the bioreactors was adjusted to 7 and sterilized by autoclaving. The sterile vitamin solution was then added into the bioreactors aseptically. The cultures were made anoxic by flushing with argon gas for 3 min. The photoheterotrophic growth mode was provided by incubating the cultures under an illumination of 100 W incandescent lamps providing circa 775 ± 25 lux on the surface of the bioreactors.

2.5. Statistical analysis

In this study, pH, growth and hydrogen production experiments were performed in duplicate. Standard deviations from the mean values were calculated. The error bars were inserted into the graphs.

3. RESULTS AND DISCUSSION
3.1. The analytical features of barley hydrolysate

The quality of barley used in this study is low and it cannot be used as human food. The percentages of fat, protein, and starch in barley were determined previously and found to be 2.45 ± 0.035, 11.19 ± 0.46 and 37.5 ± 0.49, respectively [26]. Especially, the starch content of the waste barley was almost half of the normal quality barley. In the present study, hydrolysate was prepared as 3 % (w/v) as opposed to our previous study where 9 % (w/v) hydrolysate was used [13]. Therefore, the content of 3 % (w/v) hydrolysate

was different from 9 % (w/v) hydrolysate. After acid hydrolysis, the sugar content of the 3 % (w/v) barley hydrolysate was found to be 11.58 g/L. Then, 4 different media with various concentrations of sugars (5, 6, 7 and 8 g/L) were made from this barley hydrolysate. PNS bacteria could efficiently use glucose [27] and sucrose [12] for the generation of hydrogen. Moreover, type and composition of substrate were told to strongly influence both the hydrogen production and biomass accumulation [28]. In the present study, considerable amount of simple sugars was obtained after acid hydrolysis of waste barley. Therefore, it was shown that 3 % (w/v) waste barley hydrolysate could be used as carbon source for *R. sphaeroides* O.U.001.

The ammonium content of the medium utilized for the generation of hydrogen influence the hydrogen generation ability of microorganism significantly since above 2 mM concentration, the ammonium suppresses the nitrogenase enzyme resulting in the cessation of hydrogen evolution [22]. The ammonium content of the 3 % (w/v) hydrolysate was found to be 0.139 mM which is below suppressive concentrations. After preparation of the media with different concentrations of sugar, the ammonium concentrations turned into 0.060 mM, 0.072 mM, 0.084 mM, 0.096 mM in the media having initial sugar quantities of 5, 6, 7 and 8 g/L culture, respectively. These ammonium concentrations are far below the suppressive concentration; therefore, these media are suitable for the production of biological hydrogen.

It is known that elements such as iron and molybdenum are needed for the proper functioning of Mo-nitrogenase enzyme and hydrogen generation is mediated by this enzyme in *R. sphaeroides* O.U.001 [23]. In this context, the element composition of the 3 % (w/v) barley hydrolysate was found out by ICP-MS. In the hydrolysate, the analyzed elements and their quantities were (mg/L); B (0.449), Cr (0.052), Mn (0.4), Fe (0.153), Co (-), Ni (-), Cu (0.05), Zn (0.227), Mo (0.003), Al (0.041), Ca (13.405), Mg (33.7), Na (>800), K (>400). Since sufficient

amount of Na is present in the hydrolysate, NaCl was not added to the media. The other significant factor which also affects the hydrogen generation capability of microorganisms is the presence of high amount of phenols in the waste materials which are going to be used as substrate. For instance, the quantity of whole phenol (1.9 g/L) was found to be at the toxic level in olive oil mill wastewater (OOMW) [29]. Therefore, OOMW could only be used as substrate after dilution with water for hydrogen production [30]. Total amount of phenolic substances in barley was found as 10.13 mg GAE/g barley in our previous study [13]. The overall amount of phenol in the hydrolysate is significantly lower than that in OOMW. After preparation of the media by diluting with dH₂O, the quantity of phenols becomes much lower in the culture media. Therefore, waste barley hydrolysate is also suitable for hydrogen production in terms of total phenol content.

Another important parameter which should be considered for bio-hydrogen generation processes is the availability of sufficient energy in the form of light to the cells in the bioreactor. According to Uyar et al. [31], invisible light (infrared) at which the bacteriochlorophyll a shows the maximal absorption is more effective than the visible light where the carotenoid has absorption maxima. In this context, in order to see the transmittance of the barley hydrolysate, the % transmittance of barley hydrolysate at infrared region (800 and 860 nm) was measured and it was found that the % transmittance of each media was above % 90. The suitability of the barley hydrolysate in terms of light transmittance was also demonstrated.

3.2. pH changes and bacterial growth

Several media with various sugar concentrations (5, 6, 7, and 8 g/L) were made from % 3 barley hydrolysate. After 10 % inoculation into 45 mL fresh media, 50 mL of cultures were obtained and incubated under light. pH and the turbidity of the cultures were followed at certain time intervals (Figure 1 and Figure 2). pH of the medium is mainly dependent on the type carbon source and it

is crucial for biological hydrogen production [32]. Even though the preliminary pH values of the cultures were adjusted to 7, they dropped to 6.6 after inoculation of bacteria and incubation for about 32 h (Figure 1). Then, the pH of the cultures rose back to 7 after 23 h incubation. The pH of the media remained almost the same at around 7 until 175. h. Afterward, a slight increase (pH: 7.23) occurred in especially 5 g/L sugar-containing medium. There were no significant changes in the pH of the other media. As a general tendency, the pH of the media followed a similar pattern and did not change significantly during the bioprocess. This result shows that the buffering capacity of phosphate buffer used in this study is high enough to resist the pH changes due to the metabolism of microorganisms. This uniform pH provides the bacteria with a suitable environment for hydrogen production.
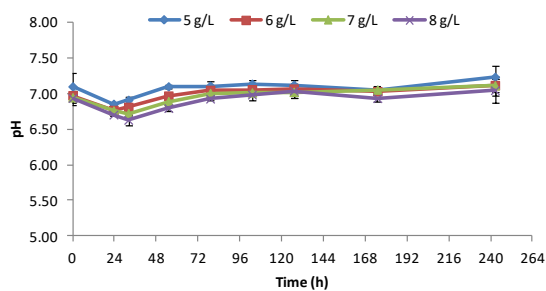
Figure 1. The pH changes during the growth of *R. sphaeroides* O.U.001. The experiment was done duplicate and standard deviations were added.

One of the aims is to find the optimal amount while using biomass as carbon source for bacterial growth. The use of high amount of hydrolysate might be toxic to the cells due to the ingredients of hydrolysate such as phenols or it might prevent light transmission in the bioreactor. Furthermore, the lower concentrations might be inadequate to sustain cell growth. For this reason, the growth of *R. sphaeroides* O.U.001 in the cultures having various concentrations of sugar was followed by taking spectrophotometric measurements periodically. In this way, the suitability of selected concentrations (5, 6, 7 and 8 g/L) in order to sustain bacterial growth was assessed. In the present study, relatively lower quantities of waste barley hydrolysate were used when compared to

our previous study [13]. As shown in Figure 2, comparable OD values were attained when compared to our previous studies [13, 23]. A rapid rise in turbidity continued until 79. h. and then the rate of increase slowed down. The maximal OD values were 1.25, 1.44, 1.50 and 1.71 in the media having initial sugar concentrations of 5, 6, 7 and 8 g/L cultures, respectively. The higher the sugar concentration, the higher the OD value (Figure 2). Demiriz et al. [33] used acetate as carbon source to produce hydrogen and poly-β-hydroxybutyric acid by *R. capsulatus* DSM 1710 and they obtained similar results such that total biomass of bacteria in the bioreactor increased in parallel to raising the amount of acetate from 10 mM to 65 mM. In our previous study which was done with 9 % waste barley hydrolysate, the highest OD value (OD$_{660}$: 1.78) was attained when using the sugar concentration at the highest concentration (11 g/L sugar) [13]. When compared to previous findings, it can be asserted that the media prepared with 3 % waste barley hydrolysate is also sufficient to sustain *R. sphaeroides* O.U.001 and the growth pattern showed the similar tendency when the literature findings were taken into account.
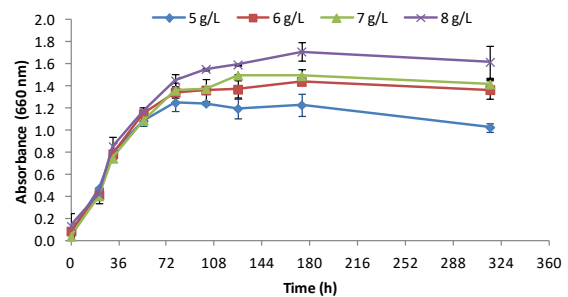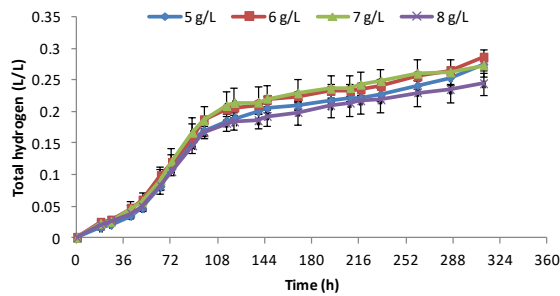

Figure 2. Growth of *R. sphaeroides* O.U.001 in media prepared by using % 3 waste barley hydrolysate. The experiment was done duplicate and standard deviations were added.

3.3. Hydrogen and 5-ALA formation by *R. sphaeroides* O.U.001

The color and content of the hydrolysate might also affect the hydrogen generation capability of *R. sphaeroides* O.U.001. For this reason, four different growth media (5, 6, 7 and 8 g/L) were prepared from 3 % (w/v) waste barley hydrolysate

and tested for hydrogen production. The total culture volume was 50 mL and the gas evolved from the culture was accumulated in the graduated glass tubes. Then, analysis of the collected gas was performed by GC. The percentage (%) of H_2 in collected gas was 81.5, 87.3, 89.2 and 80.4 in 5, 6, 7 and 8 g/L sugar-containing cultures, respectively. Remaining gas was identified as CO_2 and air. In Figure 3, total hydrogen accumulation of hydrogen was illustrated. In the preparation of graph, the pure hydrogen amounts were used not the total gas accumulated. Almost the same amount of hydrogen was accumulated in the bioreactors. The highest hydrogen accumulation (0.29 L H_2/L) was achieved in the bioreactor having initial sugar quantity of 6 g/L culture. 0.27 L H_2/L, 0.27 L H_2/L and 0.24 L H_2/L were produced in the bioreactors having initial sugar quantity of 5, 7 and 8 g/L culture, respectively. These results are comparable to our previous findings where 0.4 L H_2/L was produced in medium having an initial sugar quantity of 11 g/L culture (Table 1). The interesting point was that the hydrogen accumulation in higher amount of sugar-containing culture (8 g/L) was always lower than that in lower amount of sugar-containing media as opposed to the case observed in growth of bacteria in Figure 2. That is, increase in sugar concentration did not result in an increase in hydrogen production. This may be owing to the darker color of this medium which can prevent the access of light into the bioreactor because 34.48 mL of hydrolysate was used for the preparation of 8 g/L sugar-containing medium while 30.17, 25.86 and 21.55 mL of hydrolysate were used to make the media having sugar quantities of 7, 6 and 5 g/L culture, respectively. Moreover, the ammonium and other potentially toxic chemicals like phenols are also found in higher amount in the medium having the highest initial sugar amount of 8 g/L culture and this might negatively affect the hydrogen generation capability of the cells in the bioreactor. Light limitation and presence of ammonium seem to be harmless to the cells in terms of their growth but they are thought to be highly effective and restrictive for hydrogen production capability of bacterium. Similar findings were reported by Feng et al. [34] in their

study where hydrogen was produced using corn straw (CS) hydrolysate by *R. capsulatus* JL1. They observed that hydrogen yield increased from 1402 to 2966 mL/L when the amount of CS hydrolysate was increased from 7.0 g CS/L culture to 16.4 g CS/L culture. However, further increase in substrate concentration resulted in a decrease in hydrogen yield due to the inhibition effect of high amount of hydrolysate. In the current study, 5-ALA production was also investigated; however, 5-ALA was not detected in any of the media. Several possible explanations could be done for situation. Firstly, this may be due to the low sugar concentrations in the media. Probably, the substrate sustained the cells for hydrogen generation and growth but it was not sufficient to produce excess reducing equivalents for the generation of 5-ALA. In our earlier work where higher amounts of substrates were used, 67.4 µM of 5-ALA was obtained in the bioreactor having an initial sugar concentration of 9 g/L culture [13]. In previous study, levulinic acid and vitamin B_{12} additions were done to promote 5-ALA synthesis but in the present study such additions were not done. This might be reason why 5-ALA was not produced. Finally, the previous study was performed using 9 % (w/v) waste barley hydrolysate but the present study was done using 3 % (w/v) waste barley hydrolysate. The two hydrolysates were different in terms of sugar content, ammonium content, element composition, phenol content and transparency. In example, color of the media prepared from 3 % (w/v) waste barley hydrolysate was much darker than the color of the media prepared from 9 % (w/v) waste barley hydrolysate. These differences might also be the reason why 5-ALA could not be produced in the present study.

Figure 3. Total accumulation of hydrogen in media prepared by using 3 % waste barley hydrolysate. The experiment was done duplicate and standard deviations were added.

Table 1. Hydrogen generation by *R. sphaeroides* O.U.001 from different carbon sources.

Initial carbon source	H_2 production (L H_2/L culture)	Ref.
Simple sugars, 6 g/L	0.29	This work
Simple sugars, 11 g/L	0.40	[13]
Acetate, 30 mM	0.21	[21]
Malate, 15 mM	1.97	[21]
Sucrose, 28 g/L	1.01	[12]

4. CONSCLUSION

Different type of feedstock has been used as carbon source for biological hydrogen production for many years. The important point in these studies is to find the optimum concentration of the substrate. While inadequacy of carbon source leads to lower hydrogen yield, the excess of it leads to inhibition of hydrogen production and cell growth. In this context, in the current study, pH variations, growth of *R. sphaeroides* O.U.001, biological hydrogen production and 5-aminolevulinic acid production were investigated using waste barley as carbon source. Relatively low concentrations of sugar-containing media (5, 6, 7 and 8 g/L) were prepared from 3 % (w/v) waste barley hydrolysate. The pH of the cultures did not change significantly during the bioprocess. The initial amounts of sugars in the bioreactors sufficiently sustained cell growth. Similarly, comparable amounts of hydrogen were obtained. However, the 5-ALA was not detected in any of the media. To conclude, 3 % waste barley hydrolysate could also be used for the cultivation and hydrogen generation by *R. sphaeroides* O.U.001.

REFERENCES

[1] Aydın H. and İlkılıç C., Air pollution, pollutant emissions and harmfull effects, Journal of Engineering and Technology, 1 (2017) 8-15.

[2] Sharma B. S., Jain S., Khirwadkar P., Kulkarni S., The effects of air pollution on the environment and human health, Indian Journal of Research in Pharmacy and Biotechnology, 1-3 (2013) 391-396.

[3] Das D. and Veziroğlu T. N., Hydrogen production by biological processes: a survey of literature, Int. J. Hydrogen Energy, 26 (2001) 13-28.

[4] Reverberi A. P., Klemeš J. J., Varbanov P. S., Fabiano B., A review on hydrogen production from hydrogen sulphide by chemical and photochemical methods, Journal of Cleaner Production, 136 (2016) 72-80.

[5] Kars G., Biyokütleden biyohidrojen üretimi, Tarım Makinaları Bilimi Dergisi, 8-3 (2012) 265-270.

[6] Özgür E., Mars A. E., Peksel B., Louwerse A., Yücel M., Gündüz U., Claassen P. A. M., Eroğlu İ., Biohydrogen production from beet molasses by sequential dark and photofermentation, Int. J. Hydrogen Energy, 35 (2010) 511-517.

[7] Kars G. and Gündüz U., Towards a super H_2 producer: improvements in photofermentative biohydrogen production by genetic manipulations. Int.

J. Hydrogen Energy, 35 (2010) 6646-6656.

[8] Kars G., Improvement of biohydrogen production by genetic manipulations in *Rhodobacter sphaeroides* O.U.001. Biotechnology, Ph.D. Thesis, Middle East Technical University; October 2008.

[9] Sasaki K., Tanaka T., Nishizawa Y., Hayashi M., Production of a herbicide, 5-aminolevulinic acid, by *Rhodobacter sphaeroides* using the effluent waste from an anaerobic digestor, Appl. Microbiol. Biot., 32 (1990) 727-731.

[10] Sasaki K., Watanabe M., Suda Y., Ishizuka A., Noparatnaraporn N., Applications Of Photosynthetic Bacteria For Medical Fields, J. Biosci. Bioeng., 10-5 (2005) 481-488.

[11] Yiğit D. Ö., Gündüz U., Türker L., Yücel M., Eroğlu İ., Identification of by-products in hydrogen producing bacteria; *Rhodobacter sphaeroides* O.U.001 grown in the waste water of a sugar refinery. J. Biotechnol., 70 (1999) 125-131.

[12] Kars G. and Alparslan Ü., Valorization of sugar beet molasses for the production of biohydrogen and 5-aminolevulinic acid by *Rhodobacter sphaeroides* O.U.001 in a biorefinery concept. Int. J. Hydrogen Energy, 38 (2013) 14488-14494.

[13] Kars G. and Ceylan A., Biohydrogen and 5-aminolevulinic acid production from waste barley by *Rhodobacter sphaeroides* O.U.001 in a biorefinery concept. Int. J. Hydrogen Energy, 38 (2013) 5573-5579.

[14] Westermann P., Jorgensen B., Lange L., Ahring B. K., Christensen C. H., Maximizing renewable hydrogen production from biomass in a bio/catalytic refinery, Int. J. Hydrogen Energy, 32 (2007) 4135-4141.

[15] Rabelo S. C., Carrere H., Maciel Filho R., Costa A. C., Production of bioethanol, methane and heat from sugarcane bagasse in a biorefinery concept. Bioresour. Technol., 102 (2011) 7887-7895.

[16] Béligon V., Noblecourt A., Christophe G., Lebert A., Larroche C., Fontanille P., Proof of concept for biorefinery approach aiming at two bioenergy production compartments, hydrogen and biodiesel, coupled by an external membrane, Biofuels, 9-2 (2018) 163-174.

[17] Argun H., Gökfiliz P., Karapinar I., Biohydrogen Production Potential of Different Biomass Sources. In: Singh A., and Rathore D. (Eds.). Biohydrogen Production: Sustainability of Current Technology and Future Perspective. New Delhi: Springer, 2017; pp 11-48.

[18] Reginatto V. and Antônio R. V., Fermentative hydrogen production from agroindustrial lignocellulosic substrates, Brazilian Journal of Microbiology, 46-2 (2018) 323-335.

[19] Biebl H. and Pfennig N., Isolation of members of the family *Rhodosprillaceae*. In: Starr M. P., Stolp H., Trüper H., Balows A., Schlegel H. G. (Eds). The prokaryotes. New York: Springer-Verlag, 1981; pp 267-273.

[20] Koku H., Eroğlu İ., Gündüz U., Yücel M., Türker L., Aspects of the metabolism of hydrogen production by *Rhodobacter sphaeroides*, Int. J. Hydrogen Energy, 27 (2003) 1315-1329.

[21] Kars G., Gündüz U., Yücel M., Rakhely G., Kovacs K. L., Eroğlu İ., Evaluation of hydrogen production by *Rhodobacter sphaeroides* O.U.001 and its *hupSL* deficient mutant using acetate and malate as carbon sources, Int. J. Hydrogen Energy, 34 (2009) 2184-2190.

[22] Akköse S., Gündüz U., Yücel M., Eroğlu İ., Effects of ammonium ion, acetate, and aerobic conditions on hydrogen production and expression levels of nitrogenase genes in *Rhodobacter*

sphaeroides O.U.001, Int. J. Hydrogen Energy, 34 (2009) 8818-8827.

[23] Kars G., Gündüz U., Yücel M., Türker L., Eroğlu İ., Hydrogen production and transcriptional analysis of *nifD*, *nifK* and *hupS* genes in *Rhodobacter sphaeroides* O.U.001 grown in media with different concentrations of molybdenum and iron, Int. J. Hydrogen Energy, 31 (2006) 1536-1544.

[24] Dubois M., Gilles K. A., Hamilton J. K., Rebers P. A., Smith F., Colorimetric method for determination of sugars and related substances, Anal. Chem., 8 (1956) 350-366.

[25] Mauzerall D. and Granick S., the occurrence and determination of d-aminolevulinic acid and porphobilinogen in urine, J. Biol. Chem., 219 (1956) 435-446.

[26] Ceylan A., Biohydrogen and aminolevulinic acid production from waste barley by *Rhodobacter sphaeroides*. Biology, MSc Thesis, Selçuk University; July 2012.

[27] Liu T., Zhu L., Wei W., Zhou Z., Function of glucose catabolic pathways in hydrogen production from glucose in *Rhodobacter sphaeroides*, Int. J. Hydrogen Energy, 6016-39 (2014) 4215-4221.

[28] Pattanamanee W., Chisti Y., Choorit W., Photofermentive hydrogen production by *Rhodobacter sphaeroides* S10 using mixed organic carbon: effects of the mixture composition, Applied Energy, 157 (2015) 245-254.

[29] Yeşilada Ö., Şık S., Şam M., Treatment of olive oil mill wastewater with fungi, Turk. J. Biol., 23 (1999) 231-240.

[30] Eroğlu E., Gündüz U., Yücel M., Türker L., Eroğlu İ., Photobiological hydrogen production by using olive mill wastewater as a sole substrate source, Int. J. Hydrogen Energy, 29 (2004) 163-171.

[31] Uyar B., Eroğlu İ., Yücel M., Gündüz U., Türker L., Effect of light intensity, wavelength and illumination protocol on hydrogen production in photobioreactors. Int. J. Hydrogen Energy, 32-18 (2007) 4670-4677.

[32] Laurinavichene T. and Tsygankov A., Inoculum density and buffer capacity are crucial for H_2 photoproduction from acetate by purple bacteria, Int. J. Hydrogen Energy, 43-41 (2018) 18873-18882.

[33] Demiriz B.O., Kars G., Yücel M., Eroğlu İ., Gündüz U., Hydrogen and poly-β-hydroxybutyric acid production at various acetate concentrations using *Rhodobacter capsulatus* DSM 1710. Int. J. Hydrogen Energy, 44-32 (2019) 17269-17277.

[34] Feng J., Yang H., Guo L., The photosynthetic hydrogen production performance of a newly isolated *Rhodobacter capsulatus* JL1 with various carbon sources. Int. J. Hydrogen Energy, 43-30 (2018) 13860-13868.

The Effect of Piranha and Silane Modifications on Boron Nitride Nanosheets (BNNSs) Thin Film Formation

Duygu KURU[1] (iD) *, Alev AKPINAR BORAZAN[1,*]* (iD) *, Nuran AY[2]* (iD)

[1]*Bilecik Seyh Edebali University, Faculty of Engineering, Department of Chemical Engineering, Bilecik, TURKEY*

[2] *Eskisehir Technical University, Faculty of Engineering, Department of Material Science and Engineering, Eskisehir, TURKEY*

Abstract. In this study, the aim was to increase the adhesion between the two phases (glass substrate and BNNSs film). Surface treatment was provided by TEOS silane group and piranha solution. The retention times of the glass surfaces in the piranha solution and the adherence of different ratios of the silane solution to the glass surface were investigated. Surface characterization was carried out by Fourier Transform Infrared Spectrophotometer (FT-IR). Scanning Electron Microscopy (SEM) images were taken to characterize the surface morphology, the thickness of the thin films and the structure of boron nitride nanosheets. UV visible spectrophotometer was used to determine the efficiency of boron nitride nanosheets after the exfoliation process. Surface roughness tester (Time TR200) was used to determine surface roughness of the thin films. According to the results, it was observed that the piranha and silane solutions improved the adhesion of the glass surface. SEM images showed that the silane was coated on the glass surface and the coating material was retained on the silane. Excess silane loading caused the structure to deteriorate. Boron nitride yield was calculated and found to be 54.1% and 34.1% for different centrifugation rates after exfoliation.

*Keywords***:** Boron Nitride Nanosheet, Surface Treatment, Dip-Coating, Thin Film

Piranha ve Silan Modifikasyonlarının Bor Nitrür Nanosheets (BNNSs) İnce Film Oluşumu Üzerine Etkisi

Özet. Bu çalışmada, iki faz arasındaki (cam alt tabaka ve BNNSs filmi) yapışmanın arttırılması amaçlanmıştır. Yüzey iyileştirmesi TEOS silan grubu ve piranha çözeltisi ile sağlanmıştır. Cam yüzeylerin piranha çözeltisinde tutunma süreleri ve silan çözeltisinin farklı oranlarının cam yüzeyine yapışması incelenmiştir. Yüzey karakterizasyonu Fourier Transform Infrared Spektrofotometre (FT-IR) ile yapılmıştır. Yüzey morfolojisini, ince filmlerin kalınlığını ve bor nitrür nanosheetlerin yapısını karakterize etmek için Taramalı Elektron Mikroskobu (SEM) görüntüleri alınmıştır. Eksfoliasyon işleminden sonra bor nitrür nanosheetlerin verimliliğini belirlemek için UV görünür bölge spektrofotometresi kullanılmıştır. İnce filmlerin yüzey pürüzlülüğünü belirlemek için yüzey pürüzlülük cihazı (Time TR200) kullanılmıştır. Sonuçlara göre piranha ve silan çözeltilerinin cam yüzeyini yapışma için geliştirdiği görülmüştür. SEM görüntüleri silanın cam yüzeyinde kaplandığını ve kaplama malzemesinin silan üzerinde tutunduğunu göstermiştir. Silan yüklemesinin fazla olması yapıda bozulmalara neden olmuştur. Eksfoliasyon sonrası farklı santrifüjleme hızları için bor nitrür verimi %54,1 ve %34,1 olarak hesaplanmıştır.

*Anahtar Kelimeler***:** Bor Nitrür Nanotabaka, Yüzey Iyileştirme, Daldırarak Kaplama, Ince Film

1. INTRODUCTION

Adhesion is one of the most important factors during the forma tion of a thin film. To increase adhesion between the two phases (glass substrate and film), the glass surface must be treated before coating. There are many surface treatments applied on glass such as hydrofluoric acid (HF) abrasion, $SnCl_2$ sensitization, organic grading, sandblasting and sandpaper grinding. The etching technique using HF, a common reagent commonly used for glass treatment, causes the surface roughness to increase because of the physical treatment and promotes the formation of more silanol group (SiOH) producing hexafluorosilicic acid (H_2SiF_6). Another method is to sensitize the surface of the glass with a special treatment using $SnCI_2$, which is a special treatment with a chemical conditioning process. This process is often used to change the nature of the glass chemical. Besides chemical processes, there is also a simple physical improvement that is commonly used. Silicon carbide (SiC) paper grinding is a method that continuously increases the surface area and surface roughness. This process increases the effective area of the Van der Waals force. As a result, these processes have a positive effect on the adherence of the material to the surface [1]. There are some studies on the improvement of the glass surface. In the study of Muanpho et al. glass surface was coated by gold nanoparticles to improve the surface. In this study, the glass surfaces were primarily ultrasonic cleaned for 15 minutes in ethanol and deionized water. Glass surfaces were then treated with hydrogen peroxide that has a volume ratio of 30:70 (30%) and sulphuric acid (concentrated) for 60 minutes at 60-80ºC. Finally, the glass surfaces were washed with deionized water for 15 minutes and dried at 110°C for 45 minutes. After cleaning the surfaces, they used various silane groups (3-mercaptopropyl-trimethoxy-silane (MPTMS), 3-aminopropyl-trimethoxysilane (APTMS), polyethylenimine (PEI)) to modify the surface. Few gold nanoparticles were attached to the MPTMS-modified surface so that a homogeneous coating on the PEI-modified surface could be obtained. The first two silane groups reacted with the hydroxyl groups that were formed as a result of washing with piranha solution and formed the Si-O covalent bonds on the surface [2]. Nguyen et al. used 4 different methods for surface treatment in their study. They are Isopropyl alcohol treatment, 3% H_2O_2: H_2SO_4 piranha solution for 30 minutes, oxygen plasma treatment, piranha solution and then treatment in ammonia plasma to increase amine positive functional groups. According to the result of the analysis, it was found that the amount of carbon on the surfaces treated with oxygen and ammonia plasma was significantly reduced compared to the other two methods [3]. In another study, Wang and Awadelkarim investigated the effect of the glass surface in order to obtain a polycrystalline silicon thin film transistor on the glass. Prior to coating, they treated the glass surface at 75ºC in NH_4 / H_2O_2 / H_2O and HCl / H_2O_2 / H_2O medium for 10 minutes. Surface treated and non-treated glass have a favorable effect on the surface properties of silicon-rich surface transistors on glass surface [4]. Pacaphol and Ong investigated the effect of silanes on interfacial adhesion and surface properties of nano-cellulose film coating on glass and aluminum surfaces. Silanes containing different functional groups were used to increase the adhesion of nanocellulose films on the glass and aluminum substrates and to increase their physical and mechanical properties. It has been found that the amino group-containing silane provides the best adhesion performance compared to epoxy and methacryloxy groups; higher proportions of amino silane tended to adhere better to glass and aluminum substrates. Furthermore, the amino silane has the ability to improve the surface hardness, elastic modulus and scratch resistance of the coating film [5]. In their study, Chitvoranund et al. investigated the adhesion effects of the silver film that is produced by electrolysis coating on the glass substrate. The glass surface was treated with three different methods: HF acid etching, $SnCl_2$ activation, and silicon carbide paper milling. After this process, a glass slide was immersed in the coating solution for 90 minutes at room

temperature. The HF pickling process has created pores on the surface. The size of the pores increased with increasing immersion time. On the other hand, the sensitivity that is provided by $SnCl_2$ coating on the glass surface is similar to the untreated sample with a very smooth surface. The SiC paper grinding process made the surface smoother [1]. In their study in 2017, Ahmad et al. improved the glass surfaces with polyvinyl butyral (PVB). In order to strengthen the electro-optical properties of the R-PDLC, PVB was coated on the glass surface. It was mixed with 0.1% by weight of isopropyl alcohol to form the PVB layer and then distributed over the conductive surface of the ITO glass. After the first layer was dried, another PVB layer was produced on the first layer with the spin coating technique. According to the result of the analysis, they observed that PVB thin film improves the optical and hydrophobic properties of glass [6].

In our study, boron nitride nanosheets were produced by liquid exfoliation method, which is a high yield and low-cost process. There are several studies using this method to manufacture BNNSs with high efficiency [7-11]. Glass surfaces were kept in piranha solution at different time intervals and then modified with silane solution and surface improvement experiments were carried out.

2.   MATERIAL AND METHOD

2.1. Materials

Nano-sized boron nitride powder (Bortek Boron Technologies and Mechatronics Ind. Co.) was used as the starting material to produce 2D boron nitride nanosheets. In the exfoliation method, isopropyl alcohol and distilled water (J.T. Baker) were used as a solvent. Materials used to improve surface cleaning and wettability are; ethanol (99% purity, Sigma Aldrich), sulfuric acid (H_2SO_4, Carlo Erba 96%), hydrogen peroxide (H_2O_2, Merck 35%) and distilled water. Tetraethylorthosilicate (TEOS, ABCR GmbH 99%) was used to increase the adhesion strength between the glass surface and the coated material. The pH of the solution was adjusted with acetic acid (Riedel de Haen, 100%). Borosilicate microscope slides (25.4x76.2 mm in size and 1-1.2 mm in thickness) were used as the surface to be coated.

2.2. Method

2.2.1. Production of Boron Nitride Nanosheets

Boron nitride nanosheets were produced using sonication centrifugation technique. Low power ultrasonic bath was used to manufacture 2D boron nitride. In this method, the mixture of isopropyl alcohol and water were used as solvent. 0.2 g of bulk boron nitride powder was dispersed in 100 mL of solvent (2 mg/mL). The resulting mixture was sonicated in a 180 W ultrasonic bath for 3 hours at 45-minute intervals and centrifuged at 3200 and 4000 rpm for 30 minutes to complete the formation of boron nitride nanosheet. The supernatant was placed in a new bottle.

2.2.2. Surface treatment of glass substrates and thin film formation

In the applied method, the glass surfaces were first washed ultrasonically in the ethanol solution for 15 minutes in order to remove impurities from the surface. Then, 3:1 H_2SO_4: H_2O_2 (sulphuric acid and hydrogen peroxide) solution, also called as piranha, was prepared and the cleaned glass surfaces were kept in piranha solution for different periods (10 minutes, 20 minutes, 30 minutes) to increase the wettability of the surface. The glass surfaces in piranha solution were washed with distilled water before being immersed in boron nitride nanosheet solution. 10%, 20% and 30% methanol solutions of the silane group (TEOS) were prepared and added to the solution at the same rate as the boron nitride concentration. To accelerate the hydrolysis and condensation reactions of the silane group, acetic acid was added dropwise to bring the pH of the solution to 4. Glass surfaces were immersed into the solution 5 times and kept in the solution for 5 minutes. After immersion, the glass surfaces were dried for 1 day in room conditions to remove the excess solvent and other volatile components on the glass. The dried glasses were treated in a tube oven at 550°C for 5 hours in the presence of nitrogen gas. The experimental conditions were given in Table 1.

Table 1. Experimental conditions for surface treatment

| Sample codes	Solution concentration (mg/mL)	Piranha Solution Holding Time (minutes)	Silane Concentration (%)
BNP10	2	10	-
BNP20	2	20	-
BNP30	2	30	-
BNP30S10	2	30	10
BNP30S20	2	30	20
BNP30S30	2	30	30

2.3. Characterization

In order to determine the morphological characteristics of the surface images of thin films and boron nitride nanosheets, SEM (Zeiss Supra 40VP, Germany) analysis was performed. Images were taken from the surface and surface section at different magnifications. The presence of boron nitride and silane groups on the coating surface was investigated by FT-IR (Agilent Technologies, Cary 630) analysis with 400-4000 cm^{-1} wavelength range. The amount of boron nitride nanosheet formed in the liquid exfoliation method was determined by UV-visible region spectroscopy (Agilent Technologies, Cary 60 Uv-Vis). The surface roughness of the thin films was obtained using surface roughness tester (Time TR200).

3. RESULTS AND DISCUSSION

3.1. SEM Images of Boron Nitride Nanosheets

Figure 1 contains SEM images at 3200 and 4000 rpm of boron nitride nanosheet in which the mixture of isopropyl alcohol and water are used as solution. The surface was covered with platinum before the SEM analysis. Figure 1-b shows that the lateral dimensions of nanosheets range from 100 to 300 nm. Since nano-sized bulk h-BN powder has been used in the exfoliation process, obtained nanosheets were thick (about 20 nm). In SEM images at 4000 rpm (Figure 1-d), thinner nanosheets were formed. The separation of the boron nitride layers can be improved by increasing the rate of centrifugation [8]. Since the synthesis is done at low speed, nanosheets are seen in a stacked form.
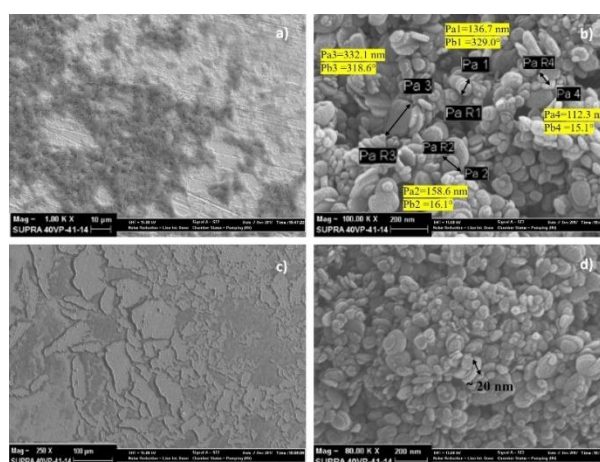
Figure 1. SEM images of boron nitride nanosheets at different centrifugal speeds and magnifications a) 3200 rpm, 1.00X b) 3200 rpm, 100.00X c) 4000 rpm, 250X d) 4000 rpm, 80.00X

3.2. SEM Images of Surface-Treated Thin Films

SEM images of coated surfaces using different piranha immersion times were given in Figure 2. Figure 2- a,b shows the images in different magnifications of the coatings obtained by immersing the glass surfaces in a solution of piranha for 10 minutes. When the SEM images are examined, it is observed that there is not much adhesion to the surface, but in some cases, the acid etching increases the area of contact of the coating with the surface. To increase the area of contact of the piranha solution with the surface and to facilitate the adhesion of the coated solution to the glass surface, the waiting time in the piranha was increased to 20 minutes. Figure 2-c, d shows the images of the coatings obtained by immersing the glass surfaces in piranha solution for 20 minutes. It

is observed that a denser part is attached to the glass surface, although not homogeneous, compared to the BNP10 sample. As the contact time with acid increased, the area occupied by the attachment increased. The coated material was stacked on the surface. In a study conducted by Chitvoranund et al. in 2013, it was determined that when the glass surfaces were eroded with acid in different time periods such as 60, 90 and 120 seconds, the pores on the surface at the end of 120 seconds were discovered to be larger than other durations. The surface before the etching was smooth and after the acid treatment, eroded and porous surfaces were obtained [1]. Figure 2-e, f is a view of the glass surfaces obtained by immersing them in a solution of piranha for 30 minutes. The images show a more homogeneous spread compared to the surfaces after 10 and 20 minutes. The surface roughness and consequently the surface area has increased, thus resulting in a better film adhesion. Waiting for glass surfaces in the piranha solution for 30 minutes increased the area where Van der Waals forces were effective and widened the surface area of boron nitride particles.
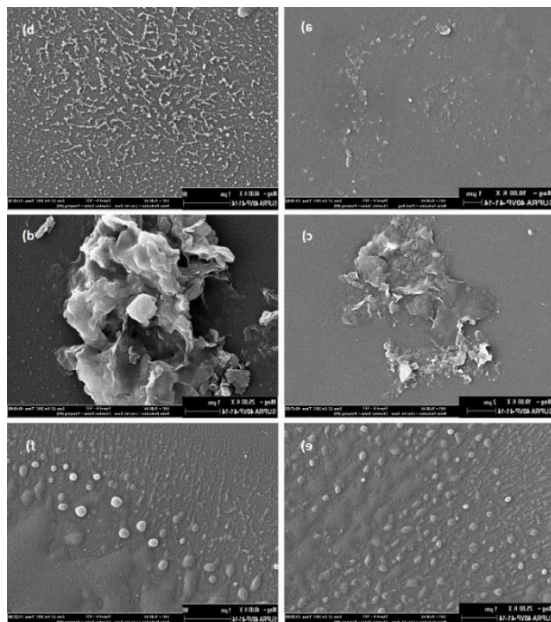
Figure 2. SEM images of coated surfaces of different piranha immersion times a,b)10 mins, b,c) 20 mins, d,e) 30 mins

Figure 3 shows the SEM images of glass surfaces modified with silane and piranha solution. In Figure 3-a, b the images of the surfaces obtained by immersing the glass surfaces in piranha solution for

30 minutes and then dipping them into a 10% silane and a boron nitride nanosheet solution were given. The addition of silane groups only improved the adhesion between the material and the surface that consisted of the coatings made with piranha, which allowed more materials to adhere to the surface. It is well known that silane groups have a very active structure on glass surfaces. They also act as a binding agent between organic and inorganic materials. Silanol groups ($^-Si^-OH$) occur in the hydrolysis event after the contact of the alkoxy groups in the structure of the silane with water. These silanol groups react with the hydroxyl groups in the condensation step to form a cross-linked silane layer between the adjacent silane molecules. As a result of these reactions, the surface of the glass is activated, and the coating material is improved by the surface [12]. In Figure 3-a, b it is observed that the adhesion between the glass surface and the material increased by 10% after the silane improvement, compared to the coating without silane. Figure 3-c, d exhibit the SEM images of the coatings obtained by immersing the glass surfaces in piranha solution for 30 minutes. From the SEM images, it is evident that the film becomes continues as the silane amount was increased. In a study conducted by Cecchin et al. in 2016, similar SEM images were obtained by coating the glass fibers that are used for surface treatment with silane groups. The acid they use, which is HF, increases the wetting properties of the surface by increasing the energy on the surface of the glass fibers [13]. The cross-sectional images and thickness of the BNP30S20 sample were also given. The thickness of the resulting film was 42.774 μm.

In Figure 3-e, f shows the SEM images of BNP30S30 film, which was prepared by pre-treating the glass surfaces in piranha solution for 30 minutes and subsequently in a mixture of 30% silane solution. The coating material, which is intended to adhere to the surface, was deposited on the silane group. It is also seen that the silane group that is coated on the glass surface is partially fragmented. It is thought that this degradation occurs after hydrolysis and condensation reactions of TEOS. The average thickness of the thin film coating is 37.25 μm. According to the images, it

was observed that a double layer coating was formed. The boron nitride particles were coated on the silane. In order to form a boron nitride coating as a single surface, silane groups must be removed from the surface.
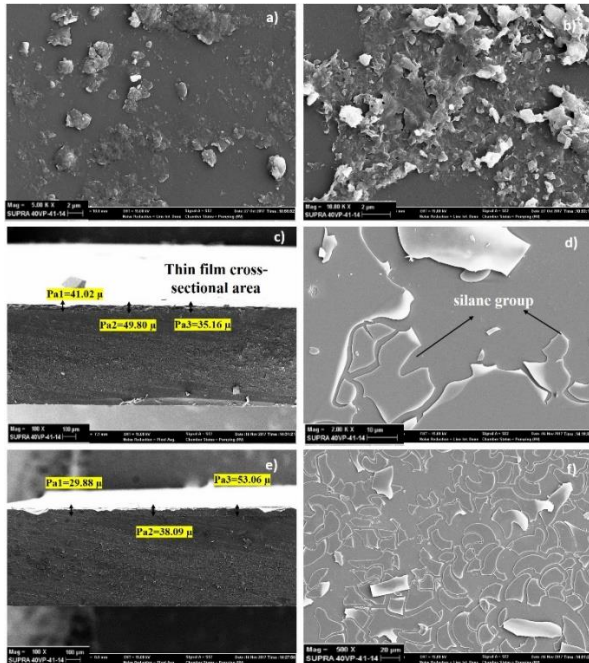

Figure 3. SEM images of coated surfaces kept in piranha solution for 30 minutes and for different silane concentrations a,b)10%, b,c) 20%, d,e) 30%.

3.3. Raman Spectroscopy Analysis Fourier Transformed Infrared Spectrophotometer (FT-IR) Analysis Results

FT-IR analyzes were performed in the wavelength range of 400-4000 cm^{-1}. Figure 4 shows the IR spectrum of the uncoated glass slide. Figure 5 and 6 shows the IR spectrum of the thin films obtained after the surface treatment. Figure 5 shows the IR spectra of thin films obtained by immersing glass surfaces in piranha solution for different time intervals. Stretching band appeared at 2949.93 cm^{-1} wavelength is related to asymmetric C-H strain. This band is belonging to the CH_3 group in the methanol structure used in all solutions. The stretching band around 2106.05 (Figure 5 and 6) shows NCO groups.
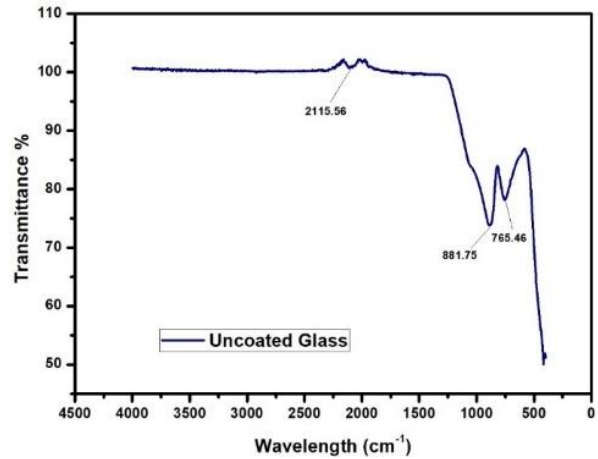
Figure 4. IR spectrum of uncoated glass slide
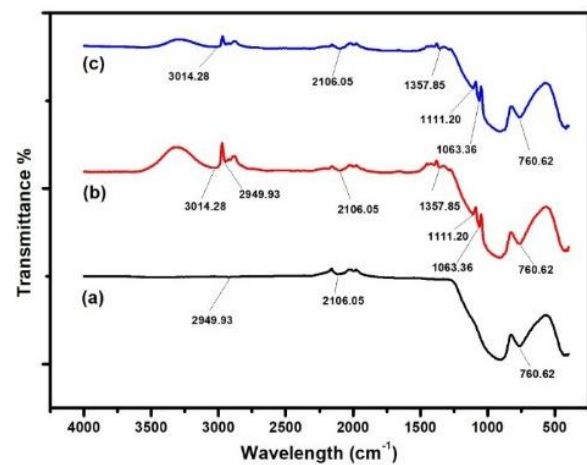
Figure 5. IR spectrum of thin films obtained as a result of surface improvement a) BNP10 b) BNP20 c) BNP30

The stretching around the wavelength of 1357.85 cm^{-1} represents the CH_2 and CH_3 groups in methanol or ethanol. Similar stretching was observed in the coatings on the surfaces which were kept in piranha solution for 20 minutes and 30 minutes while some CH_2-CH_3 stretching was not observed in the coating held in solution for 10 minutes. The stretching of 1111.20 cm^{-1} and 1063.36 belong to the C-O asymmetric band. The band at 760.62 cm^{-1} in all samples (Figure 4,5,6) refers to the oxygen-induced Si-O or Si-O-Si bonding of the silicon present in the glass structure [14]. In the coating spectrum of the solution prepared with 30% silane (Figure 6), the band at 1357.85 cm^{-1} was considered to belong to CH_3 groups in TEOS. The strain of 1007.26 cm^{-1} occurring in the 30% sample also shows C-O binding. The stretching band at 911.57cm^{-1} in all

the samples (a), (b) and (c) refers to non-bridged fractured Si-O bonds. This stretch is thought to be due to the formation of Si-O covalent bond on the surface by reacting with the hydroxyl groups resulting from washing with the piranha solution of the silane group [2].
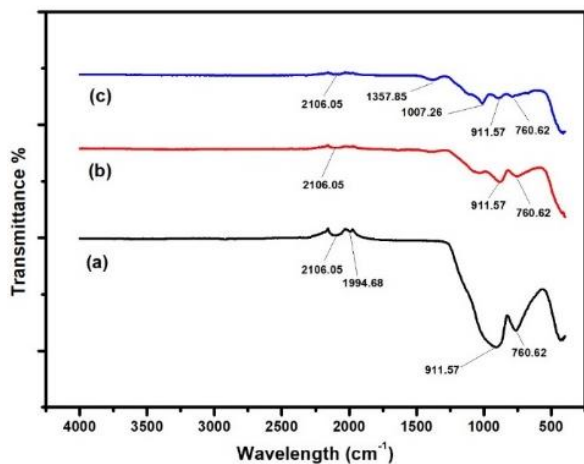
Figure 6. IR spectrum of thin films obtained as a result of surface improvement a) BNP30S10 b) BNP30S20, and c) BNP30S30

3.4. Determination of Boron Nitride Nanosheets Concentration

UV-Visible Spectrophotometer was used for the quantification of the obtained nanosheets. At 400 nm wavelength [15]. 2 ppm (2 mg/mL) suspension was prepared by diluting the mixture with isopropyl alcohol and water. Table 2 shows the absorbance values of the suspensions prepared in various ppm values.

Table 2. Absorbance values of suspensions prepared in different concentrations

Concentration (ppm)	Absorbance
0.5	3.1554
1	3.3420
1.5	3.5173
2	3.6857
BNNSs solution (3200 rpm)	3.2246
BNNSs solution (4000 rpm)	3.3658

A calibration curve was drawn according to the obtained data and the linear equation was created. The absorbance value of the boron nitride nanosheet suspension that is prepared at 3200 and 4000 rpm was calculated from this equation and the concentration value was determined to be 1.082

ppm and 0.6823 ppm (mg/mL) respectively. Sonication yield was calculated as 54.1% and 34.1 % starting from the initial amount (2 mg/mL). The peeling of the nanoparticles in the solvent is due to the strong interaction between the solvent and the nanoparticles; this means that there is little energy for exfoliation. During sonication of the boron nitride flasks in the solvent, initially large flakes are separated into smaller flakes and a greater amount of energy is obtained as the duration and rate of centrifugation increases and a small number of layers or a high concentration of nanosheets is obtained. For this reason, to perform an efficient exfoliation, the solvent should be dispersive, polar, and have H-bonding solubility parameters matching those of layered materials in order to minimize the exfoliation energy to ensure effective exfoliation [16].

3.5. Surface Roughness of BNNSs Thin Films

Roughness is the length of many scratched, irregular short wavelengths that occurs when a hand tool moves from one end of the surface to the other. One of the parameters used to determine the surface roughness is the arithmetic mean deviation (Ra) value and results in µm. This expression has been described as the average height of the central axis in the BSJ standard. Surface roughness measurement devices can be read directly. The surface roughness values of thin films prepared at different conditions were given in Table 3. It was observed that the surface roughness ranged between 0.03 and 0.14 µm. From the results, it can be concluded that roughness values increased as the surface etching increased (Figure 2).

Table 3. The surface roughness of BNNSs thin films

Sample codes	Roughness (Ra, µm)
BNP10	0.030
BNP20	0.044
BNP30	0.049
BNP30S10	0.115
BNP30S20	0.129
BNP30S30	0.140

The surface became increasingly porous and irregular because of the dissolution of the glass phase after piranha and silane modifications.

Therefore, voids and channels become larger and deeper as the etching time and silane concentration increases [17-19].

4. CONCLUSION

In general, modifications of piranha and silane group showed a positive effect on adhesion of boron nitride nanosheets to the glass surface. As the waiting time of glass surfaces in the piranha solution increased, the adhesion of the boron nitride nanosheet to the surface increased. Keeping glass surfaces in the piranha solution for 30 minutes increased the effective area of the Van der Waals forces and widened the surface area of boron nitride particles. It is also seen that the silane group coated on the glass surface is partially fragmented when the loading of the silane group is 20% and 30%. In IR spectrum of the thin films treated with silane groups, non-bridged fractured Si-O bonds were observed. This stretch is thought to be due to the formation of Si-O covalent bonds on the surface by reacting with the hydroxyl groups resulting from washing with the piranha solution of the silane group. Sonication yield was calculated as 54.1% and 34.1% for boron nitride nanosheets. According to the results if less than 20% silane group is used, surface defects can be eliminated.

REFERENCES

[1] Chitvoranund N., Jiemsirilers S., Kashima D.P., Effects of surface treatments on adhesion of silver film on glass substrate fabricated by electroless plating, J. Aust. Ceram. Soc., 49 (2013) 62-69.

[2] Muanpho K., Praserthdam P., Pavarajarn V., Surface Modification for fabrication of gold nanoparticles thin film on glass substrate, In: 4th Thailand Materials Science and Technology Conference; 31 March-1 April (2006) Bangkok, Thailand.

[3] Nguyen C.V., Bartali R., Crema L., Speranza G., Effect of glass surface treatments on the deposition of highlytransparent reduced graphene oxide films by dropcasting method, Colloid Surface A, 498 (2016) 231-238.

[4] Wang Y.Z. and Awadelkarim O.O., The Effects of Glass-Substrate's Surface-Treatment on the Characteristics of N-Channel Polycrystalline Silicon Thin Film Transistors, J. Electron. Mater., 27 (1998) 77-80.

[5] Pacaphol K. and Aht-Ong D., The influences of silanes on interfacial adhesion and surface properties of nanocellulose film coating on glass and aluminum substrates, Surf&Coat. Tech., 320 (2017) 70-81.

[6] Ahmad F., Jamil M., Jeon Y.J., Alteration of glass surface via polyvinyl butyral (PVB) layer for reverse mode polymer dispersed liquid crystal (R-PDLC) display, Phase Transit., 90 (2017) 873-881.

[7] Wang Z., Tang Z., Xue Q., Huang Y., Huang Y., Zhu M., Pei Z., Li H., Jiang H., Fu C., Zhi C., Fabrication of Boron Nitride Nanosheets by Exfoliation, Chem. Rec., 16 (2016) 1204-1215.

[8] Li X., Hao X., Zhao M., Wu Y., Yang J., Tian Y., Qian G., Exfoliation of hexagonal boron nitride by molten hydroxides, Adv. Mater., 25 (2013) 2200-2204.

[9] Wang Y., Shi Z., Yin J., Boron nitride nanosheets: large-scale exfoliation in methanesulfonic acid and their composites with polybenzimidazole, J. Mater. Chem., 21 (2011) 11371-11377.

[10] Zhi B.C., Bando Y., Tang C., Kuwahara H., Golberg D., Large-Scale Fabrication of Boron Nitride Nanosheets and Their Utilization in Polymeric Composites with Improved Thermal and Mechanical Properties, Adv. Mater., 21 (2009) 2889-2893.

[11] Liu J., Kutty R.G., Zheng Q., Eswariah V., Sreejith S., Liu Z., Hexagonal Boron Nitride Nanosheets as High-Performance Binder-Free Fire-Resistant Wood Coatings, Small, 13 (2016) 1602456.

[12] Dvir H. and Gottlieb M., Effect of Silane Sizing on Polymer-Glass Adhesion, Am.

Phys. Soc., (2007) APS March Meeting; March 5-9,2007; Denver, Colorado.

[13] Cecchin D., Farina A.P., Vitti R.P., Moraes R.R., Bacchi A., Spazzin A.O., Acid Etching and Surface Coating of Glass-Fiber Posts: Bond Strength and Interface Analysis, Braz. Dent. J., 27 (2016) 228-233.

[14] Rubio F., Rubio J., Oteo J.L., A FT-IR Study of the Hydrolysis of Tetraethylortho silicate(TEOS), Spectrosc. Lett., 31 (2013) 199-219.

[15] Marsh K.L., Souliman M., Kaner R.B., Co-solvent exfoliation and suspension of hexagonal boron nitride, Chem. Commun., 51 (2015) 187-190.

[16] Durge R., Kshirsagar R.V., Tambe P., Effect of sonication energy on the yield of graphene nanosheets by liquid-phase exfoliation of graphite, Procedia Engineer, 97 (2014) 1457-1465.

[17] Smielak B. and Klimek L., Effect of hydrofluoric acid concentration and etching duration on select surface roughness parameters for zirconia, J. Prosthet. Dent., 113 (2015) 596-602.

[18] Affatigato M., Osborne D.H., Haglund R.F., Effect of Surface Roughness on the Acid Etching of Amorphous Silica, J. Am. Ceram. Soc., 79 (1996) 688-694.

[19] Zogheib L.V., Della Bona A., Kimpara E.T., Mccabe J.F., Effect of Hydrofluoric Acid Etching Duration on the Roughness and Flexural Strength of a Lithium Disilicate-Based Glass Ceramic, Braz. Dent. J., 22 (2011) 45-50.

Electrochemical Synthesis and Characterization of ZnO Nanocomposite Copolymer Containing Fluorescent Feature Dye

Esra KILAVUZ[1], *Ersen TURAÇ[1*]*, *Ertuğrul ŞAHMETLİOĞLU[2,3]*

[1]*Niğde Omer Halisdemir University, Department of Chemistry, Niğde, 51240,TURKEY*

[2] *Erciyes University, Nanotechnology Research Center, Kayseri, 38039, TURKEY*

[3] *Kayseri University, Safiye Cikrikcioglu Vocational School, Kayseri, TURKEY*

Abstract. BODIPY (boron dipyrrolmethene) has attracted the attention of scientists although the synthesis of BODIPY from the fluorescent dye class is challenging, there are many applications such as fluorescence, ion / molecule and pH probes, sensors, redox active molecules, metal chelators, cellular imaging, photodynamic therapy, drug delivery materials and photovoltaic applications and energy storage. Firstly, it is synthesized with difficulty in synthesis but attractive fluorescence active monomer. Then, by electrochemical method, a conductive copolymer, which is an innovative material, was synthesized. The nanocomposite was synthesized with the help of a potentiostat using Zno nanoparticles to increase the strength and conductivity properties of the obtained semiconducting material and its existence was determined by advanced technological devices such as SEM-EDX, AFM-Raman. Characteristic peaks of inorganic and nano-scale compounds such as ZnO are observed in the fingerprint region and weak / medium in the conventional FT-IR device. This makes it difficult to qualitatively diagnose the compounds by infrared spectrometry. Raman spectroscopy, however, has been preferred for the determination of nanoparticles because it is relatively laborious, such as ICP-MS, and is not a complex spectral region such as FT-IR.

Keywords: Conducting Polymer, Nanocomposite, AFM-Raman.

Floresan Özellikli Boya İçeren ZnO Nanokompozit Kopolimerlerin Elektrokimyasal Sentezi ve Karakterizasyonu

Özet. Floresans boya sınıfından olan BODIPY'nin (Boron dipirolmetilen) bilim insanları tarafından sentezi uğraştırıcı olmasına karşın floresan, iyon / molekül ve pH probları, sensörler, redoks aktif moleküller, metal şelatörler, hücresel görüntüleme, fotodinamik tedavi, ilaç teslim malzemeleri ve fotovoltaik uygulamalar ve enerji depolama gibi çok çeşitli uygulamalarda kullanılması ilgi çekici olmuştur. Öncelikle çalışmada sentezi zor ama çekici floresans aktif monomer başarı ile sentezlenmiştir. Sonra elektrokimyasal yöntem kullanılarak yenilikçi malzeme olan bir iletken kopolimer sentezlenmiştir. Elde edilen yarı iletken malzemenin dayanım, iletkenlik özelliklerini arttırmak için Zno nanopartikülleri kullanılarak yine bir potansiyostat yardımı ile nanokompozit sentezlenmiş ve varlığı SEM-EDX, AFM-Raman gibi ileri teknolojik cihazlarla tayin edilmiştir. ZnO gibi inorganik ve nano ölçekli bileşiklerin karakteristik pikleri geleneksel FT-IR cihazında parmak izi bölgesinde ve zayıf/orta gözlenmektedir. Buda bahsedilen bileşiklerin kızılötesi spektrometre ile nitel teşhisini zorlaştırmaktadır. Buna karşın Raman spektroskopisi hem ICP-MS gibi nispeten uğraştırıcı hem de FT-IR gibi karmaşık bir spektrum bölgesi olmadığından nano parçacıkların tayininde tercih edilmiştir.

Anahtar Kelimeler: İletken polimerler, Nanokompozit, AFM-Raman.

1. INTRODUCTION

Boron-dipyromene, abbreviated as BODIPY, is a class of fluorescent dyes. BODIPY is a powerful electron acceptor and has unique spectroscopic and photophysical properties such as high absorption rate and high fluorescence quantum yield and strong absorption in the visible region [1-3]. The BODIPY group exhibits adjustable redox potentials [4]. The photonic properties of BODIPY can be modifiable by functionalizing with donor molecules in meso- and pyrolytic positions (positions a and b). In this study, the meso position has been derivatized and the effect on redox behavior has been investigated by electrochemical method.

The synthesized BODIPY complex is made of conductive organic-inorganic nanocomposite polymer film due to its optoelectronic properties. Intense interest in conjugated polymers has been shown, depending on the wide range of applications where they are potentially useful since the discovery of the conductivity properties of polyacetylene [5]. Photovoltaic devices [6], light emitting diodes [7], field-effect transistors [8], electrochromic devices [9], and various sensors based on conjugated polymers [10] are being investigated by a large number of researchers worldwide. In this way, the search for new functional and sensitive conjugated polymers that exhibit electrochromism [11], photochromism [12] or non-linear optical properties, is particularly sought for applications in imaging technology or data storage. [13]. Organic-inorganic composites are a good candidate for many applications such as biosensing materials, bioanalytical application, organic optoelectronic device, gas sensor, carbon nanotube, and solar cells [2]. A polymer synthesis which has a combination of several of these properties has been targeted in this study.

Electropolymerization is a versatile method for producing electrically conductive polymers due to its simplicity and repeatability. It also allows the control of the thickness of the polymer film. Generally, electrical, optical and magnetic properties of conductive polymers, zinc oxide

(ZnO), titanium oxide (TiO_2), cadmium sulfide (CdS), cadmium selenite (CdSe) and metal nanostructures etc. such as may be modified by the inclusion of inorganic materials. These inorganic materials include ZnO, wide band spacing (3,37 eV), large excitation bonding energy (60 meV), good chemical stability, interesting electrical and optical properties, and so on. It is well known for its outstanding features. Therefore, the development of ZnO / polymer nanocomposites for electrochromic device application is of great importance. Recently, ZnO-PEDOT-based nanocomposites have attracted considerable attention of material scientists in the field of optoelectronics, sensors and biomedical applications [14-17]. In this study, ZnO-PEDOT:BODIPY conductive nanocomposite copolymer film, which is an innovative material using electrochemical method, has been synthesized and characterized by advanced technologic devices such as NMR, SEM-EDX, AFM-Raman.

2. MATERIALS AND METHODS

2.1. Materials and instruments

Trifluoroacetic acid (TFA) and bortrifluoroetherate ($BF_3.OEt_2$) All other chemicals from Fluka were obtained from SigmaAldrich. Pirol was purified by filtration through an alumina-filled column prior to use. The monomers were chromatographed using 60 mesh silica using dichloromethane (DCM) as the starting phase. Polymerization Pt plate as the working electrode, Pt wire as opposite electrode and Ag / AgCl as the reference electrode were synthesized in CHI 600 potentiostat and 0.1M $LiClO_4$ / CH_3CN elektrolit pair in Niğde Ömer Halisdemir University Chemistry Department. For characterization, Scanning Electron Microscope (SEM-EDX) in Niğde Ömer Halisdemir University Central Research Laboratory Zeiss Evo 40, Ametek EDAX, Atomic Force Microscopy (AFM) Bruker Innova, RAMAN Renishaw Invia, Fourier Transformed Infrared Spectroscopy Bruker Vertex 70 instruments were used.

2.2. Synthesis

BODIPY containing monomer containing fluorescence was synthesized according to literature [4-6] as shown in Figure 1. An aldehyde derivative (335 mg, 1.5mmol) was collected in a 100 mL single-necked flask. 50 mL of dry THF was added and N_2 gas was passed through the medium for 20 minutes. Pyrol (200 mg, 3 mmol) was added. After stirring for five minutes, TFA (three drops) was added and allowed to stir under N 2 gas at room temperature until the starting material ran out (2 days). The starting material was checked by thin layer chromatography (TLC). When the starting material was finished, DDQ (284 mg 1.25 mmol) was dissolved in 20 mL dry THF and transferred to the dropping funnel and added slowly to the reaction medium. Dry Et_3N (3.63 g, 5 mL, 35 mmol) and then $BF_3.OEt_2$ (3.45 g, 3 mL, 24 mmol) were added after 30 min. After stirring at room temperature overnight, the solvent was removed under reduced pressure. After determination of hexane / dichloromethane (1/1) mixture and dichloromethane as column solvent, the material was purified by column chromatography.
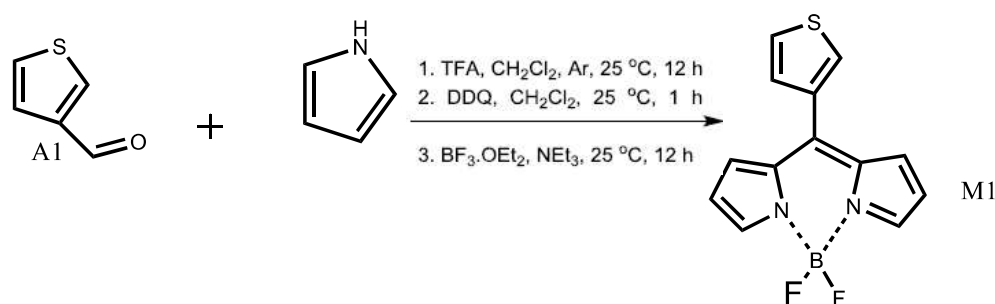
Figure 1. Synthesis scheme of M1 monomers.

2.2.1. 3-(4,4-difluoro-4-bora-3a,4a-diaza-s-indacene)-10-propyl-10H-thiophene (M1)

Thiophene 3-carboxialdehyde FT-IR spectrum in the 1700.72 cm^{-1} with the strong carbonyl peak stress, 2955 cm^{-1} aldehyde hydrogen stress is lost as a result of the reaction. 1610.98 cm^{-1} also proves the dimerization of pyrrole rings. FT-IR(cm^{-1}): 3471, 3060, 2970, 2128, 1610, 1514, 1574; ^{1}H NMR (400 MHz, $CDCl_3$) d/ppm: 7.19 (d, J ¼ 8.7 Hz, 2H), 7.08 (d, J ¼ 8.7 Hz, 2H), 4.77 (d, J ¼ 2.37 Hz, 2H, OCH2), 2.57 (t, J ¼ 2.37 Hz, 1H, CH), 2.54 (s, 6H), 2.30 (q, J ¼ 7.57 Hz, 4H), 1.32 (s, 6H), 0.98 (t, J ¼ 7.57 Hz, 6H); ^{13}C NMR (100 MHz, $CDCl_3$) d/ppm: 158.0, 153.5, 139.8, 138.3, 132.6, 131.1, 129.4, 128.9, 115.6, 78.0, 75.9, 56.1, 17.1, 14.7, 12.4, 11.9

2.2.2. Electrochemical polymerization of M1

Electropolymerization of monomers; Aggregate voltammetry using 20 mL 0.1M $LiClO_4$ as electrolyte in three-electrode electrochemical cells in which the P wire is used as the reference electrode, the platinum wire as the opposite electrode and the working electrode is separately Pt plate and the conductive and transparent indium tin oxide (ITO) coated glass surface is used. method. Copolymer synthesis was performed by adding 10ophl of EDOT (3,4-Ethylenedioxythiophene) to strengthen the electrochromic properties and to coat the film. The nanocomposite copolymer film was finalized by adding ZnO.
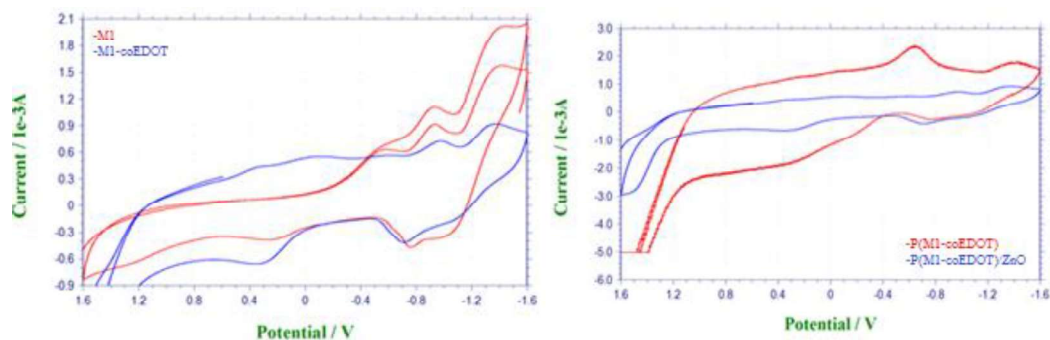
Figure 2. Cyclic voltamograms of M1, P (M1-coEDOT) and P (M1-coEDOT) / ZnO.

Table 1. Reduction and oxidation peak potentials of P(M1-co-EDOT), PEDOT, P(M1-co-EDOT)/ZnO, P-M1.

Product	Reduction Peak Potential (V)	Oxidation Peak Potential (V)
P(M1-co-EDOT)	-0.96, -1.35, -0.70	0.3, 1.5, 1.2, 0.4
PEDOT	-0.76	0.4
P(M1-co-EDOT)/ZnO	-0.65, -1.40, - 0.8	0.4, 0.96
P-M1	-0.56, -0.72, -1.0, -1.56	0,58

2.2.3. AFM-Raman analysis of P(M1-coEDOT)/ZnO nanocomposite polymer film

Figure 3 shows the AFM-Raman spectrum of the P (M1-coEDOT) / ZnO nanocomposite polymer film.

3. RESULT AND DISCUSSION

Thiophene 3-carboxialdehyde FT-IR spectrum in the 1700.72 cm^{-1} strong carbonyl peak tensile stress, 2955 cm^{-1} aldehyde in the reaction to the stress of the aldehyde lost. 1610.98 cm^{-1} also shows the dimerization of peak pyrrole rings.

In Figure 2, the cyclic voltamograms of monomer (M1), P- (M1-coEDOT) and P- (M1-coEDOT) / ZnO nanocomposite film are clearly different. Under the same conditions, the cathodic (reduction) and anodic (oxidation) peaks of EDOT are -0.76V and 0.4V as seen in Table1. The reduction and oxidation peaks of the P- (M1-coEDOT) copolymer are -0.96, -1.35, -0.70 and 0.3, 1.5, 1.2, 0.4 V, respectively, and are different from EDOT. This indicates that the copolymer was formed. In the literature, cathodic and anodic peaks belonging to ZnO are indicated as +0.106 and -0,06V [17]. The peak potentials of P- (M1-coEDOT) / ZnO nanocomposite film are given in Table 1. This difference is indicative of the nanocomposite polymer film.

The Raman shifts of ZnO nanoparticle in Figure 3 were observed at 100-400 cm^{-1} [7]. In the FT-IR spectra of the same substance, peaks correspond to the fingerprint area and make the determination difficult. At this point, Raman facilitates the determination of the trace and inorganic elements of the spectrum. The crystal structure of ZnO is hexagonal and has four atoms in the center (O-Zn-Zn-O). This four-member crystal lattice unit consists of 3n (n: member number), ie 12 lattice vibrations. 9 of these vibration movements are acoustic vibrations; 3 of them are optical vibrations. The highest vibration level called E2 was observed in Raman shift of 430 cm^{-1} [18]. Similarly, the observation of aromatic C = C raman shifts in the 1100 cm-1 and 1600 cm^{-1} range proves pyrrole and thiophene structures in the organic polymer film [3,8].

The result of the SEM-EDX with the AFM-Raman result of the copolymer nanocomposite film supports each other. As in the AFM-Raman data, SEM-EDX shows the peaks of Cα, S, N, Zn, O and Kα radiations in Figure 4. In the mapping, Zn dark green, O light green, N pink, C purple, S is represented by light purple colored speckles.
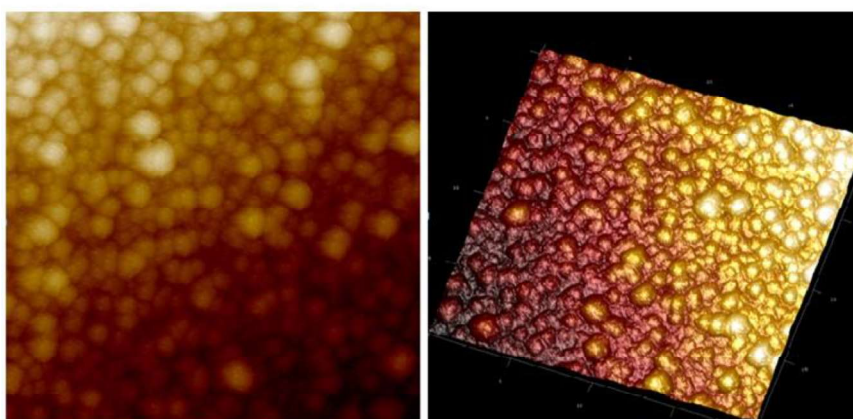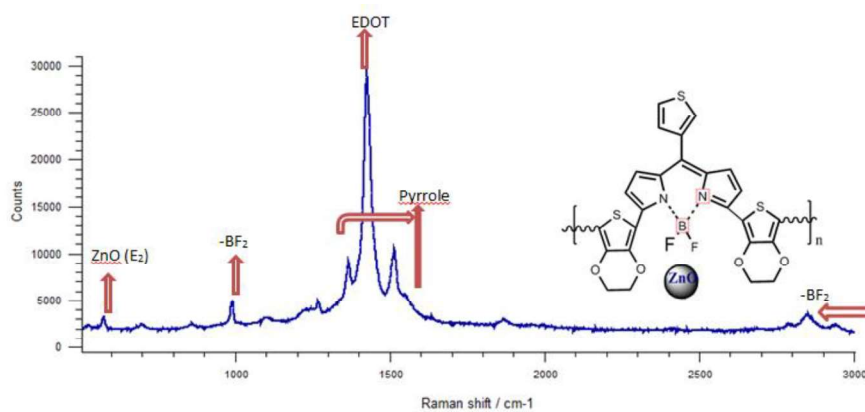
Figure 3. AFM-Raman spectrum of P(M1-coEDOT)/ZnO nanocomposite polymer film.

Figure 4. SEM-EDX analysis of P(M1-coEDOT)/ZnO nanocomposite polymer film.

* Corresponding author. *Email address:* *ersenturac@ohu.edu.tr*

In this study, the promising BODIPY monomer synthesized, promising copolymer nanocomposite film has been successfully obtained and has been proven with new generation characterization devices in Niğde Ömer Halisdemir University Central Research laboratory.

REFERENCES

[1] Değirmenci, A. and Algı, F., Synthesis, chemiluminescence and energy transfer efficiency of 2,3-dihydrophthalazine-1,4-dione and BODIPY dyad, Dyes Pigments, 140 (2017) 92-99.

[2] Turaç E., Şahmetlioğlu E. and Göktürk E., Synthesis of Conducting Polymer/Zinc Sulfide Nanocomposite Films and Investigation of Their Electrochemical and Morphological Properties, Adv. Poly Tech., 34 (2015) 21478-21486.

[3] Moraes B.R., Campos N.S. and Izumi Celly M.S., Surface-enhanced Raman scattering of EDOT and PEDOT on silver and gold nanoparticles, Vib. Spectrosc., 96 (2018) 137-142.

[4] Madhurima P., Prabhat G., Yogajivan R. and Rajneesh M., Donor–acceptor phenothiazine functionalized BODIPYs, Dyes Pigments, 146 (2017) 368-373.

[5] Kılıç B., Yeşilyurt N., Polat V., Gerçek Z. and Akkaya E.U., Bodipy-based photosensitizers with long alkyl tails at the *meso* position: efficient singlet oxygen generation in Cremophor-EL micelles, Tetrahedron Lett., 57 (2016) 1317–1320.

[6] Algı F. and Cihaner A., A novel terthienyl based polymer electrochrome with peripheral BODIPY, Polymer, 53 (2012) 3469-3475.

[7] Shijing L., Chunjiang T., Jialin L., Xin Z. and Wenzhong W., Visible light-induced charge transfer to improve sensitive surface-enhanced Raman scattering of ZnO/Ag nanorod arrays, Appl. Surf. Sci., 452 (2018) 148–154.

[8] Bukowska P., Piechowska J. and Loska R., Azine-imidazole *aza*-BODIPY analogues with

large Stokes shift, Dyes Pigments, 137 (2017) 312-321.

[9] Lu J., Song H., Li S., Wang L., Han L., Ling H. and Lu X., A poly(3,4-ethylenedioxythiophene):poly(styrene sulfonic acid)/titanium oxide nanocomposite film synthesized by sol–gel assisted electropolymerization for electrochromic application, Thin Solid Films, 584 (2015) 353-358.

[10] Sahmetlioglu E., Yilmaz E., Aktas E. and Soylak M., Polypyrrole/multi-walled carbon nanotube composite for the solid phase extraction of lead(II) in water samples, Talanta, 119 (2014) 447–451.

[11] Ak M., Sahmetlioglu E. and Toppare L., Synthesis, characterization and optoelectrochemical properties of poly(1,6-bis(2,5-di(thiophen-2-yl)-1*H*-pyrrol-1-yl)hexane) and its copolymer with EDOT, J. Electroanal. Chem., 621 (2008) 55–61.

[12] Sapp S.A., Sotzing G.A. and Reynolds J.R., High Contrast Ratio and Fast-Switching Dual Polymer Electrochromic Devices, Chem. Mater., 10 (1998) 2101-2108.

[13] Rault-Berthelot J., Raoult E. and Le Floch F., Synthesis and anodic oxidation of a dimer EDOT–dicyanomethylenefluorene and a trimer EDOT–dicyanomethylenefluorene–EDOT: towards mixed polymers with very low bandgap, J. Electroanal. Chem., 546 (2003) 29-34.

[14] Maier E., Rath T., Haas W.,Werzer O., Saf R., Hofer F., Meissner D., Volobujeva O., Bereznev S., Mellikov E., Amenitsch H., Resel R. and Trimmel G., CuInS$_2$–Poly(3-(ethyl-4-butanoate)thiophene) nanocomposite solar cells: Preparation by an in situ formation route, performance and stability issues, Sol. Energ. Mat. Sol. C., 95 (2011) 1354-1361.

[15] Madani A., Nessark B., Boukherroub R. and Chehimi M.M., Preparation and electrochemical behaviour of PPy–CdS composite films, J. Electroanal. Chem., 650 (2011) 176-181.

[16] Guptaa N., Grovera R., Singh Mehtab D. and Saxena K., A simple technique for the

fabrication of zinc oxide-PEDOT:PSS nanocomposite thin film for OLED application, Synthetic Met., 221 (2016) 261–267.

[17] Xu G.L., Li Y., Maa T., Ren Y., Wang H.H., Wang L., Wen J., Miller D., Amine K. and Chena Z., PEDOT-PSS coated ZnO/C hierarchical porous nanorods as ultralong-life anode material for lithium ion batteries, Nano Energy, 18 (2015) 253–264.

[18] Decremps F., Pellicer-Porres J., Saitta A. M., Chervin J.C. and Polian A., High-pressure Raman spectroscopy study of wurtzite ZnO, Phys

Antimutagenic and Multi-Biological Activities of *Smilax excelsa* L. Fruit Extract

Ecehan EFE[1] iD *, Emine YALÇIN[1*]* iD *, Kültiğin ÇAVUŞOĞLU[1]* iD

[1] Giresun University, Faculty of Arts and Science, Department of Biology, Giresun, TURKEY

Abstract. In this study, antimutagenic, antimicrobial and antioxidant activities of *Smilax excelsa* L. fruit extract were evaluated. The antimicrobial effect was investigated by disk diffusion method and the antimutagenic effect was investigated by Ames/Salmonella/microsom test. The antioxidant properties of S. excelsa fruit samples were determined by investigating the total phenolic, flavonoid contents and 1,1-diphenyl-2-picrylhydrazyl (DPPH) radical scavenging activity. It was observed that 200 mg plate^{-1} fruit extract was found to have a mutagenicity inhibition as 81% in the absence of S9 mixture and 67% in the presence of S9 mixture against *Salmonella typhimurium* TA1535. *S. excelsa* fruit extract produced an inhibition zone in the range of 11-16 cm against the tested microorganisms. Flavonoid and phenolic contents were found to be 0.7985±0.0124 mgQE 100 mL^{-1} and 11.9847±0.0041 mgGAE 100 mL^{-1} at the 200 mg mL^{-1} extract concentration, respectively. The DPPH removal rate was determined to be 55% at the 200 mg L^{-1} dose. As a result, it was observed that the *S. excelsa* fruit tissues exhibited a highly antimutagenic activity and has been determined as a potential natural antimicrobial and antioxidant source.

Keywords: Ames/Salmonella/microsomal test, antioxidant activity, disc diffusion test, *Smilax excelsa*.

Smilax excelsa L. Meyve Ekstresinin Antimutagenik ve Multi-Biyolojik aktiviteleri

Özet. Bu çalışmada, *Smilax excelsa* L. meyve ektraktının antimikrobiyal, antioksidan ve antimutajenik aktiviteleri araştırılmıştır. Antimikrobiyal aktivite disk difüzyon yöntemi ile antimutajenik aktivite ise Ames/Salmonella/mikrozom testi kullanılarak araştırılmıştır. *S. excelsa* meyve örneklerinin antioksidan özelliği ise toplam fenolik ve flavonoid içeriğinin tespiti ve 1,1-difenil-2-pikrilhidrazil (DPPH) giderme etkisi araştırılarak belirlenmiştir. Meyve ekstraktının 200 mg plak^{-1} dozunda *Salmonella typhimirium* TA1535 suşu ile S9 karışımı yokluğunda %81, S9 karışımı varlığında ise %67 oranında mutajenite inhibisyonu oluşturduğu belirlenmiştir. *S. excelsa* meyve eksraktının test edilen mikroorganizmalara karşı 11-16 cm aralığında inhibisyon zonu oluşturduğu gözlenmiştir. 200 mg mL^{-1} konsantrasyonunda ekstraktta flavonoid içeriği 0.7985±0.0124 mgQE 100 mL^{-1} olarak, fenolik içerik ise 11.9847±0.0041 mgGAE 100 mL^{-1} olarak tespit edilmiştir. 200 mg L^{-1} dozunda DPPH giderme oranı %55 olarak belirlenmiştir. Sonuç olarak, *S. excelsa* meyve dokularının yüksek antimutajenik aktivite sergilediği, potansiyel doğal bir antimutajenik ve antioksidan kaynak olduğu olduğu belirlenmiştir.

Anahtar Kelimeler: Ames/Salmonella/mikrozomal test, antioksidan aktivite, disk difüzyon testi, *Smilax excelsa*.

1. INTRODUCTION

The accelerated industrialization has increased the use of chemicals in various sectors, and this increase has brought the need for natural components that can eliminate the negative effects of the chemicals. Natural components that can reduce the toxicity of chemicals on living organisms can be consumed as a drug or as a diet in daily consumption. Different tissues of the plants play a protective role against many diseases such as acute/chronic diseases and degenerative defects resulting from the adverse effects of chemicals. This feature of plants is related to the active ingredients found in different tissues with different ratios. It is suggested that regular use of these active compounds in daily life may be effective in preventing cancer and genetic diseases [1, 2]. And also by this way, the secondary diseases caused by synthetic drugs, drug side effects and over-loading of the drug will be prevented [3, 4]. In this study, antimicrobial, antioxidant and antimutagenic activities of *S. excelsa* fruit extract were investigated.

Smilax excelsa L. belongs to the family of Smilacaceae, and these family members are woody, spiny, perennial plants that can be sized up to 15 m, with an average length greater than 3 m. In the Smilacaceae family *S. medica*, *S. ornata*, *S. officinalis*, *S. syphilitica*, *S. papyracea* species are grown in Central America, *S. aspera* and *S. excelsa* species are grown in Anatolia. *S. excelsa*, which is widespread throughout Northern Anatolia, has narrow, cylindrical roots and bakka type fruit [5, 6]. The shoots of *S. excelsa*, which is a spiny plant and started to give young shoots in spring, are consumed as vegetable. The rhizomes have various pharmacological properties such as immunomodulator, antibacterial, antifungal and antioxidant. *S. excelsa* has a variety of active ingredients. These active ingredients are responsible for the antitumor, anti-mutagenic, antibacterial, antifungal, antioxidant, anti-inflammatory properties of *Smilax* species. It is reported that *S. excelsa*, which is known for its blood cleaning and perspiration, is used for therapeutic purposes in the syphilis [7-9].

Because of its importance and frequently consumption in the Black Sea Region, antimicrobial, antioxidant and antimutagenic activities of *S. excelsa* fruit extract have been investigated. Antimicrobial activity was determined by disc diffusion method, antimutagenic activity was determined by Ames/Salmonella test, antioxidant activity was determined by total phenolic content, flavonoid content analysis and 1,1-diphenyl-2-picrylhydrazyl (DPPH) radical scavenging activity test.

2. MATERIALS AND METHODS

2.1. Sample Preparation and Extraction

S. excelsa fruit samples were dried under sterile conditions in an oven at 30°C. After grinding samples, 0.2 g of ground sample was extracted in 10 ml of methanol at room temperature for 24 hours in a shaking incubator. At the end of the incubation period, the extract was filtered to remove solid particles and the filtrate was centrifuged at 10000 rpm for 10 minutes. After centrifugation, the supernatant was evaporated by using liquid phase evaporator. Extracts were stored at -18°C and used for determine the antimicrobial, antioxidant and antimutagenic activity [10].

2.2. Antimicrobial Activity

The antimicrobial activity of *S. excelsa* fruit extract was determined by using disc diffusion method with the strains of *Escherichia coli*, *Pseudomonas aeruginosa*, *Staphylococcus aureus*, *Klebsiella pneumonia*, *Streptococcus mutans*, *Staphylococcus epidermidis*, *Candida albicans* and *Candida krusei*. Fresh inoculum of strains (10^7-10^8 pcs L^{-1}) was spread over the surface of Mueller Hinton Agar plates. The sterile filter paper and standart antibiotic discs (6 mm) were placed over the medium surface and 20 mg mL^{-1} extract were impregnated to free sterile discs (20 µl $disc^{-1}$). Plates were incubated for 1 hour at 4 °C and then for 18-24 hours at 37 °C [11]. At the end of the period, the inhibition zones formed around the disc were evaluated as mm.

2.3. Antioxidant Activity

2.3.1. Total Phenol and Flavonoid Determination

The phenolic content of *S. excelsa* fruit extract was determined by Folin-Ciocaltaeu method. Gallic acid was used as standard material with five different concentrations. For experimental procedures, 0.5 mL of the sample in 2.5 mL of Folin-Ciocaltaeu reagent (10%) and 7.5 mL of Na_2CO_3 (20%) were mixed in a test tube. The mixture was incubated at room temperature in the dark for 2 hours and then the absorbance was determined spectrophotometrically at 750 nm [12]. The total phenolic concentration was estimated as equivalent gallic acid (mg GAE 100 mL^{-1}).

For flavonoid determination, quercetin as a standard substance was prepared in methanol at concentrations of 50-200 mg L^{-1}. 10 mL of the sample was mixed with 1 mL of sodium nitrite (5%) and allowed to stand for 6 minutes, after 1 mL of aluminum nitrate (10%) was added. The mixture was left to stand for 6 min, 10 mL NaOH (4.3%) was added and then the volume was completed to 25 mL with dH2O. After incubation for 15 min at room temperature, the absorbance of the solution was determined spectrophotometrically at 510 nm [13]. Total flavonoid content was expressed in mg QE 100 mL^{-1}.

2.3.2. DPPH Assay

The DPPH method was used to determine the radical scavenging activity of the *S. excelsa* fruit extract. For this aim, fruit extracts, BHA and BHT solutions were prepared at a concentration of 50-200 mg L^{-1}. BHA and BHT were used as the standard substance. 80 μl of samples were mixed with 1185 μl DPPH ($6x10^{-5}$ M) solution. The mixture was allowed to stand in the dark for 60 minutes and at the end of time the absorbance of the solution was determined spectrophotometrically at 517 nm. DPPH radical scavenging activity as % Inhibition was calculated from the following equation [14].

% Inhibition=Abs $_{control}$- Abs $_{sample}$ / Abs $_{control}$ x100

2.4. Antimutagenic Activity

The antimutagenic activities of *S. excelsa* fruit extracts were determined by Ames/Salmonella test with the strains of mutant *S. typhimurium* TA1535 [15, 16]. For this aim, the mutagenity inhibition rates of extract against mutagenic substances have been investigated. 100 μl bacterial strain (1-2 x 10^9 bacteria mL^{-1}), 100 μl extract, 100 μl sodium azide as positive mutagen solution and 500 μl S9 mixture or phosphate buffer (for S9 (-) assay) were added to 2.5 ml top agar. The mixture was shaken with vortex and poured onto the surface of minimal glucose agar plates and the plates were allowed to incubate at 37 ° C for 48-72 hours. At the end of the incubation period the revertant colonies were counted by Stuart Colony meter. The rate of mutagenity in plates without extract, only contain bacterial strain and mutagenic material, was accepted as 100% (ie 0% antimutagenicity). The antimutagenic activities of the extracts were evaluated by using the following equation.

Antimutagenic activity (%)=[(A-B)/(A-C)] × 100

(A: Numbers of revertant colonies in bacteria and mutagen containing plate; B: Numbers of revertant colonies in bacteria, mutagen and extract containing plate; C: Numbers of self-returning revertant colonies).

3. RESULTS

In this study, antimicrobial, antioxidant and antimutagenic activities of *S. excelsa* fruit extract were investigated. The antimicrobial activity of *S. excelsa* fruit extract is given in Figure 1. To determine the change of antimicrobial activity according to microorganism species, disc diffusion method was tested against fungi, gram positive and gram negative bacteria. It was determined that *S. excelsa* fruit extract showed different antimicrobial activity against all tested microorganisms. The maximum antimicrobial effect of extract was obtained with a 16 mm inhibition zone against *E. coli*. The lowest antimicrobial effect was obtained with 11 mm inhibition zone against *S. aureus*. In general, it has been determined that fruit extracts are more effective against gram-negative bacteria compared to gram-positives and fungi. It is also an essential

point that the extracts have an antimicrobial activity against *Klebsiella pneumonia* and *Candida albicans* strains in which the test antibiotics are ineffective.
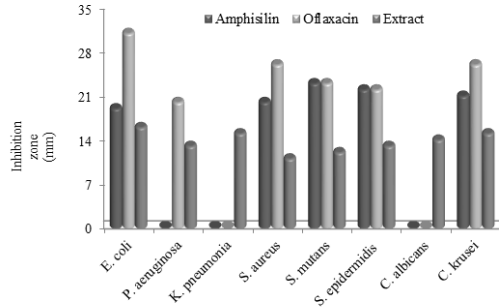
**Figure 1.** The antimicrobial activity of *S. excelsa* fruit extract

The phenolic content of *S. excelsa* fruit extract was determined by Folin-Ciocaltaeu. Phenolic and flavonoid contents were investigated at a concentration of 200 mg mL^{-1}. The flavonoid content of extract was determined as 0.7985±0.0124 mgQE 100 mL^{-1} and the phenolic content was determined as 11.9847±0.0041 mgGAE 100 mL^{-1}.

One of the methods used for evaluating antioxidant activity is the DPPH radical scavenging activity assay. DPPH removal activity of *S. excelsa* fruit extract investigated in this study is given in Figure 2. Standard substances and extract were tested at concentrations of 50-200 mg L^{-1} and it was determined that the DPPH removal efficiency increased with increasing the concentration of each sample. The highest radical scavenging activity for BHA, BHT and fruit extracts at the concentration of 200 mg L^{-1} was found as 85%, 80% and 55%, respectively. The DPPH scavenging activity obtained at the 200 mg L^{-1} dose of the fruit extract was 1.7 times higher than the effect obtained at the concentration of 50 mg L^{-1}. The DPPH removal effect of the extract may be associated with the active ingredients, especially the antioxidant phenolic compounds.
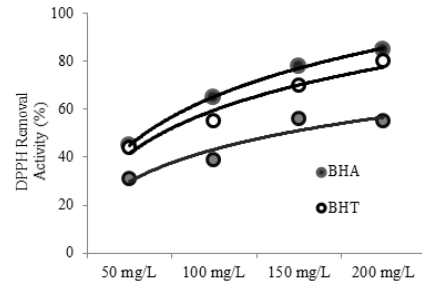

Figure 2. DPPH removal activity of *S.excelsa* fruit extract

The antimutagenicity test results of *S. excelsa* fruit extract against TA 1535 strain are given in Figure 3 and 4. It was determined that 200 mg plate^{-1} fruit extract caused an inhibition rate of 81% in the absence of S9 mixture. The inhibition rate increased with the extract dose increased and the inhibition rate obtained with 200 mg plate^{-1} extract was found to be 1.37 times higher than that obtained with 50 mg plate^{-1} extract. When the percentages of inhibition were evaluated, it was determined that the 50-200 mg plate^{-1} extracts exhibited strong antimutagenic activity in the absence of S9 mixture. In the presence of S9 mixture, the fruit extract was resulted an inhibition rate of 67% against TA 1535 strain at 200 mg plate^{-1} extract. It was determined that the inhibition rate obtained with the 200 mg plate^{-1} extract increased by 1.48 times as much as that obtained with the 50 mg plate^{-1}. It was also determined that the inhibition results obtained in the presence of the S9 mixture are lower than those obtained in the absence of the S9 mixture.
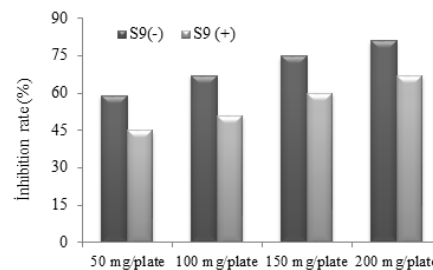
Figure 3. Antimutagenic activities of *S. excelsa* fruit extracts against TA 1535
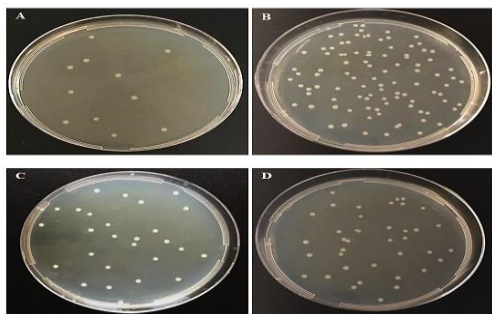
Figure 4. A: self-returning revertant colonies, B: revertant colonies in bacteria and mutagen containing plate, C: revertant colonies in bacteria, mutagen and 200 mg plate[-1] extract containing plate in the absence of S9 mixture, D: revertant colonies in bacteria, mutagen and 200 mg plate[-1] extract containing plate in the presence of S9 mixture

4. DISCUSSION

With the increase of mutagenic, carcinogenic and contaminant chemical compounds, the importance of antimicrobial, antioxidant and antimutagenic compounds in the natural structure is increasing day by day. There are many studies on the antimicrobial, antiviral and antioxidant effects of naturally active compounds. However, the increasing frequency of cancer diseases increases the importance of natural products with anticarcinogenic or antimutagenic activity. Although there are many studies on antimutagenic effects but the diversity of natural sources makes these studies insufficient. In this study, antimicrobial, antioxidant and antimutagenic activities of *S. excelsa* fruit extract were investigated. It was determined that the fruit extract provided 81% protection against mutagenity in the absence of S9 mixture at 200 mg plate[-1] dose. In the presence of S9 mixture, it was determined that it provides 67% protection. Based on the inhibition percentages, it was determined that *S. excelsa* fruit extracts exhibited strong antimutagenic activity. In literature, catechin [8], trans-resveratrol, 5-O-caffeoylbicimic acid, 6-O-caffeoyl-β-D-fructofuranosyl-(2→1)-α-D glucopyranozide [17] and phytochemical compounds [18] are reported in *Smilax* tissues. And also in this study the presence of phenolic and flavonoid compounds in

S. excelsa fruit extracts was determined. These compounds have antioxidant effect and provide protection against oxidative stress and thus show anti-mutagenic properties.

S. excelsa fruit extract showed different antimicrobial effect with the 11-16 cm inhibition zone range against tested microorganisms. This antimicrobial activity was comparable to the effect of the ampicillin and oflaxacin antibiotics tested in the study. It was determined that the oflaxacin did not show activity against *K. pneomoniae* and *C. albicans* and ampicillin did not show activity against *P. aureginosa*, *K. pneomoniae* and *C. albicans*. However, the fruit extract was also effective on these bacteria and showed a broad-spectrum antimicrobial activity. The antimicrobial activity exhibited by *Smilax* species is due to phenolic acids and the structure of the phenol group is very important in antimicrobial action. Oxygen-free phenolic compounds having a C3 side chain are classified as essential oils and exhibit high antimicrobial activity [19]. Ozsoy et al. [8] reported the presence of catechin in *S. excelsa* tissues. The antimicrobial effect observed in this study can be related to catechin which is the most reduced form of the C_3 unit from the flavonoid compounds. Another important detail of this study is that fruit extract exhibit higher antibacterial properties against gram negative bacteria than gram positive bacteria. This result can be explained by the structural differences of gram-positive and gram-negative cells. Gram-positive bacteria have thick peptidoglycan layer, while gram-positive bacteria have a thin layer. This layer acts as a barrier to reduce the transport of external molecules to the gram positive bacteria and reduces the toxic effects of extract. This structural differentiation makes the gram positives more resistant to antimicrobial agents and the gram negatives to be more sensitive to these agents [20].

The antioxidant property of *S. excelsa* fruit extract was evaluated by the DPPH removal activity, total phenolic and flavonoid content of extract. In 200 mg mL^{-1} *S. excelsa* fruit extract concentration, flavonoid and phenolic content were determined

as 0.7985±0.0124 mgQE 100mL^{-1} and 11.9847±0.0041 mgGAE 100 mL^{-1}, respectively. The DPPH removal rate of BHA, BHT and S. *excelsa* fruit extract was found to be 85%, 80% and 55%, respectively. In the literature, antioxidant activity activities of *S.excelsa* and different *Smilax* species have been reported. Ozsoy et al. [8] reported that *S. excelsa* leaf extracts have a total phenol content of 8.8–35.7 GAE mg g^{-1} and a flavonoid content of 0.61–28.7 mg g^{-1} catechin equivalent. Khaligh et al. [17] reported the isolation of trans-resveratrol, 5-O-caffeoylshikimic acid, 6-O-caffeoyl-β-D-fructofuranosyl- (2→1) -α-D glucopyranozide structures from *S. excelsa* tissues. And the antioxidant activity exhibited by the tissues was associated with these structures. The flavonoid and phenolic structures presence in the *Smilax* tissues have an active role in the prevention of diseases such as cardiovascular diseases, cancer and chronic inflammation by preventing free oxygen radicals and lipid peroxidation [21]. It is also known that flavonoids and phenolic compounds inhibit the enzymatic system involved in the radical formation of flavonoids, and decrease lipid oxidation by binding metal ions [9]. And also many studies have shown that these structures have antimutagenic and anticarcinogenic effects [18, 22].

5. CONCLUSION

Plant tissues have been used for many years in the treatment of various diseases. Increased industrial pollution and the access of contaminants to people through food chain has increased the risk of many diseases, especially cancer. In parallel with this increase, the use of synthetic drug substances increased, the side effects of drugs and the formation of various resistance mechanisms of microorganisms have brought the usage of plants for therapeutic purposes. For this aim, in literature many effects of plant tissues such as antifungal, antioxidative, antibacterial, antimutagenic, antiviral and anticarcinogenic have been studied. In this study, antimicrobial, antioxidant and antimutagenic activities of *S. excelsa* fruit exract, which is consumed as food in the Black Sea

Region, were investigated. It was determined that the fruit extracts exhibited antimicrobial activity against *E.coli*, *P. aureginosa, S. aureus, K. pneumoniae, S. mutans, S. epidermidis, C. albicans* and *C. krusei*. And also, fruit extracts have a high antioxidant phenolic and flavonoid content and have a significant DPPH removal effect as 85%. In the antimutagenic activity assay, it was determined that the fruit extract inhibited mutagenicity in the 67-81% range and could be classified as a strong antimutagenic compound. As a result, it was determined that *S. excelsa* fruit tissues are a potential natural antimicrobial and antimutagenic source and exhibit strong antioxidant activity.

REFERENCES

[1] Stein C.M., Are herbal products dietary supplements or drugs? An important question for public safety, Clin. Pharmacol. Ther., 71-6 (2002) 411-413.

[2] Süzer Ö., Serotonin, Serotonin Reseptörlerinin Baslica Etki Yerleri Ve Fonksiyonlari. Süzer Farmakoloji. 3. baskı. Istanbul: Klinisyen Tip Kitabevleri, (2005) 150-154.

[3] IARC Monographs on the Evaluation of Carcinogenic Risks to Humans. Address: https://monographs.iarc.fr/wp-content/uploads/2018/06/mono94-4.pdf. Retrieved January 9, 2019.

[4] Navarro M., Montilla M.P., Cabo M.M., Galisteo M., Cáceres A., Morales C. and Berger I., Antibacterial, antiprotozoal and antioxidant activity of five plants used in Izabal for infectious diseases, Phytother. Res., 1 (2003) 325–329.

[5] Lee S.E., Ju E.M. and Kim J.H., Free radical scavenging and antioxidant enzyme fortifying activities of extracts from *Smilax china* root, Exp. Mol. Med., 33 (2001) 263-268.

[6] Jiang J. and Xu Q., Immunomodulatory activity of the aqueous extract from rhizome of Smilax glabra in the later phase of adjuvant-induced arthritis in rats, J. Ethnopharmacol., 85 (2003) 53-59.

[7] Ozbucak T.B., Ergen A.O. and Yalcin S., Nutrition contents of the some wild edible

plants in Central Black Sea region of Turkey, IJNES, 1 (2007) 11-13.

[8] Ozsoy N., Can A., Yanardag R. and Akev N., Antioxidant activity of *Smilax excelsa* L. leaf extracts, Food Chem., 110 (2008) 571-583.

[9] Ozsoy N., Okyar A., Arda-Pirincci P., Can A., Bolkent S. and Akev N., Evaluation of *Smilax excelsa* L. use in experimentally induced nephrotoxicity, J. Fac. Vet. Med. Kafkas University, 19-5 (2013) 807-814.

[10] Efe E. *Smilax excelsa* L. meyve ekstrelerinin antimutajenik, antimikrobiyal ve antioksidan aktivitelerinin araştırılması. Giresun University Graduate School of Natural and Applied Sciences, Deparment of Biology, Master Thesiss. 16 (2017).

[11] Cooper D.G. and Paddock P.A., Production of a biosurfactant from *Torulopsis bombicola*, Appl. Environ. Microbiol., 47-1 (1984) 173-176.

[12] Singleton V.L. and Rossi J.A., Colorimetry of total phenolics with phosphomolybdic-phosphotungstic acid reagents, Am. J. Enol. Viticult., 16 (1965) 144-158.

[13] Zhishen J., Mengcheng T. and Jianming W., The determination of flavonoid contents on mulberry and their scavenging effects on superoxide radical, Food Chem., 64 (1999) 555-559.

[14] Yen G.C. and Duh P.D., Scavenging effect of methanolic extracts of peanut hulls on free-radical and active oxygen species, J. Agric. Food Chem., 42 (1994) 629-632.

[15] Maron D.M. and Ames B.N., Revised methods for the mutagenicity test, Mutat. Res., 113 (1983) 173-215.

[16] Uysal A., Zengin G., Durak Y. and Aktumsek A., Screening for antioxidant and antimutagenic properties of extracts from *Centaurea pterocaula* as well as their enzyme inhibitory potentials, Marmara Pharm. J., 20-3 (2016) 232-242.

[17] Khaligh P., Salehi P., Farimani M.M., Ali-Asgari S., Esmaeili M.A. and Ebrahimi S.M., Bioactive compounds from *Smilax excelsa* L, J. Iran Chem. Soc., 13 (2016) 1055-1059.

[18] Ivanova A., Mikhova B., Kostova I. and Evstatieva L., Bioactive chemical constituents from *Smilax excels*, Chem. Nat. Compd., 46 (2010) 295-297.

[19] Schultes R.E., The Kingdom of Plants. In: Thomson WAR., editor. Medicines from the earth. New York: McGraw-Hill Book Co, 1978; pp 208.

[20] Feng Q.L., Wu J., Chen G.Q., Cui F., Kim T.N., and Kim J.O., A mechanistic study of the antibacterial effect of silver ions on *Escherichia coli* and *Staphylococcus aureus*, J. Biomed. Mate. Res., 52-4 (2000) 662-668.

[21] Lu C.L., Zhu W., Wang M., Xu X.J. and Lu C.J., Antioxidant and anti-inflammatory activities of phenolic-enriched extracts of *Smilax glabra*, J. Evid. Based Complement Altern. Med., 2014 (2014) 1-8.

[22] Shuo X., Ming-Ying S., Guang-Xue L., Feng X., Xuan W., Cheng-Chao S. and Shao-Qing C., Chemical Constituents from the Rhizomes of *Smilax glabra* and their antimicrobial activity, Molecules, 18 (2013) 5265-5287.

Cumhuriyet Science Journal

CSJ

Some φ-Fixed Point Results in b−Metric Spaces and Applications

Müzeyyen SANGURLU SEZEN iD

University of Giresun, Department of Mathematics, Giresun, TURKEY

Abstract. The purpose of this study is to introduce the existence and uniqueness of φ-fixed point for some new contractions in complete b-metric spaces. Firstly, in this paper, we presented new definitions called $(F, \alpha, \varphi, \theta)_s$ and $(F, \alpha, \varphi, \theta)_s$ -weak contractions in complete b-metric spaces as a generalization of metric spaces. Later, we proved φ-fixed point theorems for $(F, \alpha, \varphi, \theta)_s$ and $(F, \alpha, \varphi, \theta)_s$-weak contractions in complete b-metric spaces. As applications, we derived some fixed point results in complete partial b-metric spaces as a generalization of partial metric spaces. The presented theorems extend and generalize some φ-fixed point results which are known in the literature. Also, some results in this paper generalizes many existing some fixed point results in the literature.

Keywords: b-metric space, φ-fixed point, $(F, \alpha, \varphi, \theta)_s$-contraction.

b-Metrik Uzaylarda φ-Sabit Nokta Teoremleri ve Uygulamaları

Özet. Bu çalışmanın amacı, b-metrik uzaylarda bazı yeni büzülmelerin φ-sabit noktalarının varlığını ve tekliğini göstermektir. Öncelikle, bu çalışmada, b-metrik uzaylarda $(F, \alpha, \varphi, \theta)_s$ ve $(F, \alpha, \varphi, \theta)_s$ –zayıf büzülme isimli iki tanım verilmiştir. Sonra, b-metrik uzaylarda bu tanımlar için φ-sabit nokta teoremleri ispatlanmıştır. Uygulama olarak, kısmi metrik uzayların genelleştirmesi olan tam kısmi b-metrik uzaylarda bazı sabit nokta sonuçları verilmiştir. Bu çalışmada elde edilen teoremler, literatürde bilinen φ-sabit nokta sonuçlarından daha genel ve geniş olduğu gibi, literatürde var olan bazı sabit nokta sonuçlarından da daha geneldir.

Anahtar Kelimeler: b-metrik uzay, φ-sabit nokta, $(F, \alpha, \varphi, \theta)_s$-büzülme.

1. INTRODUCTION

The Banach contraction principle is one of the most important subjects in mathematics. By using this principle, most authors have proved several fixed point theorems for various mappings in several metric spaces [1-3,5,6,8-11,16-23]. Bakhtin [12] and Czerwik [21] introduced b-metric spaces as a generalization of metric spaces and proved the contraction mapping principle in b-metric spaces that is an extension of the Banach contraction principle in metric spaces. Since then, a number of authors have investigated fixed point theorems in b-metric spaces [13, 14, 24].

On the other hand, Jleli, Samet and Vetro [13] introduced the concept of φ-fixed point and established some existence results of φ-fixed points for various classes of operators in metric spaces. Samet, Vetro C. and Vetro P. [4] introduced the notion of α−admissible mapping in metric spaces.

Later, Sintunavarat [27] introduced the concepts of α-admissible mapping type S, as some generalizations of α-admissible mapping and then he proved some fixed point theorems by using his new types of α-admissibility mapping in b-metric spaces.

In this paper, we introduced some new mappings satisfying $(F, \alpha, \varphi, \theta)_s$-contraction and $(F, \alpha, \varphi, \theta)_s$-weak contraction and proved some new φ-fixed point theorems in b-complete metric spaces. The presented theorems extend and generalize the φ-fixed point results. As applications of the obtained results, we presented some fixed point theorems in partial b-metric spaces are derived from our main theorems.

2. PRELIMINARIES

Definition 1. [21] Let X be a nonempty set and s ≥ 1 a real number. A mapping $d_b : X \times X \rightarrow [0, \infty)$ is called a b-metric if for all $x, y, z \in X$, the following conditions are satisfied:

(i) $d_b(x, y) = 0$ if and only if $x = y$,

(ii) $d_b(x, y) = d_b(y, x)$,

(iii) $d_b(x, z) \leq s[d_b(x, y) + d_b(y, z)]$.

In this case, (X, d_b) is called a b-metric space.

Definition 2. [7] A sequence $\{x_n\}$ in a b-metric space (X, d_b) is said to be:

(i) b-convergent to a point $x \in X$ if $\lim_{n \to \infty} d_b(x_n, x) = 0$.

(ii) A sequence $\{x_n\}$ in a b-metric space (X, d_b) is called a Cauchy sequence if $\lim_{n,m \to \infty} d_b(x_n, x_m) = 0$.

(iii) A b-metric space (X, d_b) is called complete if every Cauchy sequence $\{x_n\}$ in X b-converges to a point $x \in X$.

(iv) A function $f : X \rightarrow Y$ is b-continuous at a point $x \in X$ if $\{x_n\} \subset X$ b-converges to x, then $\{fx_n\} \subset Y$ b-converges to fx, where (Y, ρ) is a b-metric space.

Definition 3. [27] Let X be a nonempty set and $s \geq 1$ a given real number. Let $\alpha : X \times X \rightarrow [0, \infty)$ and $T : X \rightarrow X$ be mappings. We say T is an α-admissible mapping type S if for all $x, y \in X, \alpha(x, y) \geq s$ leads to $\alpha(Tx, Ty) \geq s$. In particular, T is called α-admissible mapping if s = 1.

Definition 4. [26] Let $s \geq 1$ be a real number. A mapping $\phi : [0, \infty) \rightarrow [0, \infty)$ is called a (b)-comparison function if

(b1) ϕ is monotone increasing,

(b2) there exists $p_0 \in N, a \in (0,1)$ and a convergent series of nonnegative terms $\sum_{p=1}^{\infty} v_p$ such that $b^{p+1}\phi^{p+1}(t) \leq ab^{p+1}\phi^p(t) + v_p$, for $p \geq p_0$ and any $t \in [0, \infty)$.

Lemma 5. [25] If $\phi : [0, \infty) \rightarrow [0, \infty)$ is a (b)-comparison function, then;

(1) the series $\sum_{p=0}^{\infty} b^p \phi^p(t)$ converges for any $t \in R^+$,

(2) the function $s_b : [0, \infty) \rightarrow [0, \infty)$ defined by $s_b(t) = \sum_{p=0}^{\infty} b^p \phi^p(t), t \in [0, \infty)$, is increasing and continuous at 0.

Lemma 6. [15] Let $\phi : [0, \infty) \rightarrow [0, \infty)$ be (b)-comparison function with constant $s \geq 1$ and $a_n \in R^+, n \in N$ such that $a_n \rightarrow 0, as \, n \rightarrow \infty$ then $\sum_{p=0}^{n} s_{n-p} \phi^{n-p}(t) \rightarrow 0, as \, n \rightarrow \infty$.

Let (X, d) be a metric space, $\varphi : X \to [0, \infty)$ be a given function and $T : X \to X$ be an operator. The set of all fixed points of the operator T will be denoted by

$$F_T = \{x \in X : Tx = x\}.$$

The set all zeros of the function φ will be denoted by

$$Z_\varphi = \{x \in X : \varphi(x) = 0\}.$$

Definition 7. [13] An element $z \in X$ is said to be a φ-fixed point of the operator T if and only if $z \in F_T \cap Z_\varphi$.

Definition 8. [13] T is a φ-Picard operator if and only if

(i) $F_T \cap Z_\varphi = \{z\}$,

(ii) $x_n \to z$ as $n \to \infty$, for all $n \in N$.

Definition 9. [13] T is a weakly φ-Picard operator if and only if

(i) $F_T \cap Z_\varphi = \emptyset$,

(ii) the sequence $\{x_n\}$ converges for each $x \in X$ and the limit is a φ-fixed point of the operator T.

We denote by $\mathcal{F}$ the set of functions $F : [0, \infty)^3 \to [0, \infty)$ satisfying the following conditions:

(F1) $max\{a, b\} \leq F(a, b, c)$ for all $a, b, c \in [0, \infty)$,

(F2) $F(0,0,0) = 0$,

(F3) F is continuous.

The following functions are given as examples:

(i) $F(a, b, c) = a + b + c$,

(ii) $F(a, b, c) = max\{a, b\} + c$,

(iii) $F(a, b, c) = a + a^2 + b + c$.

Definition 10. [13] Let (X, d) be a metric space, $\varphi : X \to [0, \infty)$ be a given function and $F \in \mathcal{F}$. The operator $T : X \to X$ is an (F, φ)- contraction if and only if for $x, y \in X$

$$F\big(d(Tx, Ty), \varphi(Tx)\varphi(Ty)\big) \leq kF\big(d(x, y), \varphi(x), \varphi(y)\big)$$

for some constant $k \in (0,1)$.

Definition 11. [13] Let (X, d) be a metric space, $\varphi : X \to [0, \infty)$ be a given function and $F \in \mathcal{F}$. The operator $T : X \to X$ is an (F, φ)-weak contraction if and only if for $x, y \in X$

$$F\big(d(Tx, Ty), \varphi(Tx)\varphi(Ty)\big) \leq kF(d(x, y), \varphi(x), \varphi(y))$$

$$+L(F(d(y, Tx), \varphi(y), \varphi(Tx)) - F(0, \varphi(y), \varphi(Tx))).$$

for some constant $k \in (0,1)$ and $L \geq 0$.

3. MAIN RESULTS

In this work, we use J_b to denote the class of all (b)-comparison functions $\theta : [0, \infty) \rightarrow [0, \infty)$ such that $\theta(t) < t$ for all $t > 0$ unless and until it is stated otherwise.

Definition 12. Let (X, d_b) be a b-metric space with coefficient $s \geq 1$, $\alpha : X \times X \rightarrow [0, \infty)$ be a mapping and $\varphi : X \rightarrow [0, \infty)$ be lower semi continuous function, $\theta \in J_b$ and $\varepsilon > 1$. A mapping $T : X \rightarrow X$ is said to be an $(F, \alpha, \varphi, \theta)_s$-contraction mapping if

$x, y \in X$ with $\alpha(x, y) \geq s \Rightarrow$

$$s^\varepsilon F\big(d_b(Tx, Ty), \varphi(Tx)\varphi(Ty)\big) \leq \theta\left(F\big(d_b(x, y), \varphi(x), \varphi(y)\big)\right). \tag{3.1}$$

Theorem 13. Let (X, d_b) be a complete b-metric space with coefficient $s \geq 1$ and $T : X \rightarrow X$ be α-admissible mapping type S. Suppose that the following conditions hold:

(1) there exists $x_0 \in X$ such that $\alpha(x_0, Tx_0) \geq s$,

(2) T is an $(F, \alpha, \varphi, \theta)_s$- contraction mapping,

(3) if $\{x_n\}$ is a sequence in X such that $\alpha(x_n, x_{n+1}) \geq s$ and $x_n \rightarrow x$ then $\alpha(x_n, x) \geq s$ for all $n \in N$.

Then

(i) $F_T \subseteq Z_\varphi$,

(ii) T is φ- Picard operator. Moreover, if $\alpha(x, y) \geq s$ for all $x, y \in F_T$, then T has a unique φ-fixed point.

Proof. (i) Assume that $\xi \in X$ is a fixed point of T such that $\alpha(\xi, \xi) \geq s$. Applying (3.1) with $x = y = \xi$, we obtain

$$F(0, \varphi(\xi), \varphi(\xi)) \leq s^\varepsilon F(0, \varphi(\xi), \varphi(\xi))$$

$$\leq \theta\left(F\big(0, \varphi(\xi), \varphi(\xi)\big)\right). \tag{3.2}$$

Then we get

$$F\big(0, \varphi(\xi), \varphi(\xi)\big) \leq s^\varepsilon F\big(0, \varphi(\xi), \varphi(\xi)\big) \leq \theta(F(0, \varphi(\xi), \varphi(\xi)))$$

then we have

$$F(0, \varphi(\xi), \varphi(\xi)) \leq \theta\left(F\big(0, \varphi(\xi), \varphi(\xi)\big)\right).$$

From the property of θ, we have

$$F(0, \varphi(\xi), \varphi(\xi)) = 0. \tag{3.3}$$

On the other hand, from (F1), we have

$$\phi(\xi) \leq F\big(0, \varphi(\xi), \varphi(\xi)\big). \tag{3.4}$$

From (3.3) and (3.4), we obtain $\varphi(\xi) = 0$, which proves (i).

(ii) Let $x_0 \in X$ be such that $\alpha(x_0, Tx_0) \geq s$. Define a sequence $\{x_n\}$ by $x_{n+1} = Tx_n$ for all $n \in N$. Since T is an α-admissible mapping and $\alpha(x_0, x_1) = \alpha(x_0, Tx_0) \geq s$, we deduce that

$\alpha(x_1, x_2) = \alpha(Tx_0, Tx_1) \geq s$. Continuing this process, we get $\alpha(x_n, x_{n+1}) \geq s$ for all $n \in N \cup \{0\}$. If $x_n = x_{n+1}$, for some $n \in N$, then $x_n = Tx_n$. Thus, x_n is a fixed point of T.

Therefore, we assume that $x_n \neq x_{n+1}$, for all $n \in N$. Using condition (1) as $\alpha(x_{n-1}, x_n) \geq s$ for all

$n \in N$, we obtain

$$F(d_b(Tx_{n-1}, Tx_n), \varphi(Tx_{n-1}), \varphi(Tx_n))$$

$$\leq s^{\varepsilon} F(d_b(Tx_{n-1}, Tx_n), \varphi(Tx_{n-1}), \varphi(Tx_n))$$

$$\leq \theta(F(d_b(x_{n-1}, x_n), \varphi(x_{n-1}), \varphi(x_n)))$$

$$\leq \theta^n(F(d_b(x_0, x_1), \varphi(x_0), \varphi(x_1))). \tag{3.5}$$

Then from (F1), we have

$$max\{d_b(x_n, x_{n+1}), \varphi(x_n)\} \leq \theta^n\left(F(d_b(x_0, x_1), \varphi(x_0), \varphi(x_1))\right) \tag{3.6}$$

which implies

$$d_b(x_n, x_{n+1}) \leq \theta^n\left(F(d_b(x_0, x_1), \varphi(x_0), \varphi(x_1))\right). \tag{3.7}$$

Now we show that $\{x_n\}$ is a Cauchy sequence. Suppose that $k \in N$ such that $k > 0$. By using the triangle inequality, we get

$$d_b(x_n, x_{n+k}) \leq sd_b(x_n, x_{n+1}) + s^2 d_b(x_{n+1}, x_{n+2}) + \ldots + s^k d_b(x_{n+k-1}, x_{n+k}))$$

$$\leq s\theta^n\left(F(d_b(x_0, x_1), \varphi(x_0), \varphi(x_1))\right) + s^2\theta^{n+1}\left(F(d_b(x_0, x_1), \varphi(x_0), \varphi(x_1))\right) + \cdots$$
$$+ s^k\theta^{n+k-1}\left(F(d_b(x_0, x_1), \varphi(x_0), \varphi(x_1))\right)$$

$$= \frac{1}{s^{n-1}}[s^n\theta^n\left(F(d_b(x_0, x_1), \varphi(x_0), \varphi(x_1))\right) + s^{n+1}\theta^{n+1}\left(F(d_b(x_0, x_1), \varphi(x_0), \varphi(x_1))\right) +$$
$$\ldots + s^{n+k-1}\theta^{n+k-1}F(d_b(x_0, x_1), \varphi(x_0), \varphi(x_1)))].$$

We denote $S_n = \sum_{p=0}^n s^p\theta^p\left(F(d_b(x_0, x_1), \varphi(x_0), \varphi(x_1))\right)$ for $n \geq 1$, then we get

$$d_b(x_n, x_{n+k}) \leq \frac{1}{s^{n-1}}[S_{n+k-1} - S_{n-1}], \ n \geq 1, \ k \geq 1.$$

From Lemma 5, we have $\sum_{p=1}^n s^p\theta^p\left(F(d_b(x_0, x_1), \varphi(x_0), \varphi(x_1))\right)$ is convergent. Hence, there exists $S = \lim_{n \to \infty} S_n$ and from above the inequality, it implies that $\{x_n\}$ is a Cauchy sequence. Since (X, d_b) is complete, then the sequence $\{x_n\}$ converges some $z \in X$ and

$$\lim_{n \to \infty} d_b(x_n, z) = 0. \tag{3.8}$$

Now, we shall prove that z is a φ-fixed point of T. Observe that from (3.6), we have

$$\lim_{n\to\infty} \varphi(x_n) = 0. \tag{3.9}$$

Since φ is lower semi continuous, from (3.8) and (3.9) we obtain

$$\varphi(z) = 0. \tag{3.10}$$

Using (3.1) and from condition (3), we have

$$s^\varepsilon F(d_b(x_{n+1}, Tz), \varphi(x_{n+1}), \varphi(z)) \leq \theta(F(d_b(x_n, z), \varphi(x_n), \varphi(z))). \tag{3.11}$$

Letting $n \to \infty$ in 3.11, using 3.8, 3.9, 3.10, (F2) and the continuity of F, we have

$$s^\varepsilon F(\lim_{n\to\infty} d_b(x_{n+1}, Tz), 0, \varphi(z)) \leq \theta(F(0,0,0)) = 0$$

which implies from condition (F1) that

$$\lim_{n\to\infty} d_b(x_{n+1}, Tz) = 0. \tag{3.12}$$

On the other hand, from the condition (iii) of definition b-metric space, we have

$$d_b(z, Tz) \leq s[d_b(z, x_{n+1}) + d_b(x_{n+1}, Tz)].$$

Taking the limit as $n \to \infty$ in above the inequality, using (3.8) and (3.12), we get $d_b(z, Tz) = 0$, that is, $Tz = z$. Hence z is a φ-fixed point of T. Now we show that z is the unique φ-fixed point of T. Assume that $w \in X$ is another φ-fixed point of T. From (3.1), we have

$$s^\varepsilon F(d_b(Tz, Tw), \varphi(Tz), \varphi(Tw)) \leq \theta(F(d_b(z, w), \varphi(z), \varphi(w)))$$

and then

$$s^\varepsilon F(d_b(z, w), 0, 0) \leq \theta(F(d_b(z, w), 0, 0))$$

which implies $d_b(z, w) = 0$, that is $z = w$.

Definition 14. Let (X, d_b) be a b-metric space with coefficient $s \geq 1$, $\alpha: X \times X \to [0, \infty)$ be a mapping and $\varphi : X \to [0, \infty)$ be lower semi continuous function, $\theta \in J_b$ and $\varepsilon > 1$. A mapping $T: X \to X$ is said to be an $(F, \alpha, \varphi, \theta)_s$-weak contraction mapping if

$x, y \in X$ with $\alpha(x, y) \geq s \Rightarrow$

$$s^\varepsilon F(d_b(Tx, Ty), \varphi(Tx)\varphi(Ty)) \leq \theta(F(d_b(x, y), \varphi(x), \varphi(y)))$$

$$+ L\left(F(d_b(y, Tx), \varphi(y), \varphi(Tx)) - F(0, \varphi(y), \varphi(Tx))\right) \tag{3.13}$$

Theorem 15. Let (X, d_b) be a complete b-metric space with coefficient $s \geq 1$ and $T: X \to X$ be α-admissible mapping type S. Suppose that the following conditions hold:

(1) there exists $x_0 \in X$ such that $\alpha(x_0, Tx_0) \geq s$,

(2) T is an $(F, \alpha, \varphi, \theta)_s$-weak contraction mapping,

(3)) if $\{x_n\}$ is a sequence in X such that $\alpha(x_n, x_{n+1}) \geq s$ and $x_n \to x$ then $\alpha(x_n, x) \geq s$ for all $n \in N$.

Then

(i) $F_T \subseteq Z_\varphi$,

(ii) T is φ-weakly Picard operator. Moreover, if $\alpha(x, y) \geq s$ for all $x, y \in F_T$, then T has a unique φ-fixed point.

Proof. (i) Assume that $\xi \in X$ is a fixed point of T such that $\alpha(\xi, \xi) \geq s$. Applying (3.13) with $x = y = \xi$, we obtain

$$F\big(0, \varphi(\xi), \varphi(\xi)\big) \leq s^\varepsilon F\big(0, \varphi(\xi), \varphi(\xi)\big)$$

$$\leq \theta(F(0, \varphi(\xi), \varphi(\xi)))$$

$$+L(F(0, \varphi(\xi), \varphi(\xi)) - F(0, \varphi(\xi), \varphi(\xi)))$$

$$= \theta\left(F\big(0, \varphi(\xi), \varphi(\xi)\big)\right). \tag{3.14}$$

$$F\big(0, \varphi(\xi), \varphi(\xi)\big) \leq s^\varepsilon F\big(0, \varphi(\xi), \varphi(\xi)\big) \leq \theta(F(0, \varphi(\xi), \varphi(\xi)))$$

then we get

$$F(0, \varphi(\xi), \varphi(\xi) \leq \theta\left(F\big(0, \varphi(\xi), \varphi(\xi)\big)\right).$$

From Lemma 5, we have

$$F(0, \varphi(\xi), \varphi(\xi)) = 0. \tag{3.15}$$

On the other hand, from (F1), we have

$$\phi(\xi) \leq F\big(0, \varphi(\xi), \varphi(\xi)\big). \tag{3.16}$$

From (3.15) and (3.16), we obtain $\varphi(\xi) = 0$, which proves (i).

(ii) Let $x_0 \in X$ be such that $\alpha(x_0, Tx_0) \geq s$. Define a sequence $\{x_n\}$ by $x_n = Tx_{n-1}$ for all $n \in N$. Since T is an α-admissible mapping and $\alpha(x_0, x_1) = \alpha(x_0, Tx_0) \geq s$, we deduce that $\alpha(x_1, x_2) = \alpha(Tx_0, Tx_1) \geq 1$. Continuing this process, we get $\alpha(x_n, x_{n+1}) \geq s$ for all $n \in N \cup \{0\}$. If $x_n = x_{n+1}$, for some $n \in N$, then $x_n = Tx_n$. Thus, x_n is a fixed point of T.

Therefore, We assume that $x_n \neq x_{n+1}$, for all $n \in N$. Using condition (1) as $\alpha(x_{n-1}, x_n) \geq s$ for all $n \in N$, we obtain

$$F(d_b(Tx_{n-1}, Tx_n), \varphi(Tx_{n-1}), \varphi(Tx_n)) \leq s^\varepsilon F(d_b(Tx_{n-1}, Tx_n), \varphi(Tx_{n-1}), \varphi(Tx_n))$$

$$\leq \theta(F(d_b(x_{n-1}, x_n), \varphi(x_{n-1}), \varphi(x_n)))$$

$$+L(F(0, \varphi(Tx_{n-1}), \varphi(Tx_n))$$

$$-F(0, \varphi(Tx_{n-1}), \varphi(Tx_n)))$$

$$\leq \theta^{n}(F(d_b(x_0, x_1), \varphi(x_0), \varphi(x_1))). \qquad (3.17)$$

The rest of the proof follows using similar argument to proof of Theorem 13.

4. APPLICATIONS

In this section, we give some fixed point results in partial b-metric spaces, using the main results in the previous section.

Firstly, let us recall some basic definitions on partial b-metric spaces.

Definition 16. [23] Let X be a nonempty set and and $s \geq 1$ be a given real number.

A function $p_b: X \times X \rightarrow R^+$ is a partial b-metric if for all $x, y, z \in X$, the following

conditions are satisfied:

(p1) $x = y \Leftrightarrow p_b(x, x) = p_b(x, y) = p_b(y, y)$,

(p2) $p_b(x, x) \leq p_b(x, y)$,

(p3) $p_b(x, y) = p_b(y, x)$,

(p4) $p_b(x, y) \leq s(p_b(x, z) + p_b(z, y) - p_b(z, z)) + (\frac{1-s}{2})(p_b(x, x) + p_b(y, y))$.

Definition 17. [28] A sequence $\{x_n\}$ in a partial b-metric space (X, p_b) is said to be:

(i) p_b-convergent to a point $x \in X$ if $\lim_{n\to\infty} p_b(x, x_n) = p_b(x, x)$.

(ii) A sequence $\{x_n\}$ in a partial b-metric space (X, p_b) is called a Cauchy sequence if $\lim_{m,n\to\infty} p_b(x_n, x_m)$ exists and is finite.

(iii) A partial b-metric space (X, p_b) is called complete if every Cauchy sequence $\{x_n\}$ in X converges to a point $x \in X$ such that, $\lim_{m,n\to\infty} p_b(x_n, x_m) = \lim_{m,n\to\infty} p_b(x_n, x) = p_b(x, x)$.

Proposition 18. [28] Every partial b-metric p_b defines a b-metric d_{p_b}, where

$d_{p_b}(x, y) = 2p_b(x, y) - p_b(x, y) - p_b(y, y)$ for all $x, y \in X$.

Lemma 19. [28] Let (X, p_b) be a partial b-metric space. Then,

(i) A sequence $\{x_n\}$ in a partial b-metric space (X, p_b) is a Cauchy sequence if and only if it is a Cauchy sequence in the b-metric space (X, d_b).

(ii) A partial b-metric space (X, p_b) is complete if and only if the b-metric space (X, d_b) is complete.

(iii) Given a sequence $\{x_n\}$ in a partial b-metric space (X, p_b) and $x \in X$, we have that

$$\lim_{n\to\infty} p_b(x, x_n) = 0 \Leftrightarrow p_b(x, x) = \lim_{n\to\infty} p_b(x, x_n) = 0 = \lim_{m,n\to\infty} p_b(x_n, x_m) = 0$$

Now, we give our some results in partial b- metric spaces.

Theorem 20. Let (X, p_b) be a complete partial b- metric space and let $T: X \rightarrow X$ is a mapping,

$\alpha: X \times X \to [0, \infty)$ and $\theta \in J_b$. Assume that the following conditions hold:

(i) $\theta(2t) = 2\theta(t)$ for all $t \in [0, \infty)$,

(ii) For all $x, y \in X$, for $s \geq 1$ and for $\varepsilon > 0$,

$$s^{\varepsilon} p_b (Tx, Ty) \leq \theta(p_b(x, y)).$$

Then

(i) T has a unique fixed point $z \in X$.

(ii) $p_b(z, z) = 0$.

Proof. Let the metric d_{p_b} on X which is defined by

$$d_{p_b}(x, y) = 2p_b(x, y) - p_b(x, y) - p_b(y, y)$$

for all $x, y \in X$ and $\varphi(x) = p_b(x, x)$ for all $x \in X$. Let $F: [0, \infty)^3 \to [0, \infty)$ be defined by

$F(a, b, c) = a + b + c$. From (i) and (ii), it is easy to verify

$$s^{\varepsilon}[2p_b (Tx, Ty) - p_b(Tx, Tx) - p_b(Ty, Ty) + p_b(Tx, Tx) + p_b(Ty, Ty))]$$

$$\leq \theta(2p_b(x, y) - p_b(x, x) - p_b(y, y) + p_b(x, x) + p_b(y, y)).$$

Then, from above the inequality, we have

$$s^{\varepsilon} F(d(Tx, Ty), \varphi(Tx), \varphi(Ty)) \leq \theta(F(d(x, y), \varphi(x), \varphi(y))).$$

Then the hypothesis of Theorem 13 is satisfied and then T has a unigue φ-fixed point. Hence, T has a unique fixed point $z \in X$ such that $p_b(z, z) = 0$. Therefore, the proof is completed.

Theorem 21. Let (X, p_b) be a complete partial b- metric space and let $T: X \to X$ is a mapping,

$\alpha: X \times X \to [0, \infty)$ and $\theta \in J_b$. Assume that the following conditions hold:

(a) $\theta(2t) = 2\theta(t)$ for all $t \in [0, \infty)$,

(b) For all $x, y \in X$, for $s \geq 1$ and for $\varepsilon > 0$,

$$s^{\varepsilon} p_b(Tx, Ty) \leq \theta(p_b(x, y)) + L(p_b(Ty, Tx) - \frac{p_b(y, y) + p_b (Tx, Tx)}{2})$$

Then

(i) T has a unique fixed point $z \in X$.

(ii) $p_b(z, z) = 0$

Taking $\theta(t) = kt$, where $k \in [0,1)$ in Theorem 20 and 21, we obtain the following corollaries.

Corollary 22. Let (X, p_b) be a complete partial b- metric space and let $T: X \to X$ is a mapping such that for all $x, y \in X$ and for some constant $k \in [0,1)$

$$s^\varepsilon p_b(Tx, Ty) \leq k p_b(x, y).$$

Then T has a unique fixed point $z \in X$. Morever $p_b(z, z) = 0$.

Corollary 23. Let (X, p_b) be a complete partial b- metric space and let $T: X \to X$ is a mapping such that for all $x, y \in X$ and for some constant $k \in [0,1)$

$$s^\varepsilon p_b(Tx, Ty) \leq \theta(p_b(x, y)) + L(p_b(Ty, Tx) - \frac{p_b(y, y) + p_b(Tx, Tx)}{2})$$

Then T has a unique fixed point $z \in X$. Morever $p_b(z,z) = 0$.

REFERENCES

[1] Ansari A., Işık H. and Radenovic S., Coupled fixed point theorems for contractive mappings involving new function classes and applications, Filomat, 31-7 (2017), 1893-1907.

[2] Akbar A. and Gabeleh M., Global optimal solutions of noncyclic mappings in metric spaces, J. Optim. Theory Appl., 153 (2012), 298–305.

[3] Latif A., Roshan J. R., Parvaneh V. and Hussain N., Fixed point results via α-admissible mappings and cyclic contractive mappings in partial b-metric spaces, Journal of Inequalities and Appl, 2014-345 (2014).

[4] Samet B., Vetro, C. and Vetro P., Fixed point theorems for α-φ-contractive type mappings, Nonlinear Anal., 75 (2012), 2154-2165.

[5] Zhu C., Xu W., Chen C. and Zhang X., Common fixed point theorems for generalized expansive mappings in partial b-metric spaces and an application, Journal of Inequalities and Appl, 2014-475 (2014).

[6] Singh D., Chauhan V. and Wangkeeree R., Geraghty type generalized F-contractions andrelated applications in partial b-metric spaces, Int. J. of Analysis, Article ID 8247925, 14 pg. (2017).

[7] Huang, H., Deng G., Chen Z. and Radenovic S., On some recent fixed point results for α-admissible mappings in b-metric spaces, J. Comp. Anal.and Appl., 25-2 (2018).

[8] Işık H. and Kumam P., Fixed points under new contractive conditions via cyclic (α, β, r)-admissible mappings, Journal of Advanced Mathematical Studies, 11-1 (2018), 17-23.

[9] Isik, H., Hussain, N. and Kutbi, M.A., Generalized rational contractions endowed with a graph and an application to a system of integral equations, J. Comp. Anal.and Appl., 22-6 (2017), 1158-1175.

[10] Isik, H. and Radenovic, S., A new version of coupled fixed point results in ordered metric spaces with applications. UPB Scientific Bulletin, Series A: Applied Mathematics and Physics, 79-2 (2017), 131-138.

[11] Isik, H. and Turkoglu, D., Generalized weakly α-contractive mappings and applications to ordinary differential equations. Miskolc Mathematical Notes, 17-1 (2016), 365-379.

[12] Bakhtin I. A., The contraction principle in quasi-metric spaces, Funct. Anal., 30 (1989), 26-37.

[13] Jleli M., Samet B. and Vetro C., Fixed point theory in partial metric spaces via φ-fixed point's concept in metric spaces, Journal of Inequalities and Appl., 2014-426 (2014).

[14] Nazam M., Arshad M. and Park C., A common fixed point theorem for a pair of generalized contraction mappings with applications, J. Comp. Anal.and Appl., 25-3 (2018).

[15] Păcurar M., A fixed point result for φ-contractions on b-metric spaces without the boundedness assumption, Fasc. Math., 43 (2010), 127-137.

[16] Sezen M.S., $(F, \varphi, \alpha)_s$ -contractions in b-metric spaces, Journal of Linear and Topological Algebra, Accepted.

[17] Hussain N., Karapınar E., Salimi P. and Akbar F., α-admissible mappings and related fixed point theorems, Fixed Point Theory Appl., 2013- 114 (2013).

[18] Kumrod P. and Sintunavarat W., A new contractive condition approach to φ-fixed point results in metric spaces and its applications, J. Comp. Appl. Math., 311 (2017) 194-204.

[19] Miculescu R. and Mihail A., New fixed point theorems for set-valued contractions in b-metric spaces, J. Fixed Point Theory Appl., 19 (2017), 2153–2163.

[20] Banach S., Sur les opérations dans les ensembles abstraits et leurs applications aux équations intégrales, Fund. Math., 3 (1922), 133-181.

[21] Czerwik S., Contraction mappings in b-metric spaces and applications, Acta Math. Inform., Univ. Ostrav. 1, 5-11 (1993).

[22] Matthews S. G., Partial metric topology, Ann. N.Y. Acad. Sci., 728: 183–197. 10.1111/j.1749-6632.1994.tb44144.x (1994).

[23] Shukla S., Partial b-metric spaces and fixed point theorems, Mediterr. J. Math., 11 (2014), 703-711.

[24] Phiangsungnoen S., Sintunavarat W. and Kumam P., Fixed point results, generalized Ulam-Hyers stability and well-posedness via α-admissible mappings in b-metric spaces, Fixed Point Theory and Appl., 2014-188 (2014).

[25] Berinde V., Generalized contractions in quasimetric spaces, Seminar on Fixed Point Theory, 3 (1993), 3-9.

[26] Berinde V., Sequences of operators and fixed points in quasimetric spaces, Stud. Univ. "Babeş-Bolyai", Math., 16-4 (1996), 23-27.

[27] Sintunavarat W., Nonlinear integral equations with new admissibility types in b-metric spaces, J. Fixed Point Theory Appl., DOI 10.1007/s11784-015-0276-6, 20 pages.

[28] Mustafa Z., Roshan J. R., Parvaneh V. and Kadelburg Z., Some common fixed point results in ordered partial b-metric spaces, Journal of Inequalities and Appl., 2013-562 (2013).

Truncated Truncated Dodecahedron and Truncated Truncated Icosahedron Spaces

Ümit Ziya SAVCI[1] iD

[1]Kütahya Dumlupınar University, Educational Faculty, Department of Mathematics Education, Kütahya, Turkey

Abstract. The theory of convex sets is a vibrant and classical field of modern mathematics with rich applications. The more geometric aspects of convex sets are developed introducing some notions, but primarily polyhedra. A polyhedra, when it is convex, is an extremely important special solid in $\mathbb{R}^n$. Some examples of convex subsets of Euclidean 3-dimensional space are Platonic Solids, Archimedean Solids and Archimedean Duals or Catalan Solids. There are some relations between metrics and polyhedra. For example, it has been shown that cube, octahedron, deltoidal icositetrahedron are maximum, taxicab, Chinese Checker's unit sphere, respectively. In this study, we give two new metrics to be their spheres truncated truncated dodecahedron and truncated truncated icosahedron.

Keywords: Polyhedron, Metric, Truncated Truncated Dodecahedron, Truncated Truncated Icosahedron.

Truncated Truncated Dodecahedron ve Truncated Truncated Icosahedron Uzayları

Özet. Konveks kümeler teorisi, zengin uygulamalara sahip modern matematiğin canlı ve klasik bir alanıdır. Konveks kümelerin geometrik yönleri, bazı kavramlar, fakat öncelikle çokyüzlülerin tanıtılmasıyla geliştirilmiştir. Konveks olduğunda bir çokyüzlü, $\mathbb{R}^n$ de çok önemli bir özel cisimdir. Öklid 3 boyutlu uzayın konveks alt kümelerinin bazı örnekleri Platonik cisimler, Arşimet cisimleri ve Arşimet dualleri veya Katalan cisimleridir. Metriklerle çokyüzlüler arasında bazı ilişkiler vardır. Örneğin, küp, sekizyüzlü, deltoidal icositetrahedron'un sırasıyla, maksimum, Taksi, Çin dama uzaylarının birim küresi olduğu görülmektedir. Bu çalışmada, kürelerinin truncated truncated dodecahedron ve truncated truncated icosahedron olan iki yeni metrik tanıtıldı.

Anahtar Kelimeler: Çokyüzlü, Metrik, Truncated Truncated Dodecahedron, Truncated Truncated Icosahedron.

1. INTRODUCTION

The word polyhedron has slightly different meanings in geometry and algebraic topology. In geometry, a polyhedron is simply a three-dimensional solid which consists of a collection of polygons, usually joined at their edges. The term "polyhedron" is used somewhat differently in algebraic topology, where it is defined as a space that can be built from such "building blocks" as line segments, triangles, tetrahedra, and their higher dimensional analogs by "gluing them together" along their faces [1]. The word derives from the Greek poly(many) plus the Indo-European hedron(seat). A polyhedron is the three-dimensional version of the more general polytope which can be defined in arbitrary dimension. The plural of polyhedron is "polyhedra" (or sometimes "polyhedrons").Polyhedra have worked by people since ancient time. Early civilizations worked out mathematics as problems and their solutions. Polyhedrons

have been studied by mathematicians, geometers during many years, because of their symmetries. Recently, polyhedra and their symmetries have been cast in a new light by mathematicians.

A polyhedron is said to be regular if all its faces are equal regular polygons and the same number of faces meet at every vertex. Platonic solids are regular and convex polyhedra. Nowadays, some mathematicians are working platonic solid's metric [2,3]. A polyhedron is called semi-regular if all its faces are regular polygons and all its vertices are equal. Archimedian soldis are semi-regular and convex polyhedra.

Minkowski geometry is non-Euclidean geometry in a finite number of dimensions. Here the linear structure is the same as the Euclidean one but distance is not uniform in all directions. That is, the points, lines and planes are the same, and the angles are measured in the same way, but the distance function is different. Instead of the usual sphere in Euclidean space, the unit ball is a general symmetric convex set [4]. Some mathematicians have been studied and improved metric space geometry. According to mentioned researches it is found that unit spheres of these metrics are associated with convex solids. For example, unit sphere of maximum metric is a cube which is a Platonic Solid. Taxicab metric's unit sphere is an octahedron, another Platonic Solid. In [1,2,5,6,7,8,9,10,11,12] the authors give some metrics which the spheres of the 3-dimensional analytical space furnished by these metrics are some of Platonic solids, Archimedian solids and Catalan solids. So there are some metrics which unit spheres are convex polyhedrons. That is, convex polyhedrons are associated with some metrics. When a metric is given, we can find its unit sphere in related space geometry. This enforce us to the question "Are there some metrics whose unit sphere is a convex polyhedron?". For this goal, firstly, the related polyhedra are placed in the 3-dimensional space in such a way that they are symmetric with respect to the origin. And then the coordinates of vertices are found. Later one can obtain metric which always supply plane equation related with solid's surface.

In this study, we introduce two new metrics, and show that the spheres of the 3-dimensional analytical space furnished by these metrics are truncated truncated dodecahedron and truncated truncated icosahedron. Also we give some properties about these metrics.

2. TRUNCATED TRUNCATED DODECAHEDRON METRIC AND SOME PROPERTIES

It has been stated in [13], there are many variations on the theme of the regular polyhedra. First one can meet the eleven which can be made by cutting off (truncating) the corners, and in some cases the edges, of the regular polyhedra so that all the faces of the faceted polyhedra obtained in this way are regular polygons. These polyhedra were first discovered by Archimedes (287-212 B.C.E.) and so they are often called Archimedean solids. Notice that vertices of the Archimedean polyhedra are all alike, but their faces, which are regular polygons, are of two or more different kinds. For this reason they are often called semiregular. Archimedes also showed that in addition to the eleven obtained by truncation, there are two more semiregular polyhedra: the snub cube and the snub dodecahedron.

Five Archimedean solids are derived from the Platonic solids by truncating (cutting off the corners) a percentage less than 1/2 [14,15]. Two of them are the truncated dodecahedron and the truncated icosahedron.

One of the solids which is obtained by truncating from another solid is the truncated truncated dodecahedron. It has 12 pent-symmetric 20-gonal faces, 20 regular hexagonal faces, 60 isosceles triangular faces, 180 vertices and 270 edges. The truncated truncated dodecahedron can be obtained by two times truncating operation from dodecahedron. Truncated dodecahedron appears with first truncation operation. Using second truncation to truncated dodecahedron gives the truncated truncated

dodecahedron. Figure 1 shows the dodecahedron, the truncated dodecahedron, the truncated truncated dodecahedron and the transparent truncated truncated dodecahedron, respectively.
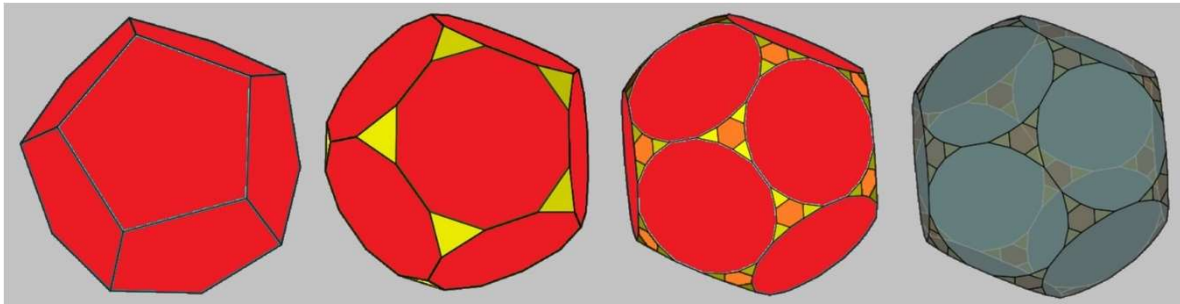

Figure 1: Dodecahedron, Truncated dodecahedron, Truncated truncated dodecahedron

Before we give a description of the truncated truncated dodecahedron distance function, we must agree on some impressions. Therefore U denote the maximum of quantities $\{|x_1 - x_2|, |y_1 - y_2|, |z_1 - z_2|\}$ for $P_1 = (x_1, y_1, z_1), P_2 = (x_2, y_2, z_2) \in \mathbb{R}^3$. Also, $X - Y - Z - X$ orientation and $Z - Y - X - Z$ orientation are called positive $(+)$ direction and negative $(-)$ directions, respectively. Accordingly, U^+ and U^- will display the next term in the respective direction according to U. For example, if $U = |y_1 - y_2|$, then $U^+ = |z_1 - z_2|$ and $U^- = |x_1 - x_2|$.

The metric that unit sphere is truncated truncated dodecahedron is described as following:

Let $P_1 = (x_1, y_1, z_1)$ and $P_2 = (x_2, y_2, z_2)$ be two points in $\mathbb{R}^3$. The distance function

$d_{TTD}: \mathbb{R}^3 \times \mathbb{R}^3 \to [0, \infty)$ truncated truncated dodecahedron distance between P_1 and P_2 is defined by

$$d_{TTD}(P_1, P_2) = \max \begin{Bmatrix} U + k_1 U^+, k_2 U + k_3 U^-, k_4 (U + U^- + U^+), k_5 U + k_6 U^-, \\ k_7 U + k_8 U^- + k_9 U^+, k_{10} U + k_{11} U^- + k_{12} U^+ \end{Bmatrix}$$

where $k_1 = \frac{\sqrt{5}-1}{2}, k_2 = \frac{7\sqrt{5}+5}{22}, k_3 = \frac{4\sqrt{5}-5}{11}, k_4 = \frac{15}{22} \frac{\sqrt{5}}{22}, k_5 = \frac{17\sqrt{5}+159}{202}, k_6 = \frac{24\sqrt{5}-31}{101}$,

$k_7 = \frac{34\sqrt{5}+15}{101}, k_8 = \frac{18\sqrt{5}+2}{101}, k_9 = \frac{39\sqrt{5}-63}{202}, k_{10} = \frac{10\sqrt{5}+46}{101}, k_{11} = \frac{-19\sqrt{5}+155}{202}$ and

$k_{12} = \frac{16\sqrt{5}+13}{101}$.

According to truncated truncated dodecahedron distance, there are six different paths from P_1 to P_2. These paths are

i) union of two line segments which one is parallel to a coordinate axis and other line segment makes $\arctan\left(\frac{1}{2}\right)$ angle with another coordinate axis,

ii) union of two line segments which one is parallel to a coordinate axis and other line segment makes $\arctan\left(\frac{\sqrt{5}}{2}\right)$ angle with another coordinate axis.

iii) union of three line segments each of which is parallel to a coordinate axis.

iv) union of two line segments which one is parallel to a coordinate axis and other line segment makes $\arctan\left(\frac{2691+860\sqrt{5}}{2242}\right)$ angle with another coordinate axis.

v) union of three line segments one of which is parallel to a coordinate axis and the others line segments makes one of $\arctan(\frac{71\sqrt{5}+585}{880})$ and $\arctan\left(\frac{575+2\ \sqrt{5}}{330}\right)$ angles with one of the other coordinate axes .

vi) union of three line segments one of which is parallel to a coordinate axis and the others line segments makes one of $\arctan(\frac{213\sqrt{5}-390}{440})$ and $\arctan\left(\frac{27+1\ \sqrt{5}}{176}\right)$ angles with one of the other coordinate axes .

Thus truncated truncated dodecahedron distance between P_1 and P_2 is for (i) sum of Euclidean lengths of mentioned two line segments, for (ii) k_2 times the sum of Euclidean lengths of mentioned two line segments, for (iii) k_4 times the sum of Euclidean lengths of mentioned three line segments, for (iv) k_5 times the sum of Euclidean lengths of mentioned two line segments, for (v) k_7 times the sum of Euclidean lengths of mentioned three line segments, and for (vi) k_{10} times the sum of Euclidean lengths of mentioned three line segments. In case of $|y_1 - y_2| \geq |x_1 - x_2| \geq |z_1 - z_2|$, Figure 2 illustrates some of truncated truncated dodecahedron way from P_1 to P_2
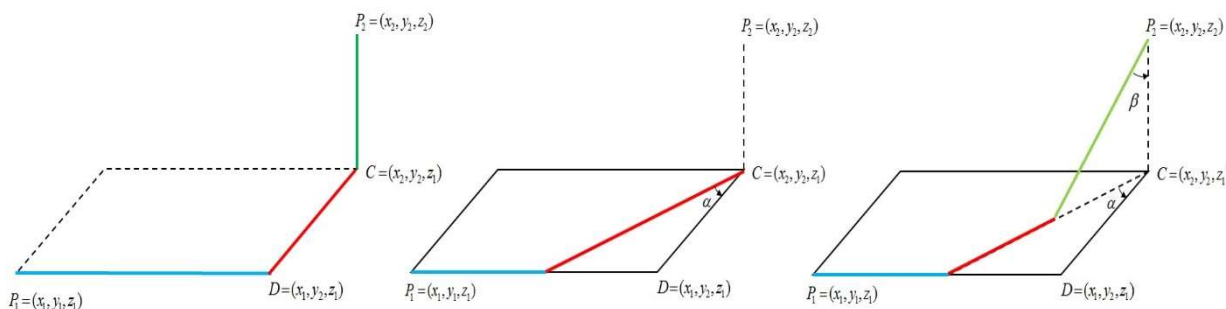

Figure 2: Some TTD way from P_1 to P_2

In [16] and [17], the authours introduce a metric and show that spheres of 3-dimensional analytical space furnished by these metric are the icosahedron and the truncated icosahedron. These metrics for $P_1 = (x_1, y_1, z_1)$, $P_2 = (x_2, y_2, z_2) \in \mathbb{R}^3$ are defined as follows:

$$d_D(P_1, P_2) = U + k_1 U^+$$

$$d_{TD}(P_1, P_2) = \max\{U + k_1 U^+, k_2 U + k_3 U^-, k_4(U + U^- + U^+)\},$$

where k_i for $i = 1,2,3,4$ are the same with definition 1.

Lemma 1: Let $P_1 = (x_1, y_1, z_1)$ and $P_2 = (x_2, y_2, z_2)$ be distinct two points in $\mathbb{R}^3$. U_{12} denote the maximum of quantities of $\{|x_1 - x_2|, |y_1 - y_2|, |z_1 - z_2|\}$. Then

$$d_{TTD}(P_1, P_2) \geq U_{12} + k_1 U_{12}^+$$
$$d_{TTD}(P_1, P_2) \geq k_2 U_{12} + k_3 U_{12}^-$$
$$d_{TTD}(P_1, P_2) \geq k_4(U_{12} + U_{12}^- + U_{12}^+)$$
$$d_{TTD}(P_1, P_2) \geq k_5 U_{12} + k_6 U_{12}^-$$
$$d_{TTD}(P_1, P_2) \geq k_7 U_{12} + k_8 U_{12}^- + k_9 U_{12}^+$$
$$d_{TTD}(P_1, P_2) \geq k_{10} U_{12} + k_{11} U_{12}^- + k_{12} U_{12}^+.$$

Proof. Proof is trivial by the definition of maximum function.

Theorem 1 The distance function d_{TTD} is a metric. Also according to d_{TTD}, the unit sphere is a truncated truncated dodecahedron in $\mathbb{R}^3$.

Proof. Let $d_{TTD}: \mathbb{R}^3 \times \mathbb{R}^3 \to [0, \infty)$ be the truncated truncated dodecahedron distance function and $P_1 = (x_1, y_1, z_1)$, $P_2 = (x_2, y_2, z_2)$ and $P_3 = (x_3, y_3, z_3)$ are distinct three points in $\mathbb{R}^3$. U_{12} denote the maximum of quantities of $\{|x_1 - x_2|, |y_1 - y_2|, |z_1 - z_2|\}$. To show that d_{TTD} is a metric in $\mathbb{R}^3$, the following axioms hold true for all P_1, P_2 and $P_3 \in \mathbb{R}^3$.

M1) $d_{TTD}(P_1, P_2) \geq 0$ and $d_{TTD}(P_1, P_2) = 0$ iff $P_1 = P_2$

M2) $d_{TTD}(P_1, P_2) = d_{TTD}(P_2, P_1)$

M3) $d_{TTD}(P_1, P_3) \leq d_{TTD}(P_1, P_2) + d_{TTD}(P_2, P_3).$

Since absolute values is always nonnegative value $d_{TTD}(P_1, P_2) \geq 0$. If $d_{TTD}(P_1, P_2) = 0$ then

$$\max \left\{ \begin{matrix} U + k_1 U^+, k_2 U + k_3 U^-, k_4(U + U^- + U^+), k_5 U + k_6 U^-, \\ k_7 U + k_8 U^- + k_9 U^+, k_{10} U + k_{11} U^- + k_{12} U^+ \end{matrix} \right\} = 0,$$

where U are the maximum of quantities $\{|x_1 - x_2|, |y_1 - y_2|, |z_1 - z_2|\}$. Therefore, $U + k_1 U^+ = 0, k_2 U + k_3 U^- = 0, k_4(U + U^- + U^+) = 0, k_5 U + k_6 U^- = 0, k_7 U + k_8 U^- + k_9 U^+ = 0$ and

$k_{10} U + k_{11} U^- + k_{12} U^+ = 0$. Hence, it is clearly obtained by $x_1 = x_2$,

$y_1 = y_2, z_1 = z_2$. That is, $P_1 = P_2$. Thus it is obtained that $d_{TTD}(P_1, P_2) = 0$ iff $P_1 = P_2$.

Since $|x_1 - x_2| = |x_2 - x_1|$, $|y_1 - y_2| = |y_2 - y_1|$ and $|z_1 - z_2| = |z_2 - z_1|$, obviously $d_{TTD}(P_1, P_2) = d_{TTD}(P_2, P_1)$. That is, d_{TTD} is symmetric.

U_{13}, and U_{23} denote the maximum of quantities of $\{|x_1 - x_3|, |y_1 - y_3|, |z_1 - z_3|\}$ and $\{|x_2 - x_3|, |y_2 - y_3|, |z_2 - z_3|\}$, respectively.

$$d_{TTD}(P_1, P_3) = \max \left\{ \begin{array}{l} U_{13} + k_1 U_{13}^+, k_2 U_{13} + k_3 U_{13}^-, k_4(U_{13} + U_{13}^- + U_{13}^+), k_5 U_{13} + k_6 U_{13}^-, \\ k_7 U_{13} + k_8 U_{13}^- + k_9 U_{13}^+, k_{10} U_{13} + k_{11} U_{13}^- + k_{12} U_{13}^+ \end{array} \right\}$$

$$\leq \max \left\{ \begin{array}{c} U_{12} + U_{23} + k_1(U_{12}^+ + U_{23}^+), k_2(U_{12} + U_{23}) + k_3(U_{12}^- + U_{23}^-), \\ k_4(U_{12} + U_{23} + U_{12}^- + U_{23}^- + U_{12}^+ + U_{23}^+), \\ k_5(U_{12} + U_{23}) + k_6(U_{12}^- + U_{23}^-), \\ k_7(U_{12} + U_{23}) + k_8(U_{12}^- + U_{23}^-) + k_9(U_{12}^+ + U_{23}^+), \\ k_{10}(U_{12} + U_{23}) + k_{11}(U_{12}^- + U_{23}^-) + k_{12}(U_{12}^+ + U_{23}^+) \end{array} \right\}$$

$$= I.$$

Therefore one can easily find that $I \leq d_{TTD}(P_1, P_2) + d_{TTD}(P_2, P_3)$ from Lemma 1.

So $d_{TTD}(P_1, P_3) \leq d_{TTD}(P_1, P_2) + d_{TTD}(P_2, P_3)$. Consequently, truncated truncated dodecahedron distance is a metric in 3-dimensional analytical space.

Finally, the set of all points $X = (x, y, z) \in \mathbb{R}^3$ that truncated truncated dodecahedron distance is 1 from $O = (0,0,0)$ is

$$S_{TTD} = \left\{ (x, y, z) : \max \left\{ \begin{array}{l} U + k_1 U^+, k_2 U + k_3 U^-, k_4(U + U^- + U^+), k_5 U + k_6 U^-, \\ k_7 U + k_8 U^- + k_9 U^+, k_{10} U + k_{11} U^- + k_{12} U^+ \end{array} \right\} = 1 \right\}.$$

Thus the graph of S_{TTD} is as in the figure 3:
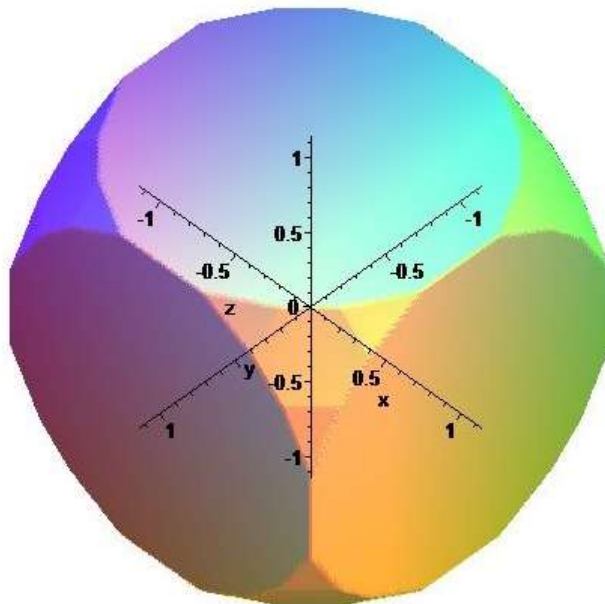
Figure 3. The unit sphere in terms of d$_{TTD}$: Truncated Truncated Dodecahedron

Corollary 1 The equation of the truncated truncated dodecahedron with center (x_0, y_0, z_0) and radius r is

$$\max\left\{\begin{matrix}U_0 + k_1 U_0^+, k_2 U_0 + k_3 U_0^-, k_4(U_0 + U_0^- + U_0^+), k_5 U_0 + k_6 U_0^-,\\ k_7 U_0 + k_8 U_0^- + k_9 U_0^+, k_{10} U_0 + k_{11} U_0^- + k_{12} U_0^+\end{matrix}\right\} = r,$$

which is a polyhedron which has 92 faces and 180 vertices, where U_0 are the maximum of quantities $\{|x - x_0|, |y - y_0|, |z - z_0|\}$. Coordinates of the vertices are translation to (x_0, y_0, z_0) all circular shift of the three axis components and all possible +/- sign changes of each axis component of $(0, C_1 r, r), (C_0 r, C_4 r, C_{20} r), (C_2 r, C_5 r, C_{19} r), (C_0 r, C_7 r, C_{18} r), (C_3 r, C_8 r, C_{17} r),$ $(C_6 r, C_{11} r, C_{16} r), (C_{12} r, C_{10} r, C_{15} r)$ and $(C_9 r, C_{13} r, C_{14} r)$, where

$$C_0 = \frac{3\sqrt{5} - 5}{30}, C_1 = \frac{5\sqrt{5} - 7}{38}, C_2 = \frac{3\sqrt{5} - 5}{15}, C_3 = \frac{5\sqrt{5} - 7}{19},$$

$$C_4 = \frac{4\sqrt{5} - 5}{15}, C_5 = \frac{7\sqrt{5} - 5}{30}, C_6 = \frac{9\sqrt{5} - 5}{38},$$

$$C_7 = \frac{\sqrt{5}}{5}, C_8 = \frac{3\sqrt{5} + 11}{38}, C_9 = \frac{\sqrt{5} + 5}{15},$$

$$C_{10} = \frac{10 - \sqrt{5}}{15}, C_{11} = \frac{27 - 3\sqrt{5}}{38}, C_{12} = \frac{\sqrt{5} + 1}{6},$$

$$C_{13} = \frac{25 - 3\sqrt{5}}{30}, C_{14} = \frac{5 + 2\sqrt{5}}{15}, C_{15} = \frac{2}{3},$$

$$C_{16} \frac{7\sqrt{5} + 13}{38}, \quad C_{17} = \frac{6\sqrt{5} + 3}{19}, \quad C_{18} = \frac{2\sqrt{5}}{5},$$

$$C_{19} = \frac{4\sqrt{5} + 5}{15} \text{ and } C_{20} = \frac{2\sqrt{5} + 10}{15}.$$

Lemma 2 Let l be the line through the points $P_1 = (x_1, y_1, z_1)$ and $P_2 = (x_2, y_2, z_2)$ in the analytical 3-dimensional space and d_E denote the Euclidean metric. If l has direction vector (p, q, r), then

$$d_{TTD}(P_1, P_2) = \mu(P_1 P_2) d_E(P_1, P_2)$$

where

$$\mu(P_1 P_2) = \frac{\max\left\{\begin{matrix}U_d + k_1 U_d^+, k_2 U_d + k_3 U_d^-, k_4(U_d + U_d^- + U_d^+), k_5 U_d + k_6 U_d^-,\\ k_7 U_d + k_8 U_d^- + k_9 U_d^+, k_{10} U_d + k_{11} U_d^- + k_{12} U_d^+\end{matrix}\right\}}{\sqrt{p^2 + q^2 + r^2}},$$

U_d are the maximum of quantities $\{|p|, |q|, |r|\}$.

Proof. Equation of l gives us $x_1 - x_2 = \lambda p, y_1 - y_2 = \lambda q, z_1 - z_2 = \lambda r, \lambda \in \mathbb{R}$. Thus,

$$d_{TTD}(P_1, P_2) = |\lambda| \left(\max \left\{ \begin{matrix} U_d + k_1 U_d^+, k_2 U_d + k_3 U_d^-, k_4(U_d + U_d^- + U_d^+), k_5 U_d + k_6 U_d^-, \\ k_7 U_d + k_8 U_d^- + k_9 U_d^+, k_{10} U_d + k_{11} U_d^- + k_{12} U_d^+ \end{matrix} \right\} \right),$$

where U_d are the maximum of quantities $\{|p|, |q|, |r|\}$, and $d_E(A, B) = |\lambda| \sqrt{p^2 + q^2 + r^2}$ which implies the desired result.

The above lemma says that d_{TTD}-distance along any line is some positive constant multiple of Euclidean distance along same line. Thus, one can immediately state the following corollaries:

Corollary 2 If P_1, P_2 and X are any three collinear points in $\mathbb{R}^3$, then

$d_E(P_1, X) = d_E(P_2, X)$ if and only if $d_{TTD}(P_1, X) = d_{TTD}(P_2, X)$.

Corollary 3 If P_1, P_2 and X are any three distinct collinear points in the real 3-dimensional space, then

$$d_{TTD}(X, P_1)/d_{TTD}(X, P_2) = d_E(X, P_1)/d_E(X, P_2).$$

That is, the ratios of the Euclidean and d_{TTD} − distances along a line are the same.

3. TRUNCATED TRUNCATED ICOSAHEDRON METRIC AND SOME PROPERTIES

The truncated truncated icosahedron can be obtained by two times truncating operation from icosahedron. Truncated icosahedron appears with first truncation operation. Using second truncation to truncated icosahedron gives the truncated truncated icosahedron. The truncated truncated icosahedron has 20 tri-symmetric dodecagonal faces, 12 regular decagonal faces, 60 equilateral triangular faces, 180 vertices and 270 edges. The truncated truncated icosahedron and the truncated truncated dodecahedron have the same number of faces, vertices and edges. Figure 4 show the icosahedron, the truncated icosahedron and the truncated truncated icosahedron, and the transparent truncated truncated icosahedron, respectively.
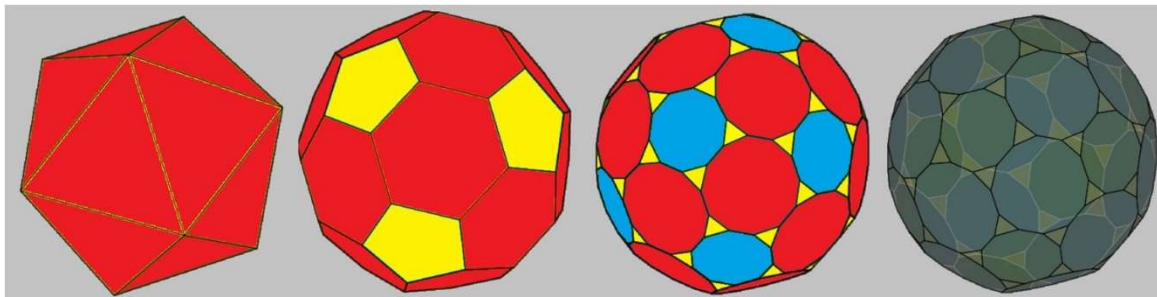
Figure 4. Icosahedron, Truncated icosahedron and Truncated truncated icosahedron

The notations U, U^+, U^- shall be used as defined in the previous section. The metric that unit sphere is the truncated truncated icosahedron is described as following:

Defnition 2 Let $P_1 = (x_1, y_1, z_1)$ and $P_2 = (x_2, y_2, z_2)$ be two points in $\mathbb{R}^3$. The distance function $d_{TTI}: \mathbb{R}^3 \times \mathbb{R}^3 \to [0, \infty)$ truncated truncated icosahedron distance between P_1 and P_2 is defined by

$$d_{TTI}(P_1, P_2) = \max \begin{Bmatrix} U + k_1 U^+, k_2(U + U^- + U^+), k_3 U + k_4 U^+, k_5 U + k_6 U^+, \\ k_7 U + k_8 U^- + k_9 U^+, k_{10} U + k_{11} U^- + k_{12} U^+ \end{Bmatrix}$$

where $k_1 = \frac{3-\sqrt{5}}{2}, k_2 = \frac{\sqrt{5}-1}{2}, k_3 = \frac{325+129\sqrt{5}+(26\sqrt{5}-90)\sqrt{3+2\sqrt{5}}}{590}, k_4 = \frac{80+49\sqrt{5}+(55-29\sqrt{5})\sqrt{3+2\sqrt{5}}}{295},$

$$k_5 = \frac{7162 + 910\sqrt{5} + (303\sqrt{5} - 789)\sqrt{3 + 2\sqrt{5}}}{9082}, k_6 = \frac{576 - 273\sqrt{5} + (1599 - 545\sqrt{5})\sqrt{3 + 2\sqrt{5}}}{4541},$$

$$k_7 = \frac{3915 + 4885\sqrt{5} + (1901\sqrt{5} - 3961)\sqrt{3 + 2\sqrt{5}}}{18164}, k_8 = \frac{7951 + 607\sqrt{5} + (337 - 751\sqrt{5})\sqrt{3 + 2\sqrt{5}}}{18164},$$

$$k_9 = \frac{1290\sqrt{5} - 77 + (2175 - 818\sqrt{5})\sqrt{3 + 2\sqrt{5}}}{9082}, k_{10} = \frac{7797 + 3187\sqrt{5} + (4687 - 2387\sqrt{5})\sqrt{3 + 2\sqrt{5}}}{18164},$$

$$k_{11} = \frac{6373+1213\sqrt{5}+(1357\sqrt{5}-1915)\sqrt{3+2\sqrt{5}}}{18164} \text{ and } k_{12} = \frac{1836\sqrt{5}-1229+(272\sqrt{5}-1003)\sqrt{3+2\sqrt{5}}}{9082}.$$

According to truncated truncated icosahedron distance, there are six different paths from P_1 to P_2. These paths are

i) union of two line segments which one is parallel to a coordinate axis and other line segment makes $\arctan\left(\frac{\sqrt{5}}{2}\right)$ angle with another coordinate axis,

ii) union of three line segments each of which is parallel to a coordinate axis.

iii) union of two line segments which one is parallel to a coordinate axis and other line segment makes $\arctan\left(\frac{1}{2}\right)$ angle with another coordinate axis..

iv) union of two line segments which one is parallel to a coordinate axis and other line segment makes $\arctan\left(\frac{(8\sqrt{5}-1)\sqrt{3+2\sqrt{5}}}{22}\right)$ angle with another coordinate axis..

v) union of three line segments one of which is parallel to a coordinate axis and the others line segments makes one of $\arctan\left(\frac{3\sqrt{5}+1+(2\sqrt{5}-2)\sqrt{3+2\sqrt{5}}}{12}\right)$ and $\arctan\left(\frac{15+7\sqrt{5}+(7-5\sqrt{5})\sqrt{3+2\sqrt{5}}}{24}\right)$ angles with one of the other coordinate axes .

vi) union of three line segments one of which is parallel to a coordinate axis and the others line segments makes one of $\arctan\left(\frac{3\sqrt{5}+1+(2-2\sqrt{5})\sqrt{3+2\sqrt{5}}}{12}\right)$ and $\arctan\left(\frac{15+7\sqrt{5}+(5\sqrt{5}-7)\sqrt{3+2\sqrt{5}}}{24}\right)$ angles with one of the other coordinate axes .

Thus truncated truncated icosahedron distance between P_1 and P_2 is for (i) sum of Euclidean lengths of mentioned two line segments, for (ii) k_2 times the sum of Euclidean lengths of mentioned two

line segments, for (iii) k_3 times the sum of Euclidean lengths of mentioned three line segments, for (iv) k_5 times the sum of Euclidean lengths of mentioned two line segments, for (v) k_7 times the sum of Euclidean lengths of mentioned three line segments, and for (vi) k_{10} times the sum of Euclidean lengths of mentioned three line segments. In case of $|y_1 - y_2| \geq |x_1 - x_2| \geq |z_1 - z_2|$, Figure 5 shows that some of the $TTI-$path between P_1 and P_2.
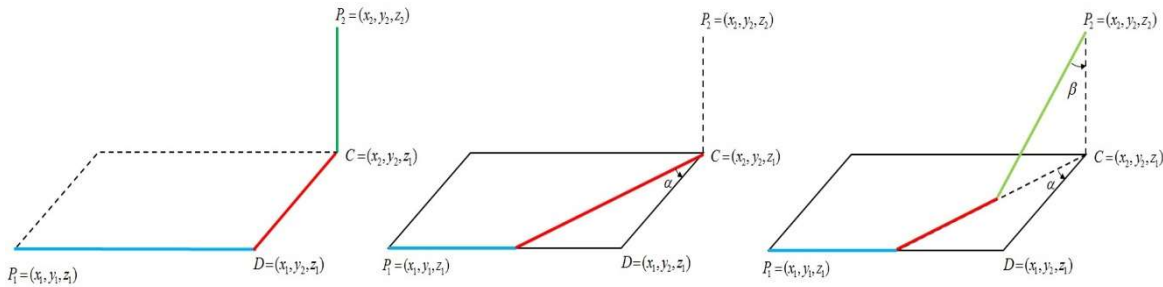

Figure 5. TTI way from P_1 to P_2

In [5] and [12], the authours introduce a metric and show that spheres of 3-dimensional analytical space furnished by these metric are the icosahedron and the truncated icosahedron. These metrics for $P_1 = (x_1, y_1, z_1)$, $P_2 = (x_2, y_2, z_2) \in \mathbb{R}^3$ are defined as follows:

$$d_I(P_1, P_2) = \max\{k_2(U + k_1 U^-), k_2(U + U^- + U^+)\}$$

$$d_{TI}(P_1, P_2) = \max\{k_2(U + U^- + U^+), U + k_1 U^-, \frac{3\sqrt{5}+27}{38}U + \frac{6\sqrt{5}-3}{19}U^+\},$$

where k_i for $i = 1,2$ are the same with definition 2.

Lemma 3 Let $P_1 = (x_1, y_1, z_1)$ and $P_2 = (x_2, y_2, z_2)$ be distinct two points in $\mathbb{R}^3$. U_{12} denote the maximum of quantities of $\{|x_1 - x_2|, |y_1 - y_2|, |z_1 - z_2|\}$. Then

$$\begin{aligned}
d_{TTI}(P_1, P_2) &\geq U + k_1 U^+, \\
d_{TTI}(P_1, P_2) &\geq k_2(U + U^- + U^+), \\
d_{TTI}(P_1, P_2) &\geq k_3 U + k_4 U^+, \\
d_{TTI}(P_1, P_2) &\geq k_5 U + k_6 U^+, \\
d_{TTI}(P_1, P_2) &\geq k_7 U + k_8 U^- + k_9 U^+, \\
d_{TTI}(P_1, P_2) &\geq k_{10} U + k_{11} U^- + k_{12} U^+.
\end{aligned}$$

*Proof.* Proof is trivial by the definition of maximum function.

Theorem 2 The distance function d_{TTI} is a metric. Also according to d_{TTI}, unit sphere is a truncated truncated icosahedron in $\mathbb{R}^3$.

Proof. One can easily show that the truncated truncated icosahedron distance function satisfies the metric axioms by similar way in Theorem 1.

Consequently, the set of all points $X = (x, y, z) \in \mathbb{R}^3$ that truncated truncated icosahedron distance is 1 from $O = (0,0,0)$ is

$$S_{TTI} = \left\{(x, y, z): \max \begin{Bmatrix} U + k_1 U^+, k_2(U + U^- + U^+), k_3 U + k_4 U^+, k_5 U + k_6 U^+, \\ k_7 U + k_8 U^- + k_9 U^+, k_{10} U + k_{11} U^- + k_{12} U^+ \end{Bmatrix} = 1 \right\},$$

where U are the maximum of quantities $\{|x|, |y|, |z|\}$. Thus the graph of S_{TTI} is as in the figure 6:
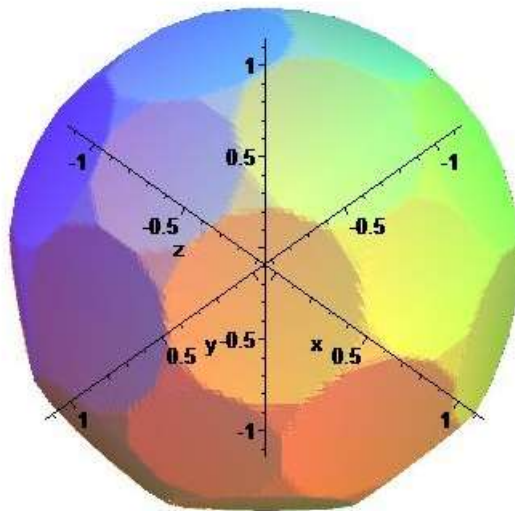
Figure 6. The unit sphere in terms of d_{TTI}: Truncated Truncated Icosahedron

Corollary 4 The equation of the truncated truncated icosahedron with center (x_0, y_0, z_0) and radius r is

$$\max \begin{Bmatrix} U_0 + k_1 U_0^+, k_2(U_0 + U_0^- + U_0^+), k_3 U_0 + k_4 U_0^+, k_5 U_0 + k_6 U_0^+, \\ k_7 U_0 + k_8 U_0^- + k_9 U_0^+, k_{10} U_0 + k_{11} U_0^- + k_{12} U_0^+ \end{Bmatrix} = r,$$

which is a polyhedron which has 92 faces and 180 vertices, where U_0 are the maximum of quantities $\{|x - x_0|, |y - y_0|, |z - z_0|\}$. Coordinates of the vertices are translation to (x_0, y_0, z_0) all circular shift of the three axis components and all possible +/- sign changes of each axis component of $(C_{19}r, 0, r), (C_1 r, C_{19} r, C_{17} r), (C_4 r, C_0 r, C_{16} r), (C_5 r, C_6 r, C_{15} r), (C_7 r, C_3 r, C_{14} r),$

$(C_2 r, C_8 r, C_{13} r), (C_{19} r, C_{10} r, C_{12} r)$ and $(C_9 r, C_0 r, C_{11} r)$, where $C_0 = \frac{81 + 1\sqrt{5} + (6\sqrt{5} - 28)\sqrt{3 + 2\sqrt{5}}}{302}$,

$$C_1 = \frac{17\sqrt{5} - 29 + (37\sqrt{5} - 72)\sqrt{3 + 2\sqrt{5}}}{151}, C_2 = \frac{169\sqrt{5} - 235 + (57 - 23\sqrt{5})\sqrt{3 + 2\sqrt{5}}}{604},$$

$$C_3 = \frac{33\sqrt{5} - 3 + (29 - 17\sqrt{5})\sqrt{3 + 2\sqrt{5}}}{151}, C_4 = \frac{26 + 16\sqrt{5} + (97\sqrt{5} - 201)\sqrt{3 + 2\sqrt{5}}}{302},$$

$$C_5 = \frac{133\sqrt{5} - 67 + (23\sqrt{5} - 57)\sqrt{3 + 2\sqrt{5}}}{604}, C_6 = \frac{305 - 33\sqrt{5} + (17\sqrt{5} - 29)\sqrt{3 + 2\sqrt{5}}}{604},$$

$$C_7 = \frac{23 + 49\sqrt{5} + (80\sqrt{5} - 172)\sqrt{3 + 2\sqrt{5}}}{302}, C_8 = \frac{299 + 33\sqrt{5} + (29 - 17\sqrt{5})\sqrt{3 + 2\sqrt{5}}}{604},$$

$$C_9 = \frac{20 + 82\sqrt{5} + (63\sqrt{5} - 143)\sqrt{3 + 2\sqrt{5}}}{302}, C_{10} = \frac{137 + 3\sqrt{5} + (85 - 29\sqrt{5})\sqrt{3 + 2\sqrt{5}}}{302},$$

$$C_{11} = \frac{50 + 54\sqrt{5} + (171 - 69\sqrt{5})\sqrt{3 + 2\sqrt{5}}}{302}, C_{12} = \frac{52 + 32\sqrt{5} + (43\sqrt{5} - 100)\sqrt{3 + 2\sqrt{5}}}{151},$$

$$C_{13} = \frac{119 + 50\sqrt{5} + (20\sqrt{5} - 43)\sqrt{3 + 2\sqrt{5}}}{302}, C_{14} = \frac{67 + 18\sqrt{5} + (57 - 23\sqrt{5})\sqrt{3 + 2\sqrt{5}}}{151},$$

$$C_{15} = \frac{32 + 101\sqrt{5} + (43 - 20\sqrt{5})\sqrt{3 + 2\sqrt{5}}}{302}, C_{16} = \frac{218 + 18\sqrt{5} + (57 - 23\sqrt{5})\sqrt{3 + 2\sqrt{5}}}{302},$$

$$C_{17} = \frac{131 + 69\sqrt{5} + (143 - 63\sqrt{5})\sqrt{3 + 2\sqrt{5}}}{302}, C_{18} = 1, \text{ and } C_{19} = \frac{84 - 18\sqrt{5} + (23\sqrt{5} - 57)\sqrt{3 + 2\sqrt{5}}}{302}.$$

Lemma 4 Let l be the line through the points $P_1 = (x_1, y_1, z_1)$ and $P_2 = (x_2, y_2, z_2)$ in the analytical 3-dimensional space and d_E denote the Euclidean metric. If l has direction vector (p, q, r), then

$$d_{TTI}(P_1, P_2) = \mu(P_1 P_2) d_E(P_1, P_2)$$

where

$$\mu(P_1 P_2) = \frac{\max \left\{ \begin{matrix} U_d + k_1 U_d^+, k_2(U_d + U_d^- + U_d^+), k_3 U_d + k_4 U_d^+, k_5 U_d + k_6 U_d^+, \\ k_7 U_d + k_8 U_d^- + k_9 U_d^+, k_{10} U_d + k_{11} U_d^- + k_{12} U_d^+ \end{matrix} \right\}}{\sqrt{p^2 + q^2 + r^2}},$$

U_d are the maximum of quantities $\{|p|, |q|, |r|\}$.

Proof. Equation of l gives us $x_1 - x_2 = \lambda p, y_1 - y_2 = \lambda q, z_1 - z_2 = \lambda r, \lambda \in \mathbb{R}$. Thus,

$$d_{TTI}(P_1, P_2) = |\lambda| \left(\max \left\{ \begin{matrix} U_d + k_1 U_d^+, k_2(U_d + U_d^- + U_d^+), k_3 U_d + k_4 U_d^+, k_5 U_d + k_6 U_d^+, \\ k_7 U_d + k_8 U_d^- + k_9 U_d^+, k_{10} U_d + k_{11} U_d^- + k_{12} U_d^+ \end{matrix} \right\} \right)$$

where U_d are the maximum of quantities $\{|p|, |q|, |r|\}$, and $d_E(A, B) = |\lambda|\sqrt{p^2 + q^2 + r^2}$ which implies the desired result.

The above lemma says that d_{TTI}-distance along any line is some positive constant multiple of Euclidean distance along same line. Thus, one can immediately state the following corollaries:

Corollary 5 If P_1, P_2 and X are any three collinear points in $\mathbb{R}^3$, then

$d_E(P_1, X) = d_E(P_2, X)$ if and only if $d_{TTI}(P_1, X) = d_{TTI}(P_2, X)$.

Corollary 6 If P_1, P_2 and X are any three distinct collinear points in the real 3-dimensional space, then

$$d_{TTI}(X, P_1)/d_{TTI}(X, P_2) = d_E(X, P_1)/d_E(X, P_2).$$

That is, the ratios of the Euclidean and d_{TTI} − distances along a line are the same.

REFERENCES

[1] Ö. Gelisgen and R. Kaya, The Isometry Group of Chinese Checker Space, International Electronic Journal Geometry, 8-2 (2015) 82–96.

[2] Z. Can, Ö. Gelişgen and R. Kaya, On the Metrics Induced by Icosidodecahedron and Rhombic Triacontahedron, Scientific and Professional Journal of the Croatian Society for Geometry and Graphics (KoG), 19 (2015) 17–23.

[3] P. Cromwell, Polyhedra, Cambridge University Press (1999).

[4] A.C. Thompson, Minkowski Geometry, Cambridge University Press, Cambridge 1996.

[5] Z. Can, Z. Çolak and Ö. Gelişgen, A Note On The Metrics Induced By Triakis Icosahedron And Disdyakis Triacontahedron, Eurasian Academy of Sciences Eurasian Life Sciences Journal / Avrasya Fen Bilimleri Dergisi, 1 (2015) 1–11.

[6] Z. Çolak and Ö. Gelişgen, New Metrics for Deltoidal Hexacontahedron and Pentakis Dodecahedron, SAU Fen Bilimleri Enstitüsü Dergisi, 19-3 (2015) 353-360.

[7] T. Ermis and R. Kaya, Isometries the of 3- Dimensional Maximum Space, Konuralp Journal of Mathematics, 3-1 (2015) 103–114.

[8] Ö. Gelişgen, R. Kaya and M. Ozcan, Distance Formulae in The Chinese Checker Space, Int. J. Pure Appl. Math., 26-1 (2006) 35–44.

[9] Ö. Gelişgen and R. Kaya, The Taxicab Space Group, Acta Mathematica Hungarica, 122-1,2 (2009) 187–200.

[10] Ö. Gelişgen and Z. Çolak, A Family of Metrics for Some Polyhedra, Automation Computers Applied Mathematics Scientific Journal, 24-1 (2015) 3–15.

[11] Ö. Gelişgen, On The Relations Between Truncated Cuboctahedron Truncated Icosidodecahedron and Metrics, Forum Geometricorum, 17 (2017) 273–285.

[12] Ö. Gelişgen and Z. Can, On The Family of Metrics for Some Platonic and Archimedean Polyhedra, Konuralp Journal of Mathematics, 4-2 (2016) 25–33.

[13] M. Senechal, Shaping Space, Springer New York Heidelberg Dordrecht London 2013.

[14] J. V. Field, Rediscovering the Archimedean Polyhedra: Piero della Francesca, Luca Pacioli, Leonardo da Vinci, Albrecht Dürer, Daniele Barbaro, and Johannes Kepler, Archive for History of Exact Sciences, 50-3,4 (1997) 241–289.

[15] http://www.sacred-geometry.es/?q=en/content/archimedean-solids Retrieved January, 5, 2019.

[16] T. Ermis, On the relations between the metric geometries and regular polyhedra, PhD Thesis, Eskişehir Osmangazi University, Graduate School of Natural and Applied Sciences, (2014).

[17] Ö. Gelişgen, T. Ermis, and I. Gunaltılı, A Note About The Metrics Induced by Truncated Dodecahedron And Truncated Icosahedron, InternationalJournal of Geometry, 6-2 (2017) 5–16.

Electronic properties of double GaAlAs/GaAs and GaInAs/GaAs quantum wells as dependent on well width

Ozan Ozturk[1]* iD *, Emine Ozturk[2]* iD *, Sezai Elagoz[3]* iD

[1] *Sivas Cumhuriyet University, Department of Nanotechnology Engineering, 58140, Sivas-TURKEY*

[2] *Sivas Cumhuriyet University, Department of Physics, 58140, Sivas-TURKEY*

[3] *ASELSAN - Microelectronics, Guidance & Electro-Optics, Ankara-TURKEY*

Abstract. Herein, the electronic properties of double $Ga_{1-x}Al_x As$/GaAs quantum wells (A model) and $Ga_{1-x}In_x As$/GaAs quantum wells (B model) have been examined related to the well width. The wave functions, the subband energies and the probability densities of these systems under effective mass approach were determined by the solution of Schrödinger equation. According to the results obtained, the major diversities of A and B models are the effective mass and the energy gap. For A model, GaAlAs is the barrier and GaAs is the well. Whereas for B model, GaAs is the barrier and GaInAs is the well. Also, the potential depth and the energy levels of A model are continuously smaller than of B model. The well width has a great impact on the electronic features of the double quantum well (DQW). These features have a convenient attention for the purpose of adjustable semiconductor devices.

Keywords: Double GaAlAs/GaAs quantum well, Double GaInAs/GaAs quantum well, Well width, Electronic properties.

Çift GaAlAs/GaAs ve GaInAs/GaAs kuantum kuyularının kuyu genişliğine bağlı olarak elektronik özellikleri

Özet. Bu çalışmada, çift $Ga_{1-x}Al_x As$/GaAs kuantum kuyularının (A yapısı) ve $Ga_{1-x}In_x As$/GaAs /GaAs kuantum kuyularının (B yapısı) elektronik özellikleri kuyu genişliğine bağlı olarak incelenmiştir. Etkin kütle yaklaşımı kullanılarak, Schrödinger denkleminin çözümüyle enerji seviyeleri, dalga fonksiyonları ve bu sistemin olasılık yoğunlukları hesaplanmıştır. Elde edilen sonuçlara göre, A ve B yapısının temel farklılıkları yasak enerji aralığı ve etkili kütledir. A yapısı için engel GaAlAs ve kuyu GaAs'dır. B yapısı için ise engel GaAs ve kuyu GaInAs'dır. Ayrıca, A yapısının potansiyel yüksekliği ve enerji seviyeleri her zaman B yapısından düşüktür. Kuyu genişliği, çift kuantum kuyusunun (DQW) elektronik özellikleri üzerinde büyük bir etkiye sahiptir. Bu özellikler, ayarlanabilir yarı iletken cihazların tasarımı için pratik bir ilgiye sahiptir.

Anahtar Kelimeler: Çift GaAlAs/GaAs kuantum kuyusu, Çift GaInAs/GaAs kuantum kuyusu, Kuyu genişliği, elektronik özellikler.

1. INTRODUCTION

The electronic features of the low-dimensional structures are highly dependent on the presence of the asymmetry of the potential profile of a semiconductor quantum well (QW). Such asymmetry in potential profile may provide an electric field or can rank the potential shape as a

---

composition, and thus it is well known that the electronic features of QW structures vary substantially. We are concerned in observing the structure of a double quantum wells (DQW) shaped by two different semiconductors (e.g, GaAs/GaAlAs and InGaAs/GaAs). These systems contain two potential wells coupled by a barrier. They are very suitable structure for observing quantum electronic transport. Because GaAlAs / GaAs QW systems are applied in modern photo-electronics and high-speed electronic devices, the electrical and optical properties of the related systems have been widely investigated under both the pressure and external fields [1-7]. The segregation of indium atoms in the GaInAs layer has been extensively researched in current times, as the understanding of high-performance devices desires sudden hetero-interfaces [8-10]. It is also known that the indium atoms are powerfully related to the growth temperature and the GaInAs/GaAs structure is allocated from the growth surface during MBE growth.

The double-quantum well (DQW) structures are very interesting for the device industry because by the interlayer distance between wells and the barrier alters, a development in the transport features is realized. The presence of a quantum limiting effect for the energy levels of a thin single quantum well is mostly considered. In DQWs, it is necessary to define the potential limiting effects that characterize the energy levels of isolated wells and the eigenstates of the systems affected weakly through a potential barrier. DQW semiconductors are important hetero-structures for technological applications because they are anticipated to be the basis for application to new electron devices [11-12]. The focus benefit of multiple semiconductor structures over single QWs is the advanced exciton electro-optic response. The opto-electronic features of the excitons in DQWs promise a range of potential applications in high-speed spatial light modulators and switches. This study focused on the theoretical research of the electronic features of $Ga_{1-x}Al_xAs/GaAs$ and $Ga_{1-x}In_xAs/GaAs$ DQW depending on the well width (WW). A model and B model will be named for $Ga_{1-x}Al_xAs/GaAs$ DQW and $Ga_{1-x}In_xAs/GaAs$ DQW, respectively. There are on the left hand side Semi V-shaped QW (SVQW) and on the right hand side Inverse Semi V-shaped QW (ISVQW). As far as we know, this is the first literature study on the electronic features of such DQW. The motivation for using many DQW with different shapes is to create multi wavelength optical devices.

2. MATERIAL and METHOD

In the effective-mass approach, the wave functions and the state energies for electrons in DQW, which are enlarged along the z-axis, may be achieved by dissolving the one-dimensional Schrödinger equation with a suitable Hamiltonian.

$$\left(-\frac{\hbar^2}{2m^*}\frac{d^2}{dz^2} + V(z) \right)\Psi(z) = E\,\Psi(z) \tag{1}$$

where $V(z)$ is the confined potential, and E and $\Psi(z)$ are the eigen-energy and eigen-function of the Eq. (1) solution. The limited potential of DQW, b being the barrier width, L_R and L_L being the right and the left quantum WWs, respectively, are given by

$$V(z) = V_0 \begin{cases} -\frac{1}{L_L}\left(z + \frac{b+L_L}{2}\right) & -\left(L_L + \frac{b}{2}\right) \le z \le -\left(\frac{L_L+b}{2}\right) \\ \frac{1}{L_L}\left(z + L_L + \frac{b}{2}\right) - \frac{1}{2} & -\left(\frac{L_L+b}{2}\right) \le z \le -\left(\frac{b}{2}\right) \\ \frac{1}{L_R}\left(z - \frac{(b+L_R)}{2}\right) + \frac{1}{2} & \left(\frac{b}{2}\right) \le z \le \left(\frac{L_R+b}{2}\right) \\ -\frac{1}{L_R}\left(z - \left(\frac{b}{2}+L_R\right)\right) & \left(\frac{L_R+b}{2}\right) \le z \le \left(\frac{b}{2}+L_R\right) \\ 1 & \text{elsewhere} \end{cases} \tag{2}$$

The effective mass of electron and the discontinuity in the conduction band edge of $Ga_{1-x}Al_xAs/GaAs$ [13-14] and $Ga_{1-x}In_xAs/GaAs$ [13, 15] are analyzed using the following equations.

$$m^*_{GaAlAs} = (0.067 + 0.083\,x)m_0 \tag{3a}$$

$$m^*_{GaInAs} = (0.067 - 0.04\,x)m_0 \tag{3b}$$

$$V_0^{GaAlAs} = \%60\left(E_g^{GaAlAs} - E_g^{GaAs}\right) \tag{4a}$$

$$V_0^{GaInAs} = \%60\left(E_g^{GaAs} - E_g^{GaInAs}\right) \tag{4b}$$

Where $E_g^{GaAlAs} = \left(E_g^{GaAs} + 1247\,x\right)$ meV, $E_g^{GaInAs} = \left(E_g^{GaAs} - 1619\,x + 555\,x^2\right)$ meV, $E_g^{GaAs} = 1424$ meV.

The confined potential of QW is significant for the enclosure of electrons. Thus, the finding possibility of the electrons in different QWs is provided by,

$$P_i^W = \int \left|\Psi_i^W(z)\right|^2 dz \quad (i = 1, 2; \quad W = L, R) \tag{5}$$

where R and L indicate the right QW (RQW) and the left QW (LQW), serially.

3. RESULTS AND DISCUSSION

We have theoretically examined the electronic features of A and B models depending on the x-concentration for DQW. In this study, $x = 0.15$, $b = 2.5$ nm, and $T = 300K$.

For different well width values (where $L = L_L = L_R$), Fig. 1 (A model) and Fig. 2 (B model) demonstrate the confinement potential, the bound energy levels and squared wave functions referred to these energies. As understood in Eq. (3) and Eq. (4), the important differences of A and B model are the energy gap and the effective mass. For A model, GaAs is the well and GaAlAs is the barrier, and the potential depth is about $V_0^{GaAlAs} = 112$ meV. For B model, GaInAs is the well and GaAs is the barrier, and the potential depth is about $V_0^{GaInAs} = 138$ meV. As estimated, the energy levels of A model with smaller potential depth are continually lower than the energy levels of B model. As seen from these figures, while A model have three bounded states for $L = 8$ nm, there are two bound conditions in B model. It is seen that the electron in the ground state is mostly located in LQW and the electron in
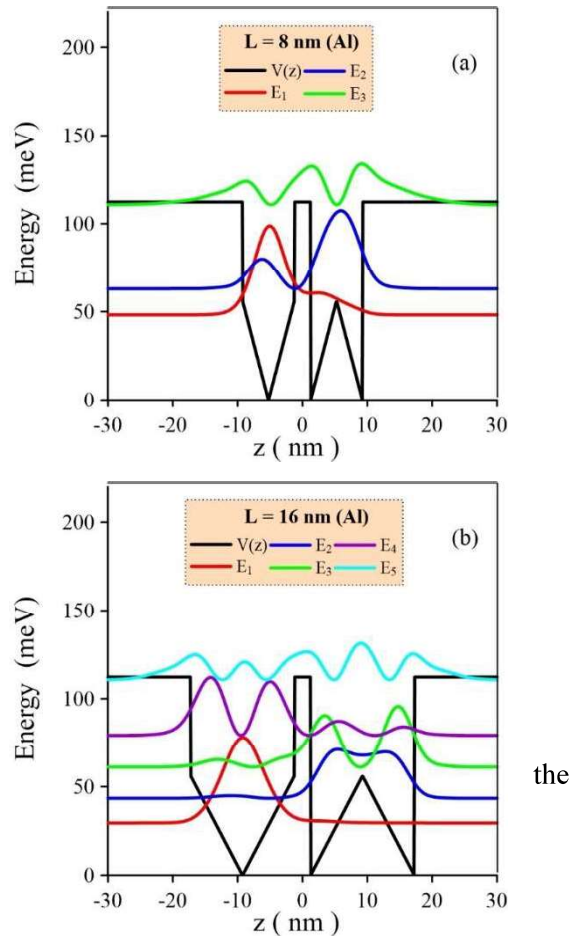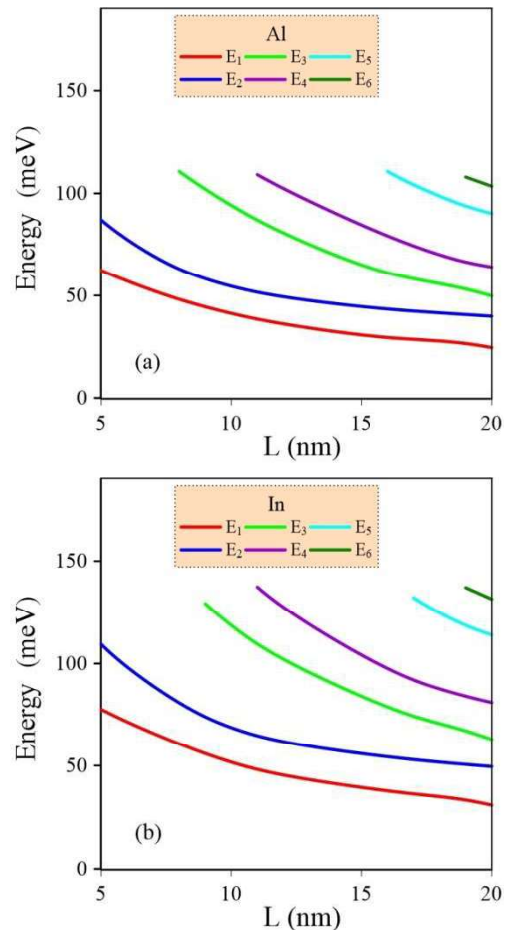

Figure 1. For DQW (A model), the confined potential and the bound energy levels with their squared wave functions for a) $L= 8$ nm, b) $L = 16$ nm.
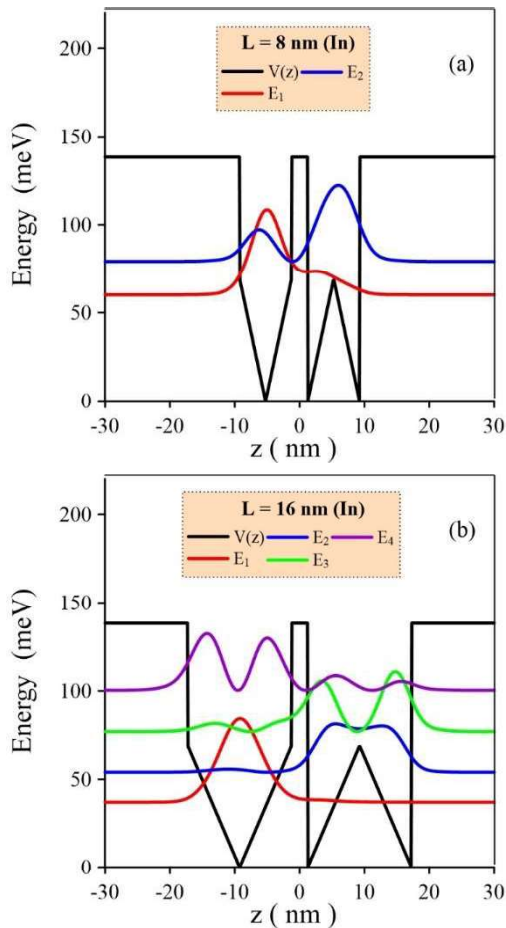
Figure 2. For DQW (B model), the confined potential and the bound energy levels with their squared wave functions for a) L= 8 nm, b) L = 16 nm.

Figure 3. For DQW the variation of bound energy levels versus the L values for a) A model, b) B model.

second energy level is localized in RQW. For L = 16 nm, there are five bounded states in A model and four bounded states in B model. The most affected by the change of the potential profile is the low energy particles, so the electron in the ground state energy is wholly found in LQW. But the electron in the second energy level behaves as if it is confined by a symmetrical double well in RQW. Other energy levels are based on the shape of QWs.

For A and B model, the variation of bound energy levels in DQW as a function of WW between L = (5 − 20) nm are shown in Fig. 3a and Fig. 3b, serially. The energy levels of DQW with different QW shapes are different from each other. As expected, all energy levels change by increasing WW values. The energy levels of A model are constantly lower than the energy levels of B model. As the wells expand, the values of the

energy levels decrease and more bounded state energy levels exist in the wells. The third bounded state energy appears in A model at L = 8 nm, while in B model it occurs for L = 9 nm. In both models, the fourth and sixth energy levels are localized in DQW at L = 11 nm and L = 19 nm, serially. The fifth energy level for A and B model was located within the wells at L = 16 nm and L = 17 nm, respectively. The differences are due to the smaller mass of the electron in B model. Therefore, if it is desired to obtain more bound state energy levels depending on L value, then A model should be preferred.

For A and B model, the finding probability of the electron in LQW and RQW for first three bounded energy states are given in Fig. 4a and Fig. 4b as a function of WW, respectively. In both models, for the initial value of L = 5 nm, the ground state and the second state energy levels are located in LQW

and RQW, serially, and they settle more as WW increases. The third energy level is found in both LQW and RQW where the well width is small ($L < 11 \, nm$), but with the increase in WW (fourth energy level appears also at $L \geq 11 \, nm$), it is located in RQW. The probability densities in A model is slightly higher than B model.
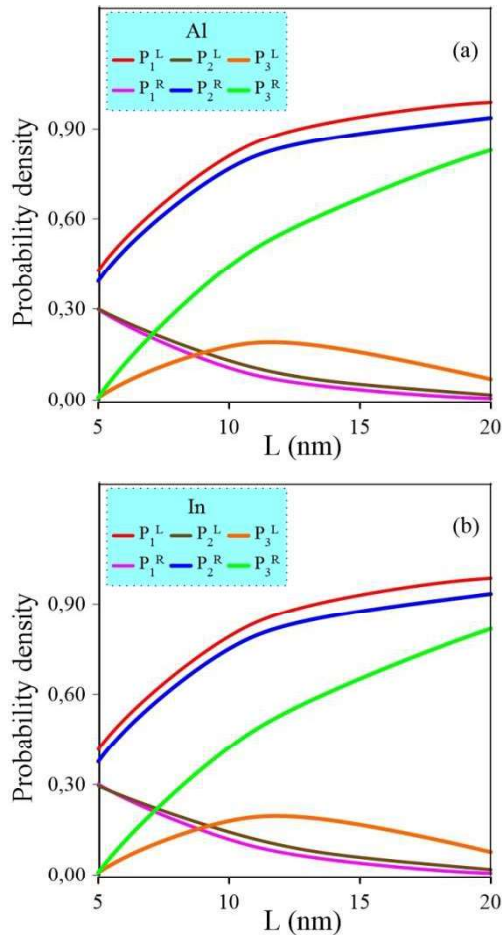
Figure 4. The probability density of the electrons in LQW and RQW for first three bound energy state as a function of the L values for a) A model, b) B model.

4.   CONCLUSIONS

In present work, the electronic features of double $Ga_{1-x}Al_xAs/GaAs$ and $Ga_{1-x}In_xAs/GaAs$ /GaAs QWs are observed related to the well width. The greatest essential difference between these models is the size of energy levels. We analyzed the bound energy levels and the finding probabilities of the electrons in DQW. In particular, we have calculated the eigen-energies and the eigen-

functions of these models. It is found that depending on the well width of the electronic features of DQW varies for A and B model. These features could be crucial in the improvement of continual wave operation of DQW semiconductor devices. So, we think that these results will provide an improvement in multiple electro-optical semiconductor devices applications, for proper selection of the structural parameters.

REFERENCES

[1]   Zhao G. J., Liang X. X., Ban S. L., Binding energies of donors in quantum wells under hydrostatic pressure, Phys. Lett. A, 319 (2003) 191-197

[2]   Ozturk E., Simultaneous effects of the intense laser field and the electric field on the nonlinear optical properties in GaAs/GaAlAs quantum well, Opt. Commun., 332 (2014) 136-143

[3]   Raigoza N., Morales A. L., Duque C. A., Effects of hydrostatic pressure on donor states in symmetrical GaAs-Ga_{0.7}Al_{0.3}As double quantum wells, Physica B, 363 (2005) 262-270

[4]   Peter A. J., Navaneethakrishnan K., Simultaneous effects of pressure and temperature on donors in a GaAlAs/GaAs quantum well, Superlattice Microst., 43 (2008) 63-71

[5]   Tung L.V., Vinh P. T., Phuc H.V., Magneto-optical properties of semi-parabolic plus semi-inverse squared quantum wells, Physica B, 539 (2018) 117-122

[6]   Kasapoglu E., Duque C. A., Mora-Ramos M. E., Restrepo R. L., Ungan F., Yesilgul U., Sari H., Sokmen I., Combined effects of intense laser field, electric and magnetic fields on the nonlinear optical properties of the step-like quantum well, Materials Chemistry and Physic, 154 (2015) 170-175

[7]   Ozturk E., Sokmen I., Nonlinear intersubband absorption and refractive index changes in square and graded quantum well modulated by temperature and hydrostatic pressure, J. Lumin.,134 (2013) 42-48

[8] Laidig W. D., Lin Y. F., Caldwell P. J., Properties of InxGa1-xAs-GaAs strained-layer quantum well-heterostructure injection lasers, J. Appl. Phys., 57 (1985) 33-37

[9] Ozturk E., Electric and intense laser field effect on the electronic properties of $Ga_{1-x}Al_xAs$/GaAs and $Ga_{1-x}In_xAs$/GaAs semi-parabolic quantum wells, Laser Physics, 26 (2016) 096102-096110

[10] Baser P., Altuntas I., Elagoz S., The hydrostatic pressure and temperature effects on hydrogenic impurity binding energies in GaAs/$In_xGa_{1-x}As$/ GaAs square quantum well, Superlattice. Microst., 92 (2016) 210-216

[11] Ohno Y., Matsusue T., Sakaki H., Gigantic negative transconductance and mobility modulation in a double-quantum-well structure via gate-controlled resonant coupling, Appl. Phys. Lett., 62 (1993) 1952-1954Liu L., Swierkowski L.,

[12] Neilson D., Szymaiski J., Static and dynamic properties of coupled electron-electron and electron-hole layers, Phys. Rev. B, 53 (1996) 7923-7931

[13] Ozturk O., Ozturk E., Elagoz S., The effect of barrier width on the electronic properties of double GaAlAs/GaAs and GaInAs/GaAs quantum wells, Journal of Molecular Structure, 1156 (2018) 726-732

[14] Niculescu E.C., Eseanu N., Spandonide A., Laser field effects on the interband transitions in differently shaped quantum wells, U.P.B. Sci. Bull., Series A, 77 (2015) 281-292

[15] Ochalski T.J., Zuk J., Reginski K., Bugajski M., Photoreflectance studies of InGaAs/GaAs/AlGaAs single quantum well laser structures, Acta Physica Polonica A, 94 (1998) 463-467.

Cumhuriyet Science Journal

CSJ

Approximate Bayes Estimation for Log-Dagum Distribution

Caner TANIŞ[1*] ID *, Merve ÇOKBARLI*[2] ID *, Buğra SARAÇOĞLU*[1] ID

[1,2,3] Selçuk University Department of Statistics, Konya, TURKEY

Abstract. In this article, the approximate Bayes estimation problem for the log-Dagum distribution with three parameters is considered. Firstly, the maximum likelihood estimators and asymptotic confidence intervals based on these estimators for unknown parameters of log-Dagum distribution are constructed. In addition, approximate Bayes estimators under squared error loss function for unknown parameters of this distribution are obtained using Tierney and Kadane approximation. A Monte-Carlo simulation study is performed to compare performances of maximum likelihood and approximate Bayes estimators in terms of mean square errrors and biases. Finally, real data analysis for this distribution is performed.

Keywords: Log-Dagum Distribution Maximum Likelihood Estimation, Asymptotic Confidence Interval, Approximate Bayesian Estimation, Tierneyand Kadane Approximation.

Log-Dagum Dağılımı İçin Yaklaşık Bayes Tahmini

Özet. Bu makalede, log-Dagum dağılımı için yaklaşık Bayes tahmini problemi düşünüldü. İlk olarak, Log-Dagum dağılımının bilinmeyen parametreleri için en çok olabilirlik tahmin edicileri ve bu tahmin edicilere dayalı asimptotik güven aralıkları oluşturuldu. Ayrıca, bu dağılımın bilinmeyen parametreleri için karesel kayıp fonksiyonu altında yaklaşık Bayes tahmin edicileri Tierney and Kadane yaklaşımı kullanılarak elde edildi. Bu tahmin edicilerin performanslarını, hata kareler ortalaması ve yan bakımından karşılaştırmak için bir Monte-Carlo simülasyon çalışması gerçekleştirilmiştir. Son olarak bu dağılım için gerçek veri analizi gerçekleştirilmiştir.

Anahtar Kelimeler: Log-Dagum dağılımı, En çok olabilirlik tahmini, Asimptotik güven aralığı, Yaklaşık Bayes tahmini, Tierney and Kadane yaklaşımı.

1.   INTRODUCTION

Statistical distributions are widely used for analysis of data in the real world. In literature, new statistical distributions have been obtained for modeling data in many areas such as science, engineering, medicine and economy. One of these statistical distributions is the dagum distribution suggested by Dagum [1,2] used for modelling wealth and income data . The cumulative distribution function (cdf) and probability density function (pdf) of a Y random variable having to Dagum distribution with parameters β, λ and δ are given by,

$$F_Y\left(y; \beta, \lambda, \delta\right) = \left(1 + \lambda y^{-\delta}\right)^{-\beta} \tag{1.1}$$

$$f_Y\left(y; \beta, \lambda, \delta\right) = \beta \lambda \delta y^{-\delta-1}\left(1 + \lambda y^{-\delta}\right)^{-\beta-1} \tag{1.2}$$

where $y > 0, \lambda > 0$, $\beta > 0$, $\delta > 0$. Domma [3] has introduced the log-Dagum (LDa) distribution by using logarithmic transformation, $X = \ln Y$, of a Y random variable having to Dagum distribution. The cdf and pdf of the log-Dagum (LDa) distribution with β, λ and δ parameters are

$$F_X\left(x;\beta,\lambda,\delta\right) = \left(1 + \lambda e^{-\delta x}\right)^{-\beta} \tag{1.3}$$

and

$$f_X\left(x;\beta,\lambda,\delta\right) = \beta\lambda\delta e^{-\delta x}\left(1 + \lambda e^{-\delta x}\right)^{-\beta-1} \tag{1.4}$$

respectively. Where $x \in \mathbb{R}$, $\beta > 0$, $\lambda > 0$ and $\delta > 0$. There are few studies about LDa distribution in literature. Domma [4] has proved that the kurtosis for log-dagum distribution depends only on parameter β. Domma and Perri [5] have examined some characteristic properties of this distribution and they have studied about maximum likelihood estimation (MLE) and asymptotic confidence interval for the unknown parameters of log-dagum distribution. The plots of pdf for various parameter values of $LDa\left(\beta,\lambda,\delta\right)$ distribution are given in Figure 1.
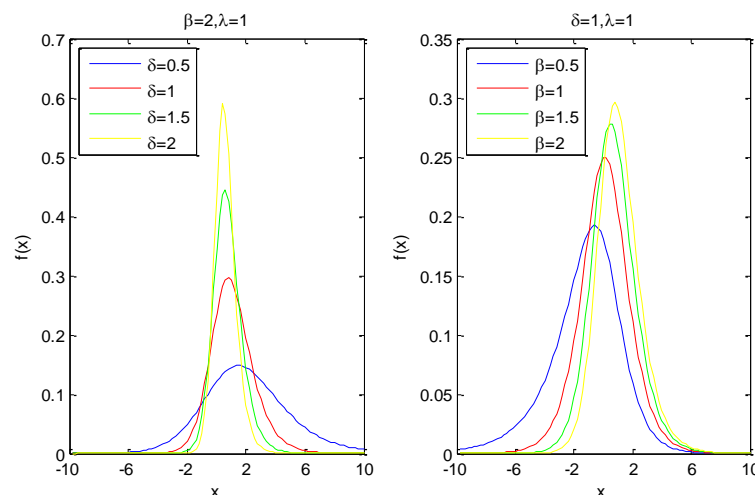
Figure 1. Density function plots of log-Dagum distribution for different parameter values

In this paper, we consider approximate Bayes estimation problem of unknown parameters (β,λ,δ) for the log-Dagum distribution. This study is organized as follows. In Section 2, maximum likelihood estimators (MLEs) for unknown parameters of the log-Dagum distribution and asymptotic confidence intervals based on these estimators are presented. In section 3, Bayes estimators with Tierney and Kadane approximation under squared loss function for unknown parameters of the log-Dagum distribution are obtained. In section 4, a Monte-Carlo simulation study is performed to compare maximum likelihood (ML) and approximate Bayes estimators in terms of mean square errors (MSEs) and biases. In addition, in this section, a simulation study based on asymptotic confidence intervals is carried out. A real data application is performed in section 5. In the last section, the conclusion of this study is given.

2. ML ESTIMATION and ASYMPTOTIC CONFIDENCE INTERVALS for LOG-DAGUM DISTRIBUTION

Let $\underline{X} = (X_1, X_2, ..., X_n)$ be a random sample with size n taken from $LDa(\beta, \lambda, \delta)$ distribution. In that case, the log-likelihood function is given by;

$$\ell(\beta, \delta, \lambda \mid \underline{x}) = n\log\beta + n\log\lambda + n\log\delta - \delta\sum_{i=1}^{n} x_i - (\beta+1)\sum_{i=1}^{n} \log\left(1 + \lambda e^{-\delta x_i}\right) \qquad (2.1)$$

In order to obtain ML estimators, the following likelihood equations should be solved.

$$\frac{\partial\ell(\beta, \delta, \lambda \mid \underline{x})}{\partial\beta} = \frac{n}{\beta} - \sum_{i=1}^{n} \log\left(1 + \lambda e^{-\delta x_i}\right) = 0 \qquad (2.2)$$

$$\frac{\partial\ell(\beta, \delta, \lambda \mid \underline{x})}{\partial\lambda} = \frac{n}{\lambda} - (\beta+1)\sum_{i=1}^{n} \frac{e^{-\delta x_i}}{1 + \lambda e^{-\delta x_i}} = 0 \qquad (2.3)$$

$$\frac{\partial\ell(\beta, \delta, \lambda \mid \underline{x})}{\partial\delta} = \frac{n}{\delta} - \sum_{i=1}^{n} x_i + (\beta+1)\sum_{i=1}^{n} \frac{\lambda x_i e^{-\delta x_i}}{1 + \lambda e^{-\delta x_i}} = 0 \qquad (2.4)$$

The solution of these non-linear equations can be obtained by using iteration methods such as Newton-Raphson method (Domma and Perri [5]).

Large-sample approach is used to obtain asymptotic confidence intervals for unknown parameters. Let $\hat{\Theta}$ is ML estimator of Θ and $I(\Theta), \Theta = (\beta, \lambda, \delta)$ is Fisher information matrix. In this case, the asymptotic distribution of $\sqrt{n}\left(\hat{\Theta} - \Theta\right)$ and the Fisher information matrix are

$$\sqrt{n}\left(\hat{\Theta} - \Theta\right) \xrightarrow{d} N\left(0, I^{-1}(\Theta)\right)$$

$$I(\Theta) = \begin{pmatrix} -E\left[\dfrac{\ell^2(\beta,\lambda,\delta \mid \underline{x})}{\partial\beta^2}\right] & -E\left[\dfrac{\ell^2(\beta,\lambda,\delta \mid \underline{x})}{\partial\beta\partial\lambda}\right] & -E\left[\dfrac{\ell^2(\beta,\lambda,\delta \mid \underline{x})}{\partial\beta\partial\delta}\right] \\ -E\left[\dfrac{\ell^2(\beta,\lambda,\delta \mid \underline{x})}{\partial\lambda\partial\beta}\right] & -E\left[\dfrac{\ell^2(\beta,\lambda,\delta \mid \underline{x})}{\partial\lambda^2}\right] & -E\left[\dfrac{\ell^2(\beta,\lambda,\delta \mid \underline{x})}{\partial\lambda\partial\delta}\right] \\ -E\left[\dfrac{\ell^2(\beta,\lambda,\delta \mid \underline{x})}{\partial\delta\partial\beta}\right] & -E\left[\dfrac{\ell^2(\beta,\lambda,\delta \mid \underline{x})}{\partial\delta\partial\lambda}\right] & -E\left[\dfrac{\ell^2(\beta,\lambda,\delta \mid \underline{x})}{\partial\delta^2}\right] \end{pmatrix}, \qquad (2.5)$$

respectively. The elements of fisher information matrix have been obtained by Domma and Perri [5]. The above approaches are used to find the approximate confidence intervals of β, λ and δ parameters. The $(1-\eta)100\%$ confidence intervals of the β, λ and δ parameters are obtained as in equations (2.6),(2.7) and (2.8).

$$P\left(\hat{\beta} - z_{\frac{\eta}{2}}\sqrt{Var\left(\hat{\beta}\right)} < \beta < \hat{\beta} + z_{\frac{\eta}{2}}\sqrt{Var\left(\hat{\beta}\right)}\right) = 1 - \eta \qquad (2.6)$$

$$P\left(\hat{\lambda} - z_{\frac{\eta}{2}}\sqrt{Var\left(\hat{\lambda}\right)} < \lambda < \hat{\lambda} + z_{\frac{\eta}{2}}\sqrt{Var\left(\hat{\lambda}\right)}\right) = 1 - \eta \tag{2.7}$$

$$P\left(\hat{\delta} - z_{\frac{\eta}{2}}\sqrt{Var\left(\hat{\delta}\right)} < \delta < \hat{\delta} + z_{\frac{\eta}{2}}\sqrt{Var\left(\hat{\delta}\right)}\right) = 1 - \eta \tag{2.8}$$

where diagonal elements of inverse of Fisher information matrix are variances of $\hat{\beta}$, $\hat{\lambda}$ and $\hat{\delta}$ (Domma and Perri [5]).

3. BAYES ESTIMATION for PARAMETERS of LOG-DAGUM DISTRIBUTION

Let $X_1, X_2,..., X_n$ be a random sample with size n taken from $LDa(\beta, \lambda, \delta)$ distribution. It is needed to prior distributions for these parameters to obtain Bayesian estimation of parameters. In this study, it is taken as following gamma priors for unknown β, λ and δ parameters.

$$\pi(\beta) \propto \beta^{d_1-1} e^{-\beta e_1} \qquad , \beta, e_1, d_1 > 0 \tag{2.9}$$

$$\pi(\lambda) \propto \lambda^{d_2-1} e^{-\lambda e_2} \qquad , \lambda, e_2, d_2 > 0 \tag{2.10}$$

$$\pi(\delta) \propto \delta^{d_3-1} e^{-\delta e_3} \qquad , \delta, e_3, d_3 > 0 \tag{2.11}$$

The joint priors and posterior distributions of β, λ and δ parameters are,

$$\pi(\beta, \lambda, \delta) = \pi(\beta)\pi(\lambda)\pi(\delta) \propto \beta^{d_1-1}\lambda^{d_2-1}\delta^{d_3-1} e^{-(\beta e_1 + \lambda e_2 + \delta e_3)}$$

$$\pi(\beta, \lambda, \delta \mid x) = \frac{f(x \mid \beta, \lambda, \delta)\pi(\beta, \lambda, \delta)}{f_x(x)}$$
$$= \frac{k(x_i; \beta, \lambda, \delta)\pi(\beta, \lambda, \delta)}{\int\limits_0^\infty\int\limits_0^\infty\int\limits_0^\infty k(x_i; \beta, \lambda, \delta)\pi(\beta, \lambda, \delta)d\beta d\lambda d\delta}, \tag{2.12}$$

respectively. Where $k(x_i; \beta, \lambda, \delta) = (\beta, \lambda, \delta)^n \exp\left(-\delta\sum\limits_{i=1}^n x_i\right)\prod\limits_{i=1}^n\left(1 + \lambda\exp(-\delta x_i)\right)^{-\beta-1}$. In this case, Bayes estimator for any function of β, λ and $\delta, u(\beta, \lambda, \delta)$, under squared loss function is as follows.

$$\hat{u}_B(\beta, \lambda, \delta) = E\left[u(\beta, \lambda, \delta) \mid x\right]$$
$$= \frac{\int\limits_0^\infty\int\limits_0^\infty\int\limits_0^\infty u(\beta, \lambda, \delta \mid x)e^{\left[\ell(\beta, \lambda, \delta \mid x) + \rho(\beta, \lambda, \delta)\right]}d\beta d\lambda d\delta}{\int\limits_0^\infty\int\limits_0^\infty\int\limits_0^\infty e^{\left[\ell(\beta, \lambda, \delta \mid x) + \rho(\beta, \lambda, \delta)\right]}d\beta d\lambda d\delta} \tag{2.13}$$

Where $\ell(\beta, \lambda, \delta \mid x)$ is log-likelihood function, $\rho(\beta, \lambda, \delta)$ is logarithm of joint prior distribution. It is very difficult to the obtain solution of above Eq. (2.13) in closed form. Some approximate methods for solution of this equation are used. One of these methods is Tierney Kadane's approximation.

a.   Bayes Estimation with Tierney and Kadane's Method

Tierney and Kadane's approximation introduced by Tierney and Kadane [6] to compute integral ratios in bayes analysis has been studied by many authors such as Gencer and Saraçoğlu [7], Howloader and Hossain [8], Mousa and Jaheen [9], Kınacı et al. [10], Tanış and Saraçoğlu [11]. Tierney and Kadane approximation can be summarized as follows.

$$I(\beta,\lambda,\delta) = \frac{1}{n}\{\rho(\beta,\lambda,\delta) + \ell(\beta,\lambda,\delta \,|\, x)\} \tag{2.14}$$

$$I^*(\beta,\lambda,\delta) = \frac{1}{n}\log u(\beta,\lambda,\delta) + I(\beta,\lambda,\delta) \tag{2.15}$$

Where, $\rho(\beta,\lambda,\delta)$ is defined as follows.

$$\rho(\beta,\lambda,\delta) = (d_1-1)\log(\beta) + (d_2-1)\log(\lambda) + (d_3-1)\log(\delta) - (\beta e_1 + \lambda e_2 + \delta e_3) \tag{2.16}$$

Bayes estimators with Tierney and Kadane approximation of $u(\beta,\lambda,\delta)$ under squared error loss function for $LDa(\beta,\lambda,\delta)$ distribution is obtained as follows

$$\hat{u}_b(\beta,\lambda,\delta) = E[u(\beta,\lambda,\delta) \,|\, x] = \frac{\int_0^\infty\int_0^\infty\int_0^\infty e^{nI^*(\beta,\lambda,\delta)}d\beta d\lambda d\delta}{\int_0^\infty\int_0^\infty\int_0^\infty e^{nI(\beta,\lambda,\delta)}d\beta d\lambda d\delta} \tag{2.17}$$

$$= \left[\left(\frac{\det\Sigma^*}{\det\Sigma}\right)^{1/2}\exp\left[n\left(I^*\left(\hat{\beta}_{I^*},\hat{\lambda}_{I^*},\hat{\delta}_{I^*}\right) - I\left(\hat{\beta}_I,\hat{\lambda}_I,\hat{\delta}_I\right)\right)\right]\right]$$

where $\left(\hat{\beta}_{I^*},\hat{\lambda}_{I^*},\hat{\delta}_{I^*}\right)$ and $\left(\hat{\beta}_I,\hat{\lambda}_I,\hat{\delta}_I\right)$ maximize $I^*\left(\hat{\beta}_{I^*},\hat{\lambda}_{I^*},\hat{\delta}_{I^*}\right)$ and $I\left(\hat{\beta}_I,\hat{\lambda}_I,\hat{\delta}_I\right)$, respectively. Σ^* and Σ are minus the inverse Hessians of $I^*\left(\hat{\beta}_{I^*},\hat{\lambda}_{I^*},\hat{\delta}_{I^*}\right)$ and $I\left(\hat{\beta}_I,\hat{\lambda}_I,\hat{\delta}_I\right)$ at $\left(\hat{\beta}_{I^*},\hat{\lambda}_{I^*},\hat{\delta}_{I^*}\right)$ and $\left(\hat{\beta}_I,\hat{\lambda}_I,\hat{\delta}_I\right)$, respectively.

4. SIMULATION STUDY

In this section, a Monte-Carlo simulation study in order to compare the performances of ML estimators and aproximate bayesian estimators according to MSEs and biases for $LDa(\beta,\lambda,\delta)$ distribution is performed. In addition, in this section, a simulation study based on coverage probabilities (cp) and lengths of asymptotic confidence intervals based on ML estimators is carried out. Firstly, it is needed to generate random samples from $LDa(\beta,\lambda,\delta)$ distribution for simulation study.

4.1. Random Sample Generation

Inverse conversion method in order to generate random number from $LDa(\beta,\lambda,\delta)$ distribution is used. Let u state a random number generated from $Uniform(0,1)$. x generated from $LDa(\beta,\lambda,\delta)$ distribution with inverse conversion method is given as follows.

$$x = \frac{1}{\delta_0}ln\left(\frac{\lambda_0}{u^{-1/\beta_0}-1}\right) \tag{3.1}$$

where β_0, λ_0 and δ_0 are initial values. (Domma and Perri [7]).

In simulation study, it is generated $N = 5000$ samples of sizes $n = 100, 200, 500, 1000$ from $LDa(\beta, \lambda, \delta)$ distribution with $(\beta_0 = 0.43, \lambda_0 = 0.2, \delta_0 = 0.5)$, $(\beta_0 = 0.8, \lambda_0 = 0.15, \delta_0 = 0.3)$ and $(\beta_0 = 0.5, \lambda_0 = 0.1, \delta_0 = 0.7)$. The biases and MSEs of ML and approximate bayes estimators for unknown parameters at different samples sizes as $n = 100, 200, 500, 1000$ are given in Table1. In this table, prior values for approximate bayes estimators are $d_1 = 0.01, e_1 = 0.01$, $d_2 = 0.01, e_2 = 0.01, d_3 = 0.01, e_3 = 0.01$. The results of asymptotic confidence intervals based on ML estimators for unknown parameters of $LDa(\beta, \lambda, \delta)$ distribution for different samples sizes as $n = 100, 200, 500, 1000$ are presented in Table 2.

Table 1. Biases and MSEs of MLE and Bayes estimators for $LDa(\beta, \lambda, \delta)$

$(\beta_0, \lambda_0, \delta_0)$	N	$\hat{\beta}_{MLE}$		$\hat{\beta}_{BAYES}$		$\hat{\lambda}_{MLE}$		$\hat{\lambda}_{BAYES}$		$\hat{\delta}_{MLE}$		$\hat{\delta}_{BAYES}$	
		bias	mse	bias	mse	bias	mse	bias	mse	bias	mse	bias	mse
$(0.43, 0.2, 0.5)$	100	-0.0261	0.0261	-0.0417	0.0352	-0.0018	0.0066	-0.0236	0.0105	-0.0247	0.0137	-0.0487	0.0201
	200	-0.0110	0.0102	-0.0154	0.0111	-0.0005	0.0027	-0.0101	0.0033	-0.0120	0.0053	-0.0225	0.0062
	500	-0.0032	0.0036	-0.0044	0.0037	-0.0005	0.0010	-0.0041	0.0011	-0.0052	0.0019	-0.0093	0.0020
	1000	-0.0020	0.0017	-0.0026	0.0017	-0.0001	0.0005	-0.0018	0.0005	-0.0022	0.0009	-0.0042	0.0009
$(0.8, 0.15, 0.3)$	100	-0.1117	2.5370	-0.3782	2.8199	0.0010	0.0037	-0.0115	0.0051	-0.0092	0.0031	-0.0159	0.0038
	200	-0.0425	0.0556	-0.0758	0.0816	0.0005	0.0016	-0.0053	0.0019	-0.0046	0.0013	-0.0079	0.0015
	500	-0.0135	0.0164	-0.0227	0.0178	-0.0001	0.0006	-0.0023	0.0007	-0.0020	0.0005	-0.0033	0.0005
	1000	-0.0076	0.0077	-0.0118	0.0080	0.0001	0.0003	-0.0010	0.0003	-0.0008	0.0002	-0.0015	0.0002
$(0.5, 0.1, 0.7)$	100	-0.0366	0.0392	-0.0645	0.0824	0.0026	0.0013	-0.0039	0.0016	-0.0294	0.0227	-0.0594	0.0327
	200	-0.0153	0.0146	-0.0224	0.0164	0.0013	0.0006	-0.0018	0.0007	-0.0148	0.0094	-0.0278	0.0108
	500	-0.0045	0.0050	-0.0067	0.0052	0.0004	0.0002	-0.0008	0.0002	-0.0066	0.0034	-0.0115	0.0036
	1000	-0.0028	0.0024	-0.0038	0.0024	0.0003	0.0001	-0.0003	0.0001	-0.0028	0.0016	-0.0052	0.0017

Table 2. Length and cp based on MLE for $LDa(\beta, \lambda, \delta)$

$(\beta_0, \lambda_0, \delta_0)$	n	$\hat{\beta}_{MLE}$		$\hat{\lambda}_{MLE}$		$\hat{\delta}_{MLE}$	
		cp	length	cp	length	cp	length
$(0.43, 0.2, 0.5)$	100	0.9298	0.5739	0.8994	0.2926	0.9456	0.4061
	200	0.9446	0.3788	0.9232	0.1982	0.9502	0.2704
	500	0.9470	0.2313	0.9388	0.1232	0.9490	0.1662
	1000	0.9512	0.1623	0.9444	0.0864	0.9514	0.1161
$(0.8, 0.15, 0.3)$	100	0.9310	1.4932	0.8988	0.2216	0.9460	0.2012
	200	0.9422	0.8406	0.9260	0.1524	0.9448	0.1370
	500	0.9488	0.4928	0.9398	0.0952	0.9538	0.0850
	1000	0.9508	0.3424	0.9460	0.0669	0.9518	0.0596
$(0.5, 0.1, 0.7)$	100	0.9340	0.6945	0.8974	0.1346	0.9480	0.5367
	200	0.9418	0.4516	0.9202	0.0942	0.9502	0.3610
	500	0.9494	0.2740	0.9380	0.0593	0.9500	0.2227
	1000	0.9506	0.1920	0.9420	0.0418	0.9506	0.1557

According to results of simulation study, it is seen that MSEs and biases values for ML and approximate bayes estimators of parameters are decreases when the number of samples increases. Furthermore, as

sample sizes increases, it is observed that cp approaches to 0.95 and the length of the asymptotic confidence interval decreases as expected.

5. REAL DATA APPLICATION

The data set consist of 76 observations about the life of fatigue fracture of Kevlar 373/epoxy which is considered in this section. These data are obtained by subject to constant pressure at the 90% stress level until all fatigue fracture had failed. (Kharazmi and Saatınık, [12]). This data set have been studied Andrews and Herzberg [13], Barlow et al. [14] and Merovci et. al. [15]. Let $x \in \mathbb{R}^+$ express data, we consider a transformation with $y = \ln(x)$ on Kevlar 373/epoxy data set. Thus, it is obtained $y \in \mathbb{R}$ data. Then, new data after transformation is given in Table 3. This data set has been analyzed to compare the log-Dagum distribution with other distributions such as, Normal, Logistic, Laplace, t location-Scale, Extreme Value and Generalized Extreme Value (GEV). Probability density functions of these distributions given by;

$$Normal: f(x) = \frac{1}{\sigma\sqrt{2\pi}}\exp\left(\frac{-(x-\mu)^2}{2\sigma^2}\right), \ \sigma > 0, \ \mu, x \in \mathbb{R}$$

$$Logistic: f(x) = \frac{\exp\left(\frac{x-\mu}{\sigma}\right)}{\sigma\left(1+\exp\left(\frac{x-\mu}{\sigma}\right)\right)^2}, \ \sigma > 0, \ x, \mu \in \mathbb{R}$$

$$Laplace: f(x) = \frac{1}{2\sigma}\exp\left(-\frac{|x-\mu|}{\sigma}\right), \ \sigma > 0, \ x, \mu \in \mathbb{R}$$

$$t\ location\text{-}Scale: f(x) = \frac{\Gamma\left(\frac{\upsilon+1}{2}\right)}{\sigma\sqrt{\upsilon\pi}\Gamma\left(\frac{\upsilon}{2}\right)}\left[\frac{\upsilon+\left(\frac{x-\mu}{\sigma}\right)^2}{\upsilon}\right]^{-\left(\frac{\upsilon+1}{2}\right)}, \ \sigma, \upsilon > 0, \ \mu, x \in \mathbb{R}$$

$$Extreme\ Value: f(x) = \sigma^{-1}\exp\left(\frac{x-\mu}{\sigma}\right)\exp\left(-\exp\left(\frac{x-\mu}{\sigma}\right)\right), \ \sigma > 0, \ \mu, x \in \mathbb{R}$$

$$GEV: f(x) = \sigma^{-1}\exp\left(-\left(1+k\frac{(x-\mu)}{\sigma}\right)^{\frac{-1}{k}}\right)\left(1+k\frac{(x-\mu)}{\sigma}\right)^{-1-\frac{1}{k}}, \ \sigma > 0, \ k, \mu, x \in \mathbb{R}$$
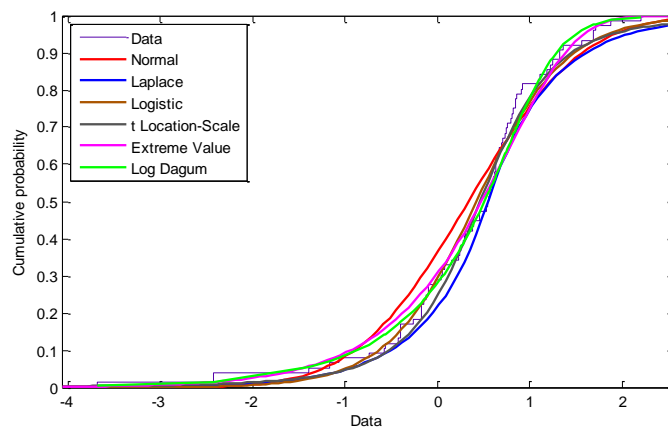
Table 3. Kevlar 373/epoxy data set

-3.6849	-2.4236	-2.4180	-1.3859	-1.1670	-1.0639	-0.7417	-0.5709
-0.5672	-0.4207	-0.3933	-0.3929	-0.3926	-0.2619	-0.1773	-0.1754
-0.1714	-0.1456	-0.1221	-0.0929	-0.0921	-0.0165	0.0472	0.0579
0.0745	0.1598	0.2287	0.2442	0.2612	0.2785	0.3003	0.3039
0.3781	0.3974	0.4529	0.4532	0.5355	0.5460	0.5573	0.5670
0.5736	0.6029	0.6084	0.6153	0.6317	0.6354	0.6356	0.6583
0.6708	0.6955	0.7133	0.7373	0.7464	0.7575	0.7930	0.8092
0.8276	0.8417	0.8531	0.8550	0.9143	0.9266	1.0956	1.1071
1.1841	1.2251	1.2484	1.3200	1.3206	1.3646	1.5701	1.6865
1.6944	1.7101	1.8801	2.2078				

MLEs and their standard errors, AIC values for seven distributions are given In Table 5. Moreover, plots fitted to cdfs, reliability functions and pdfs are presented in Figure 4-6.

Table 4. Parameter estimates (standard errors) and AIC values for Kevlar 373/epoxy data set

Distribution	ML Estimate	-2ℓ	AIC
Log-Dagum	$\hat{\beta} = 0.4248(0.1275)$, $\hat{\lambda} = 17.7962(16.7845)$, $\hat{\delta} = 3.1766(0.5964)$	**187.0024**	**193.0024**
Normal	$\hat{\mu} = 0.3379(0.1102)$, $\hat{\sigma} = 0.9610(0.0787)$	206.64	210.64
Logistic	$\hat{\mu} = 0.4244(0.0938)$, $\hat{\sigma} = 0.4810(0.0469)$	195.7154	199.1792
Laplace	$\hat{\mu} = 0.5516(0.0754)$, $\hat{\sigma} = 0.6578(0.0754)$	191.7154	195.7154
t location-Scale	$\hat{\mu} = 0.4675(0.0860)$, $\hat{\sigma} = 0.5984(0.0919)$, $\hat{\upsilon} = 2.9338(1.1357)$	189.7942	195.7942
Extreme Value	$\hat{\mu} = 0.7574(0.0911)$, $\hat{\sigma} = 0.7543(0.0647)$	191.6836	195.6836
Generalized Extreme Value	$\hat{\mu} = 0.0888(0.1271)$, $\hat{\sigma} = 1.0401(0.0873)$, $\hat{k} = -0.4695(0.0475)$	187.7040	203.7040

Also, the approximate Bayes estimation values of the unknown parameters of Log-Dagum distribution are obtained as $\hat{\beta}_{BAYES} = 0.4613$, $\hat{\lambda}_{BAYES} = 23.2287$, $\hat{\delta}_{BAYES} = 3.1277$ with prior gamma distribution $(d_1 = 0.01, e_1 = 0.01, d_2 = 0.01, e_2 = 0.01, d_3 = 0.01, e_3 = 0.01)$.

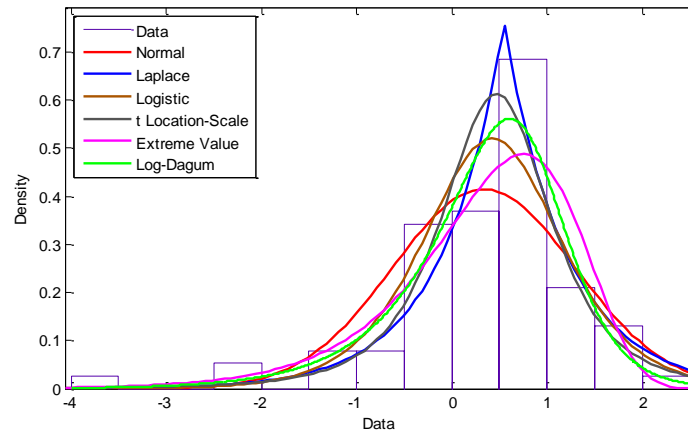**Figure 2**. Fitted cdfs plots for Kevlar 373/epoxy data set

Figure 3. Fitted pdfs plots for Kevlar 373/epoxy data set

6. CONCLUSION

We have analyzed the $LDa(\beta, \lambda, \delta)$ distribution in terms of estimation of unknown parameters. The approximate Bayesian estimators for unknown parameters of this distribution are obtained. The Bayesian estimators under squared error loss function are found using Tierney and Kadane approximation. The performances of ML and approximate Bayes estimators have been compared with the Monte Carlo simulation study according to MSE and bias criteria. A simulation study based on asymptotic confidence intervals is performed. It is seen that the biases and MSEs of ML and Bayes estimators decrease as sample size increases. It can be concluded that biases and MSEs of these two estimators are very close to each other. In interval estimation based on ML estimators of unknown parameters for the $LDa(\beta, \lambda, \delta)$ distribution, it is seen that coverage probabilities (cp) approach to 0.95 and length of asymptotic confidence intervals decreases as sample size increases. Furthermore, a real data application is performed in order to show that the $LDa(\beta, \lambda, \delta)$ distribution can be used in new areas. It is presented a real data set related to the life of fatigue fracture of Kevlar 373/epoxy. We have concluded that the $LDa(\beta, \lambda, \delta)$ distribution has to best fit between other six distributions (Normal, Logistic, Laplace, t location-Scale, Extreme Value, Generalized Extreme Value) according to AIC and -2ℓ.

REFERENCES

[1] Dagum, Camilo. New model of personal income-distribution-specification and estimation. Economie appliquée, 30-3 (1977) 413-437.

[2] Dagum, C. The Generation and Distribution of Income, the Lorenz Curve and the Gini Ratio, Economie Appliqu ée, 33 (1980) 327-367.

[3] Domma, F., Asimmetrie Puntuali e Trasformazioni Monotone. Quaderni di Statistica, 3 (2001) 145-164.

[4] Domma, F., Kurtosis diagram for the Log-Dagum distribution. Statistica Applicazioni, 2 (2004) 3–23.

[5] Domma, F., Perri, P. F., Some developments on the log-Dagum distribution. Statistical Methods and Applications, 18-2 (2009) 205-220.

[6] Tierney, L., Kadane, J. B., Accurate approximations for posterior moments and marginal densities. Journal of the american statistical association, 81(393) (1986) 82-86.

[7] Gencer, G., and Saracoglu, B. Comparison of approximate Bayes Estimators under different loss functions for parameters of Odd Weibull Distribution. Journal of Selcuk University Natural and Applied Science, 5-1 (2016) 18-32.

[8]   Howloader, H.A., Hossain, A. M., Bayesian survival estimation of Pareto distribution of second kind based on failure-censored data, Computational Statistics and Data Analysis, 38 (2002) 301-314.

[9]   Mousa, M. A., Jaheen, Z. F., Statistical inference for the Burr model based on progressively censored data. Computers and Mathematics with Applications, 43-10 (2002) 1441-1449.

[10] Kınacı, İ., Karakaya, K., Akdoğan, Y., Kuş, C., Kesikli Chen Dağılımı için Bayes Tahmini. Selçuk Üniversitesi Fen Fakültesi Fen Dergisi, 42-2 (2016) 144-148.

[11] Tanış, C., Saraçoğlu, B., Statistical Inference Based on Upper Record Values for the Transmuted Weibull Distribution. International Journal of Mathematics and Statistics Invention (IJMSI), 5-9 (2017) 18-23.

[12] Kharazmi, O., Saadatinik, A., Hyperbolic cosine-f family of distributions with an application to exponential distribution. Gazi University Journal of Science, 29-4 (2016) 811-829.

[13] Andrews, D. F., and A. M. Herzberg, Prognostic variables for survival in a randomized comparison of treatments for prostatic cancer. Data, (1985) 261-274.

[14] Barlow, R. E., Toland, R. H., and Freeman, T., A Bayes Analysis of Stress-Rupture Life of Kevlar/Eproxy Spherical Pressure Vessels, in Proceedings of the Canadian Conference in Applied Statistics, New York: Marcel Dekker (1984).

[15] Merovci, F., Alizadeh, M., Hamedani, G. G., Another generalized transmuted family of distributions: properties and applications. Austrian Journal of Statistics, 45 (2016) 71-93.

Determination of Dangerous Parts of the Energy Transmission Line by the Canopy Height Model Produced from LiDAR Data

Nuray BAŞ iD

Istanbul Technical University, Department of Geomatics Engineering, Istanbul, TURKEY

Abstract. LiDAR (Light Detection and Ranging) technique is preferable method to determine vertical metric values of High Voltage Transmission Lines (HVTL) in global regions and steep land. The importance of these facilities is increasing day by day because of the necessity of electricity energy in our daily life. Determination of vertical heights is an important problem especially in forested areas after construction. In this study, metric values of vegetation which violate vertical safety limits under voltage wires were determined by using Canopy Height Model (CHM) using LiDAR data. As a study area 450x150 m^2 was selected the existing voltage line in the region between Beykoz District and Çekmeköy located on the Anatolian side of Istanbul. Firstly, it has been made conductive classification of HVTL that is using LiDAR classification techniques. Also it is determined the dangerous limits of trees and vegetation in HVTL vertical oscillation. As a result the comparison of the values of the vertical elevation with the local methods and obtained from the LiDAR data yielded a Root Mean Square Error (RMSE) value of 0.36m was found..

Keywords: LIDAR, Classification, Canopy Height Model , Power Transmission Line.

LiDAR Verilerinden üretilen Kanopi Yükseklik Modeli Yardımıyla Enerji Nakil Hattının Tehlikeli Kısımlarının Belirlenmesi

Özet. LiDAR (Light Detection and Ranging) tekniği özellikle ulaşılması zor ve global alanlarda, Enerji Nakil Hatları (ENH) gibi tesislerin düşey metrik değerlerinin belirlenmesi konusunda tercih edilebilir bir yöntem olarak karşımıza çıkmaktadır. Elektrik Enerjisi ihtiyacının günlük yaşamımızda hayati bir ihtiyaç halini alması bu tesislerin önemini her geçen gün artırmaktadır. Tesisinden sonraki aşamada ise, düşey yüksekliklerin tespit edilmesi de özellikle ormanlık alanlık alanlarda önemli bir sorun olarak karşımıza çıkmaktadır. Bu amaçla yapılan bu çalışmada, LiDAR verileri kullanılarak oluşturulan Kanopi Yükseklik Modeli(KYM) yardımıyla gerilim telleri altındaki düşey emniyet sınırlarını ihlal eden bitki örtüsünün metrik değerleri belirlenmiştir. Çalışma alanı olarak İstanbul ilinin Anadolu yakasında yer alan Beykoz İlçesi ile Çekmeköy ilçesi arasındaki bölgedeki mevcut Enerji Nakil Hattını kapsayacak şekilde 450 x150 m2 'lik bir alan seçilmiştir. İlk olarak, Enerji Nakil Hattının LiDAR sınıflandırma teknikleri ile iletken sınıflandırması yapılmış ve elde edilen yükseklik değerlerinden, ENH düşey salınım içerisine giren bölgedeki ağaçların ve bitki örtüsünün tehlikeli sınırları tespit edilmiştir. Elde edilen sonuçlar yersel yöntemler ile elde edilen yükseklik değerleriyle karşılaştırılmış olup KOH değeri 0.36 m olarak bulunmuştur.

Anahtar Kelimeler: LiDAR, Sınıflandırma, Kanopi Yükseklik Modeli, Enerji Nakil Hatları.

_____

* Corresponding author. *Email address:*   *nuraybas@gmail.com*

1. INTRODUCTION

Light Detection and Ranging (LiDAR) is an active remote sensing technique which uses electromagnetic energy in optical range to detect an object using distance between the target and sensor [1].

System includes three basic data collection tools which is consisting of laser scanner, Global Positioning System (GPS) and Inertial Measurement Unit (IMU) systems. In recent years, LiDAR techniques have been used in many areas from mapping to urbanism and mining. Since vertical accuracy is more sensitive than positioning accuracy, there are many applications related to this technique in Digital Elevation Model (DEM) and Digital Surface Model (DSM). It is an advantage to obtain high-accuracy three-dimensional coordinate information in areas such as steep slopes, hills and forested area that cannot be reached by traditional method. Especially in corridor mapping applications for example High-voltage Transmission Lines (HVTL) project.

Many studies have been made in the literature such as object identification, DSM, DTM and accuracy management by using LiDAR data. Some studies about determination of HVTL and calculation of vertical distances have also been found in these studies. For example; HVTL and classification techniques have been studied [2]. On the other hand had practiced the risk management of lines [3]. Also identified automatic clearance with the smallest distance differential geometry calculations. Using the height threshold value applied the pylon and mask technique to the point cloud have been done [4]. They used the space, shape and symmetry properties of objects. [5] have identified the trees which is entering the Power Line corridor in the forested area. They applied random clustering method using height shape, growth characteristics in a determined area. In other study, it has been implemented plant management practices in transmission line corridor [6]. They defined the conductor wires by a semi-automatic classification process and used the buffer algorithm. Then, determined polygonal zones where vegetation on the dangerous voltage line. [7] identified the power line by using height threshold segmentation and height density segmentation algorithm.

In this study, it is aimed to determine the Canopy Height Model (CHM) segmentation of the dangerous parts of plants and trees entering into the vertical clearance of the HVTL using LiDAR data in forested area.

2. STUDY AREA

Istanbul Province, located in between the Beykoz and Çekmeköy existing HVTL route which is forested area in the district, 450x150 m^2 of a rectangle is selected (Figure 1).


F**igure 1 :** *Study Area*

3. MATERIAL AND METHOD

The LiDAR data was obtained by using the Riegle LMS-Q560 LiDAR scanner at an average speed of 700m (80km/ h) at 16.10.2016. The system parameters of the data are shown in the Table 1.

Table 1. System Parameters of Airborne LiDAR Data Used

System Parameters	
Flight Speed	80 km/h
Flight Altitude	700m
Scan Angle	30°
Pulse /second	200.000 (1/sn)
Laser Beam Divergence	0.5mrad
Raw Data Density	5point/m²
Point spacing	0.8m

In the first phase of the study, the existing Raw LiDAR data is classified as ground and nonground points. Removing the noise points before the classification process is important for both classification and model accuracy. Adaptive Triangulated Network (ATIN) filtering method was applied in the classification process [8]. LiDAR 360 commercial software was used as software.
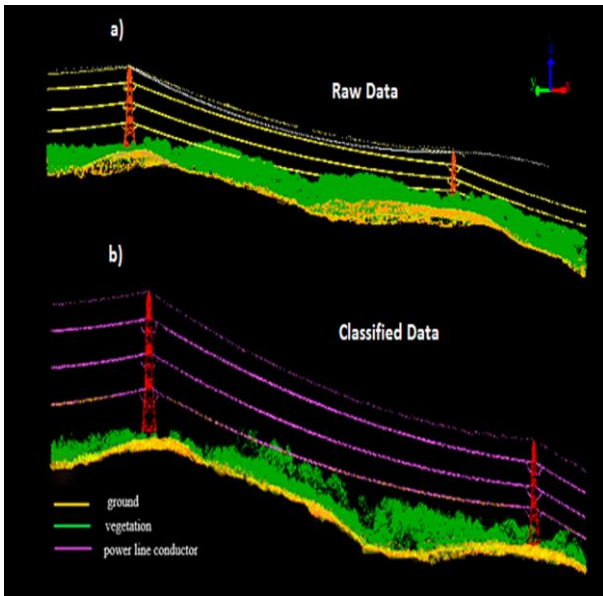
Figure 2: a) Raw LiDAR Data b) Classified Data

In the second step, point cloud data was transformed into grid structure in 1x1m cell size. Then, CHM was generated from normalized LiDAR height value using raster data. Figure 3a shows the height diagram of the classified data. Also CHM is created the differences of DSM and DTM (Figure3b-c-d).
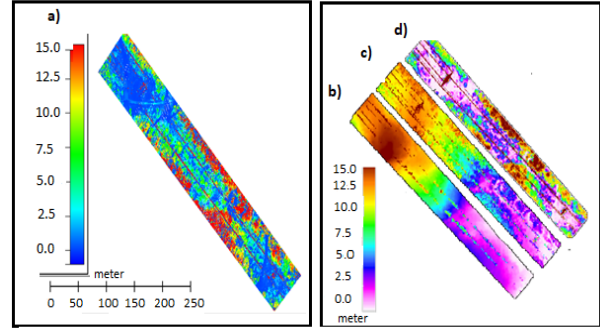
Figure 3: a) Height diagram of Point Cloud Image; b) Digital Terrain Model (DTM) c) Digital Surface Model (DSM) d) Canopy Height Model (CHM)

In the third phase; It is aimed to estimate the height values of the vegetation and trees under HVTL route and also to determine the dangerous limits for the power line wires.

In step four, the total station measurement results of the existing power transmission line obtained terrestial method from the project file of the HVTL. These values are used for accuracy management.

4. DISCUSSIONS OF RESULTS AND CONCLUSIONS

Today, new energy sources are explored every year to provide energy needs in our country. For this purpose it has been establish a new Transmission Line facility in Istanbul every year. Because the city's population and demand for energy is increasing day by day.

As a tehcnical rule, power line are planned as shortest route and pass through worthless land. But sometimes also through forested areas. In this case, vegetation or tree branches extending towards the vertical tension wires damage the voltage lines. As a result, it can be energy loss and power failure. Also, a fire hazard may ocur especially in summer period. Trees should be pruned in summer for these undesirable situations. For solution the minimum distance between the transmission line wires and the vegetation must be maintained. But ,it is difficult and wast of time to

follow the branches of trees that extend through the wires with traditional ground measurement techniques. In forested area, tree height, tree size, and canoppy area defined preciselly estimates [9] used LiDAR techniques. This technique is able to determine the elevation information of large areas both high accuracy and faster than traditional method [10].

Vertical distance from the ground to the maximum sag of the wire was measured. Buffer size is selected according to the maximum width on transmission corridor (right of way) which is determined as 60m (Figure 4).
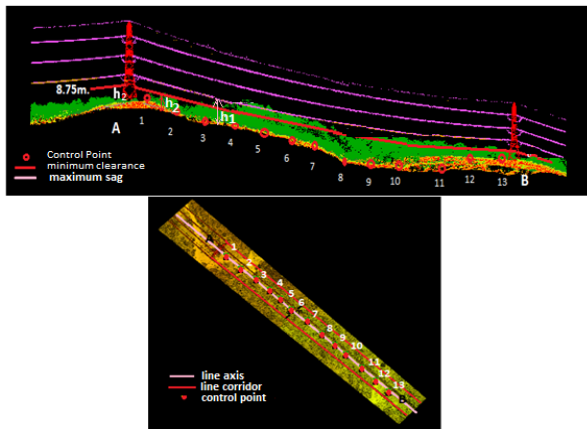
Figure 4: Horizontal and Vertical Profile of the Study Area

The minimum clearance of voltage line in the classified LiDAR data is called h1. But maximum sağ and full load in hot day determined which is 8.75m called h2. The sag lower clearance to the ground depending on ambient temperature and also operating conditions. Minimum vertical clearance which is depending at this value maintained from right of way. The safety distance from the conducter that no human plant and building into safety limits should approach. Minimum clearance limits determined by regulations for the 380 kV Lines according to the High Current Directive published in the Official Gazette numbered 24246 on 30.11.2000 [11]. According to these rules, minimum clearance to be calculated is shown with Equation 1.

$$\text{minimum safety clearance} = \text{h1-h2} \qquad (1)$$

In this study, the voltage line within the study area was determined by classification process. It is important classification process for he accuracy metric value. After the detection of voltage line and also maximum sag a point was thrown at every 25 m between the A-B length.

In principle, pixel based segmentation method was applied with the height values in each region. The parameter values used in the segmentation process are shown in the Figure 5.
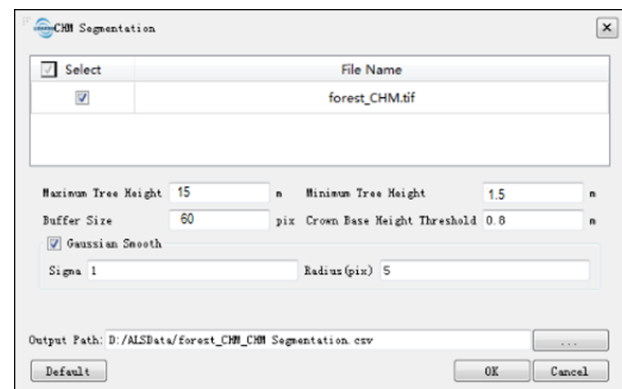
Figure 5 : Threshold Value of Segmentation Process

As a rule, CHM pixels above maximum three height threshold will not be considered in the segmentation. In the same time, CHM pixels below min tree height threshold will not be considered in the segmentation. Crown Base Height Threshold is the starting height of the crown range. A reasonable base height value is very important to improve the accuracy of the results.

As a result of this section, obtained individual tree information, such as tree location, tree height, crown diameter, crown area provides extremely precise estimates of tree height, and there are defined relationships between tree height or canopy area and tree size (i.e., diameter) [10].

Table 1 are included in minimum clearance, tree heights, volume and diameters for each numbered control point section. For implementation, If the tree height is greater than the measured minimum clearance value, it is called a danger zone. The trees in this area should be cut to the minimum clearance to avoid any danger.

Table 2: CHM Segmentasyon Result

Number	Tree height (m)	Danger zone	Min clearance (h₁-h₂)	Total Station (h₁-h₂)	Tree Diameter (m)	Volume (m³)
1	3	-	6.31	6.03	10.99	95
2	4	-	7.52	7.29	9.23	67
3	9	-	9.45	9.27	7.13	40
4	12	danger	11.21	10.97	11.62	244
5	16	danger	14.03	13.83	6.86	37
6	11	danger	9.46	9.23	5.04	20
7	10	danger	6.78	5.82	7.48	44
8	5	danger	3.96	3.71	7.73	47
9	4	danger	2.75	2.75	6.18	30
10	6	danger	2.50	2.14	9.44	70
11	7	danger	2.70	2.34	4.65	17
12	5	danger	2.21	1.95	7.31	42
13	5	danger	4.02	3.82	3.45	32

For the accuracy management, the terrestrial measurement results and the lidar height values were compared. The amount of error in height values is calculated with Root Mean Square Error (RMSE) and found as 0.36 m (2).

$$\text{RMSE}_z = \sqrt{\frac{\sum_{i=1}^{n}(Lidar_z - GPS_z)^2}{n}} = 0.36\text{m}. \qquad (2)$$

As a result it has been possible that the detection and management of the danger parts of trees and vegetation under the power line. In the forested areas that are similar to the working area, it will be difficult to mapping by the local methods, thus taking into consideration the accuracy obtained, time and power will be saved. It is also possible to monitor the dangerous occurrences on the energy transmission line if data are available at specific intervals.

Acknowledgements

REFERENCES

[1] Diaz, J.C.F., Carter, W.E., Shrestha R.L. and Glennie, C.L. Handbook of Satellite Applications, (2017) 929-980.

[2] Li, X. and Guo, Y., Application of LiDAR technology in power line inspection. IOP Conference Series: Materials Science and Engineering, 382 (2018) 052025.

[3] Chen, C., Yang, B., Song, S., Peng, X. and Huang, R. Automatic clearance anomaly detection for transmission line corridors utilizing UAV-Borne LiDAR data. Remote Sensing, 10-4 (2018) 613.

[4] Awrangjeb, M., Islam, M. K. and Systems, I., Classifier-Free Detection of Power Line Pylons From Point Cloud, 14–15 (2017). 81-87.

[5] Ko, C., Remmel, T. K. and Sohn, G.. Mapping tree general using discrete LiDAR and geometric tree metrics, Bosque (Valdivia), 33-3 (2012) 29–30.

[6] Kurinsky, B. H. and Hung, M.C. Identification and Visualization of Vegetation Encroachments along Power Line Corridors using LiDAR, International Journal of Research in Geography, (IJRG), 1-1 (2015) 38–51.

[7] Shen, X., Qin, C., Du, Y., Yu, X. and Zhang, R. An automatic extraction algorithm of high voltage transmission lines from airborne LiDAR point cloud data. Turkish Journal of Electrical Engineering and Computer Sciences, 26-4 (2018) 2043–2055.

[8] Axelsson, P.E. DEM generation from laser scanner data using adaptive TIN models. International Archives of the Photogrammetry, Remote Sensing and Spatial Information Sciences, 32 (2000) 110–117.

[9] Meador, A.J.S. and Parysow, P.F., and Moore, M.M. A new method for delineating tree patches and assessing spatial reference conditions of ponderosa pine forests in northern Arizona, Restoration Ecology 19-4 (2011) 490-499.

[10] Hodgson, M.E. and Bresnahan, P. Accuracy of Airborne LiDAR-Derived Elevation: Empirical Assessment and Error Budget, Photogrammetric Engineering and Remote Sensing, 70 (2004) 331-339.

[11] Regulation on Electric Power Installations, published in the Official Gazette No. 24246 dated 30 November 2000. http://www.resmigazete.gov.tr/eskiler/2000/11/20001130.

Discriminating between the Lognormal and Weibull Distributions under Progressive Censoring

Coşkun KUŞ [1]*, Ahmet PEKGÖR [2], İsmail KINACI[3]

[1]Selcuk University, Faculty of Science, Department of Statistics, Konya, TURKEY

[2]Necmettin Erbakan University, Faculty of Science, Department of Statistics, Konya, TURKEY

[3] Selcuk University, Faculty of Science, Department of Actuarial Sciences, Konya, TURKEY

Abstract. In this paper, the ratio of maximized likelihood and Minimized Kullback-Leibler Divergence methods are discussed for discrimination between log-normal and Weibull distributions. The progressive Type-II right censored sample is considered in the study. The probability of correct selections is simulated and compared to investigate the performance of the procedures for different censoring schemes and parameter settings.

*Keywords***:** Discrimination, Log-normal distribution, Power analysis, Simulation, Progressive type-II right censoring.

İlerleyen Tür Sansür Altında Lognormal ve Weibull Dağılımlarının Ayrımı

Özet. Bu çalışmada, log-normal ve weibull dağılımları arasında ayırım için en çok olabilirlik oran ve Kullback-Leibler uzaklık metotları tartışılmıştır. Çalışmada, ilerleyen tür sansürlü veri durumu ele alınmıştır. Doğru seçim oranları hesaplanmış ve farklı parametre ve sansür şemaları altında testlerin performansları karşılaştırılmıştır.

*Anahtar Kelimeler***:** Ayırım, Log-normal dağılım, Güç analizi, Simülasyon, İlerleyen tür sansürleme.

1. INTRODUCTION

A discrimination procedure focus on making suitable selection from two or more distributions based sample. In other words, discrimination procedure tries to get decision on which distribution is more effective to modeling the data. A lot of papers in the literature on discrimination two or three distributions. Most of them are based on Kullback-Leibler Divergence (KLD) and ratio of maximized log-likelihood (RML). There are a lot of works in this area. Some of them are Alzaid & Sultan [1], Kundu & Manglick [2], Bromideh and Valizadeh [3], Dey and Kundu [4], Dey and Kundu [5], Kundu [6], Kantam et al. [7], Ngom, et al. [8], Ravikumar and Kantam, [9], Qaffou and Zoglat, [10] and Algamal [11].

In this study, we consider on discrimination between log-normal and Weibull distributions. The probability density function (pdf) of log-normal and Weibull distribution are given, respectively, by

$$f_{\boldsymbol{\theta}_1}(x) = \frac{1}{\sqrt{2\pi}\sigma x} \exp\left\{\frac{-1}{2}\left(\frac{\log(x)-\mu}{\sigma}\right)^2\right\} I_{(0,\infty)}(x)$$

and

$$g_{\boldsymbol{\theta}_2}(x) = \alpha x^{\alpha-1}\beta^{-\alpha} \exp\left\{-\left(\frac{x}{\beta}\right)^{\alpha}\right\} I_{(0,\infty)}(x)$$

where $I_A(x)$ is an indicator function on set A and $\boldsymbol{\theta}_1 = (\mu, \sigma)'$ and $\boldsymbol{\theta}_2 = (\alpha, \beta)'$ are distribution parameter vectors.

Some papers related the discrimination between log-normal and Weibull distributions are Quesenberry & Kent [12], Dumonceaux & Antle [13], Pasha et al. [14], Dey & Kundu [4,5], Bromideh [15], Raqab, et al. [16] and Elsherpieny et al [17]. Quesenberry & Kent [12], proposed selection statistic that is essentially the value of the density function of a scale transformation maximal invariant. They considered include the exponential, gamma, Weibull, and lognormal. Note that this method works only complete sample case. Dumonceaux & Antle [13] used the difference of the RML, in discriminating between the Weibull or Log-Normal distribution based on complete sample. Kundu & Manglick [18] obtained the asymptotic distribution of the discrimination statistic RML and determined the probability of correct selection (PCS) by using asymptotic distribution in this discrimination process. Dey and Kundu [19] extended the Kundu & Manglick [18]'s results to Type-II censored sample case. Pasha et al. [14] used RML and most powerful invariant for discriminating these distributions based on complete sample. Kim & Yum [20] extended to Pasha et al. [14]'s results to Type-I and Type-II censored sample cases. Dey & Kundu [4, 5] used the RML, in discriminating between the Weibull, Generalized Exponential Distributions or Log-Normal distribution based on complete and Type-I censored sample. They obtained the asymptotic distribution of the discrimination statistic and determined the PCS by using asymptotic distribution in this discrimination process. Bromideh [15] examined the use the KLD in discriminating either the Weibull or Log-Normal distribution based on complete sample. Raqab, et al. [16] used the RML, in discriminating between the Weibull, Log-logistic or Log-Normal distribution based on doubly censored sample. Elsherpieny et al. [17] considered test based RML and Ratio Minimized Kullback-Leibler Divergence RMKLD for discrimination between Gamma and Log-logistic Distributions based on progressive Type-II right censored data. The model of progressive Type-II right censoring is of importance in the field of reliability and life testing.

Table 1. The papers related to discrimination between lognormal and Weibull distribution

Discrimination and test statistics	Type of Data Schemes				
	Complete Data	Type-I Censored	Type-II Censored	Doubly Censored	Progressively Type-II Right Censored
Kullback-Leibler (KLD)	Bromideh (2012)				Elsherpieny et al. (2017)
Ratio of the Maximized Likelihood (RML)	Kundu & Manglick (2004)	Dey & Kundu (2009)	Dey & Kundu (2012)	Raqab, et al. (2018)	
	Dumonceaux & Antle (1973)				
	Pasha et al. (2006)	Kim & Yum (2008)			
Scale Invariant Test (SI)	Quesenberry& Kent (1982)				

All the papers except for Elsherpieny et al. [17], consider complete or Type-I and Type-II censored sample. In this work, we consider discrimination under progressive Type-II right censored schemes. Progressive Type-II right censoring scheme is explained as follows: Let n identical units are subject to a lifetime test. r_i surviving units are randomly withdrawn from the test, $1 \leq i \leq m$ as soon as i-th failure is occured. Hence, if m failures are observed then $r_1 + \cdots + r_m$ units are progressively Type-II right censored; Thus, $n = m + r_1 + \cdots + r_m$. Let $X_{1:m:n}^{\mathbf{r}} < X_{2:m:n}^{\mathbf{r}} < \cdots < X_{m:m:n}^{\mathbf{r}}$ be the progressively Type-II right censored failure times, where $\mathbf{r} = (r_1, \ldots, r_m)$ denotes the censoring scheme for the life test. As a special case if $\mathbf{r} = (0, \ldots, 0)$, ordinary order statistics are obtained[21]. If $\mathbf{r} = (0, \ldots, 0, m)$, the progressive Type-II right censoring becomes type-II censoring. For more details please see [22,23,24].

In this paper, the discrimination methods are given in Section 2. In Section 3, PCS are simulated by Monte Carlo methods and results are discussed. Finally, a numerical example is provided to illustrate the methodology.

2. RULES OF DISCRIMINATION

Let $X_{1:m:n}^{\mathbf{r}} < X_{2:m:n}^{\mathbf{r}} < \cdots < X_{m:m:n}^{\mathbf{r}}$ are progressive Type-II right censored sample from log-normal (μ, σ) distribution. Then log-likelihood function [26] is given by

$$L_{LN}(\mathbf{\theta}_1) \propto -m \log(\sigma) - \sum_{i=1}^{m} \log(x_i) - \sum_{i=1}^{m} \log\left(\phi\left(\frac{x_{(i)} - \mu}{\sigma} \right) \right)$$
$$+ \sum_{i=1}^{m} (r_i + 1)\left(1 - \Phi\left(\frac{x_{(i)} - \mu}{\sigma} \right) \right), \tag{1}$$

where ϕ and Φ denotes the pdf and cdf of a standard normal distribution. Hence, ML estimate (it is denoted by $\hat{\mathbf{\theta}}_1 = (\hat{\mathbf{\mu}}, \hat{\mathbf{\sigma}})$) of $\mathbf{\theta}_1$ can be obtained numerically which maximize the likelihood function (1).

Let $X_{1:m:n}^{\mathbf{r}} < X_{2:m:n}^{\mathbf{r}} < \cdots < X_{m:m:n}^{\mathbf{r}}$ are progressive Type-II right censored sample from Weibull (α, β) distribution. Then the log-likelihood function (see [27]) is given by

$$L_W(\mathbf{\theta}_2) \propto m \log(\alpha) - m\alpha \log(\beta) + (\alpha - 1)\sum_{i=1}^{m} \log(x_i) - \sum_{i=1}^{m} (r_i + 1)\left(\frac{x_i}{\beta} \right)^{\alpha}. \tag{2}$$

Hence, maximum likelihood (ML) estimate of $\mathbf{\theta}_2$ (it is denoted by $\hat{\mathbf{\theta}}_2 = (\hat{\alpha}, \hat{\beta})$) can be obtained numerically which maximize the likelihood function (2).

One of the rules of discrimination is ratio of the maximized likelihood (RML). The ratio of maximized likelihood is defined as follows

$$RML = L_{LN}(\hat{\mathbf{\theta}}_1) - L_W(\hat{\mathbf{\theta}}_2)$$

where $L_{LN}(\boldsymbol{\theta}_1)$ and $L_W(\boldsymbol{\theta}_2)$ are defined by (1) and (2), respectively and $\hat{\boldsymbol{\theta}}_1$ and $\hat{\boldsymbol{\theta}}_2$ are ML estimates of $\boldsymbol{\theta}_1$ and $\boldsymbol{\theta}_2$. If the $RML > 0$ then log-normal distribution is selected for the modeling data otherwise Weibull distribution is selected against log-normal distribution.

Second one is based on Kullback-Leibler divergence. The KLD is a non-symmetric measure of the difference (dissimilarity) between two probability distributions $f_{\boldsymbol{\theta}_1}$ and $g_{\boldsymbol{\theta}_2}$. Kullback-Leibler divergence between models is defined by

$$D\left(f_{\boldsymbol{\theta}_1}, g_{\boldsymbol{\theta}_2}\right) = \int_0^\infty f_{\boldsymbol{\theta}_1}(x) \log\left(\frac{f_{\boldsymbol{\theta}_1}(x)}{g_{\boldsymbol{\theta}_2}(x)}\right) dx$$
$$= \int_0^\infty f_{\boldsymbol{\theta}_1}(x) \log\left(f_{\boldsymbol{\theta}_1}(x)\right) dx - \int_0^\infty f_{\boldsymbol{\theta}_1}(x) \log\left(g_{\boldsymbol{\theta}_2}(x)\right) dx.$$

It is noted that the $D\left(f_{\boldsymbol{\theta}_1}, g_{\boldsymbol{\theta}_2}\right)$ can also be written by

$$D\left(f_{\boldsymbol{\theta}_1}, g_{\boldsymbol{\theta}_2}\right) = -H\left(f_{\boldsymbol{\theta}_1}\right) - \int_0^\infty f_{\boldsymbol{\theta}_1}(x) \log\left(g_{\boldsymbol{\theta}_2}(x)\right) dx$$

where $H\left(f_{\boldsymbol{\theta}_1}\right)$ is Shannon's entropy of $f_{\boldsymbol{\theta}_1}$ defined as

$$H\left(f_{\boldsymbol{\theta}_1}\right) = -\int_0^\infty f_{\boldsymbol{\theta}_1}(x) \log\left(f_{\boldsymbol{\theta}_1}(x)\right) dx.$$

It is well known that $D\left(f_{\boldsymbol{\theta}_1}, g_{\boldsymbol{\theta}_2}\right) \geq 0$ and the equality holds if and only if $f_{\boldsymbol{\theta}_1}(x) = g_{\boldsymbol{\theta}_2}(x)$, almost surely [28], [29]. Furthermore, $D\left(f_{\boldsymbol{\theta}_1}, g_{\boldsymbol{\theta}_2}\right)$ can be considered to serve as a measure of disparity between $f_{\boldsymbol{\theta}_1}$ and $g_{\boldsymbol{\theta}_2}$.

$D\left(f_{\boldsymbol{\theta}_1}, g_{\boldsymbol{\theta}_2}\right)$ denotes the "information lost when $g_{\boldsymbol{\theta}_2}$ is used to approximate $f_{\boldsymbol{\theta}_1}$. Namely, KLD is a measure of inefficiency of assuming that the distribution of population is $g_{\boldsymbol{\theta}_2}$ when the underlying distribution is $f_{\boldsymbol{\theta}_1}$. The smaller $D\left(f_{\boldsymbol{\theta}_1}, g_{\boldsymbol{\theta}_2}\right)$ means that $f_{\boldsymbol{\theta}_1}$ is selected and large values of $D\left(f_{\boldsymbol{\theta}_1}, g_{\boldsymbol{\theta}_2}\right)$ favor $g_{\boldsymbol{\theta}_2}$ [15].

Let $f_{\boldsymbol{\theta}_1}$ and $g_{\boldsymbol{\theta}_2}$ are probability density functions of log-normal and Weibull distribution respectively. Then $D\left(f_{\boldsymbol{\theta}_1}, g_{\boldsymbol{\theta}_2}\right)$ and $D\left(g_{\boldsymbol{\theta}_2}, f_{\boldsymbol{\theta}_1}\right)$ are given by

$$D\left(f_{\boldsymbol{\theta}_1}, g_{\boldsymbol{\theta}_2}\right) = \int_0^\infty f_{\boldsymbol{\theta}_1}(x) \log\left(\frac{f_{\boldsymbol{\theta}_1}(x)}{g_{\boldsymbol{\theta}_2}(x)}\right) dx$$
$$= -1/2 - 1/2 \log(2) - 1/2 \log(\pi) - \log(\sigma) - \mu\alpha$$
$$+ \alpha \log(\beta) - \log(\alpha) + \beta^{-\alpha} \exp(1/2\alpha(2\mu + \alpha\sigma^2))$$

and

$$D\left(g_{\theta_2}, f_{\theta_1}\right) = \int_0^\infty g_{\theta_2}(x) \log\left(\frac{g_{\theta_2}(x)}{f_{\theta_1}(x)}\right) dx$$

$$= (\alpha \log(\alpha) - \alpha\gamma - \alpha \log(\beta) + \gamma - \alpha)/\alpha - (-1/12(6\alpha^2 \log(\beta)^2$$
$$+ 12\alpha^2 \log(\beta)\sigma^2 - 12\alpha^2 \log(\beta)\mu - 12\alpha \log(\beta)\gamma + 121\log(\sigma)\alpha^2\sigma^2$$
$$+ 6\log(\pi)\alpha^2\sigma^2 + 6\log(2)\alpha^2\sigma^2 + 6\mu^2\alpha^2 - 12\alpha\gamma\sigma^2 + 12\alpha\mu\gamma + 6\gamma^2 + \pi^2)/\alpha^2/\sigma^2).$$

$D\left(f_{\theta_1}, g_{\theta_2}\right)$ and $D\left(g_{\theta_2}, f_{\theta_1}\right)$ were given by Bromideh [15] but they cannot read clearly in their paper. Therefore, these equations are obtained using by Maple. Second method for discrimination is the ratio of Minimized Kullback-Leibler Divergence $\left(RMKLD\right)$ rule (Elsherpieny et al., [17]) which is defined by

$$RMKLD = \log\left(\frac{D\left(f_{\hat{\theta}_1}, g_{\hat{\theta}_2}\right)}{D\left(g_{\hat{\theta}_2}, f_{\hat{\theta}_1}\right)}\right)$$

If $RMKLD < 0,$ then we select the log-normal distribution for modeling data otherwise we select the Weibull distribution for modeling data.

3. SIMULATION STUDY

In this section, the PCS of RML and RMKLD methods are obtained and compared for different censoring schemes. The censoring schemes used in simulation are given in Table 2. Probabilities of correct selection of rules are simulated and given in Table 3-4.

Table 2. The censoring schemes used in simulation

Scheme	m	$\mathbf{r} = (r_1, \ldots, r_m)$
1	10	(5,9*0)
2	10	(9*0,5)
3	10	(5*1,5*0)
4	10	(5*0,5*1)
5	10	(4*0,5,5*0)
6	13	(2,12*0)
7	13	(12*0,2)
8	13	(2*1,11*0)
9	13	(11*0,2*1)
10	13	(4*0,2,8*0)
11	15	(15*0)
12	30	(15,29*0)
13	30	(29*0,15)
14	30	(15*1,15*0)
15	30	(15*0,15*1)
16	30	(14*0,15,15*0)
17	40	(5,39*0)
18	40	(39*0,5)
19	40	(5*1,35*0)
20	40	(35*0,5*1)
21	40	(19*0,5,20*0)
22	45	(45*0)

Let us consider the data come from log-normal distribution. From Fig. 1 and Fig. 2 the PCS of the RML and RMKLD are similar in general but the PCS of RML and KLD is slightly better than the PCS of other for some schemes. The selection of parameter values does not affect to the PCS so much.

Secondly, the PCS of the RML and RMKLD are better when the censoring is made at the beginning of the life test.

Now let us consider the data come from Weibull distribution. From Fig. 3 and Fig. 4 the PCS of RMKLD is better than the power of RML for all schemes. Secondly, the PCS of the KLD are better when the censoring is made at the end of the life test. The PCS of the RML are better when the censoring is made at the beginning of the life test.

Table 3. Probability of Correct Selection of RML and RMKLD rule when the data come from log-normal distribution

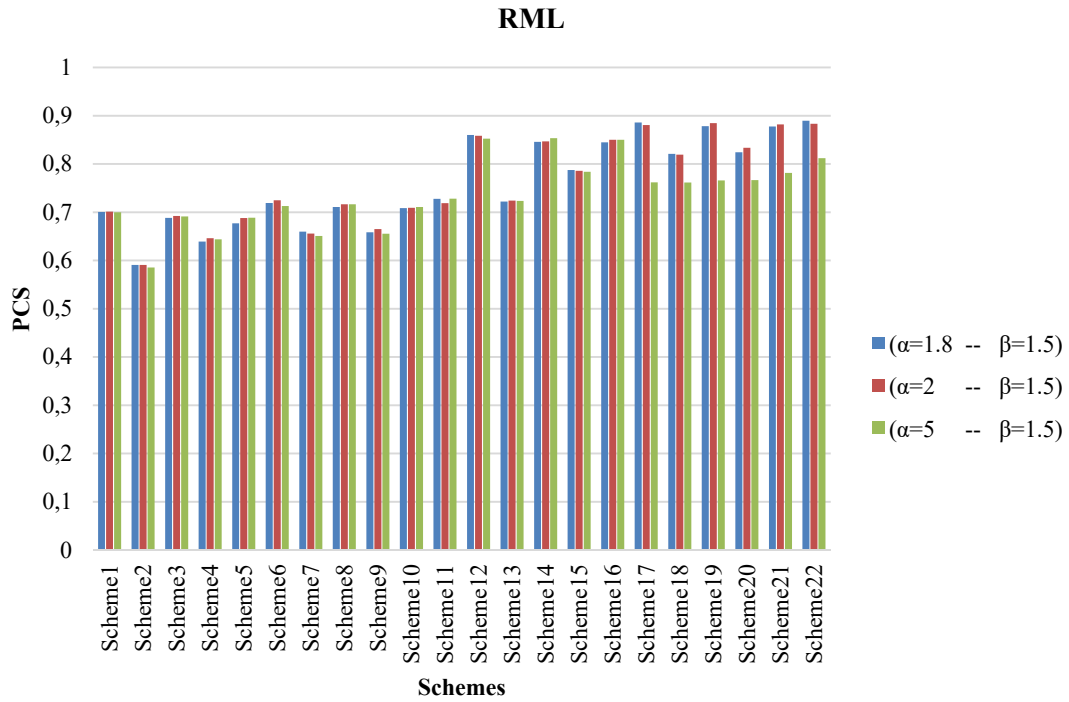|	RML			RMKLD		
	(μ=0.5,σ=1)	(μ=1,σ=1)	(μ=2,σ=1)	(μ=0.5,σ=1)	(μ=1,σ=1)	(μ=2,σ=1)
Scheme1	0.6763	0.6764	0.6802	0.7004	0.7012	0.6999
Scheme2	0.6565	0.6572	0.6568	0.5906	0.5909	0.5853
Scheme3	0.6721	0.6826	0.6737	0.6883	0.6922	0.6914
Scheme4	0.6421	0.6416	0.6384	0.6391	0.6461	0.6437
Scheme5	0.6831	0.6791	0.6820	0.6770	0.6881	0.6887
Scheme6	0.7019	0.7102	0.7116	0.7192	0.7249	0.7129
Scheme7	0.6960	0.6850	0.6920	0.6596	0.6559	0.6509
Scheme8	0.7092	0.7037	0.7054	0.7107	0.7165	0.7165
Scheme9	0.6931	0.7007	0.6950	0.6583	0.6649	0.6555
Scheme10	0.7127	0.7058	0.7054	0.7086	0.7093	0.7109
Scheme11	0.7318	0.7349	0.7235	0.7277	0.7187	0.7282
Scheme12	0.8496	0.8469	0.8499	0.8601	0.8583	0.8526
Scheme13	0.7763	0.7693	0.7654	0.7221	0.7241	0.7236
Scheme14	0.8473	0.8523	0.8486	0.8457	0.8467	0.8536
Scheme15	0.7771	0.7859	0.7868	0.7874	0.7857	0.7837
Scheme16	0.8448	0.8467	0.8378	0.8448	0.8503	0.8503
Scheme17	0.8766	0.8743	0.8790	0.8860	0.8808	0.7618
Scheme18	0.8398	0.8411	0.8371	0.8209	0.8194	0.7616
Scheme19	0.8781	0.8776	0.8772	0.8783	0.8847	0.7660
Scheme20	0.8533	0.8381	0.8394	0.8242	0.8335	0.7665
Scheme21	0.8764	0.8800	0.8798	0.8776	0.8819	0.7816
Scheme22	0.8857	0.8918	0.8859	0.8897	0.8832	0.8121
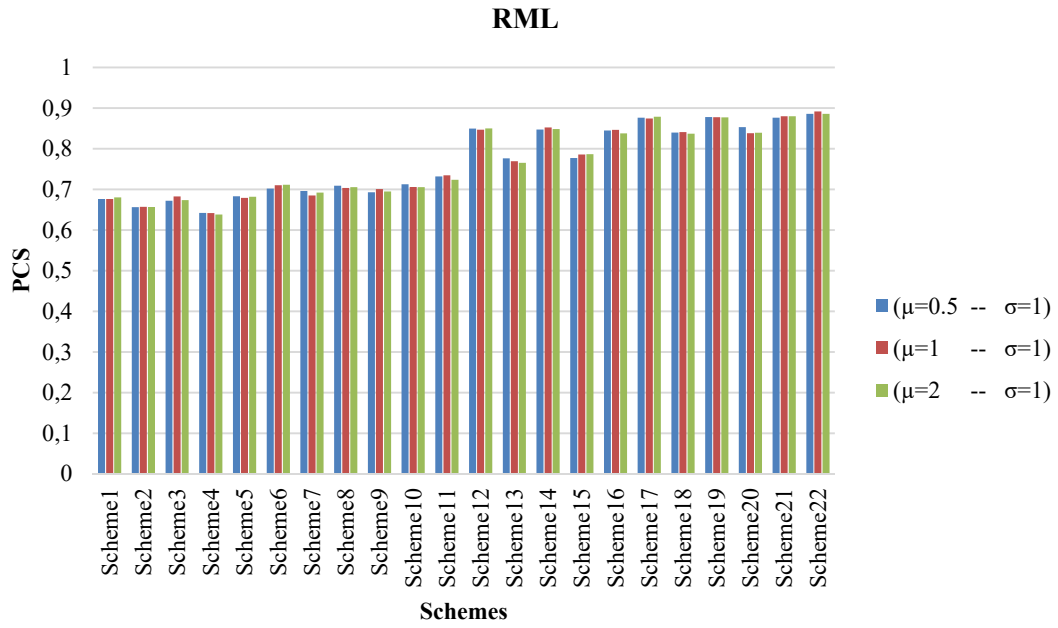
Figure 1. Probability of Correct Selection of RML rule when the data come from log-normal distribution
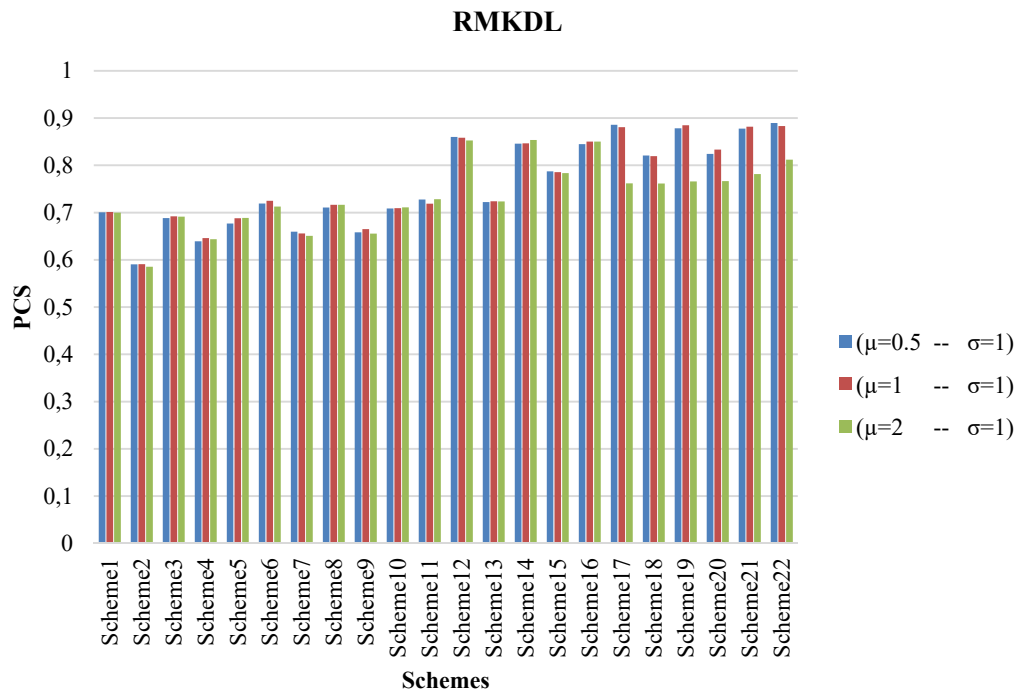
Figure 2. Probability of Correct Selection of RMKLD rule when the data come from log-normal distribution

Table 4. Probability of Correct Selection of RML and RMKLD rule when the data come from Weibull distribution

	RML			RMKLD		
	(α=1.8,β=1.5)	(α=2,β=1.5)	(α=5,β=1.5)	(α=1.8,β=1.5)	(α=2,β=1.5)	(α=5,β=1.5)
Scheme1	0.7004	0.7012	0.6999	0.8074	0.8202	0.8130
Scheme2	0.5906	0.5909	0.5853	0.9990	0.9988	0.9992
Scheme3	0.6883	0.6922	0.6914	0.8115	0.8188	0.8170
Scheme4	0.6391	0.6461	0.6437	0.9636	0.9678	0.9650
Scheme5	0.6770	0.6881	0.6887	0.8229	0.8323	0.8259
Scheme6	0.7192	0.7249	0.7129	0.7604	0.7644	0.7609
Scheme7	0.6596	0.6559	0.6509	0.9183	0.9152	0.9184
Scheme8	0.7107	0.7165	0.7165	0.7694	0.7631	0.7681
Scheme9	0.6583	0.6649	0.6555	0.9094	0.9113	0.9028
Scheme10	0.7086	0.7093	0.7109	0.7738	0.7644	0.7741
Scheme11	0.7277	0.7187	0.7282	0.7350	0.7345	0.7292
Scheme12	0.8601	0.8583	0.8526	0.9286	0.9224	0.9266
Scheme13	0.7221	0.7241	0.7236	1.0000	1.0000	1.0000
Scheme14	0.8457	0.8467	0.8536	0.9409	0.9417	0.9403
Scheme15	0.7874	0.7857	0.7837	0.9970	0.9965	0.9974
Scheme16	0.8448	0.8503	0.8503	0.9503	0.9520	0.9535
Scheme17	0.8860	0.8808	0.7618	0.8954	0.8961	0.8991
Scheme18	0.8209	0.8194	0.7616	0.9838	0.9866	0.9865
Scheme19	0.8783	0.8847	0.7660	0.8992	0.8979	0.8957
Scheme20	0.8242	0.8335	0.7665	0.9816	0.9788	0.9798
Scheme21	0.8776	0.8819	0.7816	0.9186	0.9123	0.9127
Scheme22	0.8897	0.8832	0.8121	0.8776	0.8797	0.8818

Figure 3. Probability of Correct Selection of RML rule when the data come from Weibull distribution
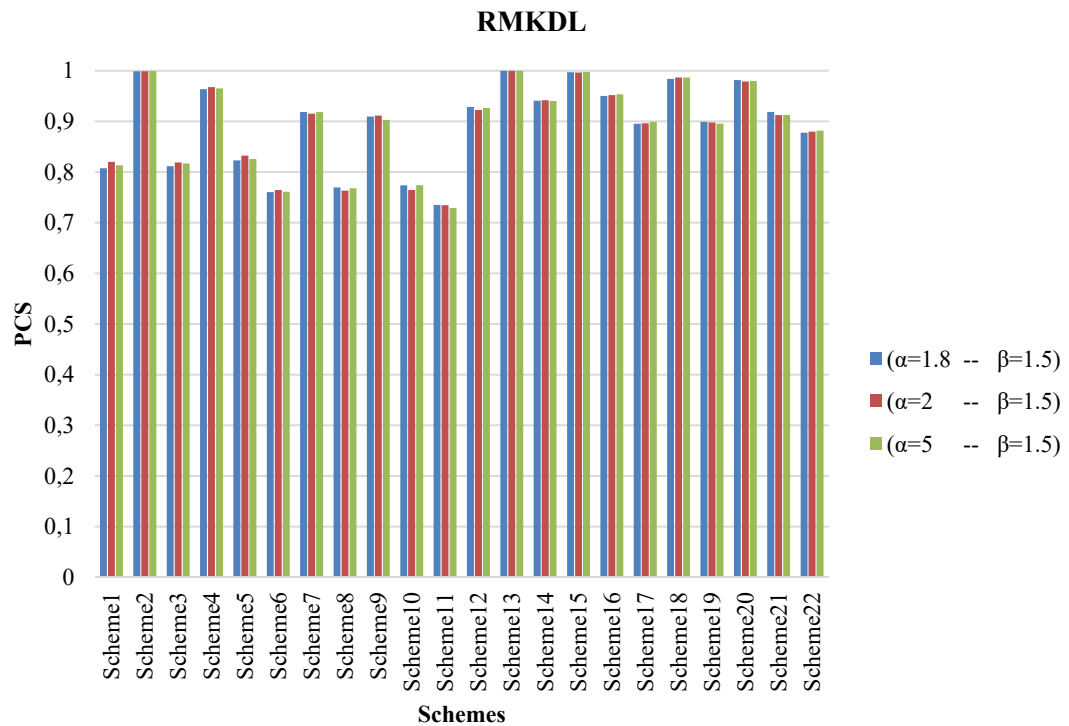
Figure 4. Probability of Correct Selection of RMKLD rule when the data come from Weibull distribution

4. Numerical Example

4.1. First Example

Let us consider the real data which is given by [30]. This data given arose in tests on endurance of deep groove ball bearings. The data are the number of million revolutions before failure for each of the lifetime tests. The progressively Type-II right censored data are obtained from complete data and it is given by

17.88 28.92 33.00 41.52 42.12 45.60 48.80 51.84 51.96 54.12 55.56 67.80 68.44 68.64 68.88 84.12 93.12 98.64 105.12 105.84 127.92 128.04 173.40 with $r = (5, 13 * 0)$ and $m = 18$.

Discrimination procedure is performed to get decision whether the data come from a Weibull or a Log-Normal. Using R code with **nlm** command (it uses Newton type algorithm), ML estimates of lognormal parameters are obtained by $\hat{\mu} = 4.3079$, $\hat{\sigma} = 0.5886$, ML estimates of Weibull parameters are obtained by $\hat{\alpha} = 2.1122$, $\hat{\beta} = 95.3497$. Test statistics are calculated as RML=0.3321 and $D\left(f_{\hat{\theta}_1}, g_{\hat{\theta}_2}\right) = \mathbf{0.1688}$ and

$D\left(g_{\hat{\theta}_2}, f_{\hat{\theta}_1}\right) = \mathbf{0.0924}$.

Since the **RML=0.3321>0** then lognormal distribution is selected for modeling this real data.
On the other hand, since the **RMKLD=0.6028>0** then Weibull distribution is selected for modeling this real data.

4.2. Second Example

Let us consider well-known data in reliability theory. This data was analyzed by many authors included in [31] and [27]. The progressive Type-II right censored data is given by
0.19 0.78 0.96 1.31 2.78 4.85 6.50 7.35 with $r = (0, 0, 3, 0, 3, 0, 0, 5)$ and $m = 8$.
Discrimination procedure is performed to get decision whether the data come from a Weibull or a Log-Normal. Using R code with **nlm** command (it uses Newton type algorithm), ML estimates of lognormal parameters are obtained by $\hat{\mu} = 1.8821, \hat{\sigma} = 1.6152$, ML estimates of Weibull parameters are obtained by $\hat{\alpha} = 0.9745$, $\hat{\beta} = 9.2253$. Test statistics are calculated as **RML=-0.1519** and $D\left(f_{\hat{\theta}_1}, g_{\hat{\theta}_2}\right) = \mathbf{0.9369}$ and

$D\left(g_{\hat{\theta}_2}, f_{\hat{\theta}_1}\right) = \mathbf{0.1395}$

Since the **RML=-0.1519<0** then Weibull distribution is selected for modeling this real data.
Since the **RMKLD=1.9042>0** then Weibull distribution is selected for modeling this real data.

REFERENCES

[1] Alzaid A. and Sultan, K.S., Discriminating between gamma and lognormal distributions with applications. Journal of King Saud University - Science, 21-2 (2009) 99-108.
[2] Kundu D. and Manglick, A., Discriminating between the log-normal and gamma distributions. Journal of the Applied Statistical Sciences, 14 (2005) 175-187.
[3] Bromideh A.A. and Valizadeh R., Discrimination between Gamma and Log-Normal Distributions by Ratio of Minimized Kullback-Leibler Divergence. Pakistan Journal of Statistics and Operation Research, 9-4 (2014) 443-453.
[4] Dey A.K. and Kundu D., Discriminating among the log-normal, Weibull, and generalized exponential distributions. IEEE Transactions on reliability, 58-3 (2009) 416-424.

[5] Dey A.K., and Kundu, D., Discriminating between the log-normal and log-logistic distributions. Communications in Statistics-Theory and Methods, 39-2 (2009) 280-292.

[6] Kundu D., Discriminating between normal and Laplace distributions. In Advances in Ranking and Selection, Multiple Comparisons, and Reliability, Springer (2005) 65-79.

[7] Kantam R. R., Priya M., and Ravikumar M., Likelihood ratio type test for linear failure rate distribution vs. exponential distribution. Journal of Modern Applied Statistical Methods, 13-1 (2014) 11.

[8] Ngom P., Nkurunziza J.D.D., and Ogouyandjou C.S., Discriminating between two models based on Bregman divergence in small samples, (2017).

[9] Ravikumar M. and Kantam R., Discrimination Between Burr Type X Distribution Versus Log-Logistic and Weibull-Exponential Distributions. i-Manager's Journal on Mathematics, 5-4 (2017) 39.

[10] Qaffou A. and Zoglat A., Discriminating Between Normal and Gumbel Distributions. REVSTAT-Statistical Journal, 15-4 (2017) 523-536.

[11] Algamal Z., Using maximum likelihood ratio test to discriminate between the inverse gaussian and gamma distributions. International Journal of Statistical Distributions, 1-1 (2017) 27-32.

[12] Quesenberry C.P., and Kent J., Selecting among Probability Distributions Used in Reliability. Technometrics, 24-1 (1982) 59-65.

[13] Dumonceaux R., and Antle C.E., Discrimination between the log-normal and the Weibull distributions. Technometrics, 15-4 (1973) 923-926.

[14] Pasha G., Shuaib K.M., and Pasha A. H., Discrimination between Weibull and Log-Normal Distributions For Lifetime data. Journal of Research (Science), Bahauddin Zakariya University, Multan, Pakistan, 17-2 (2006) 103-114.

[15] Bromideh A.A., Discriminating between Weibull and log-normal distributions based on Kullback-Leibler divergence. Ekonometri ve İstatistik e-Dergisi, 16 (2012) 44-54.

[16] Raqab M.Z., Al-Awadhi S.A., and Kundu D., Discriminating among Weibull, log-normal, and log-logistic distributions. Communications in Statistics-Simulation and Computation, 47-5 (2018) 1397-1419.

[17] Elsherpieny M.R., On Discriminating between Gamma and Log-logistic Distributions in Case of Progressive Type II Censoring, Pak.j.stat.oper.res. 13-1 (2017) 157-183.

[18] Kundu D. and Manglick A., Discriminating between the Weibull and Log-Normal Distributions, 51-6 (2004) 893-905.

[19] Dey A.K. and Kundu D., Discriminating between the Weibull and Log-normal distributions for type-II censored data, Statistics, 46-2 (2012) 197-214

[20] Kim J.S. and Yum B.J., Selection between Weibull and lognormal distributions: A comparative simulation study. Computational Statistics & Data Analysis, 53-2 (2008) 477-485.

[21] Bairamov I.G.. and Eryılmaz S., Spaciings, exceedances and concomitants in progressive type II censoring scheme. Journal of Statistical Planning and inference, 136 (2006) 527-536.

[22] Balakrishnan N. and Aggarwala R., Progressive Censoring: Theory, Methods and Applications, Statistics for Industry and Technology, Birkhauser, (2000).

[23] Saraçoğlu, B., Kınacı, İ., Kundu, D., " On Estimation of R = P(Y < X) for Exponential Distribution Under Progressive Type-II Censoring ",82 (5), , 729-744 2012

[24] Akdam, N., Kinaci, I., Saracoglu, B., "Statistical inference of stress-strength reliability for the exponential power (EP) distribution based on progressive type-II censored samples ", Hacettepe Journal Of Mathematics and Statistics, 46 239-253 2017.

[25] Demir, E., Saracoglu, B., "Maximum Likelihood Estimation for the Parameters of the Generalized Gompertz Distribution under Progressive Type-II Right Censored Samples ", Journal of Selcuk University Natural and Applied Science, 4 (2015) 41-48.

[26] Singh S. Tripathi, M.T. and Wu S.J., On estimating parameters of a progressively censored lognormal distribution, Journal of Statistical Computation and Simulation, 85-6 (2015) 1071-1089.

[27] Wu S.J., Estimation of the Parameters of the Weibull Distribution with Progressively Censored Data, Journal of the Japan Statistical Society, 32-2 (2002) 155-163.

[28] Mahdizadeh M. and Zamanzade E., New goodness of fit tests for the Cauchy distribution, Journal of Applied Statistics, 44-6 (2017) 1106-1121.

[29] Burnham K.P. and Anderson D.R., "Model selection and multimodel inference: a practical information-theoretic approach," 2nd eds., Springer, New York. (2002).

[30] Lieblein J. and Zelen M., Statistical Investigation of the Fatigue Life of Deep-Groove Ball Bearings. Journal of Research of the National Bureau of Standards, 57-5 (1956) 273-315.

[31] Viveros R. and Balakrishnan N., Interval Estimation of Parameters of Life From Progressively Censored Data, Technometrics, 36-1 (1994) 84-91.

Cumhuriyet Science Journal
CSJ

Triangles In The De-Sitter Plane

Tuğba MERT[1]* , Ümit TOKEŞER[2]

[1] Sivas Cumhuriyet University, Faculty of Science, Department of Mathematics Science, Sivas, TURKEY

[2] Kastamonu University, Faculty of Art and Science, Department of Mathematics Science, Kastamonu, TURKEY

Abstract. The triangular varieties in the de-Sitter plane were investigated and the formulas of triangles of non-degenerate   and   type of triangles were obtained in terms of dihedral angles.

Keywords: Triangle, Dihedral angles, de-Sitter plane

De-Sitter Düzleminde Üçgenler

Özet. Sitter düzlemindeki üçgen çeşitleri incelenip, bu üçgenlerin dejenere olmayanlarından olan   ve   tipindeki üçgenlerin alan formülleri dihedral açılar cinsinden elde edilmiştir.

Anahtar Kelimeler: Üçgen, Dihedral açı, de-Sitter düzlemi

1.   INTRODUCTION

The hypothesis that the shortest distance between two points is the correct part between these points is also used by Archimedes . At the end of the nineteenth century, the concept of geodesy emerged from the problem of finding the shortest path connecting two points on a surface. In 1732 Euler published a differential equation of geodesics on a surface. Thus, it was shown that the geodesics given depending on the two points can be given only depending on the type of surface. Latin translations of Archimedes and Apollonius in the Middle Ages and the introduction of Fermat and Dekart in analytical geometry in 1637 led to the development of geometric techniques used to find the tangents of plane curves in the first half of the 19th century. The algebraic formula $y^2 = x^3$ obtained by using analytical geometry, which gives the length of a nonlinear curve, was found separately by Neil van Heuraet and Fermat around 1658. In the fourth quarter of the 19th century, the Euclidean arc length element was found independently by Newton and Leibnitz and calculated the arc length of these two geometric plane curves using integral. The concept of arc length in metric spaces was entered by Menger in 1930.

The use of other metric spaces used to concretize abstract concepts (such as relativity) in which the Euclidean metric cannot be a model is inevitable. Today we see these spaces as Lorentzian, global, hyperbolic and de-Sitter. Since the curvature at one point of a curve in these spaces measures the amount of deviation at this point and the curvature of the geodesics is zero, we can correctly consider the geodesy through the two given points of the space. In the space we consider, if we solve the differential equation of geodesics with respect to two points, then we see that solution will be unique. This coincides with a single true hypothesis from two points in the Euclidean space. In this case, the correct part of the Euclidean

---

space is limited to two points and in this case it is a geodesic part limited to two points. The triangular region in the Euclidean space is the intersection of the semi-space determined by the external unit normals of the lines, and in this case it is the intersection of the semi-spaces determined by the geodesics. Furthermore, Asmus [1] obtain the type of triangles in de-Sitter plane by using geodesic segments.

Theorem 1

$p, q \in S_1^n$ and $V = Sp\{p, q\}$ is taken.

(i) If V spacelike, the parametrical equation of the line passing through p, q is

$$\alpha(t) = (\cos t) p + (\sin t) \left(\frac{q - \langle p, q \rangle p}{\|q - \langle p, q \rangle p\|} \right) , \quad t \in IR$$

(ii) If V timelike, the parametrical equation of the line passing through p, q is

$$\beta(s) = (\cosh s) p + (\sinh s) \left(\frac{q - \langle p, q \rangle p}{\|q - \langle p, q \rangle p\|} \right) , \quad s \in IR$$

(iii) If V null, the parametrical equation of the line passing through p, q is

$$\gamma(\lambda) = p + \lambda(q - p) , \quad \lambda \in IR$$

Proof

It can be seen in [2] (in Proposition 28).

Theorem 2

$p, q \in S_1^n$ and $V = Sp\{p, q\}$ is taken.

(i) If V spacelike, $\langle p, q \rangle = \cos t_0$ respectively, the length of the line segment t_0 and the parametric equation limited with p, q are

$$\alpha(t) = (\cos t) p + (\sin t) \left(\frac{q - \cos t_0 \, p}{\sin t_0} \right) , \quad 0 \le t \le t_0.$$

(ii) If V timelike, $\langle p, q \rangle = \cosh s_0$ respectively, the length of the line segment s_0 and the parametrical equation limited with p, q are

$$\beta(s) = (\cosh s) p + (\sinh s) \left(\frac{q - \cosh s_0 \, p}{\sinh s_0} \right) , \quad 0 \le s \le s_0.$$

(iii) If V null

$$\gamma(\lambda) = p + \lambda(q - p) \ , \ 0 \le \lambda \le 1$$

Proof

As Theorem 1.1 (i) is $\alpha(0) = p$, $\alpha(t_0) = q$ and α is also continuous

$\alpha(t) = (\cos t) p + (\sin t)\left(\dfrac{q - \cos t_0 \, p}{\sin t_0}\right)$, $0 \le t \le t_0$ point is on line segment limited with p, q.

As Theorem 1.1 (ii) is $\beta(0) = p$, $\beta(s_0) = q$ and β is also continuous

$\beta(s) = (\cosh s) p + (\sinh s)\left(\dfrac{q - \cosh s_0 \, p}{\sinh s_0}\right)$, $0 \le s \le s_0$ point is on line segment limited with p, q.

As from Theorem 1.1 $\gamma(0) = p$ and $\gamma(1) = q$ and $\gamma(1) = q$ and γ are continuous $\gamma(\lambda) = p + \lambda(q - p)$, $0 \le \lambda \le 1$ is parametrical equation of the line segment limited with p, q.

1.1. Triangle Types in de-Sitter Space

a. $_0\Delta_0^3$ Lightlike edged triangle
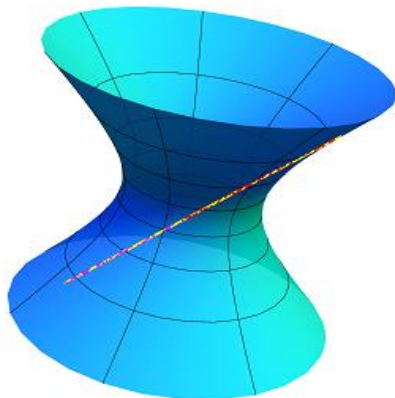
Figure 1. Lightlike edged triangle

b. $_1\Delta_0^2$ Spacelike based lightlike edged triangle
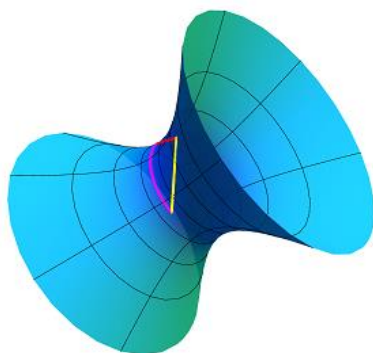
Figure 2. Spacelike based null edged triangle

c. Lightlike based timelike edged triangle

Figure 3. Null based timelike edged triangle

d. $_0\Delta_1^2$ Timelike based lightlike edged triangle
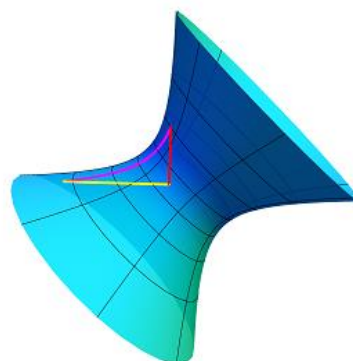
Figure 4. Timelike based null edged triangle

e. $_2\Delta_0^1$ Lightlike based spacelike edged triangle

h. $_0\Delta_3^0$ Timelike edged triangle
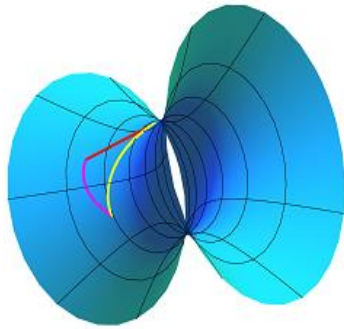
Figure 5. Null based spacelike edged triangle
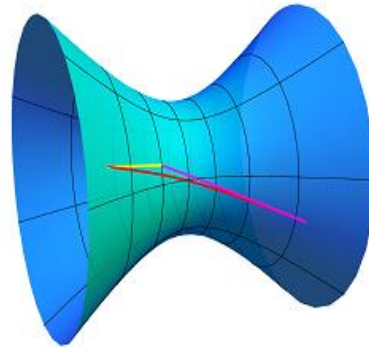
Figure 8. Timelike edged triangle

f. $_1\Delta_1^1$ Casual Scalene Triangle

ı. $_2\Delta_1^0$ Timelike based spacelike edged triangle

Figure 6. Casual Scalene Triangle
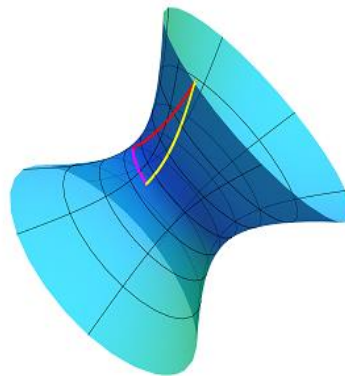
Figure 9. Timelike based spacelike edged triangle

g. $_3\Delta_0^0$ Spacelike edged Triangle

i. $_1\Delta_2^0$ Spacelike based timelike edged triangle

Figure 7. Spacelike edged triangle
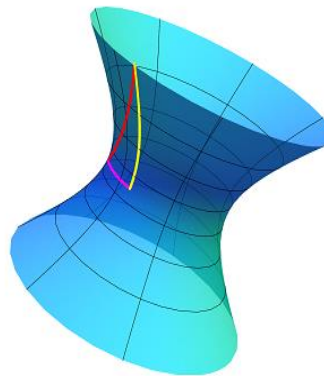
Figure 10. Timelike edged spacelike based triangle

1.2. Some Properties of the Rows Passing from Two Points in the de-Sitter Space

a. The need and sufficient condition that $V = Sp\{P_i, P_j\}$ is timelike $\langle P_i, P_j \rangle > 1$ points are on the same part of $V \cap S_1^n$ hyperbola (from ([2] Proposition 38 situation 2).

b. The need and sufficient condition that $V = Sp\{P_i, P_j\}$ is timelike $\langle P_i, P_j \rangle < -1$ points are on the same part of $V \cap S_1^n$ hyperbola (from ([2] Proposition 38 situation 2).

c. The need and sufficient condition that $V = Sp\{P_i, P_j\}$ is spacelike $|\langle P_i, P_j \rangle| < 1$ (from [2] Proposition 38 situation 1).

d. The need and sufficient condition that $V = Sp\{P_i, P_j\}$ is null $|\langle P_i, P_j \rangle| = 1$ (from [2] Proposition 38 situation 3).

Limited with P_i, P_j geodetic part is l_{ij} ,

e. The need and sufficient condition that l_{ij} is hyperbola $\langle P_i, P_j \rangle > 1$ [2].

f. The need and sufficient condition that l_{ij} is elips $|\langle P_i, P_j \rangle| < 1$ [2].

g. The need and sufficient condition that l_{ij} is null line segment $\langle P_i, P_j \rangle = 1$ [2].

2. THE AREAS OF NON-DEGENERATED EDGE TRIANGLES IN de-SITTER SPACE

Definition 1

The angle between these vectors, including

Two non-null vectors in N_1, N_2 IR_1^2 and the $\theta(N_1, N_2)$ angles between these vectors are identifed as following [3]

(i) If $\langle N_1, N_1 \rangle \langle N_2, N_2 \rangle > 0$ ve $\langle N_1, N_2 \rangle < 0$; $\theta(N_1, N_2) = \arccos h(-\langle N_1, N_2 \rangle)$,

(ii) If $\langle N_1, N_1 \rangle \langle N_2, N_2 \rangle > 0$ ve $\langle N_1, N_2 \rangle > 0$; $\theta(N_1, N_2) = -\arccos h(\langle N_1, N_2 \rangle)$,

(iii) If $\langle N_1, N_1 \rangle \langle N_2, N_2 \rangle < 0$; $\theta(N_1, N_2) = -\arcsin h(\langle N_1, N_2 \rangle)$

Definition 2

As N_1, N_2 IR_1^{n+1} are two vectors which are non-null and stretching Lorentz plane;

The θ_{12} dihedral angle in edge of $\{v \in IR_1^{n+1} : \langle v, N_1 \rangle \geq 0, \langle v, N_2 \rangle \geq 0\}$ dihedron is identified as [3]:

$$\theta_{12} = -\theta(N_1, N_2)$$

In the case of $S_1^2(1)$, 2- dimensional face are their peak points on the triangle on S_1^2 is non-degenerate since $\langle P_i, P_i \rangle = 1$. Therefore, Schülei differential formula is applicable to triangles whose edges are non-null. There are four different triangles as $_3\Delta_0^0$, $_2\Delta_1^0$, $_1\Delta_2^0$, $_0\Delta_3^0$ on S_1^2 whose edges are non-null.

Theorem 3 (Schlafli Differential Formula)

The centrifugal hyperquadiene-linked component, ε marked in $S_q^n(\varepsilon)$, IR_q^{n+1} space, the differential of the volume of $V_n(\Omega)$ non-degenerated volume on $S_q^n(\varepsilon)$ 1 and 2 coherent faces as

$$dV_n(\Omega) = \frac{\varepsilon}{n-1} \sum_F V_{n-2}(F) d\alpha_F$$

Here, $V_{n-2}(F)$, it is the volume of Ω's *n-2* face and α_F is the dihedral angle on the *F* face [3].

$n = 2$ as special condition, $\{i, j, k\}$ set is a permutation of $\{1, 2, 3\}$ and as the angle at θ_{ij}, P_k edge is;

$$dV_2(\Omega) = \varepsilon(d\theta_{12} + d\theta_{13} + d\theta_{23}) \tag{2.1}$$

2.1. Area of triangle from $_2\Delta_1^0$ type
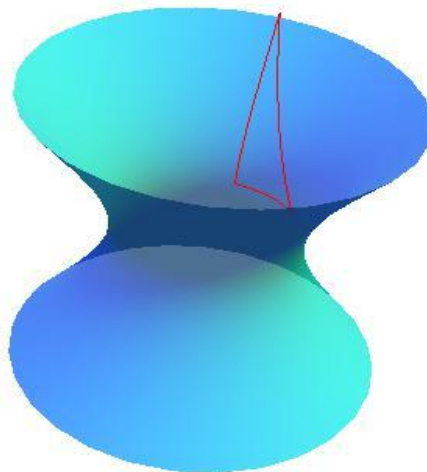
Figure 11. Triangle from $_2\Delta_1^0$ type

The edges of de-Sitter triangle from $_2\Delta_1^0$ type with $P_1 = \left(0, \dfrac{1}{\sqrt{2}}, \dfrac{1}{\sqrt{2}}\right), P_2 = (0,0,1), P_3 = \left(\dfrac{1}{2}, 0, \dfrac{\sqrt{5}}{2}\right)$

corner point are:

$$\alpha(t) = \left(0, \frac{\cos t - \sin t}{\sqrt{2}}, \frac{\cos t + \sin t}{\sqrt{2}}\right), \qquad t \in \left[0, \frac{\pi}{4}\right]$$

$$\beta(s) = (\sinh s, 0, \cosh s), \qquad s \in \left[0, \arctan h\left(\frac{1}{\sqrt{5}}\right)\right]$$

$$\gamma(u) = \left(\frac{\sqrt{3}\cos u - \sqrt{5}\sin u}{2\sqrt{3}}, \frac{2\sin u}{\sqrt{3}}, \frac{\sqrt{5}}{2}\cos u - \frac{\sin u}{2\sqrt{3}}\right), \qquad u \in \left[0, \arccos\left(\frac{\sqrt{5}}{2\sqrt{2}}\right)\right]$$

The projection of these on $z = 0$ plane is as:
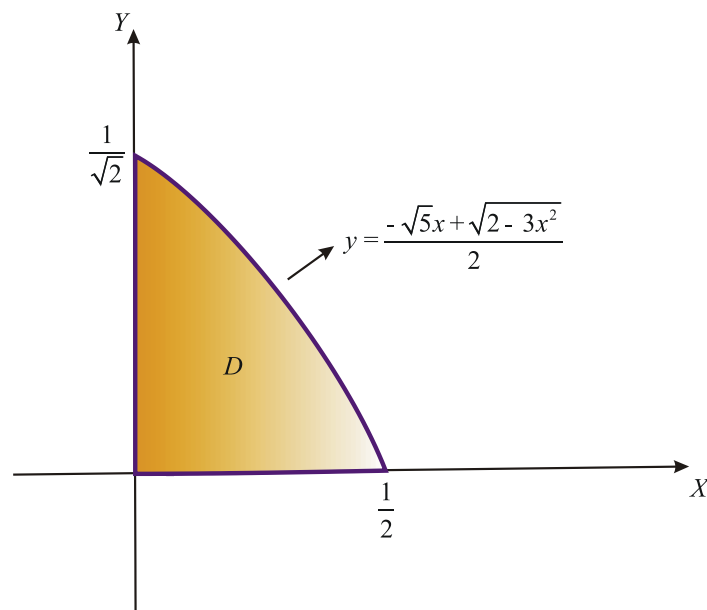
Figure 12. D zone

Since $\qquad V_2(\Delta) = \iint\limits_D \sqrt{1 + z_x^2 + z_y^2}\, dy dx$

and

$$z = \sqrt{1 + x^2 - y^2} \quad \text{is;}$$

$$V_2(\Delta) = \iint_D \sqrt{\frac{1+2x^2}{1+x^2-y^2}}\,dy\,dx$$

$$= \int_0^{1/2} \left(\int_0^{\left(-\sqrt{5}x+\sqrt{2-3x^2}\right)/2} \sqrt{\frac{1+2x^2}{1+x^2-y^2}}\,dy \right) dx \tag{2.2}$$

On the other hand, the interior angles of this triangle is;

$$P_1 \otimes P_2 = \begin{vmatrix} -e_1 & e_2 & e_3 \\ 0 & \dfrac{1}{\sqrt{2}} & \dfrac{1}{\sqrt{2}} \\ 0 & 0 & 1 \end{vmatrix} = -\frac{e_1}{\sqrt{2}} \text{ is timelike when } N_3 = -e_1,$$

$$P_2 \otimes P_3 = \begin{vmatrix} -e_1 & e_2 & e_3 \\ 0 & 0 & 1 \\ \dfrac{1}{2} & 0 & \dfrac{\sqrt{5}}{2} \end{vmatrix} = \frac{e_2}{2} \text{ spacelike; } N_1 = e_2,$$

$$P_3 \otimes P_1 = \begin{vmatrix} -e_1 & e_2 & e_3 \\ \dfrac{1}{2} & 0 & \dfrac{\sqrt{5}}{2} \\ 0 & \dfrac{1}{\sqrt{2}} & \dfrac{1}{\sqrt{2}} \end{vmatrix} = \frac{\sqrt{5}}{2\sqrt{2}}e_1 - \frac{1}{2\sqrt{2}}e_2 + \frac{1}{2\sqrt{2}}e_3 \,; N_2 = \left(\frac{\sqrt{5}}{\sqrt{3}}, \frac{-1}{\sqrt{3}}, \frac{1}{\sqrt{3}} \right),$$

$$\langle N_1, N_2 \rangle = -\frac{1}{\sqrt{3}} < 0$$

$$\langle N_1, N_3 \rangle = 0 \le 0$$

$$\langle N_2, N_3 \rangle = \frac{\sqrt{5}}{\sqrt{3}} > 0,$$

$$N_1 = e_2$$

$$N_2 = \frac{\sqrt{5}e_1 - e_2 + e_3}{\sqrt{3}}$$

$$N_3 = -e_1$$

and

since N_1 spacelike N_2 timelike, from Definition 2

$$-\arcsin h\left(\langle N_1, N_2 \rangle\right) = \bar{\theta}_{12} \Rightarrow \bar{\theta}_{12} = -\arcsin h\left(\frac{-1}{\sqrt{3}}\right),$$

Since N_1 spacelike N_3 timelike, from Definition 2

$$-\arcsin h\left(\langle N_1, N_3 \rangle\right) = \bar{\theta}_{13} \Rightarrow \bar{\theta}_{13} = \arcsin h(0) = 0,$$

Since N_2, N_3 timelike, from Definition 2

$$-\arccos h\left(\langle N_2, N_3 \rangle\right) = \bar{\theta}_{23} \Rightarrow \bar{\theta}_{23} = -\arccos h\left(\frac{\sqrt{5}}{\sqrt{3}}\right)$$

are found. From Theorem 3

$$V_2\left(\Delta\right) = \bar{\theta}_{12} + \bar{\theta}_{13} + \bar{\theta}_{23} + c. \tag{2.3}$$

By writing $V_2\left(\Delta\right)$ *and* $\bar{\theta}_{12}, \bar{\theta}_{13}, \bar{\theta}_{23}$ values on (2.2) to the place on (2.3)

$$c = V_2\left(\Delta\right) + \arcsin h\left(\frac{-1}{\sqrt{3}}\right) + \arccos h\left(\frac{\sqrt{5}}{\sqrt{3}}\right)$$

$$\tag{2.4}$$

is obtained.

Theorem 4

As $\theta_{12}, \theta_{13}, \theta_{23}$ angles are the interior angles of $_2\Delta_1^0$

$$V_2\left(_2\Delta_1^0\right) = \theta_{12} + \theta_{13} + \theta_{23} + V_2\left(\Delta\right) + \arcsin h\left(-\frac{1}{\sqrt{3}}\right) + \arccos h\left(\frac{\sqrt{5}}{\sqrt{3}}\right)$$

Proof

It is seen by writing (2.4) as in $\varepsilon = 1$ form on the place (2.1)

2.2. Area of triangle from $_1\Delta_2^0$ type
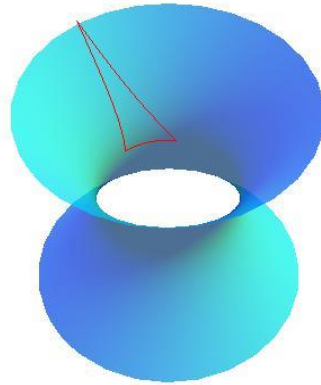
Figure 13. Triangle from $_1\Delta_2^0$ type

$_1\Delta_2^0$ de-Sitter triangle is $\overline{\Delta}$, whose edges are

$$\alpha(t) = \left(0, \frac{\cos t - \sin t}{\sqrt{2}}, \frac{\cos t + \sin t}{\sqrt{2}}\right), \qquad t \in \left[0, \frac{\pi}{4}\right]$$

$$\beta(s) = \left(\sqrt{3}\left(\cosh s - \sqrt{2}\sinh s\right), \frac{\sinh s}{\sqrt{2}}, \frac{\left(2\sqrt{2}\cosh s - 3\sinh s\right)}{\sqrt{2}}\right), \quad s \in \left[0, \log\left(1 + \sqrt{2}\right)\right]$$

$$\gamma(u) = \left(\sinh u, 0, \cosh u\right), \quad u \in \left[0, \log\left(2 + \sqrt{3}\right)\right]$$

whose corner point is

$$P_1 = \left(0, \frac{1}{\sqrt{2}}, \frac{1}{\sqrt{2}}\right), P_2 = (0,0,1), P_3 = \left(\sqrt{3}, 0, 2\right)$$

Let us show the simply closed area which is $\overline{D}$ in Figure 14 obtained from the projection of $\overline{\Delta}$ edges to $z = 0$ plane:
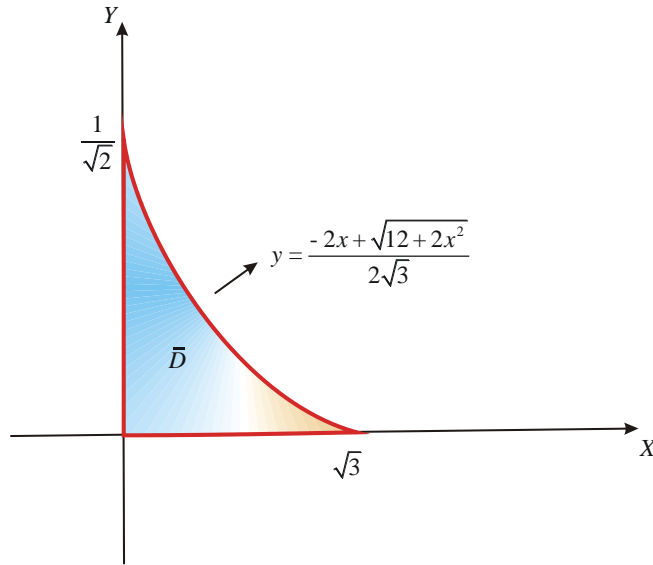
Figure 14. $\overline{\Delta}$ area

Since $\quad V_2\left(\overline{\Delta}\right) = \iint\limits_{D} \sqrt{1 + z_x^2 + z_y^2}\, dydx$

and

$$z = \sqrt{1 + x^2 - y^2}$$

$$V_2\left(\overline{\Delta}\right) = \iint\limits_{D} \sqrt{\frac{1 + 2x^2}{1 + x^2 - y^2}}\, dydx$$

$$= \int_{0}^{\sqrt{3}} \left(\int_{0}^{-2x+\sqrt{12+2x^2}/2\sqrt{3}} \sqrt{\frac{1 + 2x^2}{1 + x^2 - y^2}}\, dy \right) dx \qquad (2.5)$$

On the other hand, the interior angles of this triangle is;

$$P_1 \otimes P_2 = \begin{vmatrix} -e_1 & e_2 & e_3 \\ 0 & \dfrac{1}{\sqrt{2}} & \dfrac{1}{\sqrt{2}} \\ 0 & 0 & 1 \end{vmatrix} = -\dfrac{e_1}{\sqrt{2}} \text{ timelike; } N_3 = -e_1 \ ,$$

$$P_2 \otimes P_3 = \begin{vmatrix} -e_1 & e_2 & e_3 \\ 0 & 0 & 1 \\ \sqrt{3} & 0 & 2 \end{vmatrix} = \sqrt{3}e_2 \text{ timelike; } N_1 = e_2,$$

$$P_3 \otimes P_1 = \begin{vmatrix} -e_1 & e_2 & e_3 \\ \sqrt{3} & 0 & 2 \\ 0 & \frac{1}{\sqrt{2}} & \frac{1}{\sqrt{2}} \end{vmatrix} = \sqrt{2}e_1 - \frac{\sqrt{3}}{\sqrt{2}}e_2 + \frac{\sqrt{3}}{\sqrt{2}}e_3 ; \; N_2 = \left(\sqrt{2}, \frac{-\sqrt{3}}{\sqrt{2}}, \frac{\sqrt{3}}{\sqrt{2}} \right),$$

$$\langle N_1, N_2 \rangle = -\frac{\sqrt{3}}{\sqrt{2}} < 0$$

$$\langle N_1, N_3 \rangle = 0 \leq 0$$

$$\langle N_2, N_3 \rangle = \sqrt{2} > 0,$$

$$N_1 = e_2$$

$$N_2 = \frac{2e_1 - \sqrt{3}e_2 + \sqrt{3}e_3}{\sqrt{2}}$$

$$N_3 = -e_1$$

and

Since N_1, N_2 is spacelike, from Definition 2

$$\arccos h \left(\langle N_1, N_2 \rangle \right) = \theta'_{12} \Rightarrow \theta'_{12} = \arccos h \left(\sqrt{\frac{3}{2}} \right),$$

Since N_1 is spacelike N_3 is timelike, from Definition 2

$$-\arcsin h \left(\langle N_1, N_3 \rangle \right) = \theta'_{13} \Rightarrow \theta'_{13} = \arcsin h (0) = 0$$

Since N_2 is spacelike and N_3 is timelike, from Definition 2

$$-\arcsin h \left(\langle N_2, N_3 \rangle \right) = \theta'_{23} \Rightarrow \theta'_{23} = -\arcsin h \left(\sqrt{2} \right)$$

are found. From Theorem 3

$$V_2 \left(\overline{\Delta} \right) = \theta'_{12} + \theta'_{13} + \theta'_{23} + c . \tag{2.6}$$

If we write the values on (2.5) $V_2\left(\overline{\Delta}\right)$ *ve bu* $\theta'_{12}, \theta'_{13}, \theta'_{23}$ to the place on (2.6);

it is

$$c = V_2\left(\overline{\Delta}\right) - \arccos h\left(\sqrt{\frac{3}{2}}\right) + \arcsin h\left(\sqrt{2}\right) \tag{2.7}$$

Theorem 5

$\theta_{12}, \theta_{13}, \theta_{23}$ are the interior angles of $_1\Delta_2^0$ triangle;

$$V_2\left(_1\Delta_2^0\right) = \theta_{12} + \theta_{13} + \theta_{23} + V_2\left(\overline{\Delta}\right) - \arccos h\left(\sqrt{\frac{3}{2}}\right) + \arcsin h\left(\sqrt{2}\right)$$

Proof

It is seen by writing (2.7) as in $\varepsilon = 1$ form on the place (2.1)

REFERENCES

[1] Asmus, I., Duality Between Hyperbolic and de-Sitter Geometry, Cornell University, New York, (2008) 1-32.

[2] O'neil, B., Semi-Riemannian Geometry, AcademicPress., London, (1983) 46-49, 54-57, 108-114, 143-144.

[3] Suarez-Peiro, E., A SchlafliDifferential Formula for Implices in Semi-Riemannian Hyperquadrics, Gauss-Bonnet Formulas fo rSimplices in the de Sitter Sphere and the Dual Volume of a Hyperbolic Simplex, Pasicif Journal of Mathematics, 194-1 (2000) 229.

[4] Karlığa, B., Edgematrix of hyperbolic simplices, Geom. Dedicata, 109 (2004) 1–6.

[5] Karlığa, B., Yakut, A.T., Vertexangles of a simplex in hyperbolic space H^n, Geom. Dedicata, 120 (2006) 49-58.

Examination of the Effect of Different Projectile Geometries on the Performance of Reluctance Launcher Using 3D Finite Element Analysis

Vekil SARI [1,*] (iD) *, Ferhat DALBADAN [2]* (iD)

¹Department of Electrical and Electronics Engineering, Faculty of Engineering, Cumhuriyet University, 58140, Sivas/ Turkey
²Department of Electrical and Electronics Engineering, Faculty of Engineering, Erciyes University, 38039, Kayseri/ Turkey

Abstract. In this paper, the 3D model of a reluctance electromagnetic launcher was implemented using Maxwell program. The effect of the different projectile geometries was examined via the model. The projectile geometry with the highest velocity was determined. After constructing 3D model of the launcher, projectiles with different geometries were built and finally various projectiles with different geometries were analyzed. As a result, it was determined that the tubular projectile with 4 mm radius hole was the fastest among the tubular projectiles. Among the projectiles with notches, the projectile with 4 notches was launched faster than the others when the parameter was the number of notches, and the projectile with 0.5 mm notch radius was faster than the others when the parameter was the notch radius. In this paper, the highest velocity was reached the tubular projectile with 4 mm radius that was built with the 1050 material. The value of this velocity was 24.12 m/s.

Keywords: *Coilguns, linear accelerators, electromagnetic launching, finite elements analysis.*

3 Boyutlu Sonlu Elemanlar Analizi Kullanılarak Farklı Mermi Geometrilerinin Relüktans Fırlatıcının Performansına Etkisinin İncelenmesi

Özet. Bu çalışmada, relüktans elektromanyetik fırlatıcının 3 boyutlu modeli Maxwell programı kullanılarak oluşturulmuştur. Farklı mermi geometrilerinin etkisi model vasıtasıyla incelenmiştir. En yüksek hıza sahip mermi geometrisi belirlenmiştir. Fırlatıcının 3 boyutlu modeli oluşturulduktan sonra, farklı geometrilere ait mermiler oluşturulmuş ve analizler yapılmıştır. Bu analizlerin sonucunda boru tipi mermilerde; iç boşluk yarıçapı 4 mm olan merminin diğer boru tipi mermilere göre daha yüksek hızla fırlatıldığı tespit edilmiştir. Çentikli mermilerde ise çentik sayısına göre; 4 çentikli merminin diğer çentik sayılarına sahip mermilerden daha hızlı fırlatıldığı, çentik yarıçapına göre; çentik yarıçapı 0.5 mm olan çentikli merminin diğer mermilerden daha hızlı olduğu tespit edilmiştir. Bu çalışmada en yüksek hıza iç boşluk yarıçapı 4 mm olan 1050 den yapılmış boru tipi mermide ulaşılmıştır. Bu hız değeri 24.12 m/sn'dir.

Anahtar Kelimeler: *Bobin silahı, lineer hızlandırıcı, elektromanyetik fırlatma, sonlu elemanlar analizi.*

1. INTRODUCTION

Electromagnetic launchers were developed due to many disadvantages and velocity limitations of chemical launchers [1]. The idea of launching projectiles using electricity is not new. It's been known since 1846. However, the most significant improvements have taken place in the past few decades [2]. Electromagnetic launchers are used in many areas, but mostly in military and space applications [3]. The interest in electromagnetic launchers have increased significantly in the past few years.

Electromagnetic launchers can be divided into two categories; electromagnetic rail guns and electromagnetic coil guns [4]. Rail gun consists of two parallel metal rails and an armature that can slide on these rails. They are convenient for launching large projectiles. When the voltage was applied to the rails, the armature completes the cycle and a current flows on the armature. A force is exerted on the armature which resides in the magnetic field induced by the current flowing through the rails. Armature moves with the effect of this force. The moving armature launches the projectile in front of it [5]. The structure and the operation principle of the coil gun are more complex. It consists of a cylindrical armature, one or more coils wounded to this cylinder and a projectile to be launched [6]. In coil guns, there is almost no friction between the muzzle and the projectile, thus the acceleration system is not damaged [7].

The velocity obtained with the rail gun is higher than the velocity obtained with the coil gun. However, the required excitation current is much higher [8]. Additionally, rail guns have problems due to melting and erosion [9]. The efficiency of the coil gun is higher than the rail gun because of the strong magnetic coupling between the coils and the projectile [10, 11].

Electromagnetic coil guns can be divided into two categories according to their operation principles. These are induction-type electromagnetic launchers (IEML) and reluctance electromagnetic launchers (REML). In IEMLs, the non-magnetic projectile in the middle of the coil is accelerated and launched [12, 13]. The operation principle of the REML depends on the reluctance theory. The magnetic field induced on the coils attracts and pulls the ferromagnetic projectile towards the center of the coil [14-16]. REML have many advantages such as easy control, simple structure and high reliability when compared with other launchers [17].

In REMLs, ferromagnetic projectiles are used and their BH characteristics are non-linear [18]. Therefore, the analysis of these launchers is difficult. Finite Element Analysis (FEA) is usually preferred for the analysis of these launchers [19-23].

In a previous study, different projectile geometries for REMLs were studied and, projectiles with notches and projectiles with tail fins were examined [17]. A five-stage REML was built to launch those projectiles. For each driving coil, capacitance of the capacitor banks were 450 µF and the charge voltage was 600 V. As a result, higher launching efficiency was obtained with projectile with notches. The velocity difference between projectile with notches and normal projectiles is small. But in this paper, the highest velocity obtained using projectiles with notches increased 19% according to the highest velocity obtained using normal projectiles. This may be due to projectile material or launcher geometry.

In another study, projectiles constructed using three different materials were studied and 2, 8, and 16 slits were cut on the projectiles [24]. It was expressed that as the number of slits increased, the projectile velocity would increase, and the experiments proved this result. Additionally, it was determined that the efficiency usually tends to increase when the number of slits increase but the velocity decreased in one of the projectiles of a specific material. In this paper, the number of notches is 2, 4, and 8 respectively. The velocity increased until the number of notches exceeded 4,

thus it decreased for the projectiles with 8 notches. This is because the projectile material decreases when the number of notches increases. Because the flux cannot flow from the material.

Before implementing electromagnetic systems, the model of the system is generally constructed using electromagnetic analysis software such as Maxwell, Magnet, and Flux and then information is gathered by analyzing this model. In this study, Maxwell is used to create and analyze the 3D model of a single-coil REML. In Maxwell, the model of a system can be create in 2D or 3D [25]. 2D models are easier to build and the time required for the analysis is short. However, the 2D model does not cover the three-dimensional effects [26].

In previous studies, projectiles with notches were examined, but tubular projectiles were not examined. In this paper, the comparison of the projectiles with notches and tubular projectiles. In this paper, 3D model of a REML was used and more accurate results were obtained by including the three-dimensional effects. Then projectiles with different geometries were constructed and the launching velocity of the system was examined. The studied projectiles with different geometries are tubular projectiles and projectiles with notches. The interiors of the projectiles were drilled 1 to 5 mm-radius holes while tubular projectiles were built. The numbers of notches are 2, 4, and 8 for the projectiles with notches and the radius of the notches are 0.25, 0.5, and 1 mm. After the 3D model of the launcher system was constructed, the launcher model was analyzed. As a result, it was determined that the tubular projectile with 4 mm-radius hole was the fastest among the tubular projectiles. Among the projectiles with notches, the projectile with 4 notches was launched faster than the others when the parameter was the number of notches, and the projectile with 0.5 mm notch radius was faster than the others when the parameter was the notch radius.

2. THEORY OF RELUCTANCE ELECTROMAGNETIC LAUNCHERS

A reluctance electromagnetic launcher consists of a cylindrical tube and a coil wound around this tube. The tube used as the muzzle should not be constructed by using a magnetic material and the projectile must be constructed using ferromagnetic material. When a current flows through the coil, a magnetic field is induced around the coil. The magnetic field applies a reluctance force to the ferromagnetic projectile inside the tube and it pulls the projectile through the center of the tube. In REMLs, the projectile is pulled to the center of the coil, it is not pushed. The current of the coil must be turned off when the projectile reaches the center, or it will be pulled to the center again. This may decelerate the projectile or prevent the projectile to be launched. This should be in mind while constructing a REML. Sensors should be used to detect if the projectile reached the center.

If the REML consists of multiple coils, each coil will fasten the projectile a bit more. When the projectile gets into the attraction area of the next coil, this coil should be energized and when the projectile reaches the center of this coil, the current should be turned off. The damping time of the current flowing through the coils and the energy in the coils affect the efficiency of the launcher considerably. The timing should be adjusted using sensors.
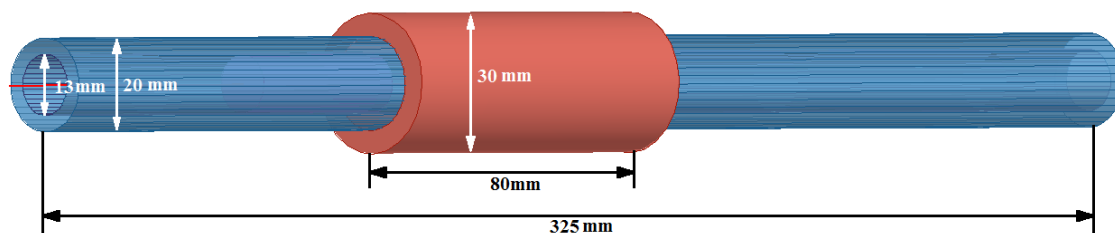

Figure 1. View of the reluctance electromagnetic launcher.

Figure 1 shows a single-coil launcher that was modelled. Launchers convert the electrical energy into the magnetic energy first, and then it converts the magnetic energy to the mechanical energy. During this conversion, there will be electrical, magnetic and mechanical losses [27].

3. 3D ANALYSIS OF RELUCTANCE LAUNCHER

In this study, FEA of a single-coil REML was realized using Maxwell software. 3D model of the launcher was constructed for FEA. The geometries of the projectiles were changed after the model was constructed and then the projectile geometry with the highest velocity was determined. The 3D Maxwell model of the launcher is shown in Figure 2. The magnetic flux density shown in Figure 3 is nearly 1.4 T inside the coil and 0.7 T at the edge of the coil.
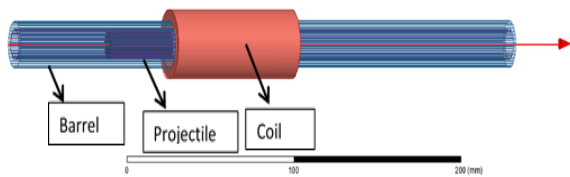
Figure 2. Maxwell model of the launcher.
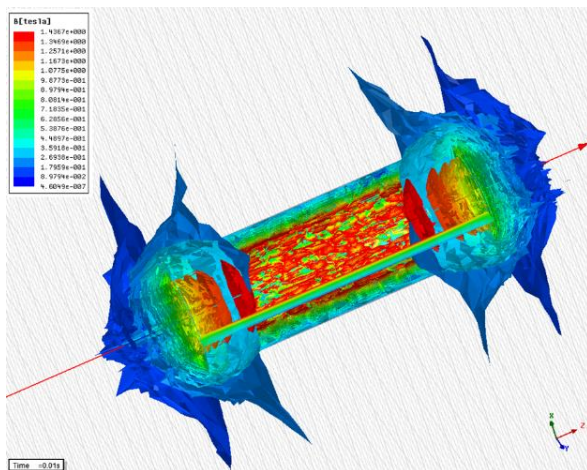
Figure 3. Magnetic flux density.

In this paper, the launching of 4 cm-length and 6.25 mm-radius projectiles constructed using different geometries and different materials such as 1020, 1050, and 12L14 was studied. BH characteristics of

these materials are shown in Figure 4 [28].
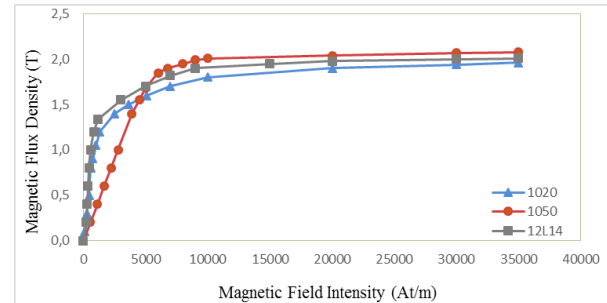
Figure 4. BH characteristics of the materials.

Table 1. Velocities of the projectiles with unmodified geometries.

Projectiles with unmodified geometry			
Velocity (m/s)			Weight (gr.)
1020	1050	12L14	
18.78	*19.24*	19.01	38.445

Then the geometry of the projectile was modified and tubular projectiles were constructed where the outer radius (r1) of the projectile is still 6.25 mm, but the interior was drilled for having a hole with radius 1 to 5 mm (r2). Tubular projectile is shown in Figure 5. Table 2 shows the velocities of each projectile.

Figure 5. View of the tubular projectile.

Table 2. Velocities of the tubular projectiles

Tubular projectiles			
Inner hole radius r_2 (mm.)	Velocity (m/s)		Weight (gr.)
	1020	1050	12L14	
1	19.38	19.48	19.45	37.461
2	20.81	20.95	20.86	34.508
3	21.68	22.09	22.05	29.587
4	23.04	*24.12*	23.71	22.698
5	21.59	22.12	21.61	13.841

Figure 6. View of projectile with notch.

Then the projectile geometry with notches was considered and 2, 4, and 8 notches were constructed at the side surfaces of the projectiles. Notches were circular-shaped. The radius of the constructed notches are 0.25, 0.5, and 1 mm, respectively. Figure 6 shows the projectile with notches. Table 3 shows the velocities of the projectiles with notches.

Table 3. Velocity results of projectiles with notch.

Projectiles with notch					
Notch radius (mm.)	Number of notches	Velocity (m/s)			Weight (gr.)
		1020	1050	12L14	
0.25	2	19.86	20.36	20.08	38.387
	4	21.3	21.87	21.6	38.329
	8	20.99	21.44	21.4	38.214
0.5	2	20.04	21.24	20.85	38.213
	4	22.52	*22.91*	22.7	37.981
	8	20.64	21.01	20.72	37.511
1	2	21.57	21.92	21.79	37.516
	4	21	21.14	21.04	36.586
	8	10.14	10.29	10.2	34.726

The highest velocity of the projectiles with unchanged geometry is 19.24 m/s. This velocity obtained with 1050 projectile. The 1020 projectile has the lowest velocity. When the relative permeability of the projectile material increases, the velocity increases too. The same result can be obtained when the velocities of tubular projectiles in Table 2 are analyzed. The velocities of all projectiles built with 1050 material are higher than the others, then comes 12L14 and 1020 projectiles respectively. When the velocities of the projectiles with unmodified geometry and tubular projectiles are compared. It can be seen that tubular projectiles are faster. When the interior hole radius is 1 mm, projectile velocities of all material types are higher. The velocity increases until the interior hole radius exceeds 4 mm, and it decreases when the interior hole radius is 5 mm. In tubular projectiles, projectiles with 4 mm interior hole radius are faster. When the interior hole radius is less or greater than 4 mm, the projectile velocity decreases. The highest velocity in tubular projectiles is 24.12 m/s. It is obtained with the projectile of 1050 material and 4 mm interior hole radius.

When the velocity results of projectiles with notches (Table 3) are interpreted, it is detected that the projectiles with the highest velocity are built with 1050 material, then comes 12L14 and 1020, respectively. If the velocity results are examined for number of notches and notch radius, we see that the velocity of the projectiles with 0.25 and 0.5 mm notch radius increases and the velocity of the projectile with 1 mm notch radius decreases when number of notches increases from 2 to 4. When the number of notches increases from 4 to 8, velocities of all the projectiles decrease. Higher velocities are obtained when the number of notches is 4. When the notch radius increases from 0.25 to 0.5 mm, velocity of projectiles with 2 notches increases while velocities of projectiles with 4 and 8 notches decrease. The highest velocity measured using projectiles with notches is 22.91 m/s. It is obtained with the projectile with 4 notches built with 1050 material and having a radius of 0.5 mm.

In this paper, the highest velocity value measured with projectiles having different geometries is 24.12 m/s. This value was obtained with the projectile of 1050 material, 4 cm-length, 6.25 mm outer radius and 4 mm inner hole radius. Therefore, the projectile with the highest velocity was analyzed. Figure 7 shows the magnetic flux density when the projectile is in the coil. Magnetic flux density is around 20 T at a very small part of the projectile, around 10-15 T at some parts, and around 3-4 T at most parts. Magnetic flux density is very high, but occurs in a very short time (milliseconds).
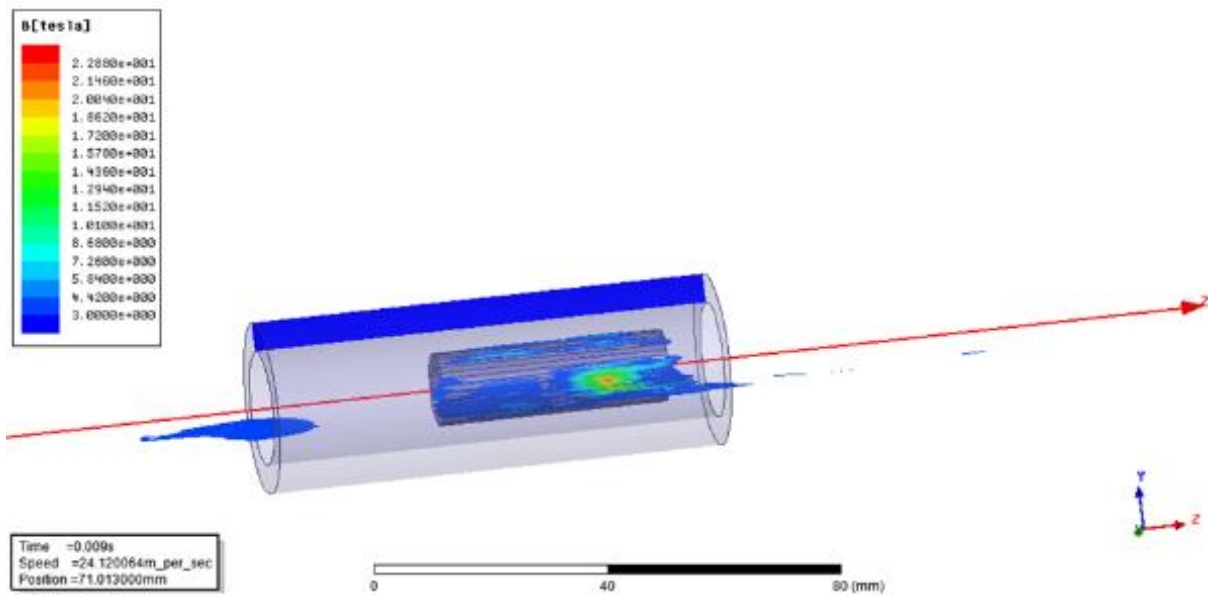
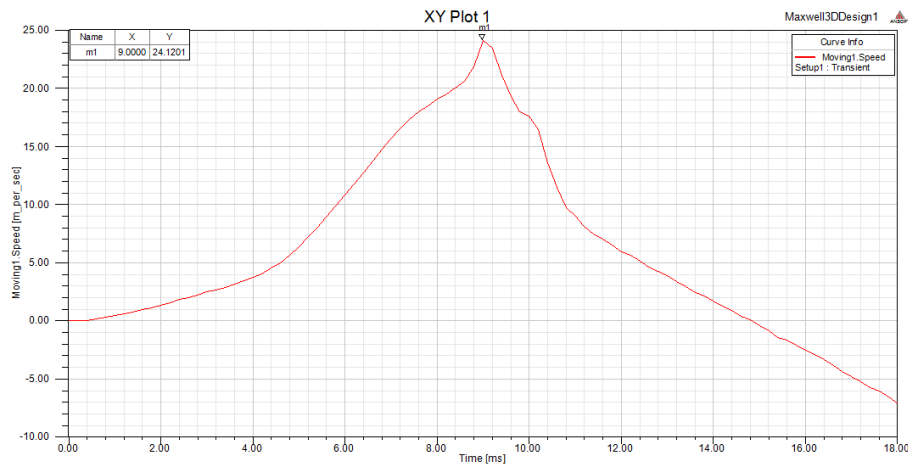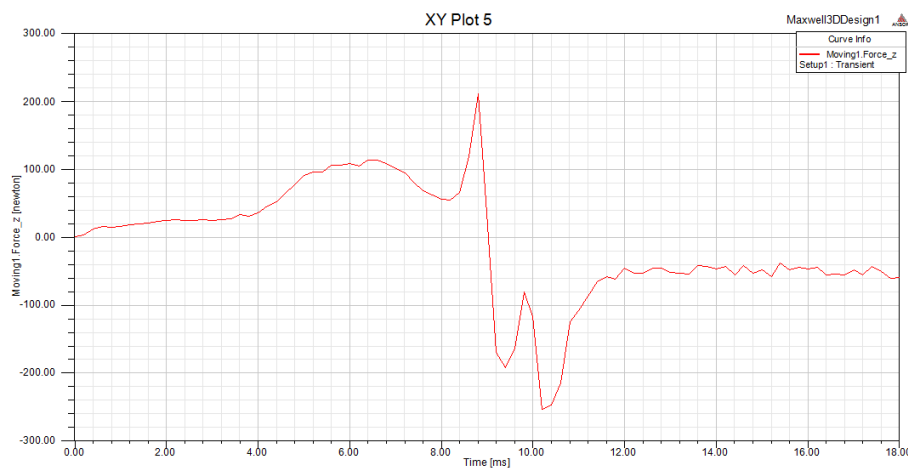**Figure 7.** Magnetic flux density when the projectile is in the coil.

Figure 8. Velocity change with time.

Figure 9. The change of force applied to the projectile.

Figure 8 shows the velocity-time graph of the projectile. The projectile reaches the highest velocity at 9 ms. The current flowing through the coil must be turned off when the projectile reaches the maximum velocity because it should not be pulled back to the center.

Figure 9 shows the force applied to the projectile in time. A forward direction force is applied to the projectile until 9 ms and the projectile is moved through the center of the coil. After 9 ms a backward force is applied and it is moved to the center of the coil again.

4. DISCUSSION

According to the analysis results, in consistence with the previous studies[20, 24], the velocity of the projectiles is proportional to the relative permeability of the projectile materials. 1050 has the highest relative permeability. Thus, the projectiles built with 1050 material have the highest velocities and then comes 12L14 and 1020, respectively. When the projectile is drilled to construct a tubular projectile, the velocity increases. The tubular projectile with 4 mm radius hole was the fastest among the tubular projectiles. Among the projectiles with notches, the projectile with 4 notches was launched faster than the others when the parameter was the number of notches, and the projectile with 0.5 mm notch radius was faster than the others when the parameter was the notch radius.

When the velocity results of the projectiles with notches are examined, it can be seen that the velocity increases until the number of notches increases up to 4, then it decreases. When the notch radius increases up to 0.5 mm, the velocity of the projectiles increases and then it decreases. The highest velocity of projectiles with notches is obtained using the projectile with 4 notches having a radius of 0.5 mm.

5. CONCLUSION

In previous studies, projectiles with notches were examined, but tubular projectiles were not examined. In this paper, the comparison of the projectiles with notches and tubular projectiles. In this paper, the 3D model of a REML was implemented and the effect of changing the projectile geometries on the projectile velocities was examined. The projectile geometry with the highest velocity was determined. In consistence with the results of the previous works, the velocity of the projectiles increase when the relative permeability of the projectile materials increases.

It is detected that the velocity increases when the projectile is drilled to construct a tubular projectile, and the velocity is at its highest value for tubular projectiles with 4 mm radius hole. It is seen that the velocity increases when the projectile is notched. The maximum velocity is reached with the projectile with 4 notches and a radius of 0.5 mm. The maximum velocity of the projectiles with notches is 19% more than the maximum velocity of the projectiles without notches, while the maximum velocity of tubular projectiles is 25.36% more than the maximum velocity of the projectiles which are not tubular.

When the velocity results of projectiles with notches are examined, it can be seen that the velocity increases until the number of notches increases up to 4, then it decreases. When the notch radius increases up to 0.5 mm, the velocity of the projectiles increases and then it decreases. The highest velocity of projectiles with notches is obtained with the 4 projectile with notches having a radius of 0.5 mm.

REFERENCES

[1] Fair H. D., Electromagnetic propulsion: A new initiative, IEEE Transactions on Magnetics, 18-1 (1965) 4-6.

[2] Mcnab I. R., Stefani F., Crawford M., Erengil M., Persad C. and Satapathy S., Development of a naval railgun, IEEE Transactions on Magnetics, 41-1 (2005) 206-210.

[3] Bresie D. A. and Andrews J. A., Design of a reluctance accelerator, IEEE Transactions on Magnetics, 27-1 (1991) 623-627.

[4] He J., Levi E., Zabar Z. and Birenbaum L., Concerning the design of capacitively driven induction coil guns, IEEE Transactions on Plasma Science, 17-3 (1989) 429-438.

[5] Bayati M. S., Keshtkar A. and Gharib L., Analyzing the near and far field using finite difference and finite element method, IEEE Transactions on Plasma Science, 41-5 (2013) 1398-1402.

[6] Marder B., A coilgun design primer, IEEE Transactions on Magnetics, 29-1 (1993) 701-705.

[7] Kim S. W., Jung H. K. and Hahn S. Y., An optimal design of capacitor driven coilgun, IEEE Transactions on Magnetics, 30-2 (1994) 207-211.

[8] Waindok A. and Mazur G., Mutual inductances in a mathematical model of the three-stage reluctance accelerator, 3rd International Students Conf. on Electrodynamics and Mechatronics, Opole, Poland, (2011) 115-118.

[9] Lv Q., Li Z., Xie S., Zhang Q., Zhao K. and Xiang H., A practical electromagnetic launcher concept–part I: Primary structure design and armature optimal simulation, 16th International Symposium on Electromagnetic Launch Technology, Beijing, China, (2012) 1-5.

[10] Hou Y., Liu Z., Yang L., Shen Z., Ouyang J. and Yang D., Analysis of back electromotive force in RCEML, 17th International Symposium on Electromagnetic Launch Technology, California, USA, (2014) 1-6.

[11] Yadong Z., Ying W. and Jiangjun R., Capacitor-driven coil-gun scaling relationships, IEEE Transactions on Plasma Science, 39-1 (2011) 220-224.

[12] He J. L., Zabar Z., Levi E. and Birenbaum L., Transient performance of linear induction launchers fed by generators and by capacitor banks, IEEE Transactions on Magnetics, 27-1 (1991) 585-590.

[13] Korkmaz F., Topaloğlu I. and Gurbuz R., Simulink model of vector controlled linear induction motor with end effect for electromagnetic launcher system, Elektronika ir Elektrotechnika, 20-1 (2014) 29-32.

[14] Waindok A. and Mazur G., A mathematical and physical models of the three-stage reluctance accelerator, 2nd International Students Conference on Electrodynamic and Mechatronics, Gora Sw. Anny, Poland, (2009) 29-30.

[15] Zhiyuan L., Youtian L., Xueping M., Hongjun X. and Shumei C., Dynamic Research of Multi-Stage Reluctance Coil Gun, 17th International Symposium on Electromagnetic Launch Technology, San Diego, California, (2014) 1-4.

[16] Cooper L. M., Vancleef A. R., Bristoll B. T. and Bartlett P. A., Reluctance accelerator efficiency optimization via pulse shaping, IEEE Access, 2 (2014) 1143-1148.

[17] Xiang H., Lei B., Li Z. and Zhao K., Design and experiment of reluctance electromagnetic launcher with new-style armature, IEEE Transactions on Plasma Science, 41-5 (2013) 1066-1069.

[18] Barhoumi E. M., Hajji M. and Salah B. B., Design of a double-stator linear switched reluctance motor for shunting railway channels, Turkish Journal of Electrical Engineering and Computer Sciences, 22 (2014) 302-314.

[19] Kalender O., The optimization of launching a bullet using electromagnetic energy, Ph.D. thesis, Gazi University, Ankara, Turkey, (2005).

[20] Hou Y., Liu Z., Ouyang J. M. and Yang D., Parameter settings of the projectile of the coil electromagnetic launcher, 16th International Symposium on Electromagnetic Launch Technology, Beijing, China, (2012) 1-4.

[21] Chang J. H., Becker E. B. and Driga M. D., Coaxial electromagnetic launcher calculations using FE-BE method and hybrid potentials,

IEEE Transactions on Magnetics, 29-1 (1993) 655-660.

[22] Chaowei Z., Pengshu D., Xiaojun D., Sanqun L., Zhiyuan L. and Guanghui Z., Analysis of reluctance coil launcher performance using coupled field-circuit method, International Conference on Electrical Machines and Systems, Wuhan, China, (2008) 4049-4052.

[23] Tarvydas P., Edge finite elements for 3D electromagnetic field modeling, Elektronika ir Elektrotechnika, 76-4 (2007) 29-32.

[24] Barrera T. and Beard R., Exploration and verification analysis of a linear reluctance accelerator, 17th International Symposium on Electromagnetic Launch Technology, California, USA, (2014) 1-6.

[25] Sveikata J., Tarvydas P. and Noreika A., Electric circuit analysis using finite element modeling, Elektronika ir Elektrotechnika, 63-7 (2005) 31-34.

[26] Michaelides A. M. and Pollock C., Effect of end core flux on the performance of the switched reluctance motor, IEE Proceedings - Electric Power Applications, 141-6 (1994) 308-316.

[27] Sen P. C., Principles of Electric Machines and Power Electronics. Singapore: John Wiley & Sons, 1989; pp 101-104.

[28] Daldaban F. and Sari V., Analysis of a reluctance launcher by finite elements method, Journal of the Faculty of Engineering and Architecture of Gazi University, 30-4 (2015) 605-614.

Evaluation of NCEP/NCAR Reanalysis Precipitable Water Data Comparing to Radiosonde Observations for Turkey

Elçin TAN[1,*] iD

[1]*Istanbul Technical University, Aeronautics and Astronautics Faculty, Department of Meteorological Engineering, Maslak, Istanbul / TURKEY*

Abstract. Precipitable Water (PW) data of NCEP/NCAR Reanalysis Project (NNRP) model is evaluated by comparing to radiosonde data obtained from 8 locations of Turkey for the years between 2015 and 2017. Two methods are utilized to extract NNRP data for the observation locations. In the first method, the nearest NNRP grid point to the radiosonde locations is selected. The second method is the application of bilinear interpolation method on NNRP data to include the weighted effects of corresponding grid locations related with the observation sites. Both NNRP and radiosonde data have 12 h interval for the times 0000 Z and 1200 Z. PW output of NNRP model is compared to observations by means of graphical evaluation of time series, error analyses (Mean Absolute Error (MAE), Root Mean Square Error (RMSE), and Root Mean Squared Error (nRMSE)), goodness of fit tests (Cp and PBIAS), and probability density functions (PDF). Error analyses of most of the observation locations indicate that bilinear interpolation method is better than utilizing the nearest grid value data which is not obtained by applying any interpolation technique. Error analyses indicate that nRMSEs of NNRP data for PW analyses are less than 10% for 6 locations of Turkey (Ankara, Diyarbakir, Erzurum, Isparta, Istanbul, and Izmir) if it is assumed that the observations have no errors for the years between 2015 and 2017. nRMSEs of the other 2 coastal locations (Adana and Samsun) are the same as 13.8% and this may indicate that local moisture sources of these locations are greater than mesoscale moisture fields, since NNRP data may not capture local effects well due to its spatial resolution. Comparisons of probability density functions (PDF) of these data sets show that NNRP model may not be successful in capturing extreme values.

Keywords: *NCEP/NCAR Reanalysis Data Project, Precipitable Water, normalized Root Mean Square Error*.

NCEP/NCAR Modelinin Yağışa Geçebilir Su Buharı Miktarındaki Başarısının Türkiye'deki Radyosonda (Radyozonde) Gözlemleri ile Karşılaştırılarak Değerlendirilmesi

Özet. NCEP/NCAR Reanaliz Projesi (NNRP) modelinin yağışa geçebilir su buharı miktarı verileri, Türkiye'nin 8 istasyonundan alınan radyosonde verileriyle 2015-2017 yılları için karşılaştırılarak değerlendirilmiştir. NNRP verilerinden gözlem noktalarına karşılık gelen zaman serilerini oluşturabilmek için iki yöntem kullanılmıştır. İlk yöntemde ilgili istasyona en yakın grid noktasından zaman serisi oluşturulmuştur. İkinci yöntem ise, istasyon konumuna yakın olan grid noktalarının ağırlıklı etkilerini dikkate alabilmek için bilinear interpolasyon yönteminin NNRP verilerine uygulanmasıdır. NNRP ve radyosonda verilerinin zaman aralığı, 0000 Z ve 1200 Z saatleri için, 12 saattir. NNRP modelinin PW çıktısı gözlemlerle karşılaştırılırken zaman serileri grafiksel olarak değerlendirilmiş, hata analizleri (Ortalama Mutlak Hata (MAE), Kök Ortalama Kare Hata (RMSE) ve Kök Ortalama Kare Hata (nRMSE)) yapılmış, uygunluk test sonuçları (Cp ve PBIAS) belirlenmiş ve olasılık

yoğunluk fonksiyonları (PDF) grafiklendirilmiştir. İstasyonların çoğunun hata analizi, bilinear enterpolasyon yönteminin, bir interpolasyon tekniği uygulamadan seçilen en yakın grid noktasının değerlerinden daha uygulanabilir olduğunu göstermektedir. Gözlemlerin hata içermediği kabulü ile, NNRP verilerinin nRMSE'lerinin, Türkiye'nin 6 istasyonu için (Ankara, Diyarbakır, Erzurum, Isparta, İstanbul ve İzmir) %10'dan az olduğu belirlenmiştir. Kıyıya yakın olan diğer 2 istasyon (Adana ve Samsun) için de nRMSE %13.8'dir. Bu sonuçlar, çözünürlüğünün düşük olmasından dolayı NNRP modelinin lokal nem etkilerini doğru kestiremediğini göstermektedir. Olasılık yoğunluk fonksiyonlarının (PDF) karşılaştırmaları ise NNRP modelinin aşırı değerleri yakalamadaki başarısının düşük olduğunu belirtmektedir.

*Anahtar Kelimeler***:** NCEP/NCAR Reanaliz Veri Projesi, Yağışa Geçebilir Su Buharı Miktarı, standartlaştırılmış Karekök Ortalama Hata Karesi.

1.   INTRODUCTION

Precipitable water is the column integrated atmospheric water vapor and it has closely correlated with precipitation [1]. Although precipitation is an output of numerical weather prediction models (NWP) and this output can be compared with rain gauge precipitation observations, precipitable water might be a better indicator than precipitation for the studies related to dynamical modeling of atmospheric moisture for several reasons. One of those reasons is that atmospheric moisture, as relative humidity and mixing ratio/specific humidity, can be both initial/boundary conditions and output of NWP models, respectively, where precipitation is an output of them only. Another reason is that microphysical processes are large sources of complexity in NWP models and this may affect the accuracy of precipitation output of these models than that of moisture fields. Thus, this study focuses on precipitable water evaluation of NCEP/NCAR Reanalysis Project (NNRP) Model [2] data for Turkey.

NNRP data have been widely evaluated for precipitable water in several studies [3-7] and their discussions mostly indicate that NNRP data should be evaluated for the specific locations before performing the studies, because the uncertainties of NNRP Model may vary depending on whether the assimilation techniques were applied for the corresponding locations [8]. For Turkey, recent studies utilized with NCEP/NCAR Reanalysis Project (NNRP) Data are mostly for downscaling or comparison purposes in climate studies [9-11]. However, especially for precipitable water, the performance of the dataset itself has not verified for

Turkey, yet. Therefore, as a first attempt, this study aims to verify the precipitable water accuracy of NNRP Dataset for Turkey to quantify the possible errors of the model. Consequently, determination of these residuals might help to understand implicitly added error sources to these data.

In the following section, data sets and the methods used for this study are explained, in detail. In Section 3, comparisons of NNRP precipitable water and radiosonde data are presented by means of visual inspections of time series, error analyses including goodness of fit tests and probability density functions for 8 observation stations. Section 4 concludes the study with suggestions for future work.

2.   MATERIALS AND METHODS
2.1. Data

Precipitable water data of 12-hourly NCEP/NCAR Global Reanalysis Model [2] are evaluated for Turkey. The NCEP/NCAR Reanalysis Project dataset (NNRP) has 2.5°x2.5° horizontal resolutions with 28 vertical sigma levels. NNRP is provided by the Research Data Archive (RDA) of the University Corporation for Atmospheric Research (UCAR) [12]. The grid locations of NNRP dataset are presented in Figure 1 with blue markers.

Precipitable water data calculated by using radiosonde observations of 8 locations in Turkey are also utilized to verify NNRP dataset. The precipitable water data is obtained from University of Wyoming [13] for the years between 2015 and

2017. The locations and names of observation stations are indicated with red markers in Figure 1. Both NNRP and radiosonde data have 12 h interval

for the times 0000 Z and 1200 Z starting from January 1, 2015 to December 31, 2017.
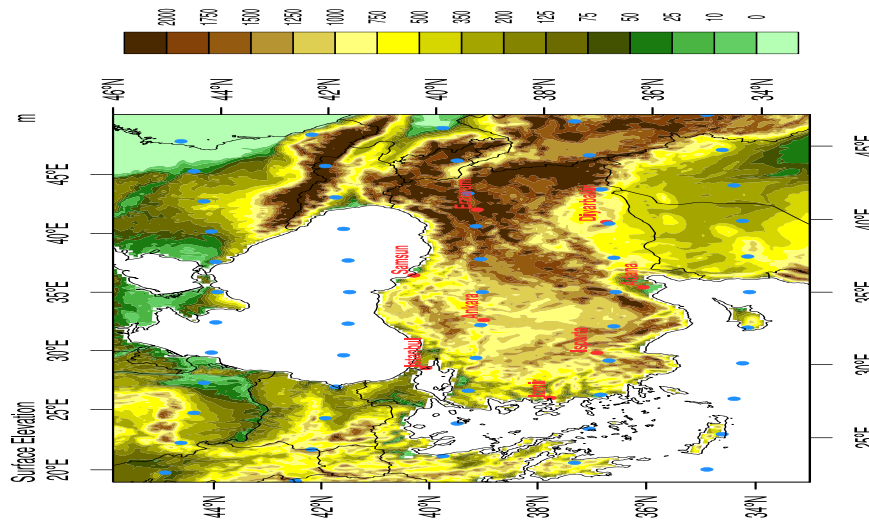
Figure 1. Surface elevation map of Turkey with the locations of 8 radiosonde stations of Turkey (red) and grid-point locations of NNRP data set (blue).

As seen in Figure 1, Turkey has a complex topography and therefore spatial variation of moisture may change abruptly. Moisture rates of Adana and Samsun are highest; rates of Istanbul (Kartal) and Izmir are moderate, and Ankara, Erzurum, Isparta, and Diyarbakir has lower rates comparing to the studied 8 station locations [14].

2.2. Methods

Construction of NNRP time series for the corresponding 8 radiosonde locations of Turkey is performed by using two methods. One is to select the nearest grid point of NNRP data with respect to the corresponding radiosonde location without applying any interpolation method. The other is to apply bilinear interpolation method to NNRP data to construct corresponding time series at the observation locations.

First of all, time series of the NNRP dataset and observations are plotted for a visual inspection starting from January 2015 to December 2017. Then, Goodness of Fit (GoF) tests, including error analyses, are calculated to evaluate the performance of NCEP/NCAR Global Reanalysis Model with respect to precipitable water (PW) radiosonde observations for the same time span. These tests, which are performed by utilizing hydroGOF-package in R, include Coefficient of

Persistence (cp), Mean Absolute Error (MAE), Root Mean Squared Error (RMSE), Normalized Root Mean Squared Error (nRMSE), and Percentage bias (PBIAS). Equations of the corresponding tests can be found in the manual of this package [15]. Finally, probable density functions are constructed for further evaluations.

3. RESULTS AND DISCUSSION

Error analyses of two methods indicate that bilinear interpolation method is better than choosing the nearest grid point approach, especially for the coastal sites. Table 1 presents the error differences of both bilinear method (indicated by the column named "Bilinear") and the nearest grid point selection method (indicated by the column named "Nearest"). For instance, the comparisons of Istanbul seem reasonable with the bilinear interpolation method (Cp>0), but the results of the nearest grid point selection do not indicate that they are reasonable (Cp<0). Therefore, the comparisons with the bilinear method will be discussed only.

As it is expected, related with the complex topography of Turkey, a visual comparison of 12 hourly NNRP and observation data time series for

eight stations of Turkey indicate that each location has own uncertainty due to local meteorological effects (Figure 2). A general evaluation may suggest that observations of Adana (a) and Samsun (h) stations do not agree with the NNRP model. Similarly, NNRP model cannot capture the highest precipitable water (PW) values observed in the beginning of 2015 for six stations. Generally, if local effects dominate PW amount more than that of mesoscale or large scale perturbations, then the accuracy of NNRP is reduced due to the fact that the resolution of the model is not high enough to resolve those local effects. On the other hand, a periodicity that observed in radiosonde time series for all stations due to seasonality is also inspected in NNRP time series for the corresponding locations.

Table 1. Error estimations and Goodness of fit measures between NNRP and radiosonde data for 8 stations of Turkey (Bilinear Interpolation is indicated by Bilinear and Nearest Grid Point Value is indicated by Nearest in the related columns)

Station Name	MAE (mm) Bilinear	Nearest	RMSE (mm) Bilinear	Nearest	NRMSE (%) Bilinear	Nearest	Cp Bilinear	Nearest	PBIAS (%) Bilinear	Nearest
Adana	**7.56**	**8.55**	**9.30**	**10.09**	**13.8**	**15**	**-2.32**	**-2.91**	**-34.30**	**-38.90**
Ankara	2.04	2.08	2.60	2.66	6.9	7.1	0.45	0.42	-12.50	-12.80
Diyarbakir	1.91	1.90	2.79	2.78	4.5	4.4	0.50	0.50	-7.60	-7.40
Erzurum	1.73	1.68	2.79	2.65	4.3	4.1	0.40	0.46	10.50	-1.10
Isparta	1.39	1.57	1.95	2.14	4.7	5.1	0.67	0.60	5.70	7.30
Istanbul	3.18	4.80	4.42	6.09	8.2	11.2	0.05	-0.81	-11.80	-22.70
Izmir	2.28	2.69	3.25	3.62	5.4	6	0.44	0.30	-9.10	-11.50
Samsun	**5.42**	**8.86**	**6.66**	**10.03**	**13.8**	**20.7**	**-1.49**	**-4.63**	**-25.40**	**-41.80**

Discrepancies which are revealed in the visual inspections of time series are quantified by means of five goodness of fit tests (Table 1). The Coefficient of Persistence (Cp) values of interested locations are evaluated first because Cp values are the first threshold in accepting the model performance. If Cp values are smaller than 0.0 then it is assumed that the model performance is not acceptable for further evaluation. In accordance with the visual evaluations of time series, Cp values of six stations indicate that they passed the threshold test except for Adana and Samsun observation locations (indicated by bold characters in Table 1.) where Cps are smaller than 0.0 and, thus, NNRP model performance for these stations are not acceptable without applying any bias correction method. MAE and RMSE values presented in the second and fourth column of Table 1, indicate fairly small errors. On the other hand, RMSEs of six stations, range between 1.95 mm and 4.42 mm, may not be considered small enough when they compare to the NNRP performance against sonde stations of the United States [8] whose RMSE range is between 0.5 mm and 1.2 mm, according to the Table 1 of this study.

PBIAS values of acceptable stations (Ankara, Diyarbakir, Erzurum, Isparta, Istanbul, and Izmir) mostly indicate a negative bias, except for Erzurum and Isparta (The tenth column of Table 1). This means that NNRP model tends to underestimate PW quantities being consistent with the corresponding time series (Figure 2). The reason of this underestimation might be related with the horizontal resolution of the model and, thus, local moisture effects observed in radiosonde data may not be captured by the model. NNRP model shows a positive bias for Erzurum and Isparta because the PW rates of this cities are the lowest (Figure 2) due to the fact that they are located at higher elevations than others.

Table 2. Mean values of NNRP and radiosonde data for 8 stations of Turkey with the number of missing values in observations

Station Name	PW-NNRP (mm)	PW-Observed (mm)	Missing Values [#/2192]
Adana	14.42	21.87	34
Ankara	12.22	13.97	11
Diyarbakir	13.01	14.07	20
Erzurum	13.97	9.14	42
Isparta	14.18	13.43	8
Istanbul	17.33	19.65	12
Izmir	17.53	19.30	16
Samsun	15.78	21.18	19

The reasons of variations in the goodness of tests depending on the location may better be seen in probability density functions (PDF) of NNRP and radiosonde data for each location (Figure 3). In Figure 3, black PDFs show observations, whereas blue lines are for NNRP distributions. The black and blue vertical lines are the mean values (Table 2.) for observations and NNRP, respectively (Table 2).

Figure 3. implies that PW distributions of NNRP and observations do not agree for Adana and Samsun, as detected with time series evaluations and GoF calculations. The negative bias of NNRP data for 4 stations (Ankara, Diyarbakir, Istanbul, and Izmir) is approved with PDFs. It is important to note that although distributions are quite similar for 6 stations, their tails demonstrate that NNRP model cannot simulate extreme values for all stations.
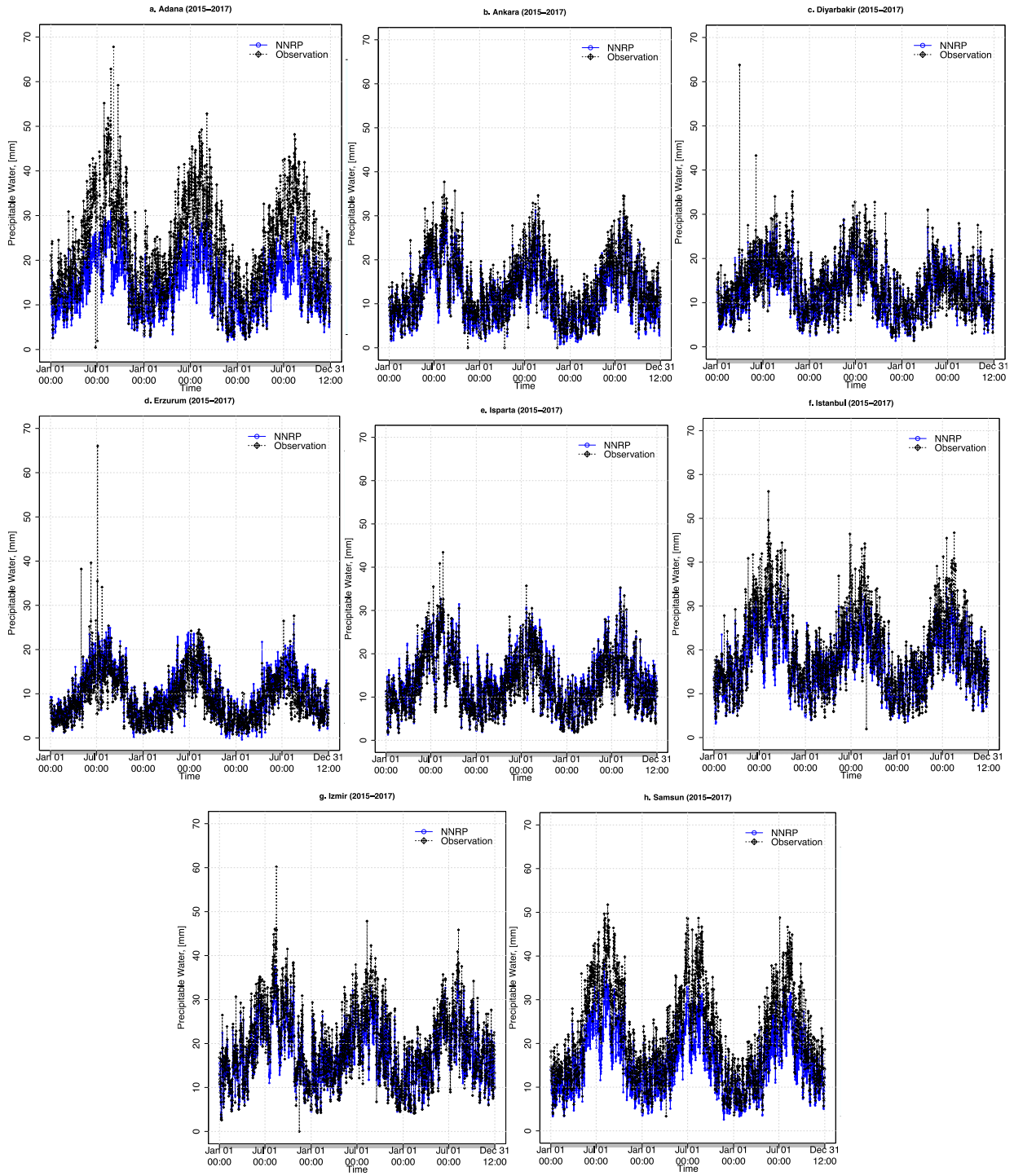
Figure 2. Precipitable Water Time Series Comparisons of NNRP data and radiosonde observations for eight stations of Turkey.
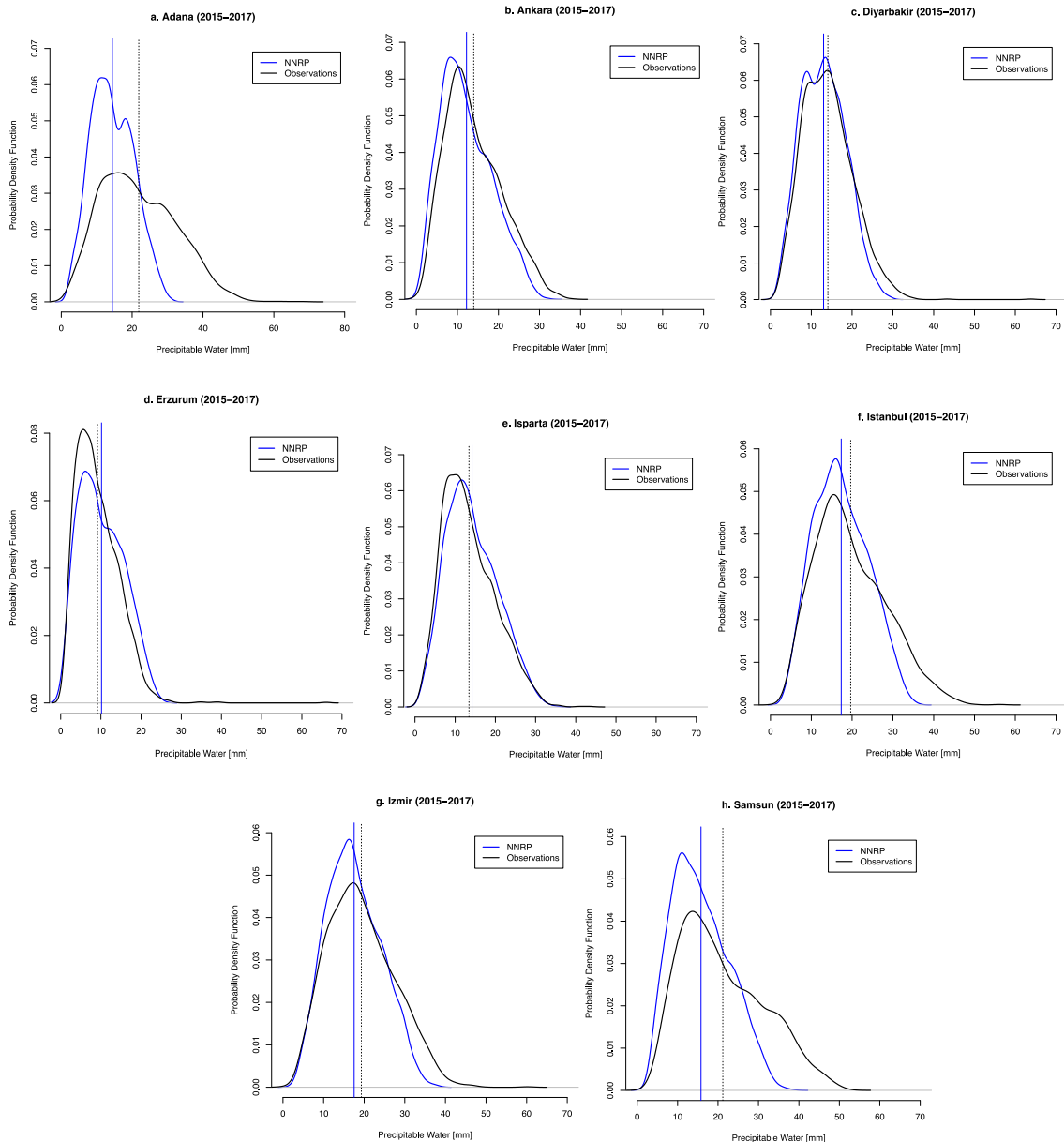
Figure 3. Probability density functions of NNRP data and radiosonde observations for 8 stations of Turkey between 2015 and 2017. Vertical lines indicate mean values of NNRP data (blue) and observations (black).

4. CONCLUSION

12-hourly Precipitable Water (PW) comparisons between NNRP data and radiosonde profiles clearly indicate that NNRP model may not capture local effects especially for the extreme PW values for Turkey. The local effects might be included to the data by applying some observational assimilation techniques or simulating the same conditions, i.e. hindcasting, with a higher resolution atmospheric model, such as the Weather Research and Forecasting Model (WRF). NNRP model results are not acceptable for the coastal cities Adana and Samsun where local moisture sources are dominant. NNRP model also produces more PW values for Erzurum where the station is located at high elevation with less moisture. NNRP data is more reliable for inland cities where moisture sources are dependent upon mesoscale effects which is consistent with the findings of [8]

that the data might have more error for mountainous regions. NNRP model tends to underestimate PW values for Turkey, except Isparta and Erzurum which are located inland and at higher elevations. Time series of radiosonde observations clearly show the diurnal and seasonal variations of PW whose values are greater during summer months than winter due to the fact that water vapor transport capacity of air depends entirely on the temperature. This periodicity and the order of magnitudes of PW for Istanbul, Izmir, and Ankara are consistent with the distributions of monthly precipitable water amounts estimated by [16] for the period of 1974 and 1984. As a result, NNRP data should be utilized after checking its consistency with observations for the interested regions of Turkey. These results imply that a subset reanalysis data of NNRP should be constructed for Turkey by assimilating remote sensing system, especially for climate change related studies.

ACKNOWLEDGMENTS

REFERENCES

[1] Precipitable water, Glossary of Meteorology, American Meteorological Society, http://glossary.ametsoc.org/wiki/Precipitable_ water. Accessed: 29 Jan 2018.

[2] Kalnay E., Kanamitsu M., Kistler R., Collins W., Deaven D., Gandin L., Iredell M., Saha S., White G., Woollen J., Zhu Y., Chelliah M., Ebisuzaki W., Higgins W., Janowiak J., Mo K.C., Ropelewski C., Wang J., Leetmaa A., Reynolds R., Jenne R. and Joseph D., The NCEP/NCAR 40-year reanalysis project. Bull. Amer. Meteor. Soc., 77 (1996) 437-471.

[3] Xie P. and Arkin P.A., Global precipitation: A 17-year monthly analysis based on gauge observations, satellite estimates, and numerical model outputs. Bulletin of the American Meteorological Society, 78 (1997) 2539–2558.

[4] Trenberth K.E. and Guillemot C.J., Evaluation of the atmospheric moisture and hydrological cycle in the NCEP/NCAR reanalyses, Clim Dyn, 14 (1998) 213–231.

[5] Bromwich D.H., Fogt R. L., Hodges K. I. and Walsh J. E., A tropospheric assessment of the ERA-40, NCEP, and JRA-25 global reanalyses in the polar regions, *J. Geophys. Res.*, 112 (2007) D10111.

[6] Ma L., Zhang T., Frauenfeld O.W., Ye B., Yang D. and Qin D., Evaluation of precipitation from the ERA-40, NCEP-1, and NCEP-2 Reanalyses and CMAP-1, CMAP-2, and GPCP-2 with ground-based measurements in China, Journal of Geophysical Research, 114 (2009) D09105. https://doi.org/10.1029/2008JD011178.

[7] Sun Q., Miao C., Duan Q., Ashouri H., Sorooshian S. and Hsu K.-L., A review of global precipitation data sets: Data sources, estimation, and inter- comparisons. Reviews of Geophysics, 56 (2018) https://doi.org/10.1002/2017RG000574.

[8] Trenberth K.E., Fasullo J. and Smith L., Trends and variability in column integrated atmospheric water vapor. Climate Dyn., 24, 7–8 (2005) 741–758.

[9] Fistikoglu O. and Okkan U., Statistical downscaling of monthly precipitation using NCEP/NCAR reanalysis data for Tahtali River basin in Turkey, ASCE J Hydrol Eng, 16(2) (2011) 157–164.

[10] Tatli H., Statistical complexity in daily precipitation of NCEP/NCAR reanalysis over the Mediterranean basin. Int. J. Climatol., 34 (2014) 155–161.

[11] Bozkurt D., Turuncoglu U., Sen O.L., Onol B. and Dalfes H.N., Downscaled simulations of the ECHAM5, CCSM3 and HadCM3 global models for the eastern Mediterranean–Black Sea region: evaluation of the reference period, Clim Dyn, 39-1,2 (2012) 207–225.

[12] National Centers for Environmental Prediction/National Weather Service/NOAA/U.S. Department of Commerce. 1994, updated monthly. NCEP/NCAR Global Reanalysis Products, 1948-continuing. Research Data Archive at the National Center for Atmospheric Research, Computational and Information Systems Laboratory.

http://rda.ucar.edu/datasets/ds090.0/.Accessed: 28 JAN 2018.

[13] University of Wyoming, College of Engineering, Upper Air Radiosonde Data. http://weather.uwyo.edu/upperair/sounding.ht ml. Accessed: 28 JAN 2018.

[14] Turkish State Meteorological Service, Statistics Report of Relative Humidty, https://www.mgm.gov.tr/FILES/resmi-istatistikler/Turkiye-Ortalama-Nem.pdf. Accessed: 1 FEB 2018.

[15] Mauricio, Z.-B., hydroGOF: Goodness-of-fit functions for comparison of simulated and observed hydrological time series. R package version 0.3-10. http://CRAN.R-project.org/package=hydroGOF, (2017).

[16] Topcu, S. Atmosferdeki Yağışa Geçebilir Su Buharı Miktarının Hesaplanması, Coğrafya Araştırmaları Dergisi, Cilt 1, Sayı 1 (1989). In Turkish. Accessed 1 FEB 2018. http://tucaum.ankara.edu.tr/wp-content/uploads/sites/280/2015/08/cadata1_9.p df

A Finite Element Investigation of the Superelevated Horizontal Curve

Murat BOSTANCIOĞLU[1,]* (iD)

[1]Sivas Cumhuriyet University, Faculty of Engineering, Civil Engineering Department, Sivas, Turkey

Abstract. Stress-strain analyses are studied under the bottom of the pavement layer, and pavement life values are calculated depending on the cross-section variation because of the superelevation in horizontal curves. For this purpose, 1st principal total mechanical strain values are analyzed with the superelevation values changing between 0-8 (%) and the different positions of wheel contact pressure. Finite element method is used for analysis. According to results of the study, it is obtained that pavement life decreases with the increasing superelevation, in the case of 8% superelevation and decreasing the distance to pavement edge, pavement life decreasing gets to 34%.

Keywords: Fatigue, finite element method, tensile strain, pavement life.

Dever Uygulaması Yapılmış Bir Yatay Kurbanın Sonlu Elemanlar Yöntemi ile İncelenmesi

Özet. Bu çalışmada dever uygulaması yapılmış bir yatay kurbanın kaplama tabakası altındaki gerilme-birim şekil değiştirme ve kaplama ömrü değerleri dever sebebiyle değişen kesitlere bağlı olarak analiz edilmiştir. Bu amaçla deverin 0-8 (%) değerleri arasında değişimine bağlı olarak ve ayrıca tekerlek temas gerilmesinin pozisyonu değiştirilerek birim şekil değiştirme değerleri sonlu elemanlar yöntemi ile analiz edilmiştir. Çalışmadan elde edilen sonuçlara göre dever değerinin artmasına bağlı olarak kaplama ömrü azalmıştır. Bu azalma değeri deverin 8% olması ve yükleme noktasının kaplama kenarına olan mesafesinin azalması ile 34% seviyesinde hesaplanmıştır.

AnahtarKelimeler: Yorulma ömrü, sonlu elemanlar yöntemi, çekme birim şekil değişimi, kaplama ömrü

1. INTRODUCTION

Roadways have vital importance for the living and development of society since they are responsible for large portion of the transportation of goods and people [1]. As a result of frequent road failure in most developing countries, the need for stronger, long-lasting and all-weather pavements has become a priority in pavement engineering as a result of rapid growth in the automobile traffic and the development of modern civilization.

In Pavement Engineering, it is known that the major causes of failure of asphalt pavement are fatigue cracking, caused by excessive horizontal tensile strain at the bottom of the asphalt layer due to repeated traffic loading and rutting deformation caused by densification and shear deformation of subgrade [2].

The fatigue resistance of asphalt concrete (AC) mixtures is its ability to withstand repeated bending

without fracture. Most analyses utilize flexure stresses or strains on the underside of the AC pavement layers to assess the pavement lives [3].

Asphalt pavements consist of four main layers as the surface layer (AC layer), base layer, subbase layer and subgrade layer (soil layer). Since these layers have a complex structure consisting a number of materials (bitumen and fine or coarse aggregates) with different properties, mathematical description of these layers may not be possible [4,5].

Mechanistic methods used in the analysis of layered pavement systems work reasonably well. These methods analyze stresses and strains that occur depending on the traffic loads and environmental factors with mechanical theories [6,7].

Finite element method (FEM) can be successfully used for analyzing pavement structures with complex geometry, boundary conditions and material properties and to investigate the effects of static and cyclic loading combined with linear and non-linear material characteristics [6,8-11].

Turkish General Directory of Highways considers the geometric characteristics of roads that are effective in pavement failure as the slopes, ramp length and the radius of horizontal curves while recommending the bitumen performance grade according to Superpave design method [12].

In this study, the effect of cross-section variation (due to superelevation) on the horizontal curves that is necessary for pavement engineering, on the pavement life is investigated by the FEM technique through these important geometric characteristics. For this reason, mechanical strain values under the bottom of pavement and pavement life are analysed depend on the superelevation and loading position change in a determined cross-section.

Paper becomes different from the other studies that consider the cross-section effect on the pavement thickness calculations.

Metal corrosion is a very important problem in various industrial processes which is widely used water, alcohol and acid. The acid solutions used cause too much corrosion in the metal that is an iron, copper, aluminum. Corrosion inhibitors that are containing nitrogen, oxygen, Sulphur and aromatic ring, are used to prevent corrosion caused by acid solutions.

As it is well known that experimental studies have been used to understand the corrosion inhibition mechanism of molecules and to explain corrosion inhibition efficiencies. Quantum chemical calculations provide preliminary information on the activities of molecules. In quantum chemical calculations, parameters related to the activity of molecules are calculated using density functional theory (DFT) that are calculated HOMO (highest occupied molecular orbital), LUMO (lowest unoccupied molecular orbital), electrophilicity, electronegativity, chemical potential, chemical hardness and nucleophilicity.

In this study, we can be seen that activity of studied molecules whose names are 2-(4-nitrophenyl) benzimidazole (4NPBI), 2-(4-aminophenyl) benzimidazole (4APBI), 2-(2-nitrophenyl) benzimidazole (2NPBI), 2-(2-aminophenyl) benzimidazole (2APBI), 2-phenyl benzimidazole (PBI), 2-(4-chlorophenyl) benzimidazole (4CPBI), 2-(4-metilphenyl) benzimidazole (4MPBI), 2-(4-bromophenyl) benzimidazole (4BPBI) in Figure 1 [1].

2. FINITE ELEMENT MODEL AND METHOD

2.1. Model geometry and material defining

Three-layered conventional flexible pavement structure is selected for this study consists of a 250 mm thick surface layer, 500 mm thick base and subbase layer and 2000 mm thick subgrade layer. The pavement configuration is shown in Figure 1. This configuration is obtained from the field work of Karadeiz Technical University on Trabzon-Arsin highway (Turkey) [7] and the values are used as the same as this work.
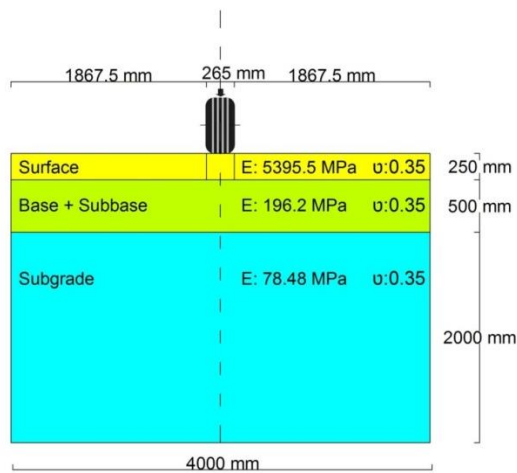
Figure 1. Pavement configuration.

Since asphaltic-pavement is a complex structure consisting of a number of materials with different properties, perfect mathematical description of the structure may not be possible. Most structural response models based on layered theory do not consider the heterogeneity of the asphalt concrete material. They are mostly based on linear elastic or linear viscoelastic theory. In the linear elastic theory, the material in each layer is assumed to be homogenous, isotropic, and linear elastic. Such material can be fully characterized by two elastic parameters such as the modulus of elasticity and Poisson's ratio [4]. In studies investigating the effect of parametric changes on the pavement performance, such as the strengthening of flexible pavements with geogrid, crack propagation modeling, the flexible pavement layers were identified by a fixed modulus of elasticity and Poisson's ratio, or they were added to the calculations by varying these values in a certain range [10,11,13].

In this study, which is particularly emphasized by the change effect at the cross-section, it is considered sufficient to define the layers as linear elastic. As can be seen in Figure 1, three different materials and their elastic material properties were used on the pavement modelling.

In the modelling of the problem, ANSYS 13.0 finite element program is used. 2 dimensional, 8 node structural solid element (PLANE183) was selected for use in the analysis [14]. The problem is considered under the plane strain condition. A plane strain model assumes that the thickness in the horizontal plane is infinite [8].

2.2. Boundary conditions, loading and failure criteria

The bottom surface of the subgrade is assumed to be fixed which means that nodes at the bottom of the subgrade can't move horizontally or vertically. The boundary nodes along the pavement edges are horizontally constrained but are free to move in the vertical direction [8].

The size of contact area between tyre and pavement depends on the contact pressure and can be represented by two semicircles and a rectangle as shown in Figure 2 (a). This shape is converted to a rectangle which's sizes are 0.8712Lx0.6L and area is $0.5227L^2$ as suggested by Huang [15] (Figure 2 (b)).
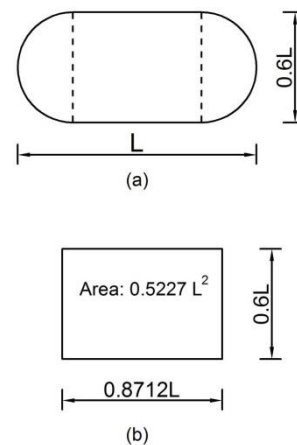
Figure 2. Contact area.

In this study the 5225 kg (51 kN) wheel load is assumed to be uniformly distributed over the contact area (26.5x29 cm^2) between tyre and pavement according to field work studied by Özcanan and Akpınar [7]. The contact pressure is assumed as equal to the tyre pressure [6] and selected as 0.667 MPa for this study. According to equivalent rectangle area suggested by Huang, contact area sizes are calculated as 23x33 cm^2 and the field measurements are in accordance with this calculation.

Due to symmetry, the pavement under a half wheel load is considered in the analysis [6]. Figure 3 shows the finite elements mesh of the model and load distribution on the surface.
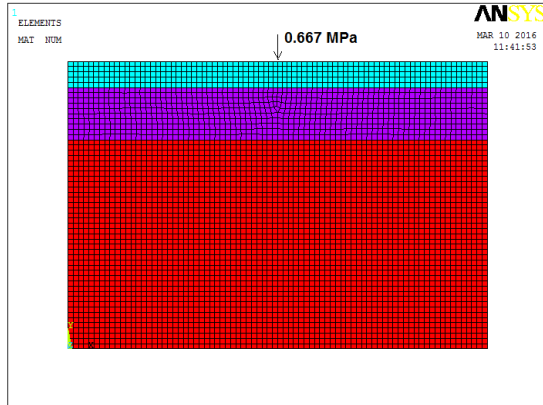
Figure 3. Finite element mesh model

According to elastic layer theory, the maximum strain is at the bottom of the asphalt surfacing layer. Most pavement design models are therefore based on straining at the bottom of the asphalt layer to predict performance with respect to fatigue cracking [14].

The failure criterion for fatigue cracking of the asphalt surfacing layer may be evaluated from the following equation;

$$\log(N_f) = 16.664 - 3.291\log\left(\frac{\varepsilon_t}{10^{-6}}\right) - 0.854\log(E) \quad (1)$$

Where N_f is the number of load applications to induce fatigue cracking over 10% of the wheel path area, ε_t is the horizontal tensile strain repeatedly applied at the bottom of the asphalt surfacing layer and E is the stiffness modulus for asphalt surfacing layer [16].

3. RESULTS AND DISCUSSION
3.1. Verification of the model

Compressive stress values measured on and under 250 mm thick asphalt surface layer of Trabzon-Arsin highway from Turkey with 20 cm diameter pressure gauge are determined as 0.68 and 0.1 MPa respectively [7]. Stress values are compared with the values obtained from finite element model and the model results are given in Figure 4. According

to Figure 4, model results are compatible with the field work. Furthermore, results obtained from the study of Walutiba and Ven [17] indicating that the vertical stress under 200 mm thick surface layer decreases 75% with regard to under wheel stress, in this study, vertical stress decreases 78% but thickness of surfacing layer is 250 mm and the results are in acceptable level.
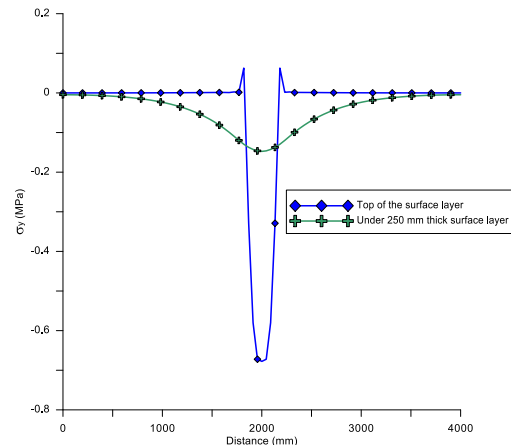
Figure 4. Compressive stress values obtained from FEM model.

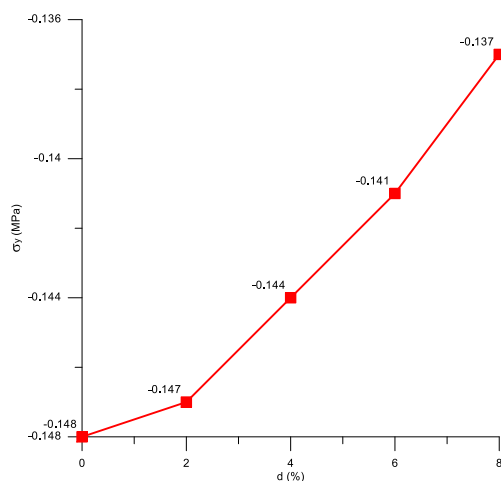### 3.2. Stress-strain analysis of the bottom of asphalt surfacing layer

For stress and strain analysis of the bottom of asphalt surfacing layer, the loading condition in which the contact pressure is performed in the middle of the traffic lane (4000 mm) is considered. 1st principal total mechanical tensile strain values at the bottom of the surfacing layer are obtained through the cross-section while the loading value and position are constant, and superelevation (d) is changing between 0 and 8%. Strain values are shown in Figure 5.
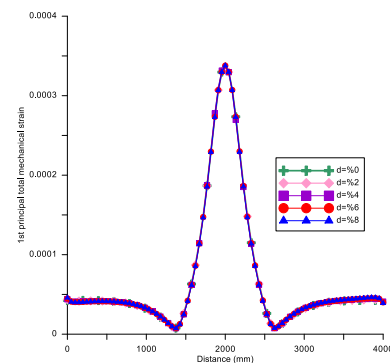
Figure 5. 1st principal total mechanical tensile strain values at the bottom of the surfacing layer

As can be seen in Figure 5, tensile strains for all superelevation values are adjacent to each other. From these results, it can be concluded that superelevation change has no significant effect on the tensile strains and pavement life while the loading is in the middle of the traffic lane (lateral supports of layers and pavement edges are strong enough).

While the loading is in the middle of the traffic lane, maximum vertical pressure stresses at the bottom of the surfacing layer are obtained as illustrated in Figure 6. According to Figure 6, increasing superelevation increases the compressive stresses. The decrease of the vertical component and the increase of the horizontal component of the loading with the steeper cross-section explain this situation.

Figure 6. Maximum vertical pressure stress values at the bottom of the surfacing layer

3.3. Strain analysis depends on the loading position and superelevation change

It is explained in the previous section that superelevation has no significant effect on the tensile strain values in the case of loading is in the middle of the cross section. But, in concern with the positioning of a standard width (2380 mm) heavy vehicle [14] on a traffic lane, Figure 7-b represents a more realistic placement than Figure 7-a.
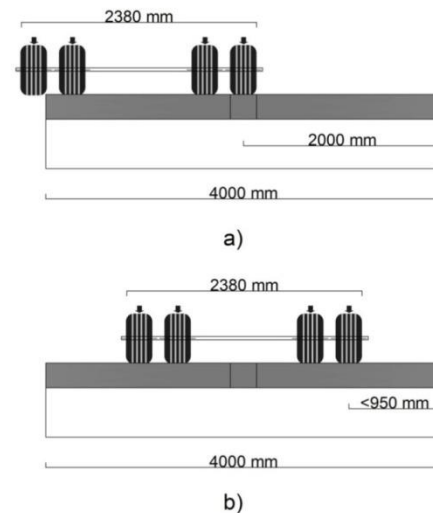
Figure 7. Positioning of a heavy vehicle on a traffic lane

The positioning of a heavy vehicle towards to horizontal curve centre and superelevation change are considered together. Hence, the contact pressure is placed in the distance of 1500 mm, 1000 mm and 500 mm from the pavement edge and strain analysis are performed with varied superelevation values (Figure 8).
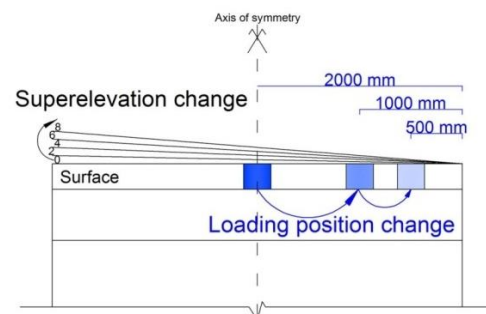

Figure 8. Illustration of loading position and superelevation change

When analyzing the tensile strain values at the bottom of the asphalt surfacing layer (under the wheel placement horizontally) for changing load position and changing superelevation, it can be seen that decreasing distance of loading to pavement edge makes superelevation-strain curves steeper (Figure 9). It means that pavement becomes more sensitive to superelevation change with decreasing distance to the edge. As a result of there is no lateral support in the horizontal direction of wheel-surfacing layer contact point and decreasing

lateral support of layers, superelevation effect on the tensile strains is more noticeable.
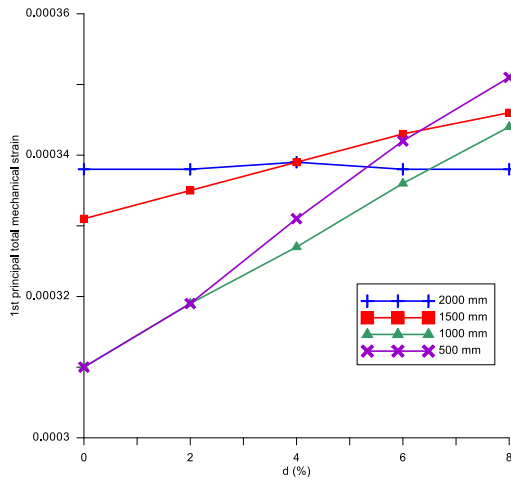
Figure 9. 1st principal total mechanical tensile strain values depend on the loading position and superelevation change

N_f values are calculated with obtained tensile strain values and stiffness modulus of surfacing layer for to evaluate the effect of superelevation to pavement life for the more sensitive loading conditions as stated above (1000 and 500 mm distance from the pavement edge) and presented in Figure 10. Nf results show that increasing superelevation decreases the pavement life. While the distance from the edge is 1000 mm, pavement life decreases 29% in comparison with 0% superelevation, and this ratio reaches to 34% for 500 mm distance.
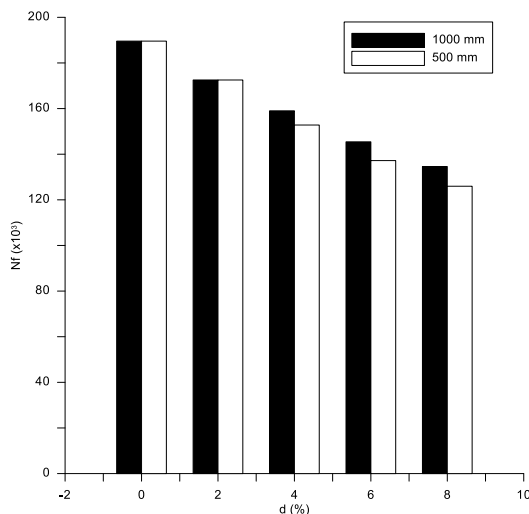

Figure 10. N_f values depend on the superelevation changing.

## 3.4. Precautions for increasing the pavement life of superelevated horizontal curves

Increasing the stiffness modulus or thickness of asphalt surfacing layer can be the solution of deteriorating effect of superelevation. In this study the most damaging conditions that are the 8% superelevation and loading at 500 mm distance from the pavement edge are considered. In this loading and cross-section condition, stiffness modulus and thickness values are calculated that equates the Nf value of 8% superelevated cross-section to Nf value of 0% superelevated cross-section (flat cross-section). Results are presented in Figure 11 and 12.

According to Figure 11, stiffness modulus value that ensures to Nf value of 0% superelevated cross-section (Nf=189572) is calculated as 10693 MPa from the curve equation so the stiffness modulus of superelevated surfacing layer must be increased just about two times.
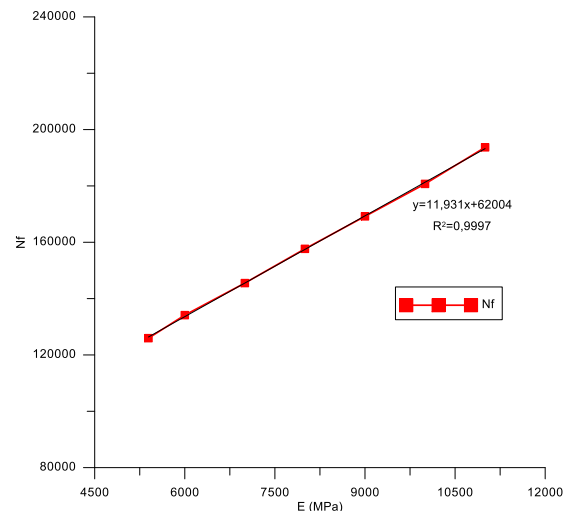
Figure 11. N_f values depend on the stiffness modulus.

While the stiffness modulus is constant, the 1st principal total mechanical strain value was calculated for different layer thickness values for obtaining the 189572 Nf value. The thickness that equates the 1st principal total mechanical strain value of 8% superelevated cross-section to flat cross-section determined from the curve equation as 296 mm (Figure 12). According to this result, surfacing layer thickness must be increased 46 mm.
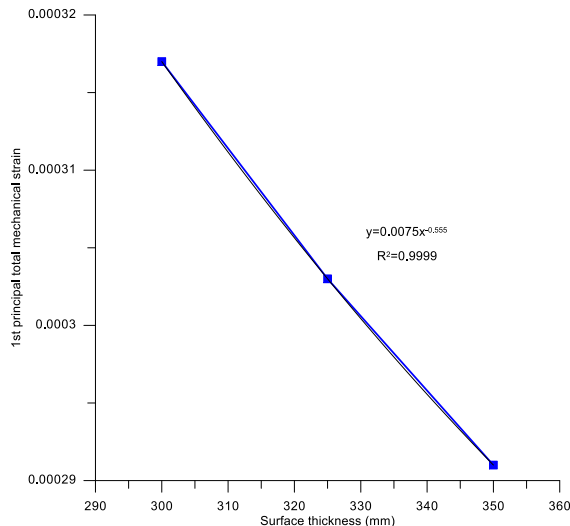
Figure 12. 1st principal total mechanical tensile strain values depend on the surfacing layer thickness.

4.   CONCLUSION

The following results can be drawn from the analysis of this study;

* FEM is an applicable method for the modelling of multilayered pavement structures

* While the contact pressure is in the middle of the traffic lane, superelevation change has no remarkable effect on the 1st principal total mechanical strain and pavement life, but compressive stress values increase 7.4% with the increasing superelevation.

* The effect of superelevation becomes more distinctive when the loading gets closer to pavement edge. Decreasing distance to pavement edge decreases the pavement life 34%.

* The deteriorating effect of superelevation can be more efficient in the fill cross-sections that their lateral support is less than the cut one.

* For increasing the pavement life in superelevated horizontal curves, stiffness modulus of pavement must be increased approximately two times, or pavement thickness must be increased dramatically.

* According to results of this study, cross-section geometry that doesn't consider in pavement thickness analysis but has an effect on it must be taken into consideration.

REFERENCES

[1] Souza F.V. and Castro L.S.,Effect of Temperature on the Mechanical Response of Thermo-Viscoelastic Asphalt Pavements, Construction and Building Materilas, 30 (2012) 574-582.

[2] Ekwulo E.O. and Eme D.B.,Expected Traffic, Pavement Thickness, Fatigue and Rutting Strain Relationship for Low Volume Asphalt Pavement, The International Journal of Engineering and Science, 2-8 (2013)62-77.

[3] Zhi S., Gun W.W., Hui L.X., Bo T., Evaluation of Fatigue Crack Behavior in Asphalt Concrete Pavements, Construction and Building Materials, 27 (2012) 117-125.

[4] Akbulut H. and Aslantas K.,Finite Element Analysis of Stress Distribution on Bituminous Pavement and Failure Mechanism, Materials and Design, 26 (2005) 383-387.

[5] Ameri M., Mansourian A., Khavas M. H., Aliha M. R. M., Ayatollahi M.R., Cracked Asphalt Pavement Under Traffic Loading – A 3D Finite Element Analysis, Engineering Fracture Mechanics, 78 (2011) 1817-1826.

[6] Hadi M.N.S. and Bodhinayake B. C.,Non-Linear Finite Element Analysis of Flexible Pavements, Advances in Engineering Software, 34 (2003) 657-662.

[7] Özcanan S. and Akpınar M. V., Determining the Critical Tire and Axle Configuration for Flexible Pavements Based on Mechanistic Analysis, Technical Journal of Turkish Chamber of Civil Engineers, 25-1 (2014) 6625-6654.

[8] Abed A.H. and Al-Azzawi A.A., Evaluation of Rutting Depth in Flexible Pavements by Using Finite Element Analysis and Local Empirical Model, American Journal of Engineering and Applied Sciences, 5-2 (2012) 163-169.

[9] Chang L. and Linglin L., Criteria for Controlling Rutting of Asphalt Concrete Materials in Sloped Pavement, Construction and Building Materials, 35 (2012) 330-339.

[10] Al-Azzawi A.A.,Finite Element Analysis of Flexible Pavements Strengthed with Geogrid, ARPN Journal of Engineering and Applied Sciences, 7-10 (2012) 1295-1299.

[11] Gajewski J. and Sadowski T., Sensitivity Analysis of Crack Propagation in Pavement Bituminous Layered Structures Using a Hybrid System Integrating Artificial Neural Networks and Finite Element Method, Computational Materials Science*, 82 (2014) 114-117.

[12] Sağlık A., Orhan F., Güngör A.G.,Bitumen Class Choosing Maps for HMA Paved Roads, Republic of Turkey Ministry of Transport, Maritime Affairs and Comminications, Ankara, (2012).

[13] Yongjie L., Shaopu Y., Jianxi W., Research on Pavement Longitudinal Crack Propagation Under Non-Uniform Vehicle Loading, Engineering Failure Analysis*, 42 (2014) 22-31.

[14] Mulungye R.M., Owende P.M.O., Mellon K.,Finite Element Modelling of Flexible Pavements on Soft Soil Subgrades, Materials and Design, 28 (2007) 739-756.

[15] Huang Y. H.,Pavement Analysis and Design, Pearson Prentice-Hall, New Jersey, (1993).

[16] Finn F., Saraf C.L., Kulkarni R., Nair K., Smith W. Abdullah A., Development of Pavement Structural Subsystems NCHRP Report 291, Transportation Research Board, Washington (DC), (1986).

[17] Walubita L.F. and Ven M.F.C.,Stresses and Strains in Asphalt-Surfacing Pavements, South African Transport Conference: Action in Transport for the New Millennium, South Africa, (2000).

Ecotoxic Effects of Cerium Oxide Nanoparticles on Bacteria

Merve ÖZKALELİ AKÇETİN[1] iD *, Ayça ERDEM[2,]* * iD

[1]*Akdeniz University, Graduate School of Natural and Applied Sciences, Dept. of Environmental Engineering, 07058, Antalya, TURKEY*
[2]*Akdeniz University, Faculty of Engineering, Dept. of Environmental Engineering, 07058, Antalya, TURKEY*

Abstract. In this study, the ecotoxic effects of cerium oxide nanoparticles (CeO_2 NPs) on both gram positive *Bacillus subtilis* and gram negative *Escherichia coli* bacteria were investigated. CeO_2 NPs were prepared in synthetic water solutions having different water contents (low, median and high ionic strength and conductivity, pH 5.5 and 6.5). Bacteria were exposed to CeO_2 NP solutions in absence and presence of light conditions for 1 h. Different NP concentrations (10, 100, 500 and 1000 mg/L) were used, and environmental scanning electron microscopy imaging was performed for morphological examination of the bacteria. Results showed an aggregation of NPs relating to both high NP concentrations and high ionic strength of the water solutions. Regardless of the test condition, CeO_2 NPs highly inhibited the bacterial growth.

Keywords:*Bacillus subtilis*, *Escherichia coli*, CeO_2 nanoparticle, inhibition, synthetic water solutions.

Seryum Oksit Nanopartiküllerinin Bakteriler Üzerindeki Ekotoksik Etkileri

Özet. Bu çalışmada, seryumoksit nanopartiküllerinin (CeO_2 NP) gram pozitif *Bacillus subtilis* ve gram negatif *Escherichia coli* bakterileri üzerindeki ekotoksik etkileri incelenmiştir. CeO_2 NPleri farklı içeriğe sahip (düşük, orta ve yüksek iyonik güç ve iletkenlik, pH 5,5 ve 6,5) sentetik su çözeltileri içinde hazırlanmıştır. Bakteriler ışıklı ve ışıksız ortamlarda CeO_2 NPlerine 1 saat süreyle maruz bırakılmıştır. Farklı NP konsantrasyonları (10, 100, 500 and 1000 mg/L) kullanılmış ve çevresel taramalı electron mikroskopi görüntüleme ile bakterilerin morfolojik incelemesi yapılmıştır. Sonuçlar yüksek NP konsantrasyonu ve yüksek iyonik güce bağlı olarak NPlerin agregasyona uğradığını göstermiştir. Test koşullarından bağımsız olarak CeO_2 NPleri bakteriyel büyümeyi yüksek oranda inhibe etmiştir.

AnahtarKelimeler: *Bacillus subtilis*, *Escherichia coli*, CeO_2 nanopartikülü, inhibisyon, sentetik su çözeltisi.

1. INTRODUCTION

Engineered nanoparticles (NPs) are used in almost every field from imaging technology to food, agriculture and cosmetics to the pharmaceutical industry. Due to this intensive use, titanium dioxide (TiO_2), zinc oxide (ZnO), cerium oxide (CeO_2) and silver NPs have the highest production volumes of 100-1000 tons/year [1]. In addition to these metal oxide NPs, cerium (Ce) with 0.0046% of rare elements, is as abundant as copper (Cu) in the earth's crust [2]. In Europe, the median Ce concentration detected as 48.2 mg/kg, 66.6 mg/kg, and 55 ng/L in soil, sediment and water,

respectively [3]. European Union (EU) Commission estimated the global production amount of nano-CeO_2 around 10000 tons in 2012 [4]. A study by the Future Markets Company predicted that the production of nano-CeO_2 in 2011 was between 7500 and 10000 tons [5]. According to Statista, the price of CeO_2 was 98217 US-\$/ton in 2011, 5516 US-\$/ton in 2018 and the predicted price will be 308 US-\$/ton in 2025 [6]. The American Geological Survey Unit (USGS) reported that 80% of the global CeO_2 production potential was reported in China [7] and other important nano-CeO_2 producer countries were located in Asia, Australia and Europe [8].

CeO_2 NPs are employed in electronics and optics [4, 9], polishing products [4, 10], exterior facade paints [4], metallurgy [4], as fuel additives due to its catalytic properties, wood coating material [11], petroleum refinery, and in fluid catalytic cracking [3]. Moreover, in medicine [12, 13], environmental chemistry [2] and in removal of pollutants from industrial wastewaters [14] CeO_2 NPs have been employed. Dai et al. [14] used SiO_2/CeO_2 catalyst (Fe_3O_4 magnetic core covered with SiO_2 in middle layer and CeO_2 in outer layer) in catalytic ozonation for acetylsalicylic acid degradation in the aqueous solution and obtained 81% removal efficiency within 1 hour.

As a result of high production volumes, high amounts of NPs tend to release into receiving environments. There are studies showing TiO_2, ZnO, Ag and CeO_2 NPs in surface waters, wastewater treatment plant effluent and sludge, sediments and landfill areas [15]. CeO_2 NP concentrations estimated in treated wastewater was between 0.003 and 1.17 μg/L, and in sludge was between 0.53 and 9.10 mg/kg [16]. It is also predicted that the increasing concentrations of NPs in receiving environments may result in ecotoxicity to organisms [15, 17, 18]. When CeO_2 NPs released into the receiving environments, it is inevitable to emerge in aquatic environments [16], and rapidly undergo an aggregation/agglomeration and interact with aquatic organisms [19, 20]. With this interaction, microorganisms, algae and macroinvertebrates, which are the basic building blocks of ecological food web, are the first and most exposed organisms to the ecotoxic effects of NPs [21].

There are limited number of studies on the ecotoxic effects of nano-CeO_2 particles to microorganisms [3, 22-27]. Thill et al. [22] showed the effects of 7 nm particle sized CeO_2 NPs on gram (-) *Escherichia coli* with an EC50 value of 5 mg/L. Moreover, they depicted that CeO_2 – *E. coli* interaction was directly by electrostatic attraction to the negatively charged bacteria wall due to the positively charged physiological pH value. Pelletier et al. [23] presented inhibitions of *E. coli* and *Bacillus subtilis*, and no effect on *Shewanella oneidensis* under CeO_2 NP treatment. In the study, different NP concentrations (50–150 μg/mL), NP sizes (6–40 nm), pH and medium were used to determine the effects of CeO_2 NPs. Dar et al. [24] treated *E. coli* HB101 K12 strains with four different sizes (3,5–6,5 nm) of CeO_2 NPs and showed the inhibition of bacteria. The studies showed the effect mechanisms of CeO_2 NPs on bacteria mostly related to a direct contact with bacterial cell wall [22, 25, 27], membrane deformation [26], cell disintegration [27] and release of free Ce(III) [25]. The evaluation of those studies revealed that the data on the ecotoxic effects of CeO_2 NPs are still inadequate, and especially the systems that represent real environmental conditions need to be carried out.

In this study, the effects of CeO_2 NPs on *E. coli* and *B. subtilis* were evaluated in terms of bacterial inhibition and cell membrane deformation. The real environmental conditions were partly fulfilled and in order to simulate them, CeO_2 NPs were prepared in synthetic water solutions (SWSs) with different water contents (low, median and high ionic strength and conductivity, pH 5.5 and 6.5). Bacteria were treated in CeO_2 NP solutions under dark and illuminated conditions. Different NP concentrations (0, 1, 10, 50 and 100 mg/L) and morphological examination were used to determine the bacterial inhibition.

2. MATERIALS AND METHODS

2.1. Preparation of Bacterial Cultures

E. coli bacteria were kindly gifted by Biology Department of Akdeniz University. Frozen bacterial culture of 1 mL was inoculated in 100 mL LB Broth and incubated at 37ºC for 18 h (OD_{600}= 1.05). Lyophilized *B. subtilis* (ATCC6633) bacteria were purchased from American Type Culture Collection (ATCC, Wesel, Germany). A pellet of lyophilized bacteria was inoculated in 100 mL of LB Broth at 37ºC for 18 h (OD_{600}= 1.03). After the incubation period, the cultures were transferred into 2 mL eppendorf tubes and centrifuged at 10,000 rpm for 5 min. Supernatants were removed and the pellets were dissolved in 10% glycerol + 90% LB Broth media. The cultures were stored at -20ºC until upon use.

2.2. Nanoparticle Solutions and Characterization

The CeO_2 NPs used in the experiments were purchased (Alfa aesar, Karlsruhe, Germany). The NPs were in 15- 30 nm size range and have 32- 40 m^2/g of surface areas. A stock NP solution of 1000 mg/L was freshly prepared in SWSs with different ionic strength (10, 50 and 100 mM), pH (5.5 and 6.5) and conductivity (0.6, 3 and 6 mS/cm). The stock solution was then diluted to 10, 100 and 500 mg/L before the experiments. All test units were continuously shaken at 100 rpm.

In order to characterize the NPs, size distribution was calculated using dynamic light scattering (DLS) technique in Dynapro Nano star particle sizer (Wyatt Tech. Corp., CA, USA), particle size analysis was performed by scanning electron microscopy (SEM, Quanta FEG 250, FEI, Hillsborough, OR, USA), zeta potential was tested using NanoZS zetasizer (Malvern Panalytical Inc., Westborough, MA, ABD), and the structure of the NPs was detected by energy dispersive X-ray (EDX) spectroscopy (Apollo X AMATEK).

2.3. Bacterial Inhibition Analysis

Overnight grown bacteria of 1 mL was added into 49 mL of NP solutions and exposed to environmental conditions (different NP concentrations, pH, ionic strength, conductivity,

and dark and light) for 1 h at 150 rpm. The used light intensity was 2.1 mW/cm^2. At the end of test duration, serial dilutions were made and bacteria+NP solutions of 100 µL was inoculated into petri dishes. The petri dishes were incubated at 37°C for 24 h. The number of the colonies on petri dishes were counted using a colony counter and reported as CFU/mL. Inhibition tests were triplicated and values were calculated as percentages (%).

2.4. Morphological Examination

Environmental scanning electron microscopy (E-SEM) imaging analysis was performed with FEI Quanta250 FEG model E-SEM in Material Research Laboratory, Izmir Institute of Technology. In fixation procedure: 2 mL of samples were centrifuged at 6000 rpm for 10 min, were washed in phosphate buffer solution (PBS, pH 7.4). Washed sample was centrifuged again and pellet was stored in PBS+cold ethanol (1:1 v/v) at -4ºC for 12 h. In E-SEM imaging, 100 µL of sample was placed onto specimen stub and dried at 30ºC for 15 min. Sample was then analyzed at 5 kV high vacuum and 50000× magnification.

3. RESULTS AND DISCUSSION

3.1. Nanoparticle Characterization

The size of the CeO_2 NPs was measured by SEM-EDX and DLS, and the zeta potential was measured by zeta sizer. Figure 1a shows the SEM image of the CeO_2 NPs (100 mg/L in ultrapure water) with agglomerated particle shapes. The average particle size was calculated as 45±1.2 nm, which is almost 1.5 to 3 times larger than those of the retailer's info. EDX analysis was applied on three different areas (yellow areas, Figure 1a), and the purity of NP sample was shown in Figure 1b that the sample was only composed of CeO_2 particles (Ce: 40.3±8.7% and O: 55.9±10.6%).

The particle size results obtained from DLS method is given in Table 1. DLS method has been effectively used in particle size measurements and usually an optimum concentration of 50 mg/L has been chosen [28, 29]. A 50 mL of NP concentration prepared in 10 and 50 mM ionic strength, 0.6 and 3

mS/cm conductivity, and pH 5.5 and 6.5 were used. The measurements were obtained at time 24 h. Our results show that the aggregated particle size was strongly ionic strength and pH dependent. At lower ionic strength (10 mM) and pH (5.5) values, the particle size was 343±11 nm. However, when the ionic strength (50 mM) and pH (6.5) increased,

micrometer sized (1497±242 nm) particles were observed. Similar finding was also reported in Kosyan et al. [30] that the CeO_2 NP size in the test media was ranged between 192±62 nm and 1.5 µm. Leung et al. [31] showed that size of the particle was highly affected by the medium content.
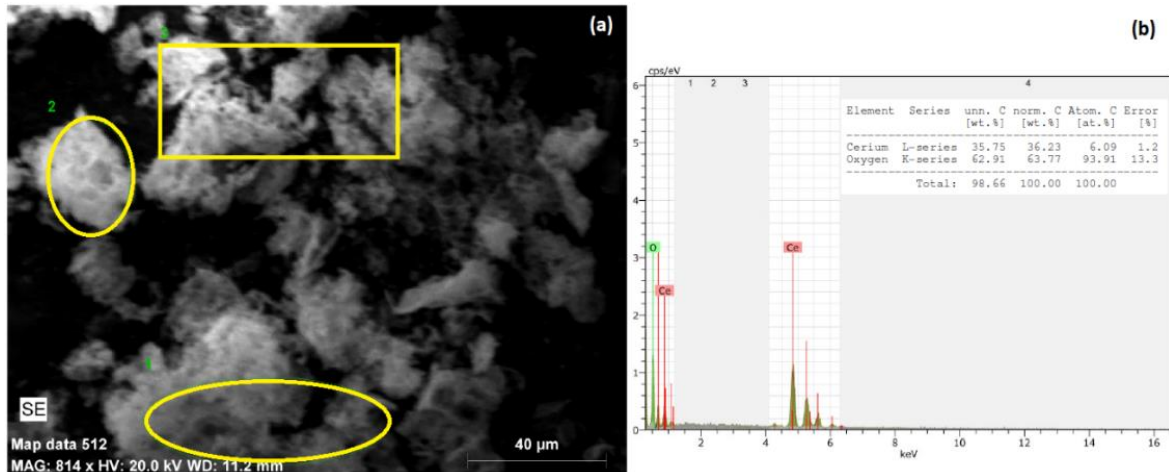
Figure 1. Scanning electron microscopy (SEM) (a) and energy dispersive X-ray (EDX) images (b) of CeO_2 nanoparticles.

Table 1. The effect of ionic strength (IS), conductivity (Cond.) and pH on CeO_2 nanoparticle size (Nanoparticle concentration: 50 mg/L)

Measurement Conditions	Particle Size (nm)
IS: 10 mM, Cond.: 0.6 mS/cm, pH: 5.5	343 ± 11
IS: 50 mM, Cond.: 3 mS/cm, pH: 5.5	1259 ± 224
IS: 10 mM, Cond.: 0.6 mS/cm, pH: 6.5	463 ± 54
IS: 50 mM, Cond.: 3 mS/cm, pH: 6.5	1497 ± 242

The zeta potential values of CeO_2 NPs used in this study were measured as 8.9 mV and 2.1 mV at pH 5.5 and 6.5, respectively. The pH, ionic strength, natural organic matter and etc. of the aquatic environment can highly effect the surface charge of nano-CeO_2 particles. Especially the surface charge of CeO_2 NPs can be negative or positive due to the pH of the solution [3, 4]. In our study, CeO_2 NPs were positively charged. According to studies, at low pH values CeO_2 NPs were positively charged and at high pH values they were negatively charged, and their isoelectric point is pH 8 [32, 33]. Buettner et al. [34] reported that CeO_2 NPs' isoelectric point is between pH 6.5

and 8.1, Berg et al. [35] noted that value as pH 6.71.
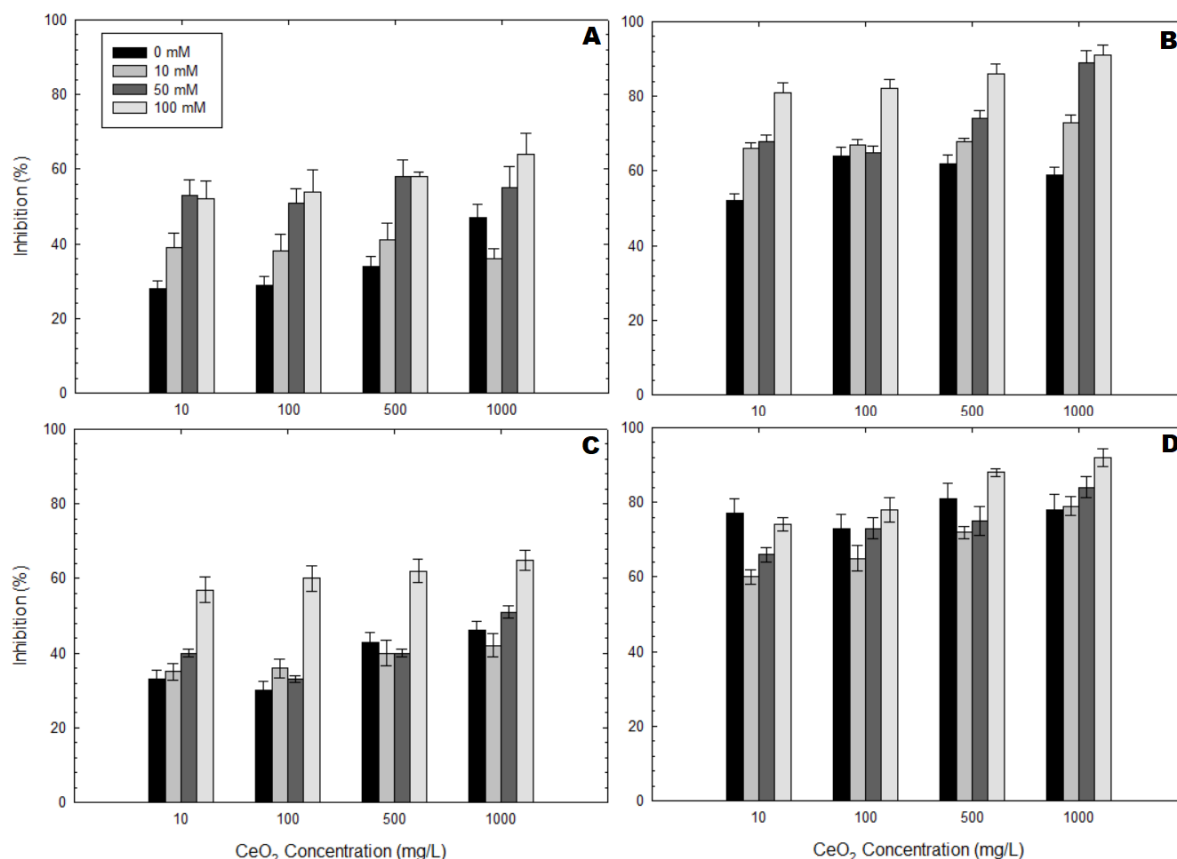
3.2. Bacterial Inhibition

The antibacterial effects of CeO_2 NPs on *B. subtilis* is depicted in Figure 1. High ionic strength and conductivity showed high negative effect on *B. subtilis*. Especially at 1000 mg/L NP concentration, 100 mM ionic strength, and 6 mS/cm conductivity under dark condition, maximum inhibition results were calculated as 64% and 68% at pH 5.5 and 6.5, respectively (Fig 2A and 2C). When 2.1 mW/cm² of light intensity was applied, the highest inhibitions were resulted from highest NP concentration and ionic strength conditions. The most antibacterial results were calculated as 92% and 95% at pH 5.5 and 6.5 in presence of light, respectively (Fig 2B and 2D).

Al-Shawafi et al. [36] studied the antimicrobial activity of CeO_2 NPs synthesized with different molar ratios of $Ce(NO_3)_3.6H_2O$ and $C_6H_{12}N_4$ (1:20, 5:20, 7:20, 12:20 and 20:20) on *E. coli* and *B. subtilis* (bacteria), and *Saccharomyces cerevisiae* (yeast). CeO_2 NPs with 12:20 ratio showed an inhibitory effect of 67% on *B. subtilis*, where NPs with 5:20 ratio displayed >70% inhibition on *E. coli*. The least antimicrobial result was obtained from NPs with 20:20 ratio on *S. cerevisiae* (45%). Krishnamoorthy et al. [36] showed that the antibacterial effect of CeO_2 NPs on *B. subtilis, E.*

coli, Salmonella typhimurium and *Enterococcus faecalis* can be attributed to membrane stress.

In this study, the optimization of the variables that could affect the extraction efficiency was carried out by monitoring the recovery. Recovery for each variable was calculated according to the following formula.

$$Recovery, \%R = \frac{c_{int}.V_{int} - c_{final}.V_{final}}{c_{int}.V_{int}} \, 100$$

Figure 2. The inhibition effect of CeO_2 NPs on *B. subtilis* bacteria (A: Dark, pH 5.5; B: Light, pH 5.5; C: Dark, pH 6.5; D: Light, pH 6.5).
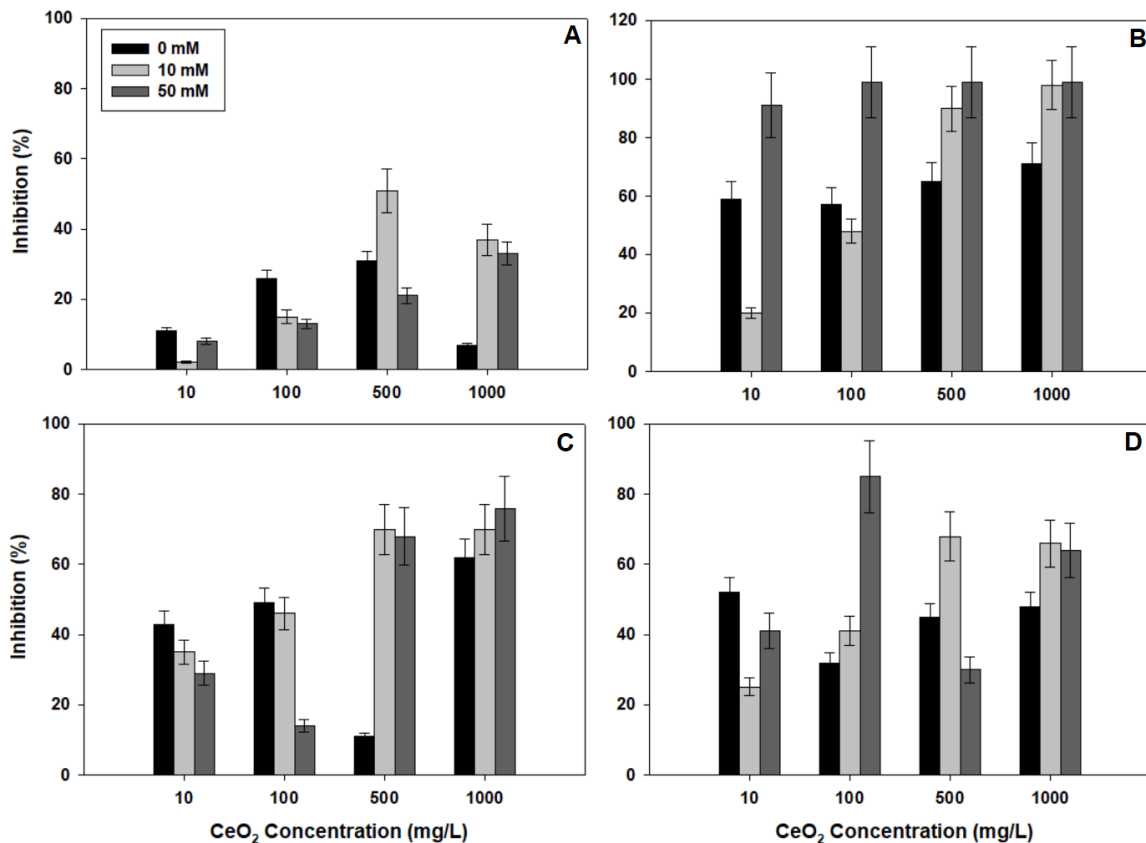
In Figure 3, the antibacterial effects of CeO_2 NPs on *E. coli* are given. The results from dark and light conditions clearly showed that illumination has a negative impact on bacteria. It is a well-known phenomenon that when CeO_2 NPs are illuminated with a light source (especially UV light), reactive oxygen species (ROS) can be formed. ROS then may disrupt cell membrane and cause stress on bacteria [38]. The most antibacterial result in absence of light was calculated as 52% when test conditions of 10 mM ionic strength, 500 mg/L NP

concentration, pH 5.5 were applied. (Fig 3A). However, when light was used, the inhibition increased to 98-99% at test conditions of 50 mM ionic strength and 100–1000 mg/L NP concentration (Fig 3B). At pH 6.5, higher antibacterial effect was observed under dark that the inhibition of bacteria increased to 78% (50 mM, 1000 mg/L) (Fig 3C). On the other hand, lower inhibition values were calculated from illuminated samples that highest result was 84% (50 mM, 100 mg/L) (Fig 3D).

Agarwal et al. [39] showed a 94% inhibition in the growth of *E. coli* after 9 h of visible light exposure. Thill et al. [22] reported the antibacterial effect of CeO$_2$ NPs (size: 7 nm) dispersed in water on *E. coli* and showed an electrostatic affinity between positively charged NPs and the negatively-charged outer membrane of bacteria. They conclude that cytotoxic effect of CeO$_2$ NPs on *E. coli* was due to the close contact of NPs and bacteria, and oxidative response. Thill et al [22] and He et al. [40] have also suggested that changing the exposure media may reverse the cytotoxic effect of CeO$_2$ NPs on *E. coli*, since surface charge density is largely responsible for antibacterial effect.

Figure 3. The inhibition effect of CeO$_2$ NPs on *E. coli* bacteria (A: Dark, pH 5.5; B: Light, pH 5.5; C: Dark, pH 6.5; D: Light, pH 6.5).

In Figure 4, E-SEM images of CeO$_2$ NPs and *B. subtilis*+CeO$_2$ NPs are given. Both samples were treated in 100 mg/L of NP concentration, pH 5.5, 50 mM of ionic strength, and 3 mS/cm of conductivity at 23±1.2ºC under light (light intensity: 2.1 mW/cm^2). The E-SEM image of CeO$_2$ NPs clearly shows that high NP concentration and high ionic strength lead to an aggregation/agglomeration of NPs. The NP size distribution was varied between 35 nm and 3.5 µm (Fig 4A). The bacteria + CeO$_2$ NP image was analyzed, a direct contact, more specifically an adsorption of CeO$_2$ NPs onto bacteria, was observed. The deformed bacteria were hidden under CeO$_2$ NPs and their different sizes were shown with red crosses in Figure 4B. The aggregated bacteria + NP size was varied between 65 nm and 6 µm. Similar results were also reported in the literature that CeO$_2$ NPs had a direct contact with bacterial cell wall [22, 25, 27]. This direct contact mostly resulted in membrane deformation [26] and cell disintegration [27].
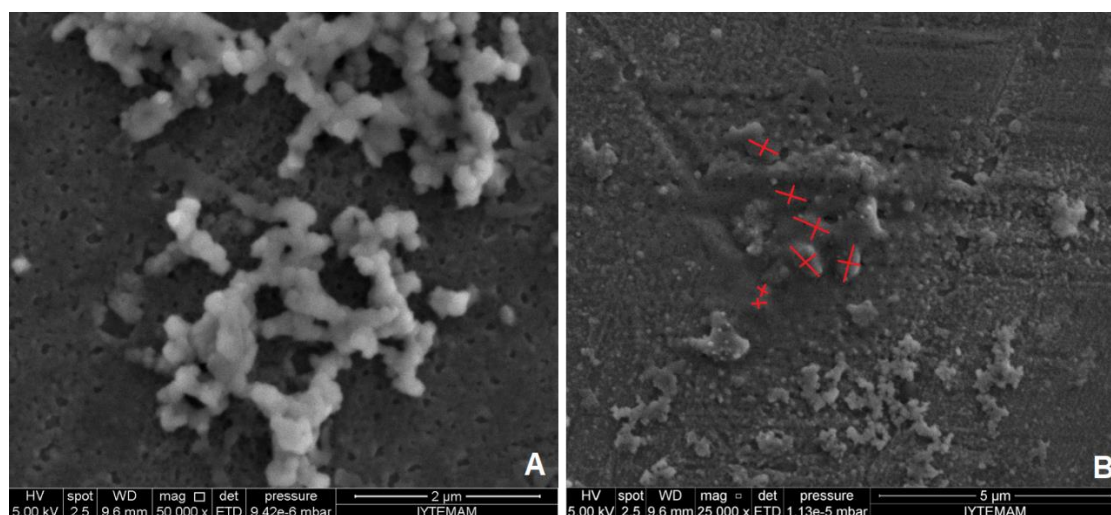
Figure 4. E-SEM images of CeO$_2$ NPs (A) and *B. subtilis*+ CeO$_2$ NPs (B) (Condition: NP concentration: 100 mg/L, pH: 5.5, ionic strength: 50 mM, conductivity: 3 mS/cm, temperature:23±1,2°C and light intensity: *2.1 mW/cm^2*)

4.   CONCLUSION

The present study examined the potential ecotoxicity of CeO$_2$ NPs on *B. subtilis* and *E. coli* bacteria. Regardless of the test conditions, CeO$_2$ NPs exhibited growth inhibition on both two bacteria. Higher growth inhibitions of bacteria in absence of light were observed compared to the those from literature. This may be attributed to cellular adsorption due to different ionic strength and high NP concentrations. In presence of light, similar results were obtained in this study that high bacterial inhibitions were resulted from high ionic strength and high NP concentration test conditions. The effects of pH varied on bacterial inhibition. It was shown that *B. subtilis* was more susceptible at pH 5.5 and *E. coli* was more sensitive at pH 6.5. The coverage of CeO$_2$ NPs on bacteria was clearly seen from E-SEM images, and it is suspected that cell damage was mainly caused by the membrane deformation.

As a conclusion of this study, the results suggest that bacteria-NP interaction is the most important factor in explaining the ecotoxic effect of CeO$_2$ NPs on *B. subtilis* and *E. coli*. However, it is still not clear whether this inhibition effect of CeO$_2$ NPs can be directly attributed to cellular adsorption. Therefore, further investigations need to be conducted to understand the interaction of NPs with bacteria, the main mechanism of growth inhibition of bacteria, and the fate of NPs in the receiving environments.

In general, CeO$_2$ NPs have been used in several sectors due to their excellent properties. Based on the results from the literature, many studies have focused on the synthesis of CeO$_2$ NPs and few of them have defined the factors leading the ecotoxic effects. The synthesis technique of the CeO$_2$ NPs should be highly efficient, economic, and practical without creating any ecotoxic effects. In overall, more researches need to be focused on environmental- friendly synthesis approaches and a life cycle assessment should be applied on all newly synthesized NPs.

ACKNOWLEDGMENTS

REFERENCES

[1] Piccinno, F., Gottschalk, F., Seeger, S., Nowack, B., Industrial production quantities and uses of ten engineered nanomaterials in Europe and the world. J Nanopart. Res., 14 (2012) 1-11.

[2] Sun, C., Li, H., Chen, L., Nanostructured ceria-based materials: synthesis, properties, and applications. Energy Environ. Sci. 5 (2012)

8475-8505.

[3] Collin, B., Auffan, M., Johnson, A.C., Kaur, I., Keller, A.A., Lazareva, A., Lead, J.R., Ma, X., Merrifield, R.C., Svendsen, C., White, J.C., Unrine, J.M., Environmental release, fate and ecotoxicological effects of manufactured ceria nanomaterials. Environ. Sci.: Nano, 1-6 (2014) 533-548.

[4] EU, Commission Staff Working Paper: Types and Uses of Nanomaterials, Including Safety Aspects, Adres: https://ec.europa.eu/health//sites/health/files/nanotechnology/docs/swd_2012_288_en.pdf, Brussels, 2012.

[5] Future Markets Inc, The Global Market for Nanomaterials 2002-2016: Production volumes, revenues and end user markets. http://www.futuremarketsinc.com/, 2012.

[6] Statista, The Statistics Portal, Cerium oxide price worldwide from 2009 to 2025 (in U.S. dollars per metric ton). Adres: https://www.statista.com/statistics/450146/global-reo-cerium-oxide-price-forecast/, 2019.

[7] Bleiwas, D.I., Potential for recovery of cerium contained in automotive catalytic converters, in Open-File Report 2013-1037. U.S. Geological Survey. Adres: https://pubs.usgs.gov/of/2013/1037/OFR2013-1037.pdf, 2013.

[8] Hendren, C.O., Mesnard, X., Droge, J., Wiesner, M.R., Estimating production data for five engineered nanomaterials as a basis for exposure assessment. Environ. Sci. Technol., 45 (2011) 2562-2569.

[9] Jasinski, P., Suzuki, T., Anderson, H.U., Nanocrystalline undoped ceria oxygen sensor. Sensors and Actuators B: Chemical, 95 (2003) 73-77.

[10] Armini, S., De Messemaeker, J., Whelan, C., Moinpour, M., Maex, K., Composite polymer core-ceria shell abrasive particles during oxide cmp: A defectivity study. J Electrochem. Society, 155 (2008) H653-H660.

[11] Auffan, M., Masion, A., Labille, J., Diot, M.A., Liu, W., Olivi, L., Proux, O., Ziarelli, F., Chaurand, P., Geantet, C., Bottero, J.Y., Rose, J., Long-term aging of a CeO$_2$ based nanocomposite used for wood protection.

Environ. Pollut. 188 (2014) 1-7.

[12] Mandoli, C., Pagliari, F., Pagliari, S., Forte, G., Di Nardo, P., Licoccia, S., Traversa, E., Stem cell aligned growth induced by CeO$_2$ nanoparticles in PLGA scaffolds with improved bioactivity for regenerative medicine. Adv. Functional Mat., 20 (2010) 1617-1624.

[13] Colon, J., Herrera, L., Smith, J., Patil, S., Komanski, C., Kupelian, P., Seal, S., Jenkins, D.W., Baker, C.H., Protection from radiation-induced pneumonitis using cerium oxide nanoparticles. Nanomed.: Nanotechnol., Biol. Med., 5 (2009) 225-231.

[14] Dai, Q., Wang, J., Yu, J., Chen, J., Chen, J., Catalytic ozonation for the degradation of acetylsalicylic acid in aqueous solution by magnetic CeO$_2$ nanometer catalyst particles. Chem. Appl. Cat. B: Environ., 144 (2014) 686-693.

[15] Gottschalk, F., Sun, T.Y., Nowack, B., Environmental concentrations of engineered nanomaterials: Review of modeling and analytical studies. Environ. Pollut., 181 (2013) 287-300.

[16] Lazareva, A., Keller, A.A., Estimating potential life cycle releases of engineered nanomaterials from wastewater treatment plants. ACS Sustainable Chem. Eng., 2 (2014) 1656-1665.

[17] Mueller, N.C. and Nowack, B., Exposure modeling of engineered nanoparticles in the environment. Environ. Sci. Technol., 42 (2008) 4447-4453.

[18] Gottschalk, F. and Nowack, B., The release of engineered nanomaterials to the environment. J. Environ. Monit., 13 (2011) 1145-1155.

[19] Quik, J.T.K., Lynch, I., Van Hoecke, K., Miermans, C.J.H., De Schamphelaere, K.A.C., Janssen, C.R., Dawson, K.A., Stuart, M.A.C., Van de Meent, D., Effect of natural organic matter on cerium dioxide nanoparticles settling in model fresh water. Chemosphere, 81 (2010) 711-715.

[20] Zhang, P., He, X., Ma, Y., Lu, K., Zhao, Y., Zhang, Z., Distribution and bioavailability of ceria nanoparticles in an aquatic ecosystem model. Chemosphere, 89:5 (2012) 530-535.

[21] Jabiol, J., McKie, B.G., Bruder, A., Bernadet, C., Gessner, M.O., Chauvet, E., Trophic

complexity enhances ecosystem functioning in an aquatic detritus-based model system. J. Anim. Ecol., 82 (2013) 1042-1051.

[22] Thill, A., Zeyons, O., Spalla, O., Chauvat, F., Rose, J., Auffan, M., Flank, A.M. , Cytotoxicity of CeO₂ nanoparticles for *Escherichia coli*: Physico-chemical insight of the cytotoxicity mechanism. Environ. Sci. Technol., 40 (2006) 6151-6156.

[23] Pelletier, D.A., Suresh, A.K., Holton, G.A., McKeown, C.K., Wang, W., Gu, B.H., Mortensen, N.P., Allison, D.P., Joy, D.C., Allison, M.R., Brown, S.D., Phelps, T.J., Doktycz, M.J., Effects of engineered cerium oxide nanoparticles on bacterial growth and viability. Appl. Environ. Microbiol., 76 (2010) 7981-7989.

[24] Dar, M.A., Gul, R., Alfadda, A.A., Karim, M.R., Kim, D.W., Cheung, C.L., Almajid, A.A., Alharthi, N.H., Pulakat, L., Size-dependent effect of nanoceria on their antibacterial activity towards *Escherichia coli*. Sci. Adv. Mat., 9:7 (2017), 1248-1253.

[25] Zeyons, O., Thill, A., Chauvat, F., Menguy, N., Cassier-Chauvat, C., Orear, C., Daraspe, J., Auffan, M., Rose, J., Spalla, O., Direct and indirect CeO₂ nanoparticles toxicity for *Escherichia coli* and *Synechocystis*. Nanotoxicology, 3 (2009) 284-295.

[26] Fang, X.H., Yu, R., Li, B.Q., Somasundaran, P., Chandran, K., Stresses exerted by ZnO, CeO₂ and anatase TiO₂ nanoparticles on the Nitrosomonas europaea. J. Colloid Interface Sci., 348 (2010) 329-334.

[27] Rodea-Palomares, I., Boltes, K., Fernández-Piñas, F., Leganés, F., García-Calvo, E., Santiago, J., Rosal, R., Physicochemical characterization and ecotoxicological assessment of CeO₂ nanoparticles using two aquatic microorganisms. Toxicol. Sci., 119 (2011) 135-145.

[28] Kato, M., Suzuki, M, Fujita, K, Horie, M, Endoh, S, Yoshida, Y, Iwahashi, H, Takahashi, K, Nakamura, A, Kinugasa, S,, Reliable size determination of nanoparticles using dynamic light scattering method for in vitro toxicology assessment. Toxicol. In Vitro, 23 (2009) 927-934.

[29] Kato, H., Fujita, K, Horie, M, Suzuki, M, Nakamura, A, Endoh, S, Yoshida, Y, Iwahashi, H, Takahashi, K, Kinugasa, S., Dispersion characteristics of various metal oxide secondary nanoparticles in culture medium for in vitro toxicology assessment. Toxicol. In Vitro, 24 (2010) 1009-1018.

[30] Kosyan D.B., Y.E.V., Vasilchenko A.S., Vasilchenko A.V., Miroshnikov S.A., Toxicity of SiO₂, TiO₂ and CeO₂ nanoparticles evaluated using the bioluminescence assay. Int. J. Geomate, 13-40 (2017), 66-73.

[31] Leung, Y.H., Yung, M.M.N., Ng, A.M.C., Mab, A.P.Y., Wong, S.W.Y., Chan, C.M.N., Ng, Y.H., Djurisic, A.B., Guo, M., Wong, M.T., Leung, F.C.C., Chan, W.K., Leung, K.M.Y., Lee, H.K., Toxicity of CeO₂ nanoparticles – The effect of nanoparticle properties. J. Photochem. Photobiol. B: Biology, 145 (2015) 48-59.

[32] Baalousha, M., Ju-Nam, Y., Cole, P.A., Gaiser, B., Fernandes, T.F., Hriljac, J.A., Jepson, M.A., Stone, V., Tyler, C.R., Lead, J.R., Characterization of cerium oxide nanoparticles-part 1: size measurements. Environ. Toxicol. Chem., 31-5 (2012), 983-993.

[33] Baalousha, M., Ju-Nam, Y., Cole, P.A., Hriljac, J.A., Jones, I.P., Tyler, C.R., Stone, V., Fernandes, T.F., Jepson, M.A., Lead, J.R., Characterization of cerium oxide nanoparticles. Part 2: Nonsize measurements. Environ. Toxicol. Chem., 31-5 (2012) 994-1003.

[34] Buettner, K.M., Rinciog, C.I., Mylon, S.E., Aggregation kinetics of cerium oxide nanoparticles in monovalent and divalent electrolytes. Colloid. Surface. A, 366 (2010) 74-79.

[35] Berg, J.M., Romoser, A., Banerjee, N., Zebda, R., Sayes, C.M., The relationship between pH and zeta potential of ∼ 30 nm metal oxide nanoparticle suspensions relevant to in vitro toxicological evaluations. Nanotoxicology, 3-4 (2009), 276-283.

[36] Al-Shawafi, W.M., Salah, N., Alshahrie, A., Ahmed, Y.M., Moselhy, S.S., Hammad, A.H., Hussain, M.A., Memic, A., Size controlled ultrafine CeO₂ nanoparticles produced by the microwave assisted route and their

antimicrobial activity. J Mater Sci: Mater Med, 28-177 (2017), 1-10.

[37] Krishnamoorthy, K., Veerapandian, M., Zhang, L.H., Yun, K., Kim, S.J., Surface chemistry of cerium oxide nanocubes: Toxicity against pathogenic bacteria and their mechanistic study. J Ind Eng Chem, 20-5 (2014), 3513-3517.

[38] Collin, B., Oostveen, E., Tsyusko, O.V., Unrine, J.M., Influence of natural organic matter and surface charge on the toxicity and bioaccumulation of functionalized ceria nanoparticles in *Caenorhabditis elegans*. Environ Sci Technol, 48-2 (2014), 1280.

[39] Agarwal, C., Aggrawal, S., Dutt, D., Mohanty, P., Cerium oxide immobilized paper matrices for bactericidal application. Materials Science and Engineering: B, 232-235 (2018) 1-7.

[40] He, X., Kuang, Y., Li, Y., Zhang, H., Ma, Y., Bai, W., Zhang, Z., Wu, Z., Zhao, Y., Chai, Z., Changing exposure media can reverse the cytotoxicity of ceria nanoparticles for *Escherichia coli*. Nanotoxicology, 6 (2012) 233-240.

AUTHOR GUIDELINES

Thank you for choosing to submit your paper to Cumhuriyet Science Journal. The following instructions will ensure we have everything required so your paper can move through pre-evaluating, peer review, production and publication smoothly. Please take the time to read and follow them as closely as possible, as doing so will ensure your paper matches the journal's requirements.

Submission

Cumhuriyet Science Journal is an international, peer-reviewed, free of charge journal covering the full scope of both natural and engineering sciences. Manuscripts should be submitted by one of the authors of the manuscript as online submission after registration to the Cumhuriyet Sciences Journal. Microsoft Word (.doc, .docx, .rtf), files can be submitted. There is no page limit. If there is a problem while uploading the files of manuscript, please try to reduce their file size, especially manuscripts including embedded figures. Submissions by anyone other than one of the authors will not be accepted. The submitting author takes responsibility for the paper during submission and peer review. If for some technical reason submission through the online submission systme is not possible, the author can contact csj@cumhuriyet.edu.tr for support.

Submission or processing charges

Cumhuriyet Science Journal does not charge any article submission, processing charges, and printing charge from the authors.

Terms of Submission

Papers must be submitted on the understanding that they have not been published elsewhere (except in the form of an abstract or as part of a published lecture, review, or thesis) and are not currently under consideration by another journal. The submitting author is responsible for ensuring that the article's publication has been approved by all the other coauthors. It is also the authors' responsibility to ensure that the articles emanating from a particular institution are submitted with the approval of the necessary institution. Only an acknowledgment from the editorial office officially establishes the date of receipt. Further correspondence and proofs will be sent to the author(s) before publication unless otherwise indicated. It is a condition of submission of a paper that the corresponding author permit editing of the paper for readability. All enquiries concerning the publication of accepted papers should be addressed to csj@cumhuriyet.edu.tr. Please note that Cumhuriyet Science Journal uses iThenticate software to screen papers for unoriginal material. By submitting your paper to Cumhuriyet Science Journal are agreeing to any necessary originality checks your paper may have to undergo during the peer review and production processes. Upon receiving a new manuscript, the Editorial office conducts initial pre-refereeing checks to ensure the article is legible, complete, correctly formatted, original, within the scope of the journal in question, in the style of a scientific article and written in clear English. Any article that has problems with any of the journal criteria may be rejected at this stage.

Peer Review

This journal operates a single blind review process. All contributions will be initially assessed by the editor for suitability for the journal. Papers deemed suitable are then typically sent to a minimum of two independent expert reviewer to assess the scientific quality of the paper. The author is required to upload the revised article to the system within 15 days by making the corrections suggested by the referee. The article will be rejected if there are no fixes in it. The Editor is responsible for the final decision regarding acceptance or rejection of articles. The Editor's decision is final

Title and Authorship Information

The following information should be included

Paper title

Full author names

Full institutional mailing addresses

Corresponding address

Email address

Abstract

The manuscript should contain an abstract. The researchers who are native speakers of Turkish have to add Turkish title and abstract as well. The abstract should be self-contained and citation-free and should be 250-300 words.

Keywords

Keywords of the scientific articles should be selected from the web address of www.bilimadresleri.com

Introduction

This section should be succinct, with no subheadings.

Materials and Methods

This part should contain sufficient detail so that all procedures can be repeated. It can be divided into subsections if required.

Conflicts of interest

Sample sentence if there is no conflict of interest: The authors stated that did not have conflict of interests.

Acknowledgements

Sample sentences for acknowledgements: The work was supported by grants from CUBAP (T-11111). We would like to acknowledge Prof. Mehmet Sözer, MD, for his precious technical and editorial assistance. We would like to thank

References

References to cited literature should be identified by number in the text in square brackets and grouped at the end of the paper in numerical order of appearance. Each reference must be cited in the text. Always give inclusive page numbers for references to journal articles and a page range or chapter number for books. References should be styled and punctuated according to the following examples

[1] Keskin B. and Ozkan A.S., Inverse Spectral Problems for Dirac Operator with Eigenvalue Dependent Boundary and Jump Conditions, Acta Math. Hungar., 130-4 (2011) 309– 320.

[2] National Cancer Institute, Surveillance Epidemiology and End Results. Cancer of the Corpus and Uterus, NOS. Available at: http://seer.cancer.gov/statfacts/html/corp.html?statfacts_page=corp. Retrieved March 2, 2008. (Sample reference of website)

[3] Isaacson K.B., Endometrial ablation. In: UpToDate, Basow, DS (Ed), UpToDate, Waltham, M.A., 2008. (Sample reference of Uptodate topics)

[4] Speroff L., Fritz M.A., Anovulation and The Polycystic Ovary. In. Speroff L., Fritz M.A., (Eds). Clinical Gynecologic Endocrinology and Infertility. 7th ed. Philadelphia, Pa: Lippincott Williams and Wilkins; 2005: chap 12. (Sample reference of online book chapters found in websites).

[5] Mazur M.T., Kurman R.J., Dysfunctional Uterine Bleeding. In: Mazur M.T., Kurman R.J., (Eds). Diagnosis of endometrial biopsies and curettings. A practical approach. 2nd ed. Berlin: Springer, 2005; pp 100-120. (Sample reference of printed book chapters)

Preparation of Figures

Each figure can be integrated in the paper body or separately uploaded and should be cited in a consecutive order. Figure widths can be 4-6 inch as 300 dpi. The labels of the figures should be clear and informative. The name and the subtitles of the figures must be 9-point font.

Preparation of Tables

Tables should be cited consecutively in the text. Every table must have a descriptive title and if numerical measurements are given, the units should be included in the column heading. Tables should be simple with simple borders and text written as left text. The name and the subtitle of the tables must be 9-point font

Proofs

Corrected proofs must be returned to the publisher within 2 weeks of receipt. The publisher will do everything possible to ensure prompt publication. It will therefore be appreciated if the manuscripts and figures conform from the outset to the style of the journal.

Copyright

Open Access authors retain the copyrights of their papers, and all open access articles are distributed under the terms of the Creative Commons Attribution license, which permits unrestricted use, distribution and reproduction in any medium, provided that the original work is properly cited.

The use of general descriptive names, trade names, trademarks, and so forth in this publication, even if not specifically identified, does not imply that these names are not protected by the relevant laws and regulations.

While the advice and information in this journal are believed to be true and accurate on the date of its going to press, neither the authors, the editors, nor the publisher can accept any legal responsibility for any errors or omissions that may be made. The publisher makes no warranty, express or implied, with respect to the material contained herein.

Ethical Guidelines

New methods and ethically relevant aspects must be described in detail, bearing in mind the following:

Human Experiments. All work must be conducted in accordance with the Declaration of Helsinki (1964). Papers describing experimental work on human subjects who carry a risk of harm must include:

A statement that the experiment was conducted with the understanding and the consent of the human subject.

A statement that the responsible Ethical Committee has approved the experiments.

Animal Experiments. Papers describing experiments on living animals should provide:

A full description of any anaesthetic and surgical procedure used.

Evidence that all possible steps were taken to avoid animal suffering at each stage of the experiment. Papers describing experiments on isolated tissues must indicate precisely how the donor tissues were obtained.

Submission Preparation Checklist

As part of the submission process, authors are required to check off their submission's compliance with all of the following items, and submissions may be rejected that do not adhere to these guidelines.

The submission has not been previously published, nor is it before another journal for consideration (or an explanation has been provided in Comments to the Editor).

The submission file is in Microsoft Word document file (Times New Roman) format.

Where available, URLs for the references have been provided.

The text is single-spaced; uses a 11-point font; employs italics, rather than underlining (except with URL addresses); and all illustrations, figures, and tables are placed within the text at the appropriate points, rather than at the end.

The text adheres to the stylistic and bibliographic requirements outlined in the Author Guidelines, which is found in About the Journal.

If submitting to a peer-reviewed section of the journal, the instructions in Ensuring a Double-Blind Review have been followed.